585

CRANFIELD INSTITUTE OF TECHNOLOGY

AERODYNAMICS DEPARTMENT

PhD THESIS

F. HEYDARI

On the Estimation of Stability and Control Characteristics of a Generalised Forward Swept Wing Aircraft

Supervisor: Mr M.V. Cook

May 1986

The research which is the subject of this thesis was sponsored by the Ministry of Defence (Procurement Executive) under the terms of Research Agreement no. 2028/0156 XR/AERO

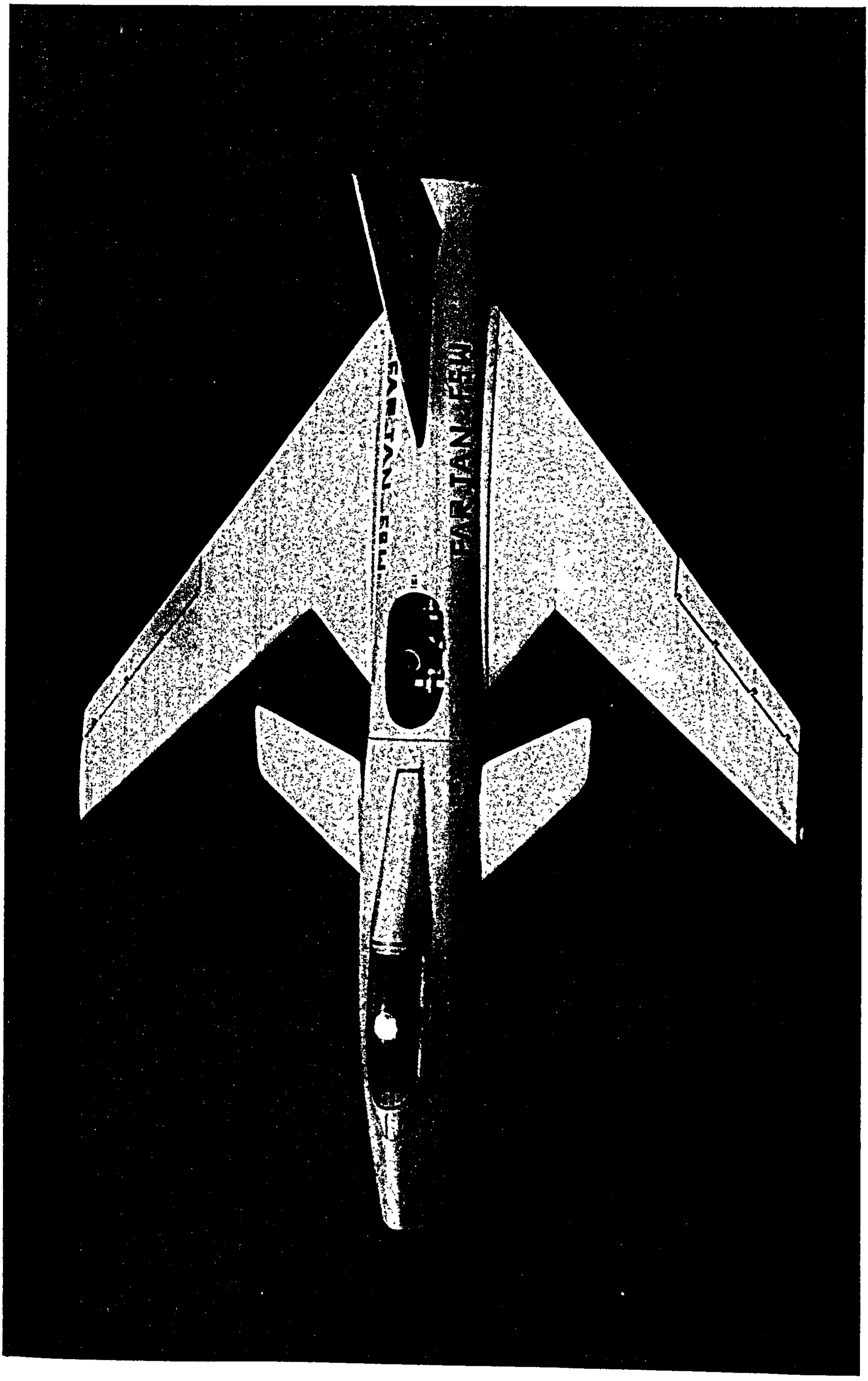

Plate-1 :- FARJAN F S W DYNAMIC MODEL

LIST OF CONTENTS

APPENDICES

FIGURES

LIST OF PLATES

PLATE

SYNOPSIS

Recent advances in composite structures and active control systems have made the concept of a forward swept wing aircraft a viable alternative to the more conventional configurations.

This thesis encompasses some of the work resulting from a three year research program covering the dynamic behaviour and characteristics of a FSW aircraft having a closely coupled canard. The dynamic model has been based on the output of a first order optimisation routine with emphasis on minimum induced drag and static margin as the two most important criteria. Stability characteristics of the dynamic model were extracted from the transient response tests in both longitudinal and lateral modes by means of a statistical method, namely Extended Kalman Filter (E.K.F.). In carrying out the dynamic tests, use was made of the facilies outlined by Ref. 8.

Validated through computer based experiments, the Extended Kalman Filter algorithm has successfully been applied to the open-loop wind tunnel tests. Simulations of the equations of motion using estimates of stability derivatives obtained in this way closely match the observed behaviour. Furthermore, substitution of aerodynamic data obtained via static wind tunnel measurements in theoretically derived expressions for some of the stability derivatives has resulted in an alternative set of stability derivative estimates.

Finally, estimates of the stability derivatives obtained with the E.K.F., first order optimisation program and static tests are compared. Although the results are limited to very low subsonic Mach numbers, nevertheless, they are very encouraging. It is hoped that future work might extend the studies into unstable flight regimes.

AKNOWLEDGEMENTS

The author wishes to express his gratitude to:

i. Mr. M.V. Cook for his invaluable advice and guidance in all matters during the course of this research programme.

ii. Dr. A.J. Ross for her support and encouragement.

iii. My wife Janet and my daughter Rokhsan for their unceasing support.

iv. Metal and wood work-shop personnel and other technicians.

v. MoD (P.E.)

LIST OF SYMBOLS

a.c.	Aerodynamic Centre
$a_{W.B.}$	Wing-Body Lift-Curve Slope
$A_{C.B.}$	Foreplane-Body Lift Curve Slope
AR	Aspect Ratio
a	Speed of Sound
b	Full Span
$\bar{c}$	Mean Aerodynamic Chord
C_D	Drag Coefficient
C_{D_o}	Zero-Lift Drag Coefficient
C_f	Friction Coefficient
C_L	Lift Coefficient
C_m	Pitching Moment Coefficient
C_l	Rolling Moment Coefficient
C_n	Yawing Moment Coefficient
C_T	Thrust Coefficient, Wing Tip Chord Length
C_R	Wing Root Chord Length
D	Drag
d	Maximum Fuselage Diameter
$\frac{dC_{L_w}}{d\alpha}$	Wing Lift-Curve Slope
$\frac{dC_{L_c}}{d\alpha}$	Foreplane Lift-Curve Slope
E, ϵ	Expected Value
$\underset{\sim}{f}$, $\underset{\sim}{g}$	Functions
$\underset{\sim}{G}(n)$	Error Covariance Matrix
h	Height
h_n	Position of Wing Aerodynamic Centre Relative to $\bar{c}$
I_{xx}, I_{yy}, I_{zz}	Principal Moments of Inertia

I.S.A.	International Standard Atmosphere
$\underset{\sim}{J}(n)$	Split Kalman Filter Gain Matrix
k_Θ, k_h	Proportional Control Gains
L	Lift
M	Mach Number, Pitching Moment
$\dot{m}$	Engine Mass Flow Rate
m	Mass
m_c	Foreplane Lift Curve Slope
m_w	Wing Lift Curve Slope
n	Load Factor, Number
p	Roll Rate
$\dot{p}$	Roll Angular Acceleration
q	Pitch Rate
$\dot{q}$	Pitch Angular Acceleration
r	Yaw Rate
$\dot{r}$	Yaw Angular Acceleration
s	Half Span
S_w	Wing Area
S_c	Foreplane Area
S_{WET}	Wetted Wing Area
S_M	Static Margin (Stick-Fixed)
T	Thrust, Tension, Period
t	Thickness
u	Velocity Perturbation in X-Direction
U	Speed
V	Measurement Noise, Speed, Volume
$\bar{V}$	Volume Coefficient
$\underline{V}$	Velocity Vector
v	Velocity Perturbation in Y-Direction
W	Weight, Process Noise
w	Velocity Perturbation in Z-Direction

$\bar{X}$, X_{CN}	X-Position of a.c. Relative to Datum
$\hat{x}$	Estimates of x
x,y,z	Axis
X_{IN}	Location of Intake Relative to Datum
X_{NP}	Position of the Neutral Point
Δ	Incremental Value
η	Foreplane Deflection Angle
ξ	Aileron Deflection Angle Positive with Starboard Aileron Up
ζ	Rudder Deflection Angle Positive to the Starboard
ζ_D	Damping Index
ω_n	Natural Frequency
ϵ_s	Blockage Coefficient
Θ	Pitch Angle
ψ	Yaw Angle
Φ	Roll Angle
ρ	Air Density
Re	Reynolds Number
α	Incidence
β	Sideslip Angle
Λ	Sweep Angle
Γ	Dihedral Angle
λ	Taper Ratio
σ,σ^*	Interference Factors
X_u, X_w, L_v, etc.	Stability Derivatives in Dimensional Form
x_v, z_w, m , etc.	Stability Derivatives in Concise Form
$\breve{X}_u$, $\breve{X}_w$, $\breve{N}_v$, etc.	Stability Derivatives in Aeronormalized Form

$\underline{X}$	State vector
$\underline{U}$	Input vector
$\underline{Y}$	Output vector
$\underline{W}$	Process noise vector
$\underline{V}$	Measurement noise vector
$\phi(m,m)$	State transition matrix
$\psi(m,q)$	Input matrix
$\theta(m,k)$	Process noise matrix
$C(n,m)$	Output matrix
$D(n,q)$	Direct input matrix

1. INTRODUCTION

1.1 Background

Although it has been recognised that wings with forward sweep may offer some aerodynamic advantages over more conventional wings, the full potential of this type of layout has not yet been totally utilised.

The first aircraft to make use of forward sweep was the German JU287 with a forward sweep angle of 15^{o} which flew in 1944. Work on this concept continued after the Second World War but due to the aero-elastic problems associated with forward-swept wings, namely wing tortional divergence, all activity was abandoned. From the design point of view the divergence speed of swept-back wings is not a matter of vital concern. On the contrary, divergence speeds of wings with forward sweep is low enough to cause this configuration option to be ruled out. This is because the additional structural mass required to assume sufficient stiffness to prevent divergence prevention more than offsets the aero-dynamic advantages of the wing with forward sweep. However true in the case of wings with conventional wing structure, it may not be so for wings constructed of composite materials. With the additional facility of aeroelastic tailoring, the flexural axis of the forward-swept wing can be aligned in such a way that the amount of wash-in caused by the aerodynamic loading is reduced as the latter increases .

New developments in composite structural technology have therefore revived the interest in forward-sweep wings. This renewed interest, though initially confined to mere analytical studies, has resulted in the implementation of such wings on experimental aircraft.

Some advantages of the forward-swept wing design are

(i) Higher L/D ratio at manoeuvring Mach numbers.
(ii) Lower trim drag.
(iii) Better lateral control at high angles of attack - lower stall and therefore slower landing.
(iv) Higher leading edge suction and therefore the extension of laminar boundary layer over a bigger section of the wing.
(v) Better volume distribution leading to less wave drag.

Furthermore, with the enormous developments in digital control and its application to active control technology, it is not only possible to augment the stability of an otherwise unstable aircraft but also to

make weight savings in its structure. This would undoubtedly lead to an unstable structure which could, through the application of active controls, behave in a stable manner. An example of this is the 'GRUMMAN' X-29 advance technology demonstrator which has an extremely high level of relaxed stability.

The aerodynamic advantages of a forward-swept wing can best be enhanced by the combination of the forward-swept wing with a closely coupled foreplane in a canard layout. So far, research into forward-swept wing aircraft has suggested that a forward-swept wing and canard layout is the only viable option which could offer some questionable advantages over the conventional combat aircraft layout.

1.2 Aims of the Research Program

Having established that a forward-swept wing and canard configuration offers a cleaner aircraft from the aerodynamic point of view, the dynamic characteristics and control of such a layout, as applied to combat aircraft, was chosen as the main research area. A purely theoretical approach to this problem has proved unsatisfactory mainly because of limited data availability. The first step towards a realistic analysis of the problem therefore, was to design an aerodynamically optimised fighter aircraft with forward-swept wings having a closely coupled foreplane. This in itself proved to be a challenging task since complete optimisation can only be possible if detailed wing and foreplane loading data are available. Despite the lack of such detailed data, use was made of available information which was then used in conjunction with computer programs to carry out the optimisation task. The main objective of the design optimisation process as applied to the present study was to minimise the induced drag resulting from the interaction of the F.S.W. and the foreplane at a particular Mach number.

A scaled dynamic model of this optimised layout was then developed having fully operational control surfaces. This generalised dynamic model of a forward-swept wing combat aircraft was then the subject of static and dynamic wind tunnel tests. The scale factor for the dynamic model was determined by the size of the test rig facilities accompanying the 42" diameter open jet "Weybridge" wind-tunnel. Details of the test rig are given in Ref. 8. This test rig allows the model to move in four degrees of freedom, namely, pitch, roll, yaw and heave.

A major part of the research program was taken up with the development of parameter identification algorithms for the purpose of the estimation of both longitudinal and lateral stability derivatives. Computer simulations of the aircraft were then used to verify the applicability of the techniques used prior to the implementation of the codes for the analysis of results of the dynamic wind-tunnel experiments. The latter consisted of short period longitudinal and lateral response tests which,with the aid of the parameter identification programs for analysis, provided some insight into the dynamic characteristics and behaviour of the model. The techniques on which the parameter identification could be based are varied in property and number. However, the extended Kalman filter (E.K.F.) technique was chosen here in particular because the estimates provided by the E.K.F. possess a maximum likelihood property which in effect makes it an optimal state estimator.

In order to gain insight into some of the more basic aerodynamic parameters,such as lift curve slopes,limited static wind tunnel tests, using the dynamic model, were carried out. Furthermore, aerodynamic data obtained from static tests carried out in the 8' x 6' wind tunnel were then used to estimate some of the stability derivatives for which theoretical expressions could also be derived. This enabled comparisons to be made between the estimates of stability derivatives obtained through,

(i) A purely theoretical approach based on aerodynamic data output of optimisation program.
(ii) Extended Kalman filtering as a means of estimation of stability derivatives.
(iii) Insertion of aerodynamic data from static tests into theoretical expressions.

Finally, an extension of the analysis to include the dynamic behaviour and characteristics of the model with relaxed stability brought the research programme to a close.

2. DESIGN OF THE F.S.W. AIRCRAFT

The primary reason for the design of a full size F.S.W. aircraft was to assess the theoretical behaviour of such aircraft and more importantly to construct a dynamically scaled version of it. The configuration was based on both computerized design and empirical data where appropriate. It must however be pointed out that all design stages were concerned with the aerodynamics rather than structure, engine placement, system design, etc. With this view in mind the following design levels were devised.

2.1 Conceptual Level

During this early stage connectivity, component placement, and approximate sizes were defined. Limited engineering calculations were performed at this stage to provide a three-view drawing and cross sections showing approximate placement and size of all the major F.S.W. aircraft components. Details of the first drawing together with initial dimensions are given in Fig. 2.1. It must be pointed out that the design at this stage was entirely based on crude approximations to the aircraft configuration, the major components of which were wing, canard, fuselage and fin. More attention was paid to the shape of components than the interaction between them, which was dealt with in the next stage of the design.

2.2 Preliminary Design Level

At this stage referred to as the preliminary design stage, emphasis was on the quantitative measures of performance in order to make comparisons. Empirical data and expressions were used since aerodynamic data such as detailed wing loading and canard-wing interactions were not available. However, with concepts that are novel or unusual, the existing engineering methods may not be applicable. Under these circumstances, significant theoretical study was required to validate the design which unfortunately was beyond the scope of the present study. Various stages of design at this level were as follows:-

(i) Define initial configuration.
(ii) Estimation of component masses.
(iii) Calculations of aerodynamic parameters.
(iv) First order optimisation of wing-foreplane geometry as regards the vertical gap between the two.
(v) Estimation of C.G. and N.P. positions and stick-fixed static margin.
(vi) Overall configuration optimisation.
(vii) Determination of principal moments of inertia.
(viii) Determination of the full size aircraft configuration.
(ix) Dynamic scaling for model.

(x) Estimation of longitudinal stability derivatives.

All these stages with the exception of 1, 3, 7 and 8 form various computational blocks of the first order optimisation computer program.

2.2.1 Initial Configuration Data.

This stage of the design level primarily served as an input to the whole of the scheme and it originates from the conceptual design. This input data includes basic dimensions, approximate positions of the aerodynamic centres of the F.S.W., canard and fin, mean aerodynamic chords, aspect ratios, etc., and in general geometric information extracted from the first drawing of the conceptual configuration. Therefore, this stage of the design could be classified as a data block since there are no computations involved with it.

2.2.2 Estimation of Component Masses.

The component masses were determined through the use of empirical formulae which are conditioned by the many different geometric properties of the components. These expressions take many forms, but in general, their estimates have a narrow scatter band. Here, use was made of Ref. 1 in order to maintain the compatibility between all the empirical information used throughout the present design level. Significant weight reduction could be achieved through the use of carbon fibre materials, in fact Ref. 1 suggests that in using carbon fibre structures the following reduction in component masses could be achieved.

(i) 25% reduction in each foreplane and fin + rudder masses.
(ii) 25% reduction in the front fuselage mass.
(iii) 30% reduction in the intake duct mass.

For a stable structure no significant mass reduction is achieved as a result of carbon fibre usage. Details of mass breakdown are given in Table B1 of Appendix B. From the point of view of program structure, this stage of the design level forms a computational block containing the empirical formulae for the estimation of component masses.

2.2.3 Calculations of Aerodynamic Parameters.

As already mentioned, one of the criteria chosen for optimisation is the minimisation of induced drag. In the absence of any other vortex shedding the induced drag represented in the computer program is entirely due to trailing edge vortices of the F.S.W. and foreplane. These surfaces cannot be treated in isolation from each other since there exists mutual interference between them which can be turned into an advantage. One of the ways in which such optimisation could be achieved is as follows:

(i) Computation of F.S.W. and canard lift distribution using extended lifting line or lifting surface theories.

(ii) Computation of induced flow fields caused by F.S.W. and canard and their effects on each other.

(iii) Computation of secondary and higher order interference between F.S.W. and canard and iteration until convergence occurs.

(iv) Repeat for different relative positions of canard with respect to wing as regards the vertical gap between the two.

(v) Compute the induced drag in each case.

(vi) Finally use a hill climbing optimisation technique to find the optimal vertical gap.

Clearly, this would involve a great deal of complex computational work which would have been beyond the scope of this thesis. Nevertheless, a first order optimisation technique was adopted here which only treats the influences of foreplane on the F.S.W. and is described in section 2.2.4.

In the absence of detailed wing and foreplane loading, important aerodynamic parameters such as wing-body and canard-body lift curve slopes, zero lift drag C_{D_o}, etc., were estimated. Details of these calculations are presented in Appendices B and G. However, these calculations are confined to Mach number range $M < 0.6$, since the study was limited to low subsonic Mach numbers.

In considering the wing-body and canard-body geometries it can be said that

$$C_{L_{\text{wing-body}}} = a_{\text{wing-body}} \cdot \alpha$$

$$C_{L_{\text{foreplane-body}}} = a_{\text{foreplane-body}} \cdot (\alpha + \eta)$$

where 'a' represents the lift curve slope

However, the geometry of the wing-body mounting has to be taken into account. For the present design, the chord lines of the wing aerofoils were chosen to be parallel to the body x-axis. Hence, the zero-lift line of the F.S.W. makes, according to characteristics of NACA 65-206 aerofoil, an angle of $\alpha_o = 1.8°$ with the body x-axis. Therefore, the lift coefficient of wing-body combination could be presented as;

$$C_{L_{W.B.}} = a_{W.B.} \cdot \alpha_{\text{Effective}}$$

or $$C_{L_{W.B.}} = a_{W.B.} (\alpha + \alpha_o)$$

with no changes in the foreplane lift coefficient presentation since the aerofoils used have symmetrical section.

2.2.4 First Order Optimisation of Wing-Foreplane Geometry

The optimisation criterion chosen was the optimum vertical gap between the F.S.W. and the foreplane which would lead to a minimisation of induced drag in trimmed flight at a Mach number of M = 0.3. From Ref. 3, the induced drag of a wing-foreplane combination is given by:

$$D_{induced} = \frac{L_{W.B.}^2}{q\pi b_W^2} + \frac{2L_{C.B.}L_{W.B.}\sigma}{q\pi b_c b_w} + \frac{L_{C.B.}^2\sigma^*}{q\pi b_c^2} \qquad \text{EQ.2.1}$$

where $q = \frac{1}{2}\rho U_\infty^2$

σ = Prandtl's interference factor

σ^* = Non-elliptic interference factor.

Fig. 2.2 represents the variation of σ and σ^* with the non-dimensional vertical gap $\bar{b} = \frac{2h}{b_c}$. Equation 2.1 can be presented in coefficient form as:

$$C_{D_{induced}} = \frac{a_{W.B.}^2(\alpha + \alpha_o)^2}{\pi AR_w} + \frac{2a_{W.B.}a_{C.B.}}{\pi AR_c} \cdot \frac{b_c}{b_w} .(\alpha + \alpha_o)(\alpha + \eta).\sigma$$

$$+ \frac{a_{C.B.}^2}{\pi AR_c} \cdot \frac{S_c}{S_w} .(\alpha + \eta)^2.\sigma^* \qquad \text{EQ.2.2}$$

By keeping $a_{W.B.}$, $a_{C.B.}$, b_c, b_w, S_c and S_w constant, the induced drag would depend upon α_{trim}, η_{trim}, σ and σ^*. It can be shown (see Appendix E) that by combining equation 2.2 and equilibrium force and moment considerations that, for a trimmed flight,

$$f(\alpha)_{trim} = \frac{A_5}{A_1} - \frac{\tan(\alpha)}{A_1}\{C_{D_o} + A_2\alpha^2 + A_3\alpha + A_4\} - 1 = 0 \qquad \text{EQ.2.3}$$

Expressions giving the values of constants A_1 to A_5 are given in Table E4 of Appendix E. The following steps were then taken to minimise the induced drag at M = 0.3.

(i) The vertical gap was set to zero and the values of σ and σ^* were determined from Fig. 2.2.

(ii) For these values of σ and σ^* the trim incidence angle α_{trim} was calculated through an iterative solution of equation 2.3.

(iii) The foreplane trim angle η_{trim} was then calculated by back substitution.

(iv) $C_{L_{W.B.}}$ and $C_{L_{C.B.}}$ and consequently $C_{D_{induced}}$, were calculated.

(v) The vertical gap was increased by a small increment Δh, and steps (ii) to (iv) repeated.

Variation of $C_{D_{induced}}$ with the non-dimensional vertical gap is presented in Fig. 2.3. Clearly, the minimum induced drag occurs for $\bar{h} = 0.1$ This value of the vertical gap was then implemented in the geometry of the aircraft. However, the induced drag cannot be determined accurately for the wing and foreplane in isolation from the fuselage since the latter induces a flow-field which could influence those of wing and foreplane. Details of calculations and derivations of equations are presented in Appendix E.

2.2.5 Estimation of C.G. and N.P. Positions and Static Margin Stick-Fixed.

Once the estimates of component masses have become available, the position of C.G. is determined by taking moments of these masses about an axis which was chosen to be the plane of the nozzle. Next the method of Appendix C was used to determine the approximate position of the neutral point and thereby the static margin. The determination of C.G. and N.P. positions were subject to the assumptions that aerodynamic data from section 2.2.2 and 2.2.3 were reasonably accurate, which cannot be fully justified. The static margin constituted the second optimisation criteria in that a design static margin of $2\%\bar{c}$ to $6\%\bar{c}$ was desirable. Therefore, it would have been necessary to relocate components in order to satisfy this criteria.

2.2.6 Overall Optimisation.

In section 2.2.4, the only geometrical parameter assumed to affect the induced drag was taken to be the vertical gap h. However, this is not entirely true since the horizontal distance between the F.S.W. and canard also affects the induced flow field, although not to the same extent. Therefore, neglecting the latter influence, the F.S.W. was chosen as the component the movement of which could result in the design static margin range. The reason behind this decision was that not only the F.S.W. constitutes a large proportion of total A.U.W. of the aircraft but also develops almost all the lift force. The overall optimisation was then achieved by fixing the value of

the vertical gap h and shifting the F.S.W. by small increments either forward or aft of the pre-assumed position provided by the conceptual design level. Details of these computations are given in Appendix B, where table B5 represents the effect of wing movement on the C.G., N.P. and thereby static margin. With the vertical gap and C.G. position fixed, the principal moments of inertia were estimated.

2.2.7 Determination of Principal Moments of Inertia.

Moment of inertia calculations could not form an integral part of the design level because the majority of aircraft components could not be assumed as being lumped masses and this would necessitate the application of parallel and perpendicular axis theorems for the determination of moments of inertia of the respective components. Details of such calculations are presented in Section H1 and Table H-2 of Appendix H. It was also assumed that the aerodynamic axes are approximately coincident with the principal axes and that is to say that the ratios of moments of inertia I_{zx}/I_{xx} and I_{zx}/I_{zz} were taken to be zero.

2.2.8 Formation of the Full Size Aircraft Configuration.

So far the results of the previous computational design stages have been limited to numbers rather than shapes. The idea here was to transform the information obtained thus far into an aircraft configuration. In order to achieve this, a three view drawing of the desired configuration with the enhancement of desired characteristics was formed. By merging the information of the three aircraft projections, a three-dimensional view of the entire aircraft was realised. This task should not be underestimated since many of the surfaces formed in this way contained double curvature. Details of this manual process are presented in Appendix D.

2.2.9 Dynamic Scaling.

It is evident from the previous design stages that no attention has been paid to the structure of the full size aircraft. This has been to no great loss since , as far as the present study is concerned, any treatment of the full size aircraft structure would not serve any purpose. However, in order to simulate the dynamic behaviour of the full size aircraft there was a need to develop a dynamic model of the full scale aircraft.

Dynamic scaling in itself is a complex subject, and detailed theoretical treatment of it is beyond the scope of this thesis. However, its application to the present design is briefly explained below. In order to scale the full size aircraft dynamically the following rules had to be observed.

2.2.9.1 Dynamic Similarity.

Two systems are said to be dynamically similar if corresponding points

of the systems are such that their position vectors referred to sets of fixed axes in the respective systems satisfy the equation

$$R_{\text{system 1}} = \lambda R_{\text{system 2}}$$

where λ is the constant linear scale factor.
If it is further assumed that the body forces measured at corresponding points and the initial velocity vectors at those points are related by

$$f_{\text{system 1}} = \mu f_{\text{system 2}}$$

and,

$$v_{\text{system 1}} = \nu v_{\text{system 2}}$$

Respectively then, for the systems to describe geometrically similar paths the 'Froude' number given by

$$F = \frac{v^2}{Lf} \quad \text{or} \quad \frac{v}{\sqrt{Lf}} \quad \text{where L is a typical length}$$

must be the same for both systems. Also, since the action and reaction are equal and opposite according to Newton, it follows that the accelerations induced by the mutual action of the two systems will remain in a fixed ratio. Hence it is, in general, necessary for similarity of behaviour that corresponding masses of the two systems shall be in a fixed ratio. 'Froude' number can be represented as

$$F = \frac{mv^2}{LP}$$

where $f = \frac{P}{m}$

P = force

m = mass of the system.

Taking P to be the weight of the system, then

$$f = \frac{P}{m} = g \quad \text{the acceleration due to gravity.}$$

Therefore, equality of F for both systems results in the correct ratio of the gravitational force. If the gravity field is the same for the A/C and model, then

$$\frac{V_{model}}{V_{A/C}} = \sqrt{\frac{L_{model}}{L_{A/C}}} = \sqrt{\lambda}$$

where L is taken to be the length of model or A/C. It must be noted that equality of 'Froude' number for the systems is a sufficient condition for similarity of behaviour but not a necessary condition for similarity of motion.

2.2.9.2 Similarity of Periodic Oscillations.

This effect is governed by the 'Strouhal' number.

$$\text{i.e. } St = \frac{\omega L}{V}$$

where ω = angular frequency
L = length
v = speed

Equality of 'Strouhal' number ensures that the angles of attack are equal.

2.2.9.3 Similarity of Flow.

Since the model is flown at a Mach number M < 0.1, compressibility effects are neglected and therefore, similarity of steady, uniform and incompressible but viscous flows is considered. This effect is governed by 'Reynolds' number given by

$$Re = \frac{\rho V L}{\mu}$$

which must be equal for both systems for similar flow fields. Again if gravitational fields are the same for both systems, then;

$$\frac{Re_{model}}{Re_{A/C}} = \frac{\nu_{A/C}}{\nu_{model}} \cdot \lambda^{3/2} = \lambda^{3/2} \text{ under I.S.A.}$$

However, having decided the overall length of the model which is equivalent to 1/14 scale, the length parameter in 'Reynolds' number was fixed together with the maximum tunnel speed. A more detailed consideration is given in Appendix G.

Furthermore, trip wires were used in order to initiate boundary layer separation over foreplane, fin and F.S.W. for similarity of flow in that respect. Details are given in Appendix K.

Details of derivations of similarity parameters can be found in Ref. 8, however the results are quoted in Table E3 of Appendix E.

2.2.10 Estimation of Longitudinal Stability Derivatives.

At this stage of design, the method of Section 2.2.4 was used to determine the aerodynamic parameters associated with the trimmed flight of the dynamically scaled model. Furthermore, from equilibrium considerations based on small perturbation theory, theoretical expressions for the estimation of longitudinal stability derivatives were derived. Estimates of the stability derivatives could then be obtained by inserting the aerodynamic parameters given earlier ,into these expressions. Details of these calculations are presented in Sections E4 - 7 of Appendix E, together with program "DERIVATIVE" shown as a block diagram on Fig.2.4.

2.3 The First Order Optimisation Code

The basis for this code was the combination of data and computational blocks of the previous sub-sections 2.2.1 - 10. A simplified representation of the complete routine is represented in Figure 2.5. Evidently there are considerable errors and deviations in the data supplied to the program in additions to the simplifications and assumptions used in developing individual sub-routines. Therefore, the errors tend to increase as the computations proceed. Unfortunately, there were no methods available to check the accuracy of the results obtained and as a result, provisions were made in the development of the dynamically scaled model in order to compensate for these discrepancies.

Clearly, the more accurate the data supplied to the optimisation code, the more realistic would be the results and, therefore, there seems to be scope for a great deal of improvement not only from the data point of view, but also from the inclusion of parameters which affect the optimisation process. It must be pointed out that the optimisation as a whole would lead to a compromise between the optimisation of individual sub-systems since some of the optimal criteria beneficial to one such sub-system may affect the optimality of other sub-systems. The optimisation program was run for the flight conditions given in Table E5 of Appendix E and the estimates of the longitudinal stability of derivatives obtained via this run are presented in Tables E6 and E7 in concise and aeronormalised forms respectively. A check on the static stability of full size configuration has also been carried out, the details of which are presented in Appendix C.

2.4 Model Construction

It was found that a 1/14th scale model of the full size F.S.W. aircraft would suit the Weybridge tunnel and test rig. Full details regarding the development of the latter are given in Reference 8. However, for the purpose of clarity, a brief review has been presented here as follows:

Figure 2.6 represents the basic layout of the rig itself, with the additional height transducer loop, developed as part of the present research programme. Plate 1, taken from Ref. 8, shows the complete test rig which includes the control unit. The basic functions of this control unit are presented in Fig. 3. The link between the rig and the control unit is via an umbilical chord. Basically the rig allows the model to have freedom of movement in heave along a vertical rod and yaw through the rod rotation. Also pitch and roll rotations are provided by the gimbal unit.

Now the purpose for which the dynamic model was developed, namely, estimation of stability derivatives, dictated the model construction. The following requirements had to be satisfied:

a) Ability to fly in trimmed straight level flight
b) Low all-up-weight so that moments of inertia and mass could be adjusted
c) Large interior space for placement of the necessary equipment.

The conditions stated above meant that conventional methods of construction could not be used since total access to the constituent parts was needed. Hence, the model was constructed on a modular basis. Furthermore, dynamic scaling was subject to appropriate ratios of moments of inertia of the full size F.S.W. aircraft to those of the model. Therefore, the wing was constructed out of foam, ply booms, thin ply covering and laminating resin to them together. An exploded view of the model minus the electronic parts and wiring is given in Fig. 2.7. The actual three dimensional picture, based on which the model was made, resulted from the cross reference of three-view drawing of the final design. Trailing edge extentions were used in order to increase the static margin as shown in Fig.2.7.

2.5 Experimental Determination of the Principal Moments of Inertia

There are several methods available for experimental determination of the moments of inertia, however, they are not often used nowadays because of aircraft size and development of weight analysis computer programs. Generally, the experimental methods are based on forced oscillations, whereby the aircraft is either hung on a supportive cradle or balanced on a knife edge. It is then made to oscillate and the oscillations are damped out by various springs placed at appropriate locations. The response is recorded and later analysed. This analysis leads to an estimate of the moments of inertia which include I_{xx}, I_{yy}, I_{zz}, I_{xy}, I_{zy}, etc.

Here, the principal moments of inertia were of interest and in order to obtain an estimate of them, the following method was developed. First, the model was balanced on the dynamic rig about the chosen C.G. position up to its estimated mass, based on the dynamic scaling, so that it was straight and level. Figure 2.8 represents the configuration and location of the damping springs for the estimation of respective principal moments of inertia. The dynamic model was then made to oscillate in the plane of interest in such a way that the rotations about the C.G. were confined to less than $\pm 10^{o}$. The application of Newton's second law of motion to the system provided the relationship between the period of the oscillations and the moment of inertia in each plane. The recorded traces of the oscillations were then used in conjunction with the derived relationships for the estimation of the principal moments of inertia. Details of the experiments and results are presented in Section G1 of Appendix G.

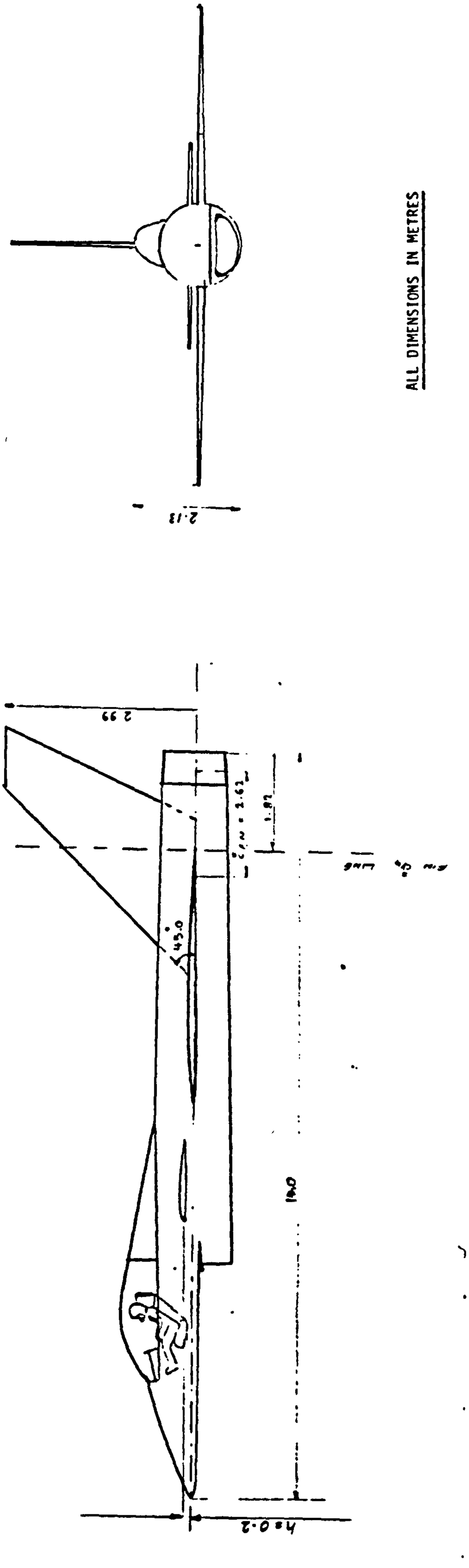

ALL DIMENSIONS IN METRES

FIG. 2.1

THIRD ANGLE PROJECTION
OF FULL SIZE AIRCRAFT.

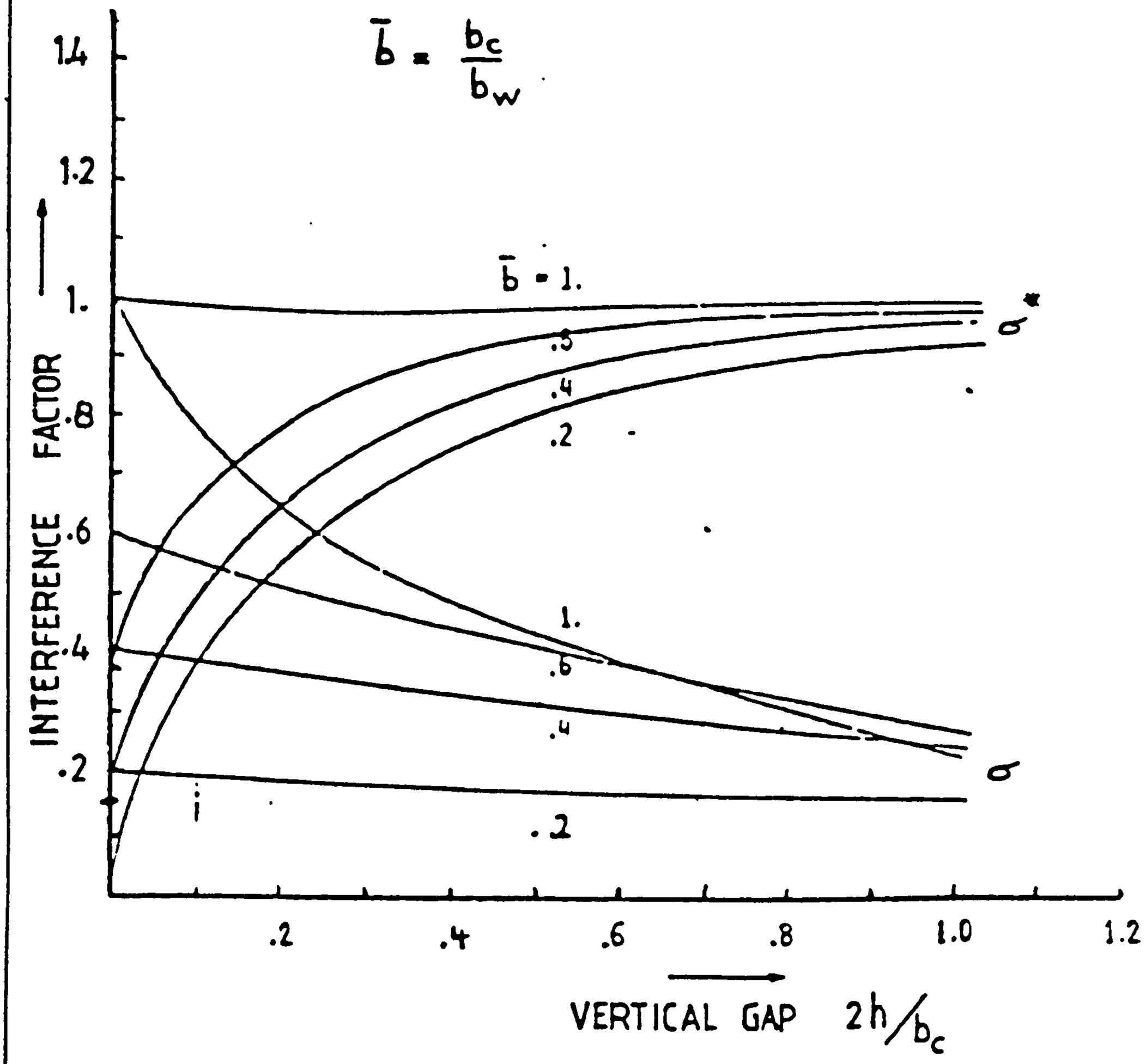

FIG. 2.2 : VARIATION OF PRANDTL'S INTERFERENCE FACTOR σ AND NON ELLIPTIC INTERFERENCE FACTOR σ^* WITH NON-DIMENSIONAL VERTICAL GAP. (Ref. 3)

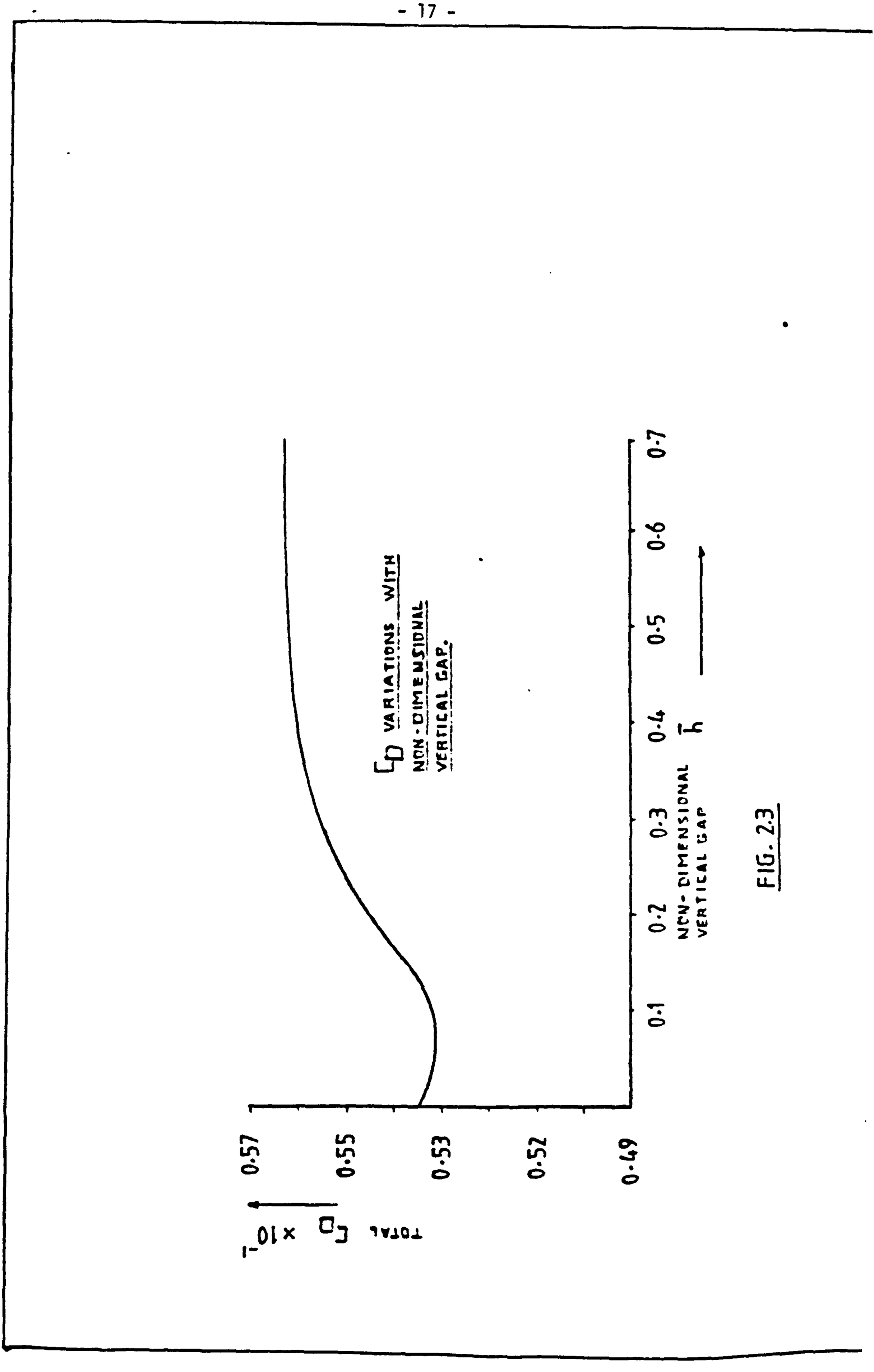
C_D VARIATIONS WITH NON-DIMENSIONAL VERTICAL GAP.
TOTAL $C_D \times 10^{-1}$
0.57
0.55
0.53
0.52
0.49
0.1
0.2
0.3
0.4
0.5
0.6
0.7
NON-DIMENSIONAL VERTICAL GAP $\bar{h}$

FIG. 2.3

PROGRAM STRUCTURE DIAGRAM

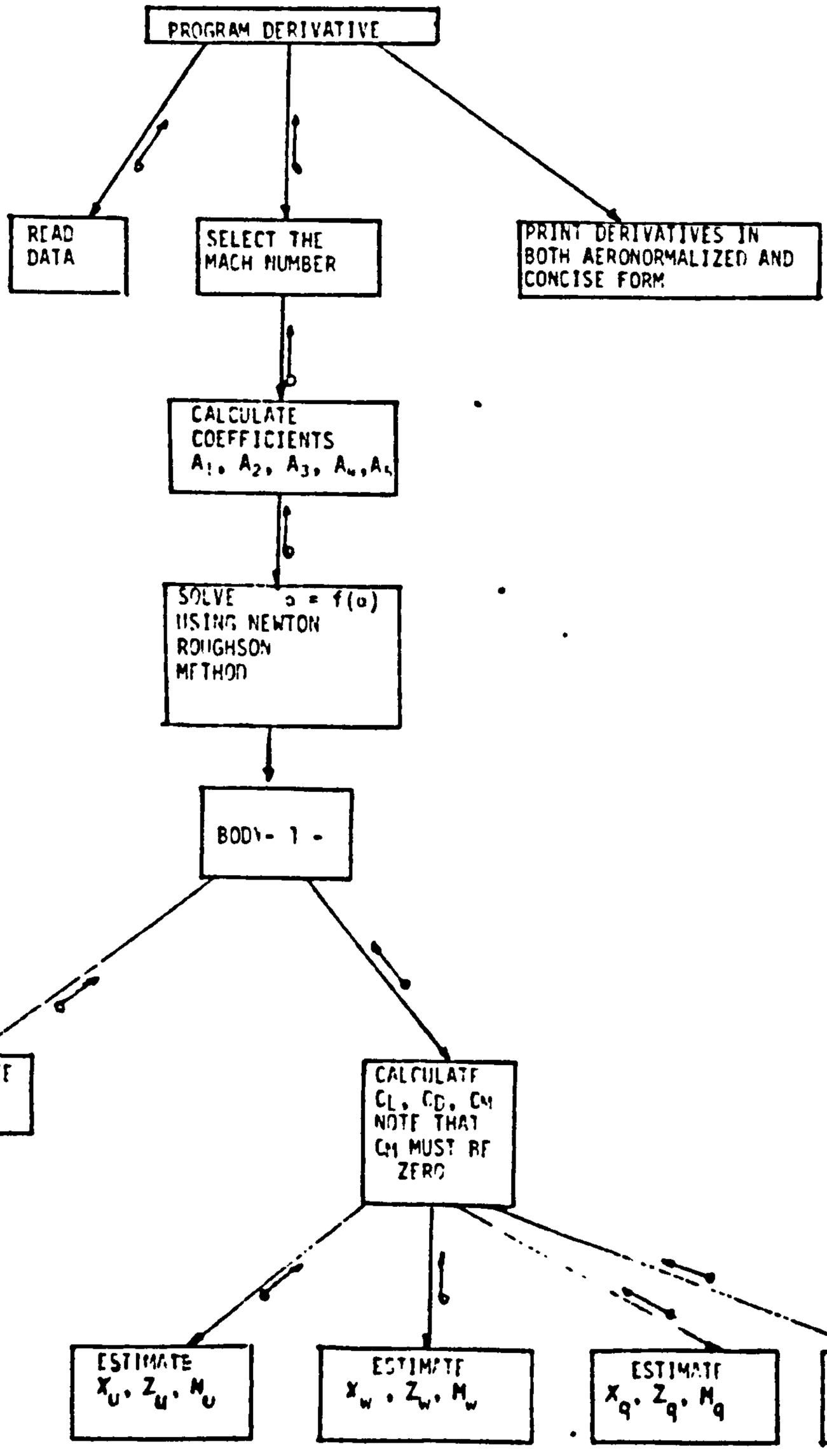

FIG. 24 .: STRUCTURE DIAGRAM OF THE SUB-ROUTINE DERIVATIVE

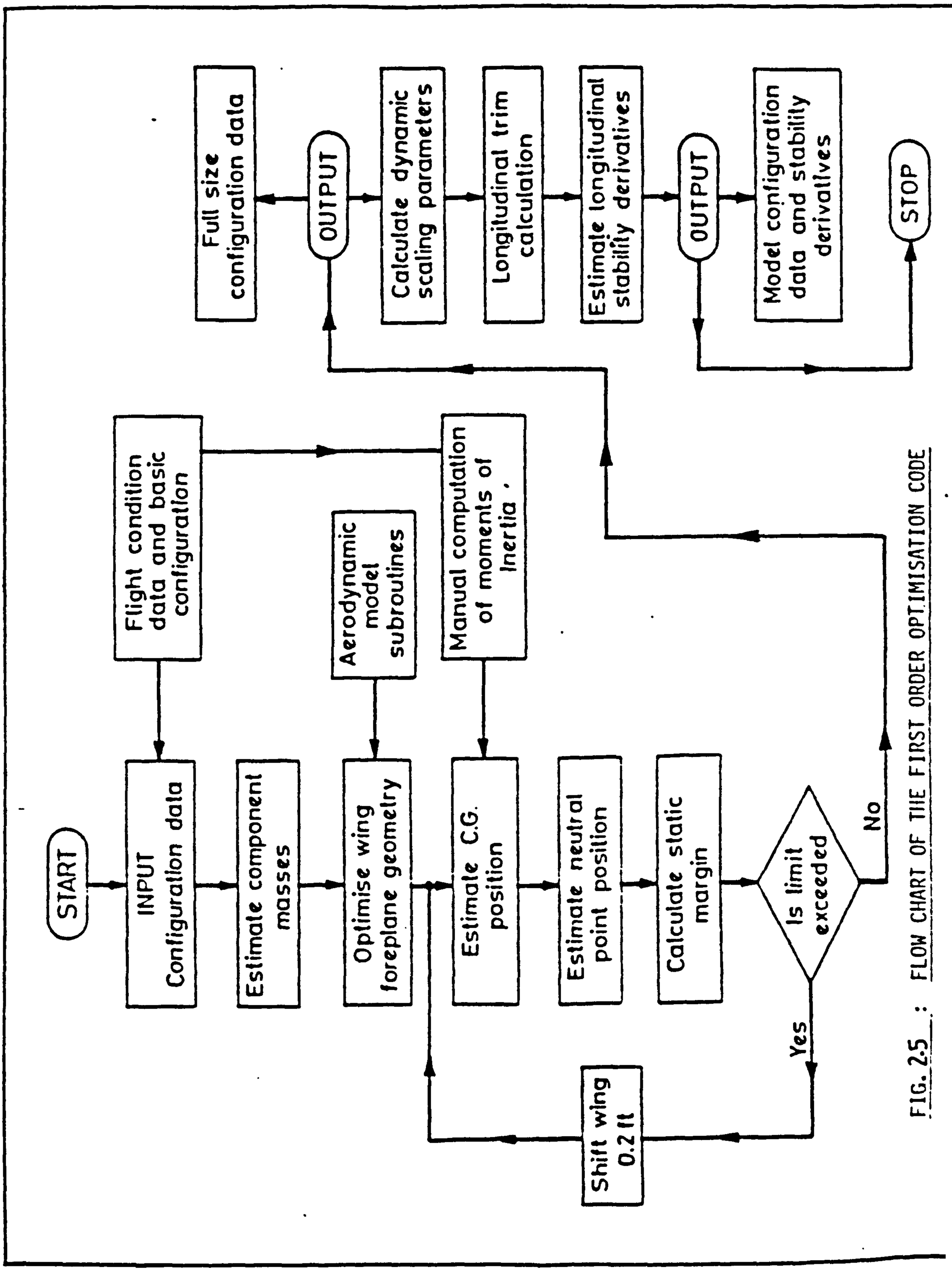

FIG. 25 : FLOW CHART OF THE FIRST ORDER OPTIMISATION CODE

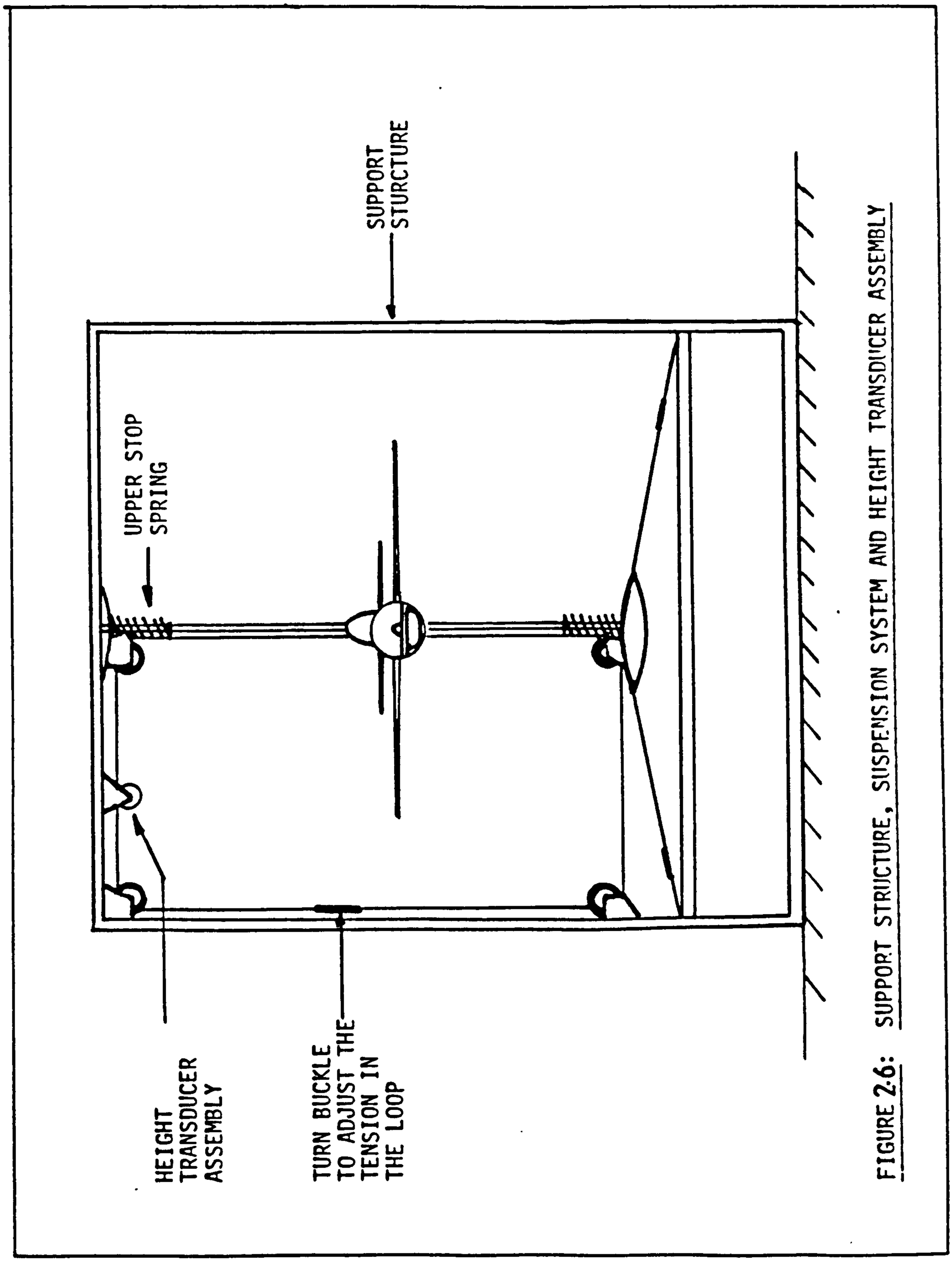

FIGURE 2.6: SUPPORT STRUCTURE, SUSPENSION SYSTEM AND HEIGHT TRANSDUCER ASSEMBLY

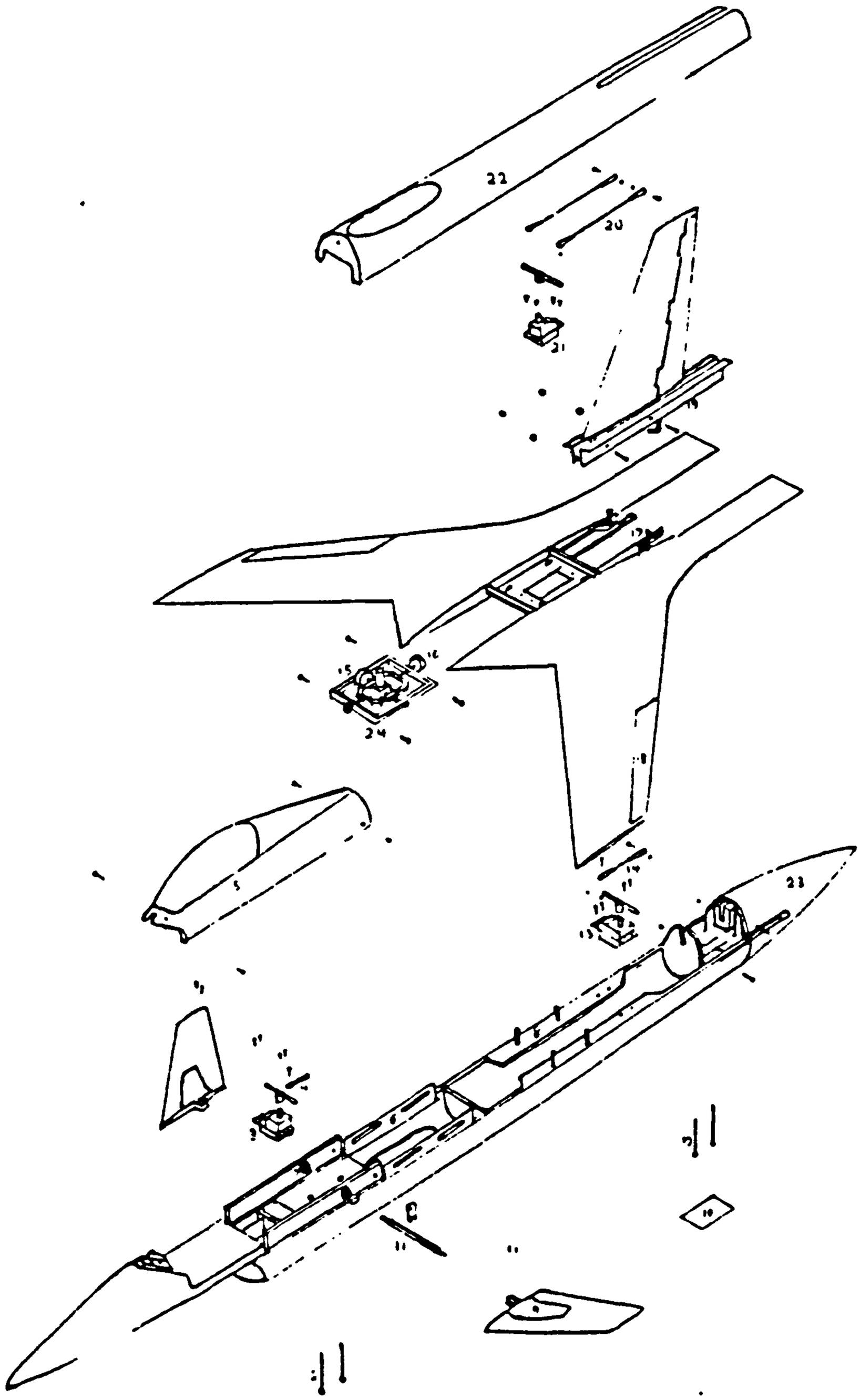

1. Front Ballast Bay Cover
2. Front Ballast Support Bolts
3. Canard Actuator
4. Canard Actuator Rod
5. Canopy Module
6. Gimbol Support Bracket
7. Support Bearing
8. FSW Fuselage Mountings
9. Canard Surface
10. Aft Ballast Bay Cover
11. Canard Rotation Shaft
12. Aft Ballast Support Bolts
13. Rudder Actuator
14. Rudder Actuator Rod
15. Pitch Pot
16. Roll Pot
17. Aileron Rotation Arm (See Ref.Drawing-1)
18. Aileron Mounting (See Ref.Drawing 1)
19. Fin & Rudder Mounting Brackets
20. Aileron Actuator Rods
21. Aileron Actuator
22. Aft Fuselage Top Cover
23. Boat Tail
24. Gimbol System

FIGURE 2.7: Exploded View of the Dynamic Model

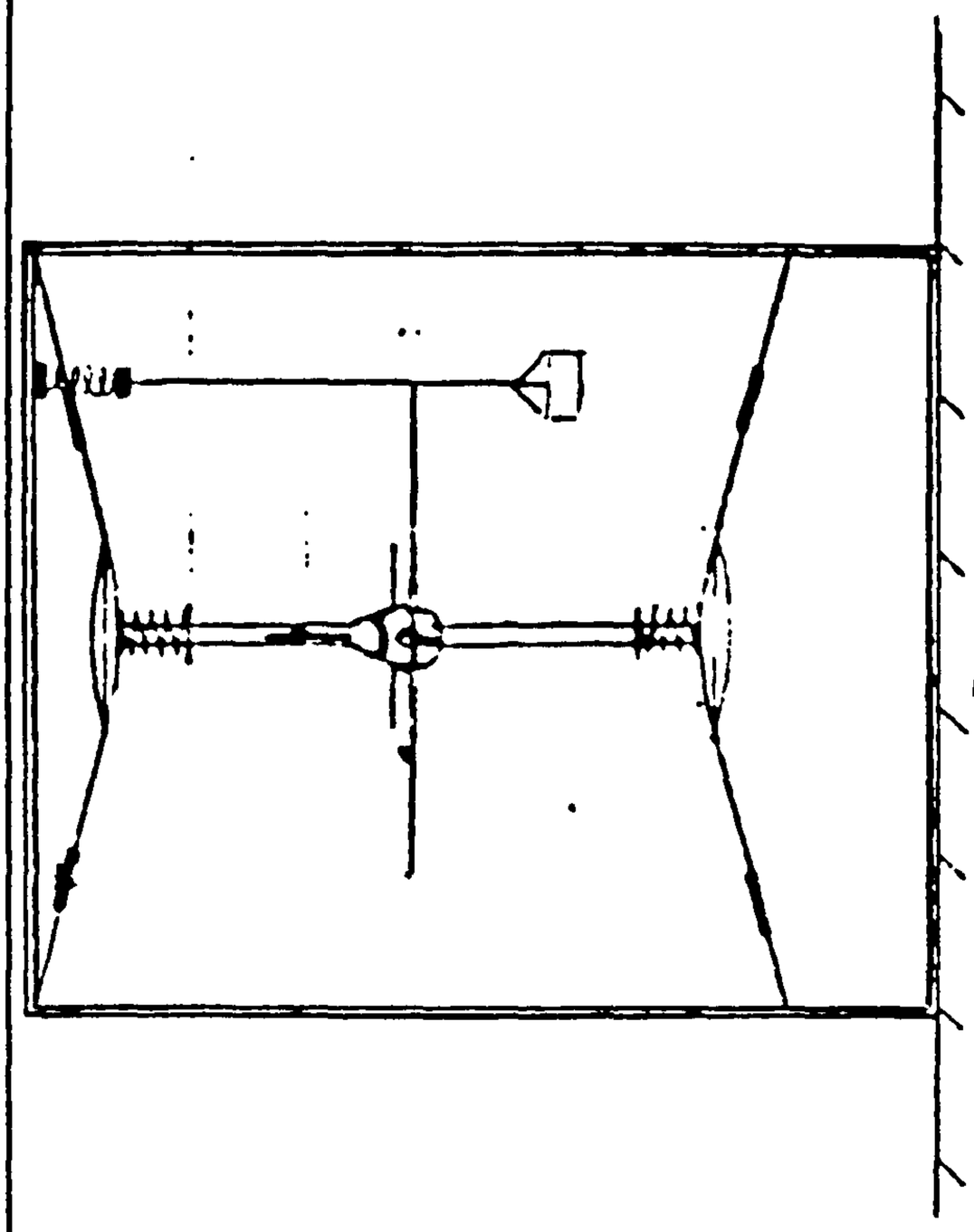

FIG. 2.8

THESE FIGURES REPPESENT THE SUSPENSION SYSTEM AND THE MASS-SPRING ARRANGEMENTS FOR THE DETERMINATION AND ADJUSTMENT OF THE PRINCIPAL MOMENTS OF INERTIA, I_{xx}, I_{yy} and I_{zz}

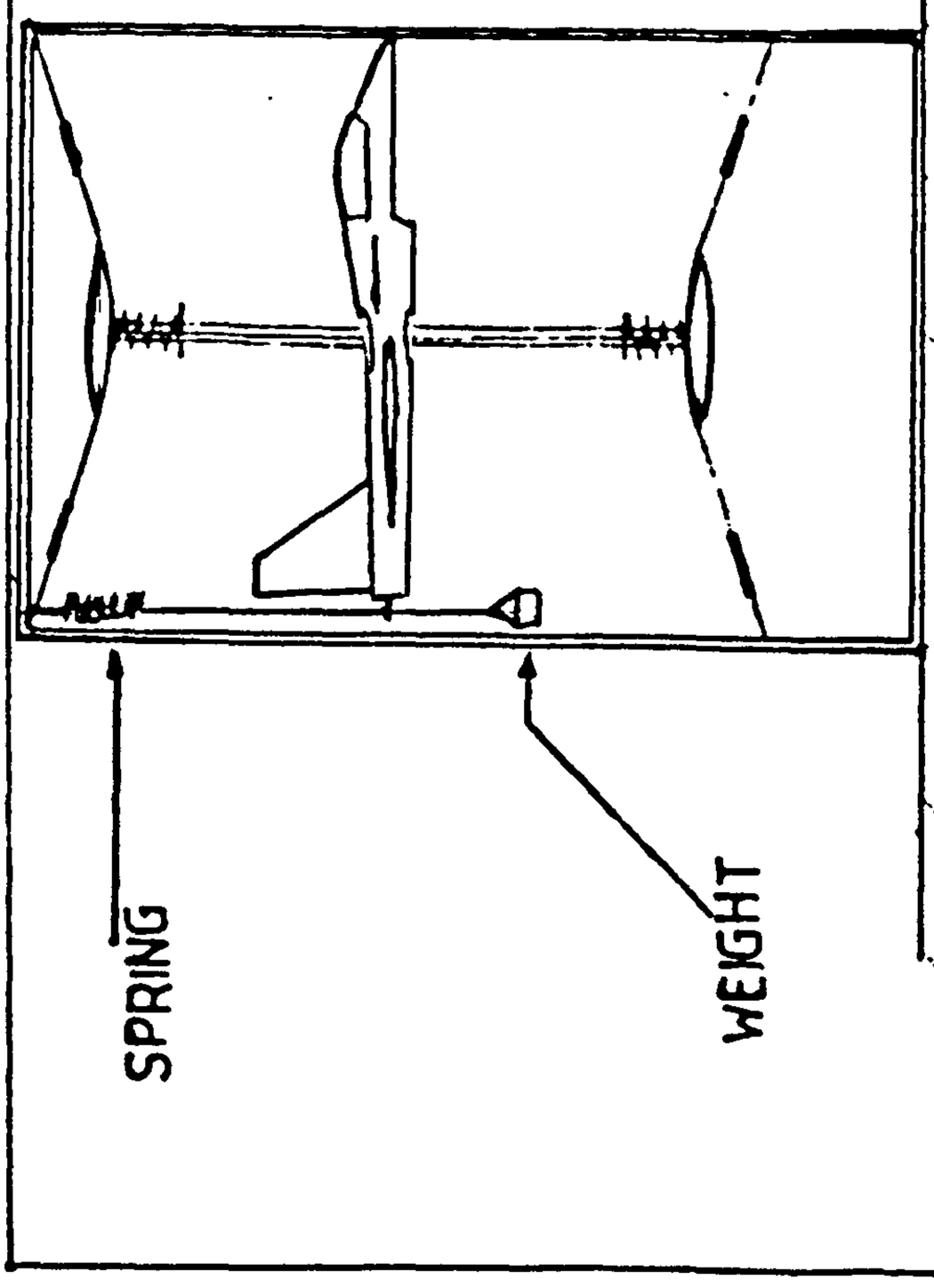

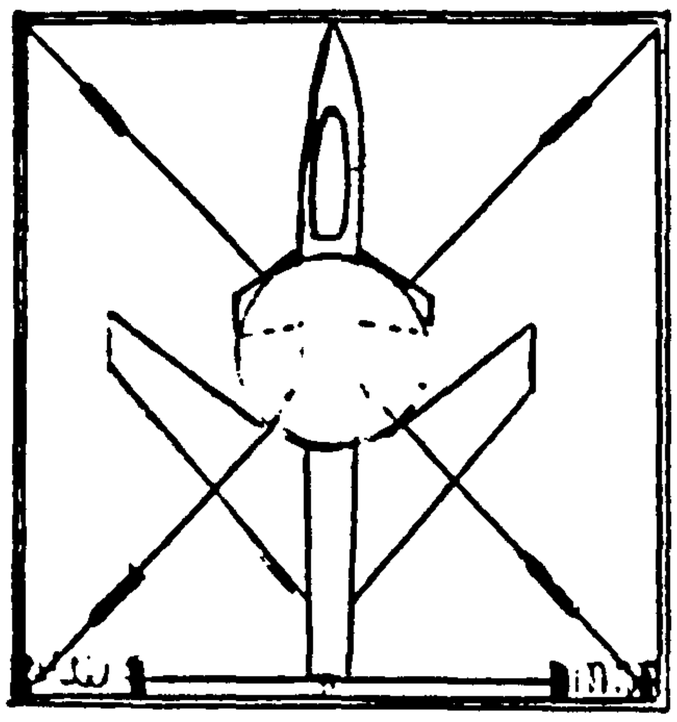

3. PARAMETER IDENTIFICATION AND KALMAN FILTERING

The evaluation of coefficients in a mathematical model of a system from measured input-output data is termed parameter identification. Over the past ten years or so, much work has been carried out on parameter identification with the result that very many techniques have now become available. Clearly, every method has its advantages and disadvantages and therefore it is up to the systems engineer to decide on the suitability of the application of one of these techniques.

Generally speaking, the parameter identification methods fall into two categories, namely those based on weighted least squares and those based on the minimisation of the probability density function. In the first category, the optimality criterion for the state estimation is a scalar quantity termed the cost function k, the minimisation of which in effect minimises the residuals between the measured and the corresponding estimated points. The difficulty with these techniques can be attributed to the problem of choosing the weights. This problem is overcome in the second category by relating the weights to the measurement and process noises assumed to be uncorrelated and white. The disadvantage however with these techniques lies in the fact that a-priori knowledge of the states is needed.

3.1 Theory of Kalman Filter Techniques

Before describing Kalman Filter theory, it is necessary to have a look at the systems and dynamical equations. In general, the equations of motion of an aircraft can be represented in the continuous time sense as,

$$\dot{\underset{\sim}{x}}(t) = \underset{\sim}{f}(x(t)\ ,\ \underset{\sim}{u}(t),\ t) \qquad \text{state equation}$$

$$\underset{\sim}{y}(t) = \underset{\sim}{g}(x(t)\ ,\ \underset{\sim}{u}(t),\ t) \qquad \text{output equation}$$

where $\underset{\sim}{u}(t)$ is a set of q input functions such as control surface movements with associated effects. i.e.

$$\underset{\sim}{u}^{\tau} = [u,\ u_2,\ u_3\ .\ .\ .\ .\ u_q]$$

Also $\underset{\sim}{y}(t)$ is a set of n output functions, which usually take the form of measurements, i.e.

$$\underset{\sim}{y}^{\tau} = [y_1,\ y_2\ ,\ y_3\ .\ .\ .\ .\ y_n]$$

Furthermore, $\underset{\sim}{x}(t)$ is a set of m state functions such as w, q, θ, z_w, z_q, etc.

i.e.

$$\underset{\sim}{x}^{T} = [x_1, x_2, x_3 \ldots . x_m]$$

and finally t is the time.

Function $\underset{\sim}{f}$ is such that the state equation has a unique solution.

Figure 3.1, below,illustrates the interconnection between state and output equations.

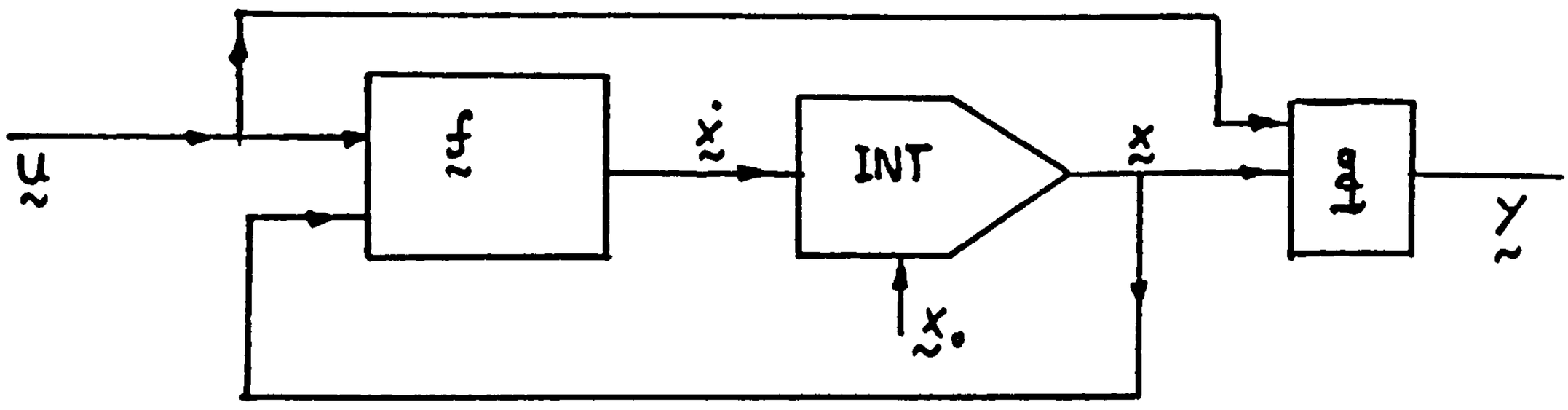

FIGURE 3.1

BLOCK DIAGRAM ILLUSTRATING THE STATE AND OUTPUT EQUATIONS

Reference can be made , Reference 5, on system design theory regarding the characteristics of a system such as time invariance, linearity, linear time invariance systems, system response, stochaistic continuous time systems, etc. However, as far as the present study is concerned, only discretised time systems are of significance.

3.2 Discrete time systems

The dynamical equations of a system in discrete time can be described by the following equations:

$$\underset{\sim}{X}(n+1) = \underset{\sim}{f}(\underset{\sim}{X}(n), \underset{\sim}{u}(n), n) \qquad \text{state equation}$$

$$\underset{\sim}{Y}(n) = \underset{\sim}{g}(\underset{\sim}{X}(n), \underset{\sim}{u}(n), n) \qquad \text{output equation}$$

with initial values of the states $\underset{\sim}{X}(0)$. $\underset{\sim}{U}(n)$ is a set of input functions such as control surface deflection.

$\underset{\sim}{Y}(n)$ is a column matrix representing the output of the system.

If the functions $\underset{\sim}{f}$ and $\underset{\sim}{g}$ are linear, the discrete time system which they describe is said to be linear. For linear systems, the above set of equations can be written as

$$\underset{\sim}{X}(n+1) = \phi(n)\underset{\sim}{X}(n) + \psi(n)\underset{\sim}{U}(n) \qquad \text{- - - - - EQ.3.1}$$

$$\underset{\sim}{Y}(n) = C(n)\underset{\sim}{X}(n) + D(n),\underset{\sim}{U}(n)$$

If the functions representing the states and the output do not depend on time explicitly then, the system is called time invariant. Therefore, if matrices $\phi(n)$, $\psi(n)$, C(n) and D(n) of the above linear system are constants, the whole system is called a linear time-invariant system.

or

$$\underset{\sim}{X}(n+1) = \phi\underset{\sim}{X}(n) + \psi\underset{\sim}{U}(n) \qquad \text{- - - - - EQ.3.2}$$

$$\underset{\sim}{Y}(n) = C\underset{\sim}{X}(n) + D\underset{\sim}{U}(n)$$

Figure 3.2 represents the block diagram of Equation 3.2.

The square matrix $\phi(m,m)$ is called the state transition matrix.

$\phi(m,m)$ is the state matrix

$\psi(m,g)$ is the input matrix

C(r,m) is the output matrix

D(r,q) is the direct matrix

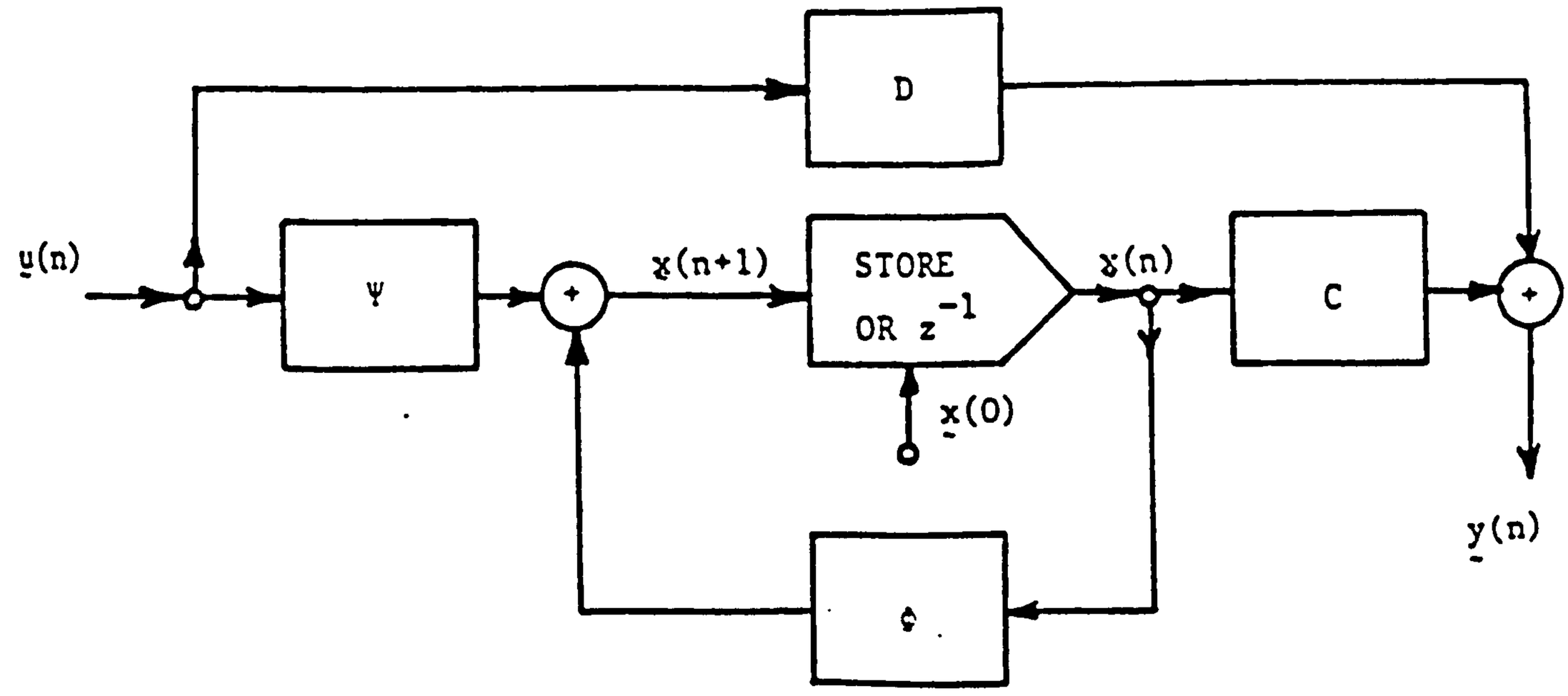

FIG. 3.2 BLOCK DIAGRAM OF EQUATIONS 3.2

3.3 The Transfer Function Matrix

Consider a linear time invariant system described by equations S4, S5. It must be noted that in departure from continuous time systems into discrete time systems it is necessary to move from s-plane onto z-plane. Therefore, taking the z-transforms of the state and output equations gives:

$$z\underset{\sim}{\bar{x}}(z) = \phi\underset{\sim}{\bar{x}}(z) + \psi\underset{\sim}{u}(z) \qquad \text{- - - - - EQ.3.3}$$

$$\underset{\sim}{\bar{y}}(z) = C\underset{\sim}{\bar{x}}(z) + D\underset{\sim}{\bar{u}}(z) \qquad \text{- - - - - EQ.3.4}$$

On substituting $\underset{\sim}{\bar{x}}(z)$ from 3.3 into 3.4 ;

$$\underset{\sim}{\bar{y}}(z) = [C(zI - \phi)^{-1}\psi + D]\underset{\sim}{\bar{u}}(z)$$

and the transfer function matrix F(z) is

$$\frac{\underset{\sim}{\bar{y}}(z)}{\underset{\sim}{\bar{u}}(z)} = F(z) = C(zI - \phi)^{-1}\psi + D$$

3.4 Stochastic Discrete Time Systems

In most of the practical applications of system design, measurements are corrupted by noise. For a linear time-invariant stochastic discrete-time system, the general state and output equations can be represented as;

$$\underset{\sim}{x}(n + 1) = \phi\underset{\sim}{x}(n) + \psi\underset{\sim}{u}(n) + \underset{\sim}{w}_d(n)$$

$$\underset{\sim}{y}(n) = C\underset{\sim}{x}(n) + D\underset{\sim}{u}(n) + \underset{\sim}{v}_d(n)$$

where:

$\underset{\sim}{w}_d(n)$ is the discrete process noise vector

and $\underset{\sim}{v}_d(n)$ is the discrete output noise vector.

These equations will be used again in Section 3.6.

3.5 Kalman Filter Estimation

In the early stages of design of aircraft, missiles, etc., it is necessary to assess the dynamic behaviour of the design. Usually, the variables of interest are impossible to measure directly. Therefore, means have to be found of obtaining them. A linear time-invariant system may be modelled by the equations:

$$\dot{\underset{\sim}{x}}(t) = A\underset{\sim}{x}(t) + B\underset{\sim}{u}(t) \qquad \text{- - - - - EQ.3.5}$$

$$\underset{\sim}{y}(t) = C\underset{\sim}{x}(t) + D\underset{\sim}{u}(t) \qquad \text{- - - - - EQ.3.6}$$

where A is the state matrix
B is the input matrix
C is the output matrix
D is the direct matrix.

The Kalman Filter estimator would have the following form:

$$\dot{\hat{\underset{\sim}{x}}}(t) = A\hat{\underset{\sim}{x}}(t) + B\underset{\sim}{u}(t) + P(\underset{\sim}{y}(t) - \hat{\underset{\sim}{y}}(t)) \qquad \text{- - - - - EQ.3.7}$$

$$\hat{\underset{\sim}{y}}(t) = C\hat{\underset{\sim}{x}}(t) + D\underset{\sim}{u}(t) \qquad \text{- - - - - EQ.3.8}$$

where P is the estimator gain which is to drive the estimated states $\hat{\underset{\sim}{x}}(t)$ into coincidence with the system states $\underset{\sim}{x}(t)$. Assuming the error in the states is thus expressed as

$$\tilde{\underset{\sim}{x}}(t) = \underset{\sim}{x}(t) - \hat{\underset{\sim}{x}}(t) \qquad \text{- - - - - EQ.3.9}$$

If $\lim_{t\to\infty} \tilde{\underset{\sim}{x}}(t) \to 0$

then the estimator is said to be an asymptotic state estimator.

Subtracting 3.6 from 3.8 gives:

$$\underset{\sim}{y}(t) - \hat{\underset{\sim}{y}}(t) = C\tilde{\underset{\sim}{x}}(t) \qquad \text{- - - - - EQ.3.10}$$

On differentiating 3.9 :

$$\dot{\tilde{\underset{\sim}{x}}}(t) = \dot{\underset{\sim}{x}}(t) - \dot{\hat{\underset{\sim}{x}}}(t) \qquad \text{- - - - - EQ.3.11}$$

Substituting for $\dot{\underset{\sim}{x}}(t)$ and $\dot{\hat{\underset{\sim}{x}}}(t)$ from 3.5 and 3.7;

$$\dot{\tilde{\underset{\sim}{x}}}(t) = (A - PC)\tilde{\underset{\sim}{x}}(t) \qquad \text{- - - - - EQ.3.12}$$

The solution to which is:

$$\tilde{\underset{\sim}{x}}(t) = \tilde{\underset{\sim}{x}}(0)e^{(A-PC)t} \qquad \text{- - - - - EQ.3.13}$$

By looking at 3.13, it is evident that in order to minimise the error $\hat{\underset{\sim}{x}}(t)$, eigenvalues of (A - PC) must be negative. In other words, they must lie in the open left half S-plane. The further to the left we place the eigenvalues of (A - PC), theoretically the faster the convergence.

However, another practical consideration is the corruption of states by noise, assumed white. Poles which are close to the imaginary axis of the S-plane will filter much more noise than poles far away from it. Therefore, a compromise has to be reached. It is the optimal choice of P, given system characteristics and noise statistics,which lead to the concept of the Kalman filter. In other words, Kalman filter is an optimal state estimator and hence a statistical method like weighted least-square curve fitting with the difference that the weights are based on the measurement and process noise.

3.6 Discrete Time Kalman Filter

Consider a linear system given by the following equations:

$$\underset{\sim}{x}(n+1) = \phi(n)\underset{\sim}{x}(n) + \psi(n)\underset{\sim}{u}(n) + \theta(n)\underset{\sim}{w}(n)$$

$$\underset{\sim}{y}(n) = C(n)\underset{\sim}{x}(n) + D(n)\underset{\sim}{u}(n) + \underset{\sim}{v}(n)$$

where

$\underset{\sim}{x}$ is the state vector

$\underset{\sim}{u}$ is the input vector

$\underset{\sim}{y}$ is the output vector

$\underset{\sim}{w}$ is the process noise vector

$\underset{\sim}{v}$ is the measurement noise vector

$\phi(m,m)$ state transition matrix

$\psi(m,q)$ input matrix

$\theta(m,k)$ process noise matrix

$C(r,m)$ output matrix

$D(r,q)$ direct input matrix

m is the number of states

q is the number of inputs

r is the number of outputs

k is the number of process noise inputs

n is the iteration number.

Also $\underset{\sim}{w}$ and $\underset{\sim}{v}$ are assumed to be white noise, Gaussian with zero-mean, uncorrelated with each other and uncorrellated with the initial states, i.e.

$$E\ \underset{\sim}{w}(n) = E\ \underset{\sim}{v}(n) = \underset{\sim}{0}$$

$$E\ \underset{\sim}{w}(n).\underset{\sim}{v}(m)^T = \underset{\sim}{0}$$

$$E\ \underset{\sim}{w}(n)\underset{\sim}{x}_o^T = E\ \underset{\sim}{v}(n)\underset{\sim}{x}_o^T = \underset{\sim}{0}$$

where E is the expected value.

Furthermore, we need to find the noise covariance matrices given by:

$$E\ \underset{\sim}{w}\ (n)\underset{\sim}{w}(n)^T = Q(n)$$

$$E\ \underset{\sim}{v}(n)\underset{\sim}{v}(n)^T = R(n)$$

From 3.7 the equations of Kalman filter can be written as:

$$\hat{\underset{\sim}{x}}(n+1) = \phi(n)\hat{\underset{\sim}{x}}(n) + \psi(n)\underset{\sim}{u}(n) + P(n)\left[\underset{\sim}{y}(n) + C(n)\hat{\underset{\sim}{x}}(n) - D(n)\underset{\sim}{u}(n)\right]$$

$$\hat{\underset{\sim}{y}}(n) = \hat{\underset{\sim}{x}}(n)$$

where $\hat{\underset{\sim}{x}}$ is the estimate of x

and P(m,n) is the gain matrix.

The estimation error is given by

$$\tilde{\underset{\sim}{x}}(n) = \underset{\sim}{x}(n) - \hat{\underset{\sim}{x}}(n)$$

with the error covariance matrix defined as

$$G(n) = E\ \tilde{\underset{\sim}{x}}(n)\tilde{\underset{\sim}{x}}(n)^T.$$

The most important elements of G(n) are the diagonal elements since the rest of the elements are very small due to uncorrelation between the states, then the filter gain matrix P which minimises trace G, i.e. minimises the sum of the squared errors $E \sum^{m} \tilde{\underset{\sim}{x}}^2(n)$, is given by:

$$P(n) = \phi(n)G(n)C(n)^T\left[C(n)G(n)C(n)^T + R(n)\right]^{-1} \qquad \text{- - - - - EQ.3.14}$$

where:

$$G(n+1) = \left[\phi(n) - P(n)C(n)\right]G(n)\phi(n)^T + \theta(n)Q(n)\theta(n)^T \qquad \text{- - - - - EQ.3.15}$$

In order to estimate $\underset{\sim}{x}(n+1)$, it is necessary to use $\underset{\sim}{v}(n)$ and $\underset{\sim}{u}(n)$. However, in many applications of the Kalman filter where the best estimate of states $\underset{\sim}{x}(n)$ is required, the filter is split as follows:

$$\hat{\underset{\sim}{x}}^{-}(n+1) = \phi(n)\hat{\underset{\sim}{x}}^{+}(n) + \psi(n)\underset{\sim}{u}(n)$$

$$\hat{\underset{\sim}{x}}^{+}(n) = \hat{\underset{\sim}{x}}^{-}(n) + J(n)[\underset{\sim}{y}(n) - C(n)\hat{\underset{\sim}{x}}^{-}(n) - D(n)\underset{\sim}{u}(n)]$$

where J(n) is defined as the split Kalman filter gain matrix and,

$$P(n) = \phi(n)J(n)$$

also

$$\left.\begin{aligned}
\tilde{\underset{\sim}{x}}^{-}(n) &= \underset{\sim}{x}(n) - \hat{\underset{\sim}{x}}^{-}(n) \\
\tilde{\underset{\sim}{x}}^{+}(n) &= \underset{\sim}{x}(n) - \hat{\underset{\sim}{x}}^{+}(n) \\
G^{-}(n) &= E\tilde{\underset{\sim}{x}}^{-}(n)\tilde{\underset{\sim}{x}}^{-}(n)^{T} \\
G^{+}(n) &= E\tilde{\underset{\sim}{x}}(n)\tilde{\underset{\sim}{x}}^{+}(n)^{T}
\end{aligned}\right\} \quad \text{- - - - - EQ.3. 6}$$

with following definitions respectively

$\hat{\underset{\sim}{x}}^{-}(n)$ = best estimate of $\underset{\sim}{x}(n)$ in the interval [n-1, n], before $\underset{\sim}{u}(n)$ and $\underset{\sim}{y}(n)$ are available.

$\hat{\underset{\sim}{x}}^{+}(n)$ = best estimate of $\underset{\sim}{x}(n)$ in the interval [n, n+1], after $\underset{\sim}{x}(n)$ and $\underset{\sim}{y}(n)$ become available.

$\tilde{\underset{\sim}{x}}^{-}(n)$ = error in the state estimation in the interval [n-1,n], before $\underset{\sim}{u}(n)$ and $\underset{\sim}{y}(n)$ are available.

$\tilde{\underset{\sim}{x}}^{+}(n)$ = error in the state estimation in the interval [n,n+1], after $\underset{\sim}{u}(n)$ and $\underset{\sim}{y}(n)$ have become available.

$G^{-}(n)$ = error covariance matrix in the interval [n-1,n], before $\underset{\sim}{u}(n)$ and $\underset{\sim}{y}(n)$ are available.

$G^{+}(n)$ = error covariance matrix in the interval [n,n+1], after $\underset{\sim}{u}(n)$ and $\underset{\sim}{y}(n)$ have become available.

Now, the split Kalman filter gain matrix J(n) which minimises both the trace of G^{+} and trace G^{-} is given by:

$$J(n) = G^{-}(n)C(n)^{T}\left[R(n) + C(n)G^{-}(n)C(n)^{T}\right]^{-1}$$

with

$$G^{-}(n+1) = \phi(n)G^{+}(n)\phi(n)^{T} + \theta(n)Q(n)\theta(n)^{T}$$

$$G^{+}(n) = [I - J(n)C(n)]G^{-}(n)$$

and $\hat{\underset{\sim}{y}}(n) = \hat{\underset{\sim}{x}}^{+}(n)$ which is the Kalman filter output equation. The calculation sequence of the split filter is given in Fig.3.3

THE CALCULATION SEQUENCE

The split Kalman filter calcuation sequence may be described as shown in

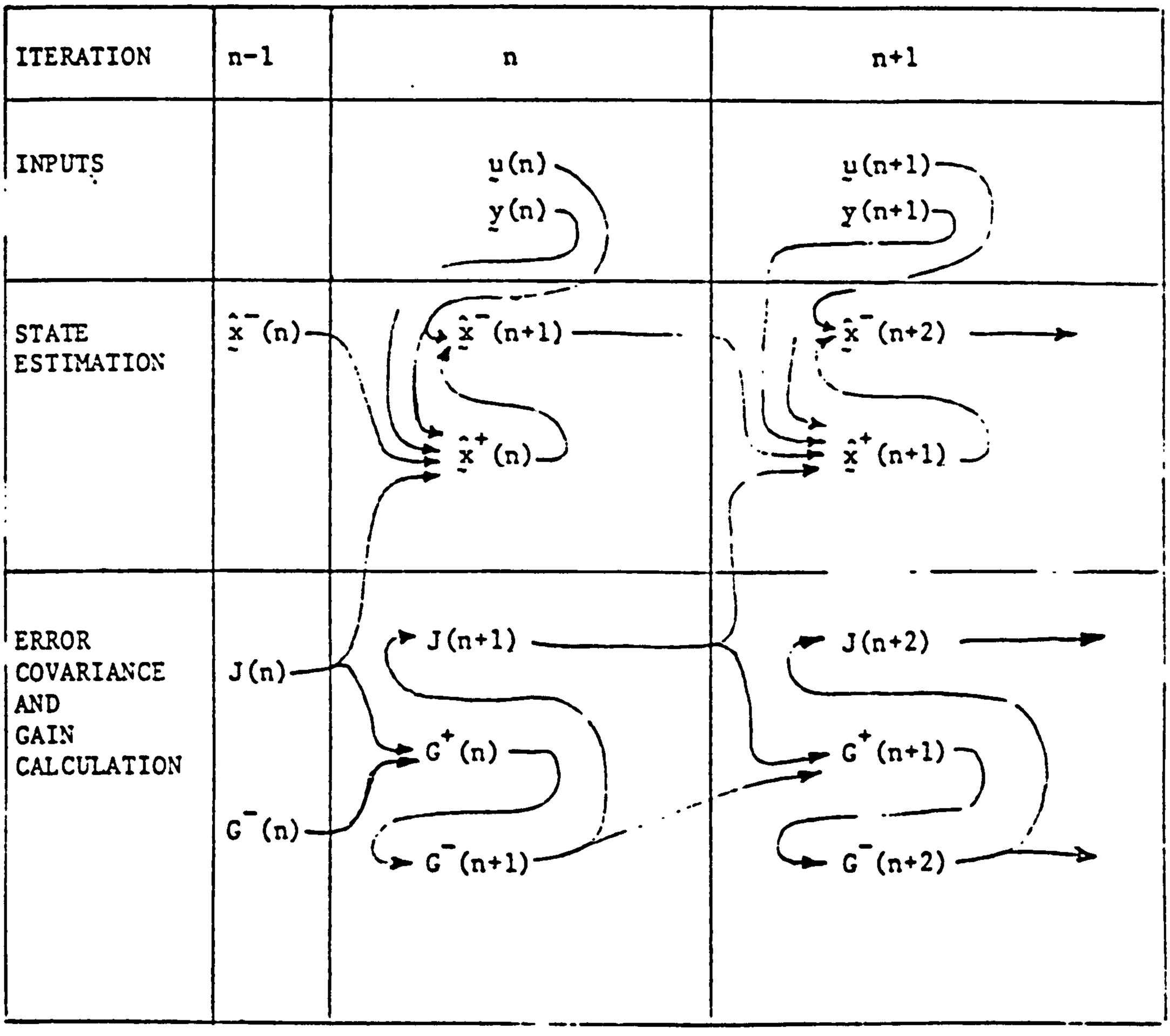

FIG. 3-3: SPLIT KALMAN FILTER CALCULATION SEQUENCE

3.7 Extended Kalman Filter

Now, consider a non-linear system described by the following equations:

$$\left.\begin{aligned} \underset{\sim}{x}(n+1) &= \underset{\sim}{f}(\underset{\sim}{x}(n)) + E(\underset{\sim}{x}(n))\underset{\sim}{w}(n) \\ \underset{\sim}{y}(n) &= \underset{\sim}{g}(\underset{\sim}{x}(n)) + \underset{\sim}{v}(n) \end{aligned}\right\} \quad \text{----- EQ.3.17}$$

where:

$\underset{\sim}{f}$ is the state function

$\underset{\sim}{g}$ is the output function

E is the process noise matrix

and it must be noted that $\underset{\sim}{f}$ and $\underset{\sim}{g}$ are non-linear continuous functions of $\underset{\sim}{x}$, with continuous first partial derivatives of $\underset{\sim}{x}$.

In this case the split Kalman filter equations can be represented as:

$$\hat{\underset{\sim}{x}}^{-}(n+1) = \underset{\sim}{f}(\underset{\sim}{x}^{+}(n)) \quad \text{----- EQ.3.18}$$

$$\hat{\underset{\sim}{x}}^{+}(n) = \hat{\underset{\sim}{x}}^{-}(n) + J(n)[\underset{\sim}{y}(n) - \underset{\sim}{g}(\hat{x}^{-}(n))] \quad \text{----- EQ.3.19}$$

$$\hat{\underset{\sim}{y}}(n) = \hat{\underset{\sim}{x}}^{+}(n) \ .$$

Equations 3.17 and 3.18 describe the split extended Kalman filter which deals with non-linear systems.

3.8 The Gain Matrix J(n)

Filter errors are defined as defined by equations 3.9 are:

$$\tilde{\underset{\sim}{x}}^{-}(n+1) = \underset{\sim}{x}(n+1) - \hat{\underset{\sim}{x}}^{-}(n+1)$$

which in substitution for $\underset{\sim}{x}(n+1)$ and $\hat{\underset{\sim}{x}}^{-}(n+1)$ from 3.17, 3.18 and 3.19 becomes:

$$\tilde{\underset{\sim}{x}}^{-}(n+1) = \underset{\sim}{f}(\underset{\sim}{x}(n)) + E(\underset{\sim}{x}(n)\underset{\sim}{w}(n) - \underset{\sim}{f}(\hat{\underset{\sim}{x}}^{+}(n)) \quad \text{----- EQ.3.20}$$

For sufficiently small $||\tilde{\underset{\sim}{x}}^{+}||$, $\underset{\sim}{f}(\underset{\sim}{x}(n))$ can be expanded using Taylor series as:

$$\underset{\sim}{f}(\underset{\sim}{x}(n)) \approx \underset{\sim}{f}(\hat{\underset{\sim}{x}}^{+}(n)) + \left(\frac{\partial \underset{\sim}{f}}{\partial \underset{\sim}{x}}\right)_{n}\Bigg|_{\underset{\sim}{x}=\hat{\underset{\sim}{x}}^{+}(n)} \cdot \tilde{\underset{\sim}{x}}^{+}(n) \quad \text{----- EQ.3.2}$$

Substitution into S22 gives

$$\tilde{\underset{\sim}{x}}^{-}(n+1) = \left(\frac{\partial \underset{\sim}{f}}{\partial \underset{\sim}{x}}\right)_{n}\Bigg|_{\underset{\sim}{x}=\hat{\underset{\sim}{x}}^{+}(n)} \cdot \tilde{\underset{\sim}{x}}^{+}(n) + E(\hat{\underset{\sim}{x}}^{+}(n))\underset{\sim}{w}(n) \quad \text{----- EQ.3.22}$$

Furthermore,

$$\tilde{\underset{\sim}{x}}^{+}(n) = \underset{\sim}{x}(n) - \hat{\underset{\sim}{x}}^{+}(n) \qquad \text{- - - - - EQ.3.23}$$

Substituting for $\hat{\underset{\sim}{x}}^{+}(n)$ from S21 and S19:

$$\tilde{\underset{\sim}{x}}^{+}(n) = \underset{\sim}{x}(n) - \hat{\underset{\sim}{x}}^{-}(n) - J(n)\,\underset{\sim}{g}(\underset{\sim}{x}(n)) + \underset{\sim}{v}(n) - \underset{\sim}{g}(\hat{\underset{\sim}{x}}^{-}(n)) \qquad \text{- - - - - EQ.3.24}$$

Assume $||\tilde{\underset{\sim}{x}}^{-}||$ is sufficiently small so that $\underset{\sim}{g}(\underset{\sim}{x}(n))$ can be expanded using Taylor series, then;

$$\underset{\sim}{g}(\underset{\sim}{x}(n) \approx \underset{\sim}{g}(\hat{\underset{\sim}{x}}^{-}(n)) + \left(\frac{\partial \underset{\sim}{g}}{\partial \underset{\sim}{x}}\right)_{n} \Bigg|_{\underset{\sim}{x}=\hat{\underset{\sim}{x}}^{-}(n)} \cdot \tilde{\underset{\sim}{x}}^{-}(n) \qquad \text{- - - - - EQ.3.25}$$

and substitution of S27 into S26 gives:

$$\tilde{\underset{\sim}{x}}^{+}(n) = \left[I - J(n)\left(\frac{\partial \underset{\sim}{g}}{\partial \underset{\sim}{x}}\right)_{n} \Bigg|_{\underset{\sim}{x}=\hat{\underset{\sim}{x}}^{-}(n)}\right]\tilde{\underset{\sim}{x}}^{-}(n) - J(n)\underset{\sim}{v}(n) \qquad \text{- - - - - EQ.3.26}$$

By comparing 3.26, 3.22 with equations 3.16 it can be shown that:

$$\phi(n) = \left(\frac{\partial \underset{\sim}{f}}{\partial \underset{\sim}{x}}\right)_{n} \Bigg|_{\underset{\sim}{x} = \hat{\underset{\sim}{x}}^{+}(n)}$$

$$C(n) = \left(\frac{\partial \underset{\sim}{g}}{\partial \underset{\sim}{x}}\right)_{n} \Bigg|_{\underset{\sim}{x} = \hat{\underset{\sim}{x}}^{-}(n)}$$

and

$$\theta(n) = E(\hat{\underset{\sim}{x}}^{+}(n))$$

where, J, G^{-}, G^{+}, Q and R are defined as before.

3.9 Effect of Sampling on E.K.F.

In order to adapt the extended Kalman filter, in this study, the measurements have to be taken at intervals of h_m. The first step in mechanising a Kalman filter on a digital computer is to use a suitable integration algorithm to numerically integrate the Kalman filter equations. Since the sampling rate was chosen to be 10 ms, then a simple forward difference method would do the job without the risk of instability and divergence associated with this type of integration. For accuracy reasons and also to give the filter time to catch up with the measurements, the algorithm routine is split into those where sampling the measurements at the rate $\frac{1}{h_m}$ and that of Kalman filter (time update

equation), $\frac{1}{h_I}$ which is higher than $\frac{1}{h_m}$. For a non-linear system the algorithm is as follows:

(i) MEASUREMENT UPDATE.

$$\hat{\underset{\sim}{x}}^{+}(n) = \hat{\underset{\sim}{x}}^{-}(n) + J(n)[\underset{\sim}{y}(n) - \underset{\sim}{g}(\hat{\underset{\sim}{x}}^{-}(n), \underset{\sim}{u}(n))] \qquad \text{-------- EQ.3.27}$$

$$G^{+}(n) = [I - J(n)C(n)]G^{-}(n)$$

(ii) TIME UPDATE at an instant a measurement is taken

$$\hat{\underset{\sim}{x}}^{-}(n+1) = \underset{\sim}{f}(\hat{\underset{\sim}{x}}^{+}(n), \underset{\sim}{u}(n)) + E(\hat{\underset{\sim}{x}}^{+}(n))S(n)R(n)^{-1}[\underset{\sim}{y}(n) - \underset{\sim}{g}(\hat{\underset{\sim}{x}}^{+}(n),\underset{\sim}{u}(n))]$$

$$\left.\begin{aligned} G^{-}(n+1) = {} & [\phi(n) - E(\hat{\underset{\sim}{x}}(n))S(n)R(n)^{-1}C(n)]\ G^{+}(n)\ . \\ & [\phi(n) - E(\hat{\underset{\sim}{x}}^{+}(n))S(n)R(n)^{-1}C(n)^{T}] + E(\hat{\underset{\sim}{x}}^{+}(n))\ . \\ & [Q(n) - S(n)R(n)^{-1}S(n)^{T}]E(\hat{\underset{\sim}{x}}^{+}(n)). \end{aligned}\right\} \text{- - - - - EQ.3.28}$$

(iii) TIME UPDATE between measurements

Between the measurement, equations S29 become;

$$\hat{\underset{\sim}{x}}^{-}(n+1) = \underset{\sim}{f}(\hat{\underset{\sim}{x}}^{+}(n),\underset{\sim}{u}(n))$$

$$G^{-}(n+1) = \phi(n)G^{+}(n)\phi(n)^{T} + \theta(n)Q(n)\theta(n)^{T} \qquad \text{- - - - - EQ.3.29}$$

where J(n) is set at zero. Therefore from the measurement update equations listed above;

$$\hat{\underset{\sim}{x}}(n) = \hat{\underset{\sim}{x}}^{-}(n)$$

$$G^{+}(n) = G^{-}(n)$$

and the time update is repeated until the next measurement arrives, i.e. h_{m/h_I} times. Also it must be noted that in S30 above;

$$\phi(n) = \left(\frac{\partial \underset{\sim}{f}}{\partial \underset{\sim}{x}}\right)_n \Bigg|_{\underset{\sim}{x}=\hat{\underset{\sim}{x}}^{+}(n)} \quad ; \quad C(n) = \left(\frac{\partial \underset{\sim}{g}}{\partial \underset{\sim}{x}}\right)_n \Bigg|_{\underset{\sim}{x}=\hat{\underset{\sim}{x}}^{+}(n)} . \qquad \text{--------- EQ.3.30}$$

and $\theta(n) = E(\hat{\underset{\sim}{x}}^{+}(n))$.

The flow diagram of Fig.3.4 illustrates the calculation sequence.

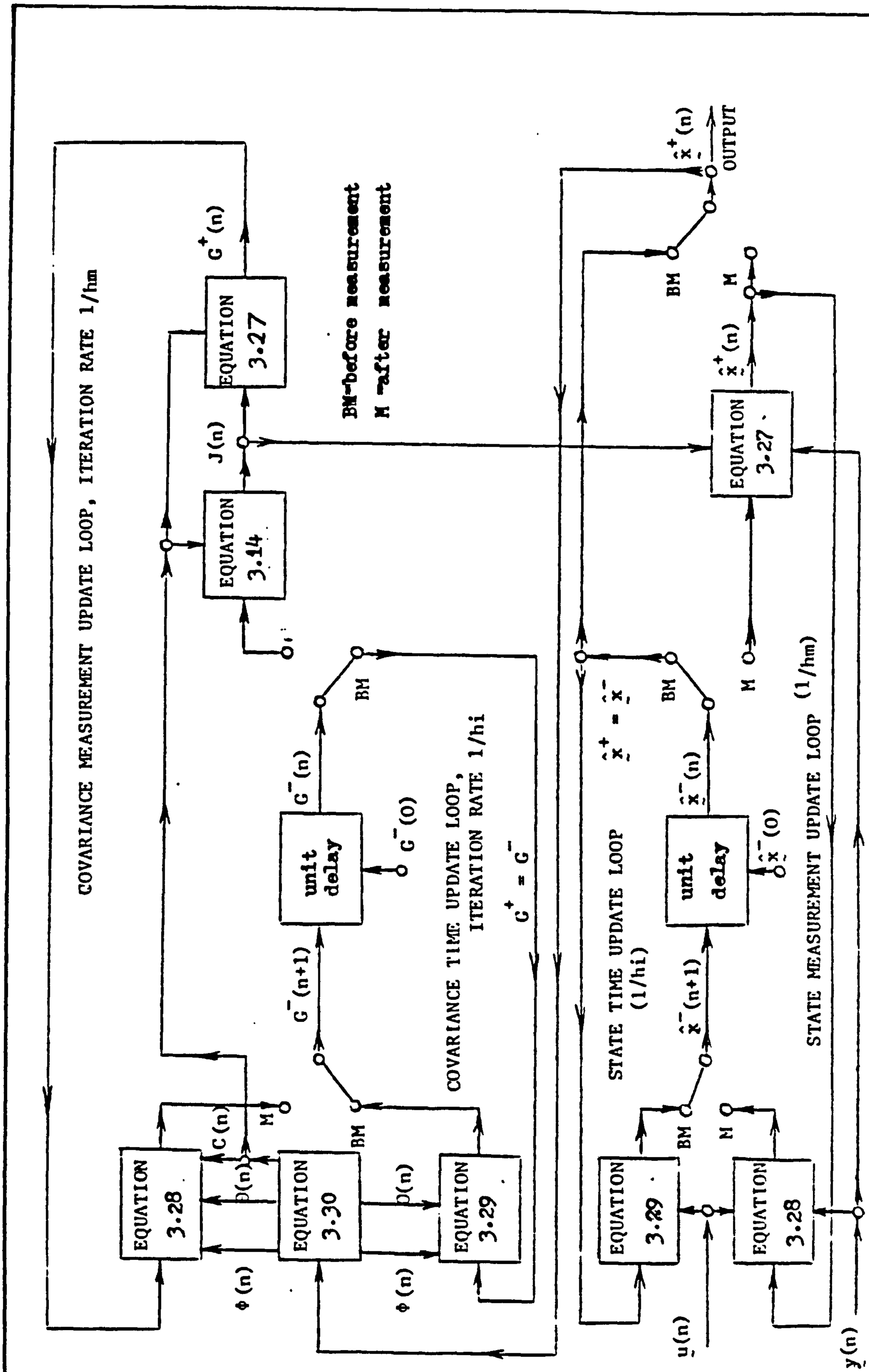

FIG. 3.4: FLOW DIAGRAM ILLUSTRATING TIE CALCULATION SEQUENCE

4. THE LINEARISED EQUATIONS OF MOTION FOR STRAIGHT SYMMETRIC FLIGHT

4.1 General Equations

For a body of fixed mass m, the laws of motion for an isolated and unconstrained rigid body state that,

$$\underline{F} = m \frac{d\underline{V}}{dt}$$

and $$\underline{G} = \frac{d\underline{h}}{dt} = \frac{d}{dt}\left[\int_{body} \underline{r} \times (\underline{\omega} \times \underline{r}) dm\right]$$

where $\underline{F}$ = resultant of all external forces

$\underline{G}$ = resultant of all the external moments about the C.G. of the body

$\underline{V}$ = linear velocity vector of C.G.

$\underline{h}$ = angular momentum of body.

Vectors $\underline{F}$, $\underline{G}$, $\underline{V}$ and $\underline{h}$ are measured relative to an inertial set of axes and the position vector $\underline{r}$ is measured with respect to the body axis as in Fig.4.1 below.

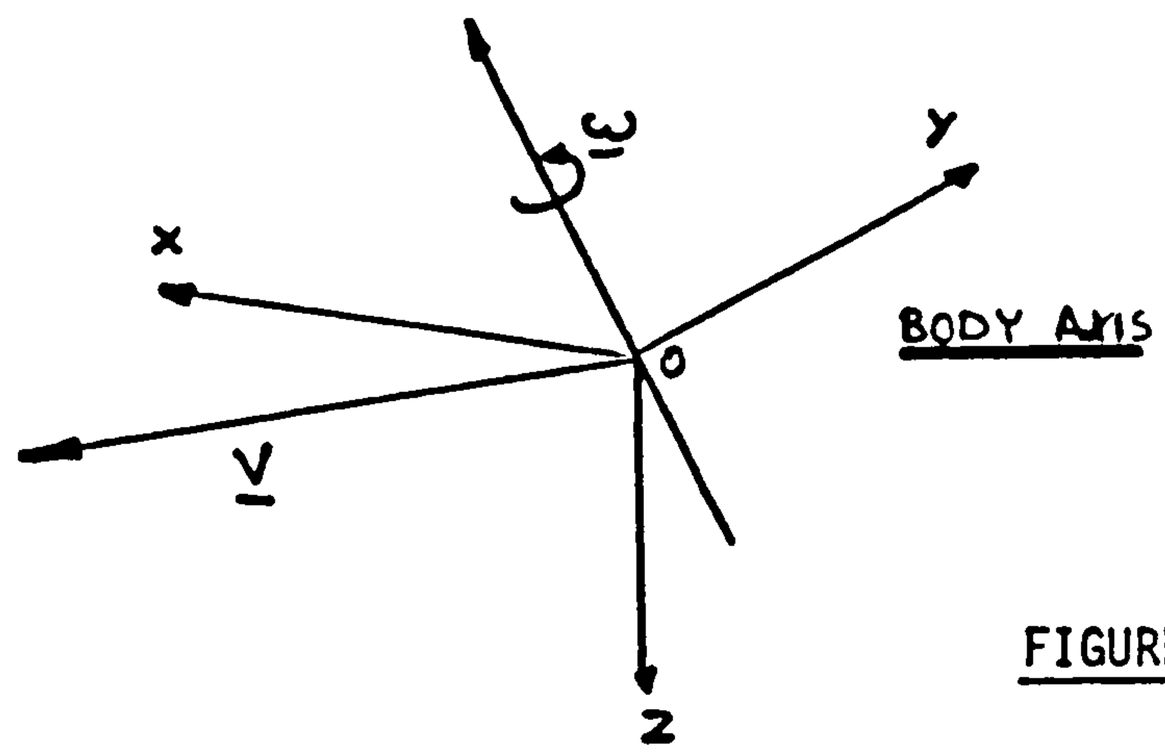

FIGURE 4.1

The vector components are defined as;

$$\underline{F} = X\underline{i} + Y\underline{j} + Z\underline{k}$$

$$\underline{V} = u\underline{i} + v\underline{j} + w\underline{k}$$

$$\underline{\omega} = p\underline{i} + q\underline{j} + r\underline{k}$$

$$\underline{h} = h_{xx}\underline{i} + h_{yy}\underline{j} + h_{zz}\underline{k}$$

$$\underline{G} = L\underline{i} + M\underline{j} + N\underline{k}$$

Now, according to the Coriolis Law which connects the rates of change of a vector as seen from non-rotating and rotating reference axes,

$$\frac{d\underline{V}}{dt} = \frac{\partial \underline{V}}{\partial t} + \underline{\omega} \times \underline{V}$$

$$\frac{d\underline{h}}{dt} = \frac{\partial \underline{h}}{\partial t} + \underline{\omega} \times \underline{h}$$

It can be shown therefore that,

$$\left.\begin{aligned} X &= m(\dot{u} + qw - rv) \\ Y &= m(\dot{v} + ru - pw) \\ Z &= m(\dot{w} + pv - qu) \\ L &= \dot{h}_{xx} + qh_{zz} - rh_{yy} \\ M &= \dot{h}_{yy} + rh_{xx} - ph_{zz} \\ N &= \dot{h}_{zz} + ph_{yy} - qh_{xx} \end{aligned}\right\} \quad \text{- - - - - EQ.4.1}$$

Also
$$h_{xx} = I_{xx}p - I_{xy}q - I_{xz}r$$
$$h_{yy} = -I_{yx}p + I_{yy}q - I_{yz}r$$
$$h_{zz} = -I_{zx}p - I_{zy}q + I_{z}r$$

where I_{xx}, I_{yy} etc. are the moments and products of inertia. For an aircraft with a longitudinal plane of symmetry,

$$I_{yz} = I_{zy} = I_{xy} = I_{yx} = 0 \quad \text{so that,}$$

$$\left.\begin{aligned} h_{xx} &= I_{xx}p - I_{xz}r \\ h_{yy} &= I_{yy}q \\ h_{zz} &= I_{zz}r - I_{zx}p \end{aligned}\right\} \quad \text{- - - - - EQ.4.2}$$

The orientation of the aircraft is defined as in Fig. 4.2

For a symmetric level flight, with small perturbations,

$$u = U_e + u' \quad , \quad v = 0 + v' \quad , \quad w = 0 + w'$$
$$p = 0 + p' \quad , \quad q = q' \quad , \quad r = r'$$
$$\phi = \phi' \quad , \quad \theta = \theta_e + \theta' \quad , \quad \psi = \psi'$$
$$X = X_e + X' \quad , \quad Y = Y' \quad , \quad Z = Z_e + Z'$$
$$L = L' \quad , \quad M = M' \quad , \quad N = N'$$

Where the subscript 'e' means equilibrium conditions. In combining the gravitational terms, aerodynamic terms representing the changes in the aerodynamic forces and moments which to the first order and for Strouhal number $\frac{\omega \ell}{U_e} < 0.02$ can be presented as:

$$X_{aero} = u\left(\frac{\partial X}{\partial u}\right)_{X=X_e} + v\left(\frac{\partial X}{\partial v}\right)_{X=X_e} \quad \ldots\ldots + \zeta\left(\frac{\partial X}{\partial \zeta}\right)_{X=X_e} \quad \text{etc.,}$$

into the equations of motion for a rigid body derived earlier and omission of the non-linear terms such as 'wq', it can be shown that the equations describing the small perturbation motion about a straight symmetric flight path in linearised form, neglecting the trust variation are,

$$\left.\begin{aligned}
m(\dot{u} + qw + \theta q Cos\theta_e) &= uX_u + wX_w + qX_q + \eta X_\eta \\
m(\dot{v} + rU_e - pw - \phi g Cos\theta_e - \psi g Sin\theta_e) &= vY_v + pY_p + rY_r + \xi Y_\xi + \zeta Y_\zeta \\
m(\dot{w} - qU_e + \theta g Sin\theta_e) &= uZ_u + wZ_w + \dot{w}Z_{\dot{w}} + qZ_q + \eta Z_\eta \\
I_{xx}\dot{p} - I_{xz}\dot{r} &= vL_v + pL_p + rL_r + \xi L_\xi + \zeta L_\zeta \\
I_{yy}\dot{q} &= uM_u + wM_w + \dot{w}M_{\dot{w}} + qM_q + \eta M_\eta \\
I_{zz}\dot{r} - I_{xz}\dot{p} &= vN_v + pN_p + rN_r + \xi N_\xi + \zeta N_\zeta
\end{aligned}\right\} \text{EQ.4.3}$$

$\dot{\phi} = p$

$\dot{\theta} = q$

$\dot{\psi} = r$ where u, w, p, q and r, represent deviations from the equilibrium conditions.

It is usually convenient to reduce these equations to a concise form by dividing the force equations through by mass and each moment equation by the appropriate moment of inertia. The set of equations above uncouple into two groups provided airframe is typically symmetrical and coupling terms are negligible, as follows:

$$\begin{bmatrix} \dot{u} \\ \dot{w} \\ \dot{q} \\ \dot{\theta} \end{bmatrix} = \begin{bmatrix} X_u & X_w & (w+X_q)q & q_1 \\ Z_u & z_{\dot{w}}D & (U_e+Z_q)q & q_2 \\ m_u & (m_{\dot{w}}D+m_w) & m_q & 0 \\ 0 & 0 & 1 & 0 \end{bmatrix} \begin{bmatrix} u \\ w \\ q \\ e \end{bmatrix} + \begin{bmatrix} X_\eta \\ Z_\eta \\ m_\eta \end{bmatrix} \eta \qquad \text{EQ.4.4}$$

where $D = \frac{d}{dt}$, $X_u = \frac{X_U}{m}$, $m_u = \frac{M_w}{Iyy}$, etc.,

Equations 4.4 represent the linearise equations of longitudinal symmetric and level flight. The second group of equations representing the lateral motion is:

$$\begin{bmatrix} \dot{v} \\ \dot{p} \\ \dot{r} \\ \dot{\phi} \\ \dot{\psi} \end{bmatrix} = \begin{bmatrix} y_v & (w_e+y_p) & (-U_e+y_r) & g_1 & g_2 \\ \ell_v & (D+\ell_p) & (e_xD+\ell_r) & 0 & 0 \\ n_v & (e_2+n_p) & (D+n_r) & 0 & 0 \\ 0 & 1 & 0 & 0 & 0 \\ 0 & 0 & 1 & 0 & 0 \end{bmatrix} \begin{bmatrix} v \\ p \\ r \\ \phi \\ \psi \end{bmatrix} + \begin{bmatrix} y_\xi & y_\zeta \\ \ell_\xi & \ell_\zeta \\ n_\xi & n_\zeta \end{bmatrix} \begin{bmatrix} \xi \\ \zeta \end{bmatrix} \qquad \text{EQ.4.5}$$

where

$$e_x = \frac{I_{zx}}{I_{xx}} \quad , \quad e_z = \frac{I_{zx}}{I_{zz}}$$

and $$D = \frac{d}{dt}$$

Equations 4.4 and 4.5 represent the longitudinal and lateral motion of an aircraft in symmetric and level flight in six degrees of freedom and are therefore inapplicable to the dynamic model. Therefore, they must be modified to represent the small perturbation symmetric and level flight of the dynamic model on the test rig.

4.2 Longitudinal Equations of Motion for the Dynamic Model

As far as the wind tunnel simulations are concerned the model is suspended on the test rig so that the X-axis is supressed thereby allowing the drag equation to be removed from the equations 4.4. Also the air velocity in the tunnel is constant during a test run so the terms describing the perturbations in U can be removed. Thus the longitudinal equations of motion reduce to:

$$\begin{bmatrix} \dot{w} \\ \dot{q} \\ \dot{\theta} \end{bmatrix} = \begin{bmatrix} z_w & z_q+U_e & 0 \\ m_w & m_q & 0 \\ 0 & 1 & 0 \end{bmatrix} \begin{bmatrix} w \\ q \\ \theta \end{bmatrix} \begin{bmatrix} w \\ q \\ \theta \end{bmatrix} + \begin{bmatrix} z_\eta \\ m_\eta \end{bmatrix} \eta \qquad \text{EQ.4.6}$$

which is of the form

$$\underline{\dot{X}} = A\underline{X} + B\underline{U}$$

The fact that the model has to travel up and down a vertical support rod does not alter Equation 4.6 since the only extra force acting would be the small friction force caused by the linear bearing of the gimbal system, the direction of which is perpendicular to and through the C.G. Also, at this stage, z_q was assumed to be small and was hence removed from Equation 4.5.

The characteristic equation of this short period motion can be realised from

$$A_{S.P.} = \begin{bmatrix} z_w & U_e \\ m_w & m_q \end{bmatrix}$$

where the third row and column have been removed since they do not affect any other state variable. The characteristic equation is given by

$$\det|sI - A| = 0$$

i.e. $$s^2 + (-z_w - m_q)s + (z_w m_q - m_w U_e) = 0$$

which has the approximate solution

$$s = -\frac{k_3}{2} \pm i\sqrt{k - \frac{k_3^2}{4}}$$

where

$$k_2 = (z_w m_q - m_w U_e)$$

and $$k_3 = (-z_w - m_q)$$

The damping index is given by,

$$-\zeta_D = -\frac{k_3}{2}$$

and the frequency by,

$$\nu = \sqrt{k_2 - \frac{k_3^2}{4}} = \sqrt{\omega_n^2 - \zeta_D^2} = \omega_n\sqrt{1 - \zeta_{REL}^2}$$

where ζ_{REL} is the relative damping index and for $\zeta_{REL} = 1$ the motion is critically damped and also ω_n is the natural frequency given by,

$$\omega_n = \sqrt{k_2}$$

4.2.1 Effect of Changes in Stability Derivatives on Short Period Motion

It can be shown from section 4.1 that

$$\omega_n = \sqrt{z_w m_q - m_w U_e}$$

$$\zeta_D = \frac{(- z_w - m_q)}{2}$$

The effect of the parameters are often shown, either one or two at a time, in the form of stability diagrams.The single most important factor determining the characteristics of longitudinal oscillations is the position of the C.G. and its effect on the static margin. The effects of C.G. movement are often shown through the derivative m_w. Fig.4.1represents the stability diagram for the short period motion.

Whilst there is a complex pair of roots, larger values of $|m_w|$ give larger frequencies but do not alter the damping. When C.G. is forward of N.P., m_w is negative which corresponds to a positive static margin stick-fixed. Further, when m_w (or static margin) becomes small so that $\frac{k_3^2}{4} > k_2$, real roots are obtained which initially give a subsidence. However, when k_2 becomes negative or in other words the static margin is negative, a divergent root is obtained i.e. $z_w m_q - U_e m_w < 0$. This is the condition for dynamic instability. It must be noted that z_w and m_q are always negative. It should be noted that movement of the C.G. behind the N.P. does not necessarily coincide with any rapid deterioration in the aircraft's handling qualities and with reasonable care, an aircraft can still be flown under these conditions.

For a satisfactorily damped oscillation, relative damping $\zeta_{rel} > 0.11$ which in other words means that the oscillation should not take more than one cycle to damp to half amplitude. But in the primary operating zone of the aircraft, ζ_{rel} should be greater than 0.25 or 0.36, depending on the role of the aircraft. (see Ref.36)

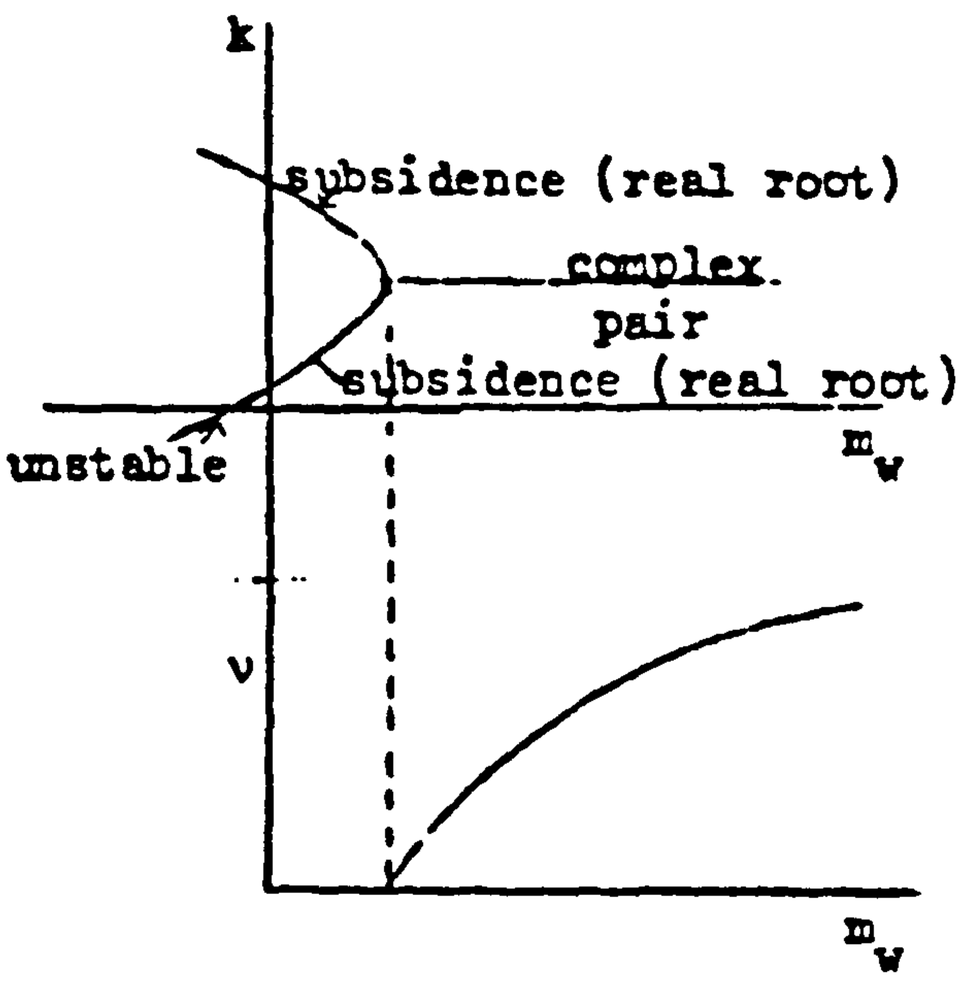

Short period motion

Whilst there is a complex pair of roots larger values of m_w give larger frequencies but do not alter the damping.

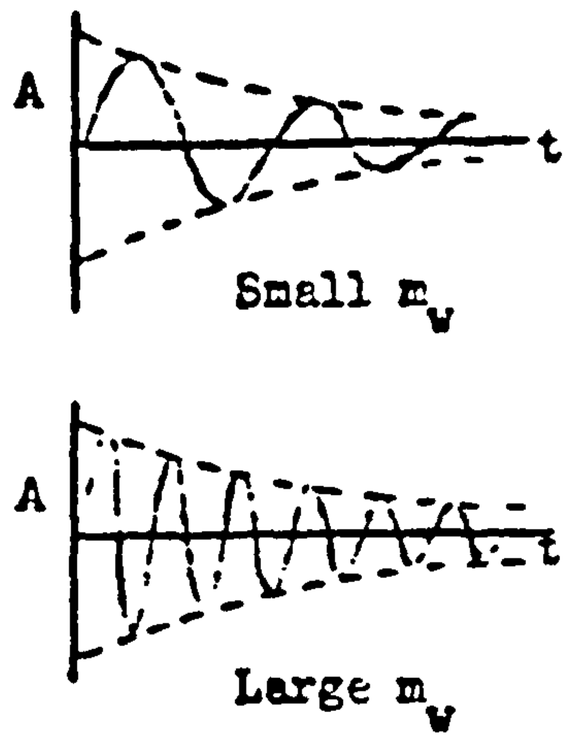

FIGURE 4.2 ONE PARAMETER STABILITY DIAGRAMS FOR THE LONGITUDINAL MOTION

4.3 Lateral Equations of Motion for the Dynamic Model

Equations 4.5 can be modified to represent the motion in the dynamic rig in the wind tunnel. The dynamic model is free to rotate in yaw but there is no translation in y-direction so the aerodynamic sideforces and gravity components are balanced by the support system. However, the fact that $\frac{dy}{dt} = 0$ implies that,

$$\dot{v} + U_e r = 0$$

since the model is locked in position during lateral wind tunnel experiments, i.e. $w_e = 0$.

Therefore the lateral equations of motion with respect to the wind-tunnel simulations for steady horizontal datum flight would become:

$$\begin{bmatrix} \dot{v} \\ \dot{p} \\ \dot{r} \\ \dot{\phi} \end{bmatrix} = \begin{bmatrix} 0 & 0 & -U_e & 0 \\ \ell_v & \ell_p & \ell_r & 0 \\ n_v & n_p & n_r & 0 \\ 0 & 1 & 0 & 0 \end{bmatrix} \begin{bmatrix} v \\ p \\ r \\ \phi \end{bmatrix} + \begin{bmatrix} 0 & 0 \\ \ell_\xi & \ell_\zeta \\ n_\xi & n_\zeta \end{bmatrix} \begin{bmatrix} \xi \\ \zeta \end{bmatrix} \qquad \text{EQ.4.7}$$

This is of the form

$$\dot{\underline{X}} = A\underline{X} + B\underline{U}$$

and therefore the characteristic polynomial can be realised from

$$A = \begin{bmatrix} 0 & 0 & -U_e \\ \ell_v & \ell_p & \ell_r \\ n_v & n_p & n_r \end{bmatrix}$$

where the fourth row and column have been removed since they do not affect any other state variable. The characteristic polynomial is given by:

$$\det |sI - A| = 0$$

$$\text{i.e.} \quad s^3 + s^2(-n_r - \ell_p) + (\ell_p n_r - \ell_r n_p + n_v U_e)s + U_e(\ell_v n_p - \ell_p n_v) = 0 \qquad \text{EQ.4.8}$$

One way of determining the stability is through the Routh-Hurwitz tests. These would lead the following stability criteria.

(i) All coefficients of Eq. 4.8 must be positive

(ii) $J_2J_1 - J_0J_3 > 0$

where

$$J_0 = 1$$

$$J_1 = (-n_r - \ell_p)$$

$$J_2 = (\ell_p n_r - \ell_r n_p - n_v U_e)$$

$$J_3 = U_e(\ell_v n_p - \ell_p n_v)$$

Therefore, provided the above conditions are satisfied, the aircraft would be stable in the semi-free flight comprising the previously defined four degrees of freedom. As far as this study is concerned, short period oscillations induced by rudder or ailerons are of interest. Hence, other lateral motions are not considered here. For this purpose, it was assumed that the lateral derivatives ℓ_p and ℓ_v would tend to zero for short period oscillations. The characteristic equation 4.8 then factorises into

$$(s - \ell_p)(s^2 - n_r s + U_e n_v)$$

or in other words, roll subsidence and dutch roll oscillations. Therefore, rudder and aileron inputs were chosen to excite oscillations rather than roll subsidence.

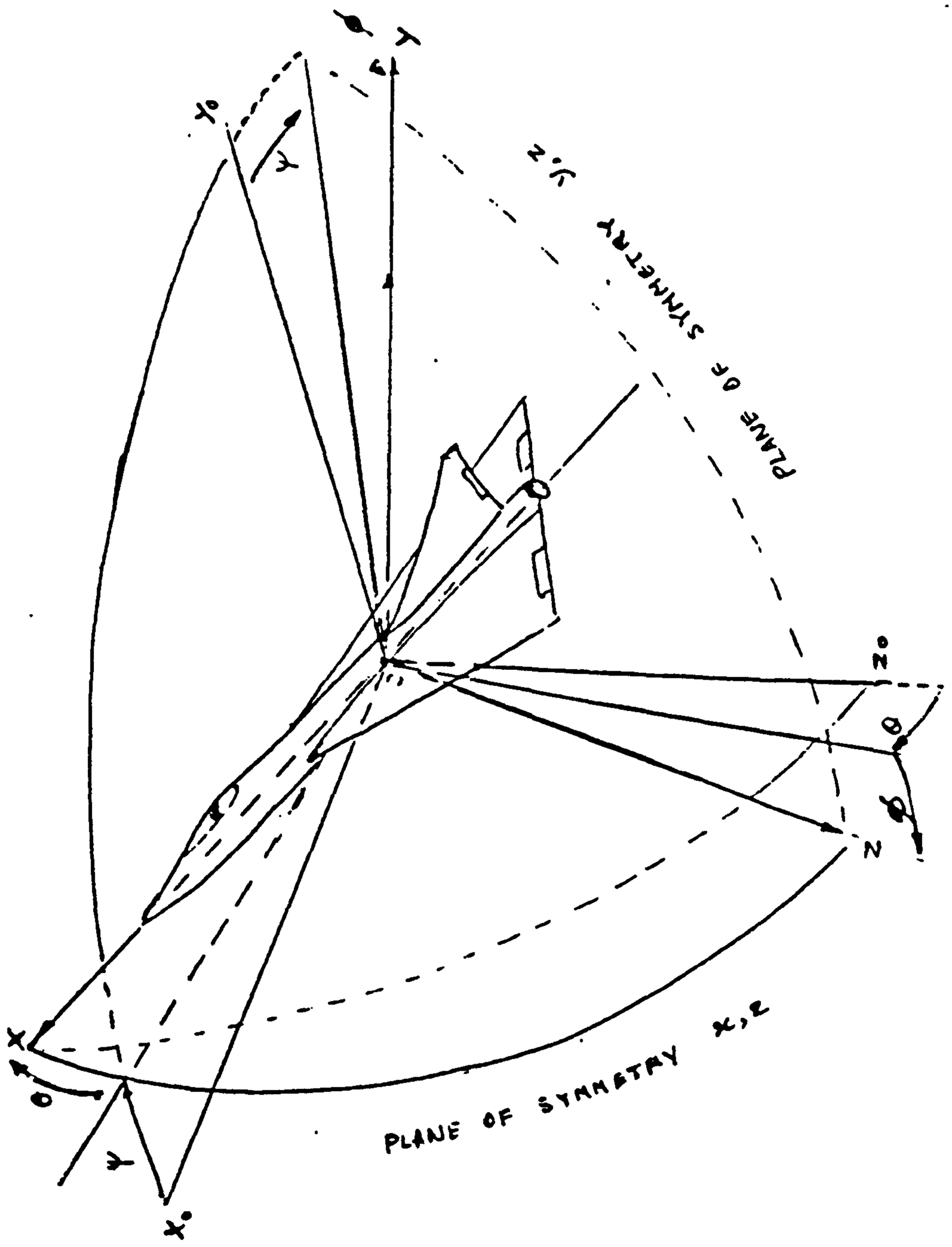

FIGURE 4.3 AIRCRAFT ATTITUDE WITH RESPECT TO A SET OF BODY-AXIS

5. APPLICATION OF EXTENDED KALMAN FILTER TO LONGITUDINAL MOTION

As it was described in Section 3, the E.K.F. can be used as a tool in the estimation of states in a non-linear system. In this section the longitudinal equations of motion given by Eq. 4.6 represent the mathematical model of the system. Where it is required to estimate the stability derivatives which appear as coefficients. Although in reality the stability derivatives are time invariant, as far as the estimation process is concerned their values vary from one iteration to the next until they approach a steady state value after a number of iterations depending on the filter convergence. Therefore the longitudinal equations of motion given by Eq. 4.6 are assumed to be non-linear and given by:

$$\dot{X}_1 = X_4.X_1 + U_e.X_2 + X_7.n$$
$$\dot{X}_2 = X_5.X_1 + X_6.X_2 + X_8.n \qquad \text{EQ.5.1}$$
$$\dot{X}_3 = X_2$$

where,

$$X_1 = w \ , \quad X_2 = q \ , \quad X_3 = \theta \ ,$$
$$X_4 = z_w \ , \quad X_5 = m_w \ , \quad X_6 = m_q \ ,$$
$$X_7 = z_n \ , \quad X_8 = m_n \ .$$

Further, let

$$\dot{X}_4 = w_1 = z_w \ , \quad \dot{X}_5 = w_2 = \dot{m}_w$$
$$\dot{X}_6 = w_3 = \dot{m}_q \ , \quad \dot{X}_7 = w_4 = \dot{z}_n$$
$$\dot{X}_8 = w_5 = \dot{m}_n$$

where $w^T = [w_1 \ w_2 \ w_3 \ w_4 \ w_5]$ is a stationary white noise vector.

Thus the general form of the state equations becomes:

$$\dot{\underset{\sim}{X}} = f(\underset{\sim}{X},\underset{\sim}{U}) + E(\underset{\sim}{w}) \quad \text{or} \ ,$$

$\dot{\underset{\sim}{X}} = \underset{\sim}{f}(\underset{\sim}{X},\underset{\sim}{U}) + E(\underset{\sim}{w})$ becomes

$$\begin{bmatrix} \dot{X}_1 \\ \dot{X}_2 \\ \dot{X}_3 \\ \dot{X}_4 \\ \dot{X}_5 \\ \dot{X}_6 \\ \dot{X}_7 \\ \dot{X}_8 \end{bmatrix} = \begin{bmatrix} X_4X_1 + U_eX_2 + X_7.\eta \\ X_5X_1 + X_6X_2 + X_8.\eta \\ 0 + X_2 \\ 0 \\ 0 \\ 0 \\ 0 \\ 0 \end{bmatrix} + \begin{bmatrix} 0 & 0 & 0 & 0 & 0 \\ 0 & 0 & 0 & 0 & 0 \\ 0 & 0 & 0 & 0 & 0 \\ 1 & 0 & 0 & 0 & 0 \\ 0 & 1 & 0 & 0 & 0 \\ 0 & 0 & 1 & 0 & 0 \\ 0 & 0 & 0 & 1 & 0 \\ 0 & 0 & 0 & 0 & 1 \end{bmatrix} \begin{bmatrix} w_1 \\ w_2 \\ w_3 \\ w_4 \\ w_5 \end{bmatrix} \qquad \text{EQ. 5.2}$$

Assuming that the motion sensors produce an output which is contaminated by a stationary and white noise vector $\underset{\sim}{V}$, then the general form of the output equation is:

$$\underset{\sim}{Y} = g(\underset{\sim}{X},\underset{\sim}{U}) + \underset{\sim}{V}$$

Since the function $g(\underset{\sim}{X},\underset{\sim}{U})$ is linear in this case, the output equation in matrix form reduces to:

$$\underset{\sim}{Y} = C\underset{\sim}{X} + \underset{\sim}{V}$$

or,

$$\begin{bmatrix} Y_1 \\ Y_2 \\ Y_3 \end{bmatrix} = \begin{bmatrix} 1 & 0 & 0 & 0 & 0 & 0 & 0 & 0 \\ 0 & 1 & 0 & 0 & 0 & 0 & 0 & 0 \\ 0 & 0 & 1 & 0 & 0 & 0 & 0 & 0 \end{bmatrix} \begin{bmatrix} X_1 \\ X_2 \\ X_3 \\ X_4 \\ X_5 \\ X_6 \\ X_7 \\ X_8 \end{bmatrix} + \begin{bmatrix} V_1 \\ V_2 \\ V_3 \end{bmatrix} \qquad \text{EQ. 5.3}$$

where Y_1 = derived vertical velocity

Y_2 = derived pitch rate

Y_3 = attitude sensor

The outputs Y_1, Y_2 and Y_3 are obtained from the mathematical model of system in the case of computer simulations, or derived from the motion sensors in the case of dynamic wind tunnel tests.

The continuous Kalman Filter equations are in general form

$$\dot{\hat{\underset{\sim}{X}}} = f(\hat{\underset{\sim}{X}}, \underset{\sim}{U}) + P(\underset{\sim}{Y} - C\hat{\underset{\sim}{X}})$$

$$\hat{\underset{\sim}{Y}} = \hat{\underset{\sim}{X}}$$

The above equations can be represented in this case as

$$\begin{bmatrix} \dot{\hat{X}}_1 \\ \dot{\hat{X}}_2 \\ \dot{\hat{X}}_3 \\ \dot{\hat{X}}_4 \\ \dot{\hat{X}}_5 \\ \dot{\hat{X}}_6 \\ \dot{\hat{X}}_7 \\ \dot{\hat{X}}_8 \end{bmatrix} = \begin{bmatrix} \hat{X}_4\hat{X}_1 + U_e\hat{X}_2 + \hat{X}_7 \cdot \eta \\ \hat{X}_5\hat{X}_1 + \hat{X}_6\hat{X}_2 + \hat{X}_8 \cdot \eta \\ 0 + \hat{X}_2 \\ 0 \\ 0 \\ 0 \\ 0 \\ 0 \end{bmatrix} + \begin{bmatrix} P_{11} & P_{12} & P_{13} \\ P_{21} & P_{22} & P_{23} \\ P_{31} & P_{32} & P_{33} \\ P_{41} & P_{42} & P_{43} \\ P_{51} & P_{52} & P_{53} \\ P_{61} & P_{62} & P_{63} \\ P_{71} & P_{72} & P_{73} \\ P_{81} & P_{82} & P_{83} \end{bmatrix} \begin{bmatrix} \underset{\sim}{Y} - C\hat{\underset{\sim}{X}} \end{bmatrix} \qquad \text{EQ. 5.4}$$

$$\begin{bmatrix} \hat{Y}_1 \\ \hat{Y}_2 \\ \hat{Y}_3 \end{bmatrix} = \begin{bmatrix} \hat{X}_1 \\ \hat{X}_2 \\ \hat{X}_3 \end{bmatrix} \qquad \text{EQ. 5.5}$$

Equation 5.5 above can be written in the discrete form using a forward difference algorithm,

$$\text{i.e. } \dot{\underset{\sim}{X}} = \frac{d\underset{\sim}{X}}{dt} \simeq \frac{\underset{\sim}{X}(n+1) - \underset{\sim}{X}(n)}{h} \qquad \text{----- EQ. 5.6}$$

Applying this to the equations above:

$$\underset{\sim}{X}(n+1) = \underset{\sim}{f}(\underset{\sim}{X}(n), \underset{\sim}{U}(n)) + E\underset{\sim}{w}(n)$$

$$\underset{\sim}{Y}(n) = C\underset{\sim}{X}(n) + \underset{\sim}{V}(n)$$

The function $\underset{\sim}{f}(\underset{\sim}{X}(n), \underset{\sim}{U}(n))$ is given by

$$\left.\begin{aligned}
f_1(\underset{\sim}{X}(n), \underset{\sim}{U}(n)) &= X_1(n) + h(X_4(n).X_1(n) + U_e X_2(n) + X_7(n).n) \\
f_2(\underset{\sim}{X}(n), \underset{\sim}{U}(n)) &= X_2(n) + h(X_5(n).X_1(n) + X_6(n).X_2(n) + X_8(n).n) \\
f_3(\underset{\sim}{X}(n), \underset{\sim}{U}(n)) &= X_3(n) + h.X_2 \\
f_4(\quad " \quad " \quad) &= X_4(n) \\
f_5(\quad " \quad " \quad) &= X_5(n) \\
f_6(\quad " \quad " \quad) &= X_6(n) \\
f_7(\quad " \quad " \quad) &= X_7(n) \\
f_8(\quad " \quad " \quad) &= X_8(n)
\end{aligned}\right\} \text{--- EQ. 5.7}$$

$$C = \begin{bmatrix} 1 & 0 & 0 & 0 & 0 & 0 & 0 & 0 \\ 0 & 1 & 0 & 0 & 0 & 0 & 0 & 0 \\ 0 & 0 & 1 & 0 & 0 & 0 & 0 & 0 \end{bmatrix}, \quad E = \begin{bmatrix} 0 & 0 & 0 & 0 & 0 \\ 0 & 0 & 0 & 0 & 0 \\ 0 & 0 & 0 & 0 & 0 \\ h & 0 & 0 & 0 & 0 \\ 0 & h & 0 & 0 & 0 \\ 0 & 0 & h & 0 & 0 \\ 0 & 0 & 0 & h & 0 \\ 0 & 0 & 0 & 0 & h \end{bmatrix}$$

Now, consider the model of the F.S.W. aircraft. It has four degrees of freedom and its longitudinal motion is expressed by the following output parameters which are measured directly or derived from measured quantities.

$$\text{Output vector} = \begin{bmatrix} \dot{w} \\ q \\ \theta \end{bmatrix}$$

Therefore, there is no need to simulate the equations of motion and the above output after being discretized through an interface can be stored in computer at each sampling instant and used in the Kalman Filter algorithm given below.

5.1 Kalman Filter Algorithm

The split extended Kalman Filter equations are:

Given the following initial values,
$\hat{\underset{\sim}{X}}(0)$, $G(0)$.

Then

$$J(n) = G^{-}(n).\underset{\sim}{C}^{T}\left[\underset{\sim}{R} + \underset{\sim}{C}.G^{-}(n)\underset{\sim}{C}^{T}\right]^{-1} \qquad \text{- - - - -} \quad \text{EQ. 5.8}$$

This can be used in the following equations to give a better estimate of the states

$$\hat{\underset{\sim}{X}}^{+}(n) = \hat{\underset{\sim}{X}}^{-}(n) + J(n)\left[\underset{\sim}{Y}(n) - C\hat{\underset{\sim}{X}}^{-}(n)\right]$$

$$G^{+}(n) = \left[I - J(n)C\right]G^{-}(n)$$

Then

$$\hat{\underset{\sim}{X}}^{-}(n+1) = \underset{\sim}{f}(\hat{\underset{\sim}{X}}^{+}(n), \underset{\sim}{U}(n))$$

$$\underset{\sim}{G}^{-}(n+1) = \phi(n)G^{+}(n)\phi^{T}(n) + EQE^{T}$$

After which let

$$\hat{\underset{\sim}{X}}^{-}(n) \quad = \hat{\underset{\sim}{X}}^{-}(n+1)$$

$$G^{-}(n) \quad = G^{-}(n+1)$$

and we go back to calculate the gain matrix $\underset{\sim}{J}(n)$ from 5.3and go through the loop again.

5.2 The state transition matrix.

The state transition matrix is given by:

$$\phi(n) = \left[\frac{\partial \underset{\sim}{f}(\underset{\sim}{X}(n), \underset{\sim}{U}(n)}{\partial \underset{\sim}{X}(n)}\right]_n \qquad \text{or,}$$

With reference to equations 5.?

$$\phi(n) = \begin{bmatrix} 1 + h.X_4(n) & h.U_e & 0 & h.X_1(n) & 0 & 0 & h.n & 0 \\ h.X_5(n) & 1 + h.X_6(n) & 0 & 0 & h.X_1(n) & h.X_2(n) & 0 & h.n \\ 0 & h & 1 & 0 & 0 & 0 & 0 & 0 \\ 0 & 0 & 0 & 1 & 0 & 0 & 0 & 0 \\ 0 & 0 & 0 & 0 & 1 & 0 & 0 & 0 \\ 0 & 0 & 0 & 0 & 0 & 1 & 0 & 0 \\ 0 & 0 & 0 & 0 & 0 & 0 & 1 & 0 \\ 0 & 0 & 0 & 0 & 0 & 0 & 0 & 1 \end{bmatrix} \qquad \text{EQ.5.9}$$

5.3 Estimation of white noise intensities

The bandwidth is defined in general sense as the frequency over which the system will have an output g(t) approximately equal to the desired output, i(t), see Ref. 5.

It was assumed that process and measurement noise vectors $\underset{\sim}{W}$ and $\underset{\sim}{V}$ were represented stationary white noise sources with zero mean, in the sense that the spectral density of these noise sources are constant over a certain range of frequency. Fig. 5.1 shows a first order filter with a cut-off frequency ω_c chosen to generate the white noise w_i over the required bandwidth. The input to this filter is the white noise intensity q_i and its transfer function given by:

$$F(s) = \frac{1}{1 + \frac{s}{\omega_c}} \qquad \text{EQ. 5.10}$$

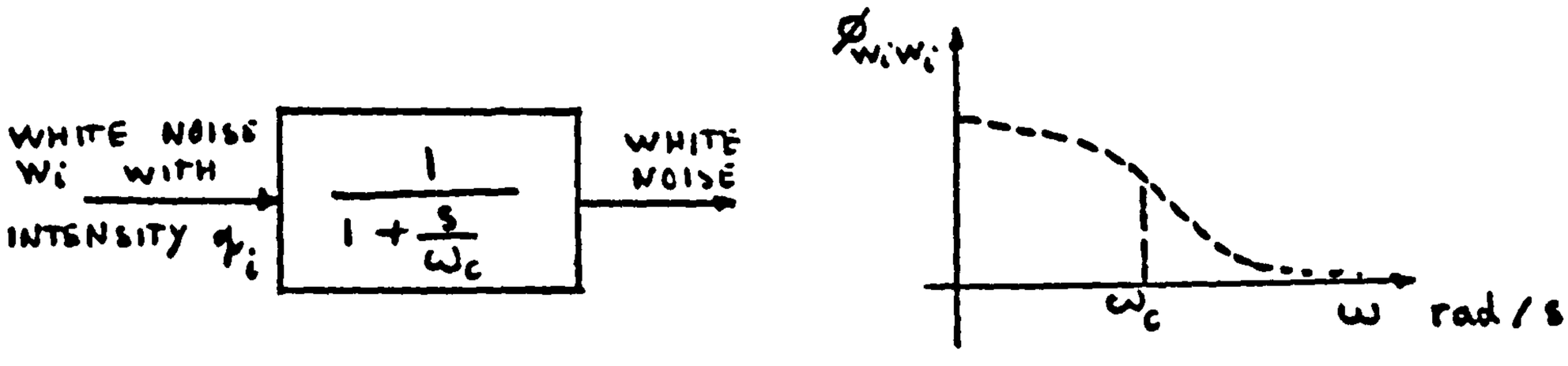

FIGURE 5.1. First Order Filter for the White Noise Generation

5.3.1 Signal Sampling

The sampling theorem states that:

> "A continuous signal can be represented completely by, and reconstructed from, a set of instantaneous measurements or samples of its voltage which are made at equally spaced times. The interval between such samples must be less than one-half the period of the highest frequency component in the signal."

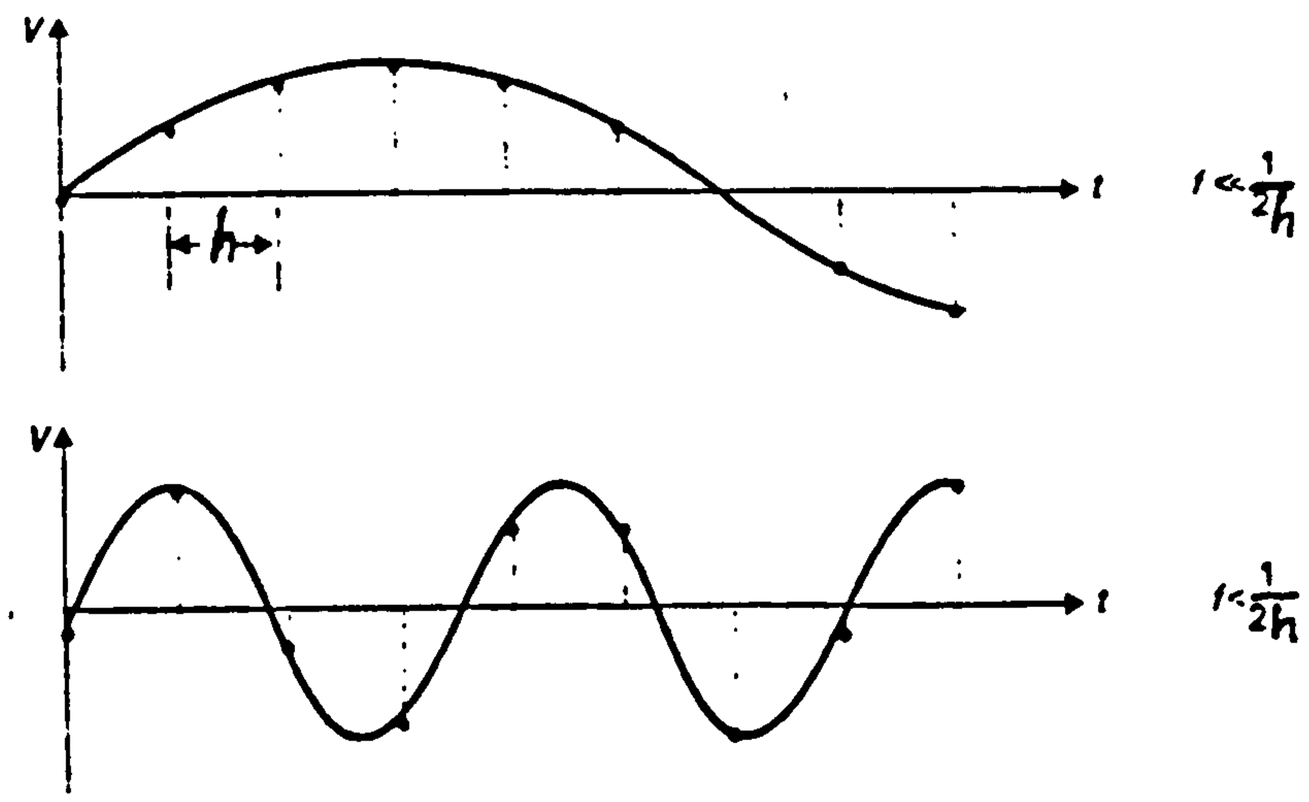

FIGURE 5.2 Effect of Sampling Rate on the Signal Representation

From the definition of the sampling theorem above, if the highest frequency is taken to be f_c then,

$$f_c = \frac{1}{T}$$

where T is the period of the highest frequency component of the signal and can be presented as,

$$T = 2nh$$

where n is the number of samples and h the sampling interval.

Thus, bandwidth

$$f_c = \frac{1}{2nh}$$

In the present application, convergent transient responses are of interest and in addition the response signals need to be differentiated numerically in order to obtain the time rates of change. Therefore, a smooth numerical variation of the signal is needed which calls for a high sampling rate.

5.4 Calculation of Covariance Matrices, R and Q

For the system under consideration the process measurement noise vectors assumed white are:

$$\underset{\sim}{w}^T = [w_1, w_2, w_3, w_4, w_5]$$

$$\underset{\sim}{v}^T = [v_1, v_2, v_3]$$

The process noise covariance matrix Q is given by

$$E(\underset{\sim}{w}\underset{\sim}{w}^T) = Q\delta \qquad \delta = \text{delta function}$$

where E means the expected value which would result if the measurements matched the expected distribution (assumed Gaussian) perfectly.

The elements of both $\underset{\sim}{w}^T$ and $\underset{\sim}{v}^T$ are assumed uncorrelated. i.e. $E(w_1 w_2)$, etc = 0.0

$$\therefore E(\underset{\sim}{w}\underset{\sim}{w}^T) = E\begin{bmatrix} w_1^2 & 0 & 0 & 0 & 0 \\ 0 & w_2^2 & 0 & 0 & 0 \\ 0 & 0 & w_3^2 & 0 & 0 \\ 0 & 0 & 0 & w_4^2 & 0 \\ 0 & 0 & 0 & 0 & w_5^2 \end{bmatrix} = Q$$

From Fig. 5.1 the white noise w_i produces a spectral density $\phi_{w_i.w_i}$ over the bandwidth specified by ω_c. From Ref. 5, the mean square value of a stationary zero-mean white noise is related to its intensity q_i by:

$$\text{mean square value} = E(w_i)^2 = \frac{C_o^2}{2d_o d_i} \cdot q_i \quad (i = 1....5) \qquad \text{EQ.5.11}$$

It can be shown that the values of the parameters C_o, d_o and d_i are related to the transfer function of the first order filter of Fig. 5.1 by:

$$C_o = 1$$

$$d_o = 1$$

$$d_i = \frac{1}{\omega_c}$$

Now, assume that $E(w_i)^2$ can be presented as the root mean square error e_i of the respective state then Eq. 5.11 becomes:

$$q_i = \frac{2}{\omega_c}.e_i^2 = \frac{2}{2\pi f_c}.e_i^2 \qquad \text{or,}$$

$$q_i = \frac{2nh}{\pi}.e_i^2 \qquad (i = 1,.....,5) \qquad \text{EQ. 5.12}$$

Equation 5.12 relates the root mean square errors of the respective states to be identified, to the diagonal elements of the Q matrix. In the same manner the diagonal elements of the R matrix are given by:

$$r_j = \frac{2nh}{\pi}.e_j^2$$

where e_j represents the root mean square error in the output states. For the purposes of the present study the errors in w, q and θ e_j were assumed to be 1% of the maximum attainable values of the output states, and for e_i, 10% of the parameters to be identified, namely, z_w, m_w, m_q, z_η and m_η.

5.5 Initial Experiments

In order to test and verify the parameter identification process based on the extended Kalman filter, a computer program was written incorporating the above algorithms. Verification of the parameter identifiability was performed according to the block diagram shown in Fig. 5.3. For the purposes of this verification exercise, the A/C was modelled using the advanced continuous simulation language (ACSL).

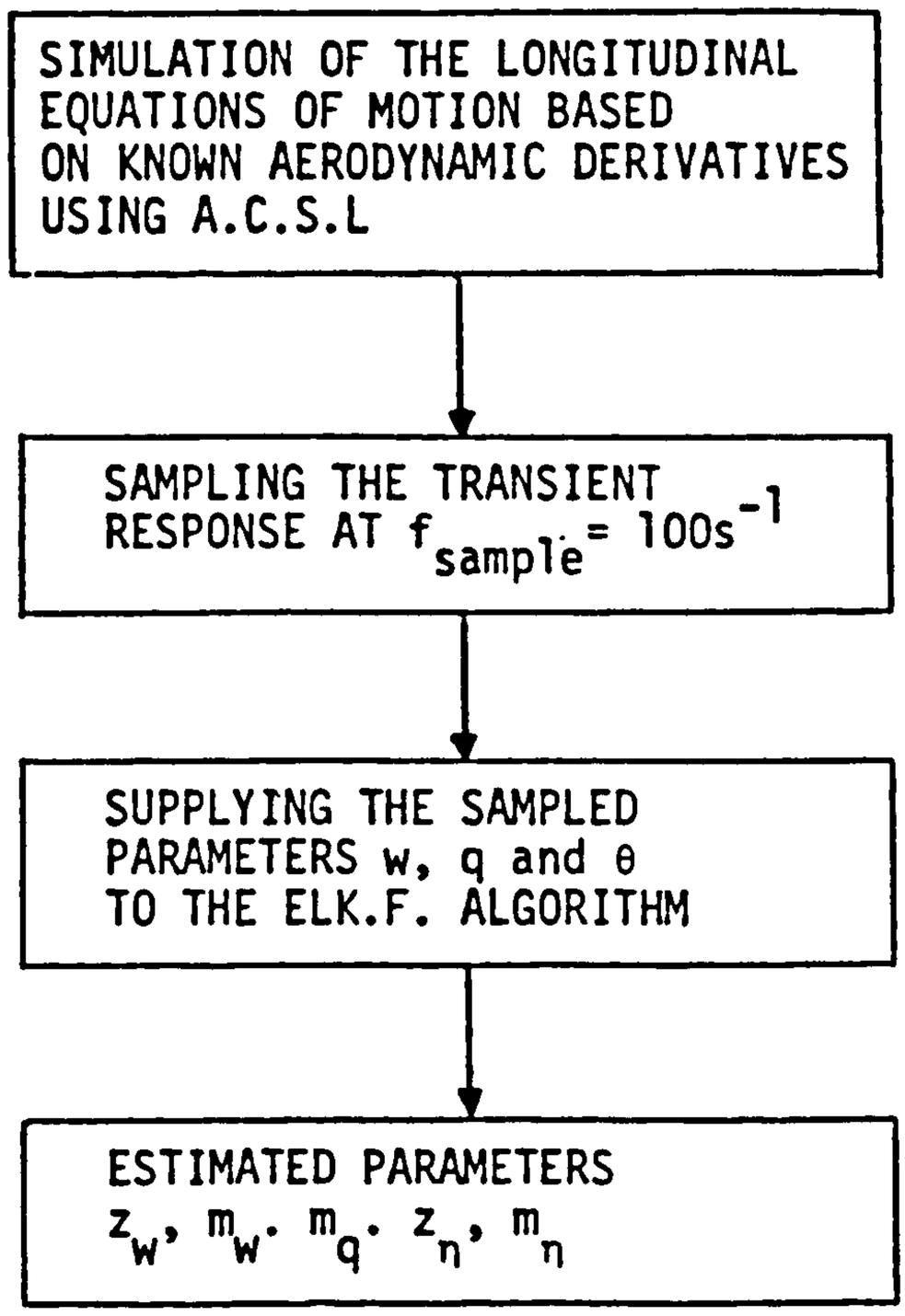

FIGURE 5.3 Verification Study Routine

5.6 Longitudinal Case Studies

The values of the longitudinal stability derivatives used in the simulation of the A/C response were chosen in an arbitrary manner. A large number of experiments were carried out in order to test and modify the analysis process and programming techniques. For illustration purposes only a few of these experiments are presented here. The experimental conditions during the computer simulations together with the key to figure numbers of the experiments and their results are presented in Table 5.1.

During the course of these experiments, it was found that control inputs in the form of pulse or dipole result in the best convergence of the estimated longitudinal stability derivatives. The input forcing functions studied here are illustrated in Figure 5.4 below.

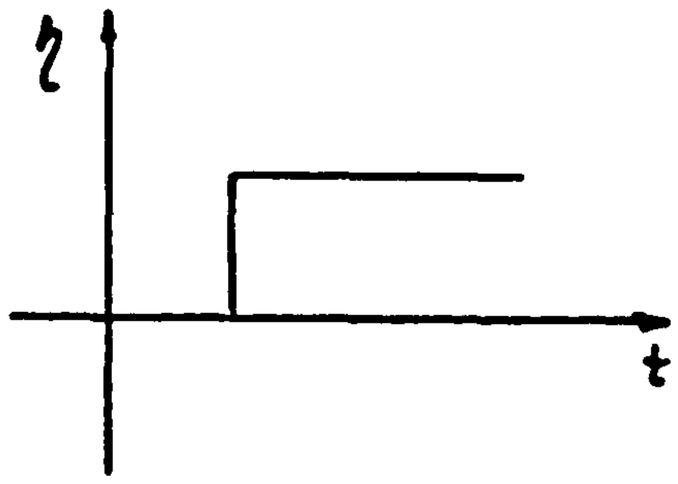

STEP INPUT

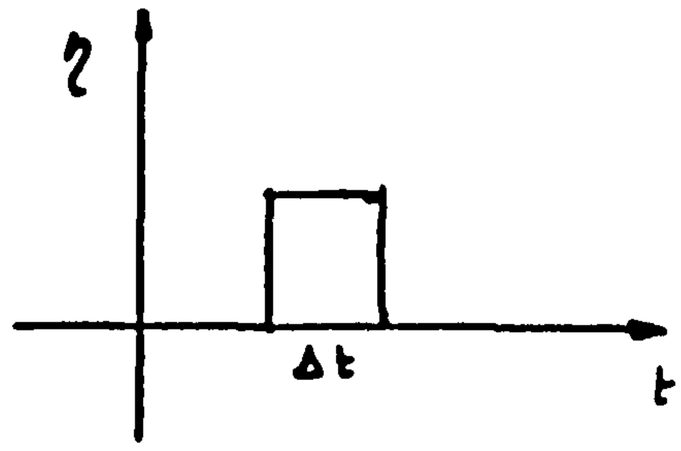

PULSE INPUT

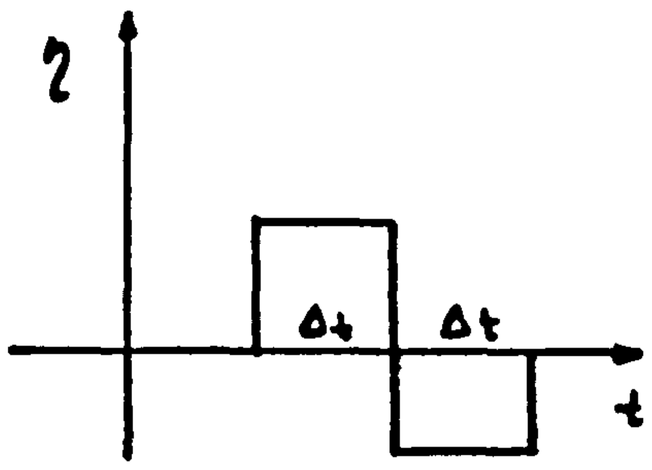

DIPOLE INPUT

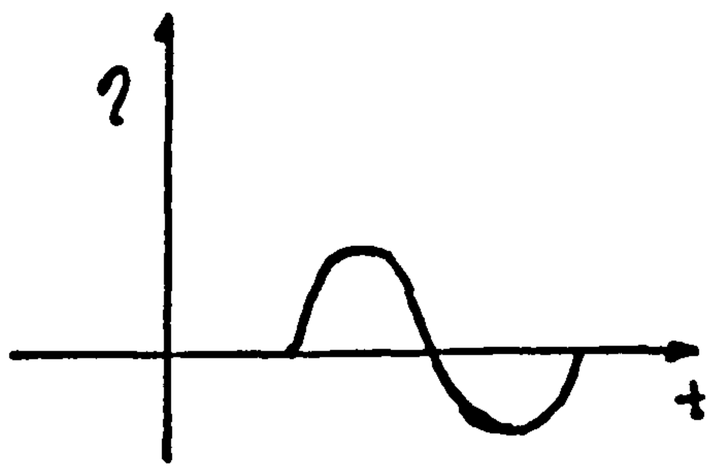

CONTINUOUS SINUSOIDAL INPUT

FIGURE 5.4 INPUT FORCING FUNCTIONS

Details of the calculation of covariance matrices G, R and Q are given in Section J1 of Appendix J. Furthermore, the known values of the longitudinal stability derivatives with which the equations of motion in four degrees of freedom were simulated and their estimates given by the extended Kalman filter program for cases included in Table 5.1, are represented in Table J1 of Appendix J, together with their respective simulation and convergence characteristics. However, the results of Case II of Table 5.1 are presented here.

Fig. 5.5 shows the simulation of the longitudinal response of the aircraft to a dipole foreplane input which is used for the purpose of parameter estimation. From Fig. 5.6 it can be seen that the estimated stability derivatives converge to their known values,given in Fig. 5.5, but the convergence characteristics of the individual estimated derivatives are different. The reason for the differences is discussed in Section 12.

CASE STUDIES	A/C SPEED(ms^{-1})	CANARD CONTROL INPUT	AMPLITUDE (rad)	DURATION (s)	SIMULATION RESULTS	EXAMPLES OF ESTIMATION CONVERGENCE	INITIAL VALUES OF ESTIMATED STATES
CASE - I	300	DIPOLE	0.05	1	FIG. J0	J.I	ALL SET TO ZERO
CASE - II	20	DIPOLE	0.05	1	FIG. J01	J.II	ALL SET TO ZERO EXCEPT $\hat{z}_\eta = -5.0$, $\hat{m}_\eta = 20.0$
CASE-III-i	20	SINOSOIDAL	0.05	T = 1	FIG. J5	J.4	ALL SET TO ZERO
CASE-III-ii	20	SINOSOIDAL	0.05	T = 1	FIG. J5	J.3	ALL SET TO ZERO EXCEPT $\hat{z}_\eta = -5.0$, $\hat{m}_\eta = 30.0$

TABLE 5.1

FLIGHT CONDITIONS OF THE LONGITUDINAL COMPUTER BASED EXPERIMENTS AND ALLOCATION OF RESULTS

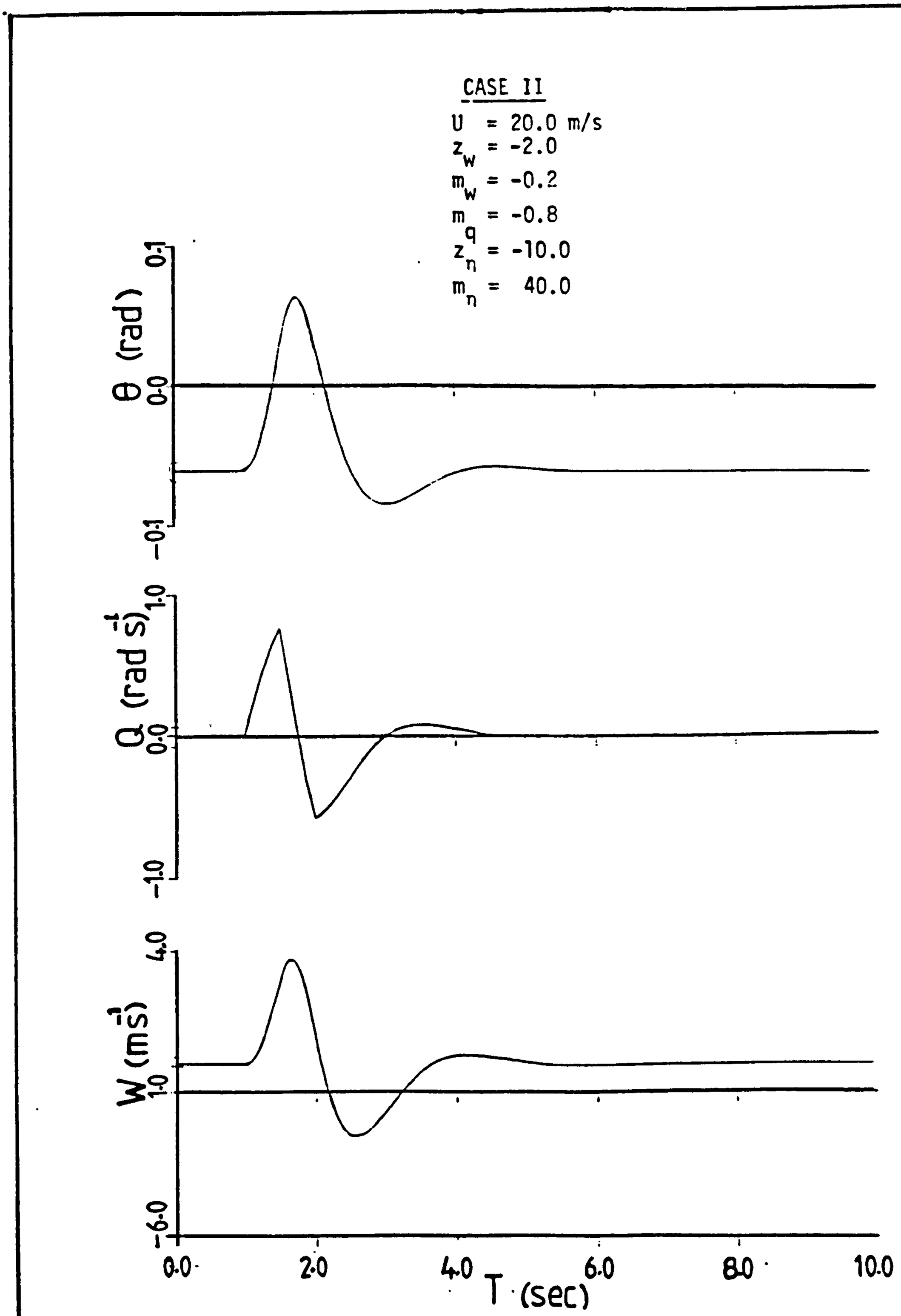

FIGURE 5.5

SIMULATED LONGITUDINAL RESPONSE OF THE A/C TO A DIPOLE FOREPLANE INPUT

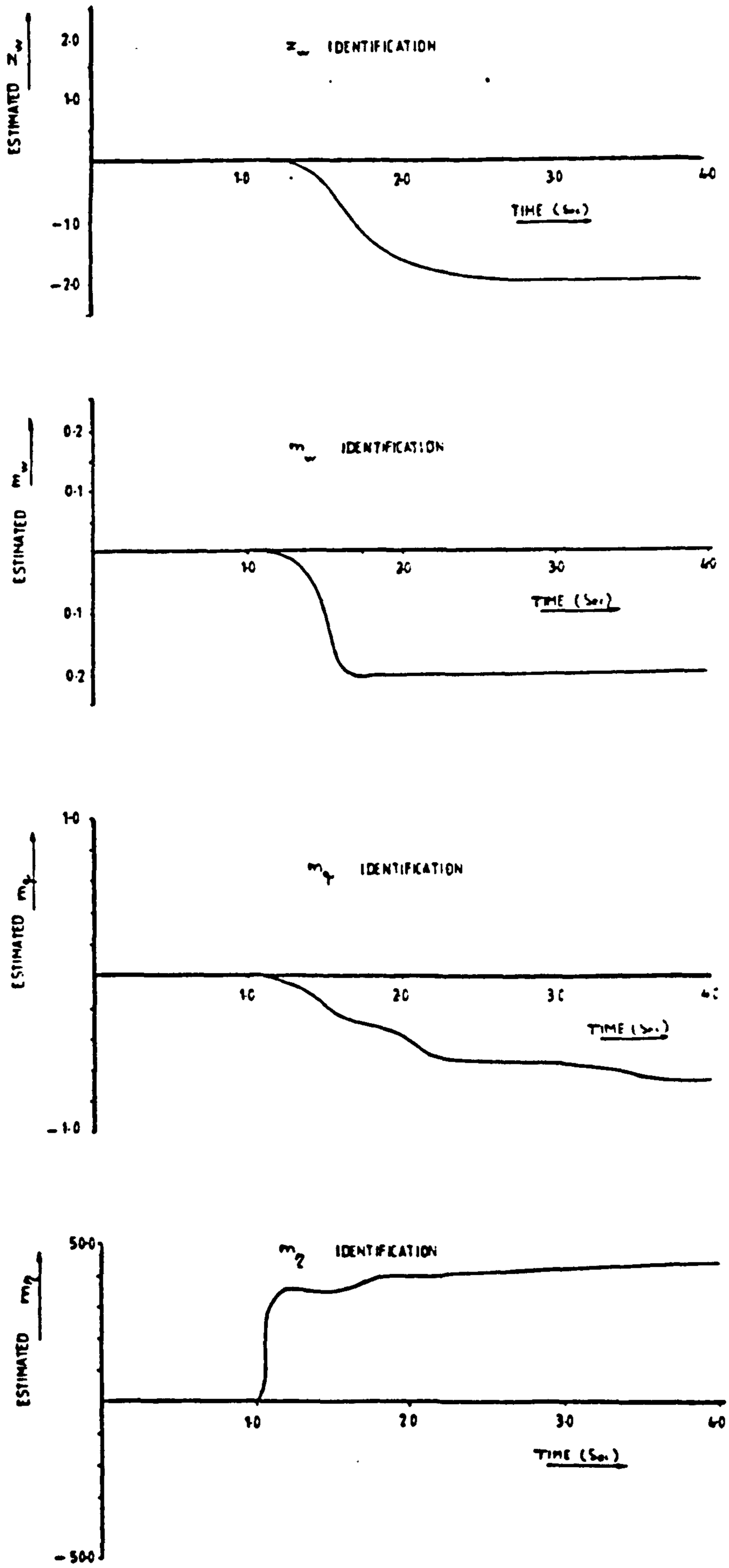

FIGURE 5.6

CONVERGENCE OF SOME OF THE ESTIMATED PARAMETERS WITH NUMBER OF ITERATIONS (CASE II)

6. APPLICATION OF EXTENDED KALMAN FILTER TO THE LATERAL MOTION

The procedure and objectives in this section are similar to those of Section 5. The lateral equations of motion given by Eq.4.7 represent the mathematical model of the system for the estimation of the lateral stability derivatives are of interest. Representation of the stability derivatives as state variables changes the linear equations of motion given by equation 4.7 to a non-linear set of equations given by:

$$\dot{X}_1 = -U_e X_3$$

$$\dot{X}_2 = X_5X_1 + X_6X_2 + X_7X_3 + X_{11}\xi + X_{12}\zeta \qquad \text{EQ. 6.1}$$

$$\dot{X}_3 = X_8X_1 + X_9X_2 + X_{10}X_3 + X_{13}\xi + X_{14}\zeta$$

$$\dot{X}_4 = X_2$$

where

$X_1 = v$

$X_2 = p$

$X_3 = r$

$X_4 = \phi$

$X_5 = \ell_v$

$X_6 = \ell_p$

$X_7 = \ell_r$

$X_8 = n_v$

$X_9 = n_p$

$X_{10} = n_r$

$X_{11} = \ell_\xi$

$X_{12} = \ell_\zeta$

$X_{13} = n_\xi$

$X_{14} = n_\zeta$

As mentioned in Section 5, although the stability derivatives are time invariant, as far as the filter is concerned their values change from one iteration to the next and therefore it is assumed that:

$$\dot{X}_5 = \dot{\ell}_v = w_1$$
$$\dot{X}_6 = \dot{\ell}_p = w_2$$
$$\dot{X}_7 = \dot{\ell}_r = w_3$$
$$\dot{X}_8 = \dot{n}_v = w_4$$
$$\dot{X}_9 = \dot{n}_p = w_5$$
$$\dot{X}_{10} = \dot{n}_r = w_6$$
$$\dot{X}_{11} = \dot{\ell}_\xi = w_7$$
$$\dot{X}_{12} = \dot{\ell}_\zeta = w_8$$
$$\dot{X}_{13} = \dot{n}_\xi = w_9$$
$$\dot{X}_{14} = \dot{n}_\zeta = w_{10}$$

where $W^T = [w_1, w_2 \ldots\ldots, w_{10}]$ is a stationary white noise vector.

6.1 State Equations

The general form of the state equations is given by,

$$\dot{\underset{\sim}{X}} = f(\underset{\sim}{X}, \underset{\sim}{U}) + E(\underset{\sim}{w})$$

and upon expansion,

$$\begin{bmatrix} \dot{X}_1 \\ \dot{X}_2 \\ \dot{X}_3 \\ \dot{X}_4 \\ \dot{X}_5 \\ \dot{X}_6 \\ \dot{X}_7 \\ \dot{X}_8 \\ \dot{X}_9 \\ \dot{X}_{10} \\ \dot{X}_{11} \\ \dot{X}_{12} \\ \dot{X}_{13} \\ \dot{X}_{14} \end{bmatrix} = \begin{bmatrix} -U_e X_3 \\ X_5X_1 + X_6X_2 + X_7X_3 + X_{11}\xi + X_{12}\zeta \\ X_8X_1 + X_9X_2 + X_{10}X_3 + X_{13}\xi + X_{14}\zeta \\ X_2 \\ 0 \\ 0 \\ 0 \\ 0 \\ 0 \\ 0 \\ 0 \\ 0 \\ 0 \\ 0 \\ 0 \end{bmatrix} + \begin{bmatrix} 0&0&0&0&0&0&0&0&0&0 \\ 0&0&0&0&0&0&0&0&0&0 \\ 0&0&0&0&0&0&0&0&0&0 \\ 0&0&0&0&0&0&0&0&0&0 \\ 1&0&0&0&0&0&0&0&0&0 \\ 0&1&0&0&0&0&0&0&0&0 \\ 0&0&1&0&0&0&0&0&0&0 \\ 0&0&0&1&0&0&0&0&0&0 \\ 0&0&0&0&1&0&0&0&0&0 \\ 0&0&0&0&0&1&0&0&0&0 \\ 0&0&0&0&0&0&1&0&0&0 \\ 0&0&0&0&0&0&0&1&0&0 \\ 0&0&0&0&0&0&0&0&1&0 \\ 0&0&0&0&0&0&0&0&0&1 \end{bmatrix} \begin{bmatrix} w_1 \\ w_2 \\ w_3 \\ w_4 \\ w_5 \\ w_6 \\ w_7 \\ w_8 \\ w_9 \\ w_{10} \end{bmatrix} \qquad \text{EQ. 6.2}$$

Further, Equation 6.2 can be discretised with the aid of Equation 5.6 of Section 5, as follows,

$$\dot{\underset{\sim}{X}} = \frac{\underset{\sim}{X}(n+1) - \underset{\sim}{X}(n)}{h} \quad \text{where 'h' is the time step.}$$

$$\therefore \quad f_1(\underset{\sim}{X}(n),\underset{\sim}{U}(n)) = X_1(n) + h.X_3(n)$$

$$f_2(\underset{\sim}{X}(n),\underset{\sim}{U}(n)) = X_2(n)+h(X_5(n).X_1(n)+X_6(n).X_2(n)+X_7(n).X_3(n)+X_{11}(n).\xi+X_{12}(n).\zeta$$

$$f_3(\underset{\sim}{X}(n),\underset{\sim}{U}(n)) = X_3(n)+h(X_8(n).X_1(n)+X_9(n).X_2(n)+X_{10}(n).X_3(n)+X_{13}(n).\xi+X_{14}.\zeta)$$

$$f_4(\underset{\sim}{X}(n),\underset{\sim}{U}(n)) = X_4(n) + h.X_2(n)$$

$$f_5(\underset{\sim}{X}(n),\underset{\sim}{U}(n)) = X_5(n)$$

$$f_6(\underset{\sim}{X}(n),\underset{\sim}{U}(n)) = X_6(n)$$

$$f_7(\underset{\sim}{X}(n),\underset{\sim}{U}(n)) = X_7(n)$$

$$f_8(\underset{\sim}{X}(n),\underset{\sim}{U}(n)) = X_8(n)$$

$$f_9(\underset{\sim}{X}(n),\underset{\sim}{U}(n)) = X_9(n)$$

$$f_{10}(\underset{\sim}{X}(n),\underset{\sim}{U}(n)) = X_{10}(n)$$

$$f_{11}(\underset{\sim}{X}(n),\underset{\sim}{U}(n)) = X_{11}(n) \qquad f_{13}(\underset{\sim}{X}(n),\underset{\sim}{U}(n)) = X_{13}(n)$$

$$f_{12}(\underset{\sim}{X}(n),\underset{\sim}{U}(n)) = X_{12}(n) \qquad f_{14}(\underset{\sim}{X}(n),\underset{\sim}{U}(n)) = X_{14}(n)$$

EQ. 6.3

6.2 The Output Equation

Assuming that the motion sensors produce output signals contaminated by measurement noise vector $\underset{\sim}{V}$ assumed white and stationary with zero mean, the general form of the output equation becomes:

$$\underset{\sim}{y} = g(\underset{\sim}{X},\underset{\sim}{U}) + \underset{\sim}{V} = C\underset{\sim}{X} + \underset{\sim}{V} \qquad \text{EQ. 6.4}$$

Since the function $g(\underset{\sim}{X},\underset{\sim}{U})$ is linear and the direct matrix D is zero. Upon expansion in matrix form, Equation 6.4 becomes:

$$\begin{bmatrix} y_1 \\ y_2 \\ y_3 \\ y_4 \end{bmatrix} = \begin{bmatrix} 1 & 0 & 0 & 0 & 0 & 0 & 0 & 0 & 0 & 0 & 0 & 0 & 0 & 0 \\ 0 & 1 & 0 & 0 & 0 & 0 & 0 & 0 & 0 & 0 & 0 & 0 & 0 & 0 \\ 0 & 0 & 1 & 0 & 0 & 0 & 0 & 0 & 0 & 0 & 0 & 0 & 0 & 0 \\ 0 & 0 & 0 & 0 & 0 & 0 & 0 & 0 & 0 & 0 & 0 & 0 & 0 & 0 \end{bmatrix} \begin{bmatrix} X_1 \\ X_2 \\ X_3 \\ X_4 \\ X_5 \\ X_6 \\ X_7 \\ X_8 \\ X_9 \\ X_{10} \\ X_{11} \\ X_{12} \\ X_{13} \\ X_{14} \end{bmatrix} + \begin{bmatrix} v_1 \\ v_2 \\ v_3 \\ v_4 \end{bmatrix}$$

where

y_1 = sideslip velocity v

y_2 = roll rate p

y_3 = yaw rate r

y_4 = roll angle ϕ

and,

$$C = \begin{bmatrix} 1 & 0 & 0 & 0 & 0 & 0 & 0 & 0 & 0 & 0 & 0 & 0 & 0 & 0 \\ 0 & 1 & 0 & 0 & 0 & 0 & 0 & 0 & 0 & 0 & 0 & 0 & 0 & 0 \\ 0 & 0 & 1 & 0 & 0 & 0 & 0 & 0 & 0 & 0 & 0 & 0 & 0 & 0 \\ 0 & 0 & 0 & 1 & 0 & 0 & 0 & 0 & 0 & 0 & 0 & 0 & 0 & 0 \end{bmatrix}$$

6.3 The State Transition Matrix

The state transition matrix is given by,

$$\phi(n) = \left[\frac{\partial f(\underset{\sim}{X}(n),\underset{\sim}{U}(n))}{\partial \underset{\sim}{X}(n)} \right]_n$$

which with reference to Equation 6.3 becomes,

$$\phi(n) = \begin{bmatrix}
1 & 0 & -U_e h & 0 & 0 & 0 & 0 & 0 & 0 & 0 & 0 & 0 & 0 & 0 \\
h.X_5 & 1+h.X_6 & h.X_7 & 0 & h.X_1 & h.X_2 & h.X_3 & 0 & 0 & 0 & h.\xi & h.\zeta & 0 & 0 \\
h.X_8 & h.X_9 & 1+h.X_{10} & 0 & 0 & 0 & 0 & h.X_1 & h.X_2 & h.X_3 & 0 & 0 & h.\xi & h.\zeta \\
0 & h & 0 & 1 & 0 & 0 & 0 & 0 & 0 & 0 & 0 & 0 & 0 & 0 \\
0 & 0 & 0 & 0 & 1 & 0 & 0 & 0 & 0 & 0 & 0 & 0 & 0 & 0 \\
0 & 0 & 0 & 0 & 0 & 1 & 0 & 0 & 0 & 0 & 0 & 0 & 0 & 0 \\
0 & 0 & 0 & 0 & 0 & 0 & 1 & 0 & 0 & 0 & 0 & 0 & 0 & 0 \\
0 & 0 & 0 & 0 & 0 & 0 & 0 & 1 & 0 & 0 & 0 & 0 & 0 & 0 \\
0 & 0 & 0 & 0 & 0 & 0 & 0 & 0 & 1 & 0 & 0 & 0 & 0 & 0 \\
0 & 0 & 0 & 0 & 0 & 0 & 0 & 0 & 0 & 1 & 0 & 0 & 0 & 0 \\
0 & 0 & 0 & 0 & 0 & 0 & 0 & 0 & 0 & 0 & 1 & 0 & 0 & 0 \\
0 & 0 & 0 & 0 & 0 & 0 & 0 & 0 & 0 & 0 & 0 & 1 & 0 & 0 \\
0 & 0 & 0 & 0 & 0 & 0 & 0 & 0 & 0 & 0 & 0 & 0 & 1 & 0 \\
0 & 0 & 0 & 0 & 0 & 0 & 0 & 0 & 0 & 0 & 0 & 0 & 0 & 1
\end{bmatrix}$$

6.4 Filter Algorithm

The split extended Kalman filter algorithm used in the present application is the same as that of Section 5.1 and therefore is not repeated here.

6.5 Lateral Case Studies

At this stage a second computer program was developed which employed the extended Kalman filter in order to identify estimates of the lateral stability derivatives. Details of the calculations included in the program leading to the initial values of the covariance matrix G and constant values of the covariance matrices Q and R are given in Section J2 of Appendix J. The sequence of events in this program were also as shown in the block diagram of fig. 5.3 of Section 5. The output transient responses of a computer simulation model of an aircraft subjected to disturbances due to aileron or rudder deflections were studied. One of these computer based experiments is discussed below as an example. Table 6.2 shows the experimental conditions and key to figure numbers of the results. For further details reference can be made to Section J2 of Appendix J.

A/C SPEED (ms^{-1})	AILERON CONTROL INPUT	AMPLITUDE (rad)	DURATION (s)	SIMULATION RESULTS	ESTIMATION CONVERGENCE
20	DIPOLE	0.1	1	Fig. J6	Fig.J7, J8
ALL INITIAL VALUES OF THE ESTIMATED STATES WERE SET TO ZERO					

TABLE 6.1

FLIGHT CONDITION AND ALLOCATION OF RESULTS, FOR THE LATERAL CASE STUDY EXAMPLE

Figs. 6.1 and 6.2 represent the simulated lateral response of the aircraft to a dipole aileron input and convergence characteristics of the estimated lateral stability derivatives respectively. It can be seen from Fig. 6.2 that the estimated stability derivatives converge to their steady state values which in actual fact are the values used in the mathematical computer simulation model. In Table 6.2 below, the estimated stability derivatives and their actual values are compared and clearly they are very close.

A/C SPEED	CONCISE LATERAL STABILITY DERIVATIVES							
	ℓ_v	ℓ_p	ℓ_r	n_v	n_p	n_r	ℓ_ξ	n_ξ
ACTUAL	-20.0	-5.0	1.5	15.0	1.5	-5.0	50.0	-6.0
ESTIMATED	-20.0	-5.0	1.0	15.0	1.5	-5.0	50.0	-4.5

TABLE 6.2 ACTUAL AND ESTIMATED LATERAL STABILITY DERIVATIVES

The apparent closeness can be explained by the fact that not only in these case studies the mathematical dynamic model used in the extended Kalman filter code is identical to that of the simulated system and also, there is no noise contamination of the responses. Therefore, in the presence of noise and mismatch in the dynamic model of the system, the experimental results of the open-loop dynamic wind tunnel tests are expected not to be as satisfactory as those above.

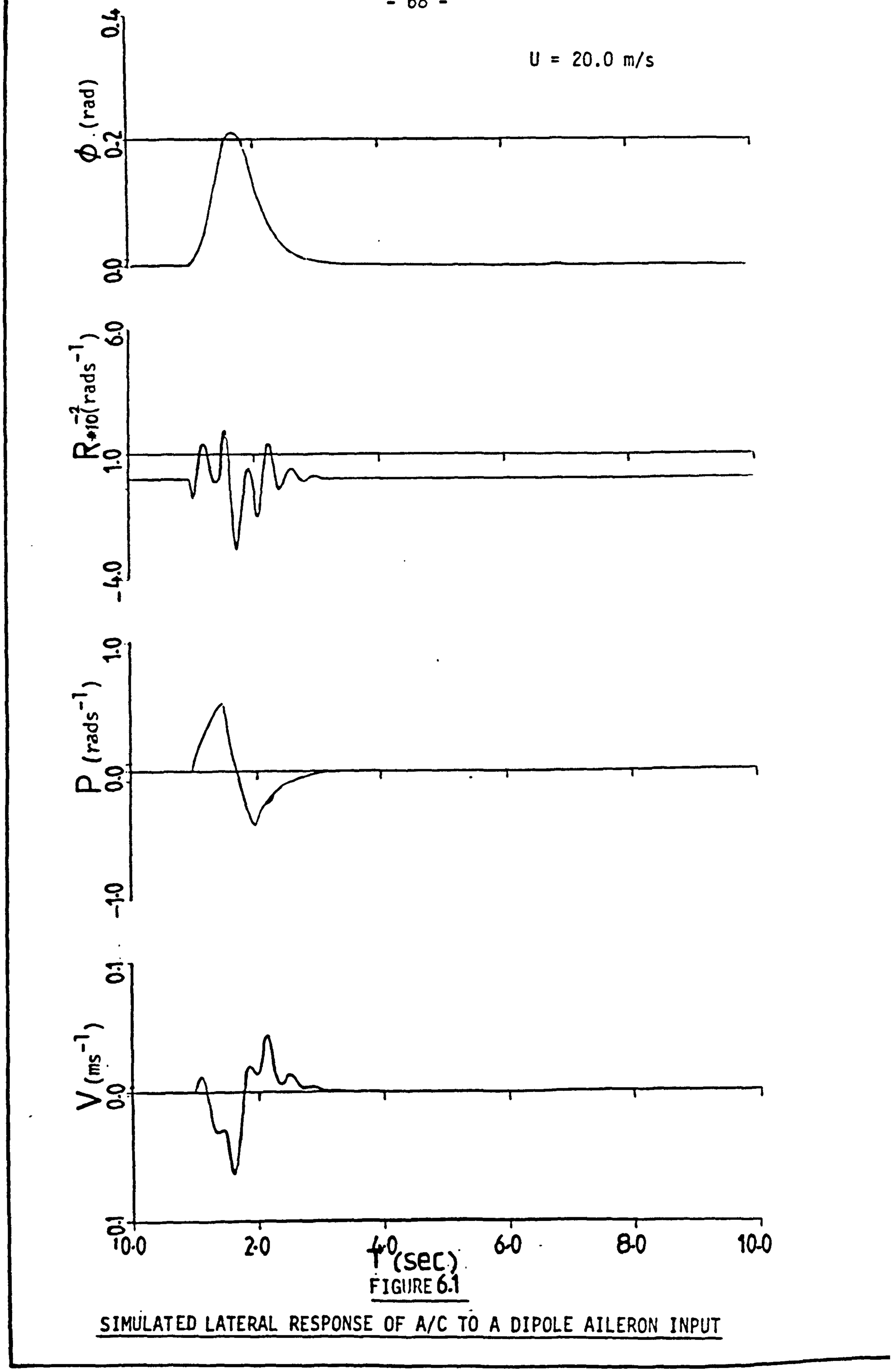

FIGURE 6.1

SIMULATED LATERAL RESPONSE OF A/C TO A DIPOLE AILERON INPUT

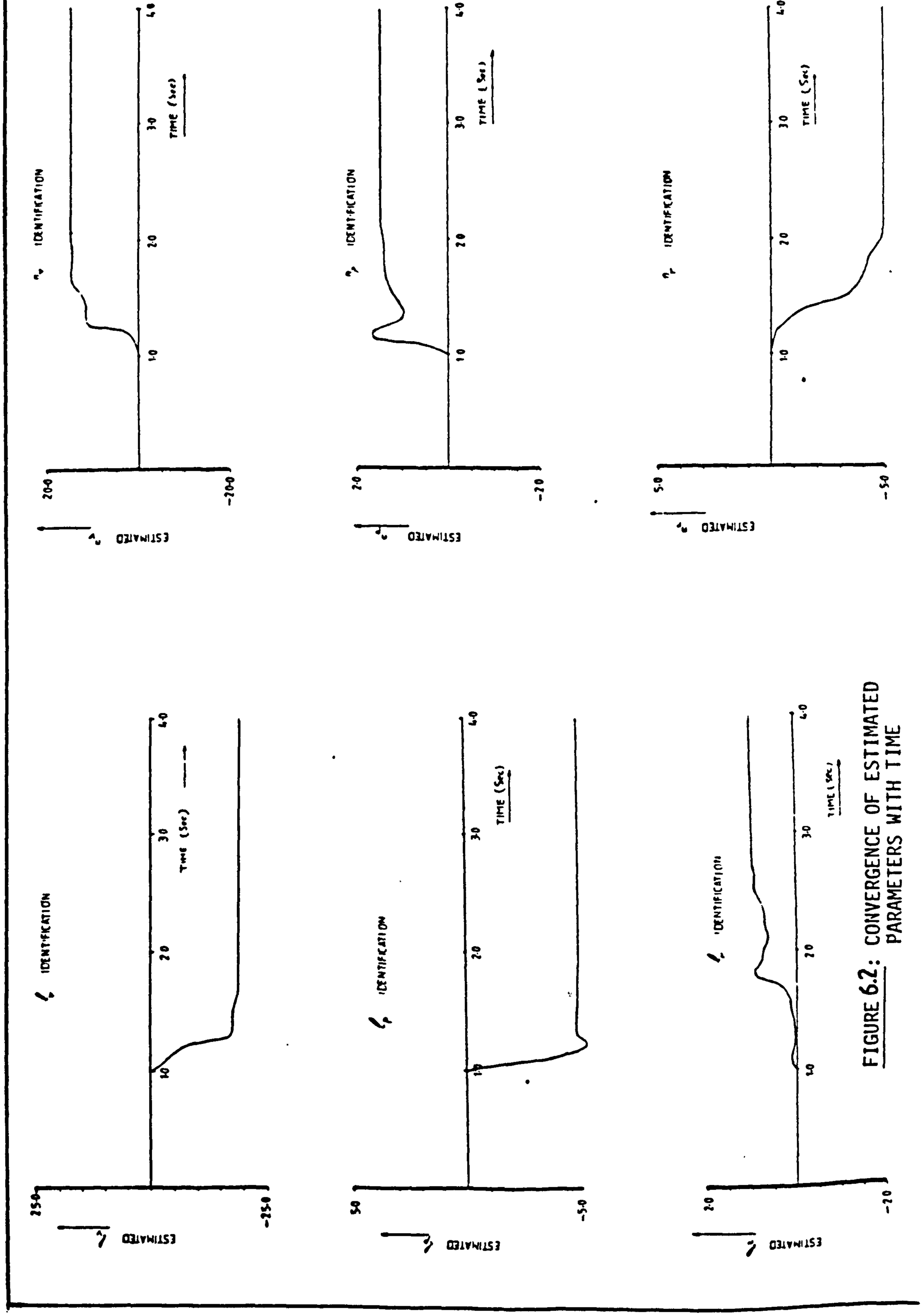

FIGURE 6.2: CONVERGENCE OF ESTIMATED PARAMETERS WITH TIME

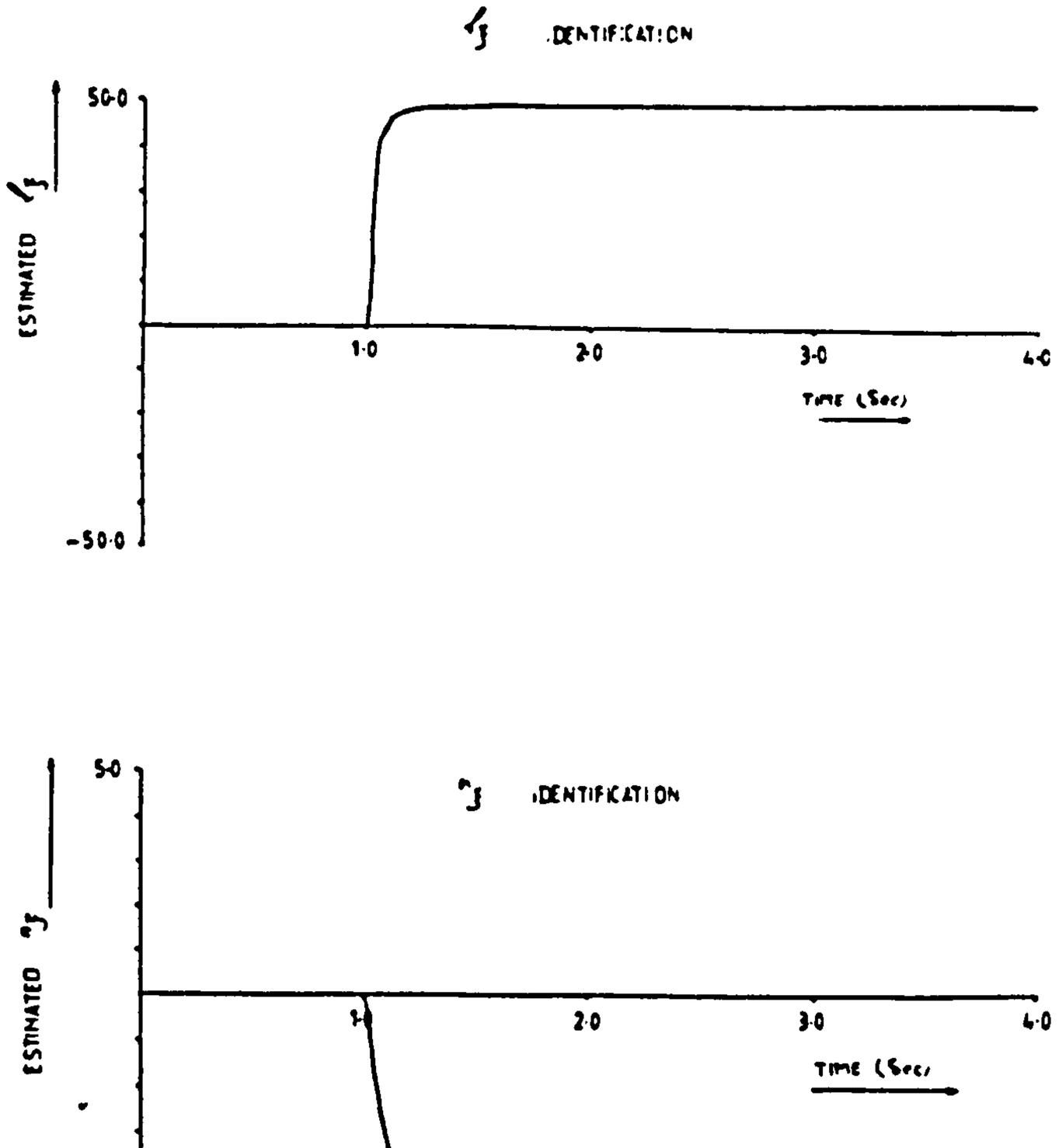

FIGURE 6.2: (continued) CONVERGENCE OF ESTIMATED PARAMETERS WITH TIME

7. EXPERIMENTAL PROCEDURES

Most of the hardware comprising the experimental facility is shown in Figure 7.4, with the exception of the height measuring transducer system which will be discussed in the following sub-section. Operation of various equipment, calibration of control surface and attitude pick-off signals, signal processing and conditioning and its analysis constitute the remainder of this section.

7.1 The Height Measuring Transducer System

In order to measure the acceleration and velocity in heave, many techniques may be used but the amount of equipment that can be placed conveniently in the dynamic model of the F.S.W. aircraft is limited. One way of measuring the above variables, namely $\dot{w}$ and w, is to measure height variations of the model with respect to a datum. The recorded height variations of the model due to the disturbance can then be digitised, and both w and $\dot{w}$ can be derived numerically at any instant of time during the transient response. Fig. 7.1 below, shows the height sensing loop together with the dynamic test rig.

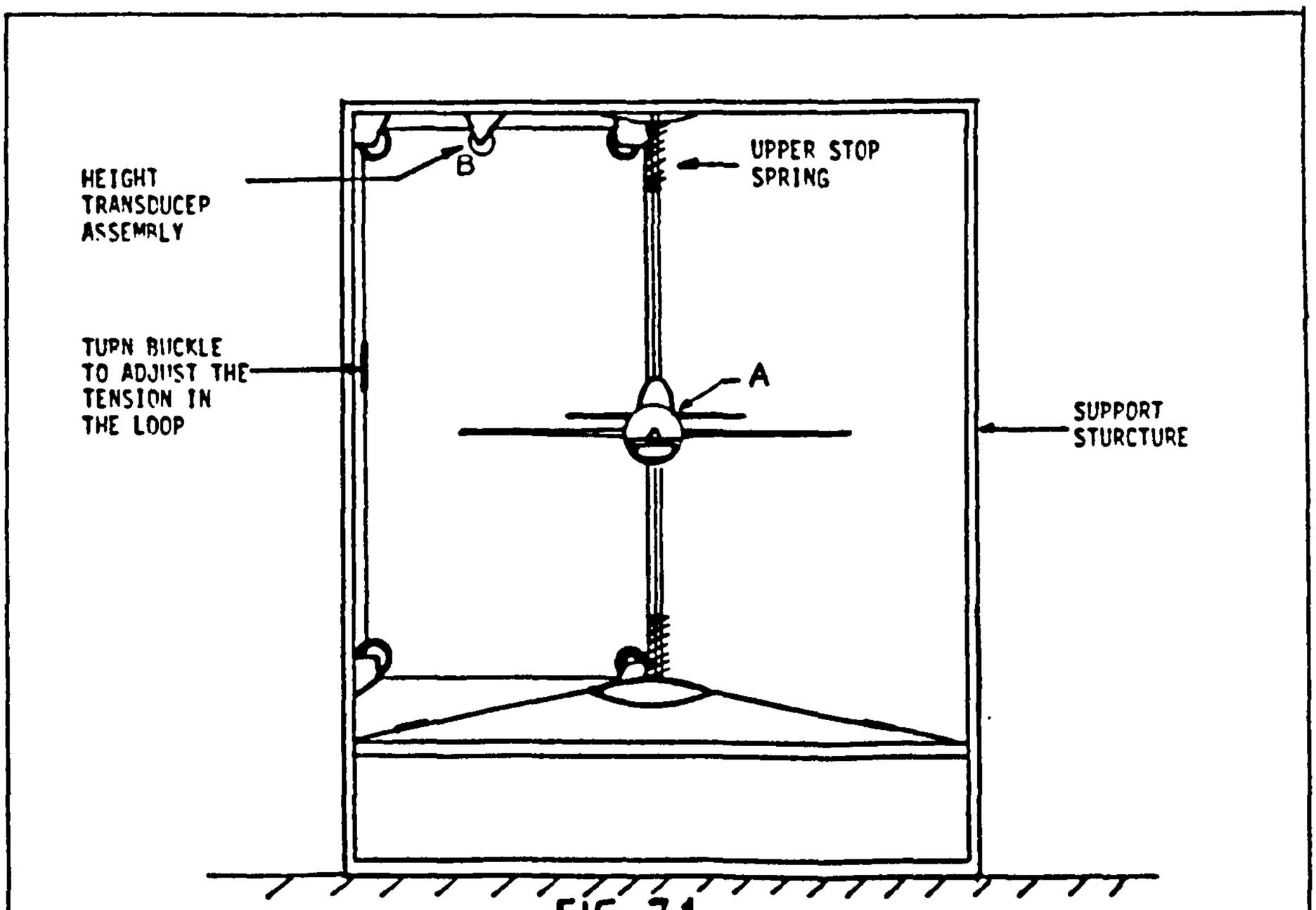

FIG. 7.1

SUPPORT STRUCTURE, SUSPENSION SYSTEM AND HEIGHT TRANSDUCER ASSEMBLY

As can be seen from Fig. F6, the cable loop was connected to the Gimbal system in the model at point 'A'. At point 'B' a 10 kΩ, 10 turn potentiometer was installed, the shaft of which was attached to a pulley. This pulley had a diameter chosen to give approximately 12 cm of linear travel per turn. This in effect meant that height variation in the order of ±50 cm could be recorded through the potentiometer which was mounted above the model suspension system. The signal from the potentiometer was digitised directly through the multifunction interface, by a process which is explained in detail in Section 7.3. Subsequently, the digitised signal was differentiated numerically to give w.

7.2 Instrumentation and Calibration Procedures

It was necessary to calibrate the control surface angle sensors in the model and the attitude sensors, namely, pitch, roll and yaw potentiometers. In order to calibrate the control surface sensors , a chart recorder and the output from the control box as detailed in Ref. 8 were used. Then datum zero angle deflections of the control surfaces were determined with the aid of a horizontal reference surface and an inclinometer. With the instruments set up, the control surfaces were moved by five degree increments and the corresponding control voltage inputs recorded via the chart recorder. It should, however, be noted that at angles above 20^{o}, non-linearities arose due to the linkage geometry between the actuator and control surface.

The model attitude sensing potentiometers were energised by a ± 10 v reference power supply, and the height measuring device was energised with a ±15 v supply. Now, with the model mounted on the rig, signals from roll and pitch potentiometers, at 5^{o} interval rotations, were recorded on the chart recorder; a tunnel mounted inclinometer was used for this purpose. The yaw potentiometer on the other hand was calibrated with the aid of a modified protractor mounted on the vertical shaft of the test rig. Finally the height measuring transducer was calibrated by recording the signal for vertical model movements at 10 cm intervals. Calibration curves and data are given by Figs. F3, F4 and F5 and Tables F2, F3 and F4 of Appendix F. The calibrated signals were conditioned and amplified through the secondary amplifiers which acted as signal summers, low-pass filters, and amplifiers. The primary reason for using summer circuits was that any signal input into the amplifier has associated with it an offset voltage which must be eliminated before amplification and this could easily be done by adding a bias signal to the signal of interest.

7.3 Digitisation of the Analogue Signals

In order to record the transient response of the F.S.W. model in digital form. in either longitudinal or lateral senses, an interface was used. In particular, a type PCI 6380 multi-function interface was employed. Being a microprocessor controlled instrument, the operating system was held in 'ROM' within the unit. Incorporated into the above multi-function interface unit were software options with which the input gains could be set to the desired value, thereby facilitating the input of analogue and the output of digital signals over the IEEE-488 bus to a CBM microcomputer, and thence to floppy disc storage. This interface operated subject to the following specifications:

Resolution (input and output)	12 bits
Calibrated accuracy (20^{o}C)	±0.1%
Hysteresis	1 bit
Power supply	220-240 v ±10%
Operating temperature	0 - 50^{o}C
Number of inputs	8
Operating time per channel	< 1 ms
Input range	Programmable ± 100 mv, ± 1 v, ± 10 v
Input noise	1 bit

When using the IEEE-488 bus, the interface unit was given a device number by means of a 4 way lever operated switch working in binary code. As far as the CBM microcomputer was concerned, numbers 0 - 4 and 8 were used in its own operating system so these numbers were avoided. The range of address values are given in Table 7.1 below:

	32K RAM MEMORY	
	BINARY	ASCII
START	(128)(0)	0 (ACTUALLY 32768)
END	(255)(255)	32767 (ACTUALLY 65535)

TABLE 7.1

This unit stored the data in digitised form starting from a given address in its 'RAM' memory and then transferring the data over IEEE-488 bus onto the computer where it was then stored on a disc. This interface unit was capable of taking up to 1000 samples per second, of the input analogue signal although the required sampling was 10 ms or 100 samples per second. Since the signals from the attitude sensors of the model were amplified, the gain was set to $\pm$10 v. On recovering the output, the digitised information was converted from ASCII form to an equivalent scaled representation by dividing each sample by the number 32768. The equivalent voltages were then rescaled to represent radians and hence time histories of attitude variations were obtained in digital form.

7.4 Data Formatting and Conditioning

After recording the response data on disc for each experiment, it was transferred onto the DEC VAX 11/750 computer. Since there were no means of measuring attitude rates directly, they had to be derived by differentiation of attitude time histories . Once this data was transferred, it was formatted. Now, in its original form, data obtained from the experiment was contaminated with noise. Taking into account the fact that attitude time histories from the model were represented by noisy samples meant that any attempt to differentiate it numerically would be quite unsatisfactory as is evident by such an experiment illustrated graphically in Fig. 1.

Therefore, the time histories obtained from the model had to be conditioned so that numerical differentiation could be sensibly carried out to yield the rates of changes of pitch angle, etc. A possible alternative solution was to use rate gyros of the type used in model helicopters, but this was not a practical solution since the space inside the F.S.W. model aircraft was very limited.

It was concluded that the best way to condition the attitude time histories was to use a curve fitting routine using a weighted least-square technique. For this purpose, a least-square Chebyshev-polynomial curve fitting routine was used. Since the number of points was quite large, a very smooth curve fit was obtained. Fig. 7.3 shows the result of this process as applied to the pitch angle time history of Fig. 7.2. A computer program was written to read in the experimental values and then curve-fit them and store the resultant signals and their derivatives in a formatted form ready for the parameter identification program.

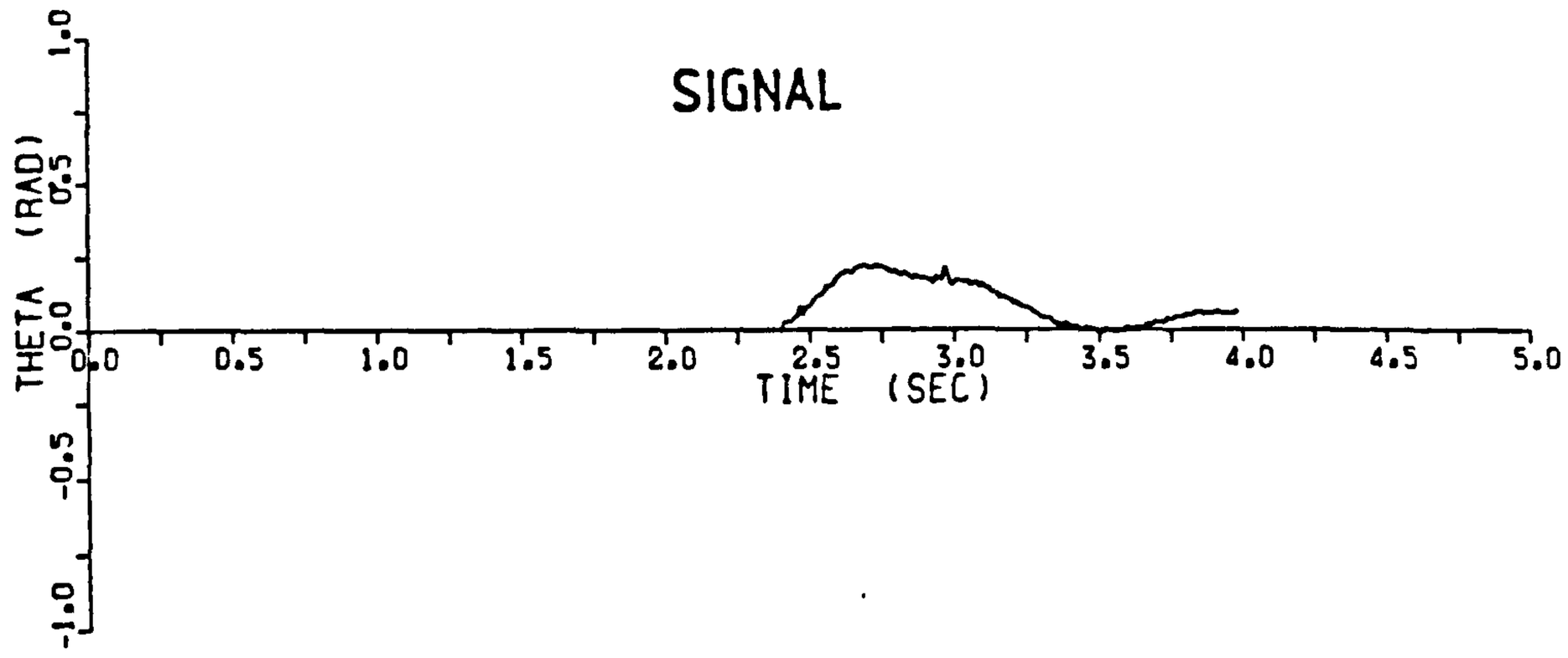

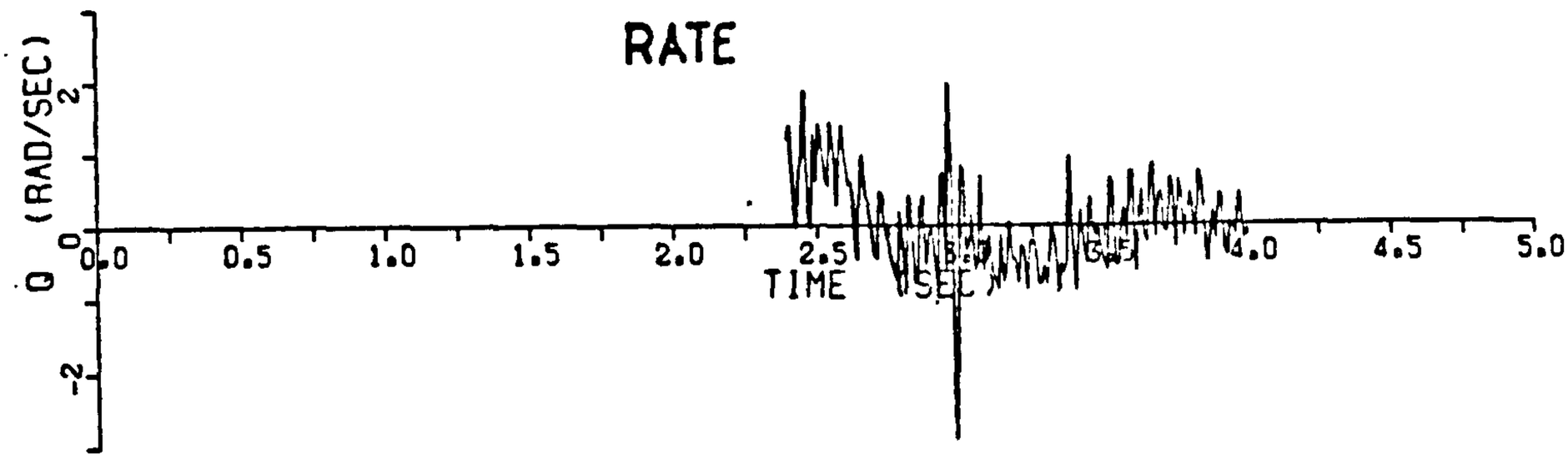

FIG. 7.2

NUMERICAL DIFFERENTIATION OF A NOISY SIGNAL

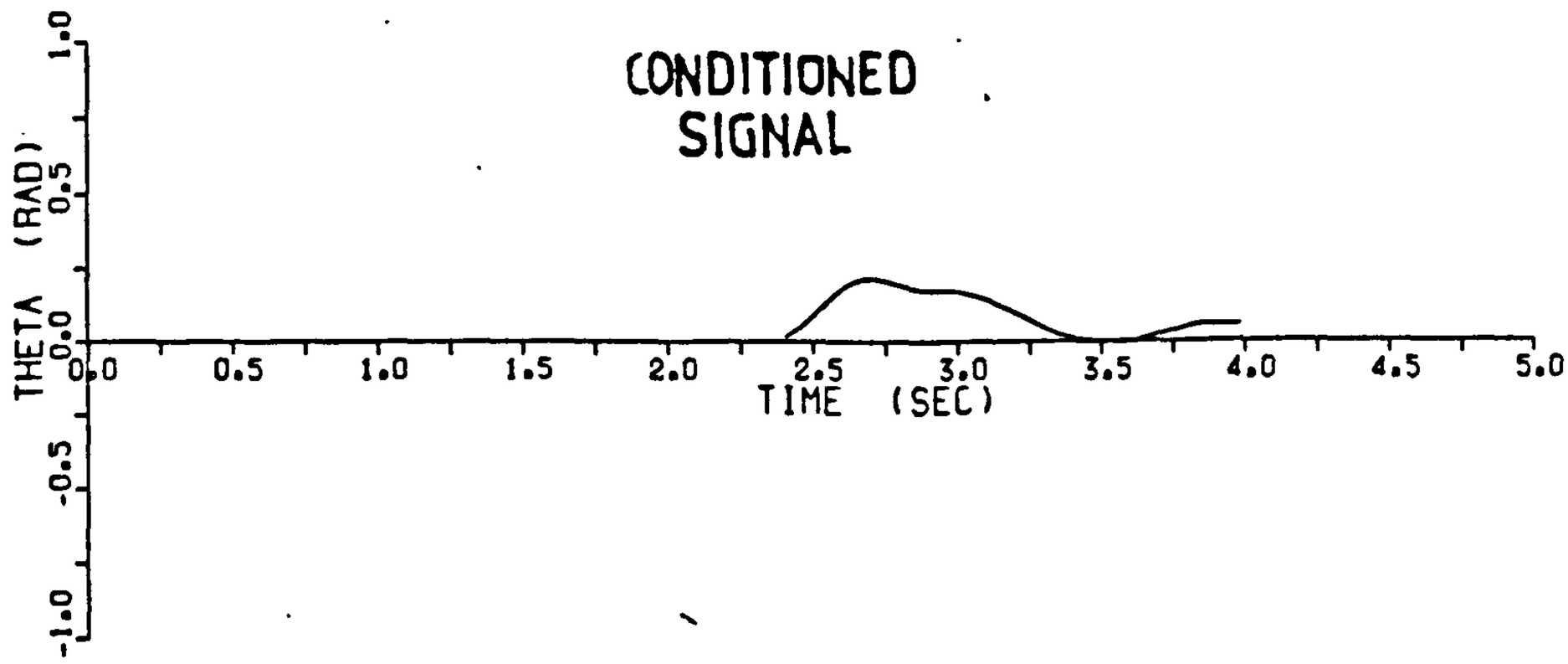

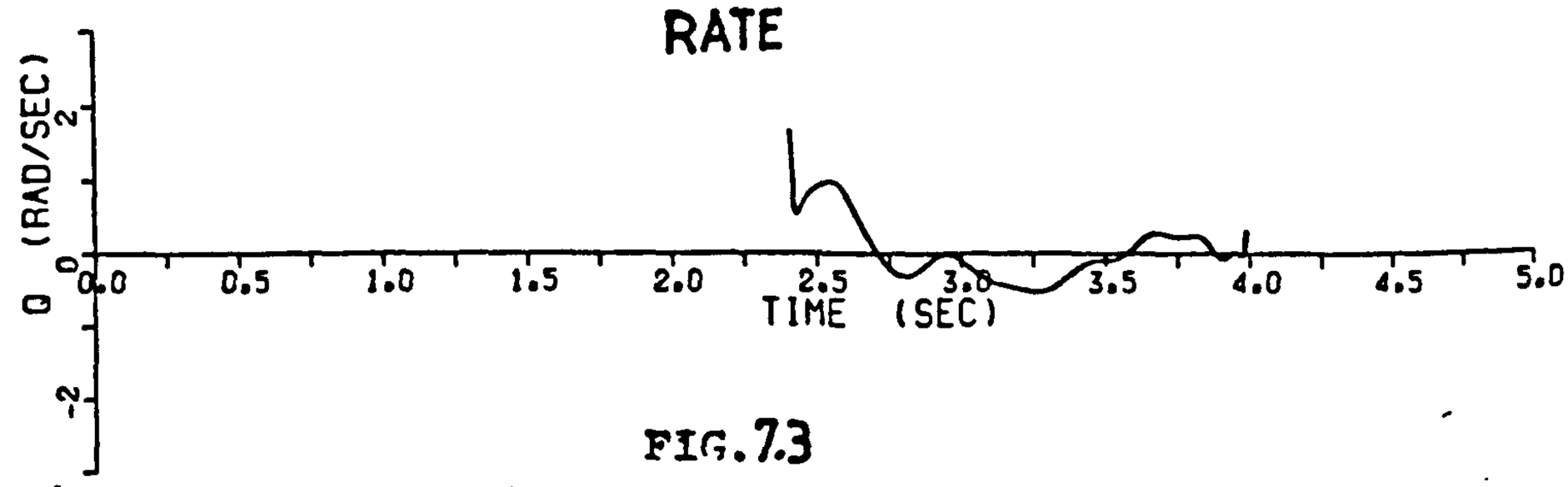

FIG. 7.3

NUMERICAL DIFFERENTIATION OF THE SIGNAL AFTER CURVE FITTING PROCESS

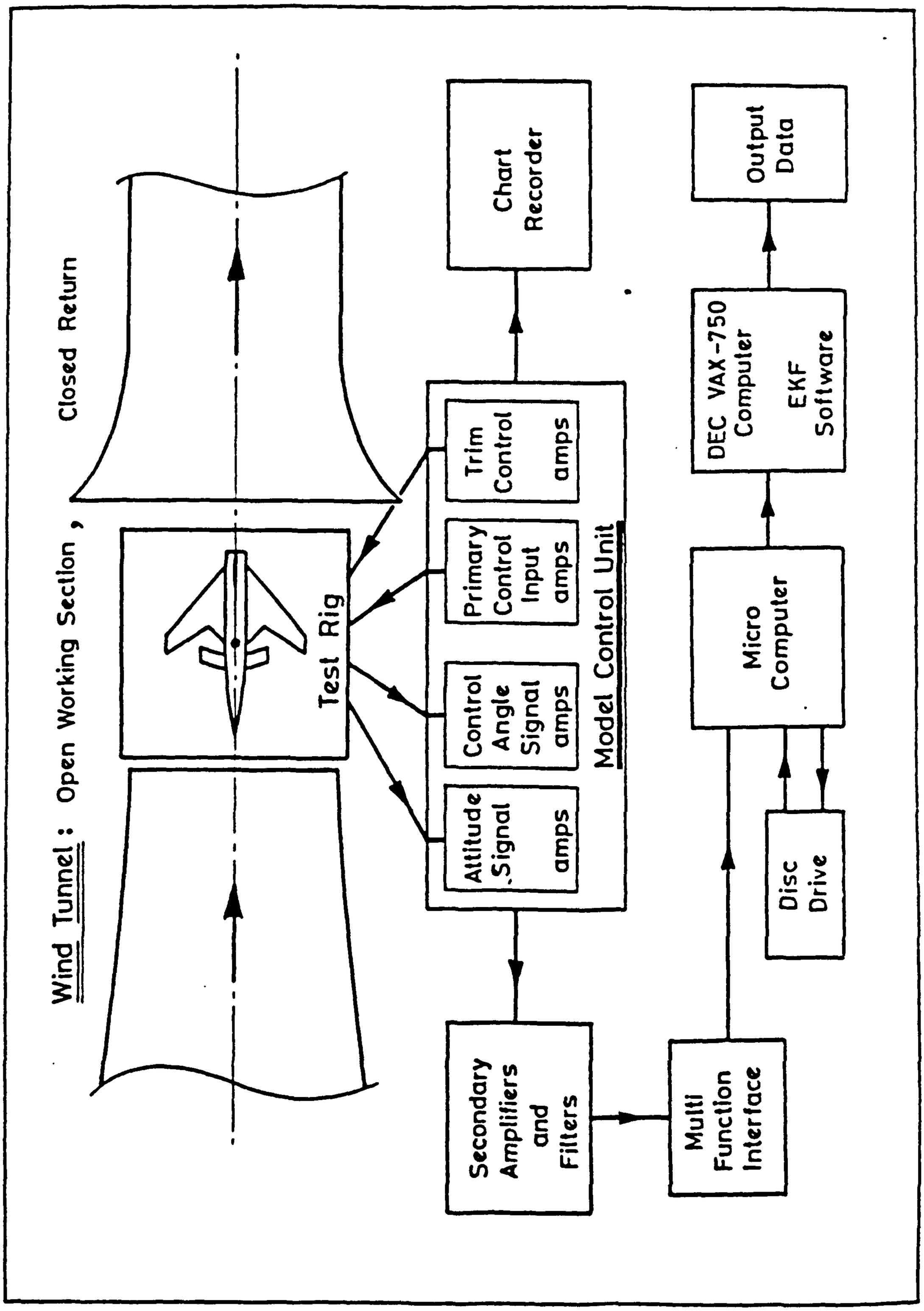

FIGURE 7.4 BLOCK DIAGRAM REPRESENTING THE EXPERIMENTAL PROCESS OF OPEN-LOOP DYNAMIC TESTS

7.5 Kalman Filtering

Two codes were developed and tested, one for longitudinal and one for lateral studies, for the purpose of implementing the parameter identification technique, whose validity and scope was discussed above. The process noise was included in the covariance matrices for both the longitudinal and lateral parmaeter identification algorithms and then the programs were run for the various tunnel speeds and experiments and the results were output either as data or in graphical form.

7.6 Data Output and Plots

In order to gain confidence in the results obtained from the Kalman filtering algorithms, a plotting routine was written to plot the unprocessed and Kalman filter outputs on the same axes. Provided the covariance matrices are of the right order and magnitude, all responses should be coincident when the estimation process results are ideal.

8. LONGITUDINAL DYNAMIC WIND TUNNEL EXPERIMENT

In Section 5, the application of the extended Kalman filter to the computer simulation of longitudinal short period oscillations was studied which gave an insight into the behaviour of the filter and how to improve its mechanisation. This knowledge was crucial in the present application where it was required to estimate the dynamic stability and control characteritics of the dynamic model from response data. Because of the limitations of the dynamic model and suspension system all longitudinal dynamic wind tunnel tests were concerned with the short period motions only and consisted of short period transient response to foreplane control inputs. The analysis of the transient responses by means of the extended Kalman filter then resulted in the estimates of the respective longitudinal stability derivatives.

8.1 Initiation of the Disturbances

The linearised equations of motion in four degrees of freedom were valid as long as the disturbance introduced results in a pitch attitude variation in order of $\pm 10°$. Experiments showed that a foreplane deflection not exceeding $\pm 5°$ would satisfy this requirement. However, foreplane deflections were limited to the positive sense only due to the motion contraints of the test-rig. In other words, the model was made to ascend. Furthermore, the limited vertical freedom for the model meant that the experiments could only be performed at a limited tunnel speed range since any foreplane deflection at higher speeds would result in catastrophic damage to the model. In addition, every experiment had to be repeated several times before a good response was obtained. A response was considered good when, following the foreplane deflection, the F.S.W. model climbed to a certain height and remained in that position until the attitude response had died away. For this purpose, two tunnel speeds, namely 27 and 30 m/s were found to be most suitable. With two C.G. positions this defined a total of four test cases. Further longitudinal experiments were performed after incorporation to the development of a height control system together with the incorporation of the latter into the equations of motion listed above. This was necessary since lack of vertical velocity signal would have resulted in failure of E.K.F. parameter identification algorithm.

8.2 Validity of the Longitudinal Short Period Equations

Preliminary experiments involving the short period oscillations of the F.S.W. model revealed that the set of equations describing the motion given by equation (4.6) do not represent the transient response completely. That is to say the stability derivatives estimated through the extended Kalman filter would oscillate and thus not converge to a definit: value. The most likely cause

was considered to be the omission of z_q from the equations.

Therefore z_q was included inthe longitudinal equations of motion describing the short period oscillations of the F.S.W. model on the test rig. The revised equations are;

$$\left.\begin{aligned} \dot{w} &= z_w.w + (z_q + U_e)q + z_\eta.\eta \\ \dot{q} &= m_w.w + m_q.q + m_\eta.\eta \\ \dot{\theta} &= q \end{aligned}\right\} \quad ----- \quad EQ.8.1$$

The transition matrix $\Phi(n)$ was also modified and another state was added to the Extended Kalman Filter equations representing $\hat{z}_q$. Now the new characteristic equation became,

$$s^2 + s(-z_w - m_q) + (z_w m_q - m_w(z_q + U_e) = 0$$

Therefore,

$$\left.\begin{aligned} \omega_n &= \sqrt{z_w m_q - m_w(z_q + U_e)} \\ \zeta_D &= \left(\frac{-z_w - m_q}{2}\right) \end{aligned}\right\} \quad ----- \quad EQ.8.2$$

Clearly the inclusion of z_q has not altered the damping. Earlier tests regarding the determination of the position of N.P. has suggested (see Appendix G) that the F.S.W. model had a static margin stick-fixed of approximately -1% $\bar{\bar{c}}$ with the model balanced at the forward C.G. of 0.444 m from datum. This would obviously produce a positive value for m_w.

8.3 Analysis of the Longitudinal Experiments

As stated above, the longitudinal experiments were limited to two C.G. positions for each tunnel speed. Table 8.3 lists the conditions of each experiment. It must however be pointed out that experiments 1 to 4 were selected as the best from many similar experiments. After conditioning and formatting the experimental data for each experiment, four data files were generated within the computer which were then used for the analysis of longitudinal transient responses with the parameter identification algorithm. Details of calculations and results derived from the tests listed in Table 8.3 are given in Appendix J. In order to illustrate the effect of variations in the elements of measurement covariance matrix R, for every experiment two longitudinal transient responses with varying covariance matrix R are presented

in Appendix J. Evidently, the choice of the values of the R matrix elements was found to be very important and therefore, their values were adjusted during the course of the computational analysis. Estimated longitudinal stability derivatives are given in Tables J3a and J3b of Appendix J for forward and aft C.G. locations respectively. These estimates were then used in the computer simulation of the equations of motion given by equation 8.1 which correspond to dynamic tests listed in Table 8. The simulated plots are coded as in Table 8 and presented in Appendix J. As an example experiment 2 is discussed here. Fig. 8.1 shows the actual and estimated transient response corresponding to experiment 2. The agreement between the two responses is clearly very close and proves that the filter is performing the required task. The matching of the actual and estimated responses does not necessarily mean that the filter has produced the right estimates of the stability derivatives. One way of testing this is to simulate the mathematical model of the longitudinal shortperiod oscillations using the estimated derivatives. Fig. 8.2 shows such simulation for the results of experiment 2 of Table 8. Comparison of Figures 8.1 and 8.2 shows the close similarity of the simulated and observed responses.

As mentioned in Section 3, the 'Kalman' filtering was based on the representation of measurement and process noises in the form of white noise. Certainly, the assumption that the measurement noise was white could not be fully justified since during the experiments the wind tunnel was running at somewhere around its resonant speed. This produced periodic oscillations in the flow which in turn affected the model behaviour. This is obviously contrary to the definition of white noise. In cases where these periodic disturbances were pronounced such as that of experiment 3, mismatching occurred. This resulted in poor convergence mainly for control derivatives z_η and m_η.

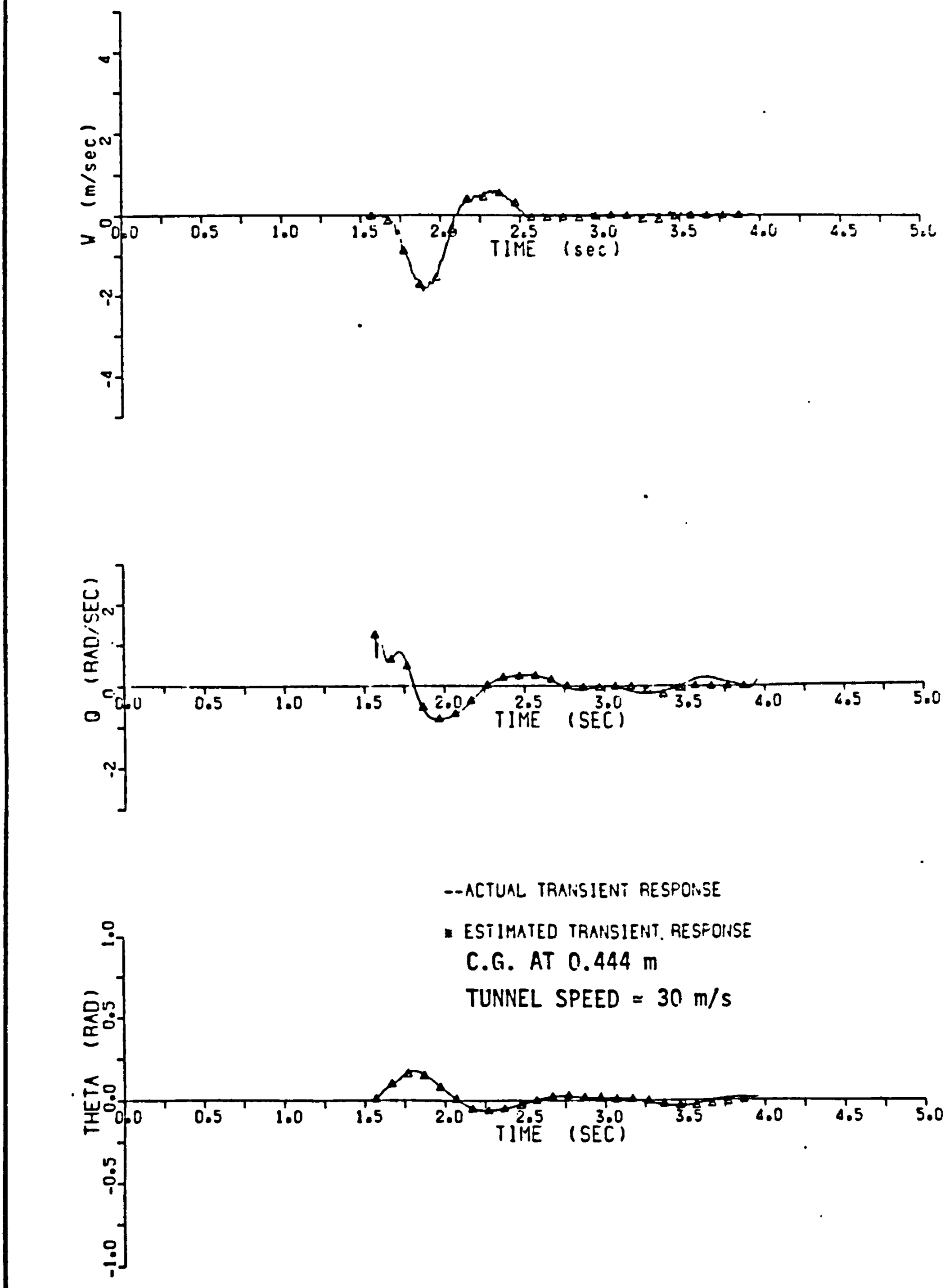

FIGURE 8.1 LONGITUDINAL TRANSIENT RESPONSE TO FOREPLANE PULSE INPUT

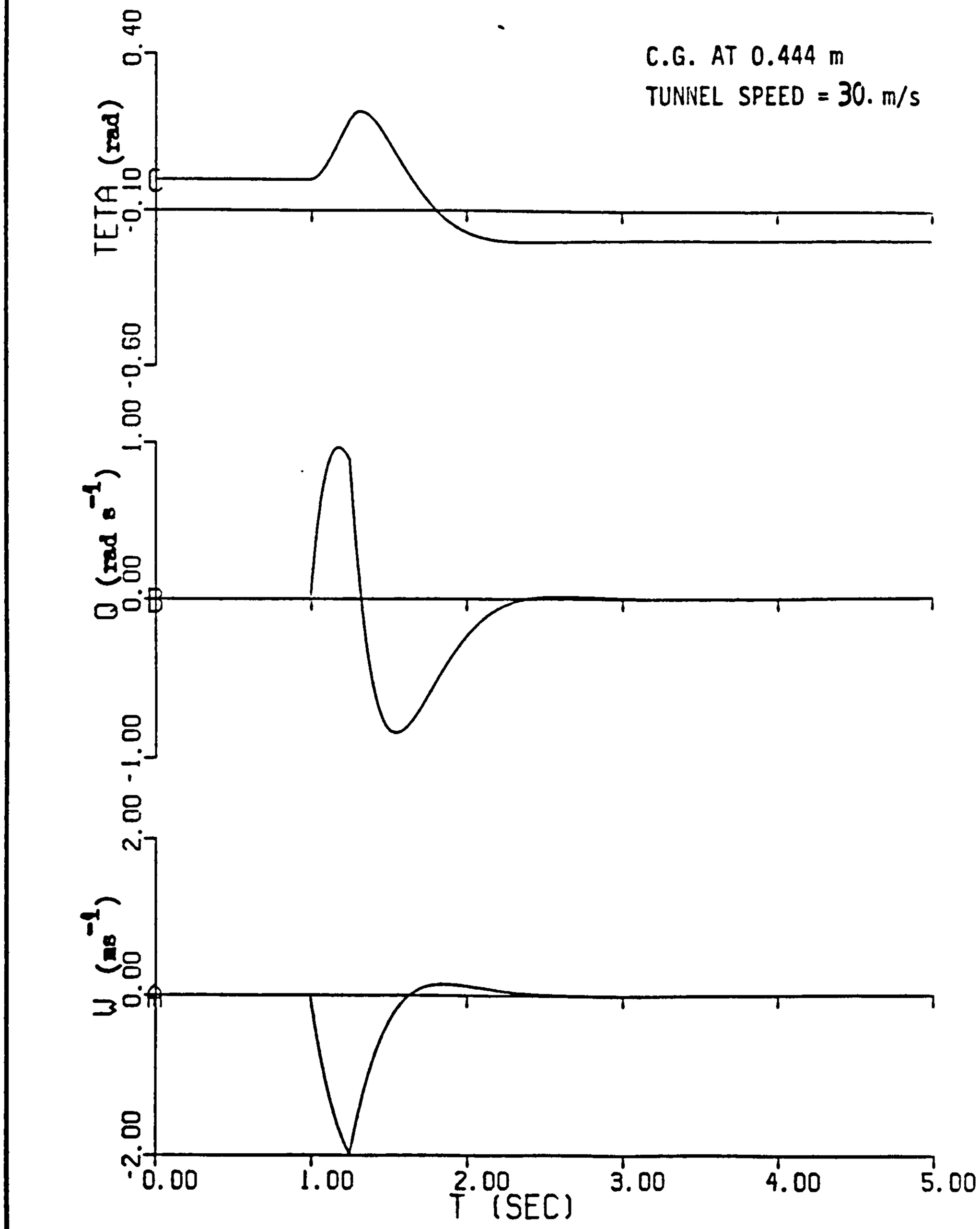

FIGURE 8.2.. SIMULATION OF LONGITUDINAL TRANSIENT RESPONSE USING ESTIMATED DERIVATIVES

LONGITUDINAL EXPFRIMENTS AND THEIR ALLOCATION						
	EXPERIMENT NUMBER	TUNNEL SPEED (m/s)	AMPLITUDE OF FORPLANE INPUT (rad)	DURATION OF INPUT (sec)	FIG. NO.	SIMULATION FIG. NO.
FORWARD C.G. AT 0.444m	EXPERIMENT 1	27.0	0.091	0.4	J12, J13	J 14
	EXPERIMENT 2	30.0	0.091	0.24	J15, J16, J17	J18
AFT C.G. AT 0.440m	EXPERIMENT 3	26.0	0.098	0.24	J19, J20	-
	EXPERIMENT 4	28.0	0.07	0.12	J21, J22	J23

TABLE 8.

FLIGHT CONDITIONS CORRESPONDING TO THE LONGITUDINAL DYNAMIC EXPERIMENT AND KEY TO FIGURE NUMBERS OF RESULTS

9. LATERAL DYNAMIC WIND TUNNEL EXPERIMENTS

The broad outline and objectives in this section are similar to those of Section 8. In particular the lateral dynamic wind tunnel tests which consisted of the lateral transient response to control surface inputs were analysed by means of the extended Kalman filter algorithm from which the respective lateral stability derivatives were estimated. These experiments were subject to the following assumptions.

(i) - for small perturbations in response to rudder and aileron control inputs the heave motion could be neglected.

(ii) - in the absence of a lateral translation the sideslip velocity could be represented as:

$$v = -\beta U_e$$

Under these assumptions the lateral equations of motion are given by Equation 4.7 of Section 4 as:

$$\begin{bmatrix} \dot{v} \\ \dot{p} \\ \dot{r} \\ \dot{\phi} \end{bmatrix} = \begin{bmatrix} 0 & 0 & -U_e & 0 \\ \ell_v & \ell_p & \ell_r & 0 \\ n_v & n_p & n_r & 0 \\ 0 & 1 & 0 & 0 \end{bmatrix} \begin{bmatrix} v \\ p \\ r \\ \phi \end{bmatrix} + \begin{bmatrix} 0 & 0 \\ \ell_\xi & \ell_\zeta \\ n_\xi & n_r \\ 0 & 0 \end{bmatrix} \begin{bmatrix} \xi \\ \zeta \end{bmatrix} \quad \text{- - - - - EQ(9.1)}$$

9.1 Initial Experiments

Initial experiments were undertaken to obtain basic response data for rudder or aileron impulse disturbances at a limited number of flight conditions. As a consequence of assumption (i) above, there was no need to record the heave motion. Thus, with the C.G. set at its forward position of 0.444 m from datum, the model was fixed at the centre of the vertical rod, being free to traverse ±0.01 m up and down the rod. This was done in order that, prior to the introduction of disturbances, the model was flying straight and level in the centre of the tunnel flow. Disturbances were then initiated by means of rudder or aileron pulse control inputs. A total of 16 experiments were conducted as listed in Table 9.1 below.

	FORWARD C.G.		AFT C.G.	
TUNNEL SPEED	AILERON I/P	RUDDER I/P	AILERON I/P	RUDDER I/P
27	✓	✓	✓	✓
29	✓	✓	✓	✓
31	✓	✓	✓	✓
33	✓	✓	(data lost)	(data lost)
			×	×

TABLE 9.1

9.2 Validity of the Lateral Equations

As the model was extremely responsive and the tunnel flow less than ideal, the roll motion under trimmed flight conditions was subject to large perturbations. Therefore, for the unaugmented aircraft model the roll responses were so contaminated by these perturbations and they were not suited for analysis. Furthermore, by limiting the experiments to those involving rudder pulse control inputs, there was no need to include the control derivatives associated with the aileron. The equations of lateral motion subject to these omissions then become:

$$\begin{bmatrix} \dot{v} \\ \dot{p} \\ \dot{r} \\ \dot{\phi} \end{bmatrix} = \begin{bmatrix} 0 & 0 & -U_e & 0 \\ \ell_v & \ell_p & \ell_r & 0 \\ n_v & n_p & n_r & 0 \\ 0 & 1 & 0 & 0 \end{bmatrix} \begin{bmatrix} v \\ p \\ r \\ \phi \end{bmatrix} + \begin{bmatrix} 0 \\ \ell_\zeta \\ n_\zeta \\ 0 \end{bmatrix} \zeta \qquad \text{- - - - - EQ(9.2)}$$

Equations 9.2 were then implemented in the Extended Kalman Filter parameter identification program through which the rudder initiated lateral transient responses were analysed. Table 9.2 below lists these experiments and the various parameter changes associated with them.

However, it should be pointed out that the outcome of the lateral dynamic experiments, namely the estimated lateral stability derivatives,

differed from those of an unconstrained model since in Equation 9.2 the lateral forces y_p, y_r and especially y_v were neglected whereas ℓ_v and n_v were retained. Further, the inclusion of y_v in the equations of motion would confuse the filter since the sideslip velocity v cannot be measured independently.

9.3 Analysis of the Lateral Experiments

The analysis process applied to the lateral experiments was similar to that applied to the longitudinal dynamic tests. However, the choice of measurement covariance matrix R in this case was critical since initial experiments showed that the extended Kalman filter estimator would match the transient response for a wide range of values of R matrix, whereas, the convergence of the estimated lateral stability derivatives seemed to be best for a much more limited range of values of the elements of the covariance matrix R.

Due to the correlation between roll and yaw motions, estimates of the stability derivatives ℓ_v and n_v oscillate in value which was found to be a function of the R matrix. These observations are discussed in detail in Section 12. The results of the analysis in the form of estimated lateral derivatives based on an average of ten runs for each dynamic test are presented in Tables J4, J5 and J6, J7 of Appendix J together with transient response plots coded as listed in Table 9.2 for forward and aft C.G. positions respectively. Furthermore, the initial value of the elements of the covariance matrices G, R and Q are given in Section J4 of Appendix J, which are based on the method of calculations of Section J1. Unfortunately, dynamic experiments, Exp. 10 and Exp. 11, failed to produce any meaningful results, since, as Figure J38 and Figure J39 of Appendix J indicate despite matching the response, the estimated stability derivative values determined by the extended Kalman filter algorithm would not converge. This behaviour would be expected since the mathematical model implemented in the extended Kalman filter is not representative of the observed response. As an example, the results of experiment 5 of Table 9.2 are included here as Figs.9.1 and 9.2. Fig. 9.1 shows the lateral transient response due to rudder pulse input together with the estimated response. The estimated response is certainly very close to the observed response but as mentioned in Section 8, not necessarily an indication that the filter estimates of the respective lateral derivatives are of the right order and sign.thus it was essential to simulate the mathematical model of the lateral transient reponse given by Eq. 9.2 using the estimated derivatives. This simulation is shown in Fig. 9.2 and clearly the simulated response matches the observed response as shown in Fig. 9.1.

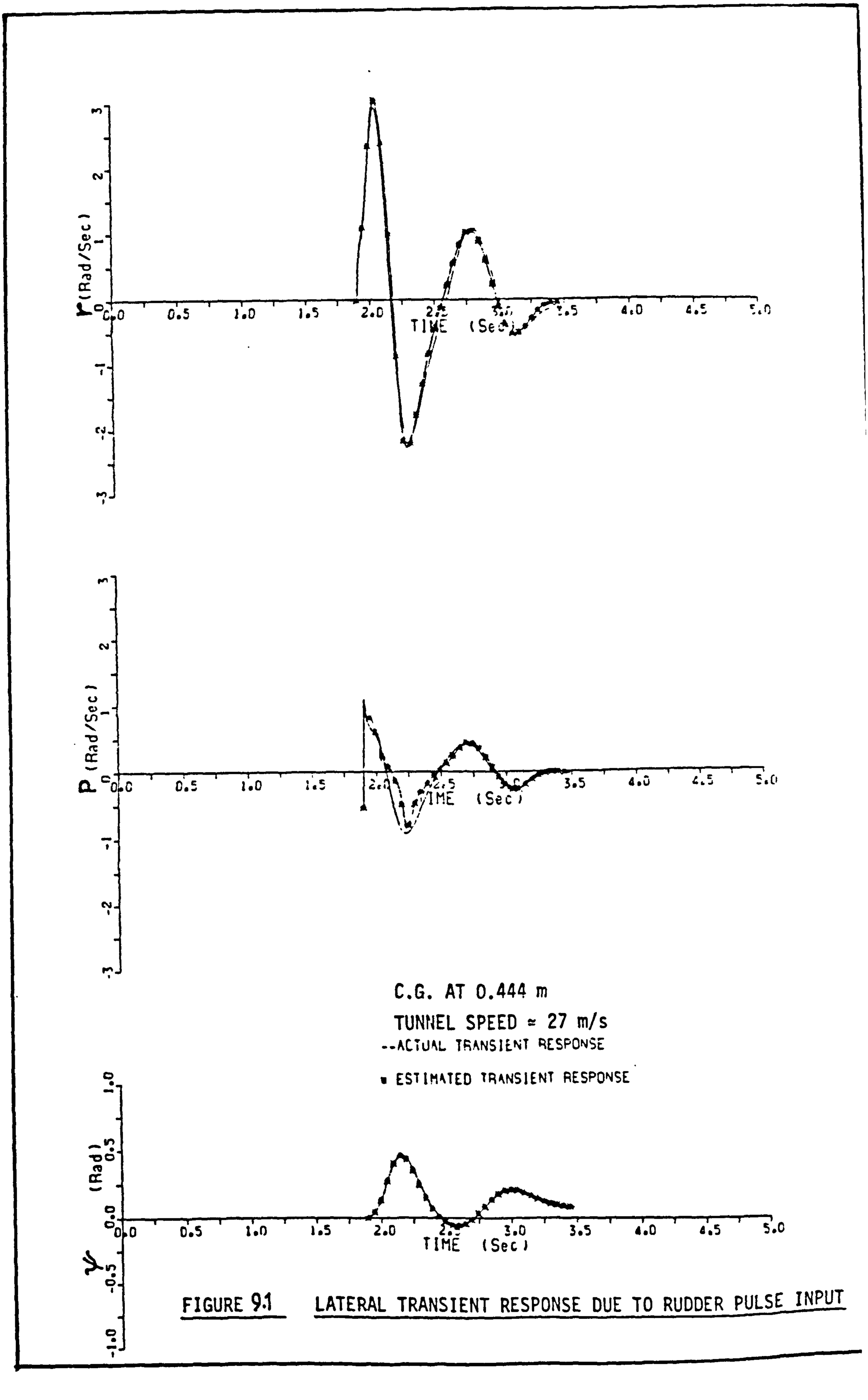

FIGURE 9.1 LATERAL TRANSIENT RESPONSE DUE TO RUDDER PULSE INPUT

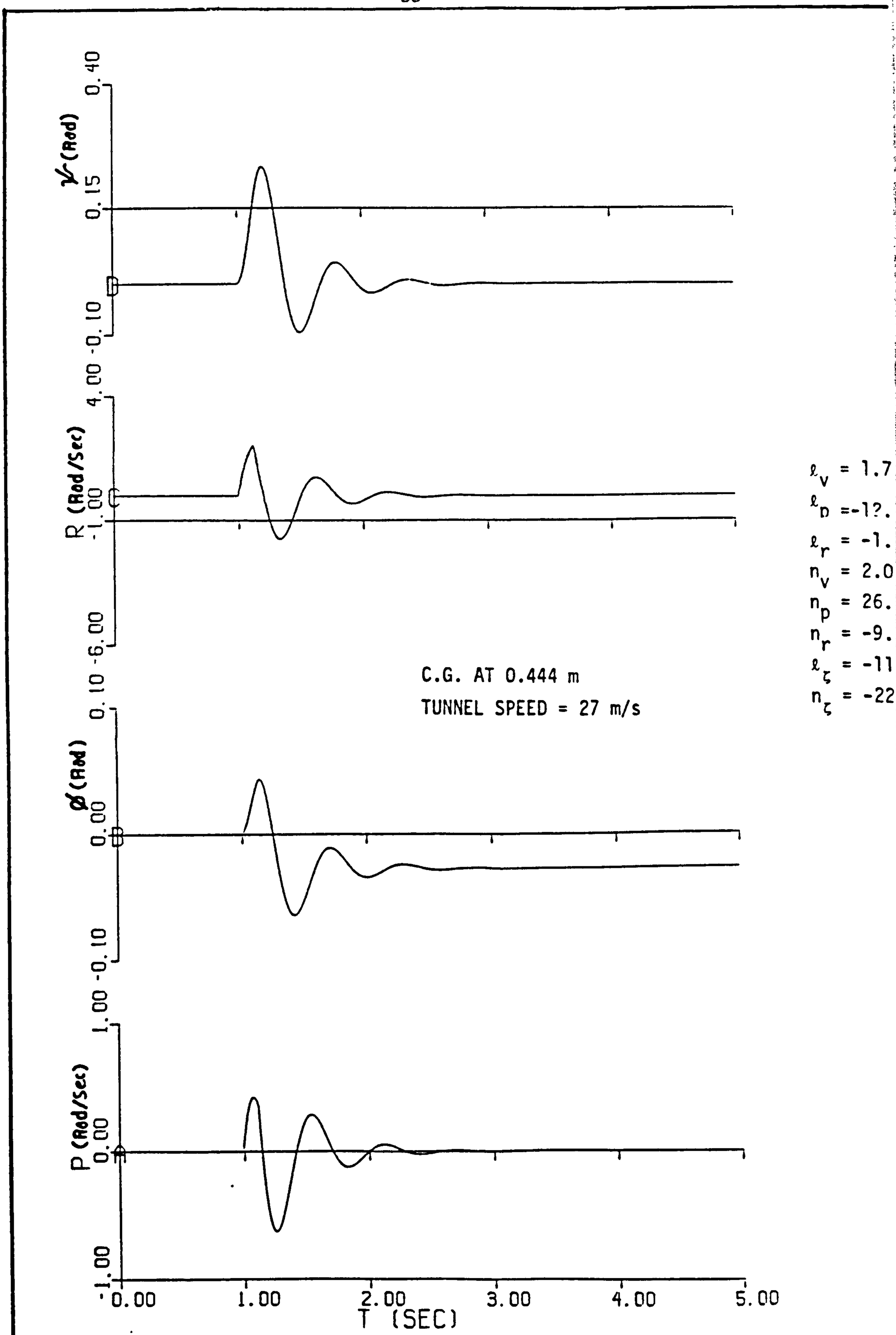

ℓ_v = 1.7
ℓ_n =-1?.
ℓ_r = -1.
n_v = 2.0
n_p = 26.
n_r = -9.
ℓ_ζ = -11
n_ζ = -22

C.G. AT 0.444 m
TUNNEL SPEED = 27 m/s

FIGURE 9.2 SIMULATED LATERAL TRANSIENT RESPONSE USING ESTIMATED DERIVATIVES

LATERAL EXPERIMENTS				RESULTS GIVEN IN SECTION R2 OF APPENDIX R: FIGURE NOS.		
TUNNEL SPEED (m/s)	EXPERIMENT NUMBER	AMPLITUDE RUDDER DEFLECTION (rad)	DURATION OF PULSE CONTROL INPUT (sec)	EXPERIMENT	SIMULATION	
27	EXP - 5	0.089	0.12	J24, J25	J26	FORWARD C.G. AT 0.444m FROM DATUM
29	EXP - 6			J27, J28	J29, J30	
31	EXP - 7			J31, J32	-	
33	EXP - 8			J33, J34	J35	
27	EXP - 9	0.089	0.12	J36	J37	AFT C.G. AT 0.44m FROM DATUM
29	EXP - 10			J38	-	
31	EXP - 11			J39	-	

TABLE 9.2

FLIGHT CONDITIONS CORRESPONDING TO THE LATERAL DYNAMIC EXPERIMENTS AND KEY TO FIGURE NUMBERS OF RESULTS

10. STATIC WIND TUNNEL MEASUREMENTS

In the work discussed in the preceding sections, most of the aerodynamic parameters assumed were based on theoretical estimates. In order to assess the validity of these parameters it was decided to conduct limited static wind tunnel tests so that some of the more important aerodynamic characteristics of the dynamic model could be measured and analysed, and for this purpose the CoA 8' x 6' low speed wind tunnel was used.

The support structure consisted of a streamlined vertical strut which was attached to the gimbal brackets in the model. The strut was designed in such a way that the centre of the balance and the centre of gravity of the model were coincident. As a result, no axis transformations were necessary as far as the symmetric force and moment measurements were concerned. The support structure was completed by tail wires which could be adjusted remotely and in doing so, change the incidence of the model. Fig. 10.1 shows diagramatically the model and the supporting structure. Obviously the presence of the support structure would lead to small errors in the measured values of lift, drag, moments, etc . these corrections were obtaine by conducting appropriate force and moment measurements on the support structure in the absence of the model.

It must be emphasised that the F.S.W. aircraft model was primarily designed for dynamic, rather, than static tests. In general, static models are made with a safety factor of 8 to 10 in mind which literally means a solid construction. Dynamic tests however, had indicated that the model could withstand the stresses at speeds and incidences of up to 30 m/s and 25^{o} respectively while free to fly in four degrees of freedom. As a result the support structure was designed to accommodate the latter limits.

Generally, static wind tunnel measurements are rather tedious, the reason being that the tunnel has to be stopped and restarted every time there is a need to change the control surface setting, etc. In the case of large tunnels the restart procedure is time consuming since the tunnel speed has to be increased gradually until steady state conditions at the required tunnel speed are reached. As far as the dynamic model was concerned, measurements could be taken continuously since all the control surfaces were actuated remotely via the umbilical chord. Figure 10.2 represents a block diagram of the instrumentation.

10.1 Tunnel Corrections

The presence of a model in the wind tunnel disturbs the flowfield in the working section and therefore, the measurements have to be corrected for these interference effects. From Ref. 12, the interference effects relevant here are;

(i) Solid blockage
(ii) Wake blockage
(iii) Lift effect

These are discussed below.

10.1.1 Solid Blockage

This involves a change of axial velocity around the model since the presence of the model has blocked part of the working section, thereby reducing the section area. It is convenient to express the blockage in terms of a factor ε_s defined by

$$U_F = U_T(1 + \varepsilon_s)$$

where U_T is the tunnel speed and U_F is the corresponding free-air speed which is taken to be the speed at the working section. The solid blockage is considered to have two contributory components, namely blockage due to fuselage ε_{s_F} and blockage due to a wing of finite aspect ratio ε_{s_W}. Then in the notation of Ref. 12,

(i)- for a body of revolution,

$$\varepsilon_{s_F} = (\tfrac{\pi}{4})^{\frac{1}{2}}\tau(1 + 0.4\,\frac{t}{c})\,\frac{V}{A^{3/2}}$$

(ii)- for a finite wing,

$$\varepsilon_{s_W} = (\tfrac{\pi}{4})^{\frac{1}{2}}\tau(1 + 1.2\,\frac{t}{c})\,\frac{V}{A^{3/2}}$$

where $\frac{t}{c}$ is the fineness ratio, V is the volume of the model fuselage or wing as the case may be, A is the tunnel cross-section area at the working section and $(\frac{\pi}{4})^{\frac{1}{2}}\tau = 0.723$ for a tunnel with a square cross-section at the working section.

10.1.2 Wake Blockage

This is a similar effect to that of sub-section 10.1.1, but it corresponds to a reduction of speed within the wake of the model. This effect is represented by the factor ε_W and as before,

$$U_F = U_T(1 + \varepsilon_W)$$

In the notation of Ref. 12, ε_W can be expressed by,

$$\varepsilon_W = \tfrac{1}{4} \frac{S}{bh} C_D$$

where S is the area on which the drag coefficient is based, h and b are the tunnel height and breadth respectively. This expression can be used for both a body of revolution and a wing of finite AR. This effect is usually negligible for streamlined bodies and therefore was not taken into account in the analysis of the static wind tunnel measurements in the present study.

10.1.3 Lift Effect

This arises from the tunnel boundary constraints put on the velocity field induced by the bound and trailing vortices. For a wing of finite aspect ratio Ref. 12 gives,

$$\alpha_F - \alpha_T = \delta \frac{S}{C} C_{L_T}$$

where subscripts F and T have the previous meanings, S and C are the wing and tunnel cross-section areas respectively and δ is a factor whose value is dependent on the shape of the working section. As a result of the change in incidence, the lift vector is inclined to its correct direction and the drag has to be approximately corrected, viz,

$$C_{D_F} - C_{D_T} = (\alpha_F - \alpha_T) C_{L_T}$$

Figure 254 of Ref. 12 is reproduced in Appendix M and shows the interference due to lift effect in three-dimensional flow for a closed rectangular tunnel as a function of wing span to tunnel breadth ratio.

10.2 Test Procedures for Force and Moment Measurements

With the instruments set up, the model was given the required attitude and the wind-off balance force readings were set to zero and recorded. With wind-on the control surface and/or model incidence were varied remotely without the need to shut the tunnel down between readings and the corresponding force readings were recorded. In the case of moment measurement, the balance had to be set to zero for every attitude and in order to save time, the following technique was adopted. For every control surface setting the model was taken through the incidence range and the balance readings recorded. This process was repeated for all control surface angle settings. From the analysis of these measurements, the required results were extracted. Tables 10.1 and 10.2 represent the flight-attitude conditions covered by the static tests.

10.3 Data Acquisition and Analysis

The complete data acquisition process is shown in diagrammatic form on Fig. 10.2, where model reference attitude and tunnel balance measurements were recorded on a chart recorder and mini computer respectively. In recording the data and its subsequent analysis, use was made of two computer programs both of which were interactive in nature. Although part of a standard 8' x 6' tunnel data acquisition system, both of the programs had to be modified to a great extent before they could be used specifically for the dynamic model. By the implementation of tunnel corrections and appropriate axis transformations the measured data from the first computer program were analysed by the second program, the output of which was the aerodynamic data. The output of this process was then formed into graphs from which the aerodynamic data were then obtained. Tables H2 and H4 of Appendix H list the results of the static tunnel measurements. For simplicity all forces and moments are given in non-dimensional form. The values of aerodynamic parameters given in Tables H2 and H4 have been extracted from Figures H1 - H14, which include $C_L - \alpha$, $C_m - \alpha$, $C_n - \zeta$, $C_D - \alpha$, and $C_\ell - \xi$ variations. Some examples of the results are presented here. Figures 10.3, 10.4, 10.5, 10.6 and 10.7 represent the $C_L - \alpha$, $C_D - C_L^2$, $C_m - \alpha$, $C_n - \zeta$ and $C_\ell - \xi$ variations respectively. The appropriate tunnel speeds are indicated on the respective figures.

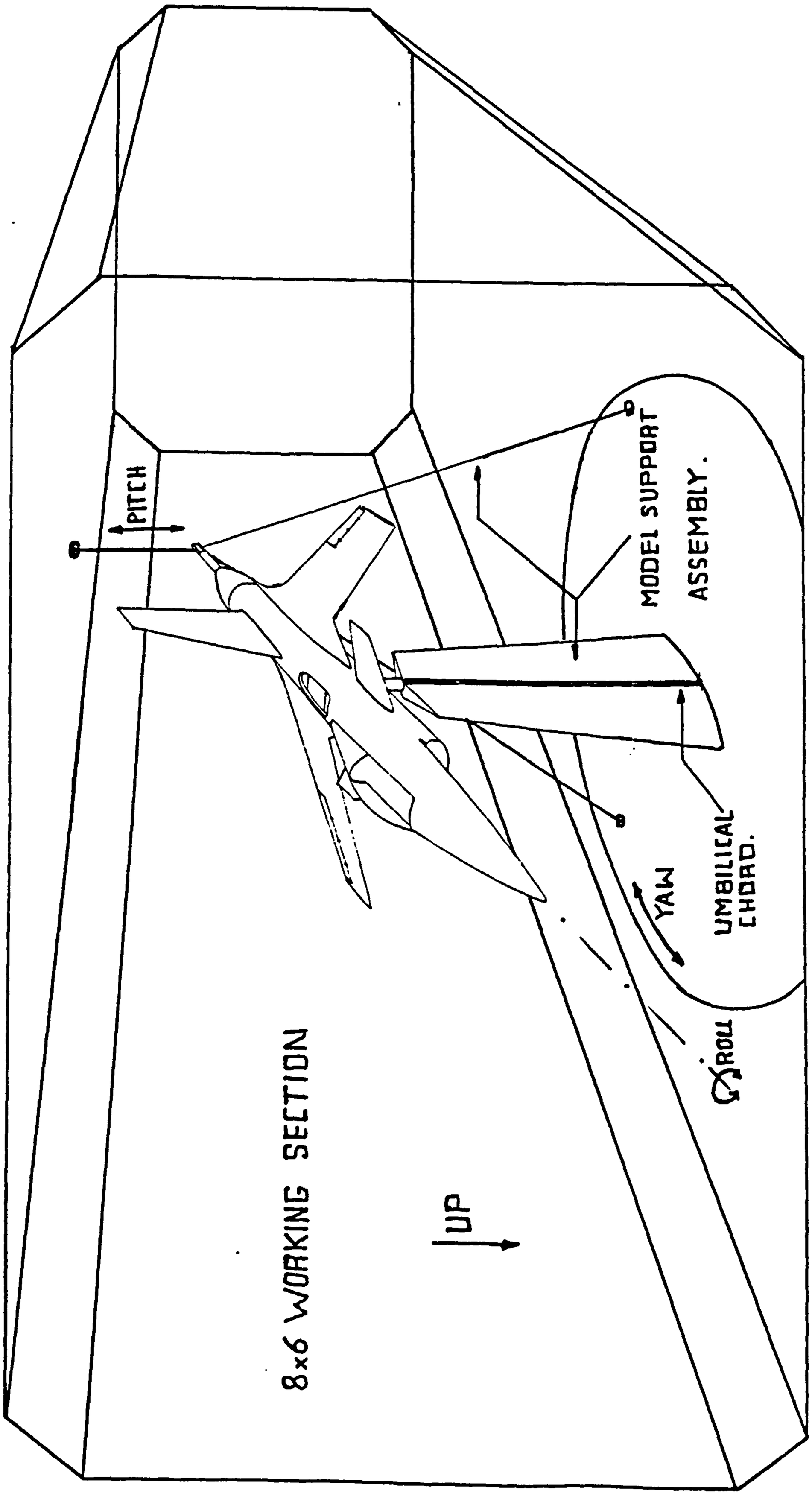

FIG.10.1 LAY-OUT OF STATIC WIND TUNNEL MEASURMENTS.

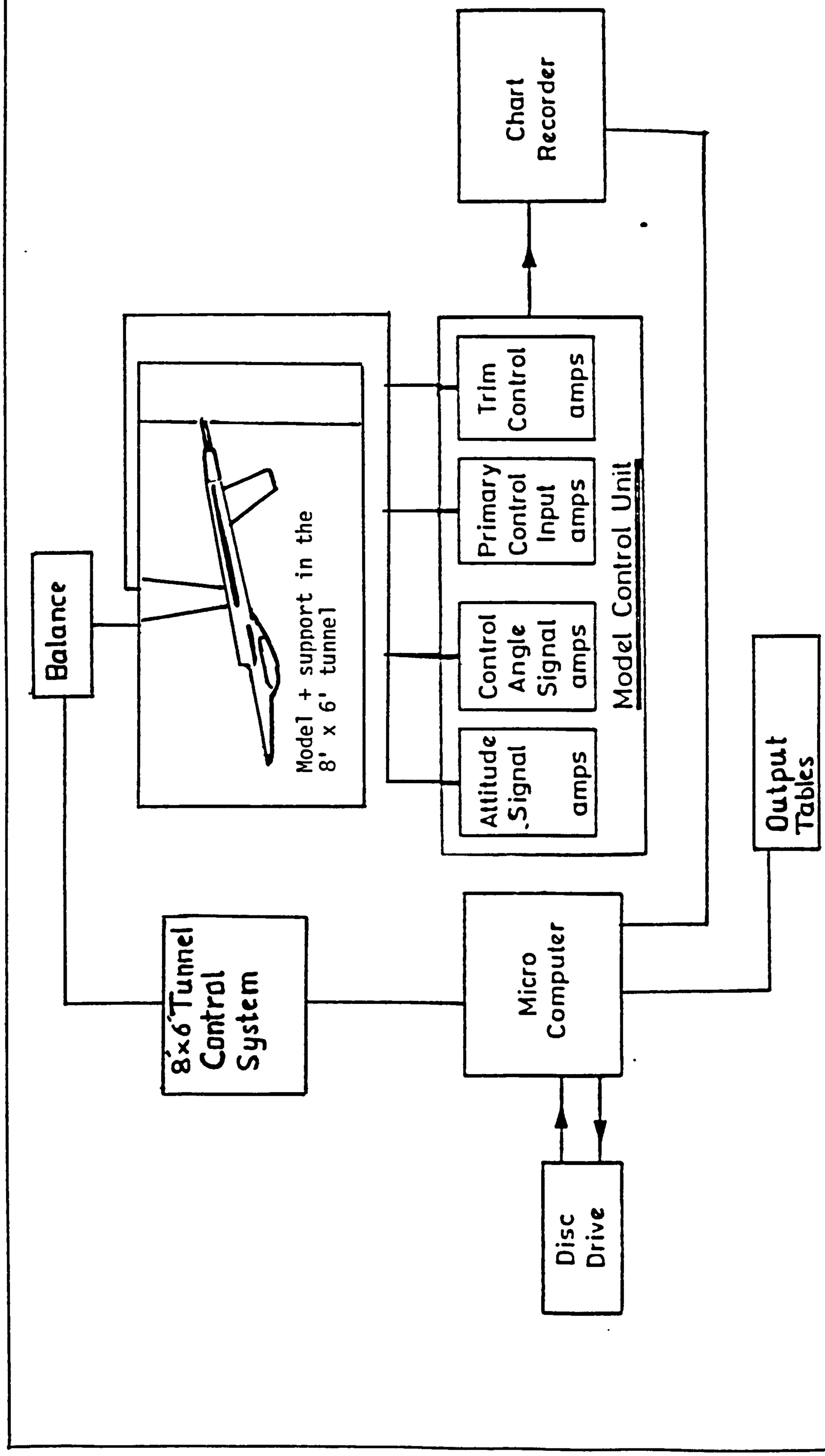

FIGURE.10.2 DATA ACQUISITION AND INSTRUMENTATION FACILITY FOR THE STATIC TUNNEL MEASUREMENTS

C.G. AT 0.435 m FROM DATUM	TUNNEL SPEED ≃ (m/s)	VARIATION OF C_L WITH α^o (CANARD ON)	VARIATION OF C_M WITH α^o (CANARD OFF)	DRAG POLARS		VARIATION OF C_L WITH α^o (CANARD OFF)
				CANARD ON	CANARD OFF	
	19	FIG. M3	FIG. M4	FIG.M	-	-
	25	FIG. M2	-	FIG.M7	-	-
	28	FIG. M1	FIG. M5	FIG.M6	FIG.M15	FIG. M12

TABLE 10.1

SYMMETRICAL FORCE-MOMENT MEASUREMENTS CORRESPONDING TO COVERED FLIGHT-ATTITUDE CONDITIONS

C.G. AT 0.435 m FROM DATUM	TUNNEL SPEED ≃ (m/s)	VARIATION OF C_n WITH ζ^o AT $\alpha = 0^o, 20^o$ WITH $\psi = 0^o$	VARIATION OF C_n WITH ζ^o AT $\alpha = 0^o, 20^o$ WITH $\psi = 10^o, 15^o$ IN EACH CASE	VARIATION OF C_ℓ WITH ξ^o AT $\alpha = 0^o$ $\psi = 0^o$
	19.0	FIG. M9	FIG. M10	-
	25.0	-	-	FIG. M11

TABLE 10.2

ASYMMETRICAL FORCE-MOMENT MEASUREMENTS CORRESPONDING TO COVERED FLIGHT-ATTITUDE CONDITIONS

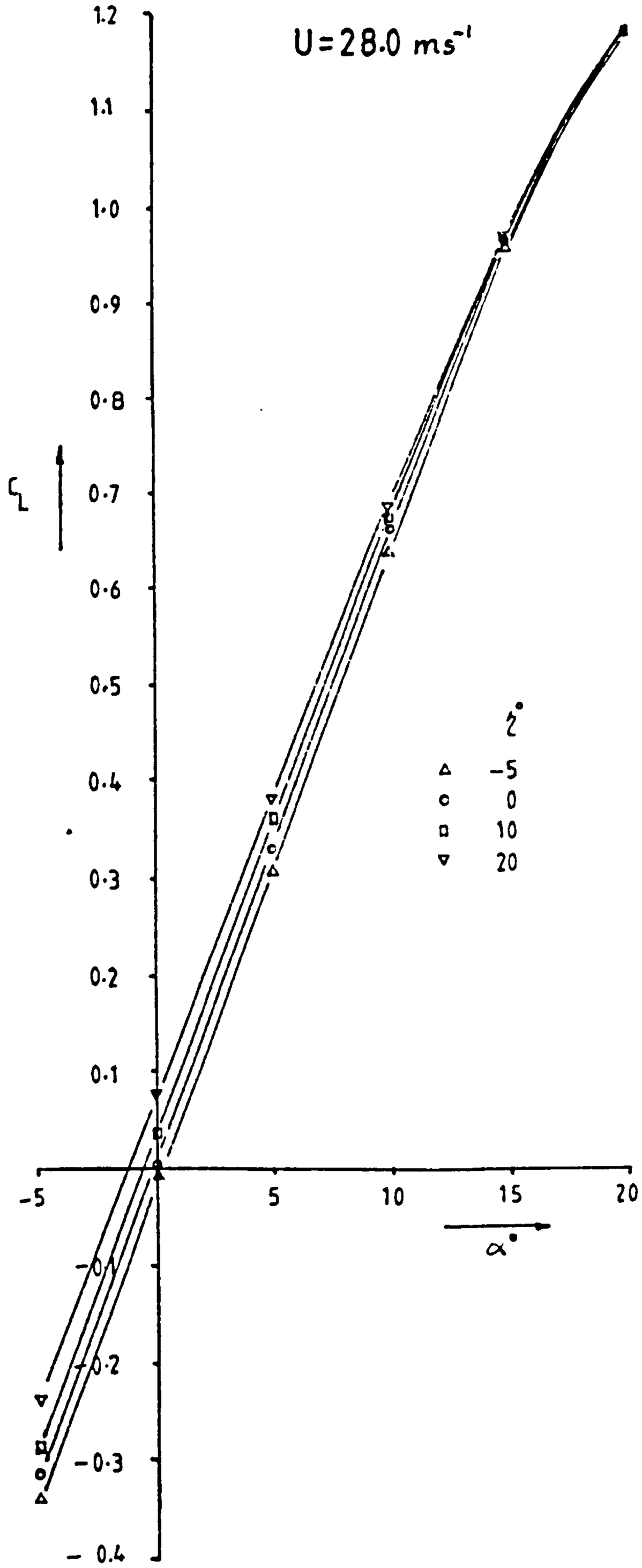

FIGURE 10.3

C_L - α VARIATION - FOREPLANE ON

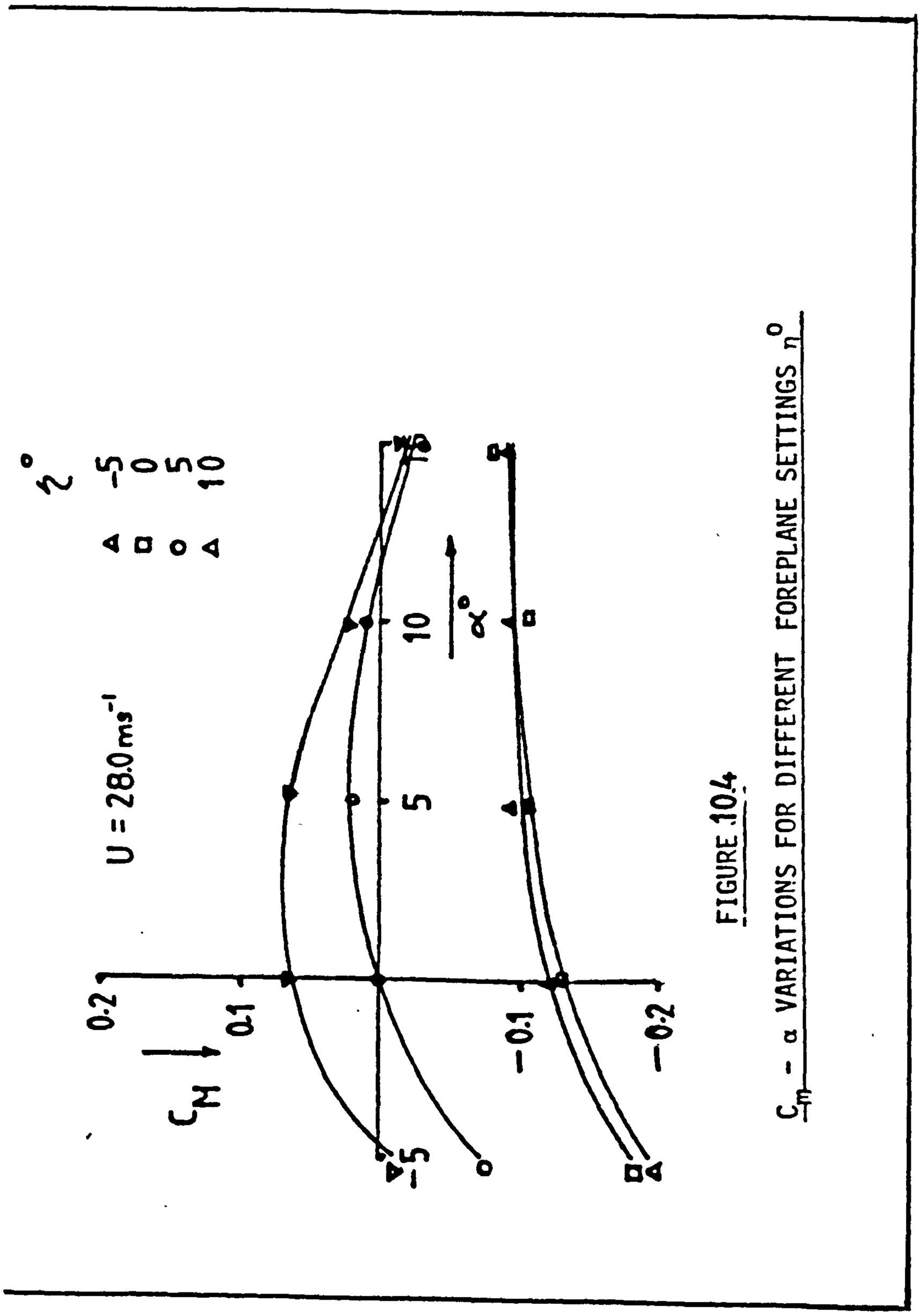
C_m - α VARIATIONS FOR DIFFERENT FOREPLANE SETTINGS η^o
C_M
α°
U = 28.0 ms⁻¹
0.2
0.1
-0.1
-0.2
5
10
-5
0
5
10

FIGURE 10.4

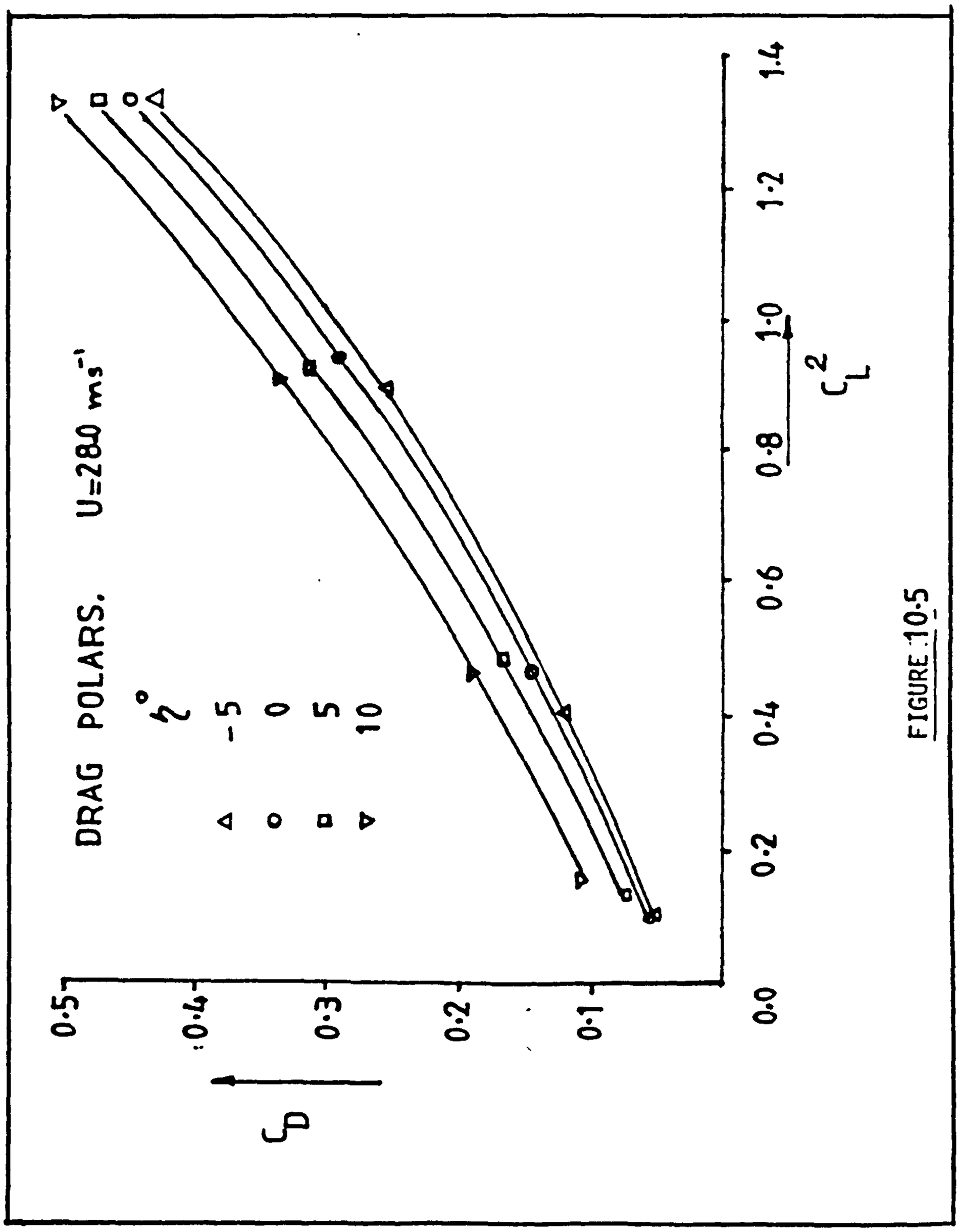
DRAG POLARS.
U=280 ms⁻¹
α°
-5
0
5
10
0·5
0·4
0·3
0·2
0·1
0·0
0·2
0·4
0·6
0·8
1·0
1·2
1·4
C_L^2
C_D

FIGURE 10.5

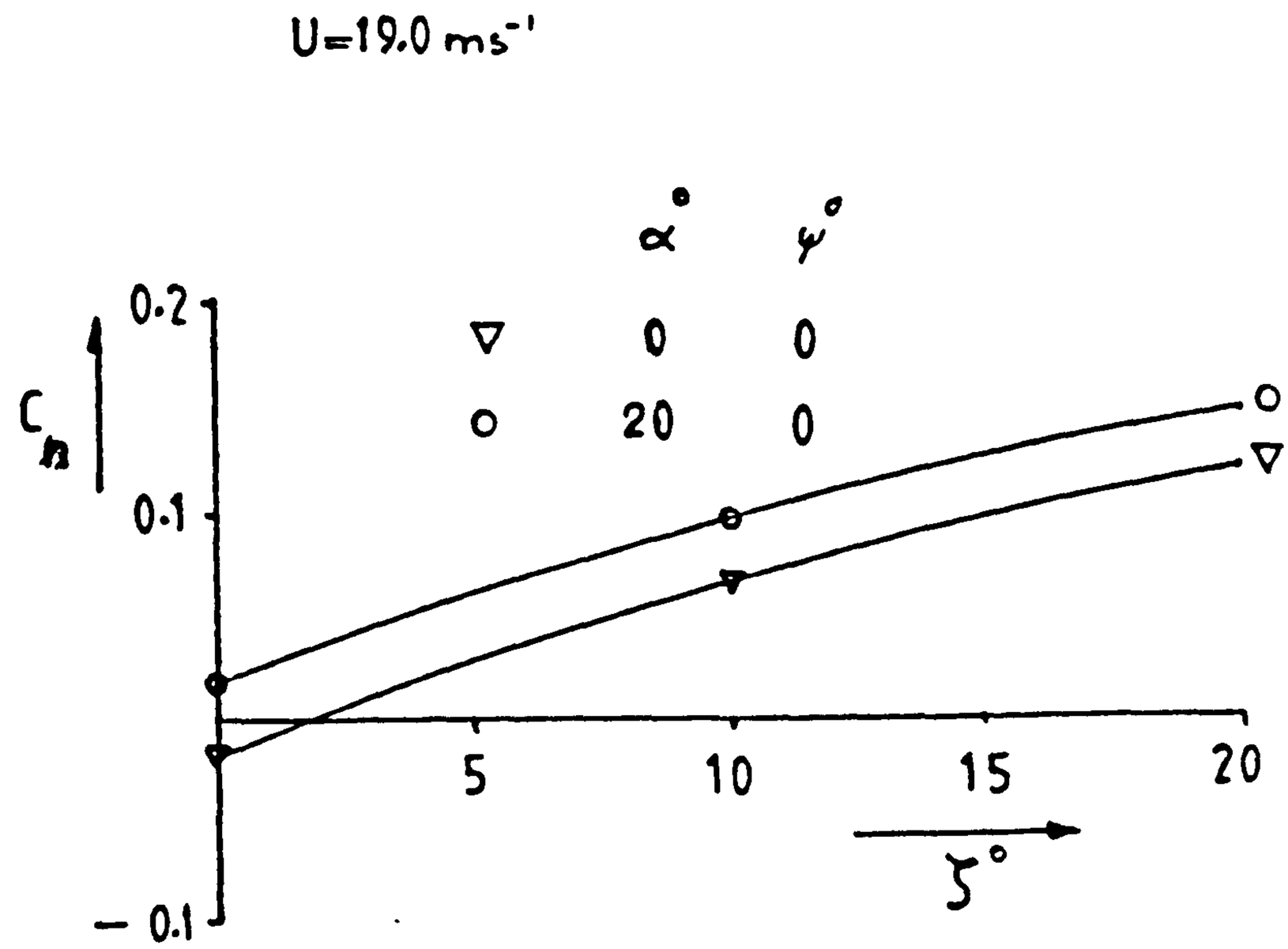

(i)- C_n - ζ^o VARIATIONS FOR DIFFERENT INCIDENCES α^o

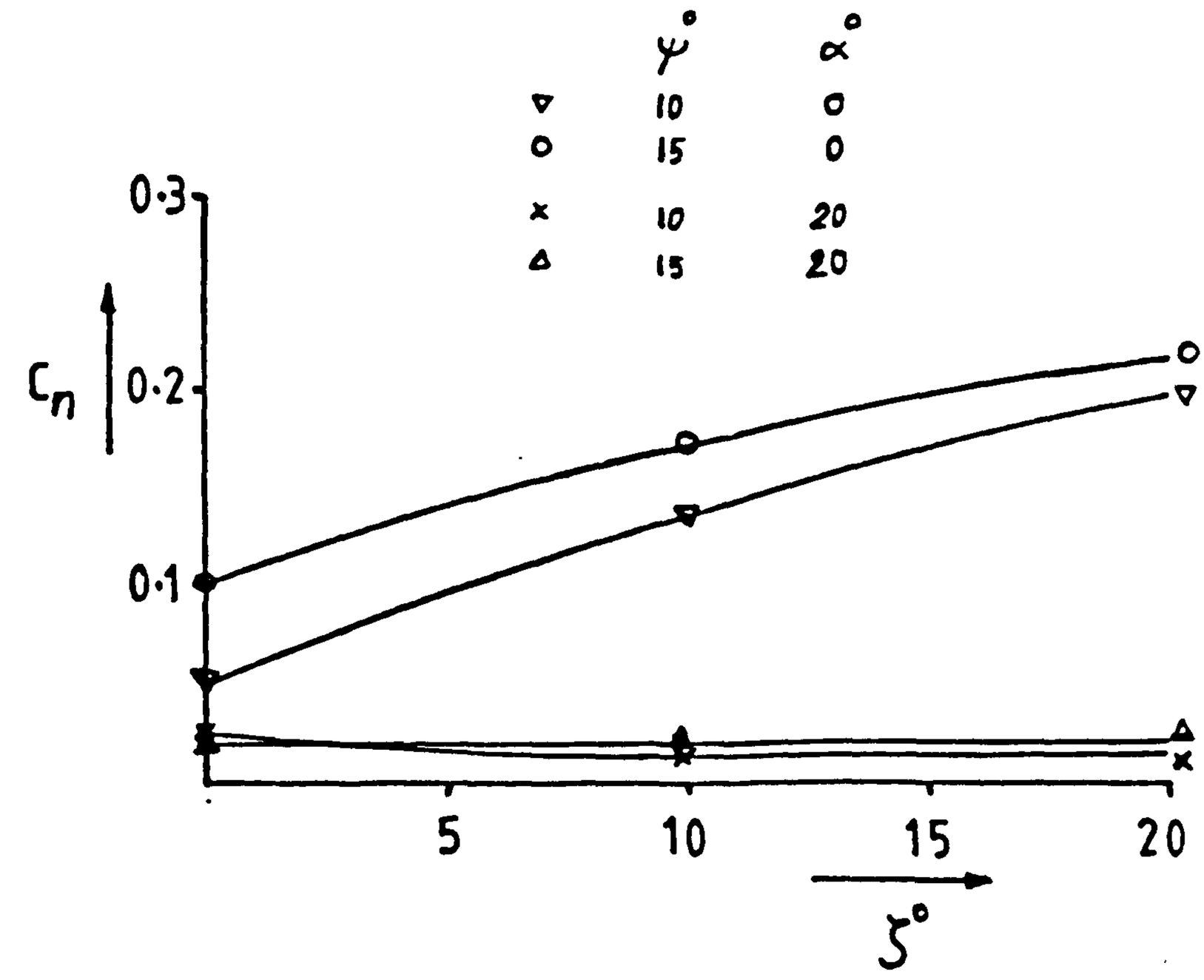

FIGURE 10.6

(ii)- C_n - ζ^o VARIATIONS FOR DIFFERENT INCIDENCES α^o

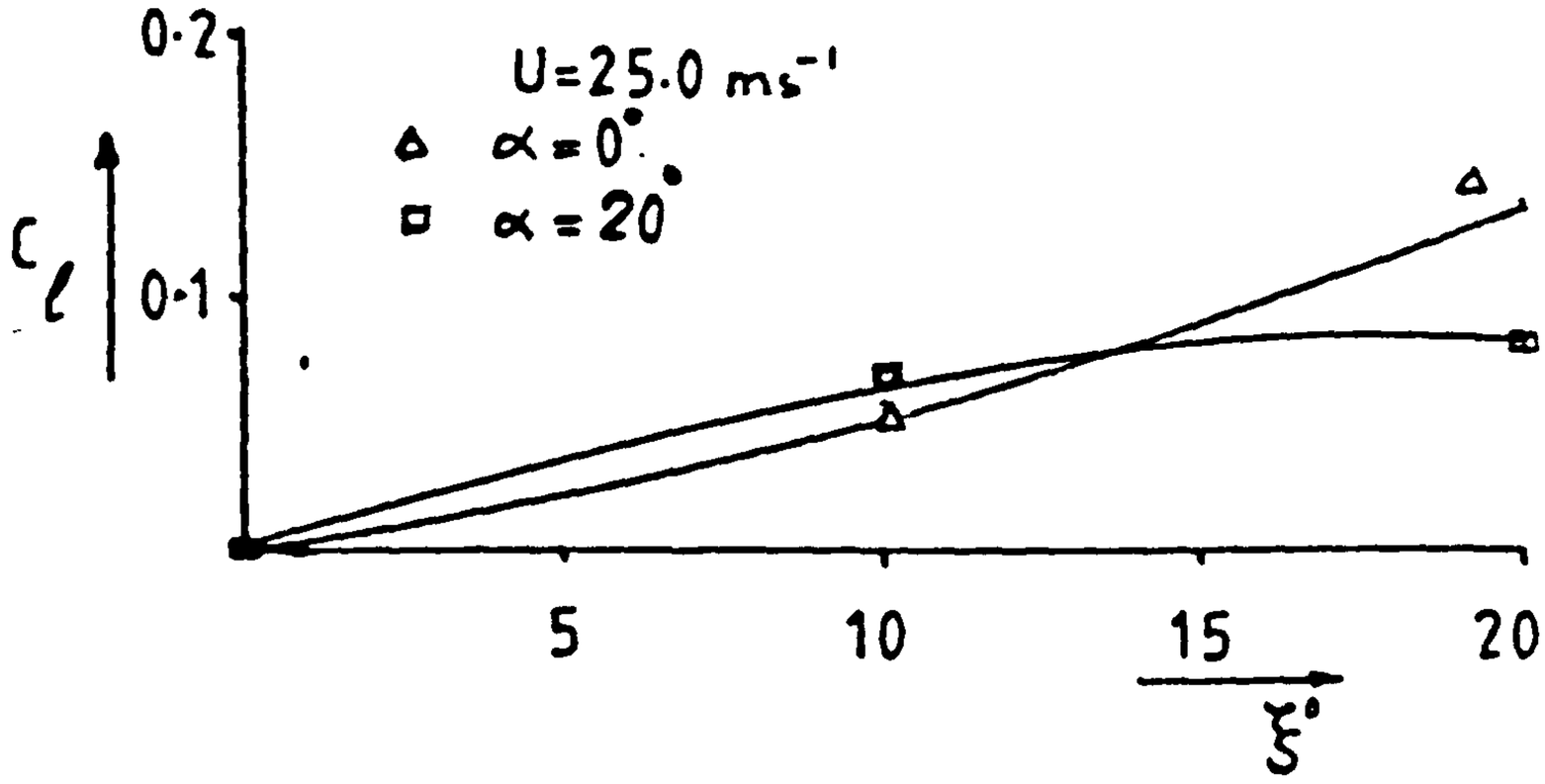

FIGURE 10·7

C_ℓ - ξ^o VARIATION

11. THE DESIGN OF AN ANALOGUE HEIGHT HOLD CONTROL SYSTEM

As was mentioned in Section 8, longitudinal experiments involving the short period oscillations of the model on the test rig were limited to a finite range of tunnel speed. This was because foreplane deflections of magnitude sufficient to disturb the short period pitching oscillation would also result in relatively large vertical motions in which the model would impact the end stops. In order to increase the experimental speed range, a height hold autopilot system was designed. The control command demands the model position on the vertical rod and any subsequent departures from this position would automatically activate the control system to return the model to its original position and attitude.

Clearly, in order to design such a control system the longitudinal dynamic characteristics of the model would be needed. These characteristics were identified here through the mathematical model of the model response. Analysis of the system was then based on the substitution of the longitudinal stability derivatives with the extended Kalman filter algorithm.

It must be noted that even in a steady level flight condition, the model would be subjected to external disturbances which are a direct result of turbulence in the tunnel. The turbulence induces symmetric aerodynamic loads on the model which affect its vertical position. Due to the complexity of representing the transfer function of this behaviour, the effect of such disturbances was assumed negligible, which was justifiable if a lateral auto-pilot were to be used to suppress rolling motion.

Initial experiments employing a simple height feedback control loop proved unsatisfactory in many ways, therefore, a two-state feed-back control system was developed, the analysis of which, together with the possible inclusion of a heave velocity feed-back loop, constitutes the rest of this section.

11.1 Design of the Control System

The equations representing the short period oscillations with the inclusion of height are,

$$\underbrace{\begin{bmatrix} s - z_w & -s(U_e + z_q) & 0 \\ -m_w & s^2 - s\,m_q & 0 \\ 1 & -U_e & s \end{bmatrix}}_{A} \underbrace{\begin{bmatrix} \bar{w} \\ \bar{\theta} \\ \bar{h} \end{bmatrix}}_{x} = \begin{bmatrix} z_\eta \\ m_\eta \end{bmatrix} \bar{\eta}$$

where $\bar{w}$, $\bar{\theta}$ and $\bar{h}$ mean w(s), θ(s) and h(s) respectively. Therefore unless otherwise stated the latter notation is used throughout this section.

Pitch attitude response to foreplane control input, with the application of Cramer's rule is given by:

$$\frac{\bar{\theta}}{\bar{\eta}} = \frac{N_\eta^\theta(s)}{\Delta(s)} = \frac{1}{\det A}\begin{vmatrix} s - z_w & z_\eta & 0 \\ -m_w & m_\eta & 0 \\ 1 & 0 & s \end{vmatrix}$$

where

$$\det A = \Delta(s) = s^2(s^2 + s(-z_w - m_q) + (m_q z_w - m_w(U_e + z_q)))$$

$$\therefore \quad \frac{N_\eta^\theta(s)}{\Delta(s)} = \frac{s(s\,m_\eta + z_\eta m_w - z_w m_\eta)}{s^2(s^2 + s(-z_w - m_q) + (m_q z_w - m_w(U_e + z_q)))}$$

$$= \frac{s\,m_\eta + z_\eta m_w - z_w m_\eta}{s(s^2 + s(-z_w - m_q) + (m_q z_w - m_w(U_e + z_q)))} \qquad \text{- - - - - EQ.11.1}$$

Similarly, the height response to elevator transfer function is given by,

$$\frac{\bar{h}}{\bar{\eta}} = \frac{N_\eta^h(s)}{\Delta(s)} = \frac{1}{\Delta(s)}\begin{vmatrix} s - z_e & -s(U_e + z_q) & z_\eta \\ -m_w & s^2 - sm_q & m_\eta \\ 1 & -U_e & 0 \end{vmatrix}$$

$$\therefore \quad \frac{\bar{h}}{\bar{\eta}} = \frac{-s^2 z_\eta + s(U_e m_\eta - m_\eta(U_e + z_q) + z_\eta m_q) + U_e(z_\eta m_w - z_w m_\eta)}{s^2(s^2 + s(-z_w - m_q) + (m_q z_w - m_w(U_e + z_q)))}$$

The design of the height control system was split into two parts, namely a pitch loop and a height loop control system.

11.2 Pitch Loop Design

Pitch control is achieved via the θ-feedback loop of Fig. 11.1 below.

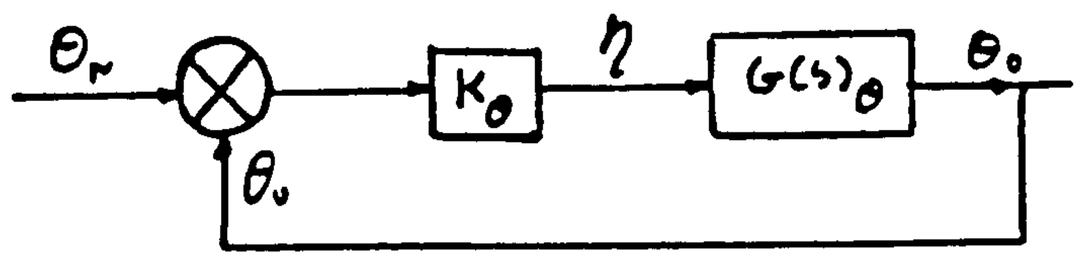

FIGURE 11.1 PITCH LOOP SYSTEM

where the open-loop transfer function is given by.

$$\frac{\bar{\theta}_o}{\bar{\theta}_r - \bar{\theta}_o} = k_\theta k_n G(s)_\theta$$

i.e.

$$\frac{\bar{\theta}_o}{\bar{\theta}_r - \bar{\theta}_o} = k_\theta k_n \cdot \frac{sm_n + z_n m_w - z_w m_n}{s(s^2 + s(-z_w - m_q) + (m_q z_w - m_w(U_e + z_q)))} \quad \text{- - EQ.10.2}$$

Further, the closed-loop transfer function is given by;

$$\frac{\bar{\theta}_o}{\bar{\theta}_r} = \frac{k_\theta k_n G(s)_\theta}{1 + k_\theta k_n G(s)_\theta}$$

At this stage a CASD package was used to determine the value of k for a satisfactory response, details of these calculations are presented in Section I1 of Appendix I. Fig.11.4 represents the response of the pitch control system to a step input.

Now by adopting the control law,

$$\bar{\eta} = k_\theta k_n(\overline{\theta_r - \theta_o})$$

The equations of motion describing the short period mode would become,

$$\begin{bmatrix} s - z_w & -s(U_e + z_q) & 0 \\ -m_w & s^2 - sm_q & 0 \\ 1 & -U_e & s \end{bmatrix} \begin{bmatrix} \bar{w} \\ \bar{\theta} \\ \bar{h} \end{bmatrix} = \begin{bmatrix} z_n \\ m_n \\ 0 \end{bmatrix} k_\theta k_n(\overline{\theta_r - \theta})$$

or

$$\begin{bmatrix} s - z_w & -s(U_e + z_q) + k_\theta k_\eta z_\eta & 0 \\ -m_w & s^2 - sm_q + k_\theta k_\eta m_\eta & 0 \\ 1 & -U_e & s \end{bmatrix} \begin{bmatrix} \bar{w} \\ \bar{\theta} \\ \bar{h} \end{bmatrix} = \begin{bmatrix} k_\theta k_\eta z_\eta \\ k_\theta k_\eta m_\eta \\ 0 \end{bmatrix} \bar{\theta}_r$$

Application of Cramer's rule leads to the following transfer function,

$$\frac{\bar{h}_o}{\bar{\theta}_r} = \frac{1}{\Delta(s)} \begin{vmatrix} s - z_w & -s(U_e + z_q) + k_\theta k_\eta z_\eta & k_\eta k_\theta z_\eta \\ -m_w & s^2 - sm_q + k_\theta k_\eta m_\eta & k_\eta k_\theta m_\eta \\ 1 & -U_e & 0 \end{vmatrix}$$

i.e.

$$\frac{\bar{h}_o}{\bar{\theta}_r} = \frac{-k_\theta k_\eta z_\eta s^2 + k_\theta k_\eta (m_\eta U_e - m_\eta (U_e + z_q) + m_q z_\eta)s + k_\theta k_\eta U_e (z_\eta m_w - m_\eta z_w)}{s(s^3 + s^2(-z_w - m_q) + s(k_\theta k_\eta m_\eta + z_w m_q - m_w (U_e + z_q)) + k_\theta k_\eta (m_w z_\eta - m_\eta z_w))}$$

- - - - - EQ.11.3

11.3 Height Loop Design

The complete control system can be represented as in Fig. 11.2 below;

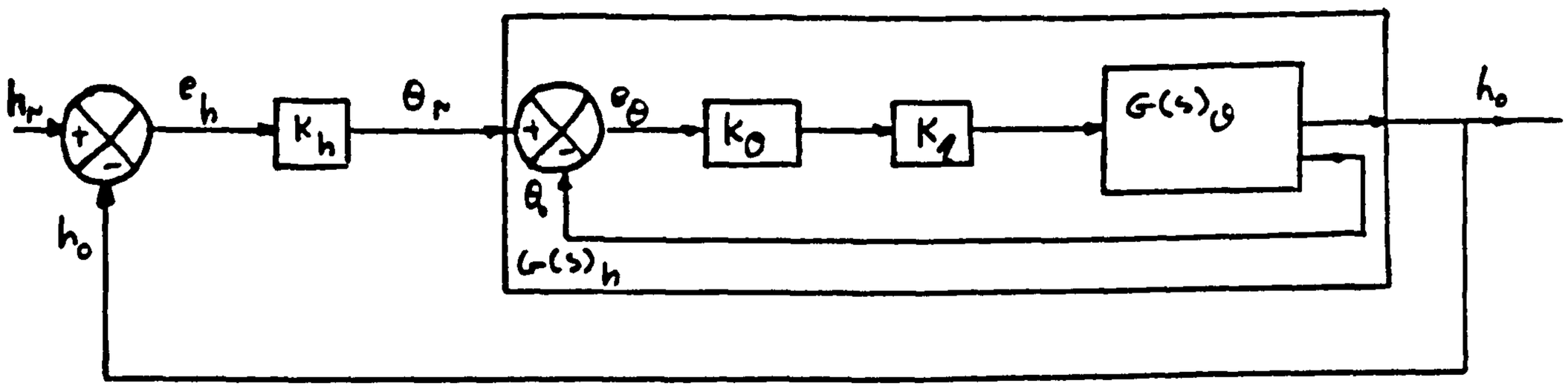

FIGURE 11.2 HEIGHT LOOP SYSTEM

The open and closed-loop transfer functions of this system are;

$$\frac{\bar{h}_o}{\bar{e}_h} = k_h G(s)_h$$

and

$$\frac{\bar{h}_o}{\bar{h}_r} = \frac{k_h G(s)_h}{1 + k_h G(s)_h}$$

- - - - - EQ.11.4

A control law of the form,

$$\bar{\theta}_r = k_h(\overline{h_r - h_o})$$

was adopted.

Therefore, the equations governing the response of the model to a height change are given by,

$$\begin{bmatrix} s - z_w & -s(U_e + z_q) + k_\theta k_\eta z_\eta & 0 \\ -m_w & s^2 - sm_q + k_\theta k_\eta m_\eta & 0 \\ 1 & -U_e & s \end{bmatrix} \begin{bmatrix} \bar{w} \\ \bar{\theta} \\ \bar{h} \end{bmatrix} = \begin{bmatrix} k_\theta k_\eta z_\eta \\ k_\theta k_\eta m_\eta \\ 0 \end{bmatrix} k_h(\overline{h_r - h})$$

$$\text{or} \quad \begin{bmatrix} s - z_w & -s(U_e + z_q) + k_\theta k_\eta z_\eta & k_\theta k_\eta k_h z_\eta \\ -m_w & s^2 - sm_q + k_\theta k_\eta m_\eta & k_\theta k_\eta k_h m_\eta \\ 1 & -U_e & s \end{bmatrix} \begin{bmatrix} \bar{w} \\ \bar{\theta} \\ \bar{h} \end{bmatrix} = \begin{bmatrix} k_\theta k_\eta k_h z_\eta \\ k_\theta k_\eta k_h m_\eta \\ 0 \end{bmatrix} \bar{h}_r$$

$$\therefore \begin{bmatrix} \dot{w} \\ \dot{q} \\ \dot{\theta} \\ \dot{h} \end{bmatrix} = \begin{bmatrix} z_w & (U_e + z_q) & -k_\theta k_\eta z_\eta & -k_\theta k_\eta k_h z_\eta \\ m_w & m_q & -k_\theta k_\eta m_\eta & -k_\theta k_\eta k_h m_\eta \\ 0 & 1 & 0 & 0 \\ -1 & 0 & U_e & 0 \end{bmatrix} \begin{bmatrix} \bar{w} \\ \bar{q} \\ \bar{\theta} \\ \bar{h} \end{bmatrix} + \begin{bmatrix} k_\theta k_\eta k_h z_\eta \\ k_\theta k_\eta k_h m_\eta \\ 0 \\ 0 \end{bmatrix} \bar{h}_r \quad \text{- - - - - EQ.11.5}$$

The above set of equations describes the short period transient response of the model due to a disturbance from the required height. These equations were simulated with the aid of a real time computer simulation package in order to verify the characteristics of the height-lock control system. Figs. 11.5 & 11.6 represent such simulations for various values of a correction factor defined as;

$$C_F = \frac{k_\theta}{k_{\theta_o}}$$

where k_θ = -0.1. In this way the effect of changes in the value of k_θ could be observed. The performance of this two-state feedback control system will be discussed in Section 12. Suffice to say here that the performance of this control system was not satisfactory and therefore other techniques were examined. A more detailed description of the analysis and simulation exercise are included in Appendix I.

11.4 Velocity Feedback as a Means of Reducing the Response Time

One way of increasing the damping of a control system is to use velocity feed-back. Fig. 11.3 below shows this system in block diagram form.

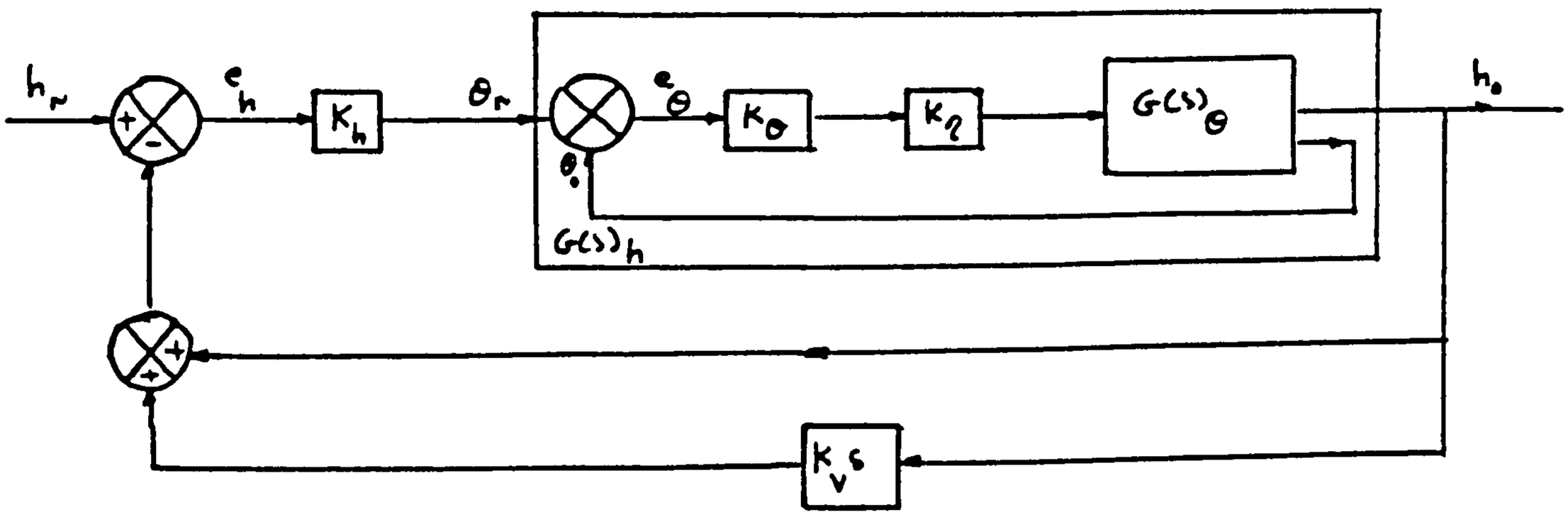

FIGURE 11.3 CONTROL SYSTEM WITH VELOCITY FEEDBACK

The open and close-loop transfer functions of this system are given by;

$$\frac{\bar{h}_o}{\bar{e}} = k_h(k_v s + 1).G(s)_h$$

where steady state error can be shown to be zero, and

$$\frac{\bar{h}_o}{\bar{h}_r} = \frac{k_h.(k_v s + 1).G(s)_h}{1 + k_h(k_v s + 1).G(s)_h} \qquad \text{- - - - - EQ.11.6}$$

respectively.

Figs.11.7 and 11.8 represent the system response to a step height command of 1 and the Bode plot of system respectively for,

$$k_v = 2$$

and

$$k_h = 0.015$$

Details of calculations are contained in Section I4 of Appendix I together with the modified circuitary given by Fig.I11

Further in adopting the control law

$$\bar{\theta}_r = k_h\left[\bar{h}_r - \bar{h}(k_v s + 1)\right] .$$

The equations of motion representing the height auto-pilot control system with velocity feed-back would become,

$$\begin{bmatrix} s - z_w & -s(U_e + z_q) + k_\theta k_\eta z_\eta & 0 \\ -m_w & s^2 - sm_q + k_\theta k_\eta m_\eta & 0 \\ 1 & -U_e & s \end{bmatrix} \begin{bmatrix} \bar{w} \\ \bar{\theta} \\ \bar{h} \end{bmatrix} = \begin{bmatrix} k_\theta k_\eta z_\eta \\ k_\theta k_\eta m_\eta \\ 0 \end{bmatrix} k_h\bar{h}_r - k_h\bar{h}(k_v s + 1)$$

or

$$\begin{bmatrix} s - z_w & -s(U_e+z_q) + k_\theta k_\eta z_\eta & k_\theta k_\eta k_h(k_v s+1)z_\eta \\ -m_w & s^2 - sm_q + k_\theta k_\eta m_\eta & k_\theta k_\eta k_h(k_v s+1)m_\eta \\ 1 & -U_e & s \end{bmatrix} \begin{bmatrix} \bar{w} \\ \bar{\theta} \\ \bar{h} \end{bmatrix} = \begin{bmatrix} k_\theta k_\eta k_h z_\eta \\ k_\theta k_\eta k_h m_\eta \\ 0 \end{bmatrix} \bar{h}_r \qquad \text{- - EQ.11.7}$$

Equation (11.7) is readily simulated on a digital computer and hence enables the entire performance to be analysed for various gain settings.

11.5 Analysis of Longitudinal Dynamic Tests with the Inclusion of Auto-Pilot

As was mentioned in Section 10, the turbulence effects comprised the primary source of external disturbances which needed to be suppressed. This was achieved by employing two additional proportional feedback systems controlling the roll and yaw motion of the model, which in effect rid the longitudinal flight mode of the unsymmetric induced aerodynamic loads. Initial tests have shown this to be the case.

However, in order to analyse the dynamic tests, the new mathematical model representing the response of the model has to be implemented in the extended Kalman filter parameter identification code. Initially, the system could have been simulated with the aid of a simulation language and subsequently analysed. Once the method was verified, it could then have been applied to the physical system. Unfortunately, this was beyond the time available and the scope of this thesis.

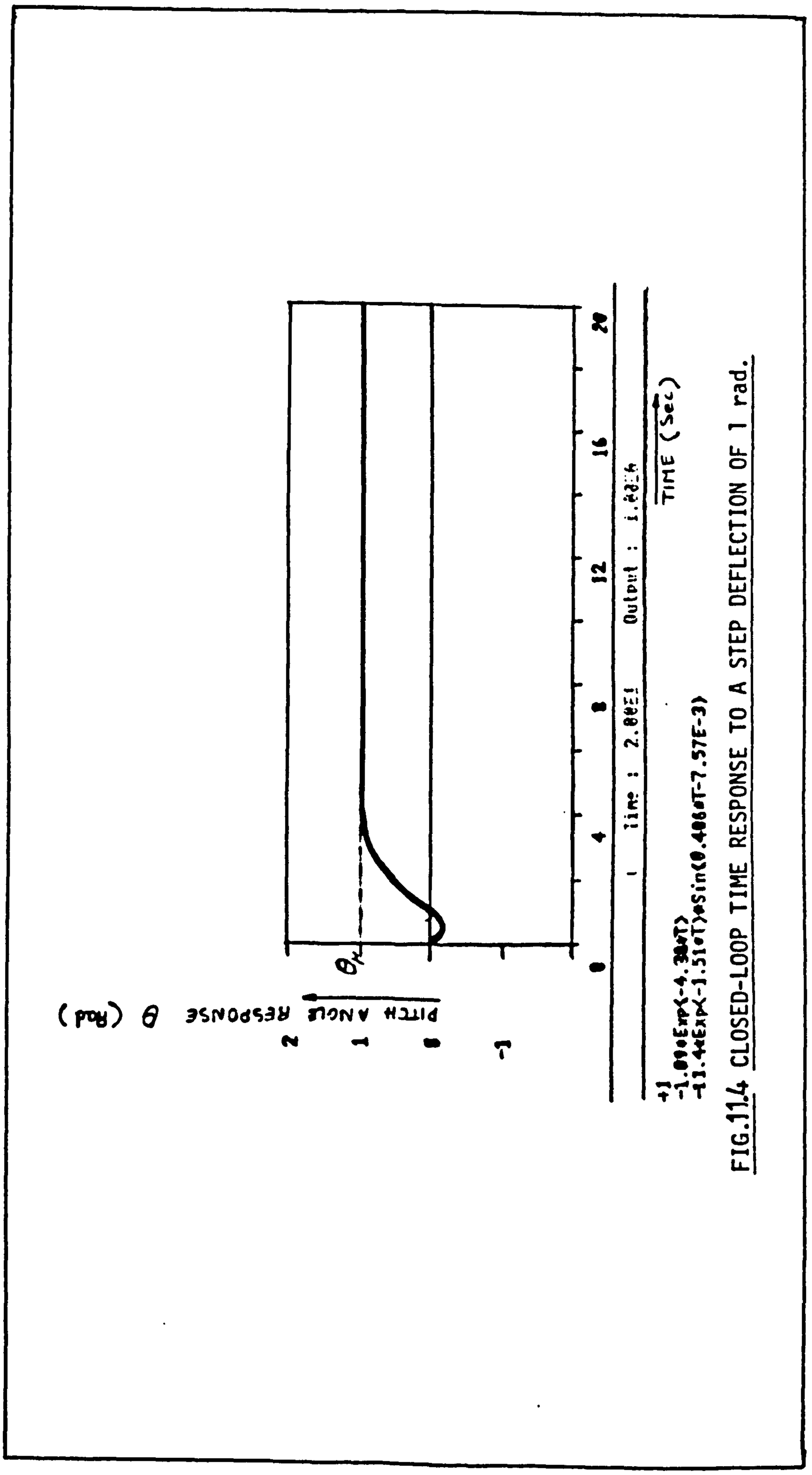

FIG.11.4 CLOSED-LOOP TIME RESPONSE TO A STEP DEFLECTION OF 1 rad.

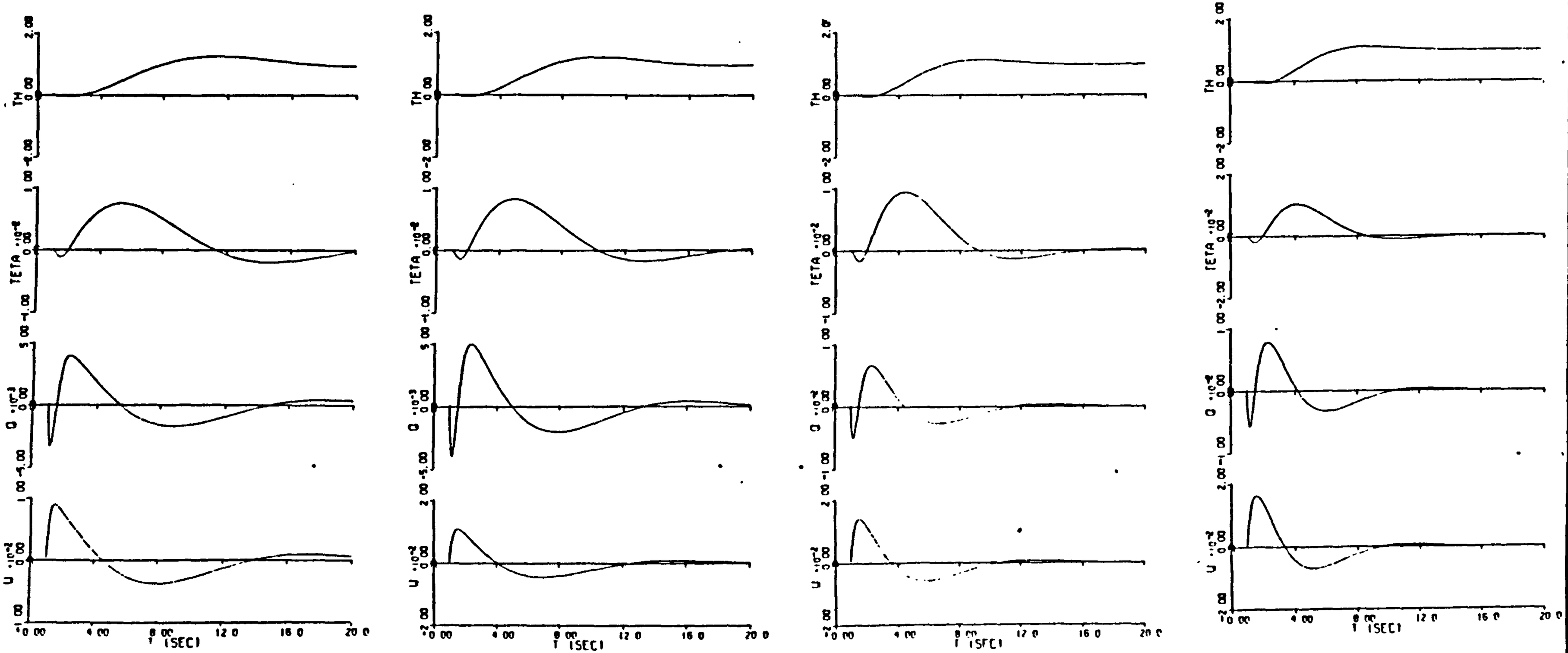

$C_F = 1$ $C_F = 1.2$ $C_F = 1.5$ $C_F = 1.7$

FIGURE 11.5

SIMULATION OF EQUATIONS 11.7

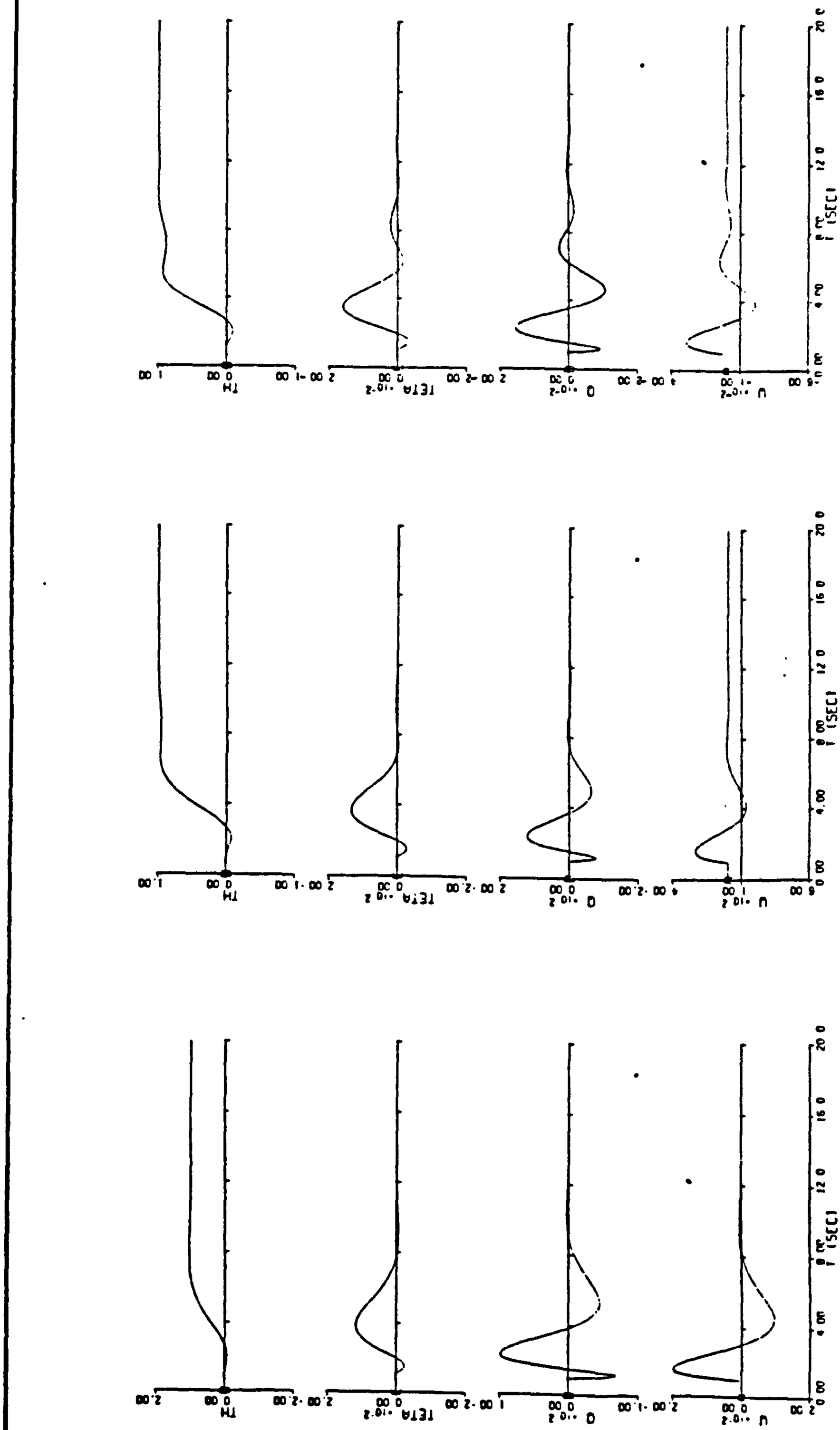

FIGURE 11.6 SIMULATION OF EQUATIONS 11.7

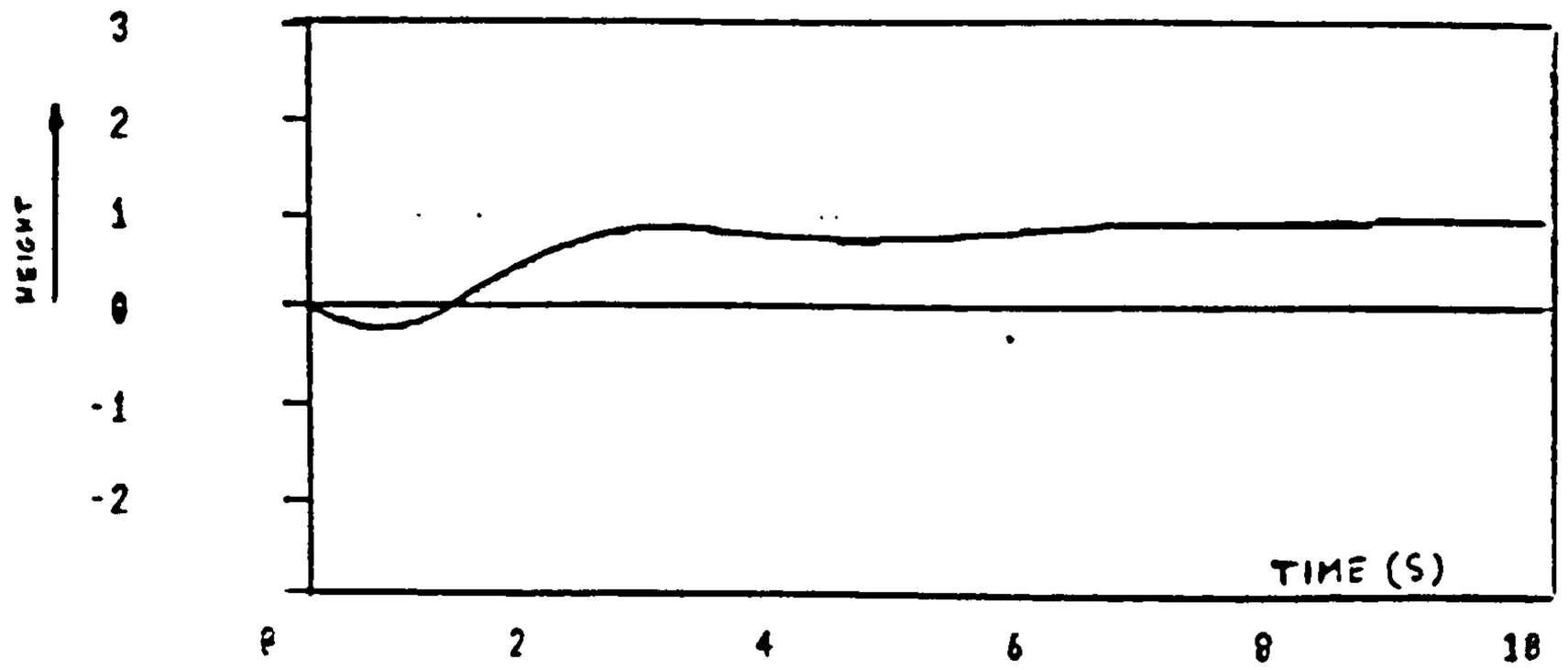

FIGURE 11.7

SYSTEM RESPONSE WITH VELOCITY FEEDBACK TO A HEIGHT STEP INPUT

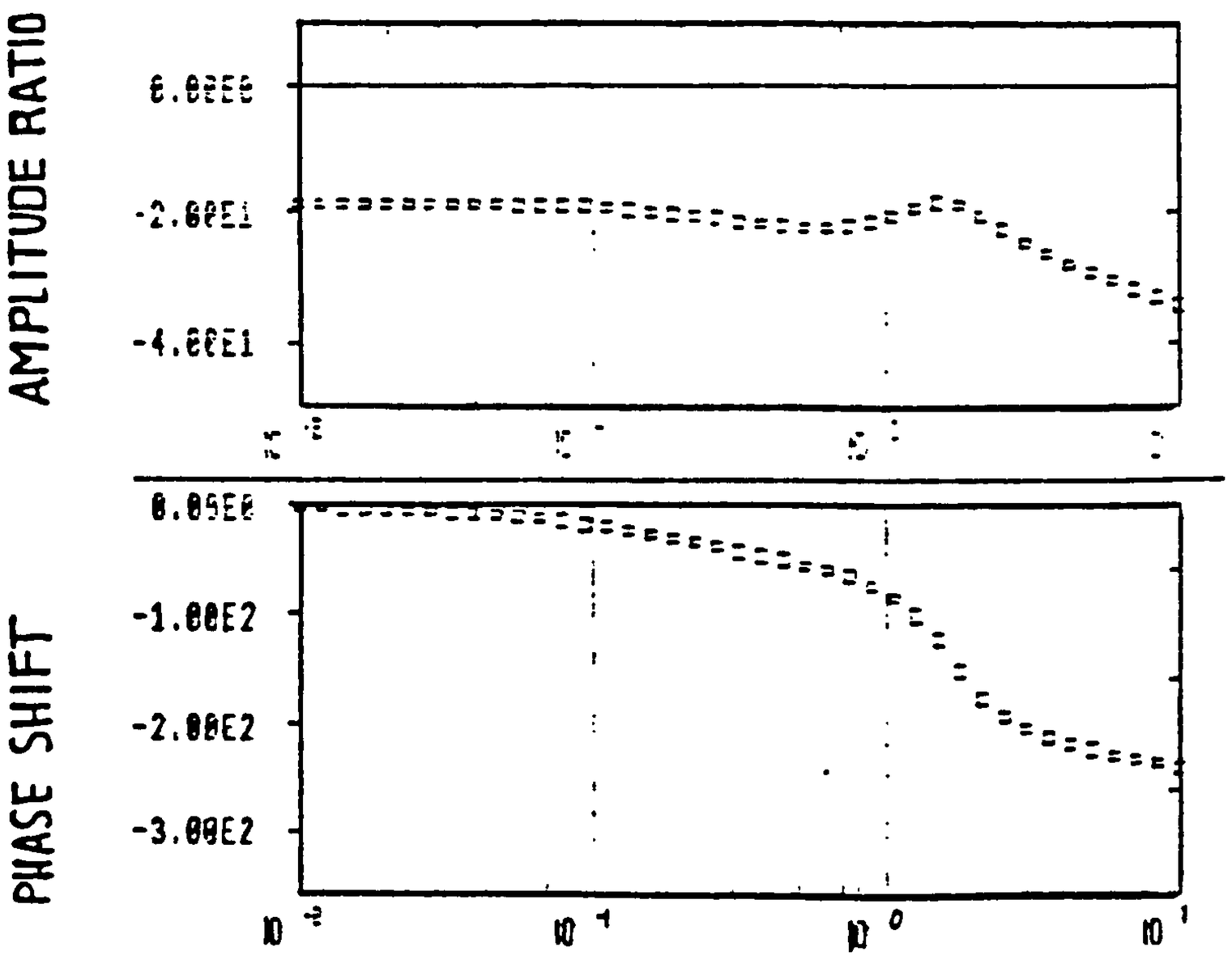

FIGURE 11.8

BODE PLOT OF SYSTEM WITH VELOCITY FEEDBACK

12. RESULTS AND DISCUSSION

Clearly, from what has been presented in the preceding sections, three alternative methods have been used to estimate the stability derivatives of the F.S.W. aircraft. The first set of estimates were obtained from the first order design optimisation program. The second method of estimation was the extended Kalman filter algorithm and finally the static wind tunnel measurement data from which some of the stability derivatives were estimated. In this section each of these methods is discussed in detail with respect to its efficiency as a mean for estimating stability derivatives, the validity of the results and possible ways in which these might be improved.

12.1 The Results of the First Order Optimisation Program, their Validity and Scope

In the absence of detailed wing and foreplane loading data and the limited availability of aerodynamic data the first order optimisation program yielded the following results. First and foremost was the data from which, a three view drawing of the full scale aircraft was produced. Input data as far as this design stage was concerned, was mostly based on linearised theory and the relevant calculations are given in Appendices A and B.

In order to achieve an optimized layout, two criteria were chosen, namely, static margin stick-fixed and minimum induced drag. Therefore in theory, the full size aircraft was designed to meet these two criteria. However, with respect to the construction of a dynamic model, based on the full size aircraft obtained in this way, the assumptions needed to be re-examined. In doing so, the following had to be justified.

(i) Application of linearised theories to wing and foreplane in isolation.

(ii) Neglecting interference effects due to vortex shedding of the fuselage.

(iii) Assumption that the lift generated is totally due to circulation. In other words, slender wing theory not to be applied.

(iv) Assumption that the linearised theory would still be applicable at $M = 0.3$ or, in other words, incidence not greater than 10^{o} below such a Mach number.

Clearly all these assumptions are interrelated and therefore not entirely justifiable. Nevertheless, by making provision for variation of the centre of gravity in the development of the dynamic model, any error in the determination of static margin could be compensated for. Checks on static longitudinal and lateral stability of the full size aircraft were carried out (see Appendix C) which proved the design to be satisfactory.

A rather more drastic result of the above assumptions was the manifestation of errors in the estimates of stability derivatives, which formed the output of the second stage of the optimisation routine. Basically, linearised theories base the estimates of stability derivatives upon trimmed flight conditions such as foreplane trim angle at a given incidence, $C_{L_{trim}}$, C_D, etc. These values in turn depend on the accuracy of the methods with which they have been calculated. Therefore, the derivative estimates obtained at this stage were assumed to be unreliable to an extent that could not be assessed until later in the research program. Calculations supporting the second stage of the optimisation program are given in Appendices B and E.

12.2 Verification of the Extended Kalman Filter Parameter Identification Code Using Computer Based Simulations

After the development of the Extended Kalman Filter code, it was necessary to verify it before actually applying it to wind-tunnel based dynamic tests. As mentioned in Section 5, the equations of motion in four degrees of freedom were simulated using predetermined stability derivatives. The aim was to see whether or not, by feeding these simulated responses to the estimating program, it would produce estimates of the stability derivatives matching the original values. A typical simulated response using the original stability derivatives (see Sections 5.6 and 6.2) is shown on Fig. 12.1, together with Fig. 12.2 showing the convergence characteristics of the estimated derivatives to their known values. More detailed examples are contained in Appendix J. Results from these simulations proved beyond a shadow of a doubt that under steady-state conditions and from a theoretical point of view the estimates of stability derivatives and their known values, as used in the simulations, represented a perfect match.

However, as with all theoretical approaches, the following limitations were applied to the validation study,

(i) Absence of coloured noise, i.e. all noise assumed white with no correlation between them.

(ii) Equations of motion in four degrees of freedom would represent the actual physical motion of the model on the test rig.

By making sure that the departure from trimmed flight remains within the bounds of linearised theory the above assumptions can be justified.

12.3 Use of the Dynamic Model for the Purpose of the Open-Loop Dynamic Tests

12.3.1 Dynamic Model

In order to be able to apply the extended Kalman filter algorithm to the physical responses, it was necessary to design and build a 1/14 scale dynamic model of the full size aircraft. Appendix E contains the dynamic scale relationships between the model and full size aircraft as discussed in Section 2.3.

As far as the similarity of flow was concerned, calculations leading to an estimate of zero-lift drag revealed that the Reynolds number for the model does not correspond to a fully turbulent flow. Therefore, use was made of trip wires on the flying surfaces of the model in order to trip the boundary layer into an early transition. Calculations to determine the diameter of the wire and its chordwise position on the F.S.W. foreplane and fin are given in Appendix F. Although these calculations were based on a 2-D treatment, ref. 2 suggests that for a F.S.W. they would be sufficiently representative to ensure a good approximation to the actual position of transition from laminar to turbulent boundary layer. The dynamic similarity analysis formed the basis on which the dynamic model was developed. The model was designed and built to comply with these fundamental requirements and also to comply with some additional requirements as described in Section 2.5.

The experimental test facilities described in Ref. 8 were also further developed, mainly from the instrumentation point of view (see Sections 7.1 and 7.3). As pointed out in Section 12.1, the model was constructed so that the gimbal system, on which the model was suspended, could be moved ±0.02 m fore and aft from the predicted centre of gravity. This C.G. range was chosen in accordance with Fig. B2 of Appendix B, which suggests that for a static margin stick-fixed range of -6% $\bar{c}$ to +6% $\bar{c}$ a C.G. movement of 0.279 m for the full size aircraft, and therefore 0.02 m for the 1/14th scale dynamic model was necessary.

The principal moments of inertia were then adjusted in compliance with the dynamic similarity requirements. Initial test flights showed that the model was unstable although the level of instability was unknown at

this stage. In an attempt to secure a stable airframe for initial experiments two extensions were added to the trailing edge of the wing root in order to move the neutral point aft and, additionally, the C.G. was moved to its forward limit. With this configuration, the model could be made to fly with great ease although no stability analysis was carried out at this stage.

The next step was to establish the position of the neutral point. Calculations and experiments leading to the determination of this position are given in Appendix G. These calculations revealed that with the C.G. at 0.444 m from the plane of the nozzle, the model had a static margin stick-fixed of approximately -1%; in other words, the model was statically unstable. Despite this fact, the model was behaving in a dynamically stable manner. The reason for this was not known until some static tests were carried out, the results of which are discussed below.

Having established that the model was capable of flying in trimmed condition, dynamic tests were carried out. These transient response tests were carried out to evaluate firstly the longitudinal open-loop dynamics, and secondly, the lateral open-loop dynamics of the aircraft model.

12.3.1.1 Longitudinal open-loop tests

Instrumentation noise was one of the major obstacles to progress. Without adequate suppression of signal noise, signal rates could not have been properly derived. Due to the magnitude of the signal sampling rate $h_s = 10^{-2}$ sec, 200 data points were available for the digitisation of an analogue transient signal for a period of 2 seconds. Noise suppression of the attitude signals was achieved by curve fitting the recorded points and differentiation of the fitted function could then follow. (See Section 7.3.4) In this way pitch and other attitude responses were curve fitted and differentiated in order to acquire pitch rate q, etc. It was found that the signals from the height measuring transducer (Section 7.1) were relatively noise free and therefore it was not necessary to apply this process to obtain height rate.

As explained in Section 7.3.1, the initial analysis of the short period responses with the Kalman filtering indicated that the equations of motion were not consistent with the observed physical motion. It was then decided to invlude z_q in the longitudinal equations of motion. The inclusion of z_q clearly stabilized the filter and in this way convergent estimates of

the stability derivatives z_w, z_q, m_w, m_q, z_η and m_η were obtained. Although the estimates converged to a value, oscillations with low frequency and small amplitude were apparent. Through a series of experiments with different measurement noise matrices R, is was found that these oscillations could be minimised. Table 7.1 lists the experiments and conditions under which they were carried out. Instrumented results include two runs of the parameter identification program for the same flight condition but with different measurement noise matrices R. As an example, the results of experiment 2 of Table 7.1, are shown on Figures 12.3 and 12.4. Further, Fig. 12.7 shows the simulated short period oscillations using the estimated stability derivatives with the extended Kalman filter program. From these figures it can be seen that the simulated result shown on Fig. 12.5 agrees favourably with the observed response shwon on Fig. 12.5.

However, it must be noted that the observed transient response is affected by two main factors. Firstly, gimbal frictional effects which manifest themselves as additional motion damping such as friction in pitch freedom pivot and in the heave motion linear bearing. Secondly, the non-uniformity of the airflow across the tunnel test section and blockage effects. These factors could, and in some instances did, cause the model to assume a different incidence at various vertical positions prior to the introduction of the disturbance, following a foreplane control input.

This effect can clearly be seen from the pitch attitude time history of the experiments 3 and 4 as on Fig. 12.6. Here, after the transient response has died away, there is a steady state error in the pitch attitude response. Computer experiments showed that in the more severe cases, this steady state error could cause oscillations and possible divergence of the extended Kalman filter parameter identification program.

12.3.1.2 Lateral Open-Loop Tests

Clearly, as the lateral equations of motion in four degrees of freedom indicate, see Section 6, the need to measure heave motion does not arise. Therefore, in carrying out the lateral dynamic tests, the model was locked in position halfway up the vertical rod in such a way that a heave movement of 0.02 m was possible. This was done, in order to make sure that prior to the introduction of disturbances,the model was flying straight and level.

For both fore and aft C.G. positions, observations showed that even under trimmed flight conditions, random oscillations in roll were evident. The maximum amplitude of these oscillations were within $\phi = \pm 10^{o}$ of the wing-level condition.

The inability to return to the flight attitude prior to the introduction of an aileron control input made the analysis of the response of the model to aileron control inputs impossible mainly because of the low signal to noise ratio. These observations were demonstrated in the poor quality of the recorded responses. Therefore, it was realised that without a feedback control system, as far as the roll degree of freedom was concerned, no useful information would result from the analysis of such responses. As a result of the above argument, only the responses due to rudder control inputs were analysed. The experiments conducted at this stage are listed in Section 9. In deriving the extended Kalman filter code, it was assumed that the white noise components of the various signals were uncorrelated. This assumption is more justified in the case of longitudinal than in the case of lateral dynamic response experiments because some correlation between signals is evident when the motion exceeds the limits associated with linear approximation. Although, in the case of computer based experiments, this could be achieved, it was not possible in the physical experimentation environment.

Therefore, unlike the results of Section 5.5 as discussed in Section 11.2, oscillations in the estimates of lateral derivatives, especially ℓ_v, n_v and ℓ_p, n_r were predicted. This was verified as the lateral responses under different flight conditions were analysed. By way of example refer to Figures 12.7 and 12.8, which show the observed response due to rudder control input but with two different measurement noise matrices R. Although the extended Kalman filter seems to match the response closely, the estimated lateral derivatives, especially ℓ_v and n_v, constantly oscillate in order for the extended Kalman filter to match the response. It was found that the frequency and amplitude of these oscillations were sensitive to small changes in the measurement noise matrix R, although this sensitivity was not evident in the matching of the response. The best estimates were obtained when elements of the R matrix were of the order of 10^{-6}. Simulation of the lateral equations of motion using the estimated derivatives for the same flight conditions is shown on Fig. 12.9, which agrees favourably with the observed response in frequency, amplitude and damping.

What became evident firstly from the observed responses at different tunnel speeds and consequently from the simulated responses, was that the damping became less and less as the tunnel speed was increased, as shown on Figures 12.9 to 12.11. By changing the C.G. position from 0.444 m to 0.44 m the response due to rudder control input became erratic and indeed, except for a tunnel speed of 27 ms^{-1}, analysis of the responses, although matched by the extended Kalman filter code, would not lead to convergent estimates of

the lateral stability derivatives. Just as for the case of the responses to aileron control inputs, only through a yaw axis feedback control system would it be possible to first stabilise the response and then analyse it. Although roll and yaw control could be achieved independently of each other for small deviations from the equilibrium conditions, some autostabilisation would be necessary to cope with large perturbations. The treatment of large perturbations however, was beyond the scope of this thesis.

During the course of the initial computer based experiments described in Section 5 and in Section 6, the dynamic response simulations and extended Kalman filter estimator were both based on the same mathematical model, which in effect eliminated any mismatch between the two systems. As far as the dynamic experiments described in Sections 8 ant 9 were concerned, the difficulties arose once an attempt was made to represent a physical motion by a mathematical model which clearly has its shortcomings as it depends on the assumptions made.

12.4 Static Wind Tunnel Results

Static wind tunnel tests were carried out to obtain the basic aerodynamic characteristic data which would extend and verify the data obtained from the earlier dynamic experiments. The background to this work is discussed below followed by a more detailed description of the results obtained from the various tests.

12.4.1 Preliminary Results

Due to the nature of the research program and the availability of wind tunnels, the static wind tunnel measurements had to be conducted after the dynamic model was designed and built. Nevertheless, results from this part of the programme helped in the understanding of the results of earlier work. Prior to carrying out the static wind tunnel tests, some of the dynamic experiments had already been conducted. The latter were partially concerned with the approximate determination of the neutral point of the model.

The method adopted here to estimate the neutral point is explained in detail in Appendix G. The following assumptions had been made:

(i) Frictional effects such as those in the bearing and pivots of the gimbal were neglected.

(ii) Downwash effects were not accounted for.

(iii) Forces due to the weight of the umbilical connection were assumed to act along the vertical rod of the test rig.

Results from these dynamic experiments indicated that with the trailing edge extension (see Section 11.3.1), the static margin stick-fixed was around -1%. Assuming at this stage that the results were meaningful, it was deduced that the pitching moment was acting in a nose up sense. In other words the stability derivative m_w was positive, which was in accordance with the results of the extended Kalman filter parameter identification of that derivative.

12.4.2 Static Wind Tunnel Measurements

The prime purpose of these measurements was to obtain the basic aerodynamic characteristics of the model. However, due to the nature of the support structure, incidence variations were limited to $\pm 20^{o}$ relative to the horizontal plane, but the actual experimental range was from -5^{o} to $+20^{o}$. Yaw angle variations were within $\pm 20^{o}$ of the tunnel centre line. Results of the static tests are accumulated in Appendix H. Although dynamic tests had indicated that the model possessed a high strength to weight ratio, the tunnel speed for the static tests was not taken beyond approximately 28 m/s, since, in the event of structural failure, the remainder of the research program would have been jeopardised.

12.4.2.1 Pitching moment variation with incidence

From Section 12.4.1, it was predicted that under normal flight conditions, i.e. positive incidence, a nose-up pitching moment would be associated with all positive incidences. Figures 12.12 and 12.13 show the variation of pitching moment coefficient with incidence α for various canard angle settings η in the absence of the wing trailing edge extensions. Since from the dynamic tests the minimum lift-off speed, defined as the minimum speed at which the model could support its own weight, was found to be approximately 22 m/s, only Figure 12.13 is discussed here. From this figure it is clear that under normal flying conditions, which would correspond to a positive incidence of between 0^{o} and 5^{o} and a foreplane trim angle η_{trim} of 4^{o} to 8^{o}, the position of the neutral point must lie ahead of the C.G. Furthermore, for the range of incidence $\alpha \approx \pm 5^{o}$ and $\alpha = 5^{o}$ to 15^{o}, $\frac{dC_M}{d\alpha}$ is positive and then negative respectively.

Since $\frac{dC_M}{d\alpha} < 0$ for static stability, the model is unstable for $-5^{o} < \alpha < +5^{o}$, but stable for $5^{o} < \alpha < 15^{o}$. These results conform to the observations. All the static tests were performed in the absence of the trailing edge extensions and through correlation between pitching moment and lift data obtained from these tests it was possible to estimate the position of the neutral

point. This was approximately 0.025 m ahead of the C.G. which would correspond to stick-fixed static margin of approximately -14% $\bar{c}$. On the other hand, from Section G2 of Appendix G, the stick-fixed static margin with the inclusion of trailing edge extension and a C.G. position corresponding to that of static tests, i.e. 0.435 m from datum, is given as -6% $\bar{c}$. In conformity with these results the stability derivative m_w must be positive, as was predicted by the extended Kalman filter estimator.

12.4.2.2 Wing and Foreplane-body Aerodynamic Forces

Results of the static wind tunnel tests covering these aspects are given in Table H2 of Appendix H. Included in the same table are the corresponding aerodynamic parameters obtained theoretically, as discussed in Appendix B. The comparison between the experimental and theoretical values of the aerodynamic parameters will be undertaken in Section 12.5 below. Consider figures 12.14, 12.15 and 12.16, which show the variation of lift coefficient with incidence α for different foreplane angle settings η and three tunnel speeds. Clearly, as the incidence is increased, the foreplane stalls and towards the upper incidence range all the C_L-α curves for various foreplane angle settings η converge. Further, it is evident that wing stall occurs at an incidence greater than $\alpha = 20^o$. Therefore, at high angles of incidence the F.S.W. seems to behave like a delta wing. Theoretical extrapolations indicate that the incidence corresponding to $C_{L_{max}}$ would be somewhere between 25^o to 35^o.

The results are in agreement with experimental results of reference 2 and reproduced on Figure 12.17. In order to compare the variation of C_L with incidence for foreplane-on and foreplane-off configurations, use was made of Figure 12.18. Here the tunnel speed with corrections was approximately 28 m/s and the foreplane angle was set at $\eta = 0^o$. Evidently, there exists a non-linear relationship between C_L and α when α varies between 0^o to 3^o. This non-linearity was expected since at these near zero incidences interference effects between model components become predominant. It can also be seen that for $\eta = 0$, zero-lift incidence is approximately $\alpha \approx 0.6^o$. Further, due to foreplane-body interference effects, the variation of C_L with foreplane angle η is seen to be non-linear. Here interference effects are more dominant mainly because of the body diameter to foreplane span ratio.

12.4.2.3 Rolling Moment Measurements

Here, results were limited to rolling moment variation with aileron angle deflection ξ^o, with incidence $\alpha = 0$ and a tunnel speed of approximately 24 m/s. With reference to Figure 12.21, it can be seen that the variation is almost linear. Further, the rolling moment coefficient C_ℓ corresponding

to $\alpha = \xi = 0^{o}$ is zero which again gave a good indication that the model was not twisted or warped. The average slope of the $C_{\ell} - \xi$ curve is given in Table H4 of Appendix H. This value $\frac{dC_{\ell}}{d\xi}$ can be used to give an estimate of the lateral power derivative $C_{\ell_{\xi}}$. Clearly the value of $\frac{dC_{\ell}}{d\xi}$ would vary with incidence assuming that the ailerons remain within an undisturbed flow region which is one of the advantages of F.S.W. layout. The change in $\frac{dC_{\ell}}{d\xi}$ would then result in a variation in $C_{\ell_{\xi}}$.

12.4.2.4 Yawing Moment and Side Force Measurements

These measurements were carried out at a tunnel speed of approximately 19 m/s and they include the variation of yawing moment with yaw angle ψ for angles of incidences 0^{o} and 20^{o}. With reference to figures 12.20 and 12.21, which show the variation of yawing moment coefficient with yaw angle, the following observations were made:

(i) For various yaw angles ψ, with rudder angle ζ set to zero, there exists a yawing moment, the direction and magnitude of which varies with incidence α. This is particularly evident from Figure H9.

(ii) The variation of C_{n} with ζ is slightly non-linear over the incidence range.

(iii) For yaw angles greater than $\psi \approx 10^{o}$ and incidence angles in the region of 20^{o}, the fin and rudder become immersed in the wake of the wing and body and are rendered less effective. This was also observed during the dynamic tests.

Average values of the slopes of the C_{n} ζ curves are given in Table H4 of Appendix H. Values of $\frac{dC_{n}}{d\zeta}$ obtained in this way can be used to give an estimate of the lateral control derivative n_{ζ} at an approximate tunnel speed of 19 m/s. It must be noted that the wing trailing edge extensions were not used in this static test. Furthermore, the estimated lateral control derivative n_{ζ} corresponds to $\frac{dC_{n}}{d\zeta}$ at U ≈ 19 m/s. Usually , the value of $\frac{dC_{n}}{d\zeta}$ would change with incidence. Unfortunately, the manner in which this change might occur could not be investigated since it was thought that the model was not capable of sustaining the high frequency vibrations experienced at high incidence and yaw angles.

12.4.2.5 Drag Measurements

Measurements covering this aspect of the static wind tunnel tests are given in Tables H1 and H2 of Appendix H. Comparison between the theoretical estimates of drag and the actual measurements are discussed in Section 12.5, below. As a typical example, results corresponding to drag variation

at a tunnel speed of approximately 28 m/s shown on Figure 12.22 will be discussed here. Clearly from Figure 12.22 there is a marked increase in drag coefficient as the foreplane angle η was varied.

Protruberances are one of the contributing factors to drag force. In developing models for the purpose of static wind tunnel measurements, gaps and cavities are avoided since they would otherwise distort the flow and cause a substantial drag increase. Dynamic models on the other hand have to accomodate instruments and mechanisms which inevitably lead to the existence of such gaps and cavities, although the severity of this is dependent on the application to which the model is subjected.

Therefore, dynamic models are unsuitable for drag measurements since they do not represent the clean aircraft. Finally, Figure 12.23 shows the variation of C_D wigh C_L with $\eta = 0$, the tunnel speed was approximately 28 m/s for foreplane-on and foreplane-off cases. Evidently in the absence of foreplane there is a drag increase at the same lift coefficient for incidence angles greater than 10^o. This is due to the fact that the mutually beneficial interaction between wing and foreplane has been eliminated, which in effect has increased the induced drag.

12.5 Comparison of Common Results

During the course of this research programme a lot of data was compiled, as a result of which some of the variables have been estimated or calculated by different methods and means. Where appropriate, these have been compared as follows:

(i) Comparison between design C.G. and N.P. positions and those obtained experimentally.
(ii) Comparison between design and experimental lift curve slopes.
(iii) Comparison between predicted and measured C_D variations.
(iv) Comparison of estimated stability derivative.

These are discussed further below.

12.5.1 Comparison between Design C.G. and N.P. Positions and those Obtained Experimentally

As discussed in Section 12.3.1, the dynamic model initially lacked the design stability margin due to an error in the estimation of neutral point position which was not unexpected. The first order design optimisation program with an objective design static margin of +2% $\bar{c}$ had estimated the position of C.G. and neutral point to be at 0.425 m and 0.422 m respectively

ahead of the datum. Initial dynamic tests revealed that the neutral point lay ahead of the design C.G. and in order to compensate for the apparent lack of stability, two trailing edge extensions were fitted to the model and the C.G. was moved to its forward limit of 0.444 m from datum. From Appendix G, the estimated static margin stick fixed associated with the present model configuration was -1% $\bar{c}$ which corresponds to C.G. and neutral point positions of 0.444 m and 0.445 m respectively. Therefore the errors in design C.G. and neutral point positions with respect to those corresponding to the dynamic tests would be approximately 4% and 5% of the experimental values respectively. The error in the position of the C.G. was within the tolerance of the gimbal support bracket of ±0.02 m.

Due to friction between the linear bearing of the gimbal and vertical support rod, there is an extra force acting on the dynamic model. Ordinarily, with the model balanced the effect of this force may be neglected. However,with the model slightly unbalanced, the situation represented in Fig.12.24 comes into play

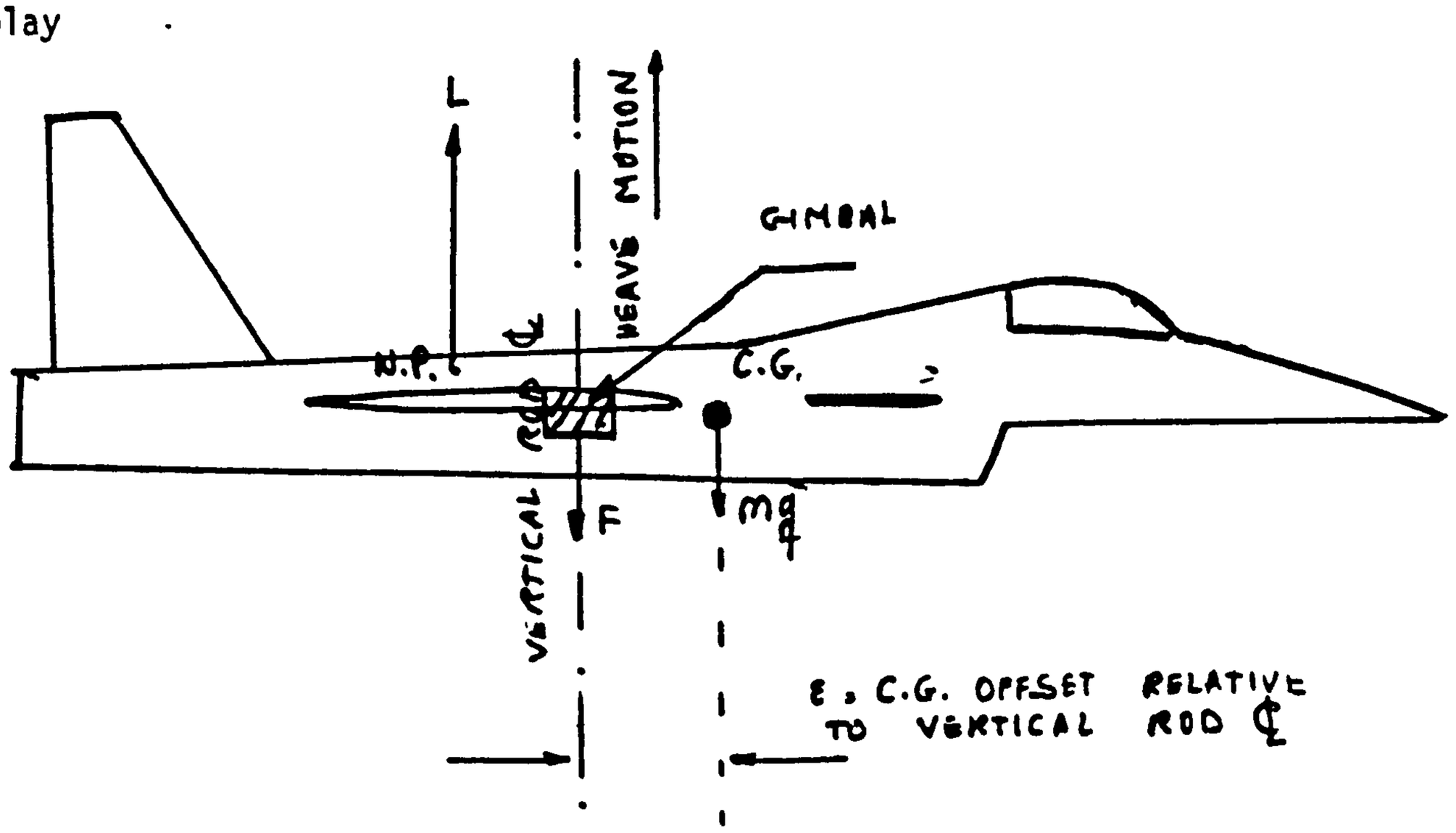

FIGURE 12.24

FORCES ACTING ON A SLIGHTLY UNBALANCED MODEL

From this figure it can be seen that however minute, the friction force F has a detrimental effect on the stability of the model since it always acts in the opposite direction and has a stiction property. That

is to say, that initially this frictional break-out force has to be overcome if the model is to heave. From Fig. 12.24 it can be seen that not only the force F reduces the lift, but also brings the resultant force closer to the C.G. and thus reduces the static margin.

12.5.2 Comparison between Design and Experimental Lift Curve Slopes

Table 12.1 lists the theoretical and experimental component lift curve slopes. From the compatibility point of view, they have all been based on the wing area. Clearly, the theoretical values of lift curve slope in all cases have been over-estimated to various degrees. Detailed theoretical lift curve slope calculations are given in Appendix B. In the case of the total lift curve slope $(\frac{dC_L}{d\alpha})_{total}$, with foreplane on and off configurations, two theoretical values are presented in Table 12.1. These correspond to the inclusion and exclusion , respectively, of the interference factor given by Fig. 11.3 of reference 1. Evidently the latter gives a better agreement with experiment as far as the dynamic model is concerned. The interference effects cannot be ignored and the apparent lack of agreement between theory and experiment is caused by the fact that the aspect ratios of both wing and foreplane in the absence of the fuselage have been used in Equation (1) of Appendix B. Better agreement could be achieved if corrected aspect ratios, corrected for the presence of the fuselage, were used.

The same argument can be applied to the foreplane-body lift curve slope. Included in Table 12.1 is the experimental foreplane-body lift curve slope in isolation from the wing at $\alpha = 0^o$. Unfortunately, as a result of foreplane angle variations relative to the fuselage, no theoretical value of $(\frac{dC_L}{d\eta})_{\alpha= 0^o}$ could be estimated.

12.5.3 Comparison between Predicted and Measured C_D Variations

In the light of the discussion in Section 12.4.2.5, the various protruberances contributed a large proportion of the drag force. Naturally, therefore, a substantial agreement between predicted and measured drag could not be expected. Other contributing factors to the expected difference were,

(i) Induced drag due to strakes

(ii) Induced drag due to vortices emanating from the flat underside of the front . of the fuselage

(iii) Secondary influences of (i) and (ii) on the mutual interference between the F.S.W. and the closely coupled foreplane.

Figure 12.25 shows the variation of total drag coefficient C_D with lift coefficient C_L as obtained theoretically and experimentally corresponding to a speed of U ≈ 28 m/s. The agreement between theory and experiment is not impressive, which merely confirmed the above arguments. The effect of this disagreement on the theoretically estimated longitudinal stability derivatives and on the experimentally estimated values is discussed in the following section. Measured and estimated values of zero lift drag are given in Table 12.1. Further details are contained in Appendix H.

12.5.4 Comparison of Theoretically and Experimentally Estimated Stability Derivatives

In order to make such comparisons, the ways in which the derivatives were estimated have to be discussed. The first set of estimates were obtained through the first order design optimisation program.. Here, theoretically derived lift curve slopes and drag characteristics, for trimmed flight, see Appendix E, were used to estimate the longitudinal stability derivatives. As discussed in Sections 12.4.1 to 12.4.3, substantial discrepancies exist between measured and estimated values of C_L and especially C_D, bearing in mind also the differences between real and estimated positions of C.G. and neutral point.

Details of the theoretical procedure with which estimates of longitudinal stability derivatives were made are given in Appendix E. Tables 12.2 and 12.3 represent the results of a run of the design optimisation program to obtain the longitudinal stability derivatives in concise and aeronormalised form, respectively. The flight conditions corresponding to this run are given in Table 12.4.

On the other hand, factors affecting the estimates of longitudinal stability derivatives as obtained with the extended Kalman filter algorithm were discussed above in Section 12.3.1.1. Finally, it was possible to obtain another set of longitudinal stability derivative estimates by inserting data from the static wind tunnel measurements into theoretical expressions for the stability derivatives as used in the design optimisation program. These derivatives are listed in Table 12.5 and discussed in more detail in Appendix E. Comparison of the three sets of derivatives reveals that the estimates based on the static tests data agrees more favourably with that of the Kalman filter estimator. Unfortunately, it has not been possible to evaluate z_q by any other means, therefore the estimate given by the extended Kalman filter has been relied upon since in using it in the simulation of dynamic responses favourable agreement with the observed responses is evident.

In order to compare the theoretical estimates of the lateral derivatives with those obtained from the extended Kalman filter estimator, Table 12.6 was formed. From this table it is clear that the theoretical estimates of L_p and N_v agree favourably with those of the extended Kalman filter estimator. However, there is a great deal of discrepancy between $L_{v_{theoretical}}$ and $L_{v_{E.K.F.}}$. By assuming that the E.K.F. estimates were representative of the actual model, a fact justified by simulations, the discrepancy could be put down to the fact that the theoretical expression for L_v does not take into account the contribution due to fuselage and especially the large canopy.

Values of $\frac{dC_n}{d\zeta}$ and $\frac{dC_\ell}{d\xi}$ from Table 12.4 can be used to estimate the lateral control derivatives N_ζ and L_ξ respectively. However, the estimates of N_ζ and L_ξ obtained in this manner could not be compared with those of the extended Kalman filter algorithm since the latter estimates correspond to a tunnel speed of U > 27 m/s whereas the measured value of $\frac{dC_n}{d\zeta}$ and $\frac{dC_\ell}{d\xi}$ correspond to tunnel speeds of 19 m/s and 25 m/s respectively.

12.6 Initial Computer Based Simulations of the Flight Control System

In moving from experiments in stable flight regime to experiments in an unstable flight regime it became necessary to design a suitable auto-stabilisation system for the model. Details of the design philosophy and calculations were given in Section 10. Initial experiments involving the implementation of the autostabiliser have been limited to observations, the most important of which are listed below.

(i) The height-locking control system of the F.C.S. was affected by the stiction in the heave motion due to friction between the gimbal linear bearing and the vertical support rod.

(ii) Partly as a result of (i) and partly because of the backlash in the servomechanisms, there was always a steady state error in attitude.

(iii) An attempt to use an integrator to overcome (ii) reduced the phase margin and the system became unstable.

(iv) Theoretical values of proportional gains were found to be too small for the physical height-lock control system.

(v) An attempt to increase the proportional gains of the height-lock control system for a quicker and better response shifted the system poles to the right half s-plane and resulted in oscillatory and divergent characteristics.

(vi) The implementation of a lead network in the system provides a marginal improvement in the height lock control system.

(vii) Independent roll and yaw control loopsresulted in a reduction in perturbations to within $\pm 10^{o}$ of the trimmed flight datum values. Any departure beyond these limits would have required a control law to cope with the resulting roll-yaw coupling.

A computer simulation of the height holding control system response to a height step input showed a satisfactory performance as Figures 12.25 and 12.26 indicate. It may be deduced from these two figures that the response time was about 6 s, at best. By using heave velocity feedback the response time was halved and this is shown in Fig. 12.27. A more detailed evaluation of the system is contained in Appendix I. With the application of the flight control system to the dynamic model and its incorporation into the extended Kalman filter parameter estimation program, it was hoped that estimates of the longitudinal stability derivatives of the dynamic model with relaxed stability could be obtained.

CASE II

$U = 20.0$ m/s
$z_w = -2.0$
$m_w = -0.2$
$m_q = -0.8$
$z_\eta = -10.0$
$m_\eta = 40.0$

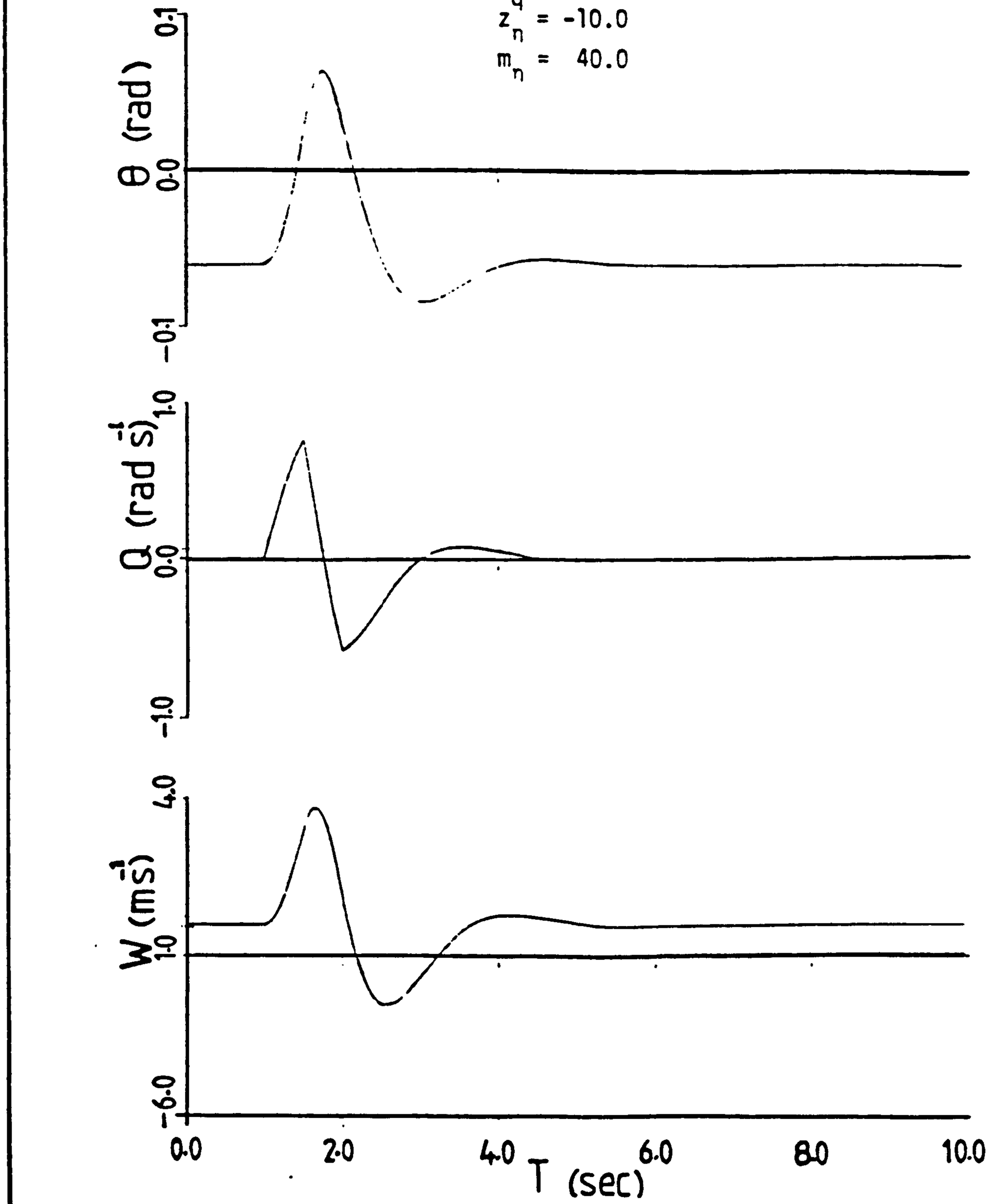

FIGURE 12.1

SIMULATED LONGITUDINAL RESPONSE OF THE A/C TO A DIPOLE FOREPLANE INPUT

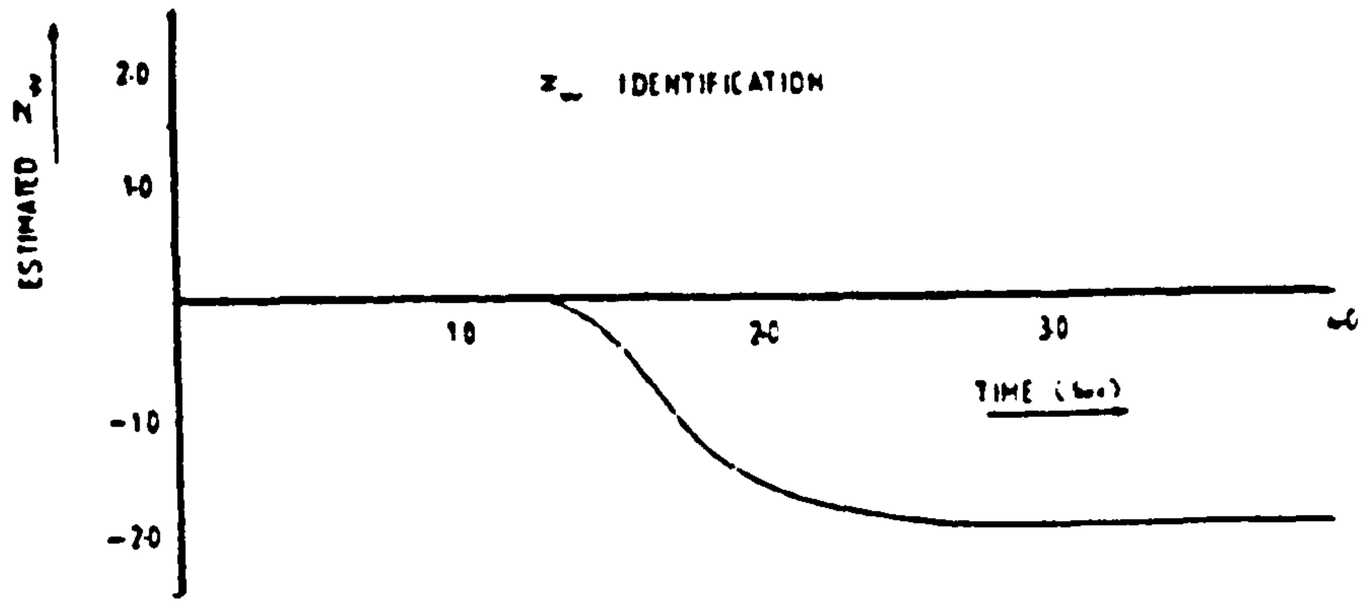

FIGURE 12.2

CONVERGENCE OF SOME OF THE ESTIMATED PARAMETERS WITH NUMBER OF ITERATIONS (CASE II).

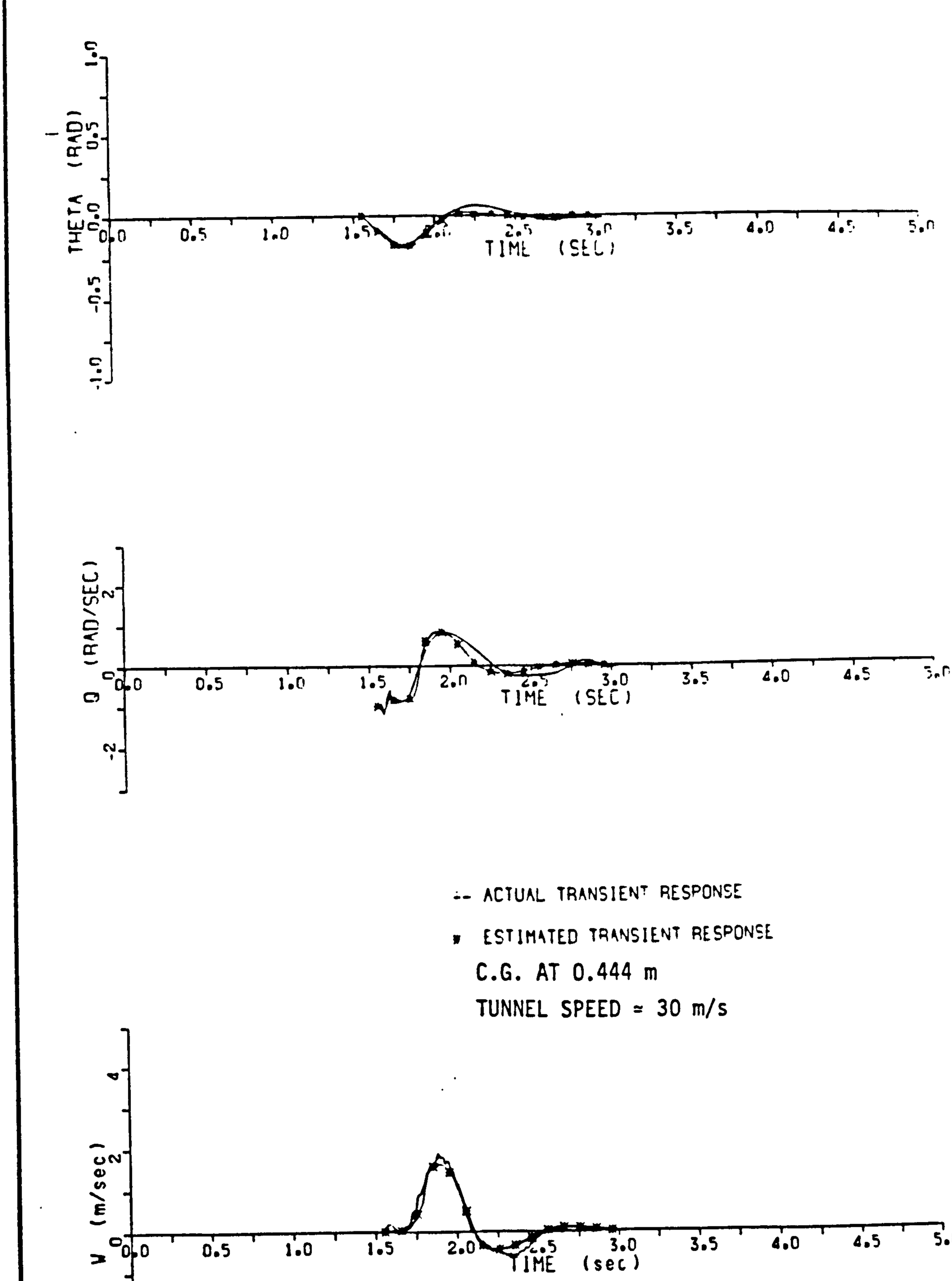

FIGURE 12.3 .LONGITUDINAL TRANSIENT RESPONSE TO A FOREPLANE PULSE INPUT

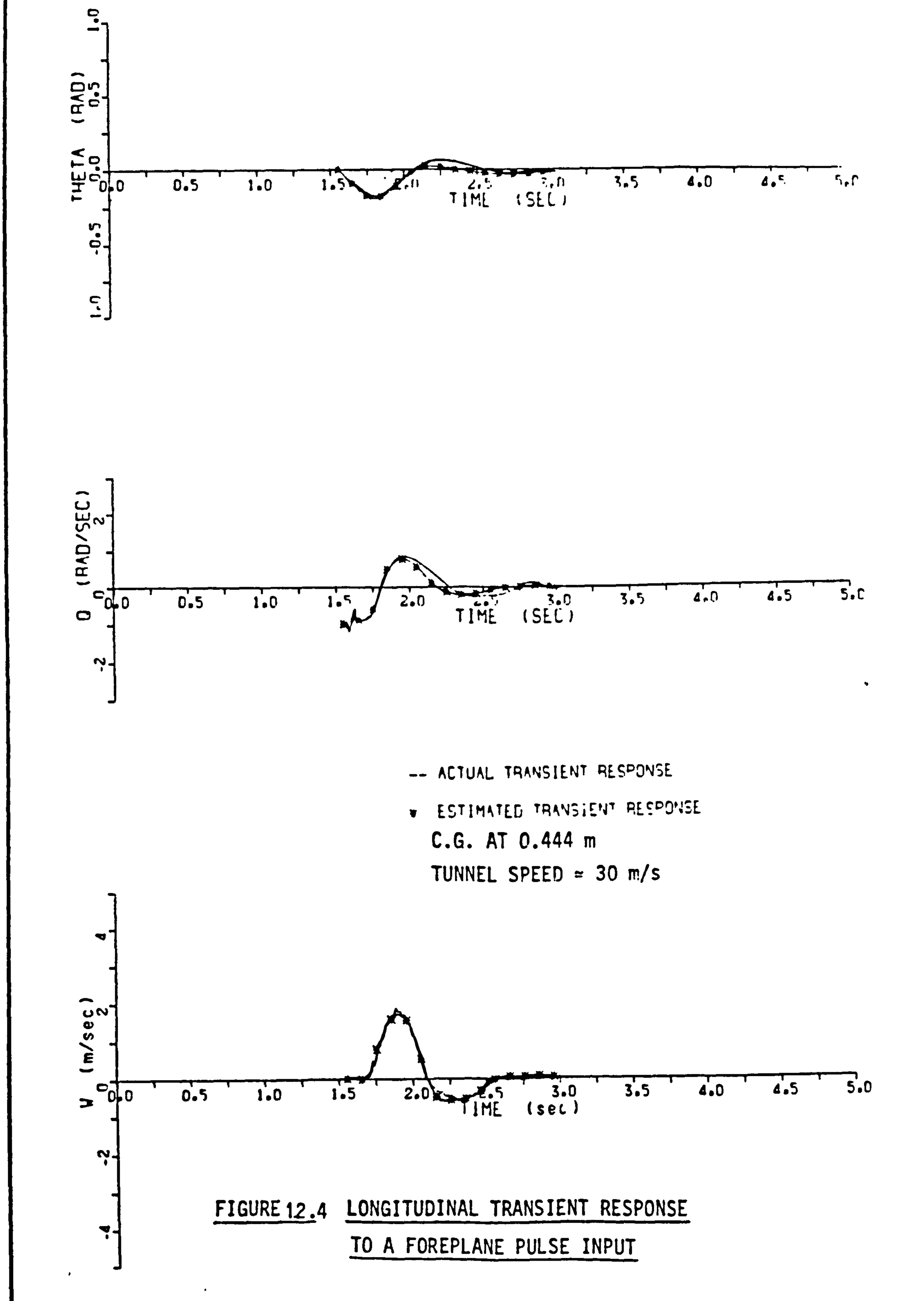

FIGURE 12.4 LONGITUDINAL TRANSIENT RESPONSE TO A FOREPLANE PULSE INPUT

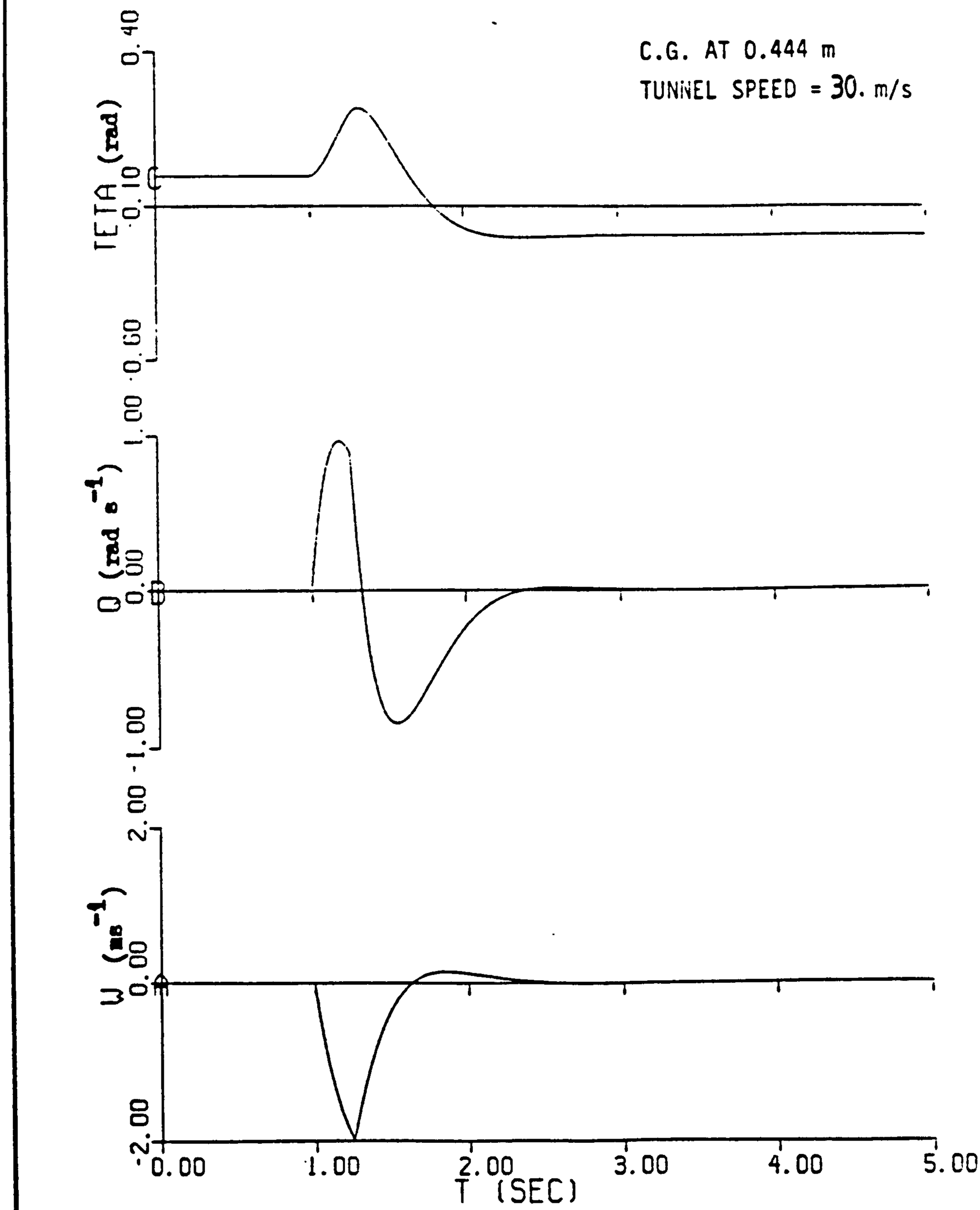

FIGURE 12.5. SIMULATION OF LONGITUDINAL TRANSIENT RESPONSE USING ESTIMATED DERIVATIVES

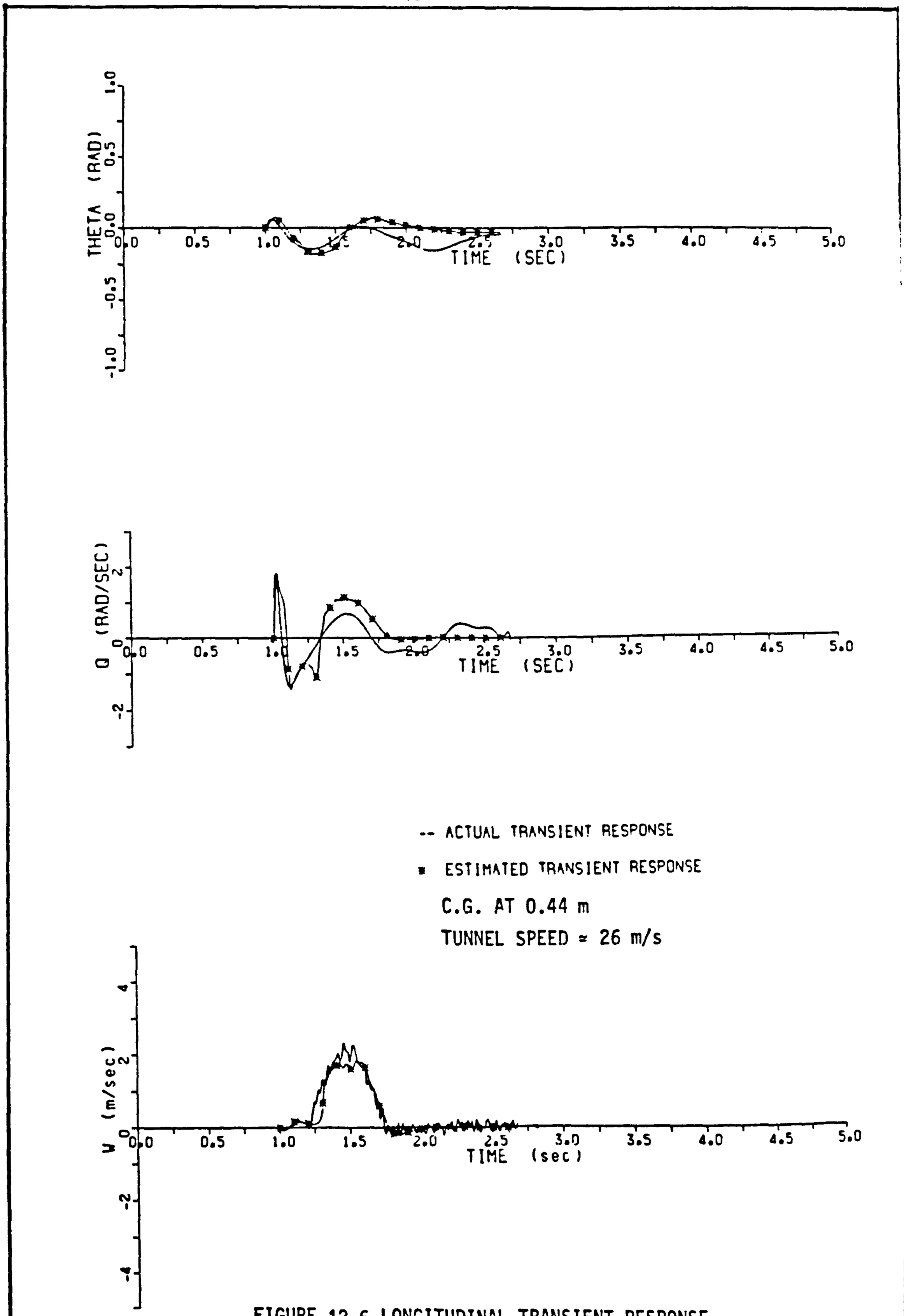

FIGURE 12.6 LONGITUDINAL TRANSIENT RESPONSE TO A FOREPLANE PULSE INPUT

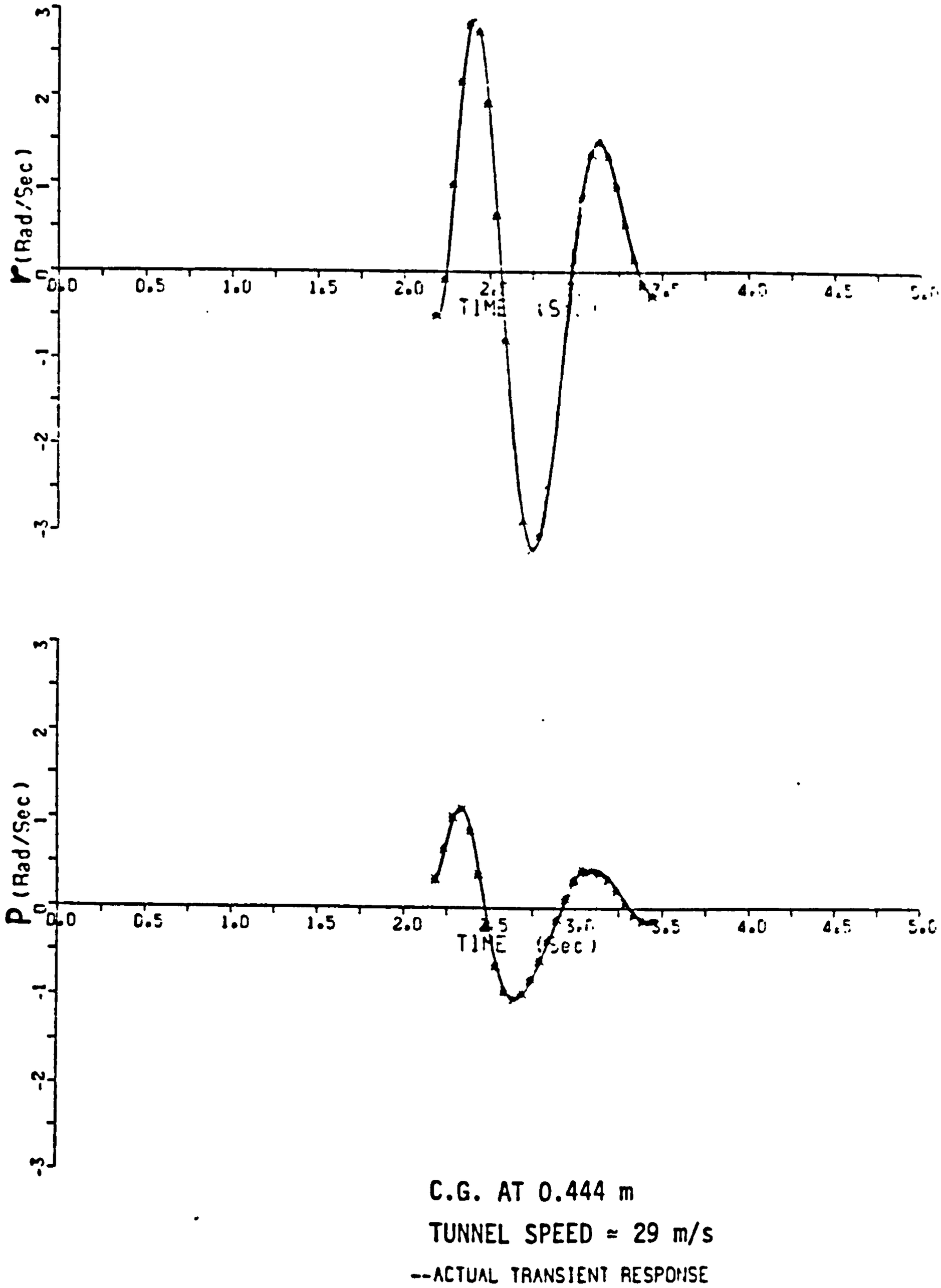

FIGURE 12.7 LATERAL TRANSIENT RESPONSE DUE TO RUDDER PULSE INPUT

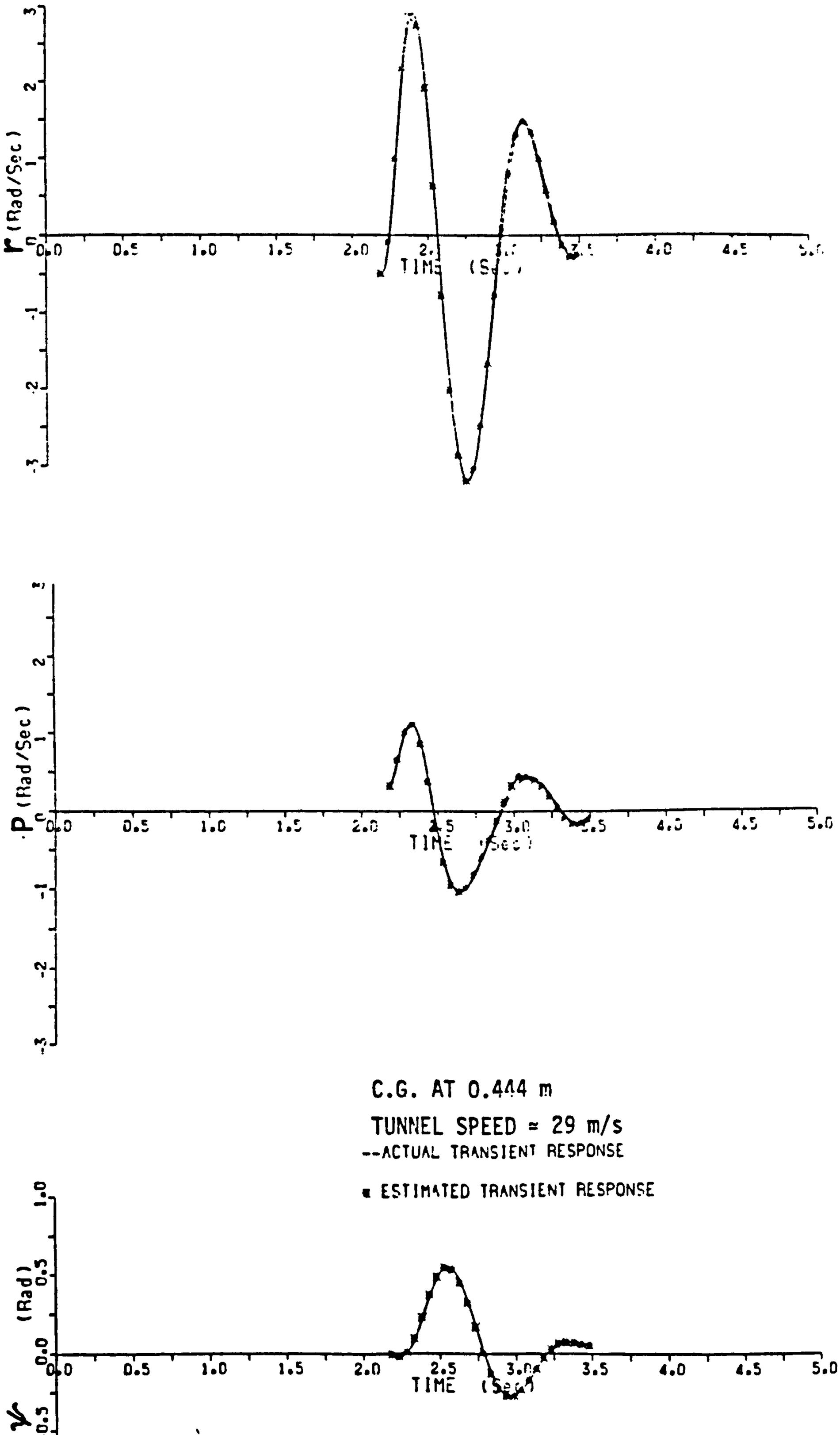

FIGURE 12.8 LATERAL TRANSIENT RESPONSE DUE TO RUDDER PULSE INPUT

Text cut off in original

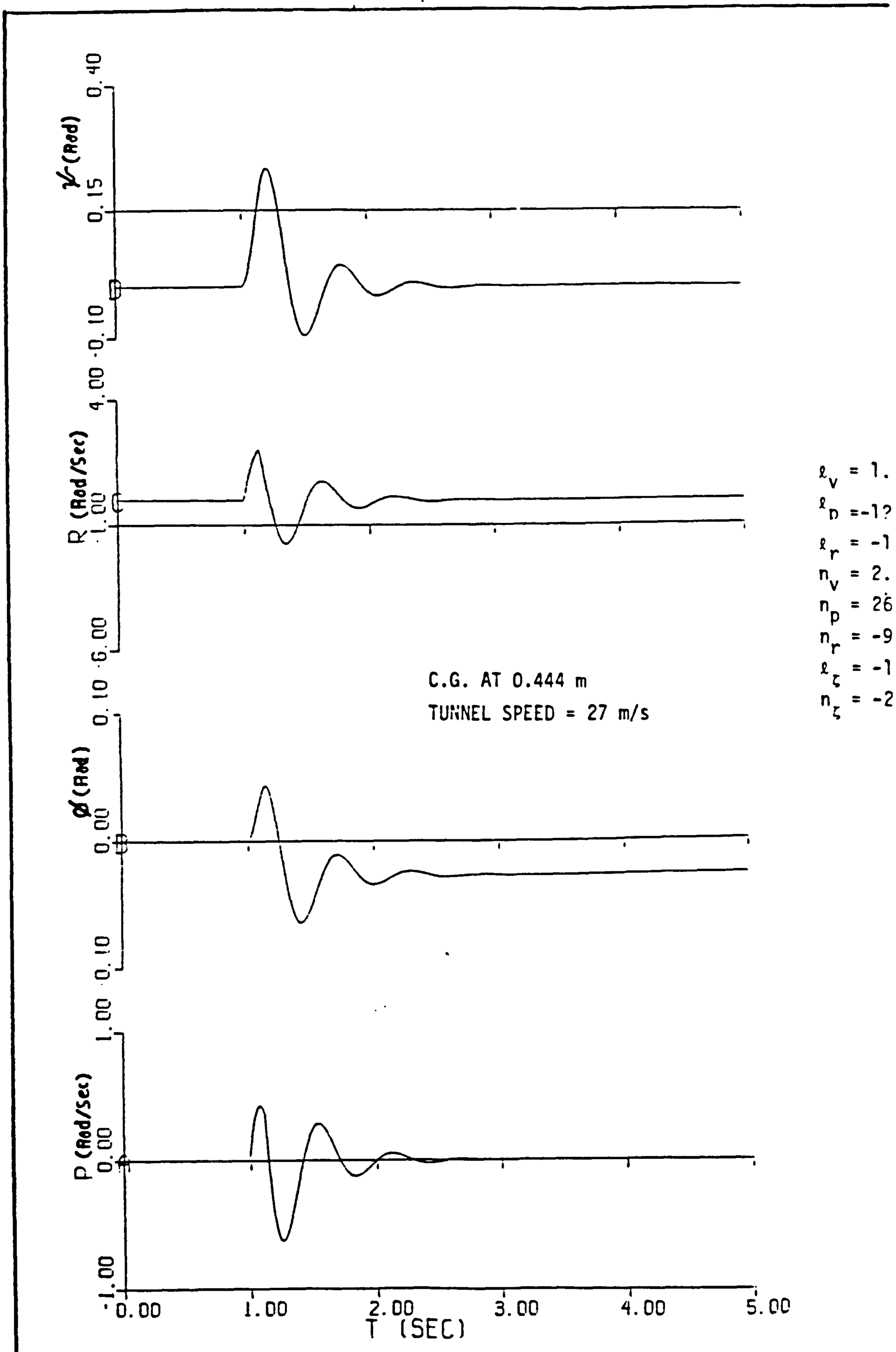

ℓ_v = 1.
ℓ_n =-1?
ℓ_r = -1
n_v = 2.
n_p = 26
n_r = -9
ℓ_ζ = -1
n_ζ = -2

C.G. AT 0.444 m
TUNNEL SPEED = 27 m/s

FIGURE 12.9 SIMULATED LATERAL TRANSIENT RESPONSE USING ESTIMATED DERIVATIVES

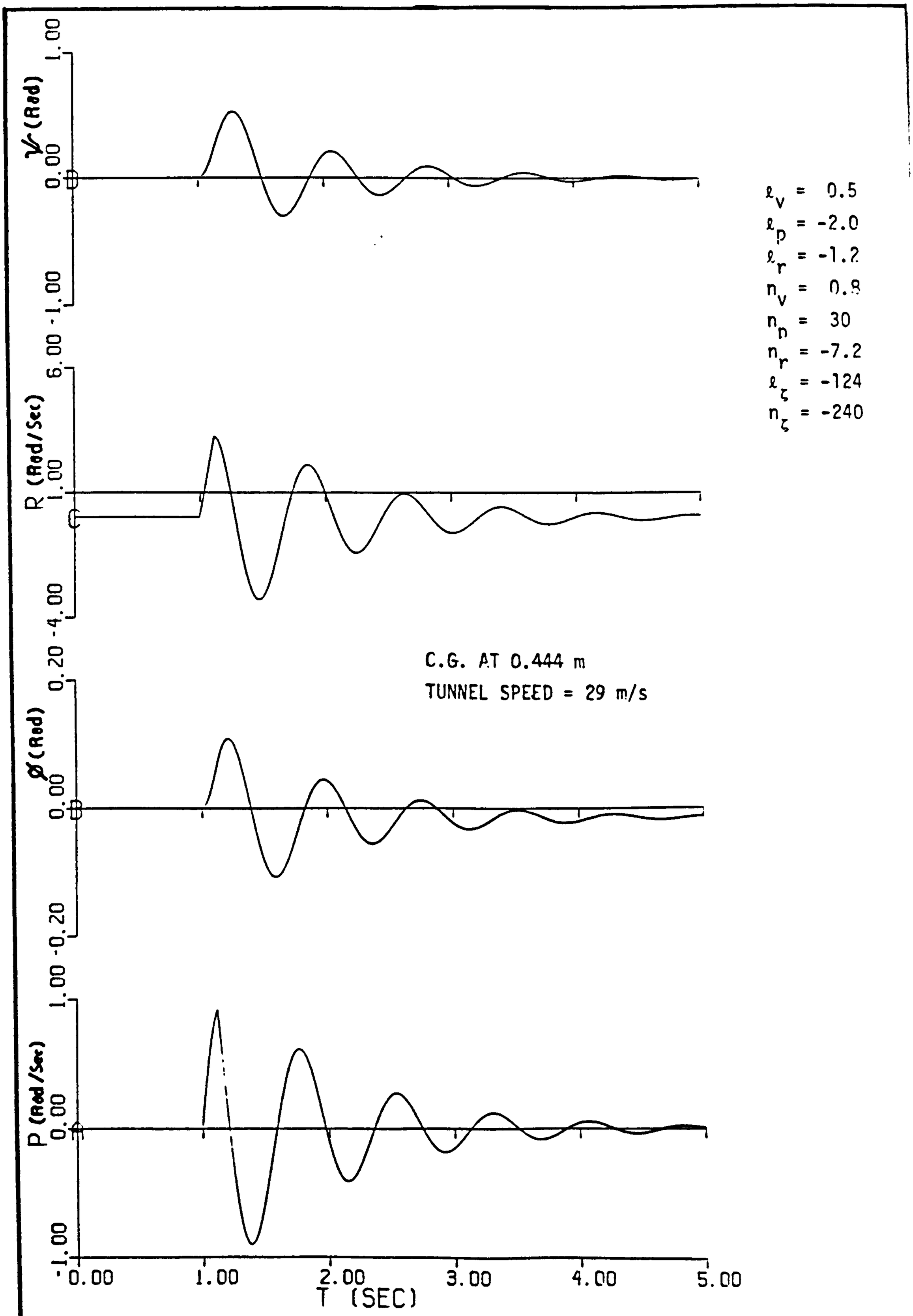

FIGURE 12.10SIMULATED LATERAL TRANSIENT RESPONSE USING ESTIMATED DERIVATIVES

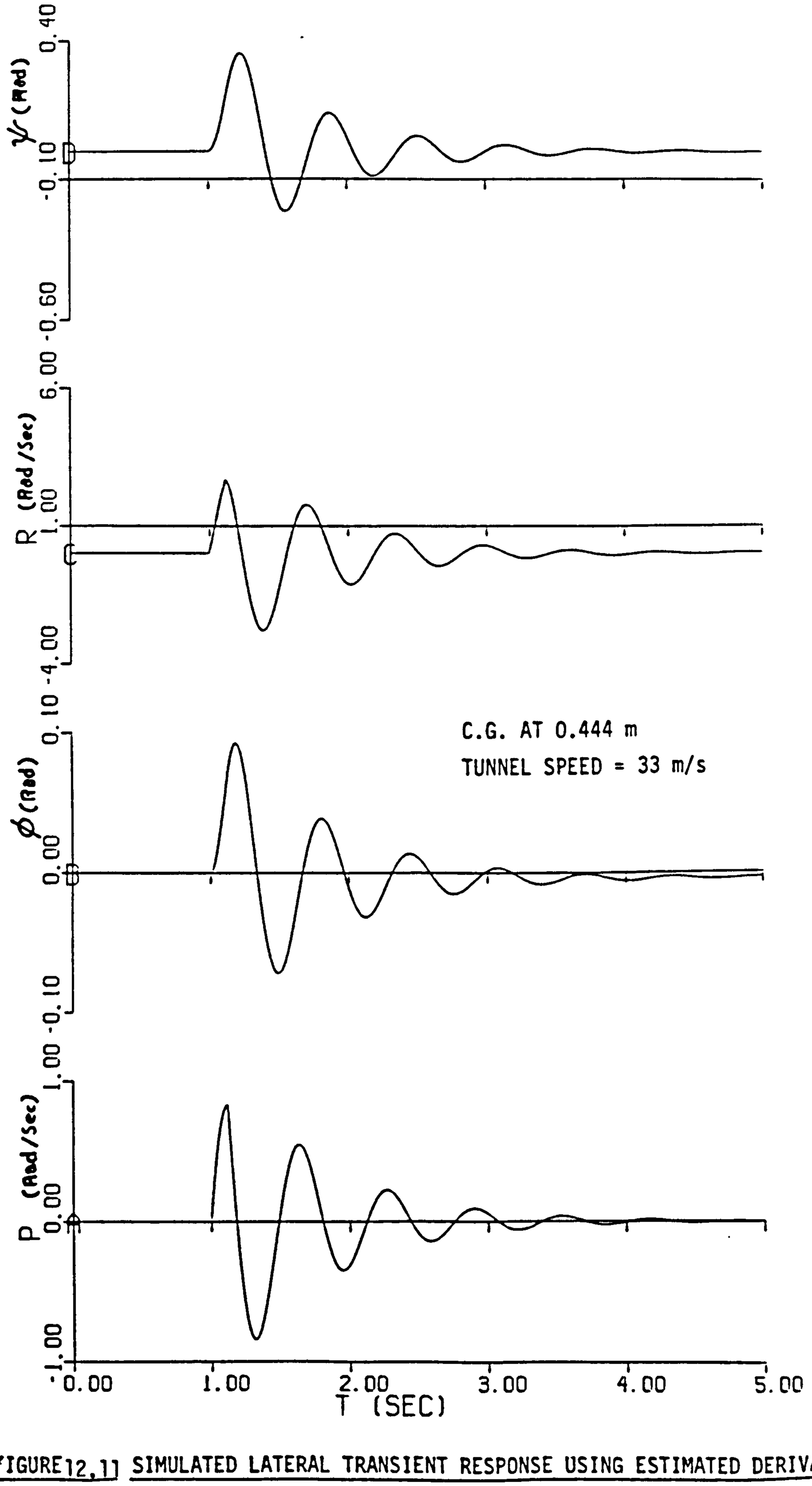

FIGURE 12.11 SIMULATED LATERAL TRANSIENT RESPONSE USING ESTIMATED DERIVATIVES

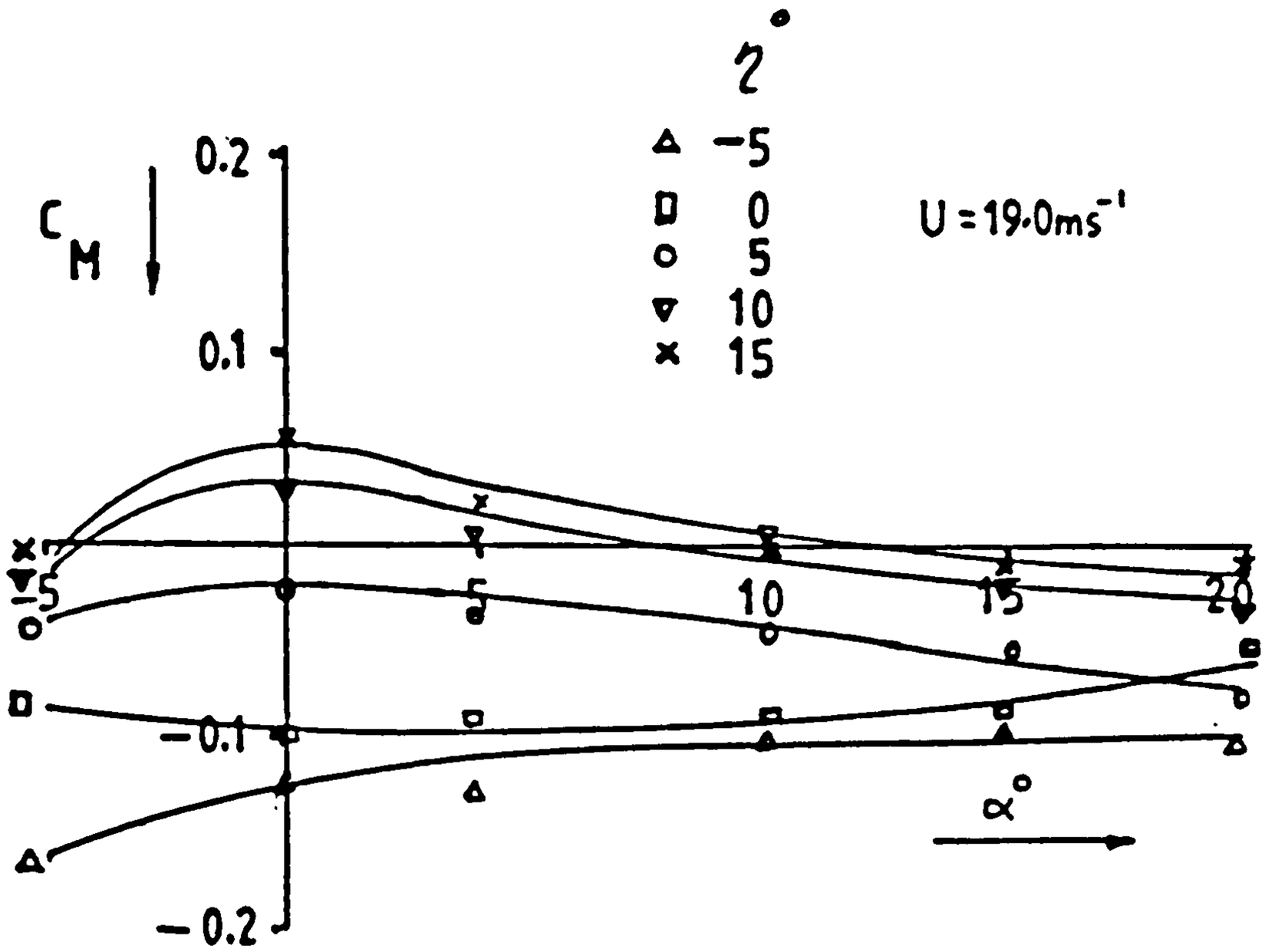

FIGURE 12.12

C_m - α VARIATIONS FOR DIFFERENT FOREPLANE SETTINGS n°

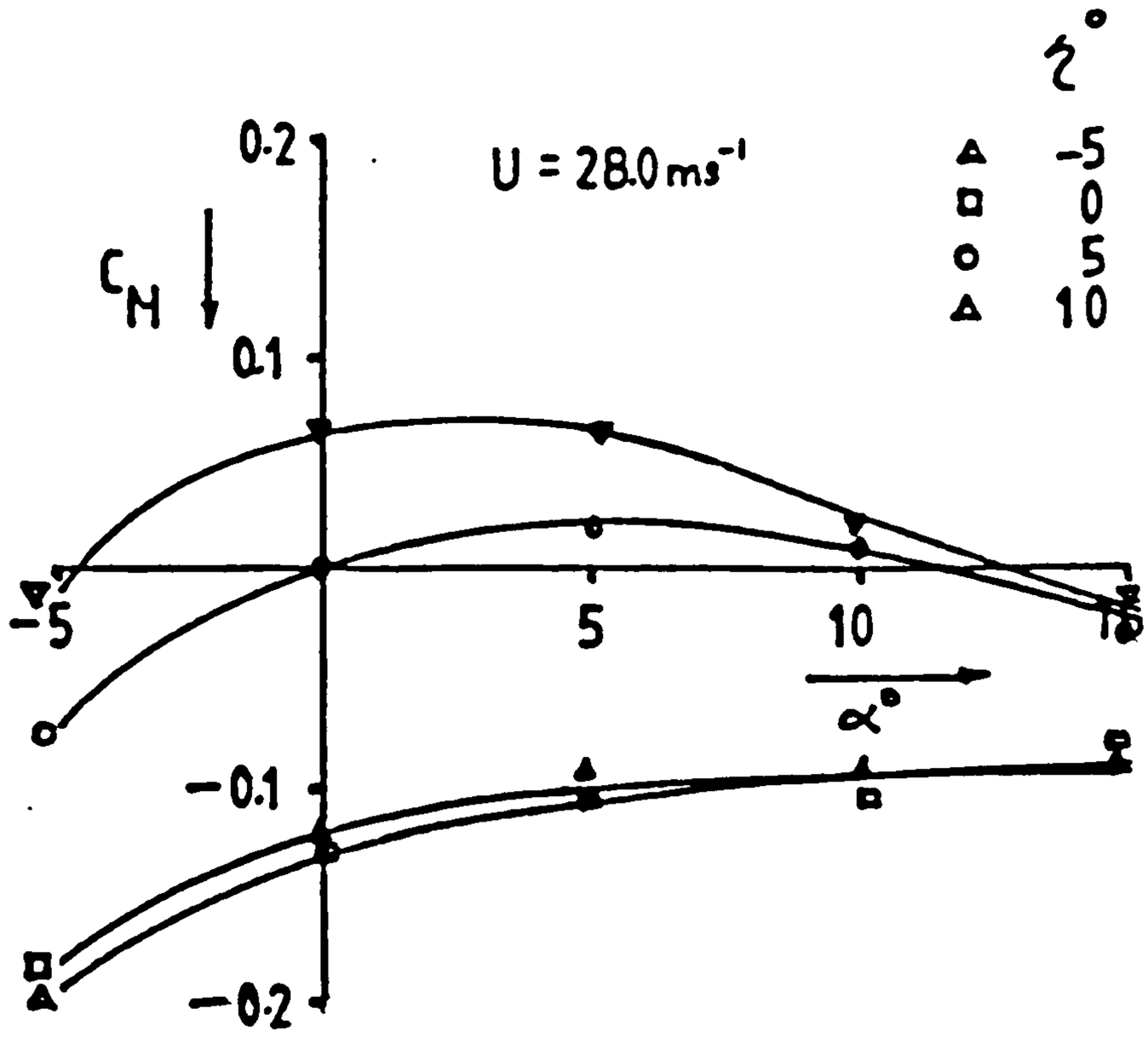

FIGURE 12.13

C_m - α VARIATIONS FOR DIFFERENT FOREPLANE SETTINGS n°

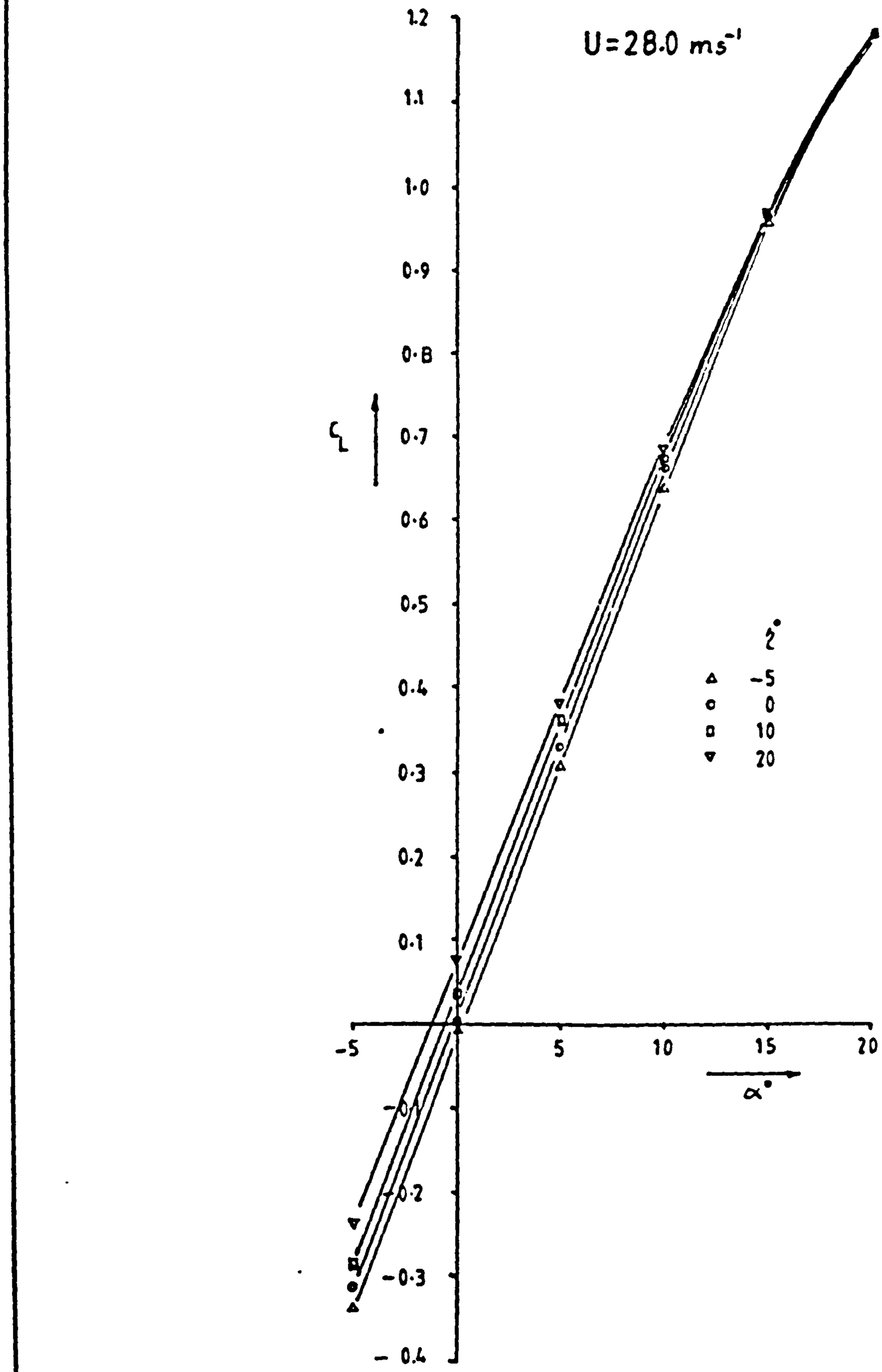

FIGURE 12.14

C_L - α VARIATION - FOREPLANE ON

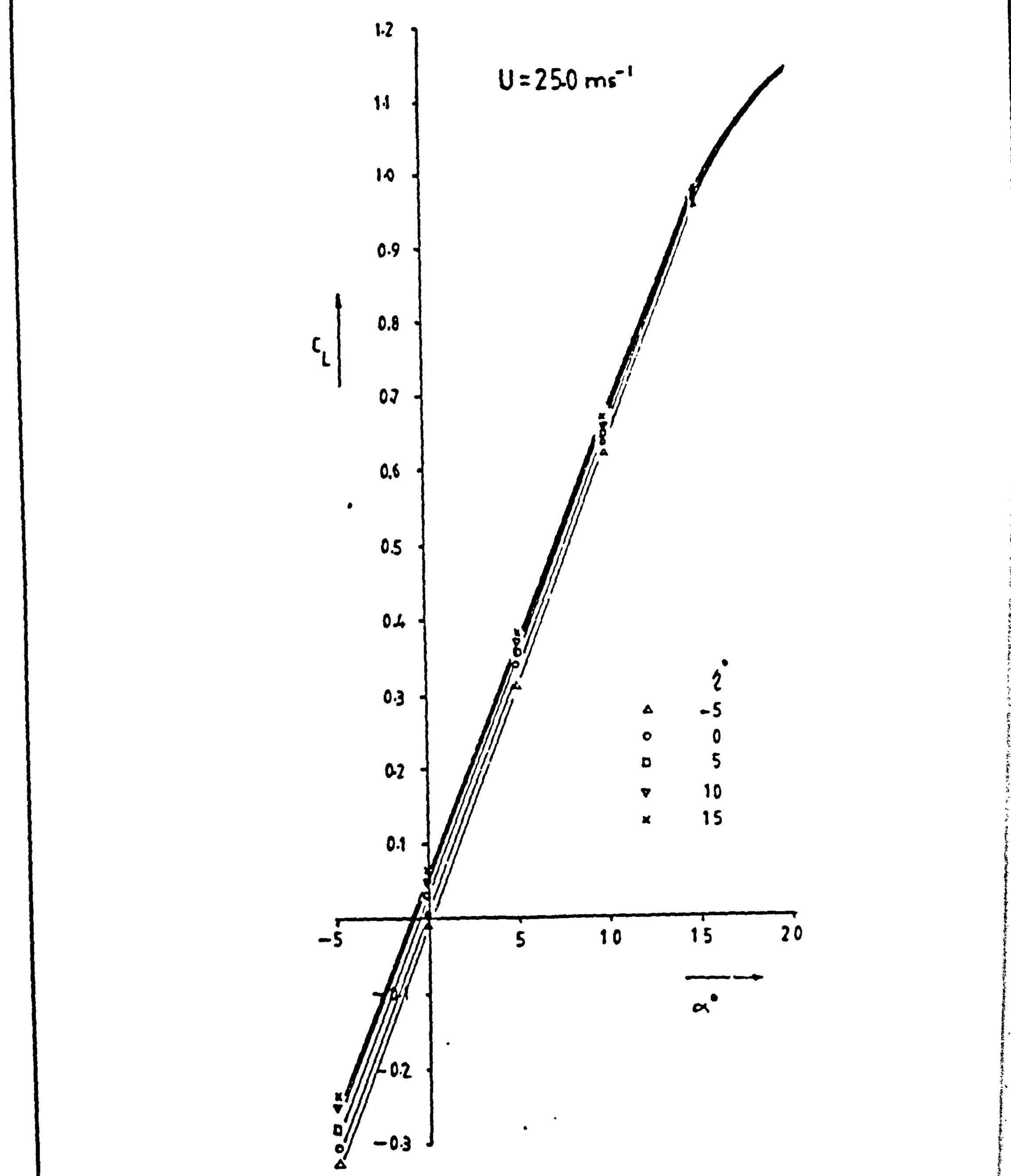

FIGURE 12.15

C_L - α VARIATION - FORFPLANE ON

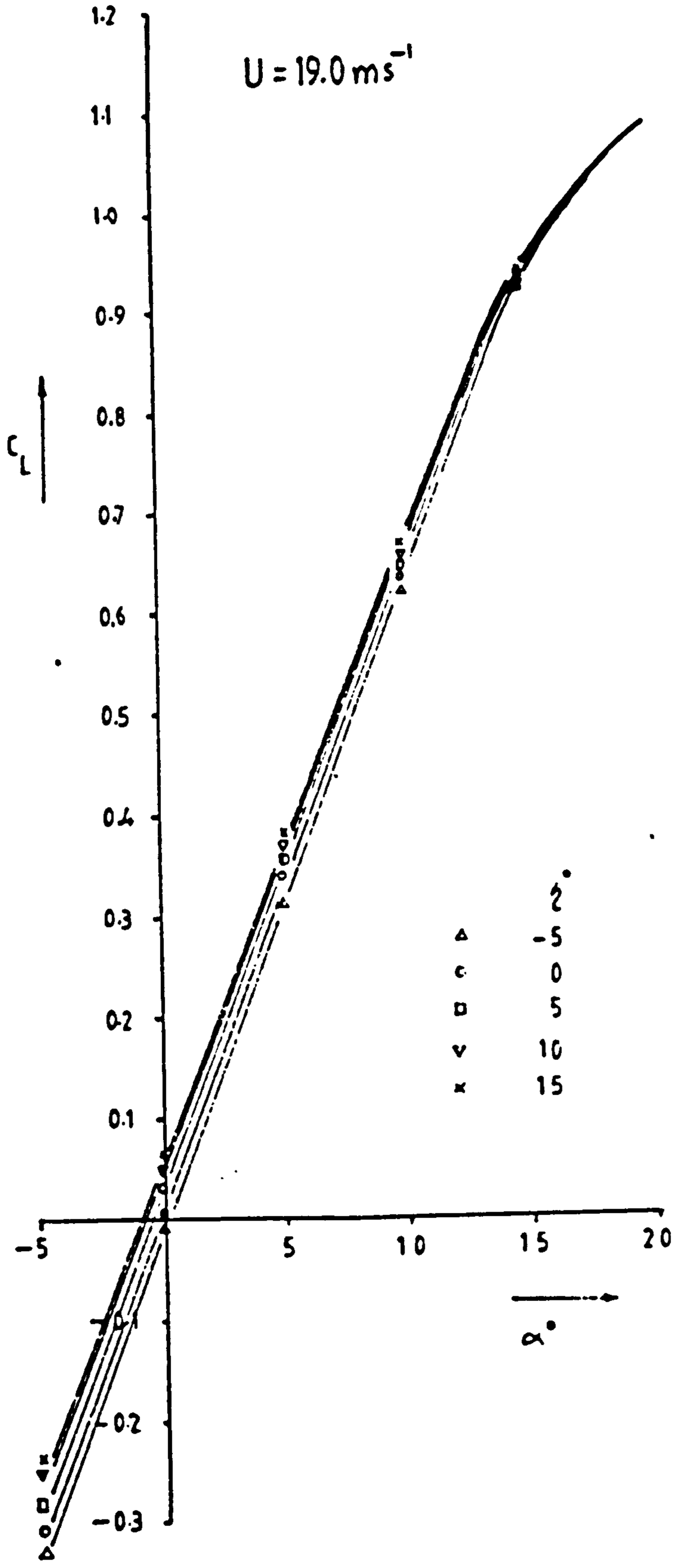

FIGURE 12.16

C_L - α VARIATION - FOREPLANE ON

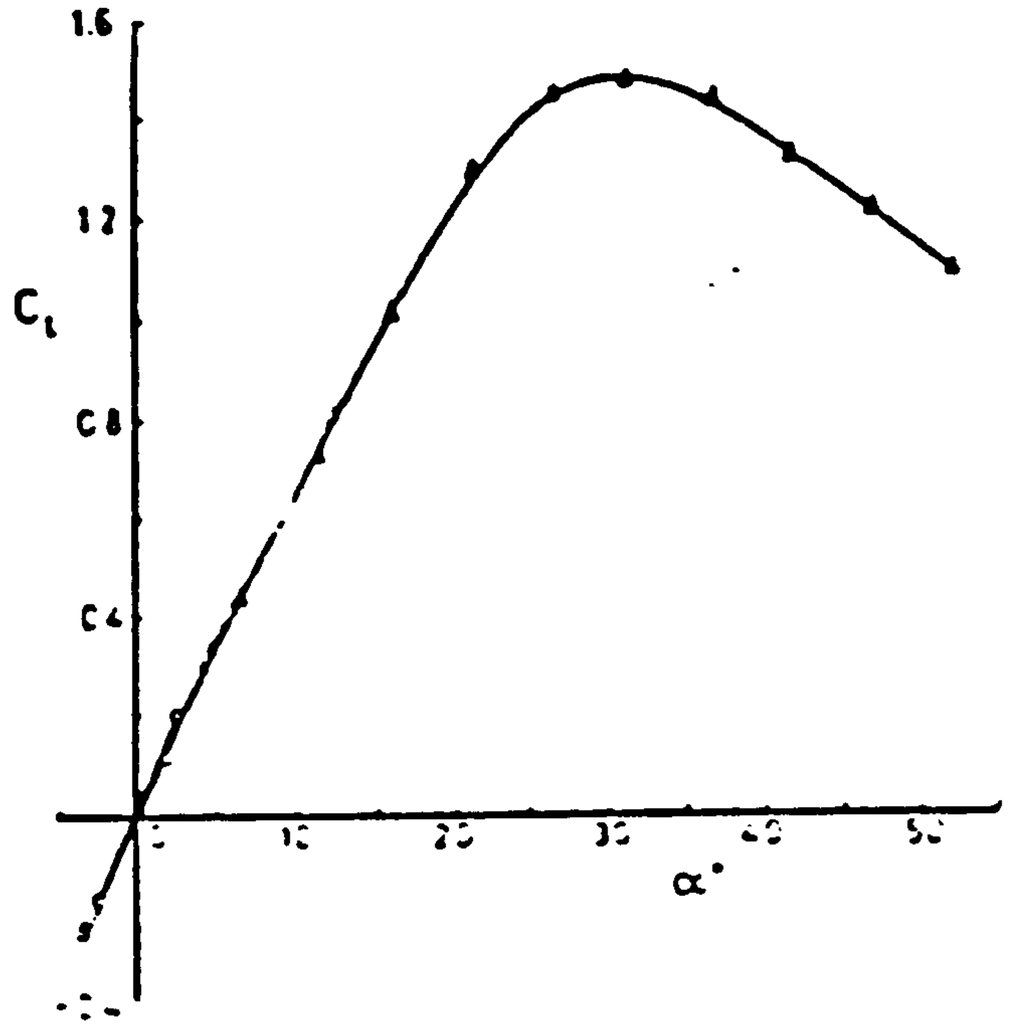

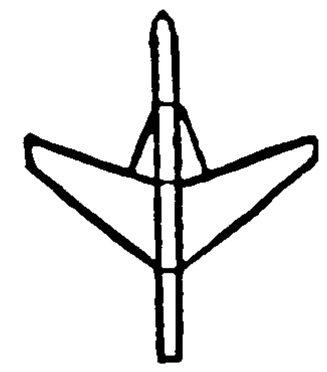

Force and moment measurements for above planform.

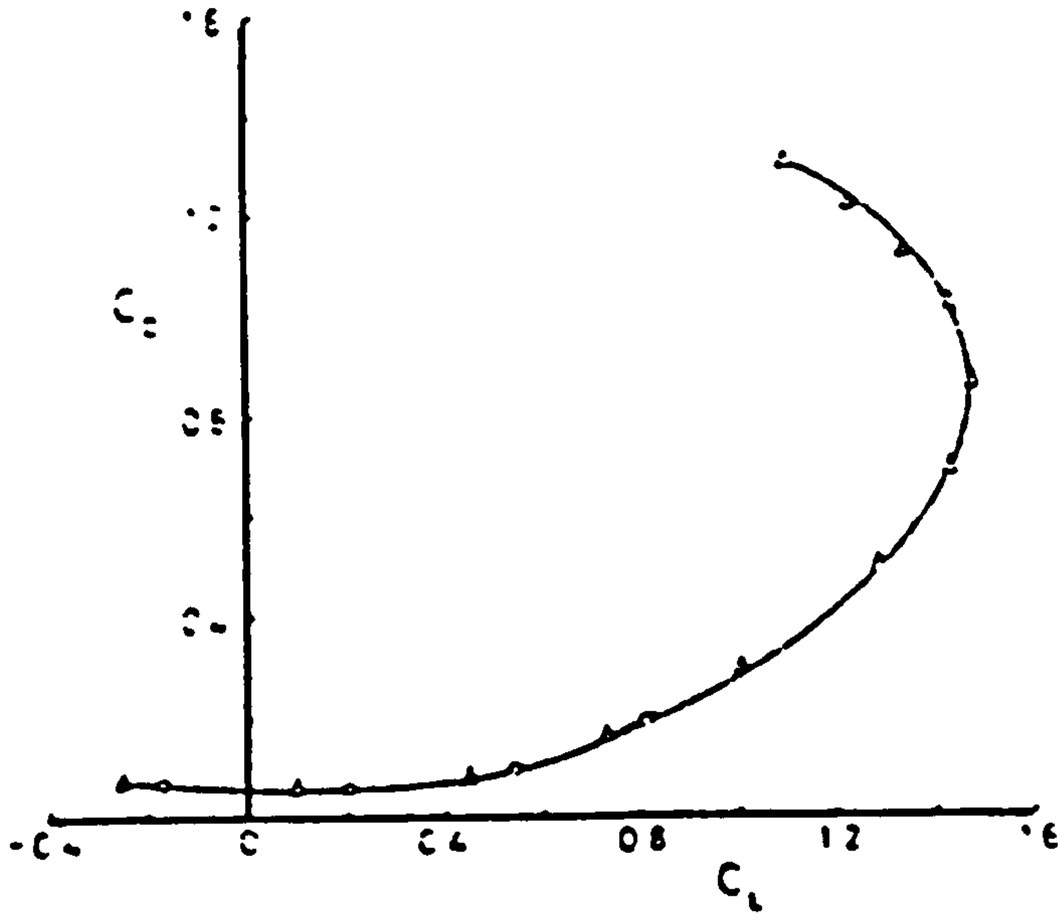

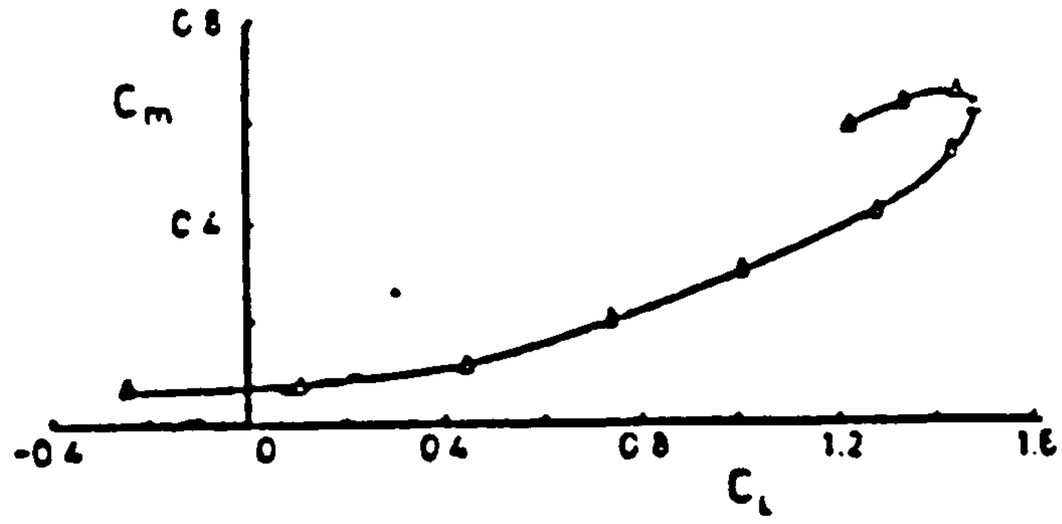

FIGURE 12.17 (Ref 2)

AERODYNAMIC CHARACTERISTICS OF A F.S.W. WITH STRAKES

PAGE

MISSING

IN

ORIGINAL

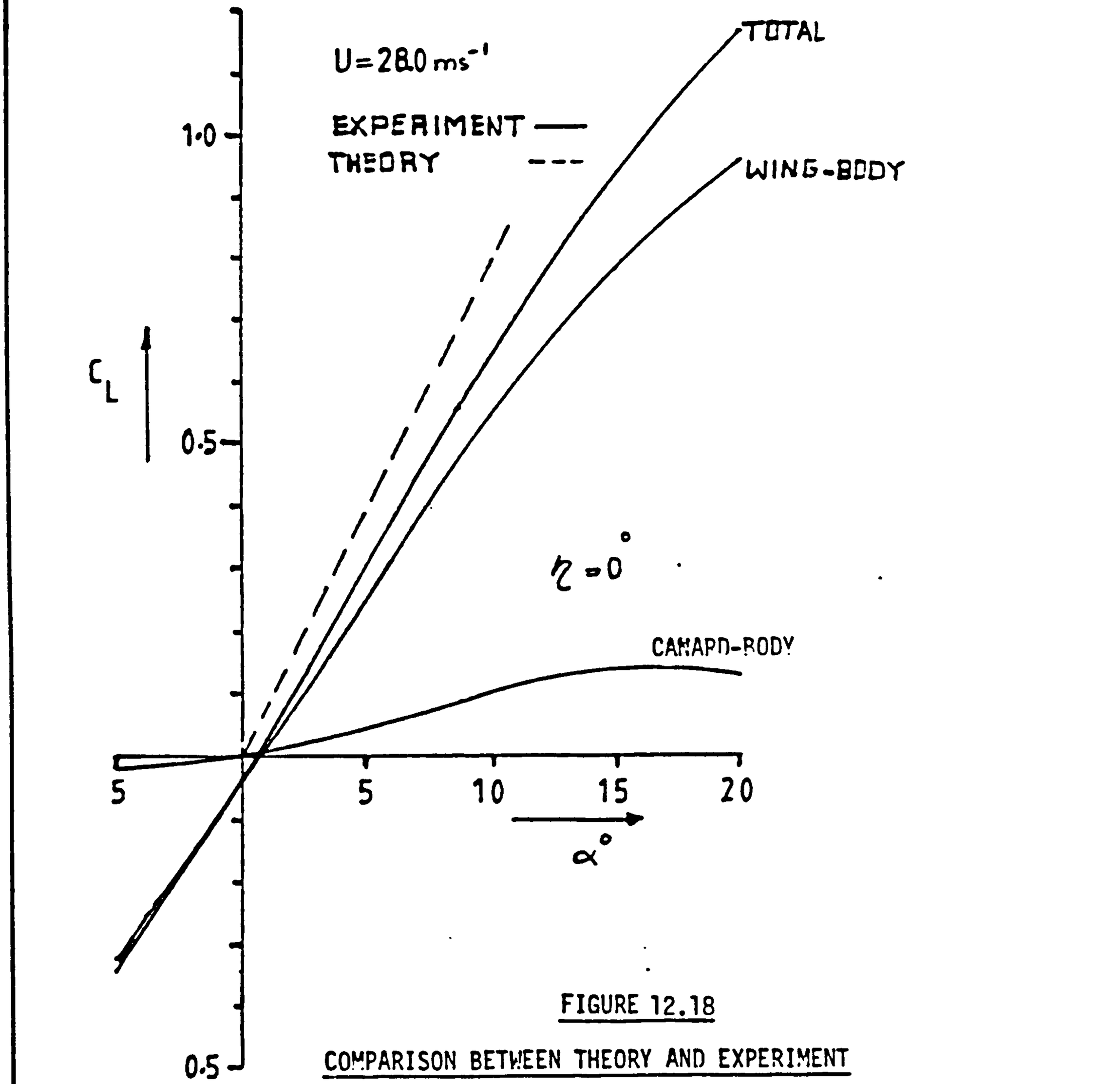

FIGURE 12.18

COMPARISON BETWEEN THEORY AND EXPERIMENT

REGARDING LIFT CURVES

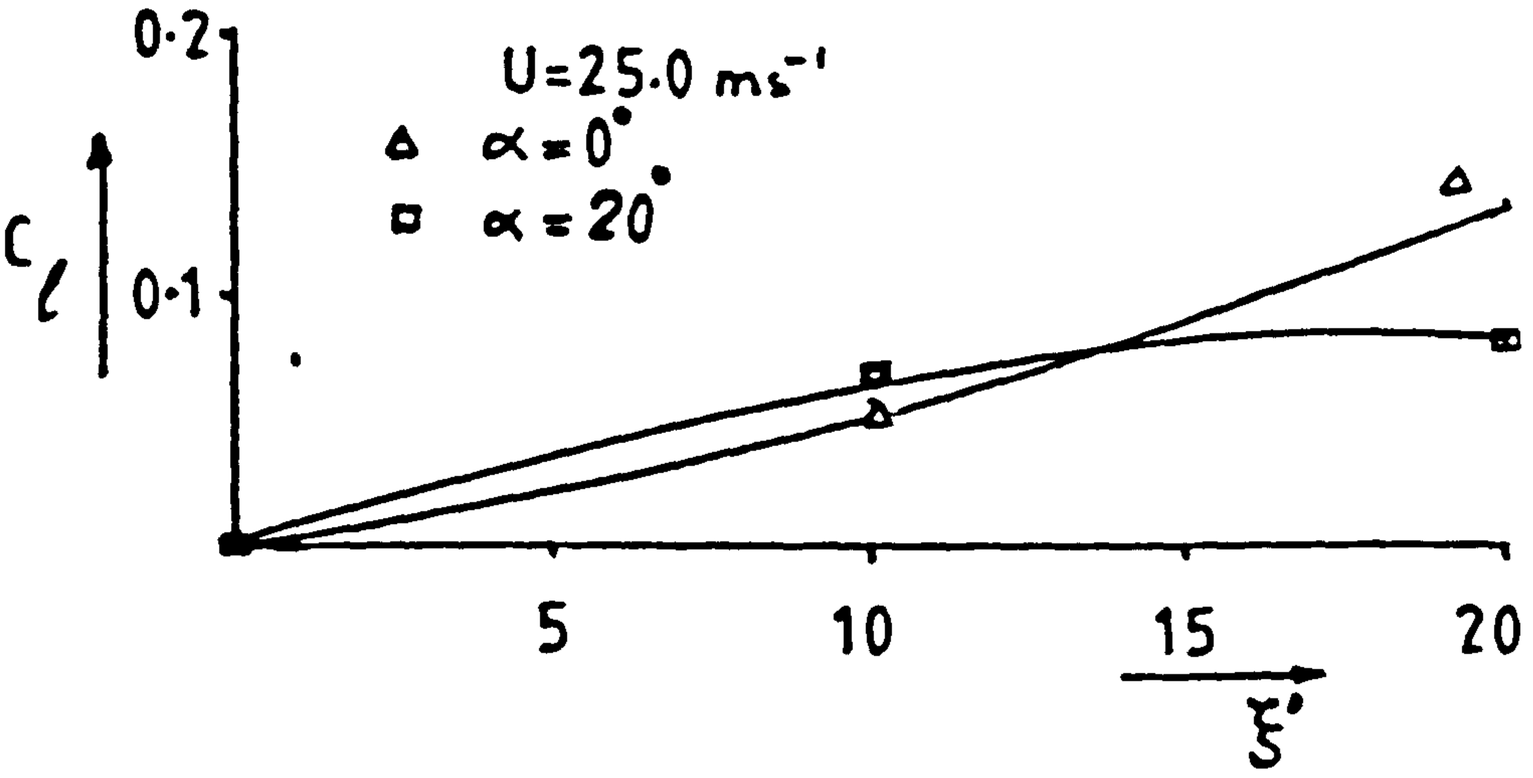

FIGURE 12.19

C_l - ξ^o VARIATION

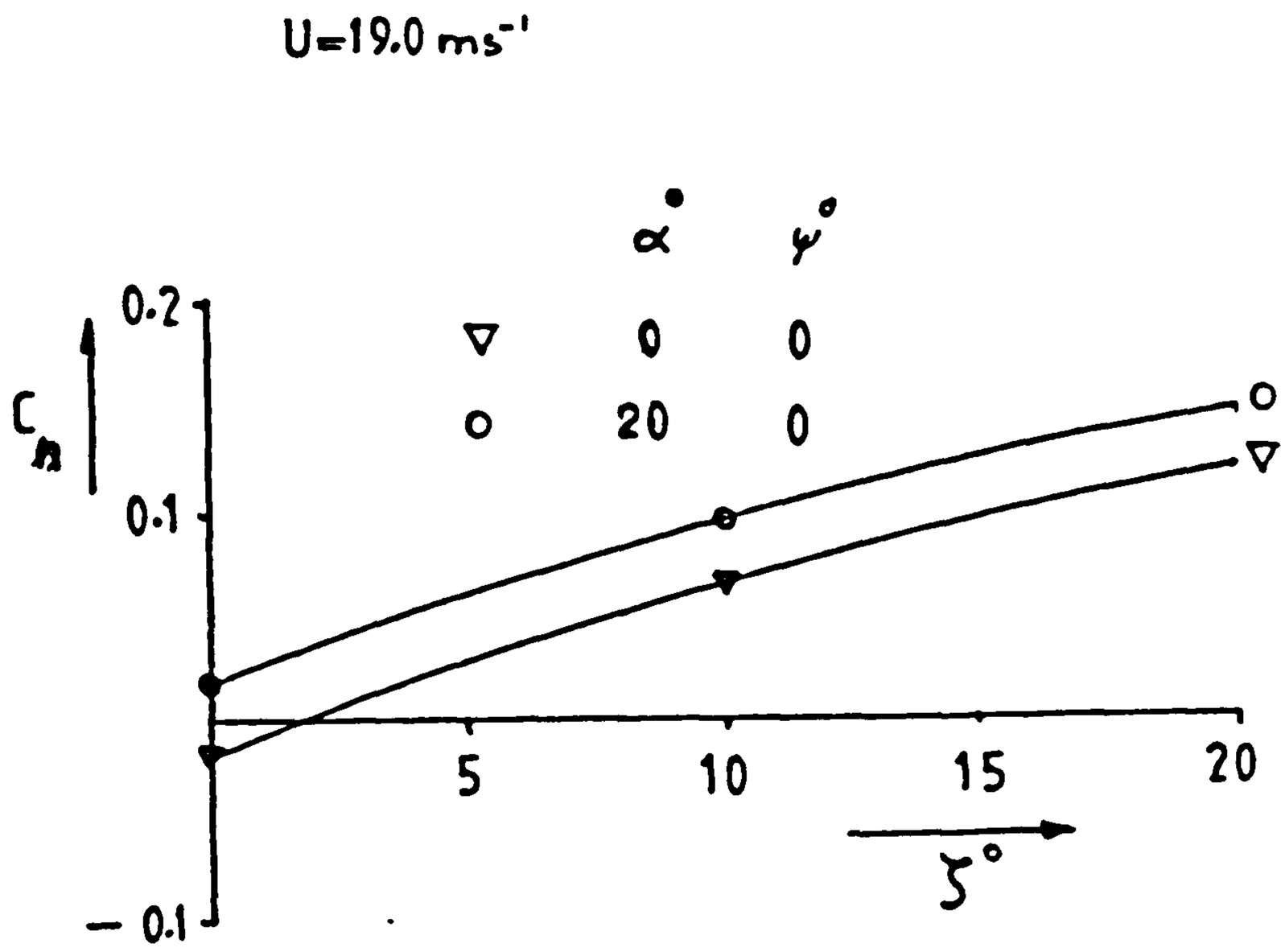

FIGURE 12.20

C_n - ζ^o VARIATIONS FOR DIFFERENT INCIDENCES α^o

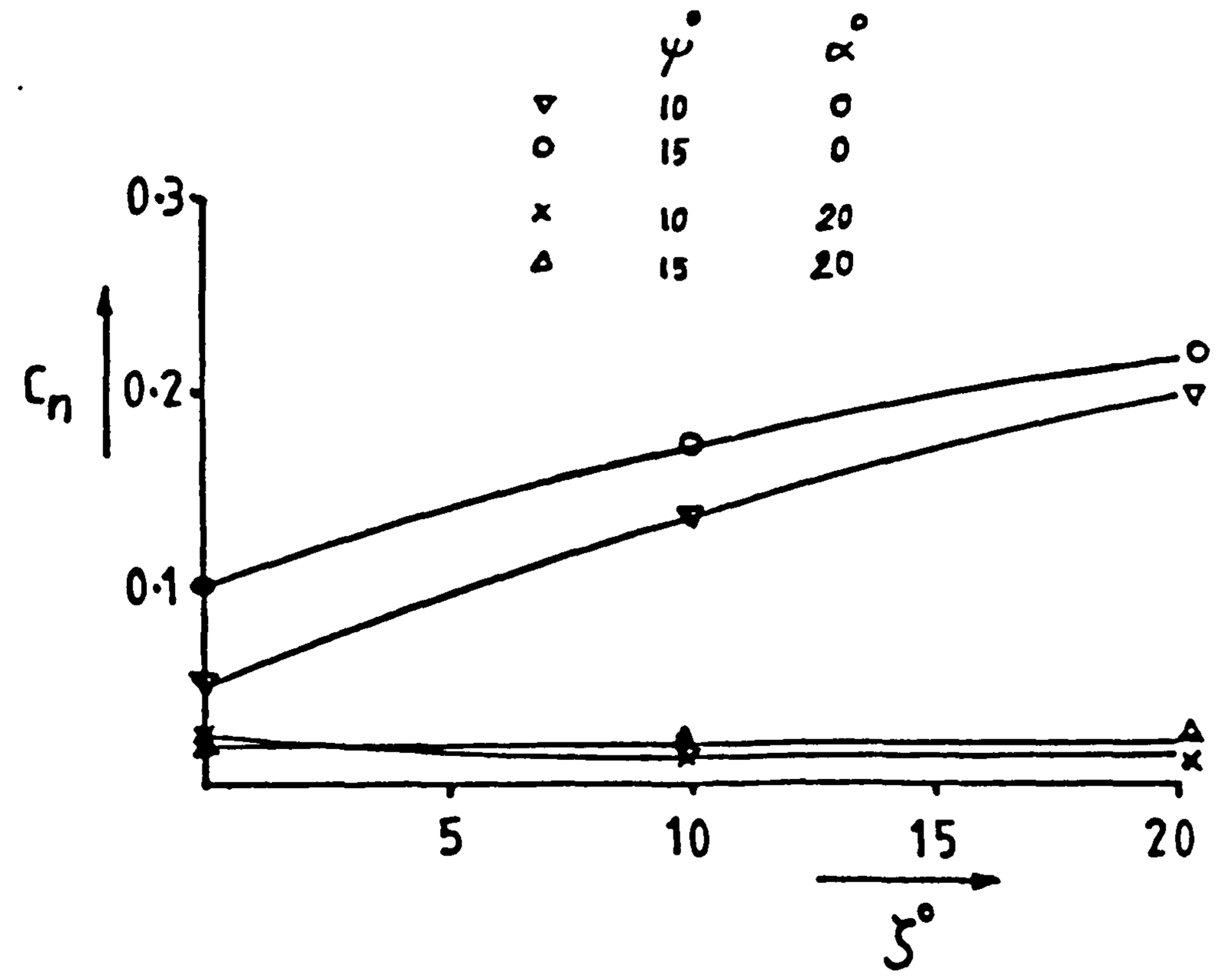

FIGURE 12.21

C_n - ζ^o VARIATIONS FOR DIFFERENT INCIDENCES α^o

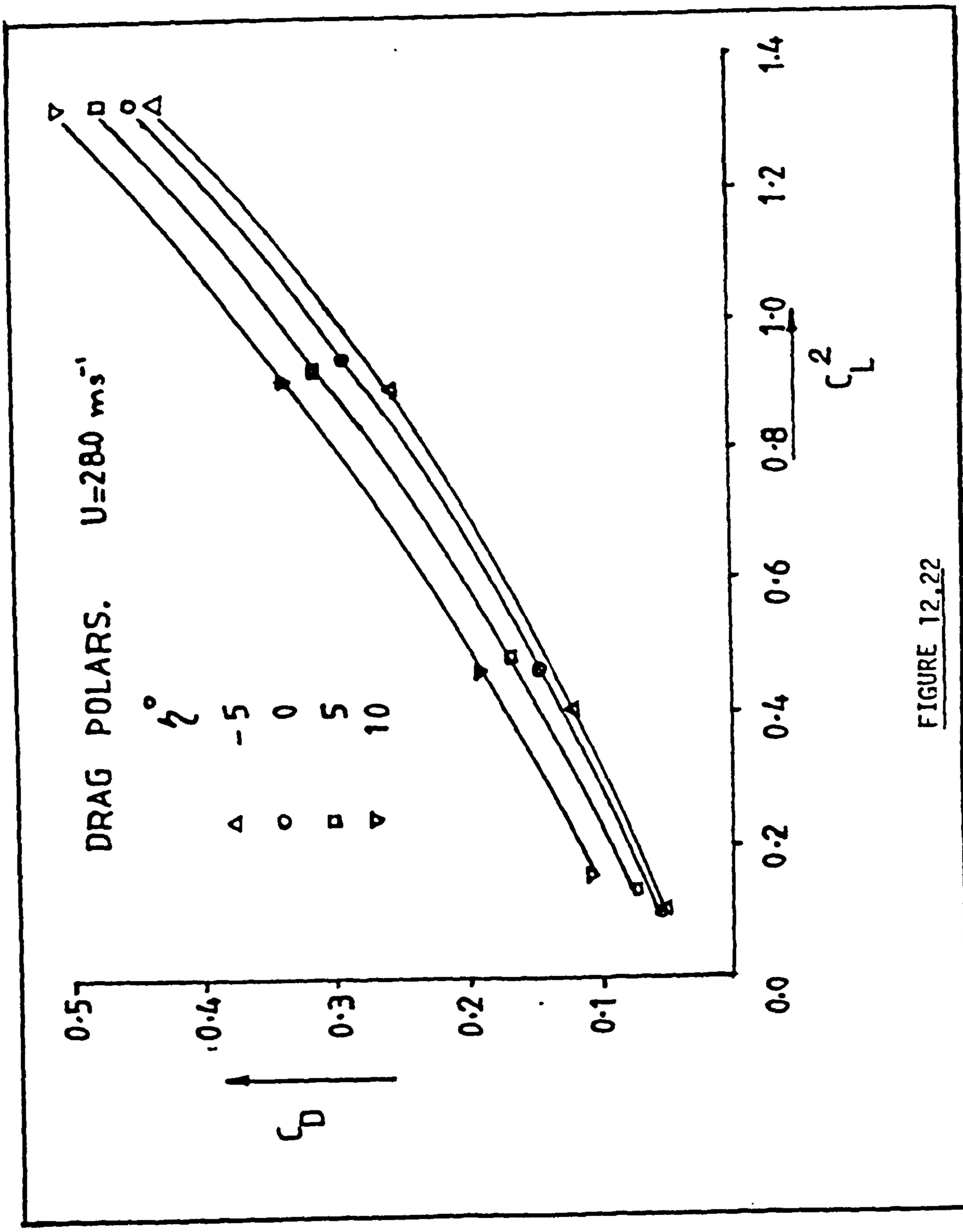
DRAG POLARS.
U=280 ms⁻¹
α°
-5
0
5
10
C_D
C_L^2
0·5
0·4
0·3
0·2
0·1
0·0
0·2
0·4
0·6
0·8
1·0
1·2
1·4

FIGURE 12.22

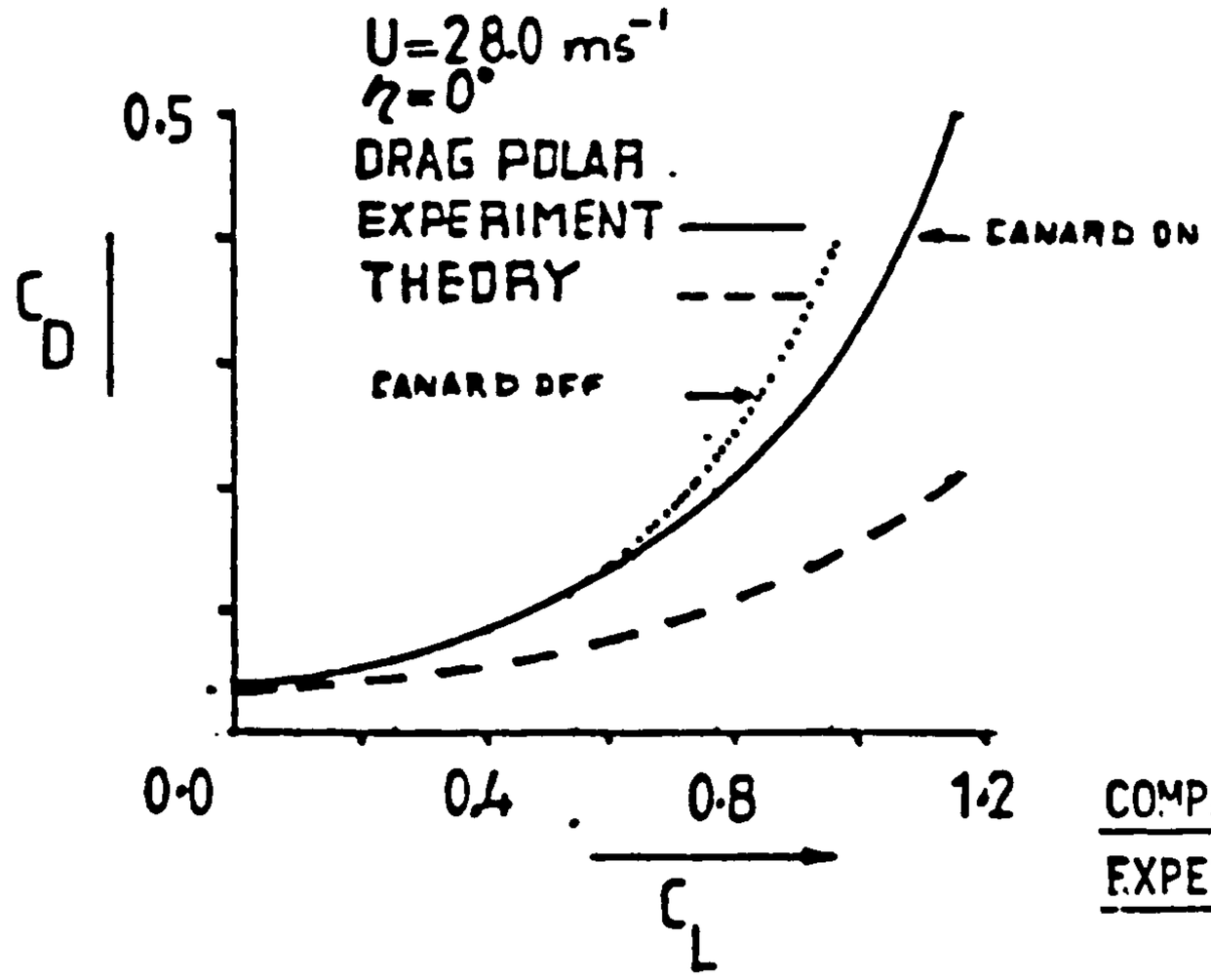

FIGURE 12.23

COMPARISON BETWEEN THEORY AND EXPERIMENT REGARDING DRAG POLARS

TUNNEL SPEED (m/s)	WING -FOREPLANE - BODY						FOREPLANE LIFT SLOPE A PROPORTION OF TOTAL LIFT SLOPE						
	WIND TUNNEL		THEORY (WITH THE INTERFERENCE FACTOR)		THEORY (WITHOUT THE INTERFERENCE FACTOR)		WIND TUNNEL	THEORY WITH INTER-FERENCE	THEORY WITHOUT INTER-FERENCE	WIND TUNNEL	THEORY	WIND TUNNEL	THEORY
	$(\frac{dC_L}{d\alpha})$ (rad^{-1}) total		$(\frac{dC_L}{d\alpha})$ (rad^{-1}) total		$(\frac{dC_L}{d\alpha})$ (rad^{-1}) total		$(\frac{dC_L}{d\alpha})_{\eta=0^o}$ (rad^{-1}) ≈	$(\frac{dC_L}{d\alpha})_{\eta=0^o}$ (rad^{-1})	$(\frac{dC_L}{d\alpha})_{\eta=0^o}$ (rad^{-1})	C_{D_o} for $\eta = 0^o$ ≈	C_{D_o} for $\eta=0^o$	C_{m_o}	$(\frac{dC_L}{d\eta})_{\alpha=0^o}$ (rad^{-1}) ≈
	CANARD ON $= 0^o$	CANARD OFF ≈	CANARD ON $= 0^o$	CANARD OFF	CANARD ON $= 0^o$	CANARD OFF							
19.0	3.76	3.38	4.63	3.68	3.66	3.07	0.46	0.95	0.59	0.041	0.036	-0.095	0.74
25.0												-0.098	
28.0												-0.12	

TABLE 12.1

AERODYNAMIC PARAMETERS CORRESPONDING TO FLIGHT-ATTITUDES OF TABLE-H1

* All lift slopes in Table-H2 are based on the wing area

MACH NO.	α^o	η^o_{trim}	C_L	C_D	C_M	X_u	Z_u	M_u
0.06	9.42	4.12	1.19	0.16	0.0	-0.6	-2.4	0.0
0.08	4.46	3.60	0.68	0.08	0.0	-0.26	-1.36	0.0
0.1	2.13	3.35	0.44	0.05	0.0	-0.17	-0.87	0.0

X_w	Z_w	M_w	X_q	Z_q	M_q	X_η	Z_η	M_η
0.15	-4.9	-0.13	1.1	0.33	-0.42	-0.32	-1.25	1.26
0.14	-4.84	-0.13	0.64	0.33	-0.42	-0.19	-1.25	1.26
0.13	-4.82	-0.13	0.42	0.33	-0.42	-0.12	-1.25	1.26

TABLE 12.2 ESTIMATED LONGITUDINAL STABILITY DERIVATIVES IN AERONORMALISED FORM

MACH NO.	α^o	η^o_{trim}	C_L	C_D	C_M	X_u	Z_u	m_u
0.06	9.42	4.12	1.19	0.16	0.0	-0.23	-0.95	0.0
0.08	4.46	3.60	0.68	0.08	0.0	-0.14	-0.72	0.0
0.1	2.13	3.35	0.44	0.05	0.0	-0.11	-0.57	0.0

x_w	z_w	m_w	x_q	z_q	m_q	x_η	z_η	m_η
0.06	-1.94	-0.21	0.08	0.1	-0.69	-2.61	-10.11	40.9
0.07	-2.55	-0.28	0.06	0.13	-0.85	-2.67	-17.97	72.7
0.09	-3.17	-0.35	0.05	0.16	-1.06	-2.73	-28.01	113.6

TABLE 12.3 ESTIMATED LONGITUDINAL STABILITY DERIVATIVES IN CONCISE FORM

TUNNEL SPEED	$(\frac{dC_n}{d\zeta})_{\psi=0^o}(rad^{-1})$		$(\frac{dC_n}{d\zeta})_{\psi=10^o}(rad^{-1})$		$(\frac{dC_n}{d\zeta})_{\psi=15^o}(rad^{-1})$		$(\frac{dC_\ell}{d\xi})_{\psi=0^o}(rad^{-1})$	$(\frac{dC_n}{d\beta})_{\alpha=0}(rad^{-1})$	
(m/s)	$\alpha = 0^o$	$\alpha = 20^o$	$\alpha = 0^o$	$\alpha = 20^o$	$\alpha = 0^o$	$\alpha = 20^o$	$\alpha = 0^o$	WIND TUNNEL	THEORY
19.0	0.401	0.401	0.415	0.0	0.329	0.0	-	0.47	0.32
25.0	-	-	-	-	-	-	0.448	-	

TABLE 12.4

AERODYNAMIC PARAMETERS CORRESPONDING TO FLIGHT-ATTITUDE CONDITIONS OF TABLE-H3
BASED ON THE WING AREA

* It must be noted that the values of $\frac{dC_n}{d\zeta}$ and $\frac{dC_\ell}{d\xi}$ are average values due to non-linearity.

		ESTIMATED LONGITUDINAL STABILITY DERIVATIVES											
		CONCISE FORM						AERONORMALISED FORM					
	METHOD	z_w	m_w	z_q	m_q	z_η	m_η	$\check{Z}_w$	$\check{M}_w$	$\check{Z}_q$	$\check{M}_q$	$\check{Z}_\eta$	$\check{M}_\eta$
C.G. AT 0.444 m FROM DATUM U = 28 m/s M = 0.08	E.K.F ESTIMATES	-4.5	7.0	-31.0	-1.4	-92.0	108.0	.8.0	3.3	-328.2	-4.0	-6.1	1.9
	STATIC TEST DATA	-2.21	3.1	-	-1.96	-99.0	96.0	-3.93	1.48	-	-5.56	-6.52	1.69
	OPTIMISATION PROGRAM	-2.54	-0.28	0.13	-0.85	-17.98	72.7	-4.84	-0.13	0.33	-0.42	-1.25	1.26

TABLE 12.5 ESTIMATED LONGITUDINAL DERIVATIVES

	LATERAL STABILITY DERIVATIVES	E.K.F. ESTIMATES	THEORY	E.K.F. ESTIMATES	THEORY
CONCISE FORM	ℓ_v	2.0	-1.21	0.7	-0.1
	ℓ_p	-12.0	-8.8	-8.0	-7.9
	ℓ_r	-2.0	-	-3.2	-
	n_v	2.0	2.48	2.2	2.23
	n_p	26.0	-	-2.0	-
	n_r	-9.0	-	-8.0	-
	ℓ_ζ	118.0	-	100.0	-
	n_ζ	222.0	-	380.0	-
AERONORMALISED FORM	$\breve{L}_v$	0.08	-0.06	0.03	0.00
	$\breve{L}_p$	-1.15	-1.14	-1.03	-1.02
	$\breve{L}_r$	-0.26	-	-0.41	-
	$\breve{N}_v$	0.49	0.61	0.54	0.55
	$\breve{N}_p$	19.83	-	-1.53	-
	$\breve{N}_r$	-6.86	-	-6.1	-
	$\breve{L}_\zeta$	0.16	-	0.15	-
	$\breve{N}_\zeta$	1.83	-	3.49	-
		U ≈ 30 m/s		U ≈ 27 m/s	
		C.G. AT 0.444 m FROM DATUM		C.G. AT 0.44 m FROM DATUM	
		ζ POSITIVE TO STARBOARD			

TABLE 12.6 ESTIMATED LATERAL DERIVATIVES

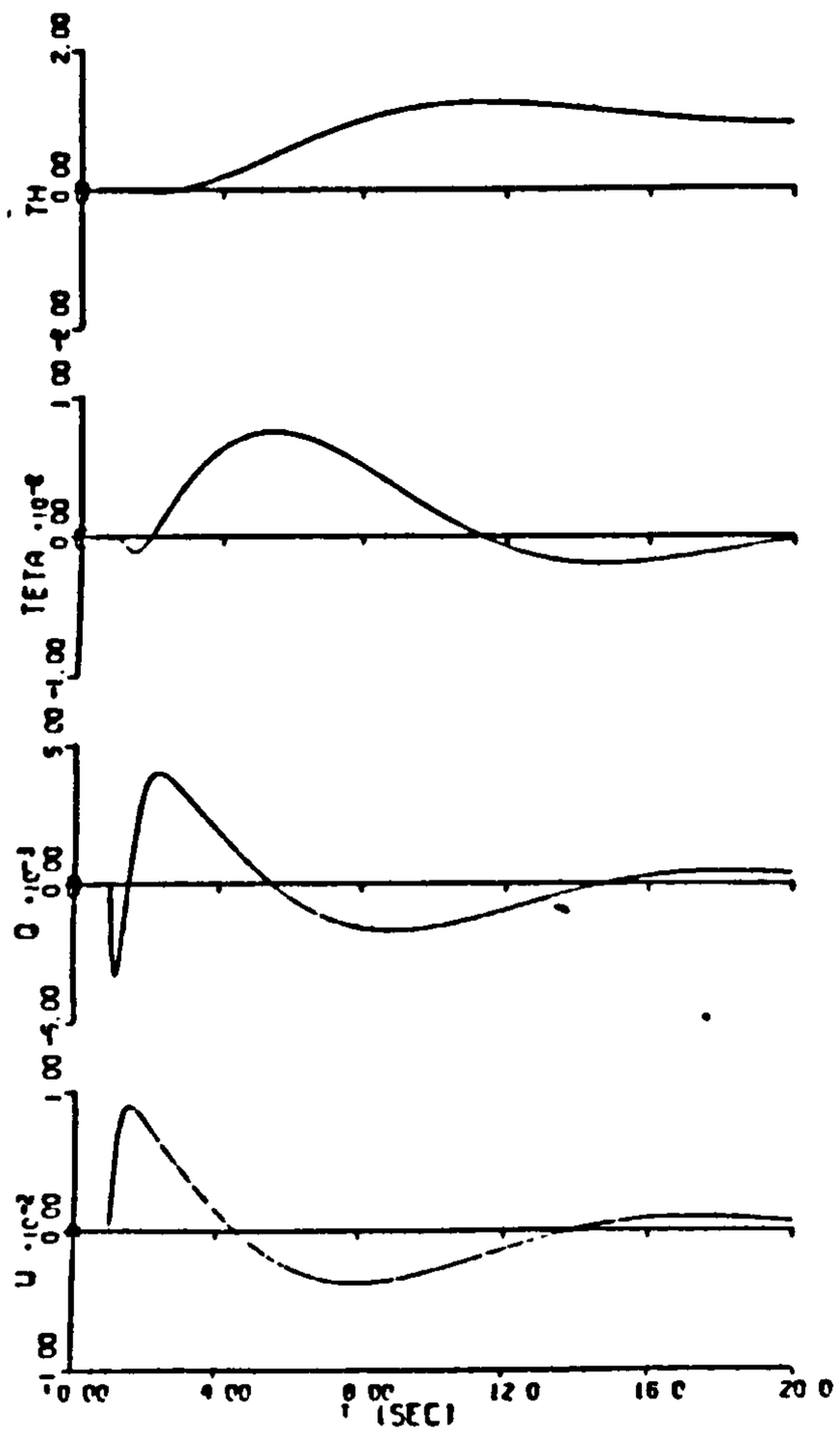

$C_F = 1$

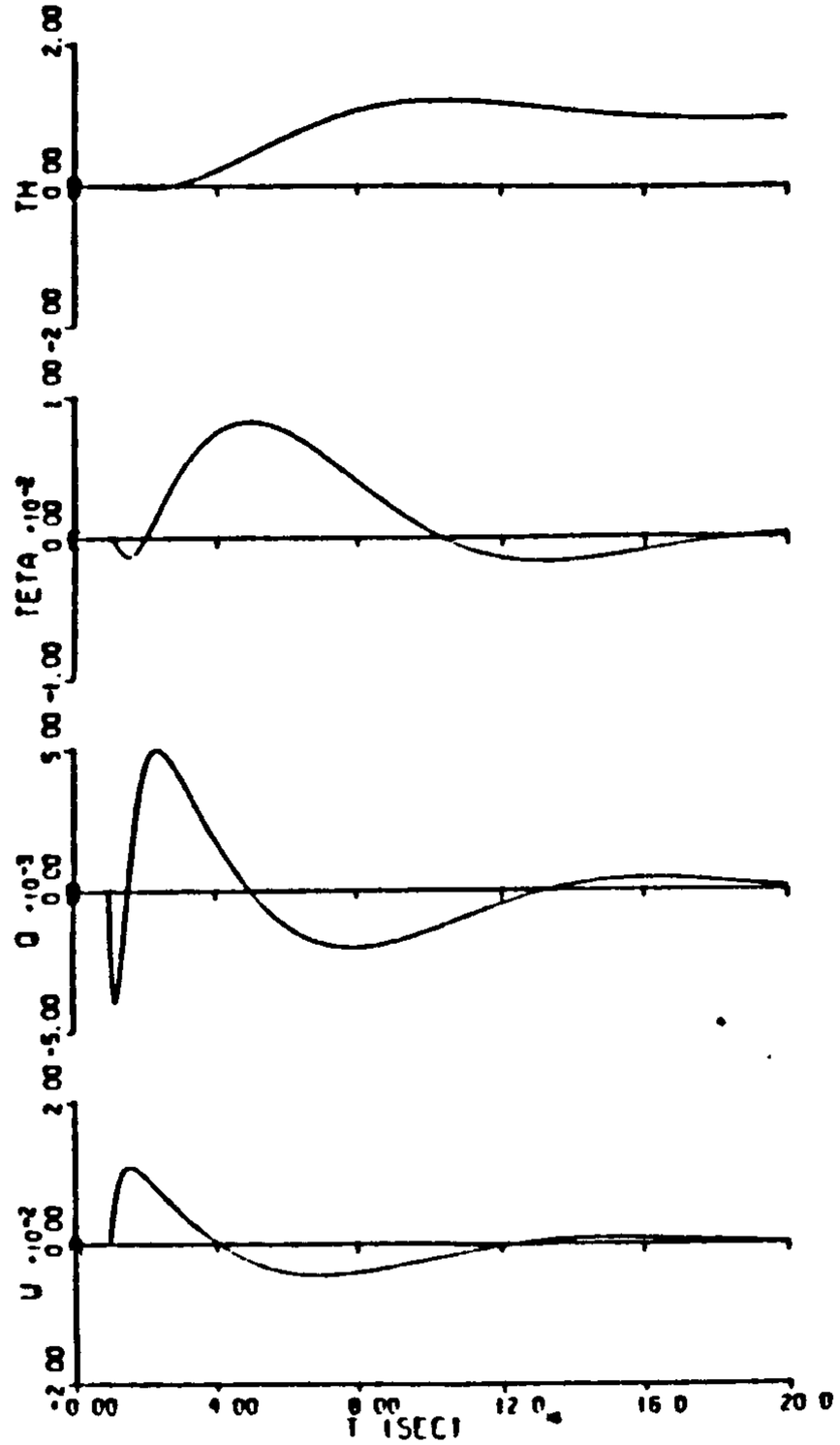

$C_F = 1.2$

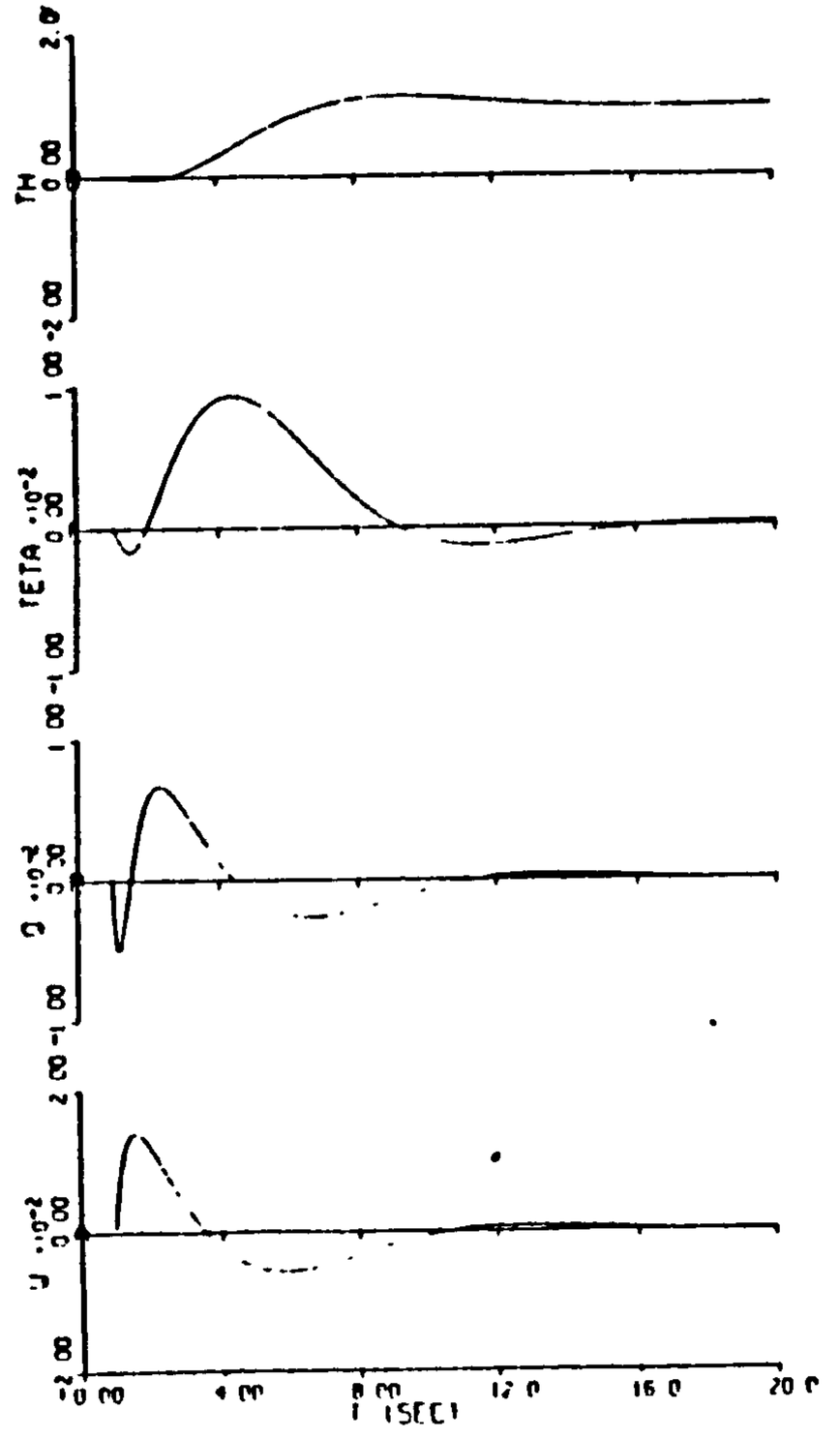

$C_F = 1.5$

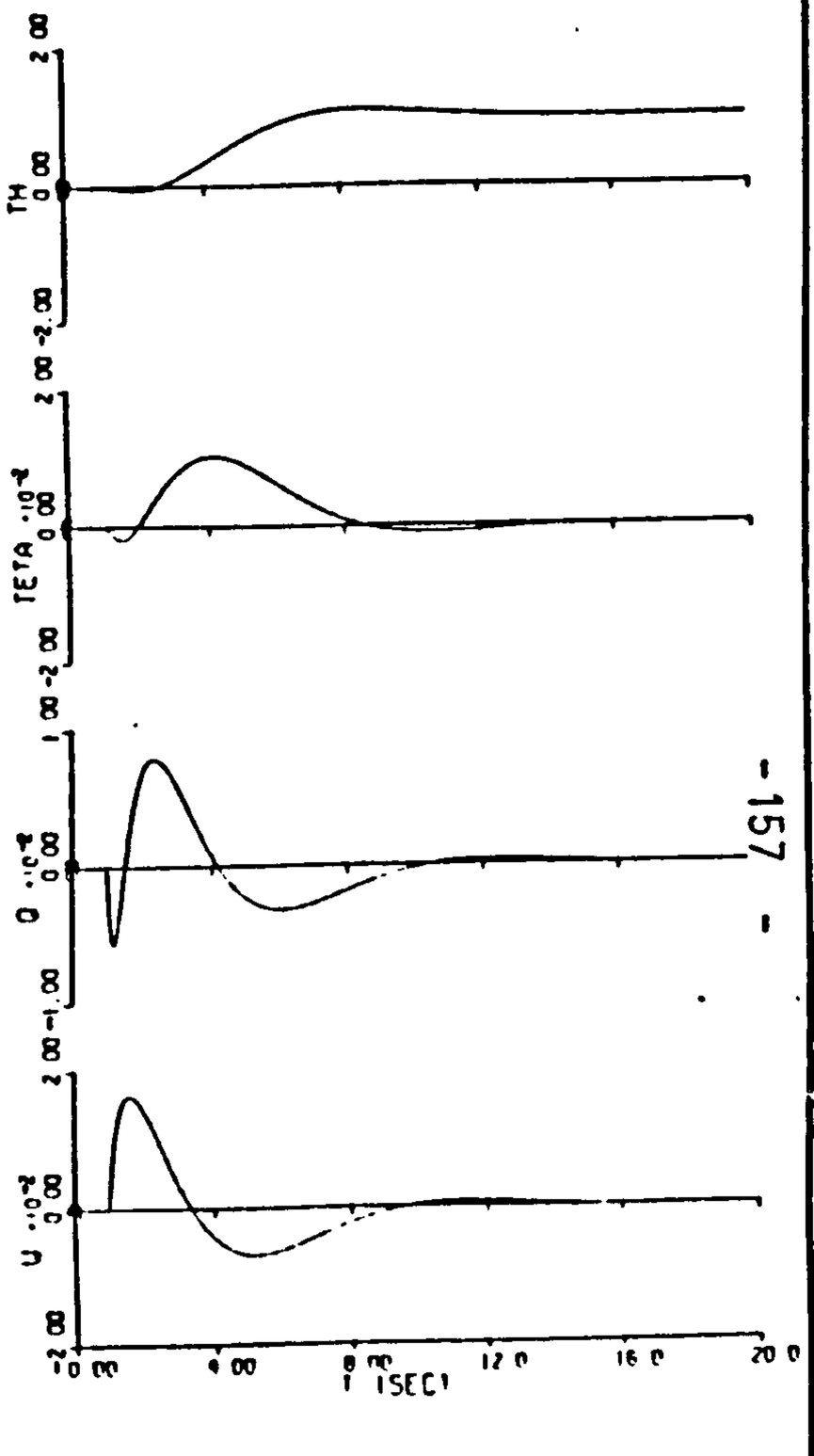

$C_F = 1.7$

FIGURE 12.25

SIMULATION OF EQUATIONS

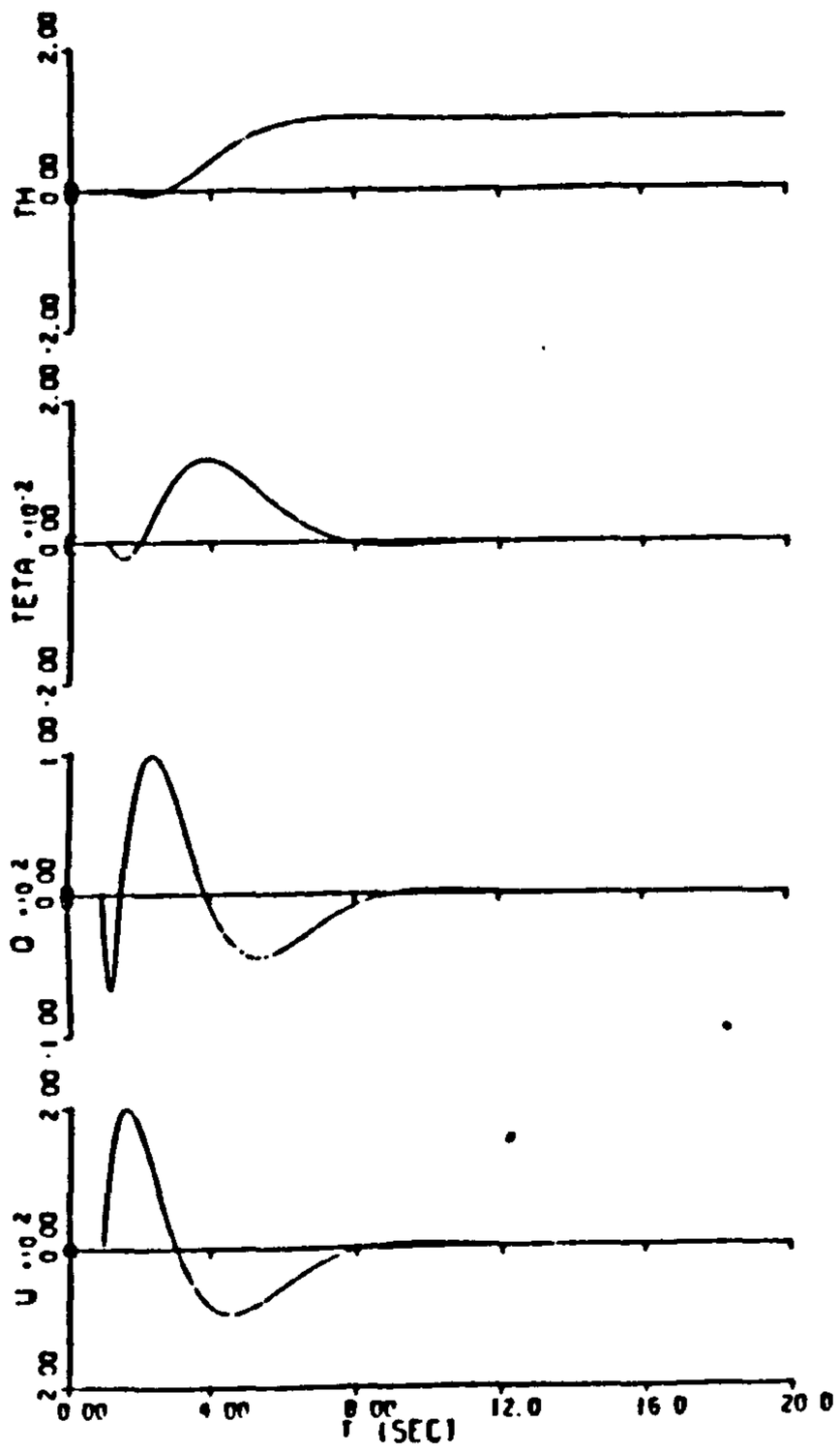

$C_F = 2.0$

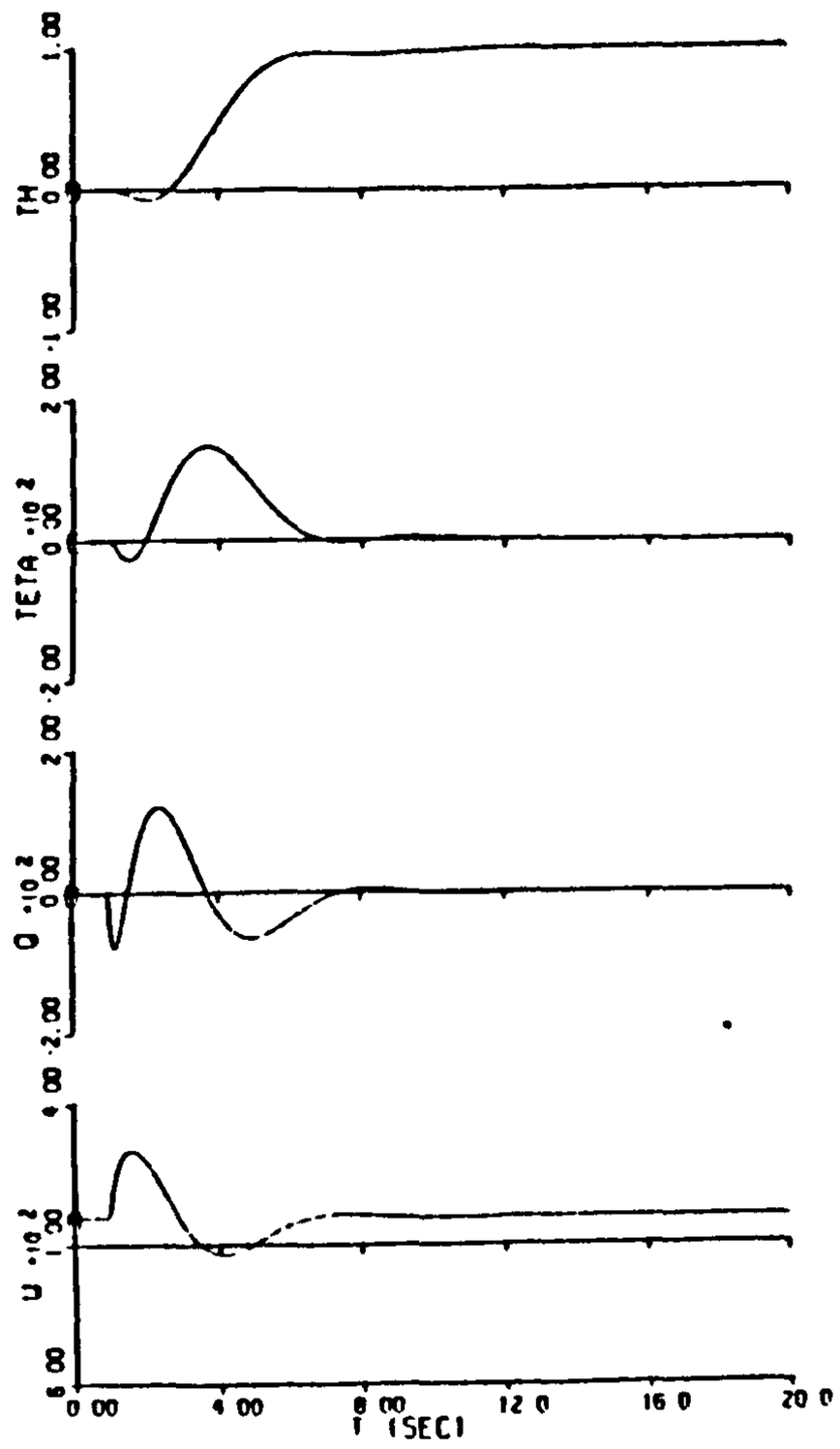

$C_F = 2.3$

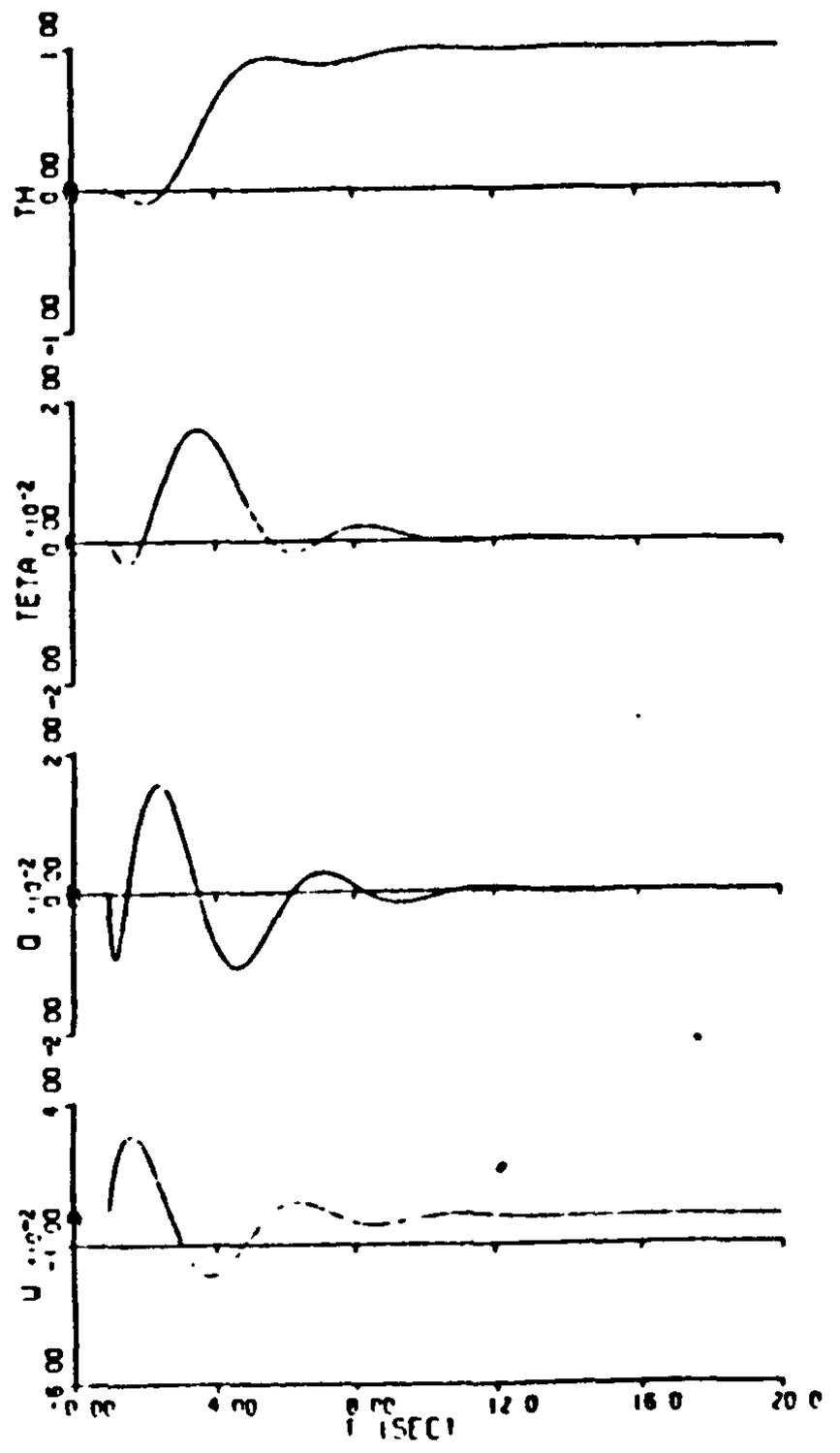

$C_F = 2.7$

FIGURE 12.26

SIMULATION OF EQUATIONS

13. COMMENTS AND CONCLUSIONS

13.1 Comments on the Test Rig

In carrying out the dynamic wind tunnel experiments, use was made of the test rig facilities described in ref. 8. However modifications to the test rig were needed in order to make it suitable for the present work. These modifications are explained below and other than these there were no major departures from the original test rig.

13.1.1 Gimbal System

There were no major design changes to the gimbal system described in ref. 8 other than a change of size and improved bearings. Due to the lateral movement of the model and the lack of suitable restraints, problems were experienced with the original design. That is to say, that because of un-constrained lateral movements the wiper on the pitch attitude potentiometer frequently came off the track and hence disrupted the output signal. This problem has been overcome in the present design. Also repeated use of the gimbal system resulted in some backlash between the relative motion of the linear bearing of the gimbal system and the vertical rod. Under normal flight conditions the latter shortcoming could be tolerated. However, the use of a yaw auto-stabilisation system required the monitoring of the yaw-attitude signal obtained from yaw-attitude potentiometer, the shaft of which is fixed to the vertical rod. Any backlash in this link would have a direct effect on the stability of the control system and its performance. Therefore, further developments were needed to improve this. Also the cables supporting the vertical rod tended to slacken off with use, as a result of tunnel resonance, resulting in vertical mis-alignment of the support rod. This could lead to asymmetrical friction force along the rod.

13.1.2 Installation of a Height Transducer

Studies of the mathematical model of the short period motion of the dynamic model showed that heave velocity measurement is essential to a proper analysis of the motion. Therefore, some simple means of obtaining this information had to be devised. Full details of the subsequent design are given in section 7.1. Despite its simplicity, the performance of the height transducer was extremely satisfactory, the friction in the pulleys was assumed negligible.

13.1.3 Power Supply Modifications

Due to the characteristics of the servoactuators fitted to the F.S.W. dynamic model, there was a need to change the voltages of the power supplies to the model control equipment. Details of the functions of the various power supplies can be found in ref. 8. As a result of these changes, the electronic control unit and model reference input and output signals were recalibrated.

13.2 Comments on the Model Construction and Peformance

Mainly because of the modular construction of the dynamic model internal access was extremely straightforward, even with the model mounted on the test rig. Three servo-actuators, the specifications of which are listed in Appendix D were used to actuate the control surfaces. In order to minimise control system back-lash, miniature bearings were used for the foreplane and aileron actuation mechanism. The foreplane mechanism was, however, spring-loaded to suppress any residual backlash in the sytem. Details of these mechanisms are given in Appendix D. Despite its low weight, the F.S.W. model aircraft was found to possess a very high strength to weight ratio, mainly because of the composite structure shown in Fig. 13.1. No noticeable vibrations or twist of the model were observed, even at speeds well beyond the experimental range. After initial installation of the servo-actuators they were energised via two voltage regulators which were placed in the model and designed specifically for this purpose. It was then found that, due to mutual electrical interference, the servos were interacting with each other. This problem was found to be due to an earthing fault and was therefore remedied completely.

As far as the model structure was concerned, it was found that despite the complexities of the modular design, the model possessed an accurate structural geometry , as confirmed by the static wind tunnel measurements.

13.3 Conclusions

The conclusions of the present research program covering the various aspect of the work presented in the preceding sections are listed below.

(i) The first order design optimisation code based on linearised theories predicted the position of the neutral point reasonably well and minimises the induced drag due to wing and foreplane mutual interference. This optimization was limited to the vertical gap between wing and foreplane.

(ii) Estimates of the longtudinal stability derivatives obtained with the first order design optimisastion code to not represent the dynamic characteristics of the F.S.W. model accurately.

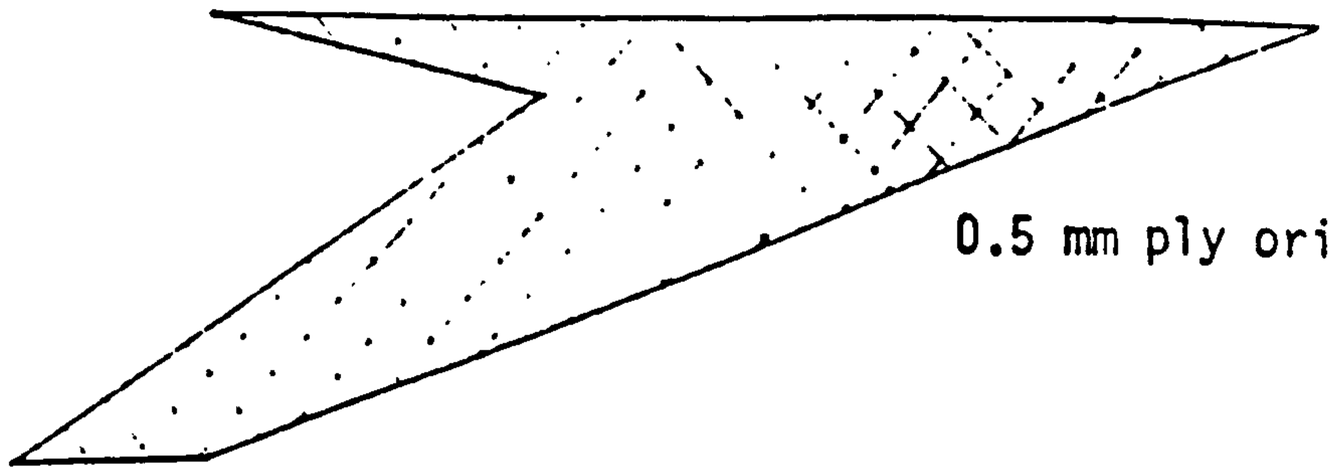

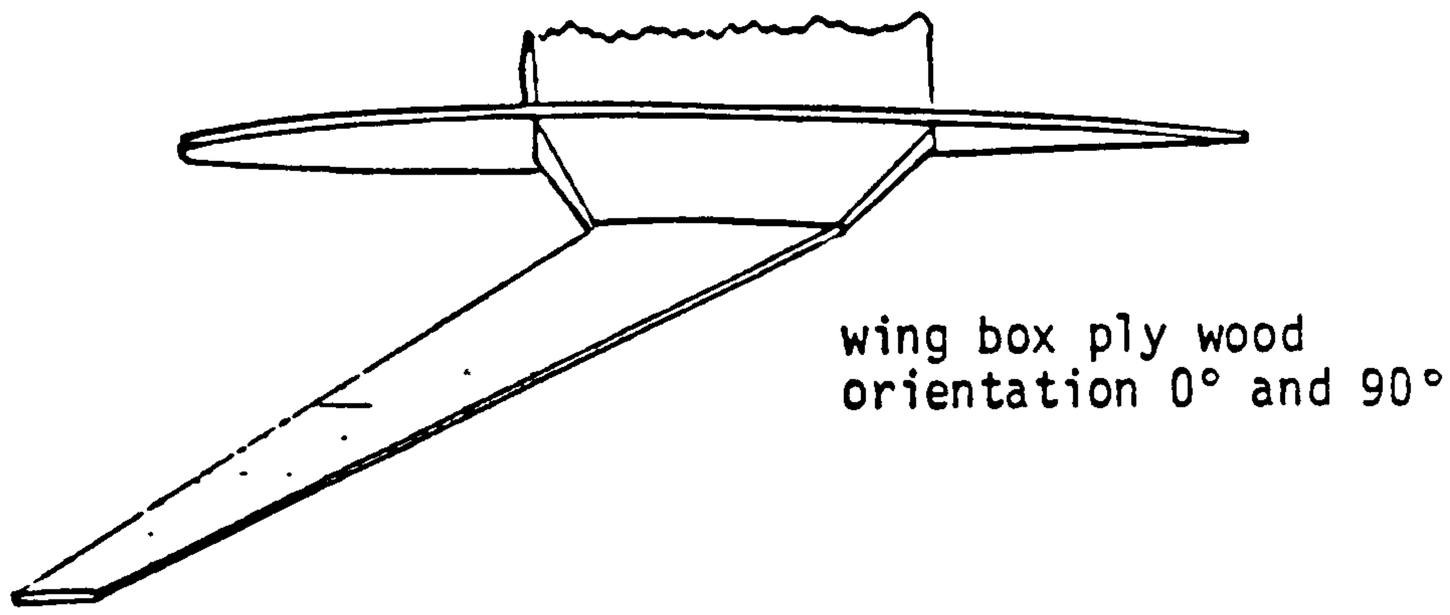

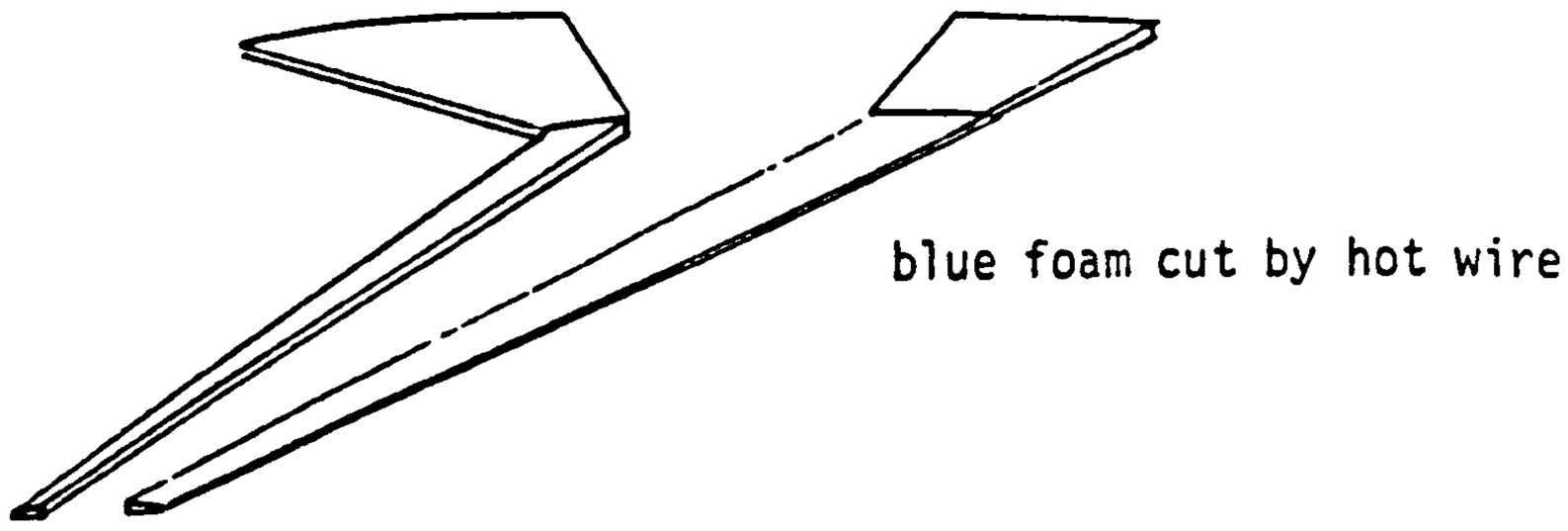

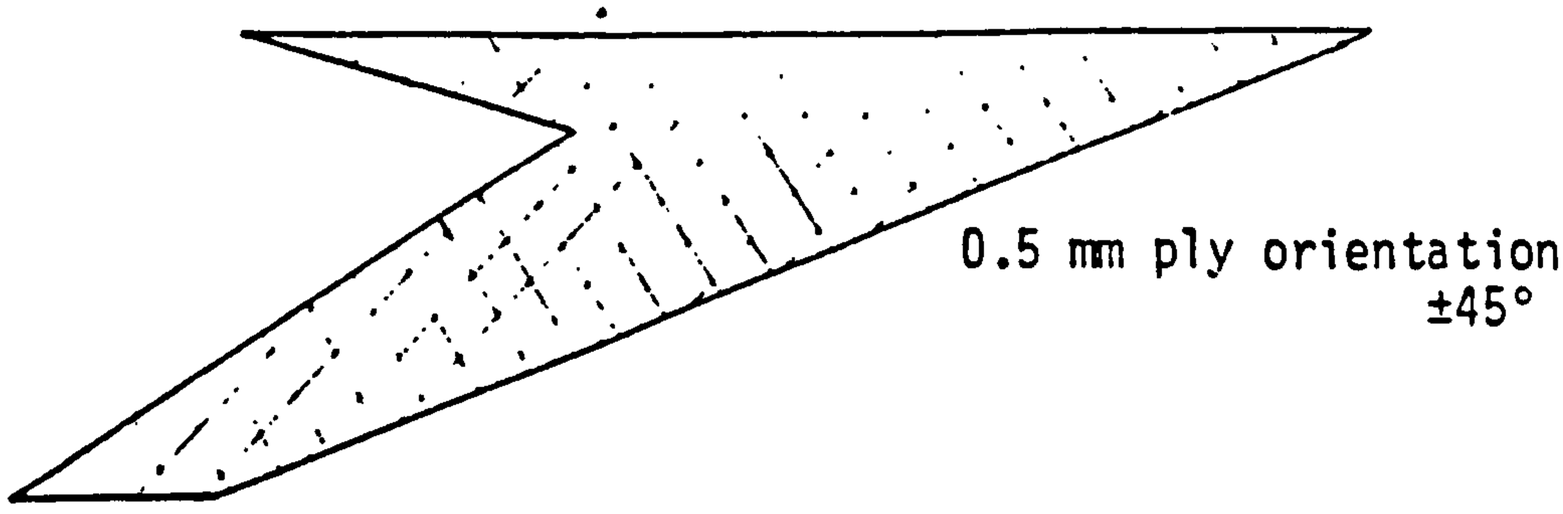

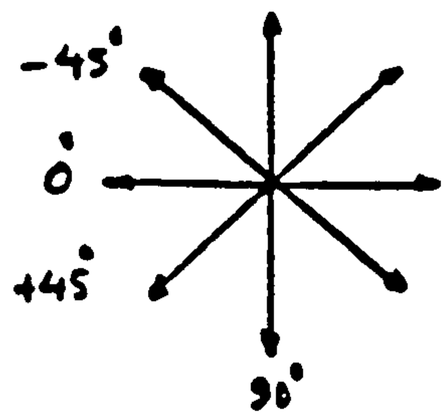

FIGUPE 13.1 F.S.W. STRUCTURE

iii) The predictions of stability derivatives made by the first order design optimisation code can be much improved in accuracy if more representative aerodynamic data, such as wing lift curve slope, etc., are available from experimental measurements.

(iv) Computer based experiments regarding flight simulation and its analysis through the developed Extended Kalman Filter parameter identification software, provided an effective means of gaining insight into the behaviour of the filter code as applied to this particular system. This information proved invaluable when analysing observed motion of the model in the wind tunnel. However, parameter estimation was almost perfect since the flight simulation and Kalman filter are based on the same mathematical model, a fact which cannot be fully justified when the mathematical model of the Kalman filter is assumed to represent the physical dynamic behaviour of the model.

(v) The 1/14 th scale dynamic model constructed on a modular basis offers much easier access to model components than a solid construction.

(vi) By using composite materials the need, especially for a solid F.S.W. construction is eliminated and the moments of inertia of the model can readily be adjusted by placement of lumped masses at the appropriate radii of gyration.

(vii) In order to trim the model at high tunnel speeds the backlash in the actuation mechanisms must be minimised so as to achieve the precise trimming required. Use of miniature bearings proved to be an effective way of eliminating some of the problems.

(viii) The performance of the test rig described in ref. 8 with the new gimbal design provided a satisfactory performance in the intended four degrees of freedom.

(ix) The electronic control unit described in ref. 8 provides effective control of the F.S.W. dynamic model although the model reference attitude outputs needed further amplification and noise filtering before they could be digitized.

(x) At the lower range of flying speeds, the friction force in the heave motion due to the gimbal linear bearing, influenced the heave motion by introducing additional damping and stiction.

(xi) The model was found to have exceptionally good flying qualities although it was critically stable from the static stability point of view, which can be attributed to the pitching moment characteristics of the model.

(xii) Auto-stabilisation in roll and yaw was achieved in a relatively simple way. However, the height holding control system design could not be optimised due to stiction in heave motion on the test rig.

(xviii) Independent roll and yaw auto-stabilisation control systems were effective for small perturbations only and for larger deviations from the trimmed flight conditions, more sophisticated control laws would have to be devised in order to cope with coupling between roll and yaw motions.

(xix) It was established that the flight control system was capable of providing auto-stabilisation for relatively large negative static margins also.

(xx) The parameter identification code was effectively applied to the dynamic wind tunnel tests and provided estimates of both longitudinal and lateral derivatives which upon substitutitution in the mathematical model of the motion and its subsequent simulation,resulted in a similar behaviour to the observed responses.

REFERENCES

1. Nicolai, M. — Fundamentals of aircraft design. 1975.

2. Poll, D.I.A. and Cheng-Hao Qiu — A comparison of the aerodynamic characteristics of swept forward and swept back wings including the effect of strakes. International Conference Proceedings on Forward Swept Wing Aircraft. University of Bristol, March 1982.

3. Kroo, I.M. — Minimum induced drag of canard configurations. Stanford University, Stanford, California AIAA Engineering Notes.

4. Perkins, C.D. and Hage, R.E. — Airplane performance stability and control. John Wiley and Sons, 1949.

5. Newton, Gould, Kaiser — Analytical design of linear feedback controls. Chapman and Hall Ltd., 1957.

6. Prandtl, L. — Induced drag of multiplanes. NACA TN-182, March 1924

7. Munk, M. — Minimum induced drag of aerofoils. NACA Report 121, 1921

8. Malik, I.A. — The design and evaluation of an active control aircraft model wind tunnel facility. Ph.D. Thesis. Department of Aerodynamics, Cranfield Institute of Technology, September 1982.

9. Cook, M.V. and O'Riordan, S.J.P. — A technique for optimising the aerodynamic design of a generalised combat aircraft with forward swept wings for the purposes of stability and control investigation. College of Aeronautics Report 8325, Cranfield Institute of Technology, Cranfield, January 1984.

10. Bierman, G.J. — Factorization methods for discrete sequential estimation. Mathematics in Science and Engineering. Vol. 128. Academic Press, California Institute of Technology, California, 1977.

11. Maybeck, P.S. — Mathematics in Science and Engineering. Vol. 141, Academic Press, 1979.

12. Pankhurst, R.C. and Holder, D.W. — Wind Tunnel Techniques. Sir Issac Pitman and Sons Ltd., 1954

13. The Open University Course Units — Second level technology courses T291 and T391 in instrumentation and control engineering. The Open University Press, 1981.

14. Cebeci, T. and Smith, A.M. — Analysis of turbulent boundary layer. Academic Press, 1974.

15. Jenkinson, L.R. and Simos, D. — A computer program for assisting in the preliminary design of twin-engined propellor-drifen general aviation aircraft. Loughborough University, September 1984.

16. Stannizand, D.R. — The effect of deflecting flaps on strike/ fighter aircraft wing design. Aeronautical Journal, December 1974.

17. Manitius, A.Z. — Feedback controllers for a wind tunnel model involving a dealy: Analytical and numerical simulation. IEEE, Transactions on Automatic Control, Vol. AC-29, No. 12, December 1984.

18. Grafton, S.B., Gilbert, W.D., Croon, M.A. and Murri, D.G. — High angle of attack characteristics of a forward swept wing fighter configuration. NASA Technical Memorandum 81863, November 1960.

19. Doggett, R.V. Jr. and Ricketts, R.H. — Dynamic response of a forward swept wing model at angles of attack up to 15° at a Mach number of 0.8. NASA Technical Memorandum R55563. November 1980.

20. Anderson, D. — X-29 forward swept wing flight control system. AIAA/IEEE Fifth Digital Avionics Systems Conference, November 1983.

21. Frei, D.R. — X-29 forward swept wing demonstrator airplane. NASA Report 820600, Langley Research Center, 1981.

22. Moore, M. and Frei, D. — X-29 forward swept wing aerodynamic review. AIAA Paper 83-1834, presented at the AIAA applied aerodynamic conference, Danvers, Massachusetts, July 1963.

23. Lovell, D.A. — Some experiences with numerical optimisation in aircraft specification and preliminary design studies. Technical Memorandum, Aero 185, RAE, May 1980.

24. Spacht, G. — The forward swept wing: A unique design challenge. AIAA Paper 80-1885 presented at AIAA Aircraft Systems Meeting, Anaheim, California, August 1980.

25. Kukemann, D. — The aerodynamic design of aircraft. Pergamon Press, 1978.

26. Krone, N.J. — Divergence eliminated with advanced composites. AIAA Paper 75-1009. AIAA Aircraft Systems and Technology Meeting, Los Angeles, August 1975.

27. Deyoung, J. and Harper, c.W. — Theoretical symmetric span loading at subsonic speeds for wings having arbitrary planform. NACA Report 921, 1948.

28. McCormack, G.M. and Cook, W.L. — A study of stall phenomena on a 45° swept forward wing. NACA TN 1797, 1949.

29. Hopkins, E.J. — Lift, pitching moment and span load characteristics of wings at low speeds as affected by variations of sweep and aspect ratio. NACA TN 2284, 1950.

30. Bozk, S.M. — Digital and Kalman filtering. Edward Arnold Publishers Ltd., 1979.

31. Sorenson, H.W. — Least squares estimation from Gauss to Kalman. IEEE Spectrum, 7, 63-8, July 1970.

32. Sorenson, H.W. — Kalman filtering techniques, advances in control systems. Academic Press, 1966.

33. Scovell, G. — A guided tour through the implementation of a Kalman filter. University of Birmingham (England), Bosworth Course, April 1977.

34. McCormack, G.M. and Cook, W.L. — Effects of boundary layer control on a 45° forward swept wing-fuselage combination. NACA RM A9K02a, 1950.

35. Gunston, B. — The encyclopaedia of the world's combat aircraft. Salamander Books Ltd, 1976.

36. Miele, A. — Theory of optimum aerodynamic shapes. Academic Press, 1965.

37. Hertz, T.J. — On the track of practical forward swept wings. Astronautics and Aeronautics Journal. January 1982.

38. Butler, G.F. — Effect of downwash on the induced drag of canard-wing combinations. AIAA 82-4111, May 1982.

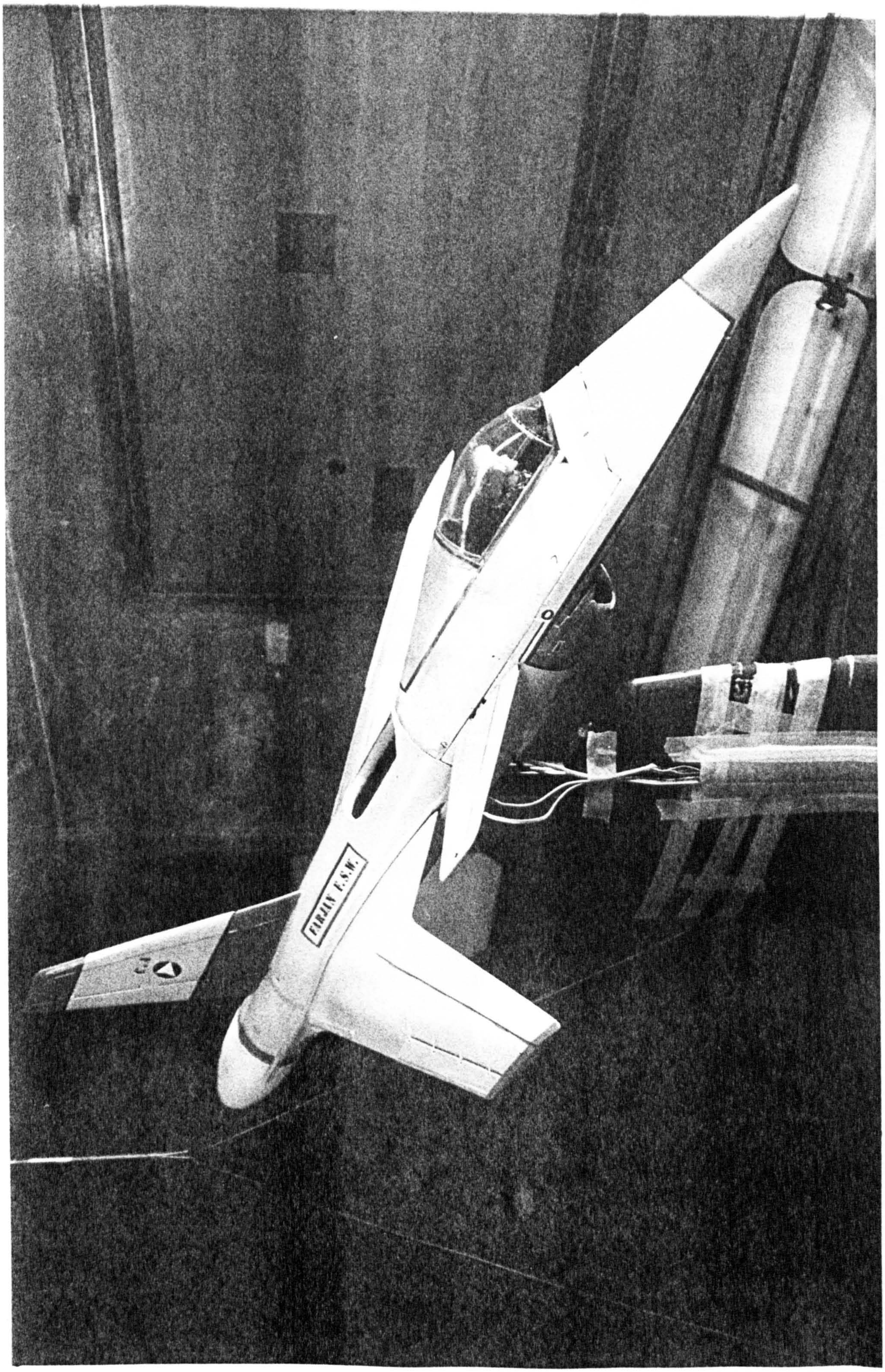

Plate-2 :- DYNAMIC MODEL UNDERGOING STATIC TESTS IN THE 8'x6' WIND TUNNEL

Plate-3:- PARTIAL VIEW OF THE DYNAMIC TEST RIG AND THE INTERIOR OF THE F S W MODEL.

NOTE: Throughout the Appendices the foreplane has been referred to as Canard,

APPENDIX A: Initial Geometric Data of the Full-Scale F.S.W. Aircraft.

Forward Swept Wing Parameters		
¼ chord sweep angle	$\Lambda_{\frac{1}{4}c_w}$	$= -45^o$
taper ratio	λ_w	$= 0.4$
aspect ratio	AR_w	$= 4.0$
wing area	S_w	$= 20.0\ m^2$
Canard Parameters		
leading edge sweep angle	$\Lambda_{L.E._c}$	$= 45^o$
aspect ratio	AR_c	$= 3.0$
canard area	S_c	$= 25\%$ x wing area
taper ratio	λ_c	$= 0.5$
Fin Parameters		
leading edge sweep angle		$= 45^o$
aspect ratio	AR	$= 1.6$
fin + rudder area	S_F	$= 28\%$ x wing area
taper ratio	λ_F	$= 0.43$

TABLE A1 INITIAL DATA

Determination of the Mean Aerodynamic Chords

The aerodynamic chord in terms of taper ratio and root chord is given by;

$$\bar{c} = \frac{2}{3} c_{root} \left(\frac{1 + \lambda + \lambda^2}{1 + \lambda}\right)$$

Based on this expression,

$$\bar{c}_{wing} = 2.35\ m$$
$$\bar{c}_{canard} = 1.34\ m$$
$$\bar{c}_{fin+rudder} = 1.12\ m$$

Aerodynamic Centre Positions

The position of this point is given by;

$$\bar{X} = \frac{2}{S} \int_0^{b/2} c(y).x(y).dy$$

which could be represented by the following numerical approximation,

$$\bar{X} \simeq \frac{2}{S} \sum_{o}^{n} c_n X_n \Delta y$$

with $n = 9$

$\bar{X}_{wing} = 4.75$ m

$\bar{X}_{canard} = 8.0$ m

$\bar{X}_{fin+rudder} = 1.82$ m

where $\bar{X}$ is measured from the plane of the nozzle.

APPENDIX B

B.1 Mass Breakdown and Aerodynamic Data Evaluation.

Generic equations of reference 1 were used to estimate masses of the aircraft components with the following coding.

MW	=	mass of the wing
MC	=	mass of the canard
MFR	=	mass of the fin + rudder
MF1 & MF2	=	masses of front and rear fuselage sections
MUC	=	mass of the U/C
ME	=	mass of the engine F100-pw-100
MINTS	=	mass of the intake and support structure
MIND	=	mass of the internal duct
MFC	=	mass of the fuel cells
MFSS	=	mass of the fuel support structure
MDD	=	mass of dump and drain
MAHP	=	mass of the actuators, hydraulic and pneumatics
MEC	=	mass of engine controls
MFIN	=	mass of flight instruments
MEIN	=	mass of engine instruments
MELEC	=	mass of electrics
MMIN	=	mass of miscellaneous indicators
MPIL	=	mass of the pilot
MEJS	=	mass of ejection seat
MACON	=	mass of airconditioning equipment
MEMER	=	mass of emergency equipment
MGUN	=	mass of gun
MAVIN	=	mass of avionics
MSW	=	mass of sidewinder missiles
MAMRAM	=	mass of AMRAM
MCGC	=	mass of c.g. controls
TFF	=	total fuselage fuel
TWF	=	total wing fuel
MRADAR	=	mass of radar

Table B1, lists these components together with their respective distances from x, y and z axes.

COMPONENT	$\bar{X}$ (m)	$\bar{Y}$ (m)	$\bar{Z}$ (m)	MASS OF THE COMPONENT (kg)
MW	1.23^{-}	1.83	0	988.0
MC	2.3	0	0.2	98,4
MFR	4.39^{-}	0	1.77^{-}	162.1
MF1	2.44^{-}	0	0	1049.4
MF2	4.56	0	0	1399.2
0.25 MUC	2.06	0	0.62	89.9
0.75 MUC	0.94^{-}	$1.75^{\pm}$	0.62	260.8
ME	2.62^{-}	0	0	1450.2
MINTS	1.21	0	0.2	62.1
MIND	1.21	0	0.2	117.1
(MFC+MFSS)	1.23^{-}	0	0.5^{-}	73.2
MDD	2.44^{-}	0	0.5^{-}	8.8
(MAHP+MEC)	1.23^{-}	0	0.5^{-}	366.2
(MFIN+MEIN)	5.21	0	0.29^{-}	9.3
MELEC	3.82	0	0.1	157.8
MMIN	5.21	0	0.3^{-}	1.4
(MPIL+MEJS)	4.56	0	0.3^{-}	236.7
MACON	3.06	0	0.4^{-}	69.0
MEMER	4.36	0	0.3^{-}	18.8
MGUN	2.81	0.55	0	238.0
MAVIV	5.21	0	0.3^{-}	133.4
MSW	2.11	$4.65^{\pm}$	0	214.0
MAMRAAM	0.46	$0.6^{\pm}$	0.6	300.0
MCGC	1.23^{-}	0	0.5	13.3
TFF*3.637	0.26	0	0.55^{-}	185.1
69%TWF*3.637	0.47^{-}	$2.6^{\pm}$	0	804.8
31%TWF*3.637	1.89^{-}	$0.25^{\pm}$	0	361.6
MRADAR	6.36	0	0.2	84.8

TOTAL MASS ≈ 895.4 kg

TABLE B1

Component masses and their positions relative to the plane of the nozzle

PAGES

MISSING

IN

ORIGINAL

Finite Wing Linear Lift Curve Slope

This is given by:

$$\frac{dC_L}{d\alpha_{wing}} = \frac{2\pi AR}{2 + \sqrt{4 + AR^2\beta^2\left(1 + \frac{\tan^2\Lambda(\text{max.thickness line})}{\beta^2}\right)}} \qquad \text{Eq.B1.1}$$

where

$\Lambda_{\text{max.thickness line (wing)}} = -47^o$

$\Lambda_{\text{max.thickness line (canard)}} = 40^o$

$AR_{wing} = 4.0$

$AR_{canard} = 3.0$

The table below shows the variation of wing and canard lift curve slope variation with Mach number.

M	$\frac{dC_L}{d\alpha_{wing}}$ per rad	$\frac{dC_L}{d\alpha_{wing}}$ per deg	$\frac{dC_L}{d\eta_{canard}}$ per rad	$\frac{dC_L}{d\eta_{canard}}$ per deg
0.1	3.07	0.054	2.95	0.051
0.2	3.08	0.054	2.96	0.052
0.3	3.11	0.054	2.98	0.052
0.4	3.14	0.055	3.02	0.053
0.5	3.19	0.056	3.07	0.054
0.6	3.25	0.057	3.13	0.055
0.7	3.33	0.058	3.21	0.056
0.8	3.43	0.06	3.31	0.058
0.9	3.56	0.062	3.44	0.06

TABLE (B2)

NOTE: It can be assumed that the values of lift curve slopes M < 0.1 are the same as the ones for M = 0.1.

Equation (1) gives the theoretical value of the lift curve slope with the wing in isolation. However, the wing and canard lift curve slopes are affected by the presence of fuselage. Fig. 11.3 of Ref. 1 gives interference factors of 1.5 and 2.3 for wing-body and canard body combinations respectively. It must be pointed out that unlike the wing, canard is free to rotate relative to the fuselage. This gives rise to two lift curve slopes.

i) $(\frac{dC_L}{d\alpha})$, which is the contribution to total C_L by canard when $\eta = 0^o$

ii) $(\frac{dC_L}{d\eta})$, which is the contribution to total C_L by canard when $\alpha = 0$ and canard is rotated.

Table B3 gives the wing-body lift curve slopes.

TABLE B3

WING-BODY LIFT SLOPES		
M	$\frac{dC_L}{d\alpha}_{WB}$ Rad^{-1}	$\frac{dC_L}{d\alpha}_{WB}$ Deg^{-1}
≤0.1	3.86	0.064
0.2	3.70	0.064
0.3	3.73	0.065
0.4	3.77	0.065
0.5	3.83	0.066
0.6	3.91	0.068

Further, the values of canard lift curve slope are based on the wing area when the total lift coefficient is required. Therefore, canard lift slope is corrected for:

i) canard-body interference $(\frac{dC_L}{d\alpha})_{corrected} = (\frac{dC_L}{d\alpha})_{C.B.} \times 2.3$

ii) data correction $(\frac{dC_L}{d\alpha})_{corrected} = (\frac{dC_L}{d\alpha})_{C.B.} \times 0.56$

iii) reference area correction $\left(\frac{dC_L}{d\alpha}\right)_{C.B.} = \left(\frac{dC_L}{d\alpha}\right)_{C.B.} \times \frac{S_c}{S_w}$

TABLE B4

CANARD -BODY LIFT SLOPES			
M	$\left(\frac{dC_L}{d\alpha}\right)_{\substack{\eta=0 \\ canard}}$ (Rad^{-1})	$\left(\frac{dC_L}{d\alpha}\right)_{\substack{\eta=0 \\ canard}}$ (deg^{-1})	$\left(\frac{dC_L}{\eta}\right)_{canard}$ (Rad^{-1})
0.1	0.95	0.016	0.73
0.2	0.95	0.016	0.74
0.3	0.96	0.016	0.74
0.4	0.97	0.017	0.75
0.5	0.98	0.017	0.76
0.6	1.00	0.017	0.78

$$\left(\frac{d}{b}\right)_{canard} = \frac{1.5}{3.87} = 0.387$$

$$\left(\frac{d}{b}\right)_{wing} = \frac{1.5}{9.0} = 0.167$$

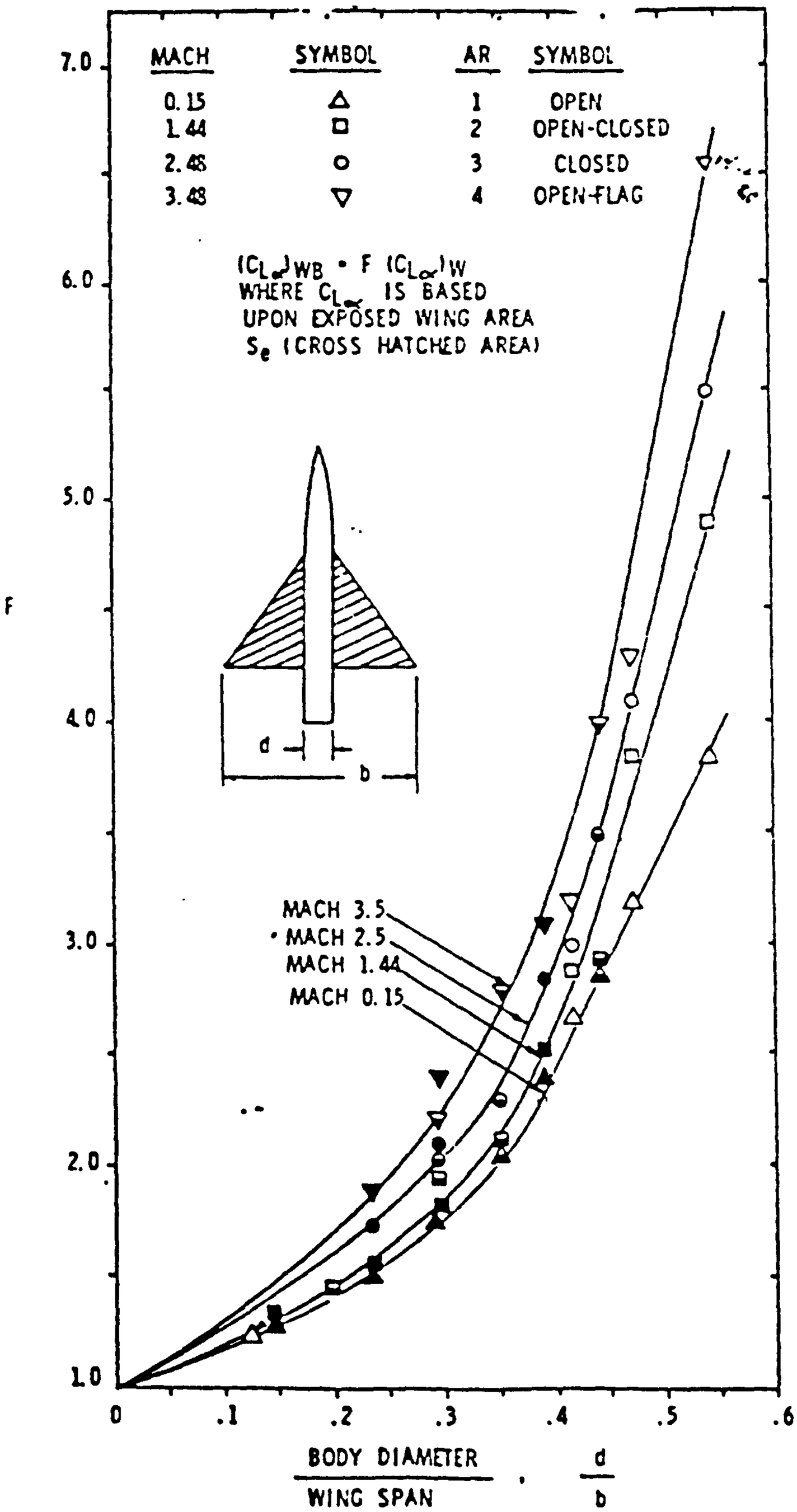

Fig. 11.3 Wing-Body Lift Interference Factor (Reference 10)

To find the position of the aerodynamic centre of the wing and canard, use was made of Fig.21.13 of Reference 1 with the following adoption.

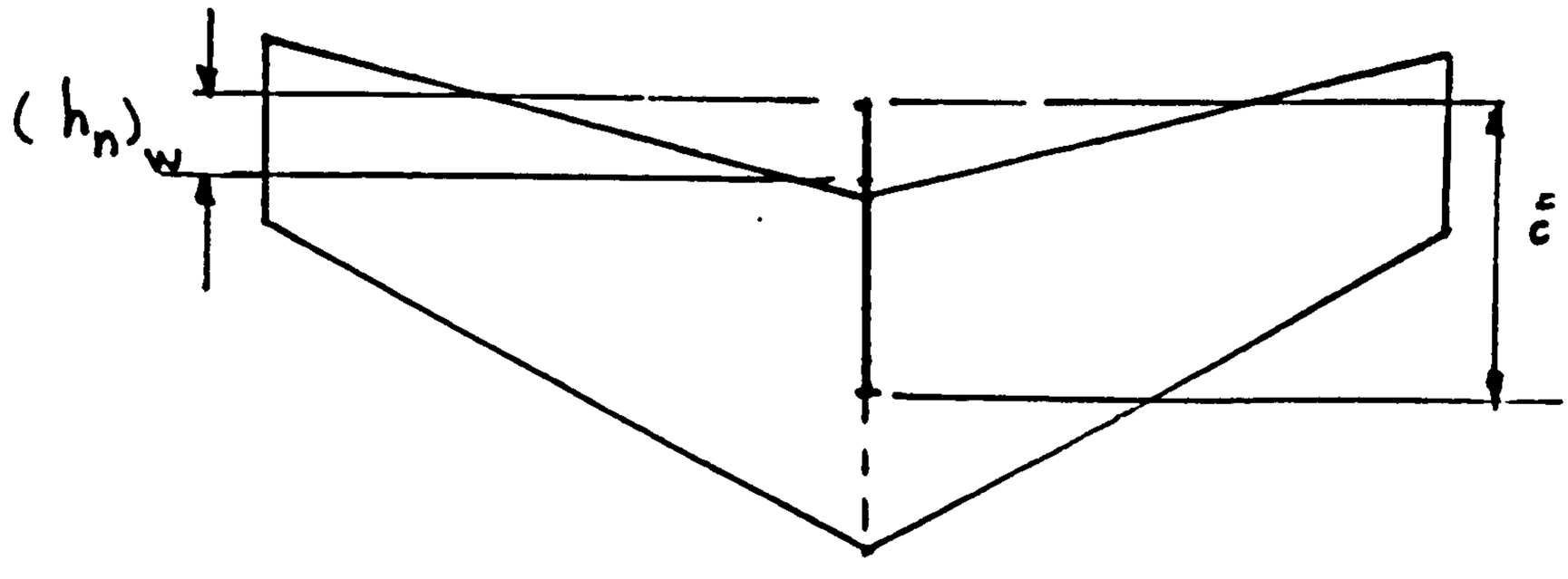

where $(h_n)_w$ is the theoretical position of the aerodynamic centre.

For the wing:

AR = 4.0

Taper ratio= 0.4

β = Prandtl-Glavert's correction factor = $\sqrt{|1- M_1^2|}$

$AR*\tan(\Lambda_{\frac{1}{2}})$ = 4.44 $\Lambda_{\frac{1}{2}}$ = ½ chordwise sweep angle = -48.0^o

$\bar{\bar{C}}_w$ = 2.35 m.

Table (B3) gives the variation of $(h_n)_w$ with Mach number.

For the canard:

AR = 3.0

$\Lambda_{\frac{1}{2}}$ = 33.0^o

Taper ratio= 0.5

$AR*\tan(\Lambda_{\frac{1}{2}})$ = 1.95

$\bar{C}_c$ = 1.34 m.

Table (B4) gives the variation of $(h_n)_c$ with Mach number.

$$AR_w.\tan(\Lambda_{\frac{1}{2}}) = 4.44$$

$$AR_c.\tan(\Lambda_{\frac{1}{2}}) = 1.95$$

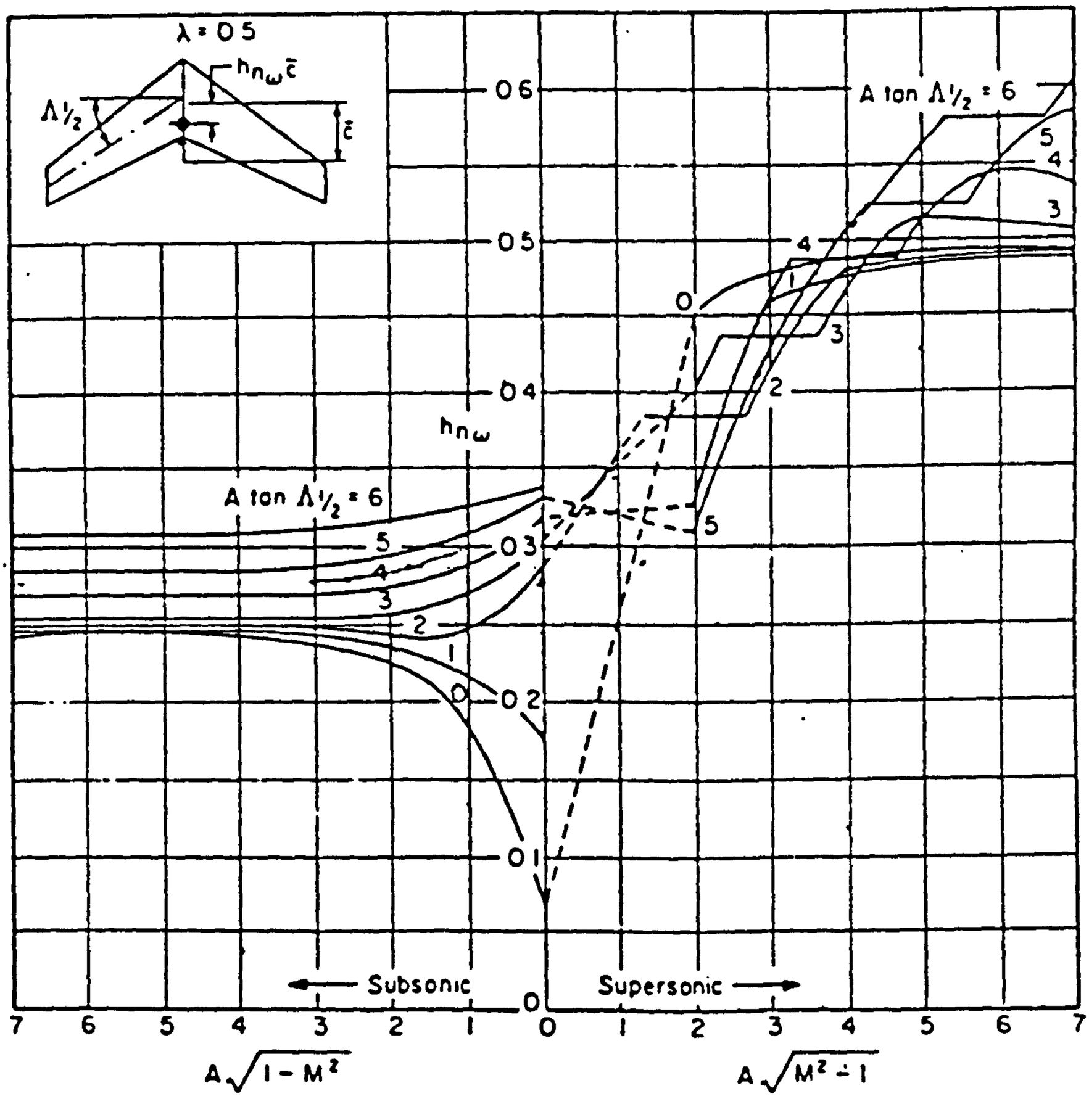

Fig. 21.13 Theoretical Chordwise Position of the Aerodynamic Center (Data courtesy of the Royal Aeronautical Society Data Sheets)

POSITION OF W.B. AERODYNAMIC CENTRE				
M	AR β	$(h_n)_w$	$(h_n)_w x\bar{\bar{C}}$ (m)	distance from datum (m)
0.2	3.92	0.278	0.648	4.675
0.6	3.2	0.278	0.648	4.675
0.8	2.4	0.28	0.652	4.671
0.9	1.74	0.289	0.673	4.625
0.95	1.25	0.297	0.692	4.625
1.0	0.00	0.324	0.755	4.562
1.05	1.28	0.322	0.750	4.56
1.1	1.83	0.317	0.739	4.575
1.2	2.65	0.411	0.958	4.375
1.3	3.32	0.475	1.107	4.200
1.4	3.92	0.508	1.184	4.120
1.6	4.99	0.508	1.184	4.12

TABLE B3

POSITION OF CANARD-BODY AERODYNAMIC CENTRE				
M	$AR_c\beta$	$(h_n)_{canard}$	$(h_n)x\bar{\bar{C}}_{canard}$ (m)	distance from datum (m)
0.2	2.94	0.250	0.33	approximately constant at 8.0 m
0.6	2.4	0.24	0.317	
0.8	1.8	0.237	0.313	
0.9	1.31	0.237	0.313	
1.0	0.0	0.276	0.364	
1.05	0.96	0.346	0.457	
1.1	1.37	0.385	0.508	
1.2	1.99	0.388	0.512	
1.3	2.49	0.388	0.512	
1.4	2.94	0.408	0.538	
1.6	3.75	0.470	0.62	

TABLE B4

Aerofoil Sections

The wing aerofoil section was chosen to be NACA 65-206 with the following characteristics:

$\alpha_{OL} = -1.6^{o}$

$C_{mo} = -0.031$

$\frac{\partial C_l}{\partial \alpha} = 0.105$ /deg

Aerodynamic centre at 0.257 $\bar{\bar{C}}$

$^{\alpha}C_{L_{max}} = 12.0^{o}$

$C_{L_{max}} = 1.03$ at $\alpha = 6.0^{o}$ (without flaps)

The inner wing aerofoil section is of the NACA 66-206 type with coordinates given in Table B7.

Fin and Canard Aerofoil Section

TYPE: NACA 65.006 (symmetrical)

Characteristics: $\alpha_{OL} = 0.0$

$C_{mo} = 0.0$

$\frac{\partial C_l}{\partial \alpha} = 0.105 \quad deg^{-1}$

a.c = 0.264 C

$^{\alpha}C_{L_{max}} = 12.0^{o}$

$C_{L_{max}} = 0.92$ at $\alpha^{*} = 7.6^{o}$

It must be pointed out that the characteristics of these aerofoils are based on a 2-D treatment.

A more likely trend is given below:

With reference to page I.20-8 of Reference 2, it is evident that for a forward swept wing with strakes, maximum lift coefficient is achieved at an angle of incidence of around 30-35 degrees and moreover, at such incidences lift coefficient has a value between 1.4 - 1.6 without using either leading of trailing edge flaps.

Typical C_L v. α, C_D v. C_L and C_m v. C_L are given in Figure B1. Also maximum lift to drag ratio is about $(L/D)_{max} \simeq 5$ at $C_L \simeq 0.45$ which is within the linear part of C_L v. α curve. It should be noted that the strake contributes around 12% to the lift coefficient and therefore is beneficial.

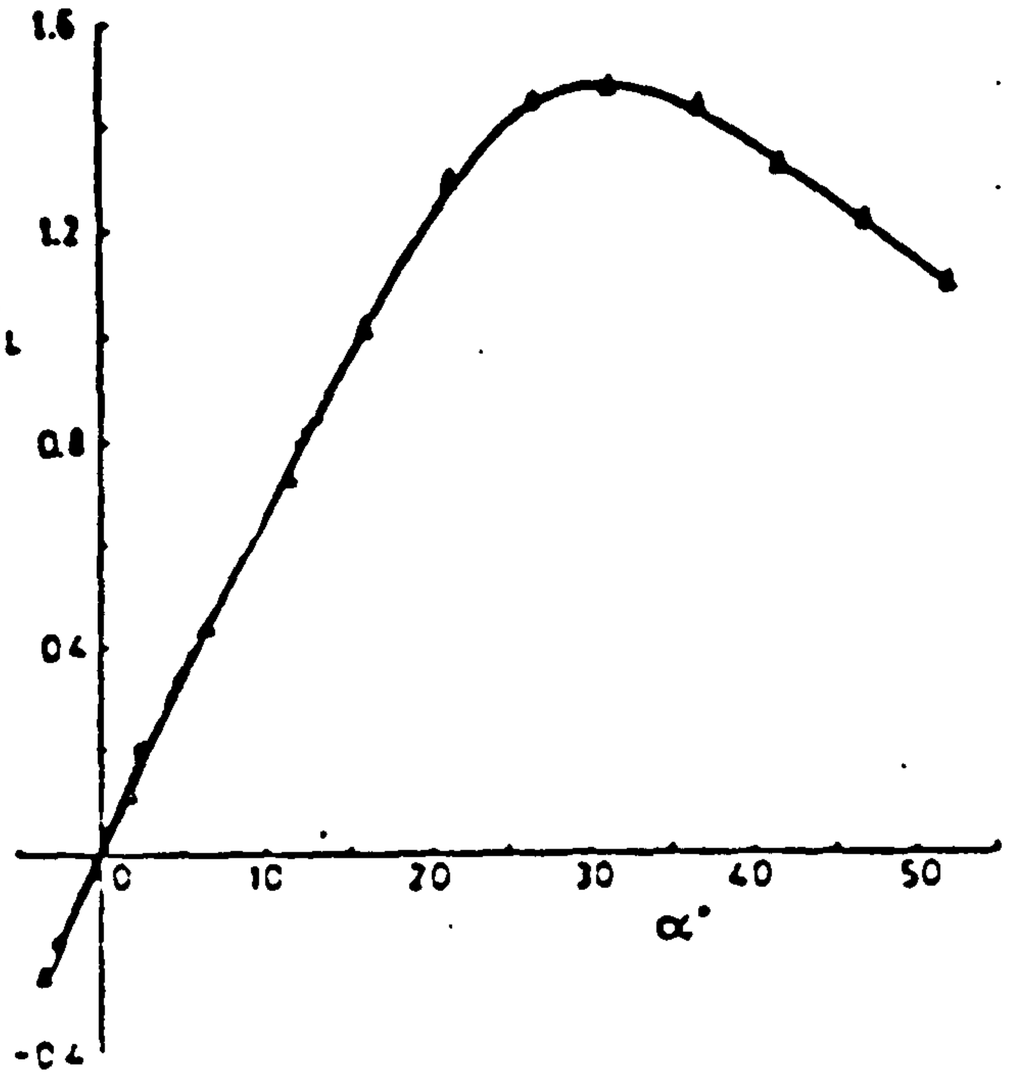

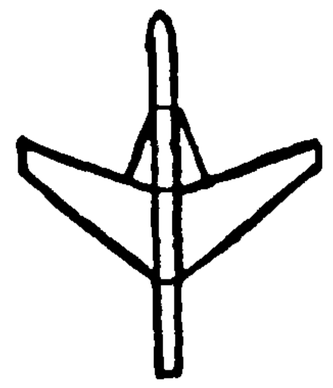

Force and moment measurements for above planform.

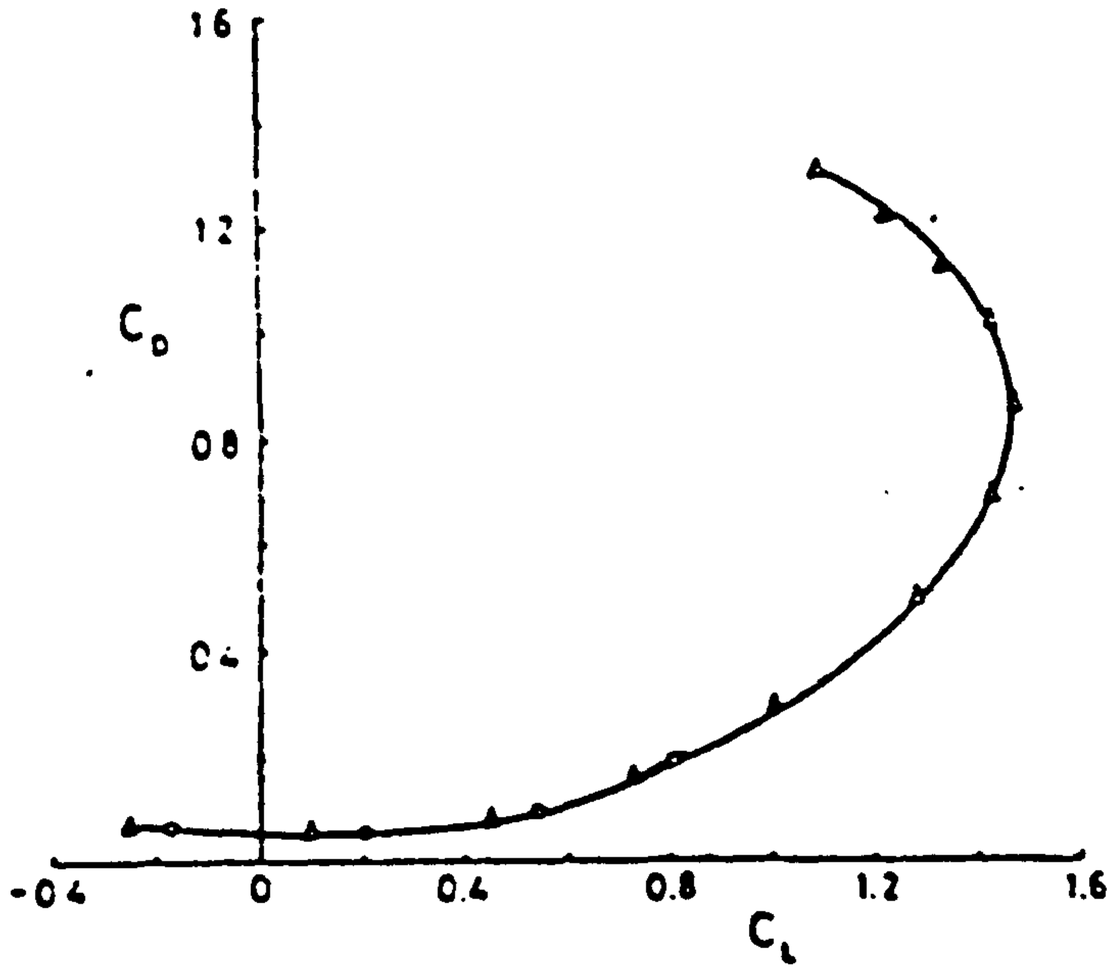

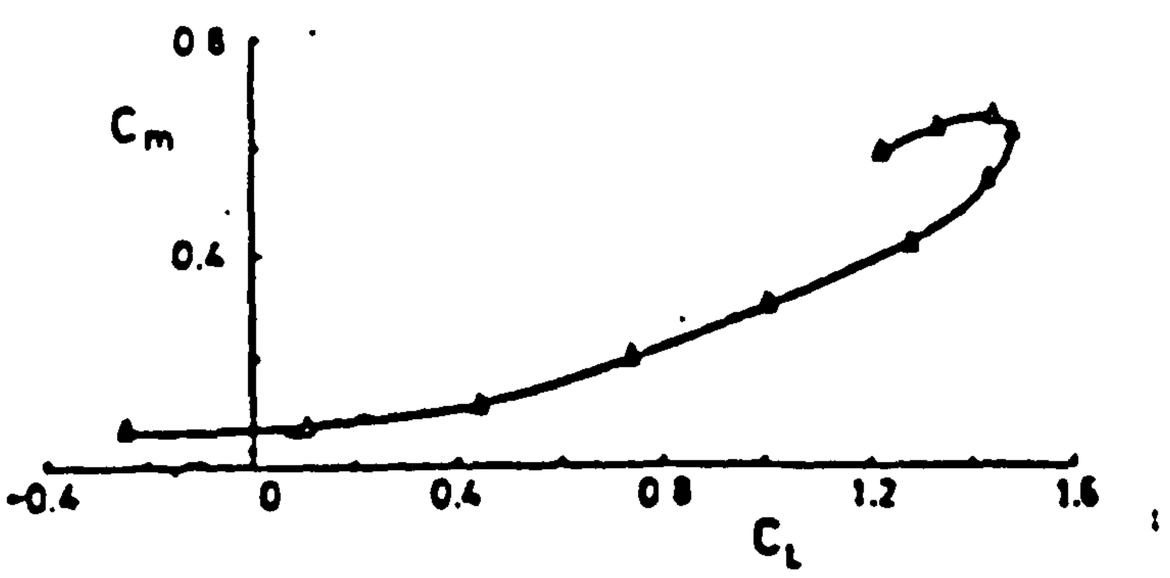

FIGURE B1 (Ref. 2)

AERODYNAMIC CHARACTERISTICS OF A F.S.W. WITH STRAKES

B2 .: Determination of the static margin stick-fixed

Static margin is defined as -

$$S_M = \frac{X_{NP} - X_{CF}}{\bar{\bar{C}}} \qquad \text{- - - - - EQ.B2.1}$$

where,

X_{NP} = location of neutral point (relative to datum)

X_{CG} = location of aircraft centre of gravity.

Since $X_{C.G}$ is already determined by the layout and weight distribution, (Appendix B), it only remains to establish the position of neutral point X_{NP}.

For the position of N.P.

$$\frac{\partial C_{M_{C.G.}}}{\partial \alpha} = 0$$

From Reference 1, page 21-7 for a canard layout

$$\frac{\partial C_{M_{C.G.}}}{\partial \alpha} = V_c . a_c - \frac{X_w}{\bar{\bar{C}}} . a_w + \left(\frac{\partial C_M}{\partial \alpha}\right)_{intake} \qquad \text{- - - - - EQ.B2.2}$$

where $V_c = \frac{P_c S_c}{\bar{\bar{C}} S_w}$, $a_c = \left(\frac{\partial C_L}{\partial \eta}\right)_{canard}$ - - - - - EQ.B2.3

$$a_w = \left(\frac{\partial C_L}{\partial \alpha}\right)_{wing}$$

If N.P were to be at C.G., terms in (C-2) could be written as

$$V_c = \left(\frac{X_{NP} - X_{CN}}{\bar{\bar{C}}}\right)\left(\frac{S_c}{S_w}\right)$$

where X_{CN} = location of canard aerodynamic centre.

Also,

X_w = $(X_{AC} - X_{NP})$ where X_{AC} = location of wing body aerodynamic centre.

Moreover,

$$\left(\frac{\partial C_M}{\partial \alpha}\right)_{intake} = \frac{2\dot{m}}{\rho V_\infty S_w \bar{C}} - \frac{\partial \beta}{\partial \alpha}\,(X_{NP} - X_{IN})$$

$\frac{\partial \beta}{\partial \alpha}$ = rate of change of flow deflection angle at intake w.r.t. incidence.

where X_{IN} = location of air intake

$\dot{m}$ = engine mass flow rate

Now the criterion for combat aircraft would be agility at combat Mach number, Having decided on combat Mach number say M = 0.3, and data from Appendix B together with engine characteristics given in Table (C1) below.

M	0.0	0.1	0.2	0.3	0.4	0.5	0.6	0.7	0.8	0.9	1.0
$\dot{m}$ lb/s	216.75	220.0	223.75	232.0	24.10	253.25	266.25	282.5	302.5	322.5	346.25

TABLE C-1. PRATT & WHITNEY F100-PW-100 AFTERBURNING TURBOFAN CHARACTERISTICS

and also X_{IN} = 3.74 m

$\frac{\partial \beta}{\partial \alpha}$ = 1.69 (from Reference 1)

Equation (C-1) becomes

$$\frac{\partial C_M}{\partial \alpha} = 0 = \left(\frac{(X_{NP} - X_{CN})}{\bar{C}}\right)\cdot\left(\frac{S_c}{S_w}\right)\cdot a_c - \frac{(X_{AC} - X_{NP})}{\bar{C}}\cdot a_w + \frac{2\dot{m}}{\rho V_\infty S_w \bar{C}} - \frac{\partial \beta}{\partial \alpha}(X_{NP} - X_{IN})$$

which gives

$$X_{NP} = \frac{\left\{(X_{CN}\cdot\frac{S_c}{S_w}\cdot a_c) + (X_{AC}\cdot a_w) + (X_{IN} - \frac{2\dot{m}}{\rho V_\infty S_w}\cdot\frac{\partial \beta}{\partial \alpha})\right\}}{\left\{(\frac{S_c}{S_w}\cdot a_c) + (a_w) + (\frac{2\dot{m}}{\rho V_\infty S_w} - \frac{\partial \beta}{\partial \alpha})\right\}} \qquad \text{----- EQ.B2.4}$$

This expression was adopted in the optimisation code so that the position of N.P. and hence the static margin could be determined.

Stick-Fixed Static Margin Data and C.G. Movement for the Full-Size Aircraft

Table B5 below represents the variation of static margin stick-fixed with the wing location.

X_{NP} = estimated location of neutral point

X_{MW} = estimated location of wing C.G.

SMSF = Static margin stick-fixed

X_{MW} (m)	$X_{C.G.}$ (m)	$X_{N.P.}$ (m)	SMSF $\simeq$ %$\bar{c}$
4.16	5.8	5.47	14
4.22	5.82	5.52	13
4.28	5.84	5.57	11
4.34	5.85	5.62	10
4.4	5.87	5.67	9
4.46	5.89	5.72	7
4.52	5.9	5.77	6
4.58	5.92	5.82	5
4.64	5.94	5.87	3
4.7	5.95	5.92	2

TABLE B5

Here the F.S.W. was fixed at a point 4.64 m relative to the plane of the nozzle corresponding to a static margin of 3%$\bar{c}$. By moving the C.G. the variation of static margin with C.G. was determined. This variation is presented in Fig. B2. Clearly, for a static margin range of -6%$\bar{c}$ - 6%$\bar{c}$ a C.G. movement of 0.28 m is required.

Flight condition.

Level flight $n = 1$

$w = mg$

I.S.A. prevails.

$$C_w = \frac{W}{\frac{1}{2}\rho V^2 S_w}$$

mass of A/C = 19544 lb ≈ 8865 kg.

$\rho = 1.225\ kg/m^3$

$S_w = 20\ m^2$

M	Lw (m)	LC (m)	$a_{w.B}$ (rad^{-1})	$a_{c.g}$ (rad^{-1})	V (m/s)	total C_{D_o}	DCMDAI (rad^{-1})	C_w
≤0.2	≈ 0.713	2.368	3.7	4.77	68.06	0.0257	0.0099	1.532
0.4			3.78	4.87	136.12	0.0264	0.0053	0.383
0.6			3.91	5.04	204.18	0.0265	0.0039	0.170

TABLE B6

AERODYNAMIC CHANGES OVER THE MACH NUMBER

RANGE OF UP TO M = 0.6

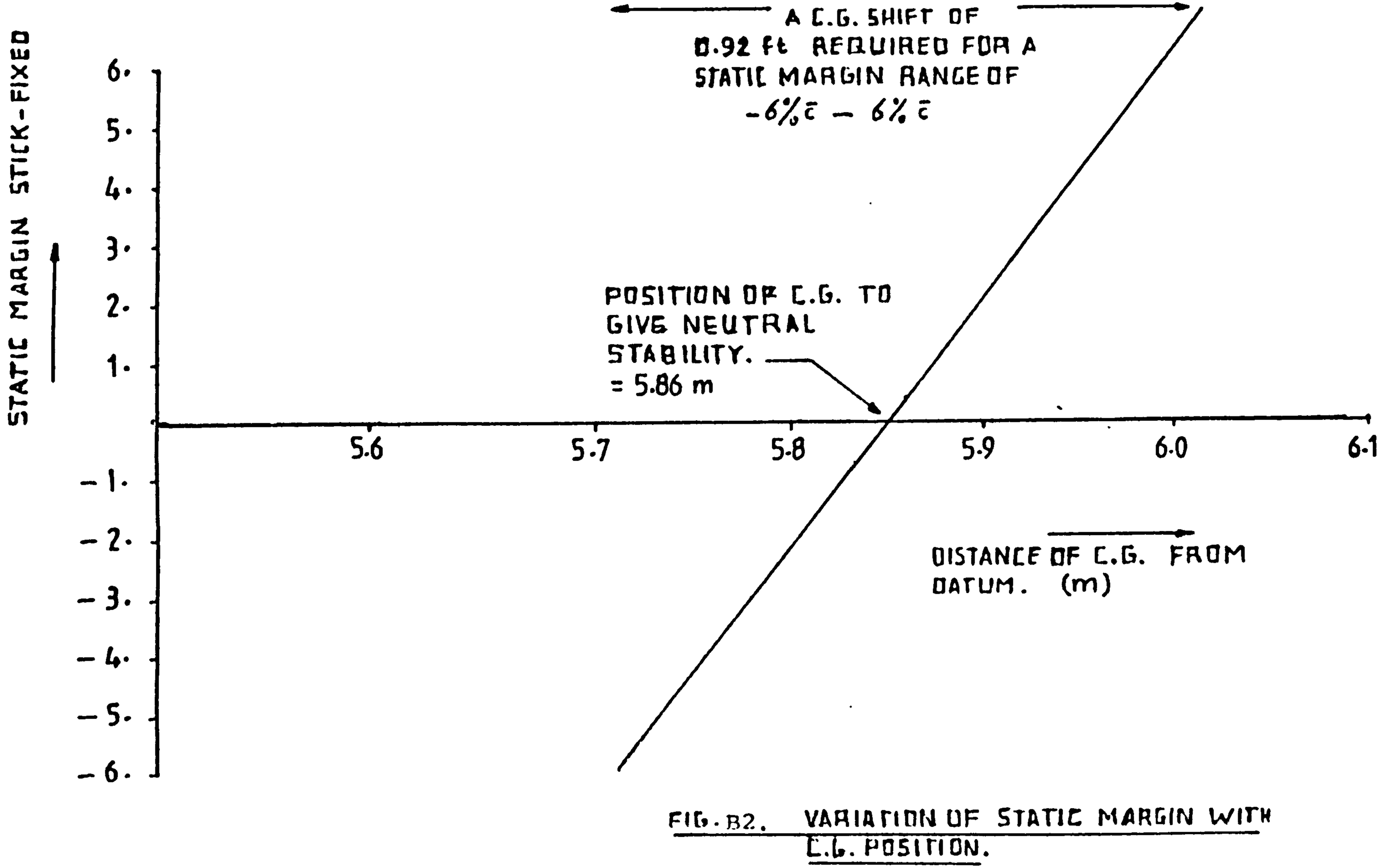

FIG. B2. VARIATION OF STATIC MARGIN WITH C.G. POSITION.

B.4 . Zero Lift Drag Calculations for the F.S.W. Model.

We would like to test the model at a speed corresponding to Mach number M = 0.3 for A/C

$V_{A/C} = M \times a$ where a is the speed of sound

$V_{A/C} = 0.3 \times 340.3 = 102.1$ m/s

For Fraud number to be the same, for both model and aircraft we must have the following relationships:

$$\frac{V_M}{V_{A/C}} = \sqrt{\lambda} \quad \rightarrow \quad V_M - 102.1 \times \sqrt{\frac{1}{14}} = 27.29 \text{ m/s}$$

$$\text{or } V_M = \frac{V_{A/C}}{3.74}$$

Now for this to be true, that is to say, for A/C and model to fly under the same gravitational acceleration Reynolds numbers must have the ratio -

$$\frac{Re_M}{Re_{A/C}} = \lambda^{3/2}$$

$$\text{Now } Re_{A/C} = \frac{102.1 \times 2.35}{1.461 \times 10^{-5}} = 1.6 \times 10^7$$

$$Re_M = 1.6 \times 10^7 \times (\frac{1}{14})^{3/2} \simeq 3 \times 10^5$$

Now for our model

$$Re_M = \frac{27.29 \times 0.168}{1.461 \times 10^{-5}} = 3 \times 10^5$$

which is the same as above.

Now generally airflow over the wing becomes turbulent at $Re \simeq 4 \times 10^5$. Therefore it may be necessary to use a trip wire over the wings.

(i.) Wing-zero lift drag subsonic

C_{D_o} is due to skin friction. The expression for $(C_{D_o})_w$ is based upon the wing reference area (S_{ref}) here taken as the exposed wing area, S_e

EO. 11.13, Ref.1 $S_e \approx 16.65$ m

$$(C_{D_o})_w = C_f\left[1 + L\left(\frac{t}{c}\right) + 100\left(\frac{t}{c}\right)^4\right] R. \frac{S_{wet}}{S_{ref}}$$

L = aerofoil thickness location parameter
= 1.2 for $^t/_c$ max at $x \geq 0.3\bar{c}$
= 2.0 for $^t/_c$ max at $x < 0.3\bar{c}$

For our wing

$L = 1.2$

$\frac{t}{c} = 0.06$

$S_{wet} = 2 \times S_e = 2 \times 16.65 = 33.3\ m^2$

R = lifting surface correlation factor obtained from Ref.1, Fig.11.8, see Table below.

C_f = turbulent flat plate skin friction coefficient.

M	R
≤0.2	0.950
0.4	0.980
0.6	1.025
0.7	1.080
0.8	1.130
0.85	1.160
0.9	1.22

The turbulent flat plate skin friction coefficient is determined from the combination of the following source data.

Ref.1, Table 11.1 - to select a type of surface and to determine the roughness height.

Ref.1, Fig.11.9 - to determine the cut-off Reynolds number (Re) suitable for $^{l}/_{k}$ and to compare with Re for the flow, where 'K' is the equivalent sand roughness.

Ref.1, Fig. E.2 - to find C_f, based on the smaller Re or R_{e_L}

From Table 11.1

For camouflage paint - $K = 0.4 \times 10^{-3}$ inch $\simeq 0.01 \times 10^{-3}$m

$\simeq 1 \times 10^{-5}$m

$$l_{model} = \bar{c}_{model} = \frac{2.35}{14} = 0.168 \text{ m}$$

$$\frac{l}{k} = \frac{\bar{c}}{k} = \frac{0.168}{10^{-5}} = 1.68 \times 10^4$$

From Ref.1, Fig. 11.9, when $\frac{l}{k} = 1.68 \times 10^4$ for $0 < M < 1$

$$R_{e_L} = 10^6$$

$$Re = \frac{V\bar{c}}{\gamma}$$

At sea level at I.S.A. conditions, $\gamma = 1.461 \times 10^{-5}$

The table below shows variations of Re with M.

M	$R_{e\,(FLOW)}$
$\leqslant$0.2	7.8×10^5
0.4	1.6×10^6
0.6	2.3×10^6
0.8	3.1×10^6
0.9	3.5×10^6

Since Re is greater than Re_L we choose Re to determine C_f.

From Fig. E-2 for our Re range, C_f can be found approximately from formula

$$C_f = \frac{0.455}{\left[\log_{10} Re\right]^{2.58}} - \frac{1700}{Re} \qquad \text{(for a turbulent flow)}$$

$\therefore$ $(C_{D_o})_w$ subsonic is

$$(C_{D_o})_w = C_f \left[1 + (1.2)(0.06) + 100(0.06)^4\right] R. \frac{2 \times 16.65}{-6.65}$$

$$(C_{D_o})_w = 2.1466.C_f.R$$

The table below shows $(C_{D_o})_w$ at various M and R.

M	R	$C_f \times 10^{-3}$	$(C_{D_o})_w \times 10^{-3}$
$\leq$0.2	0.95	2.5	5.09
0.4	0.98	3.04	6.39
0.6	1.025	3.1	6.82
0.8	1.13	3.1	7.52
0.9	1.22	3.1	8.12

(ii) Body Drag - Subsonic

At subsonic speeds, (C_{D_o}) of smooth slender bodies is primarily due to body skin friction. $(C_{D_o})_{body}$ is referenced to the maximum x-sectional area S_B. Now, since the intake is open, air is allowed to circulate through the fuselage. As a first approximation drag due to fuselage was doubled in order to take this into account.

$$(C_{D_o})_B = (C_{D_{o_F}})_B + C_{D_{o_b}} \qquad \text{(Ref.1, Eq. 11.21a)}$$

$(C_{D_{o_F}})_B$ = body skin friction coefficient

$C_{D_{o_b}}$ = base pressure coefficient

Skin friction coefficient

From Ref.1 Eq. 11.22.

$$(C_{D_{oF}})_B = C_f \left[1 + \frac{60.0}{(l_{B/d})} + 0.0025\left(\frac{l_B}{d}\right)\right] \frac{S_S}{S_B}$$

$l_{B_{model}}$ = body length = $^{14}/_{14.0}$ = 1 m

d_{model} = body diameter $^{1.4}/_{14.0}$ = 0.1 m

$\frac{l_B}{d}$ = body fineness ratio = 10

S_S = wetted area of the body surface ≈ 47.33 m^2

S_B = 1.54 m^2

To find C_f we have to find R_e referenced to $l_{B_{model}}$

M	Re
≤0.2	4.6×10^6
0.4	9.3×10^6
0.6	1.4×10^8
0.8	1.9×10^8
0.9	2.1×10^8

Now since for this range of Re the flow is fully turbulent from Fig. E.2
C_f is given by

$$C_f \approx \frac{0.455}{\left[\log_{10} Re\right]^{2.58}}$$

NOTE: Since we have the ratio $\frac{S_S}{S_B}$ there is no need to scale the areas down.

$$\therefore \quad (C_{D_{OF}})_B = C_f \left[1 + \frac{60}{(10)^3} + 0.0025 \times 10\right] \frac{47.33}{1.54}$$

$$= \quad (C_{D_{OF}})_B = 33.346\ C_f$$

M	$C_f \times 10^{-3}$	$(C_{D_{OF}})_{B_{model}} \times 2$
≤0.2	3.42	0.114
0.4	3.03	0.101
0.6	2.85	0.095
0.8	2.71	0.0905
0.9	2.67	0.089

* Since our engine nozzle * completely fills the base region, base drag * is zero. *

(iii) Miscellaneous Drag Items C_{D_o}

Use was made of Fig. 11.22 of Ref.1 . However the data on this figure is referenced to a wing area of 280 square feet. Thus, the data must be corrected for the appropriate S_{ref} where

S_{ref} = 16.65 m^2

$S_{ref} = S_e \approx 16.65\ m^2$

$$\therefore \quad \Delta C_{D_{0_{\substack{\text{canopy}\\\text{our}\\\text{A/C}}}}} = C_{D_{0_{\substack{\text{canopy}\\\text{from}\\\text{fig 11.22}}}}} \times \frac{26.01285}{16.65}$$

$0 < M < 0.9$

$$\Delta C_{D_{0_{\text{canopy}}}} = 0.0006 \times \frac{26.01285}{16.65} = 0.00094$$

$$\Delta C_{D_{0_{\substack{\text{nozzle}\\\text{boat}\\\text{tail}}}}} = 0.00125 \times \frac{26.01285}{16.65} = 0.00195$$

$$\Delta C_{D_{0_{\substack{\text{protruberances}}}}} = 0.0014 \times \frac{26.01285}{16.65} = 0.0022$$

ΔC_{D_0} for 2 x sidewinder AIMD $\simeq 0.0008$

Assume twice for AMRAM

$\therefore \quad \Delta C_{D_0}$ for 2 x AMRAM $\simeq 0.0016$

$$\Sigma \Delta C_{D_{0_{\text{miscellaneous}}}} = 0.00748$$

As a first approximation to canard and fin drag $(C_{D_0})_{\text{stabilizer}}$

Assume $(C_{D_0})_{\text{stabilizer}} = (C_{D_0})_{\text{wing}} \times \frac{S_C + S_F}{S_{ref}}$

where

S_F = fin area (wetted) = 5.59 m^2

M	$(C_{D_0})_{\text{stabilizer}} \times 10^{-3}$
≤ 0.2	2.57
0.4	3.22
0.6	3.44
0.8	3.79
0.9	4.09

S_C = canard area(Wetted) = 2.81 m^2

S_{ref} = 16.65 m^2

$\therefore \quad (C_{D_0})_{\text{stabilizer}} = 0.5045 \times (C_{D_0})_{\text{wing}}$

B4.1 Zero-Lift Drag Coefficient $(C_{D_o})_{total}$

For the first approximation let this be the sum of individual C_{D_o} components.

i.e.

$$(C_{D_o})_{total} = (C_{D_o})_w + (C_{D_o})_{stab} + (C_{D_o})_B^{**} \times \frac{S_B}{S_{ref}} + \Sigma\Delta C_{D_o} \quad - - - - \quad EQ(1)$$

M	$(C_{D_o})_{total}$
<0.2	↑
0.4	≃ 0.036
0.6	↓

TABLE B6

**: This is because $(C_{D_o})_B$ was based on S_B and the rest of the terms in EQ(1) are based on $S_{ref} = S_e$ so we multiply it by $\frac{S_B}{S_{ref}}$ to make it based on S_{ref}.

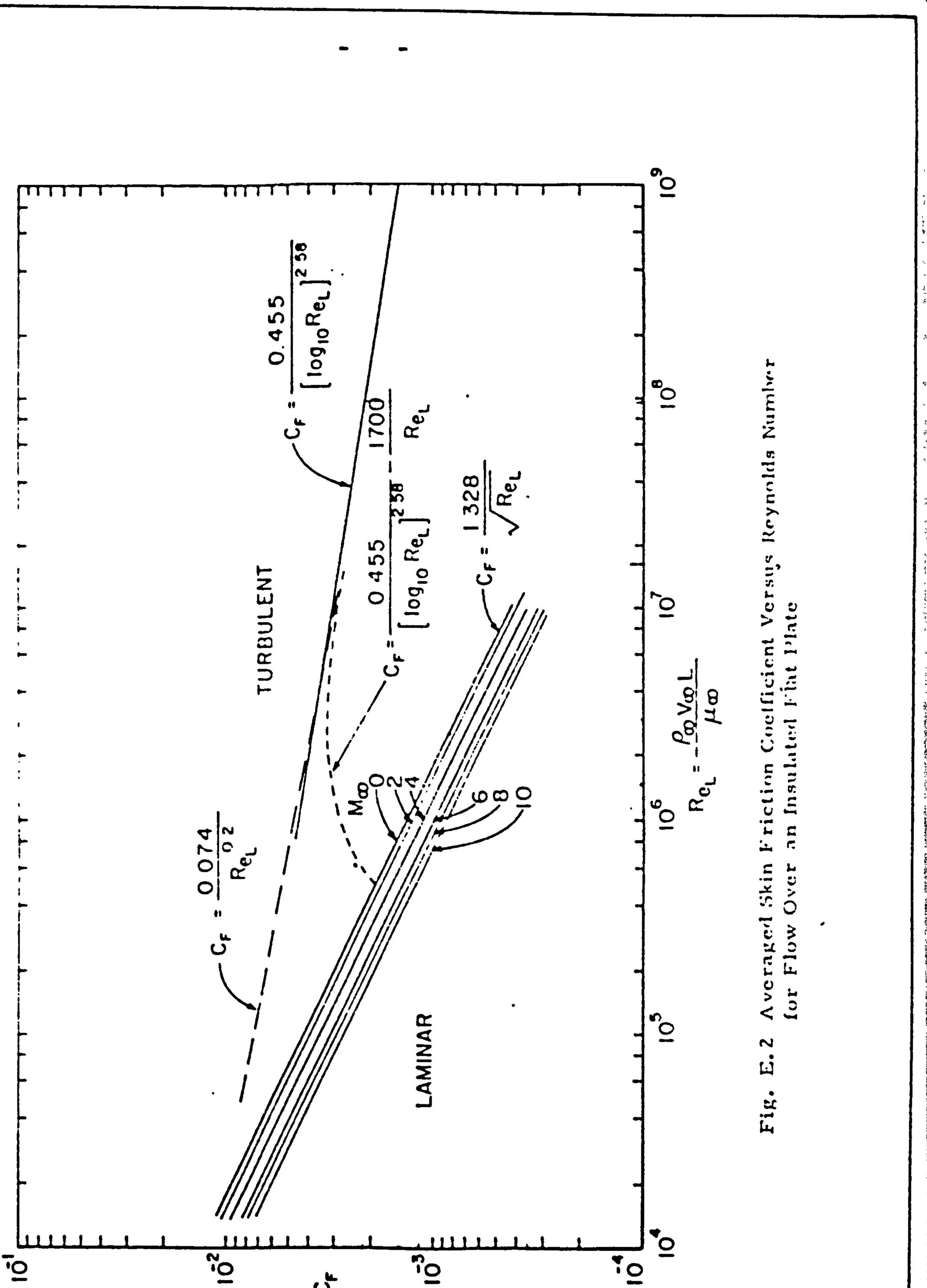

Fig. E.2 Averaged Skin Friction Coefficient Versus Reynolds Number for Flow Over an Insulated Flat Plate

APPENDIX C: Check on the Canard and fin sizes regarding the static longitudinal and directional stabilities at M = 0.3

(i) Check on the canard size

From Ref. 1, pitching moment equation can be presented as,

$$\frac{dC_M}{d\alpha} = \overline{V}_c . a_{C.B.} - \frac{X_w}{\overline{c}} + \left(\frac{dC_M}{d\alpha}\right)_{INTAKE} \qquad \text{EQ.C1}$$

where $\overline{V}_c = \frac{\ell_c S_c}{\overline{c}\, S_w}$, $a_{C.B.} = \left(\frac{dC_{L_{C.B.}}}{d\alpha}\right)_{\eta=0}$

$$a_{W.B.} = \left(\frac{dC_L}{d\alpha}\right)_{W.B.}$$

and $$\left(\frac{dC_M}{d\alpha}\right)_{INTAKE} = \frac{2\dot{m}}{\rho V_\infty S_c \overline{c}} \cdot \frac{d\beta}{d\alpha}\left(|X_{C.G.} - X_{IN}|\right)$$

From appendices A and B the above parameters have the values of,

ℓ_c = 2.06 m

$_W$ = 0.74 m

$X_{C.G.}$ = 5.94 m

$(|X_{C.G.} - X_{IN}|)$ = 3.71 m

X_{IN} = 9.65 m

$a_{C.B.}$ = 0.96 rad^{-1}

$a_{W.B.}$ = 3.73 rad^{-1}

$\dot{m}$ = engine mass flow rate = 146.12 kg/s

$\frac{d\beta}{d\alpha}$ = 1.69

$\overline{c}$ = 2.35 m

S_W = 20.0 m^2

S_c = 5.0 m^2

V_∞ = 103.0 m/s

ρ = 1.225 kg/m^3

Therefore from equation C1,

$$\frac{dC_M}{d\alpha} = \frac{2.06 \times 5.0}{2.35 \times 20.0} \times 0.96 - \frac{0.74}{2.35} \times 3.73$$

$$+ \frac{2 \times 146.12}{1.225 \times 103 \times 5 \times 2.35} \cdot 1.69 \times 3.71$$

$$\cong 0.32 \text{ rad}^{-1}$$

A typical value for $\frac{dC_M}{d\alpha}$ as regards the fighter aircraft would be in the region of -0.3 - -0.4 rad^{-1}. Therefore canard is assumed to be of the right size.

(ii) CHECK FIN SIZE

Directional stability for a canard layout can be expressed as

$$\frac{dC_n}{d\beta} = C_{n_\beta} = (C_{n_\beta})_{\text{fuselage}} + (C_{n_\beta})_{\text{wing}} + V_{vs}(C_{L_\beta})_{vs}\left(1 + \frac{d\sigma}{d\beta}\right)\frac{q_{vs}}{q}$$

"vs" refers to vertical stabilizer.

where

$$V_{vs} = \frac{\ell_{vs}\ S_{vs}}{s\ S_w} = \frac{\ell_F\ S_F}{S_w\ s} = \text{fin volume coefficient.}$$

$(C_{n_\beta})_{\text{power}}$ is neglected.

For directional stability $\frac{\partial C_n}{\partial \beta}$ must be > 0

From Reference 1

$$\left(1 + \frac{d\sigma}{d\beta}\right) - \frac{q_{vs}}{q} = 0.724 + \frac{3.06\ \frac{S'_{vs}}{S_w}}{1 + \text{Cos}\Lambda_{C/4}} + 0.4\ \frac{Z_w}{d} + 0.009\ AR$$

and

$$(C_{n_\beta})_{vs} = V_{vs}(C_{L_\alpha})_{vs}\left(1 + \frac{d\sigma}{d\beta}\right)\frac{q_{vs}}{q}$$

where

S'_{VS} = fin + rudder area with this area extended to the fuselage centre line = 7.734 m^2 =

Z_w = distance along the aircraft z-axis from the wing root chord to the fuselage centre line.

d = maximum fuselage depth.

C.1 A CHECK ON DIRECTIONAL STABILITY

The static directional stability derivative can be expressed as (Nicolai equation 21-20, Ref.4, Sec 5.4 from the same chapter)

$$\frac{dC_n}{d\beta} = C_{n_\beta} = (C_{n_\beta})_{fuselage} + (C_{n_\beta})_{wing} + \frac{L_{fin} \cdot S_{fin}}{b\ S_w}$$

$$- \left(\frac{dC_L}{d\beta}\right)_{fin} \cdot \left(0.724 + \frac{3.06 \frac{S'_{fin}}{S_w}}{1 + \cos\Lambda_{c/4_{fin}}} + 0.4 \cdot \frac{Z_w}{d} + 0.009AR\right)$$

where

S'_{fin} = area of the fin extended to the fuselage centre line

= 7.734 m^2

Z_w = the distance along the aircraft z-axis from the wing root chord to the fuselage centre line

= 0.7 m

d = maximum fuselage depth = 2.24 m

AR = wing aspect ratio = 4.0

$\left(\frac{dC_L}{d\beta}\right)_{fin}$ = lift curve slope of the fin based on the fin planform area plus an effective aspect ratio of 1.55 times the geometric aspect ratio of the fin since the fuselage acts as a large tip plate.

$\Lambda_{c/4_{fin}}$ = 42°

S_w = 20 m^2

b = 9.0 m

S_{fin} = 5.6 m^2

L_{fin} = 4.11 m

For a finite wing the linear lift curve slope is given by

$$\left(\frac{dC_L}{d\beta}\right)_{fin} = \frac{2\pi AR_{fin/compensated}}{2 + \sqrt{4 + AR^2_{fin_{compensated}}\left(1 + \frac{\tan\Lambda_{max.thickness\ line}}{\beta^2}\right)}}$$

where β = angle of sideslip

subsonic $\beta = \sqrt{1 - M^2}$

$\Lambda_{maximum\ thickness} = 37^o$

$AR_{fin_{compensated}} = 1.55 \times AR_{fin} = 1.55 \times 1.6 = 2.48$

M	$\frac{dC_L}{d\beta}$ rad^{-1}
$\leq$ 0.2	2.68
0.4	2.73
0.6	2.81
0.8	2.94
0.9	3.04

TABLE C1

(i) FIN CONTRIBUTION

Fin contribution to C_{n_β} is given by (see Ref. 1)

$$V_{fin}\left(\frac{dC_L}{d\beta}\right)_{fin}\left(0.724 + \frac{3.06\frac{S'_{fin}}{S_w}}{1 + \cos\Lambda_{c/4_{fin}}} + 0.4\frac{Z_w}{d} + 0.009\ AR\right)$$

$$(C_{n_\beta})_{fin} = \frac{4.11 \times 5.6}{9 \times 20} \times 2.68 \times \left(0.724 + \frac{3.06 \times \frac{7.734}{20}}{1 + \cos(42)} + 0.4 \times \frac{0.7}{2.24} + 0.009 \times 4\right)$$

$$= 0.536 \text{ rad}^{-1}$$

(ii) WING CONTRIBUTION

Wing contribution (subsonic) is given by (Ref. 1 equation 21-22)

$$(C_{n_\beta})_{wing} = C_L^2\left[\frac{1}{4\pi AR} - \frac{\tan\Lambda_{c/4}}{\pi AR(AR + 4\cos\Lambda_{c/4})}\left(\cos\Lambda_{c/4} - \frac{AR}{2} - \frac{AR^2}{8\cos\Lambda_{c/4}} + \frac{6X_w}{\bar{c}}\frac{\sin\Lambda_{c/4}}{AR}\right)\right]$$

where X_w = wing distance between wing-body aerodynamic centre and c.g.

$= 2.424$ ft $= 0.739$ m

$\Lambda_{c/4} = -45^o$

Assuming a C_L of 0.67 at M = 0.3

then

$(C_{n_\beta})_{wing} = -0.014 \text{ rad}^{-1}$

(iii) FUSELAGE CONTRIBUTION

This is given by (Ref. 1 equation 21-23)

$$(C_{n_\beta})_{fuselage} = -1.3 \frac{\text{volume of fuselage}}{S_w.b} \cdot \frac{h}{w}$$

where volume of fuselage $\simeq 20$ m^3

$\frac{h}{w}$ = the ratio of mean fuselage depth to mean fuselage width

$\simeq 1.0$

b = wing span = 9.0 m

S_w = wing area = 20 m^2

$$\therefore (C_{n_\beta})_{fuselage} \approx -1.3 \times \frac{20}{20 \times 9} .1 = -0.1444$$

$$\text{Total } (C_{n_\beta}) \approx -0.014 - 0.1444 + 0.536 = 0.38$$

Since this is positive the aircraft has static directional stability. However, the fin C_{n_β} increases and then decreases with increasing Mach number due to the variation in $(\frac{dC_L}{d\beta})_{fin}$. Since $(\frac{dC_L}{d\beta})_{fin}$ can decrease by a factor of three from subsonic to Mach 3, the static directional stability decreases at high Mach numbers. Therefore, fin area should be more than what is required for subsonic range to compensate for this effect.

C2. CHECK ON LATERAL STABILITY (STATIC)

The static lateral stability derivative is

$\frac{dC_\ell}{d\beta} = C_{\ell_\beta}$ where C_ℓ is the rolling moment coefficient

This stability derivative is influenced by the wing, the fin and the wing-fuselage interaction.

Therefore C_{ℓ_β} can be expressed as

$$C_{\ell_\beta} = (C_{\ell_\beta})_{wing} + (C_{\ell_\beta})_{fin} + (C_{\ell_\beta})_{wing\text{-}fuselage}$$

(i) WING CONTRIBUTION

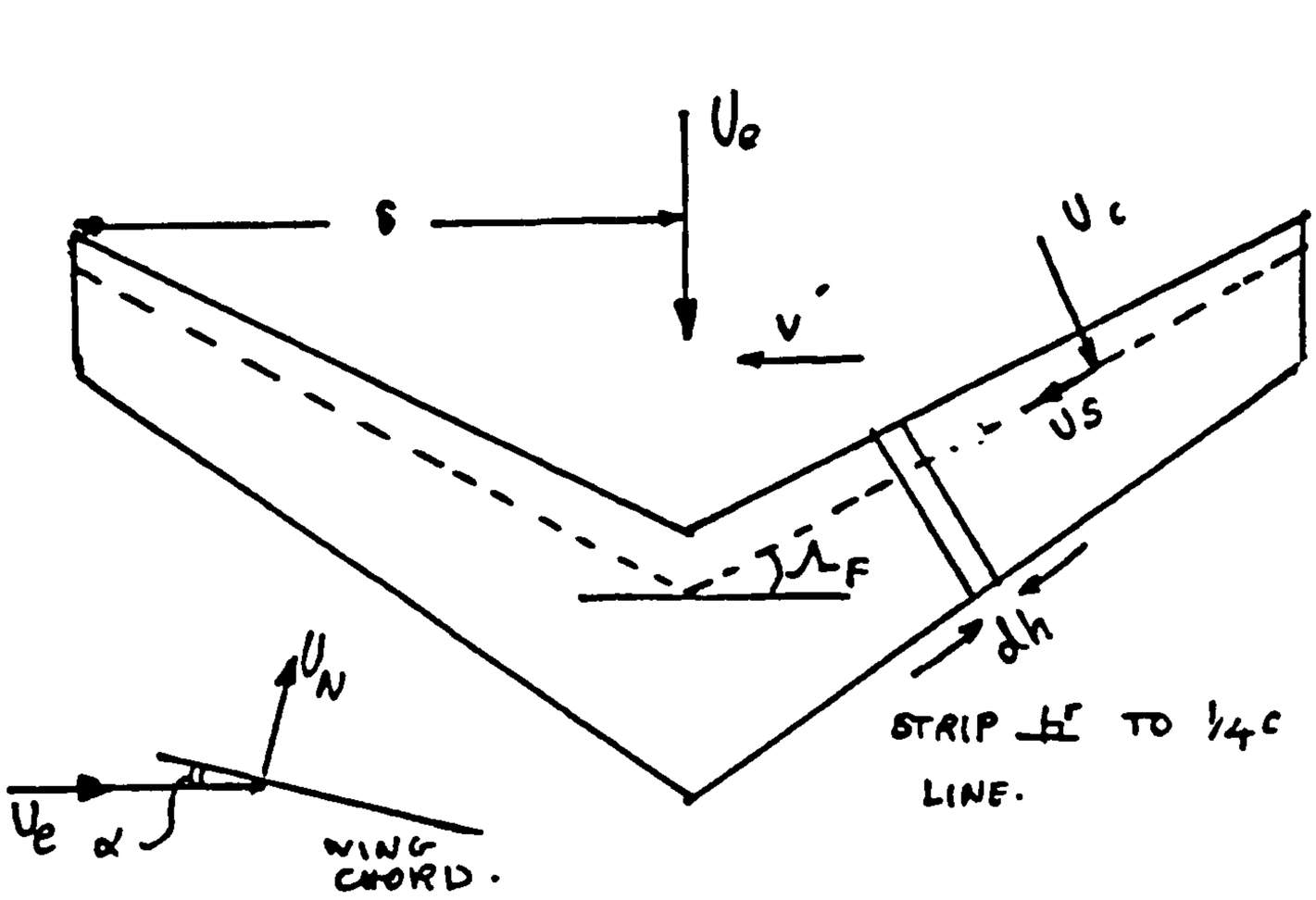

V' = sideslip velocity

$\beta \simeq \frac{V'}{V_e}$

U_e = free stream velocity

U_c = component of U_e ⊥r to ¼c.line

U_s = component of U_e ||l to ¼c.line

U_s has negligible effect of lift due to sideslip.

Now $U_N \simeq U_e.\alpha$ and $U_c = U_e Cos\Lambda_F - V' Sin\Lambda_F$

$$\text{or } U_c = U_e Cos\Lambda_F\left(1 - \frac{V'}{U_e} Tan\Lambda_F\right)$$

Now $V' \simeq U_e.\beta$

$$\therefore \quad U_c = U_e.Cos\Lambda_F(1 - \beta.Tan\Lambda_F)$$

For a chordwise strip on the starboard wing. The incidence of the chordwise strip is U_N/U_C so that lift on the starboard wing is approximately

$$\int_0^{S/\cos\Lambda_F} \tfrac{1}{2}\rho_e U_C^2 \left(\frac{dC_L}{d\alpha}\right)' \cdot \frac{U_N}{U_C} \cdot C(h)dh$$

$$= \int_0^{S/\cos\Lambda_F} \tfrac{1}{2}\rho_e U_e Cos\Lambda_F \left(\frac{dC_L}{d\alpha}\right)' U_N.C(h).(1 - \beta.Tan\Lambda_F).dh$$

where $(\frac{dC_L}{d\alpha})'$ is the local value of the lift curve slope. With no sideslip, the lift on starboard wing is

$$\tfrac{1}{2}\rho_e U_e^2 \frac{S_w}{2}.C_L = \int_0^{S/\cos\Lambda_F} \tfrac{1}{2}\rho_e U_e \cos\Lambda_F (\frac{dC_L}{d\alpha})' U_N - C(h).dh$$

Hence, the lift on the starboard wing

$$= (1 - \beta\tan\Lambda_F).\tfrac{1}{2}\rho_e U_e^2 \frac{S_w}{2} C_L$$

on the port wing,

$$U_c = U_e\cos\Lambda_F + V'\sin\Lambda_F$$

and the lift

$$= (1 + \beta\tan\Lambda_F)\ \tfrac{1}{2}\rho_e U_e^2 \frac{S_w}{2}.C_L$$

The rolling moment can be written as

$$L = +\beta\tan\Lambda_F.\tfrac{1}{2}\rho_e U_e^2 S_w C_L.d$$

where d is the moment arm measured in the O_y direction and the contribution to L_β due to wing sweep forward is then

$$L_\beta = \frac{dL}{d\beta} = +\ \tfrac{1}{2}\rho_e U_e^2 S_w.d.C_L.\tan\Lambda_F \qquad \text{. . . . .} \qquad \text{EQ.C2}$$

NOTE: Λ_F is the absolute value of angle of sweep.

Therefore, it can be seen that the forward sweep has a destructive effect on C_{ℓ_β} which for static lateral stability must be negative

From equation (F) above

$$C_{\ell_\beta}{}_{wing} = \frac{\frac{1}{2}\rho_e U_e^2 S_w . d . C_L}{\frac{1}{2}\rho_e U_e^2 S_w . s} \cdot \text{Tan}\Lambda_F = \frac{d}{s} . C_L$$

Assuming 'd' to be the y-coordinate of aerodynamic centre of half the wing

i.e. $d = 1.85$ m

also $s = 4.5$

$$\therefore (C_{\ell_\beta})_{wing} = \frac{0.132}{0.321} . C_L = 0.41 . C_L$$

As a first approximation for the model

C_L at M = 0.3 is given by

$$C_L = \frac{W}{\frac{1}{2}\rho U^2 S_W} = \frac{8953.4 \times 9.81}{0.5 \times 1.225 \times 103^2 \times 20} = 0.67$$

$$\therefore (C_{\ell_\beta})_{wing} = 0.41 \times 0.67 = 0.27$$

(ii) <u>WING-FUSELAGE CONTRIBUTION</u>

From reference 4, where $(C_{\ell_\beta})_{wing\text{-}fuselage}$ is obtained empirically, the following applies.

High wing $(C_{\ell_\beta})_{wing\text{-}fuselage} \approx -0.0344 \text{ rad}^{-1}$

Mid wing $(C_{\ell_\beta})_{wing\text{-}fuselage} \approx 0$

Low wing $(C_{\ell_\beta})_{wing\text{-}fuselage} \approx +0.0458 \text{ rad}^{-1}$

For our model, we have a mid wing

$$\therefore (C_{\ell_\beta})_{wing\text{-}fuselage} = 0.0$$

(iii) FIN CONTRIBUTION

From reference 1 (page 21-15) this is estimated to be

$$(C_{\ell_\beta})_{fin} = -\left(\frac{dC_L}{d\beta}\right)_{fin}\left(0.724 + \frac{3.06\,\frac{S'fin}{S_w}}{1 + \cos\Lambda_{c/4}} + 0.4\,\frac{Z_w}{d} + 0.009AR\right)$$

$$\times \frac{S_{fin}}{S_w} \cdot \frac{Z_w}{b}$$

b = span

where the terms are the same as before.

At M = 0.3, $\left(\frac{dC_L}{d\beta}\right)_{fin}$ is given from table E-2 as

$$\left(\frac{dC_L}{d\beta}\right)_{fin} \simeq 2.68\ \text{rad}^{-1}$$

$$\therefore (C_{\ell_\beta})_{fin} = -2.68\left(0.724 + \frac{3.06\,\frac{7.734}{20}}{1 + \cos(42)} + 0.4 \times \frac{0.7}{2.24} + 0.009 \times 4\right)$$

$$\times \frac{5.6}{20} \times \frac{0.146}{0.642}$$

$$\simeq -0.268\ \text{rad}^{-1}$$

Therefore, total (C_{ℓ_β}) is given by

$$(C_{\ell_\beta})_{total} \simeq -0.268 + 0.27 \simeq 0.0 \quad \text{at M = 0.3}$$

This is not of the right sign and magnitude.

NOTE: $Z_{w_{model}}$ = the distance from the vertical position of aerodynamic centre of the fin to c.g.
= 2.04 . m.

APPENDIX-D: Drawings, Calibration Tables/Graphs and a Summary of Full-Size and 1/14th Scale Dynamic Model Dimensions.

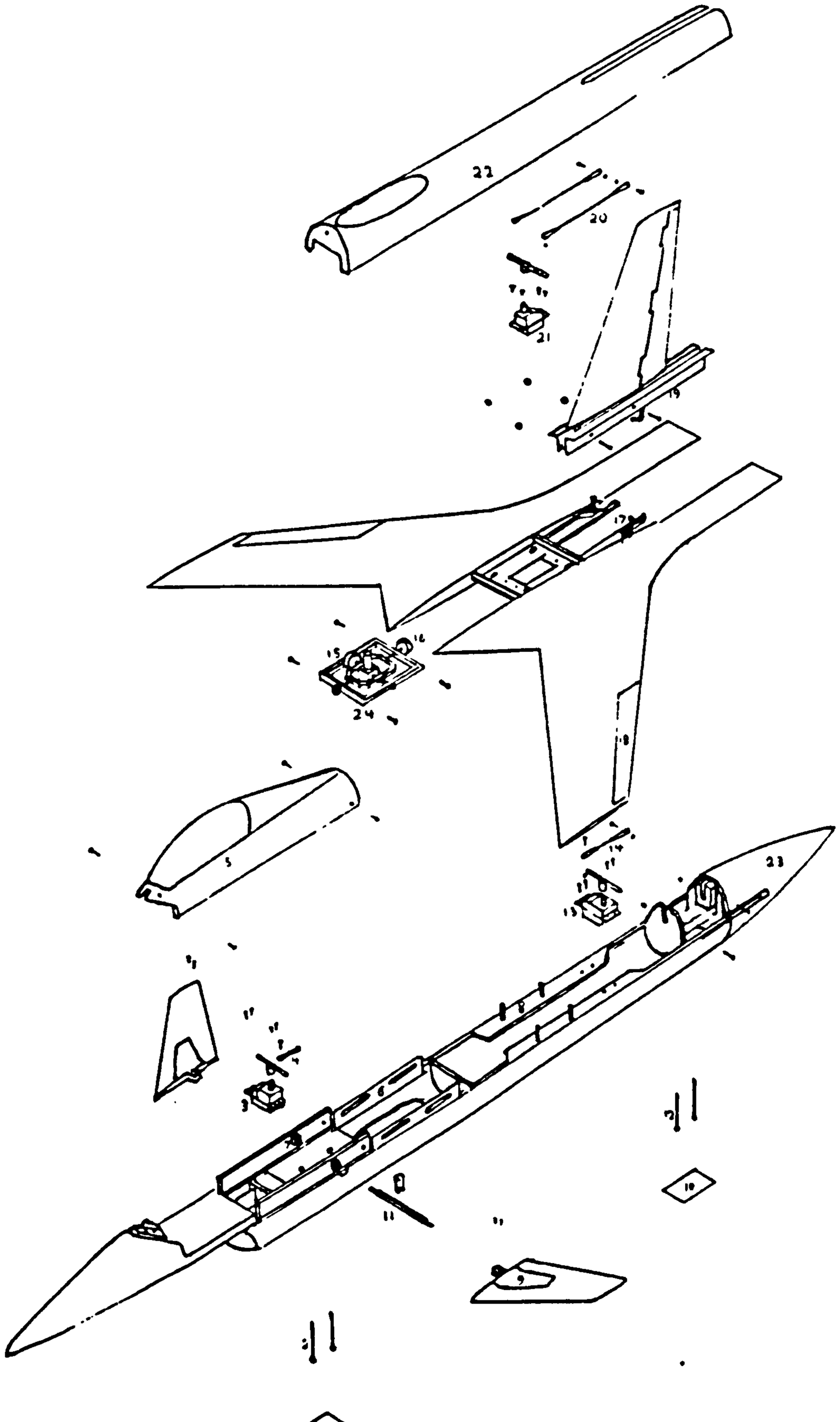

1. Front Ballast Bay Cover
2. Front Ballast Support Bolts
3. Canard Actuator
4. Canard Actuator Rod
5. Canopy Module
6. Gimbol Support Bracket
7. Support Bearing
8. FSW Fuselage Mountings
9. Canard Surface
10. Aft Ballast Bay Cover
11. Canard Rotation Shaft
12. Aft Ballast Support Bolts
13. Rudder Actuator
14. Rudder Actuator Rod
15. Pitch Pot
16. Roll Pot
17. Aileron Rotation Arm (See Ref.Drawing-1)
18. Aileron Mounting (See Ref.Drawing 1)
19. Fin & Rudder Mounting Brackets
20. Aileron Actuator Rods
21. Aileron Actuator
22. Aft Fuselage Top Cover
23. Boat Tail
24. Gimbol System

FIGURE D1: Exploded View of the Dynamic Model

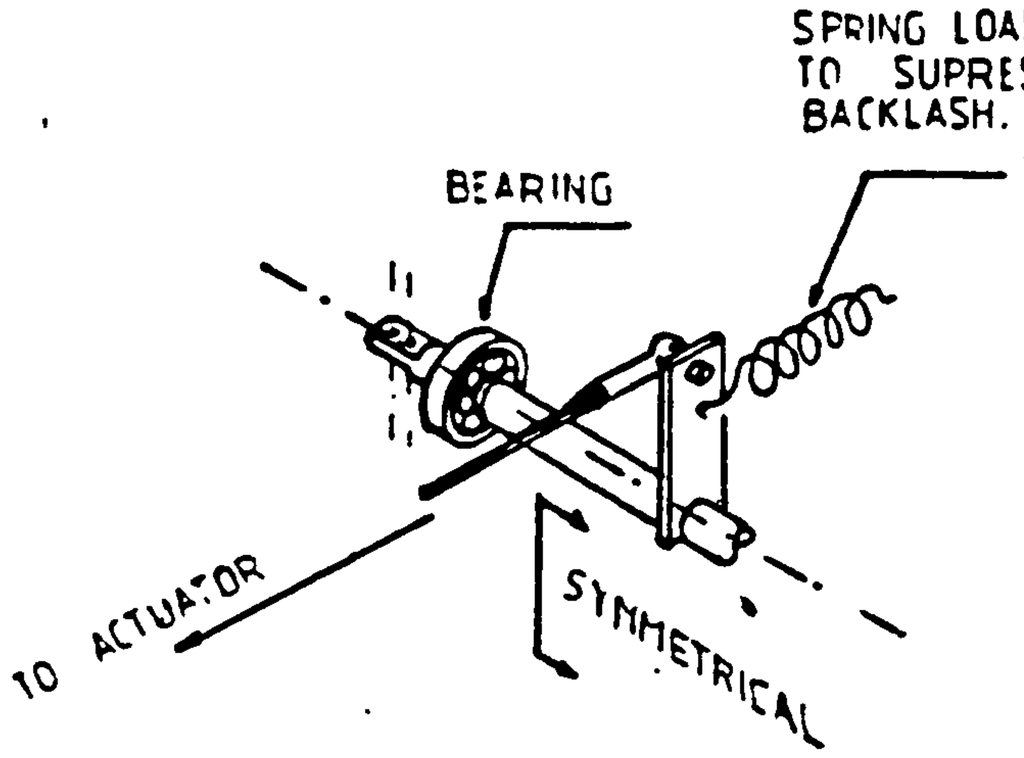

DETAILS OF CANARD ASSEMBLY.

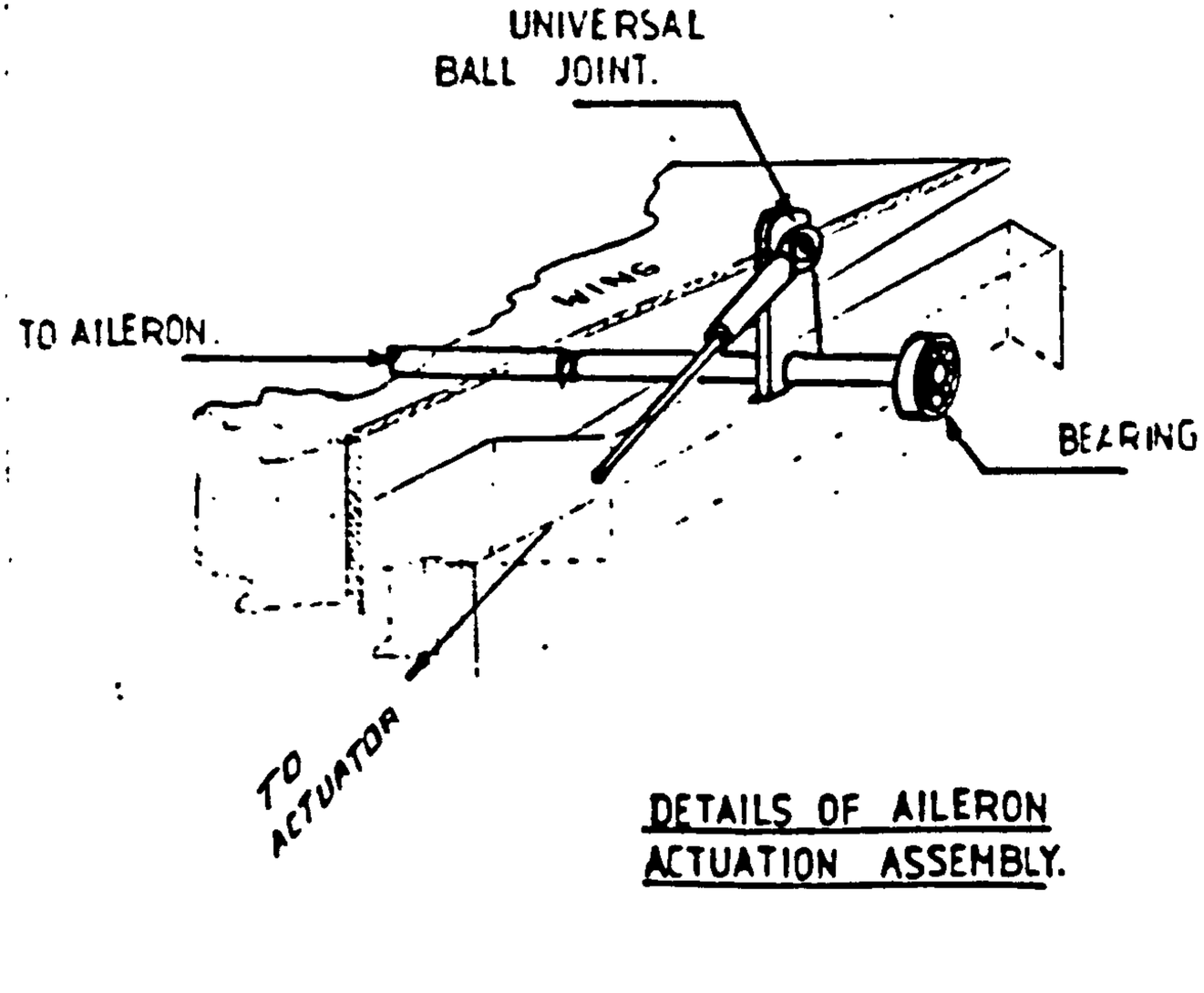

DETAILS OF AILERON
ACTUATION ASSEMBLY.

FIGURE D1: Supplement

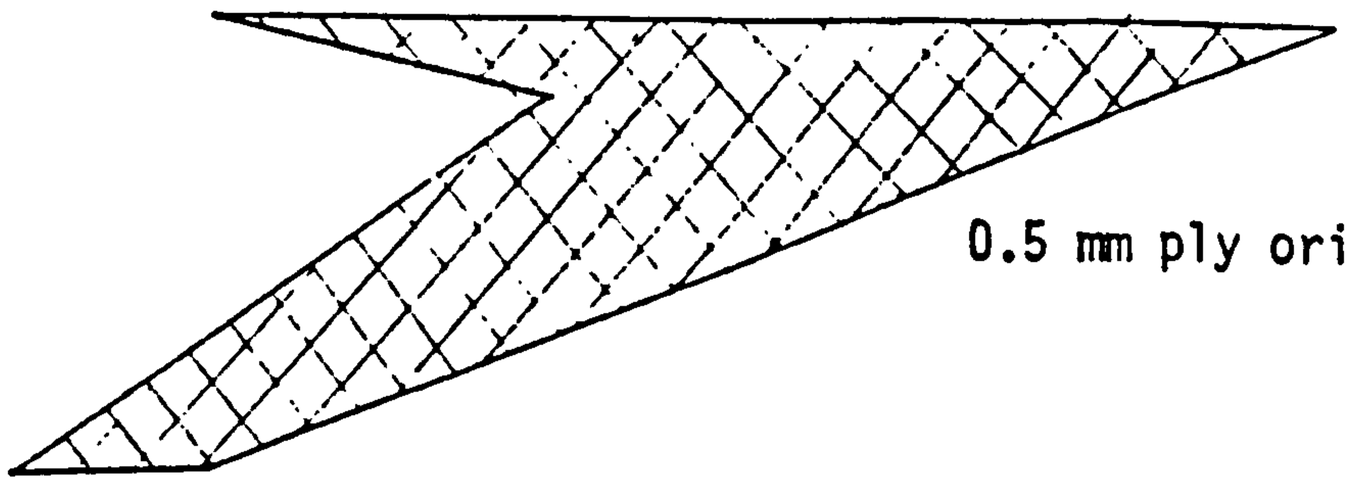

0.5 mm ply orientation
±45°

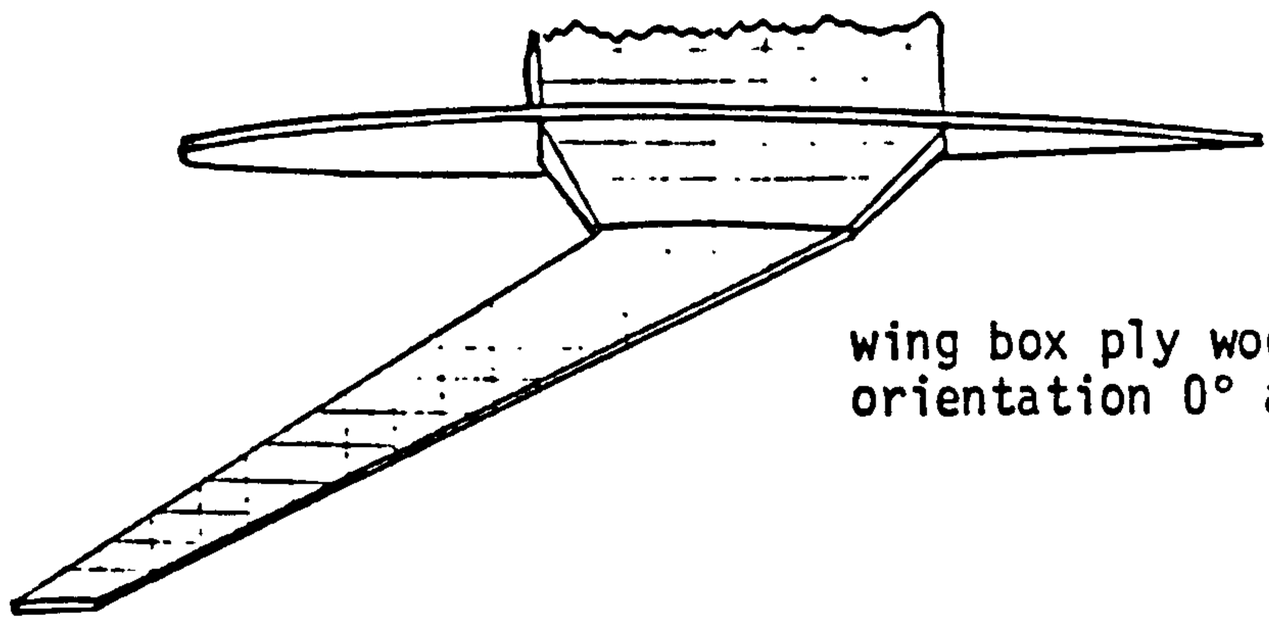

wing box ply wood
orientation 0° and 90°

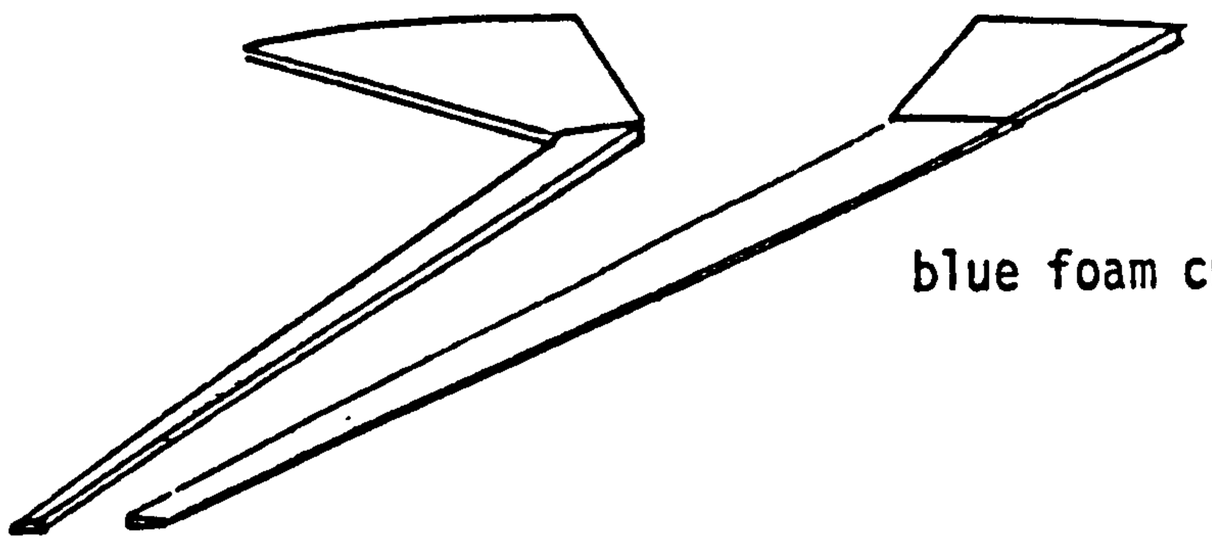

blue foam cut by hot wire

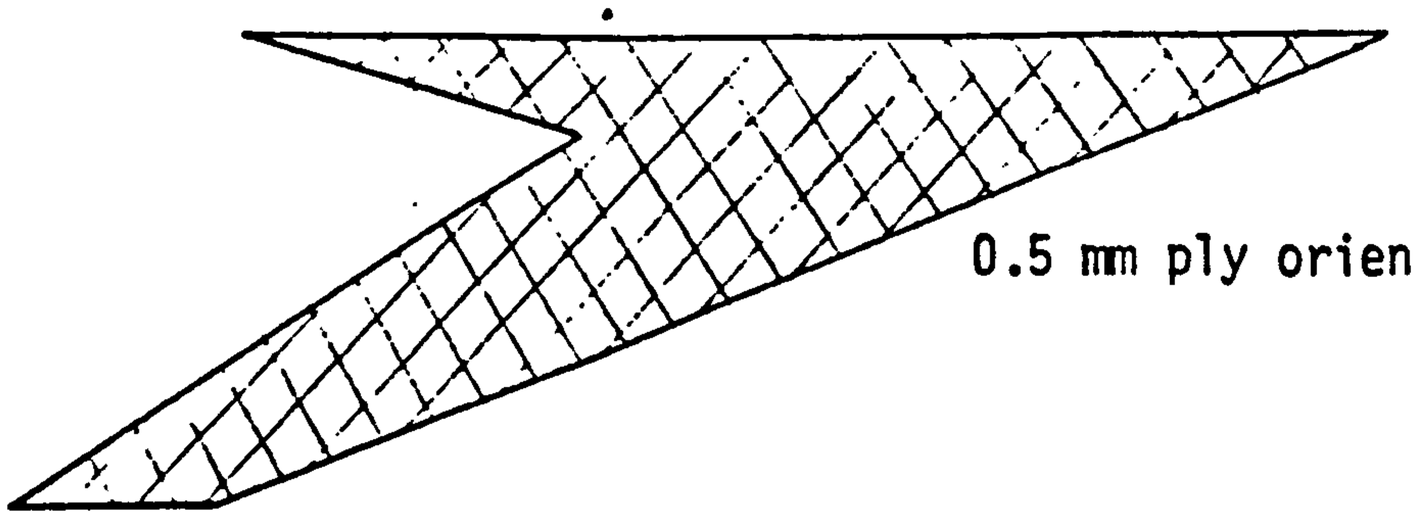

0.5 mm ply orientation
±45°

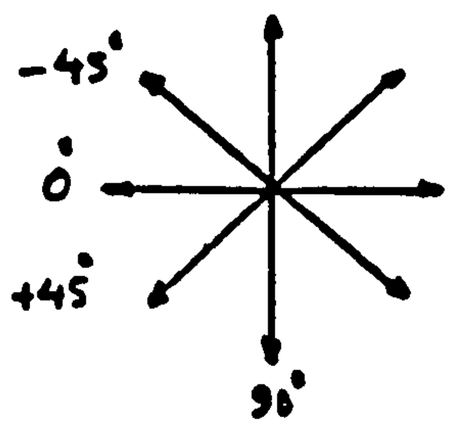

ORIENTATION

FIGURE 02: F.S.W. STRUCTURE

SUMMARY OF AIRCRAFT AND 1/14th SCALE MODEL DIMENSIONS

WING-SECTION Outer NACA 65-206 Inner NACA 66-206	A/C	MODEL
Area (gross) m^2	20.0	0.102
Full span m	9.0	0.65
¼ chord line sweep Λ^o	-45^o	-45^o
Distance of a.c. of half wing from $\mathcal{C}_L$ m	1.85	0.13
Mean aerodynamic chord m	2.35	0.17
Aspect ratio	4.0	4.0
Taper ratio	0.4	0.4
Root chord m	3.16	0.23
Tip chord m	1.27	0.09
Zero-lift angle α_o^o	-1.8^o	-1.8^o

CANARD-SECTION NACA 65-006	A/C	MODEL
Area (Gross) m^2	5	0.026
Full span m	3.92	0.28
L.E. sweep Λ^o	45^o	45^o
Mean aerodynamic chord m	1.34	0.096
Aspect ratio	3.0	3.0
Taper ratio	0.5	0.5
Root chord m	1.72	0.123
Tip chord m	0.86	0.061

FIN + RUDDER SECTION NACA 65-006	A/C	MODEL
Area (gross) m^2	5.49	0.028
Span m	3.64	0.26
L.E. sweep Λ^o	45^o	45^o
Mean aerodynamic chord m	1.96	0.14
Taper ratio	0.43	0.43
Aspect ratio	1.6	1.6
Root chord	2.62	0.19
Tip chord	1.12	0.08

TABLE D1

(cont. over)

FUSELAGE	A/C	MODEL
Length m	14.0	1.0
Fineness ratio	0.1	0.1

TABLE D1 (continued)

CONTROL SURFACE DEFLECTION (deg)	CANARD REF O/P (volt)	AILERON REF O/P (volt)	RUDDER REF O/P (volt)
5	-0.125	-0.075	0.15
10	-0.25	-0.15	0.3
15	-0.375	-0.225	0.45
20	-0.5	-0.3	0.6
SCALES	0.025 v/deg	0.015 v/deg	0.03 v/deg

TABLE D2

ATTITUDE INDICATORS DEFLECTION (deg)	PITCH (volt)	ROLL (volt)	YAW (volt)
0	0.0	0.0	0.0
10	1.5	1.5	1.5
20	3.0	3.0	3.0
30	4.5	4.5	4.5
SCALES	0.15 v/deg	0.15 v/deg	0.15 v/deg

TABLE D3

VERTICAL HEIGHT (m)	REFERENCE VOLTAGE (volt)
0.0	0.0
0.1	0.8
0.2	1.6
0.3	2.4
0.4	3.2

TABLE D4

CALIBRATION TABLES

CANARD CALIBRATION CURVE

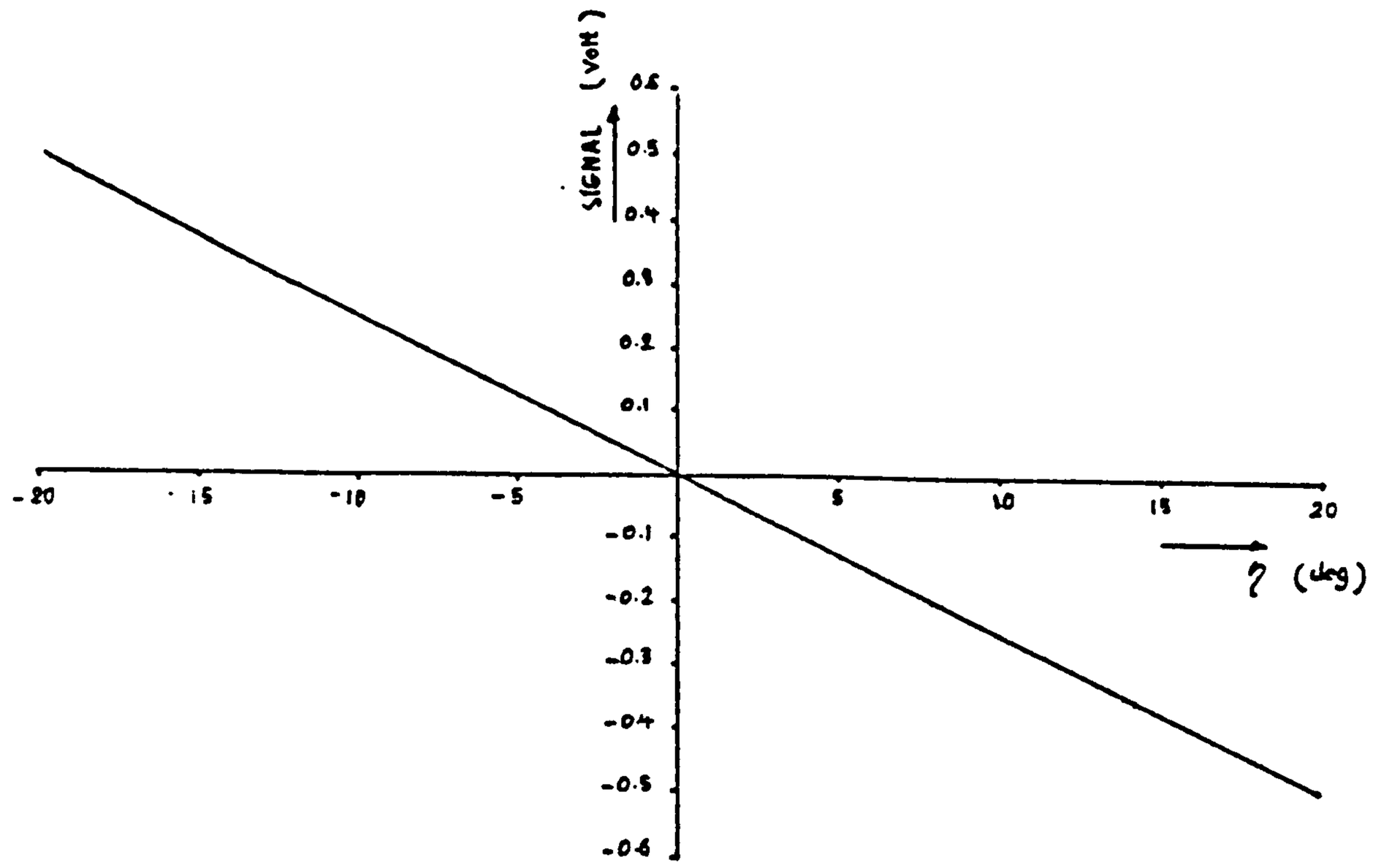

FIG.D3

RUDDER CALIBRATION CURVE

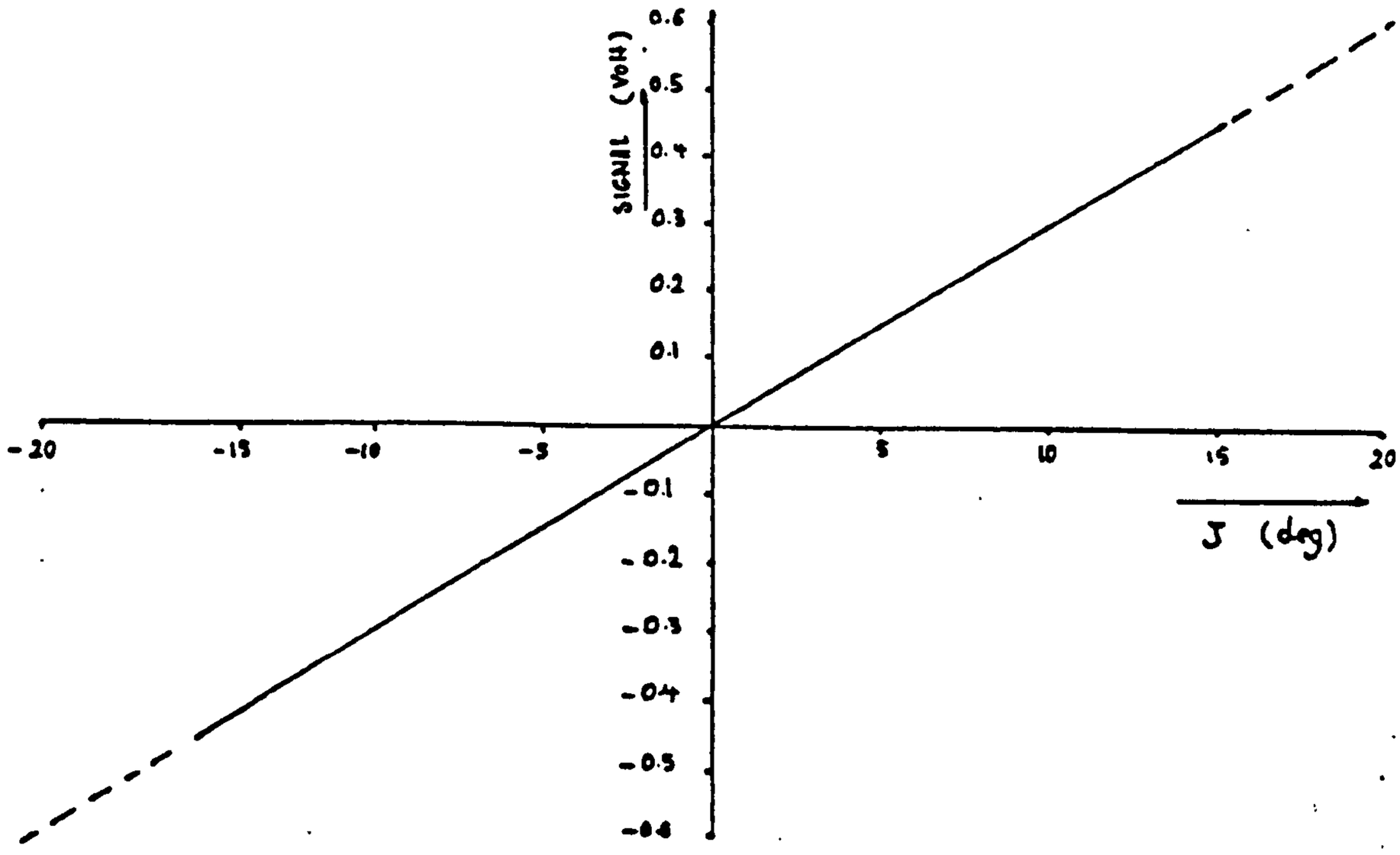

FIG. D4

AILERON CALIBRATION CURVE

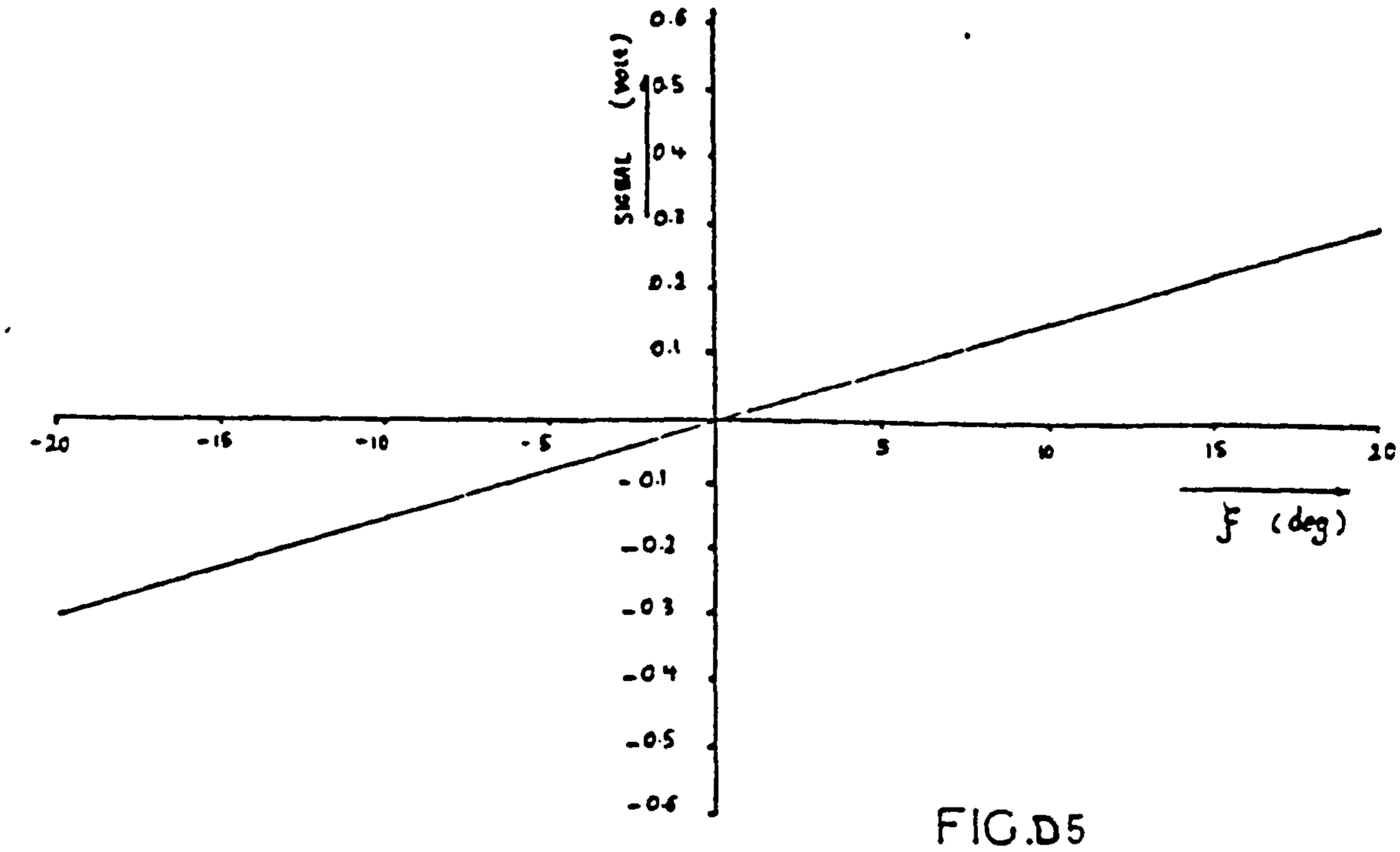

FIG.D5

The calibration of the above plots was conducted with the model suspended on the test rig. An inclinometer and suitable scale + pointer arrangements were employed to find attitude changes versus the output voltage from signal conditioning amplifiers.

SKYLEADER SRC 4BB (ROTORY SERVO)

SIZE AND WEIGHT

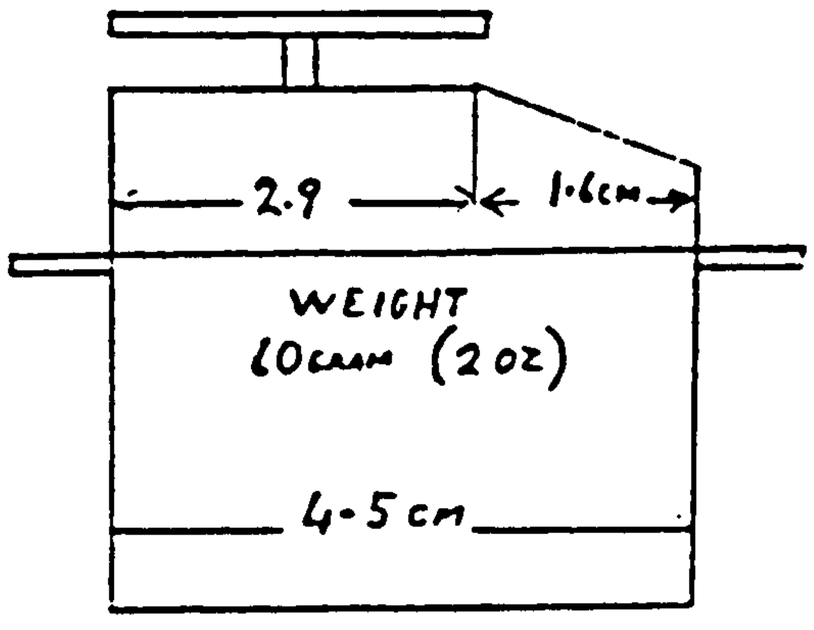

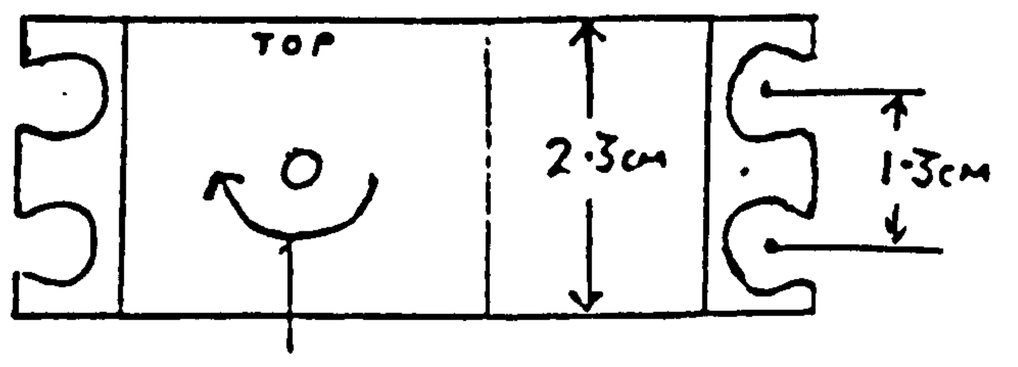

XRAE 01 DIAGRAM

SERVOS

ISSUE 1 DATE 29 9 82

PROVISIONAL TEST RESULTS OF EVALUATION.

RESULTS OF TESTS ON ONE DEVICE (SUPPLY VOLTS = 5V)	VALUE
CURRENT NO LOAD NOT MOVEING	6 mA
CURRENT NO LOAD MOVEING	200 mA
CURRENT STARTING AND STALL	900 mA
CURRENT PEAK (MOTOR REVERSAL AND OVERSHOOT CORRECTION SPIKES)	1 AMP
NO LOAD SPEED	200°/SEC
EFFECT OF INPUT PULSE	103°/ms
TOTAL MOVEMENT	220°
WORKING RANGE OF INPUT PULSE (OUT OF RANGE CAUSES STALL)	0.28ms TO 2.25ms
MAXIMUM TORQUE SERVO CAN MOVE	0.34N/m
MAXIMUM TORQUE SERVO CAN HOLD	OVER 0.46N/M
MAXIMUM TORQUE SERVO CAN HOLD (NO SUPPLY OR INPUT PULSE)	0.14N/M

TABLE D5: SPECIFICATION OF THE SERVO-ACTUATORS

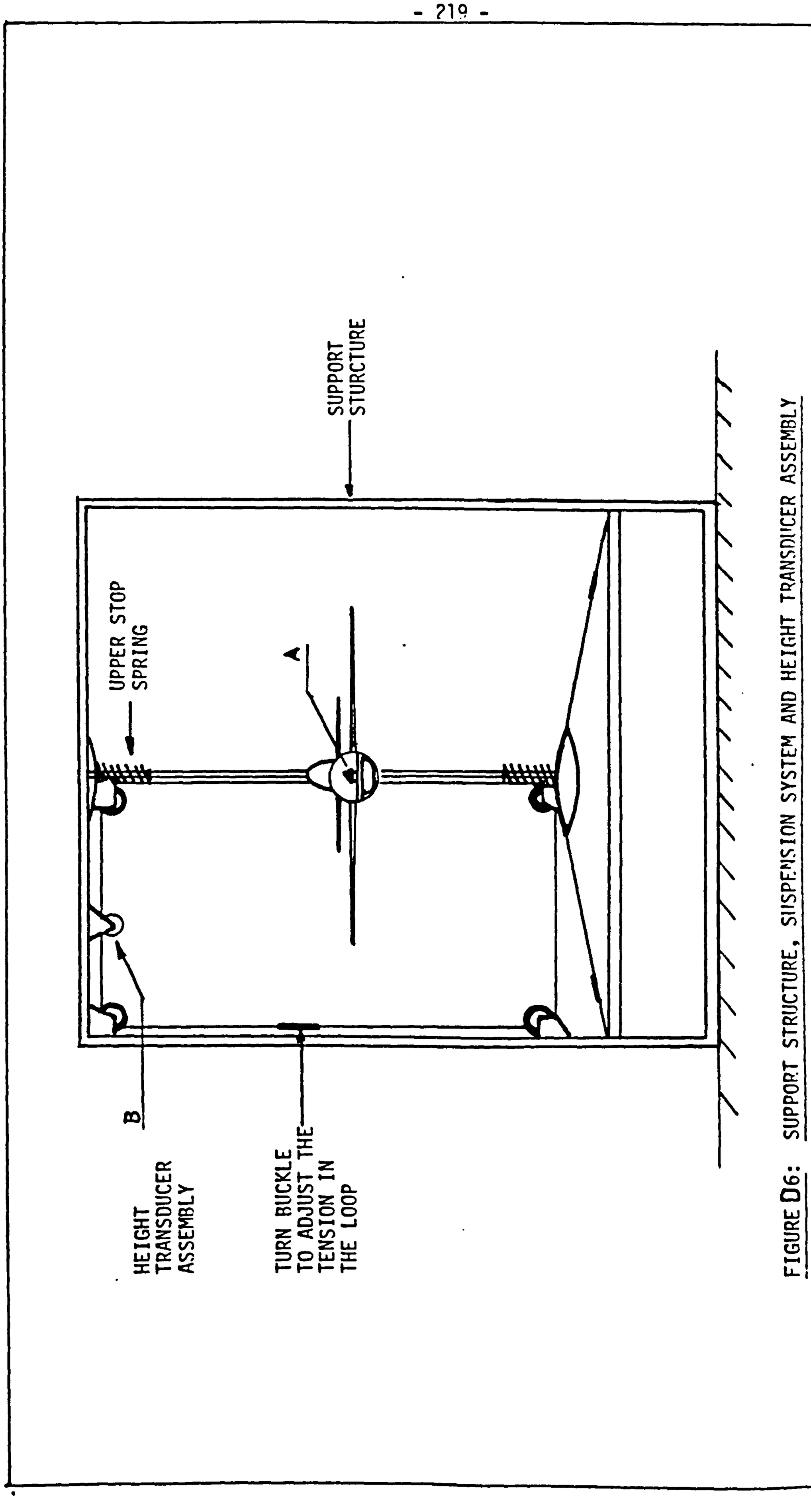
SUPPORT STURCTURE
UPPER STOP
SPRING
A
B
HEIGHT TRANSDUCER ASSEMBLY
TURN BUCKLE TO ADJUST THE TENSION IN THE LOOP
SUPPORT STRUCTURE, SUSPENSION SYSTEM AND HEIGHT TRANSDUCER ASSEMBLY

FIGURE D6:

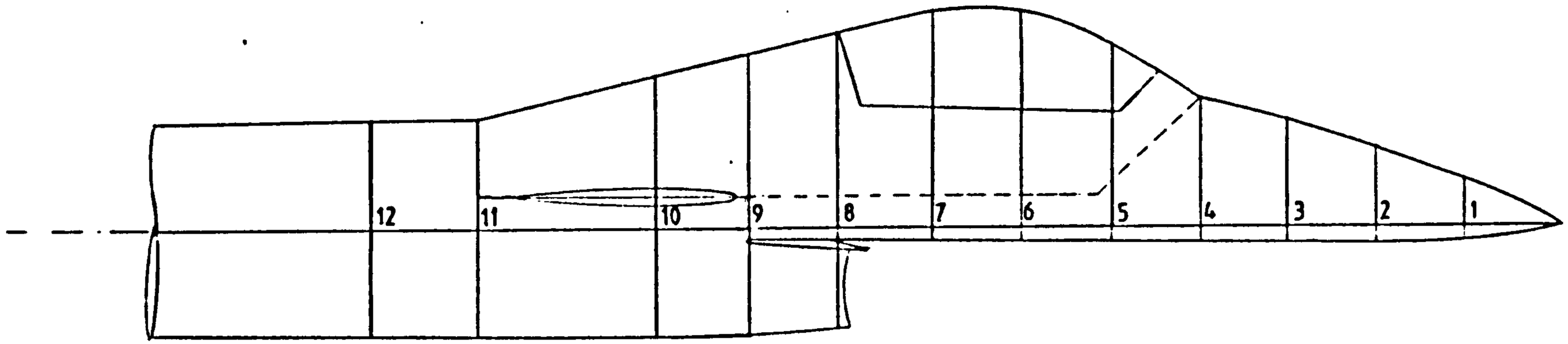

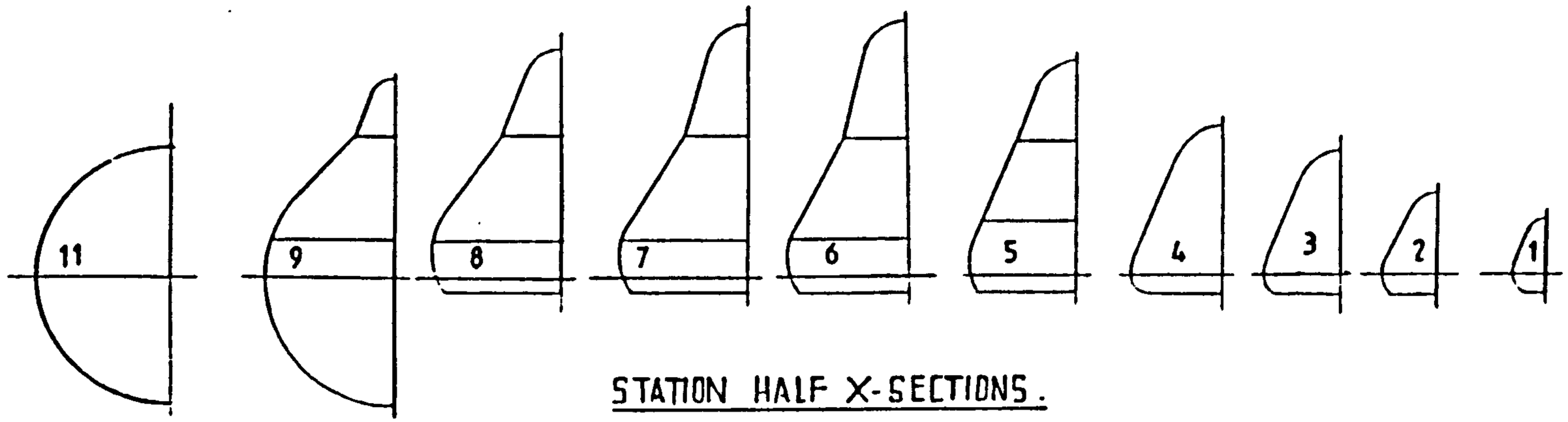

STATION HALF X-SECTIONS.

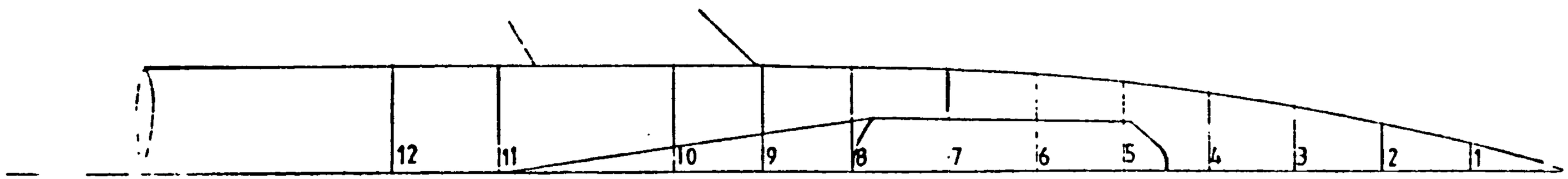

FIG.D7: X-REFERENCE OF NON-CIRCULAR FRONT FUSELAGE.

KEY TO CUTAWAY DRAWING.

1 - wing
2 - canard
3 - fin + rudder
4 - front and rear fuselage sections
5 - U/C
6 - engine F100-pw-100
7 - intake and support structure
8 - internal duct
9 - fuel cells
10 - fuel support structure
11 - dump and drain
12 - the actuators, hydraulic and pneumatics
13 - engine controls
14 - flight instruments
15 - engine instruments
16 - electrics
17 - miscellaneous indicators
18 - the pilot
19 - ejection seat
20 - airconditioning equipment
21 - emergency equipment
22 - gun
23 - avionics
24 - sidewinder missiles

25 - fuselage fuel
26 - wing fuel
27 - radar

Table 8 lists these components together with their respective distances from x, y and z axes.

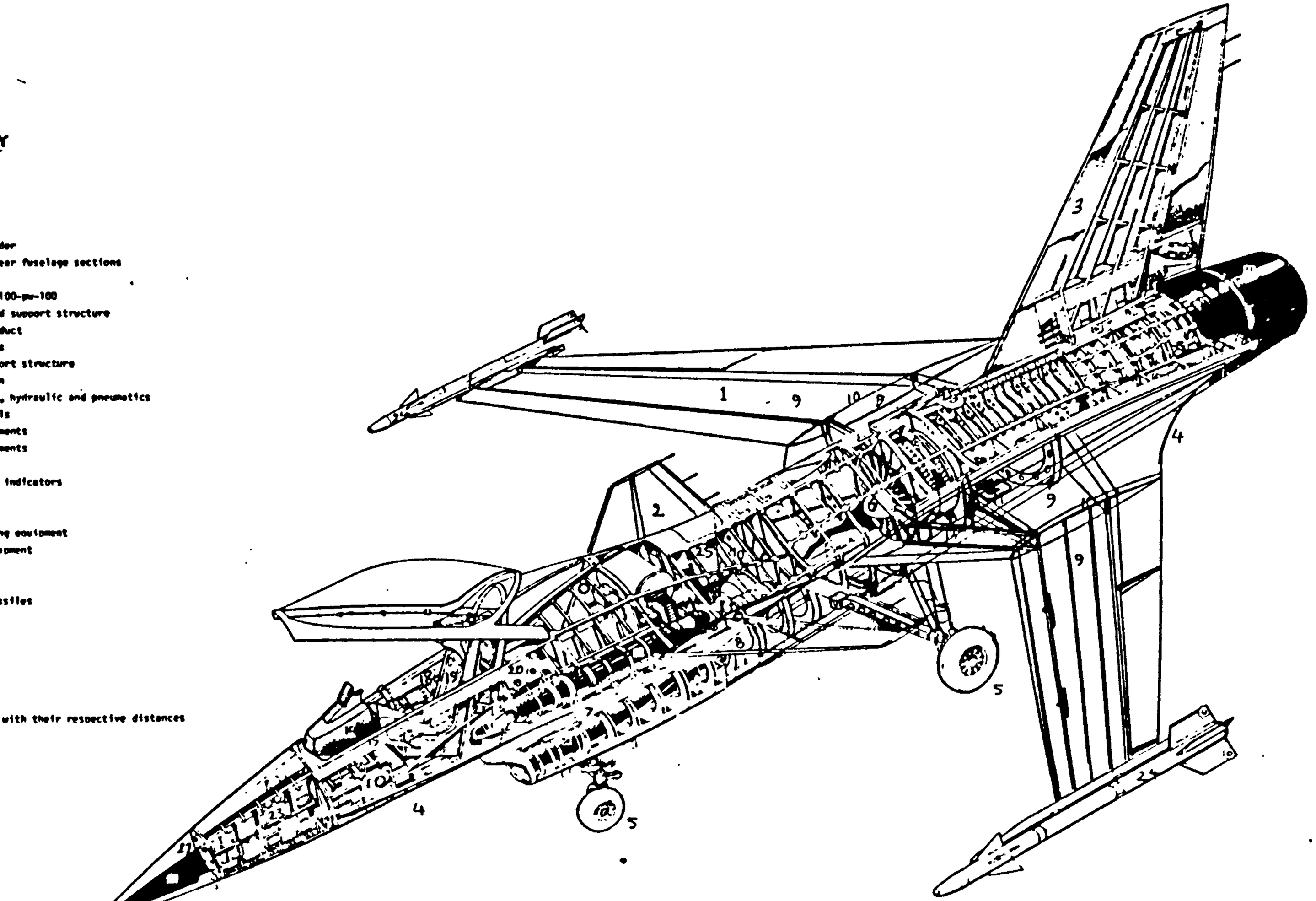

FIG. D8 (TAKEN FROM REF . 35)

CUTAWAY DRAWING OF 'FARJAN' F.S.W A/C BASED ON THE GENERAL DYNAMICS F.16 (Ref. 35) ILLUSTRATING COMPONENT PLACEMENTS.

APPENDIX-E: Estimation of Principal Moments of Inertia I_{xx}, I_{yy}, I_{zz}, Trim C_D, C_L, C_m and Stability Derivatives of the Dynamic Model.

In order to estimate the moments of inertia namely, I_{xx}, I_{yy}, I_{zz}, Table (H-1) was constructed in which the masses of different components are multiplied by the square of their respective distances from their centres of gravity. However, this is inaccurate in itself and therefore parallel and perpendicular axis theorems were used whereever necessary.

All masses are in 'kg'.
All dimensions are in 'm'. unless otherwise stated.

E.1 Moment of Inertia Calculations

Assuming uniform density, the following calculations were made.

..1.1 WING MOMENT OF INERTIA

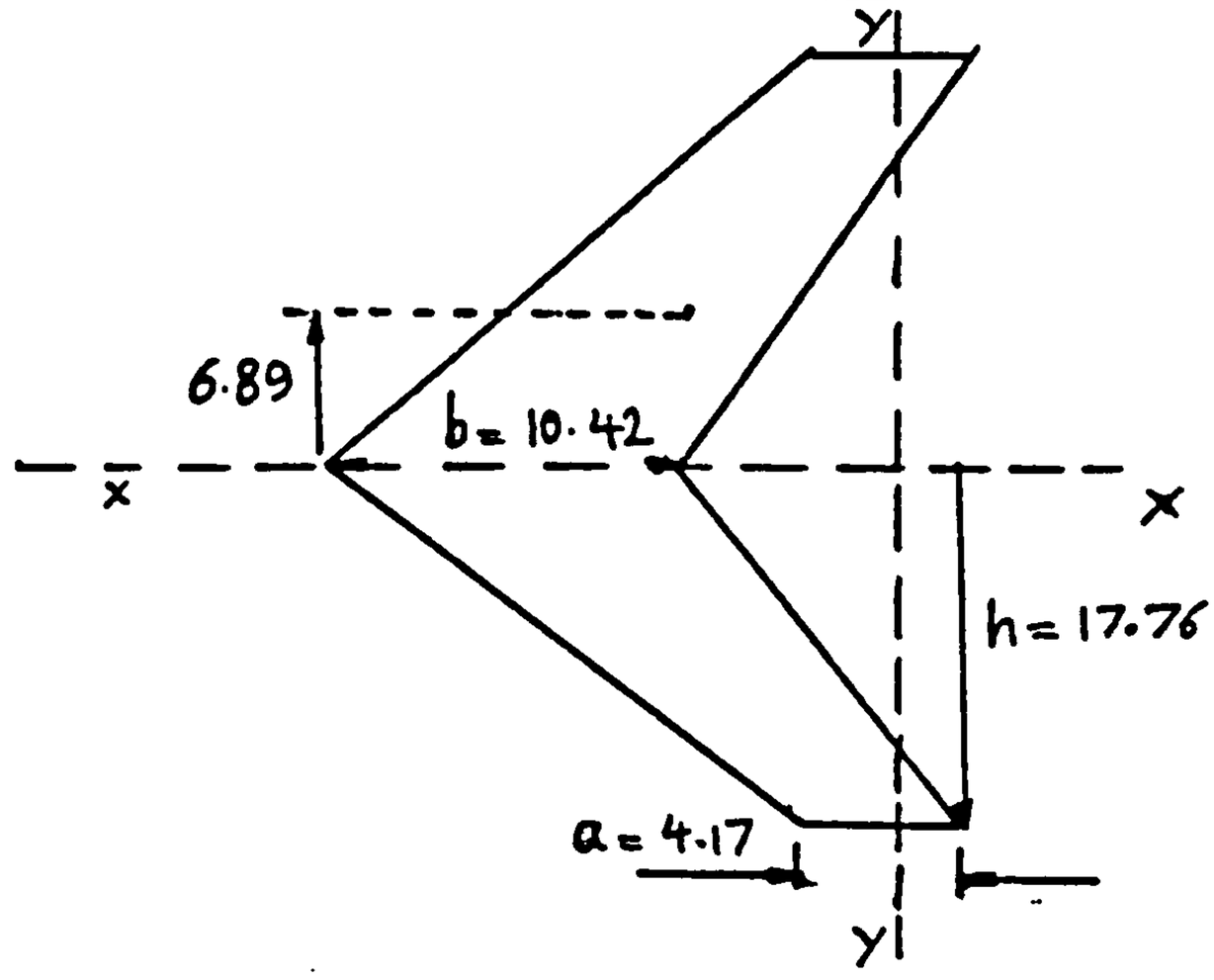

$$I_{xx} \approx M_w\left(\frac{h^2(a^2 + 4ab + b^2)}{18(a + b)^2} + 6.89^2\right)$$

$$I_{xx} \approx 2178.01\left(\frac{17.76^2(4.17^2 + 4 \times 4.17 \times 10.4 + 10.4^2)}{18(4.17 + 10.4)^2} + 6.89^2\right)$$

$$\approx 6622.5 \text{ kg m}^2$$

To estimate I_{yy}, wing was transformed into the following planform.

Where,

$$b = 4.17 + \left(\frac{10.4 - 4.17)}{2}\right)$$

Then I_{yy} is given by the standard formulae,

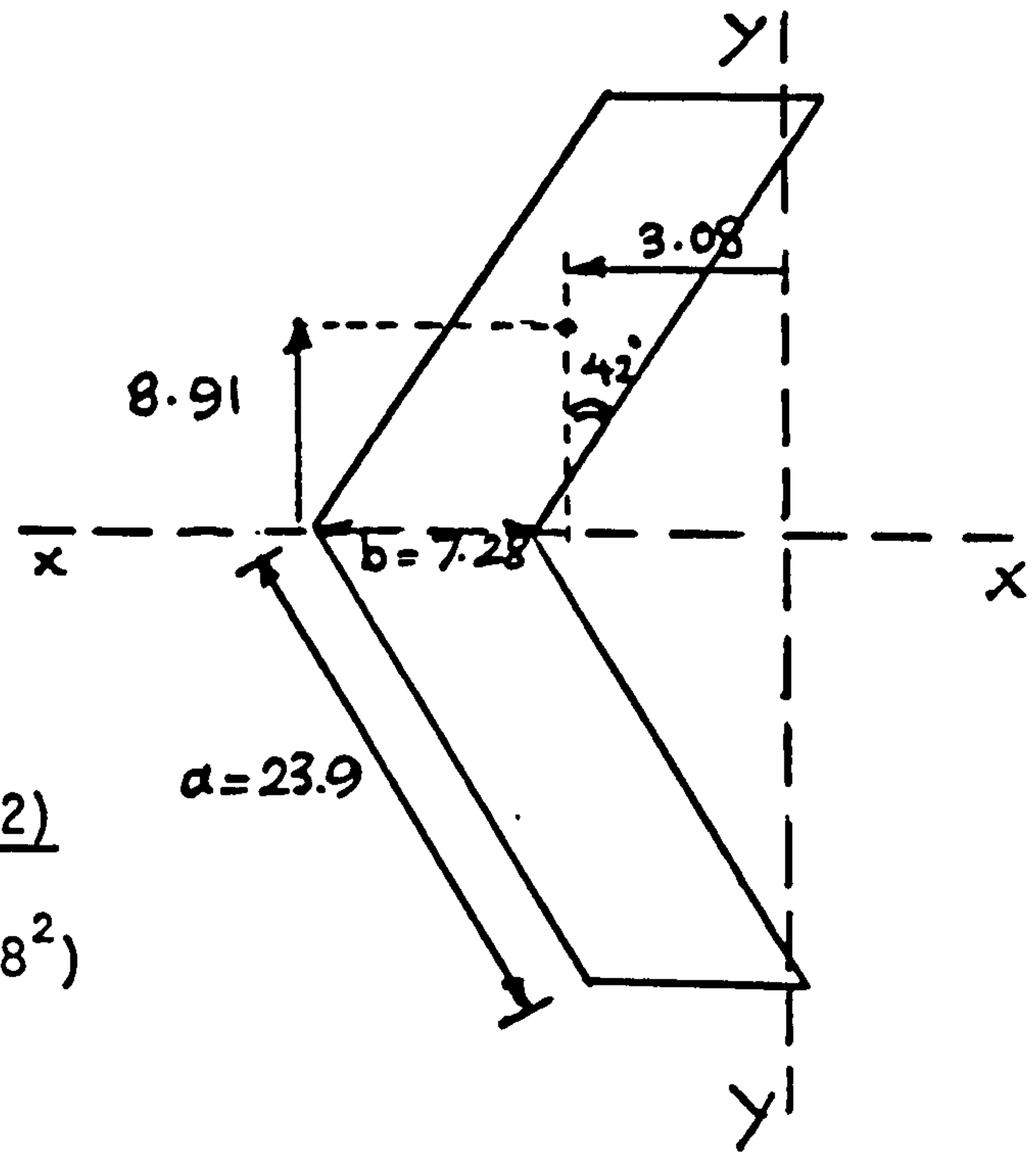

$$I_{yy} \approx M_w\left(\frac{b^2 + a^2\text{Cos}^2(42)}{12} + 4.88^2\right)$$

$$\approx 2178.01\left(\frac{7.28^2 + 23.9^2\text{Cos}^2(42)}{12} + 3.08^2\right)$$

$$\approx 3688.8 \text{ kg}\cdot\text{m}^2$$

By the application of perpendicular axis theorem

$I_{zz} \approx 244691.04$ lb ft^2

CANARD MOMENTS OF INERTIA

$$I_{xx} = M_c\left(\frac{h^2(a^2 + 4ab + b^2)}{18(a + b)^2}\right) + 2.22^2)$$

$$= 216.91\left(\frac{6.35^2(2.82^2 + 4 \times 2.82 \times 5.64 + 5.64^2)}{18(2.82 + 5.64)^2}\right.$$

$$\left. + 2.22^2\right.$$

$$= \quad 74.6 \text{ kg m}^2$$

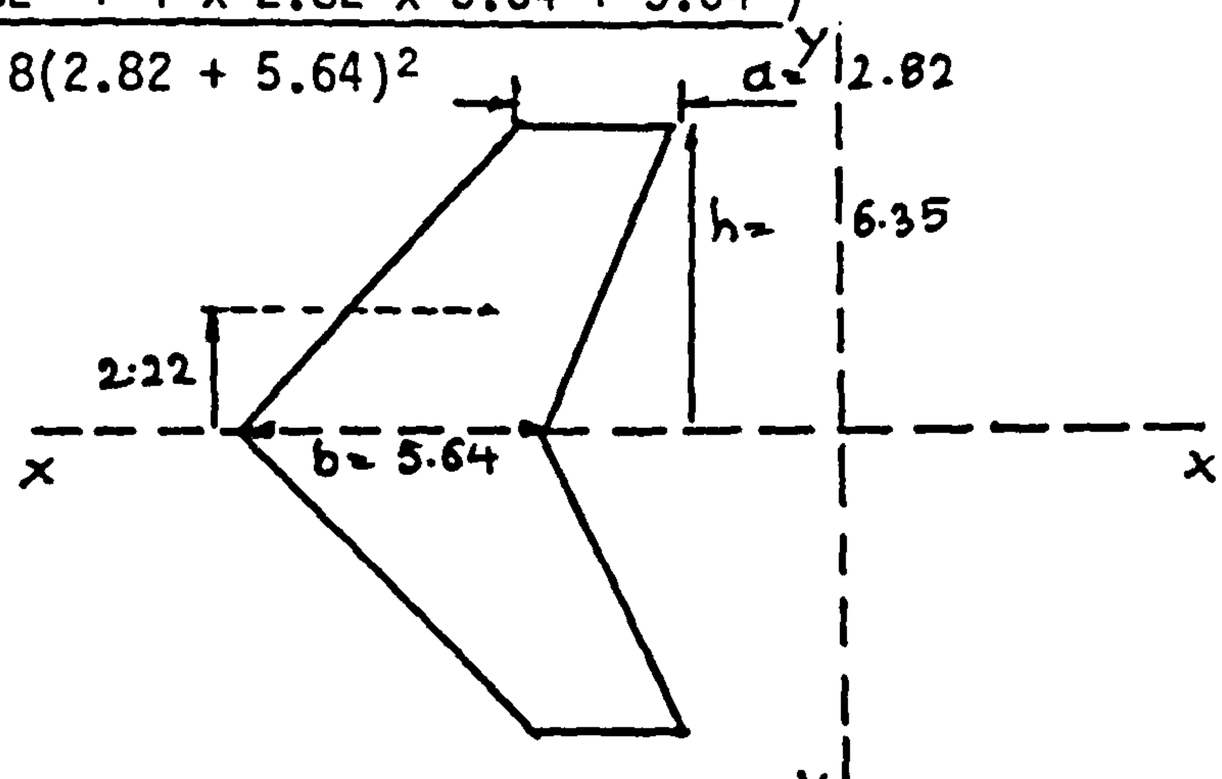

In order to estimate I_{yy}, canard planform was replaced by the following planform.

Where,

$$b = \left(\frac{5.64 - 2.82}{2}\right) + 2.82$$

$$I_{yy} = M\left(\frac{b^2 + a^2\text{Cos}^2(45)}{12} + 7.52^2\right)$$

$$= 216.91\left(\frac{4.23^2 + 8.98^2\text{Cos}^2(45)}{12}\right.$$

$$\left. + 7.52^2\right)$$

$$= 561.2 \text{ kg m}^2$$

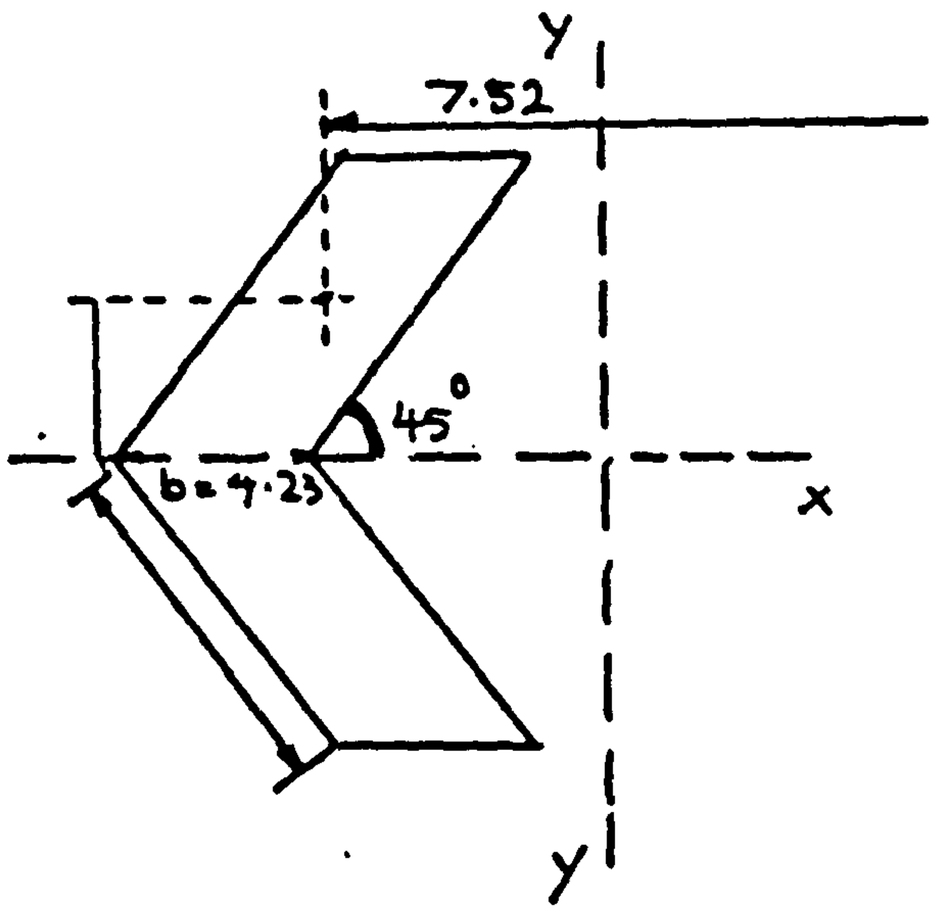

By the application of perpendicular axis theorem, I_{zz} was found to be,

$$I_{zz} \approx 635.9 \text{ kg m}^2$$

Text cut off in original

E.1.2 MOMENT OF INERTIA OF FIN + RUDDER

I_{xx} is given by:

$$I_{xx} = 357.38\left(\frac{9.82^2(3.69^2 + 4 \times 3.69 \times 8.58 + 8.58^2)}{18(3.69 + 8.58)^2} + 5.81^2\right)$$

$$= 623.0 \text{ kgm}^2$$

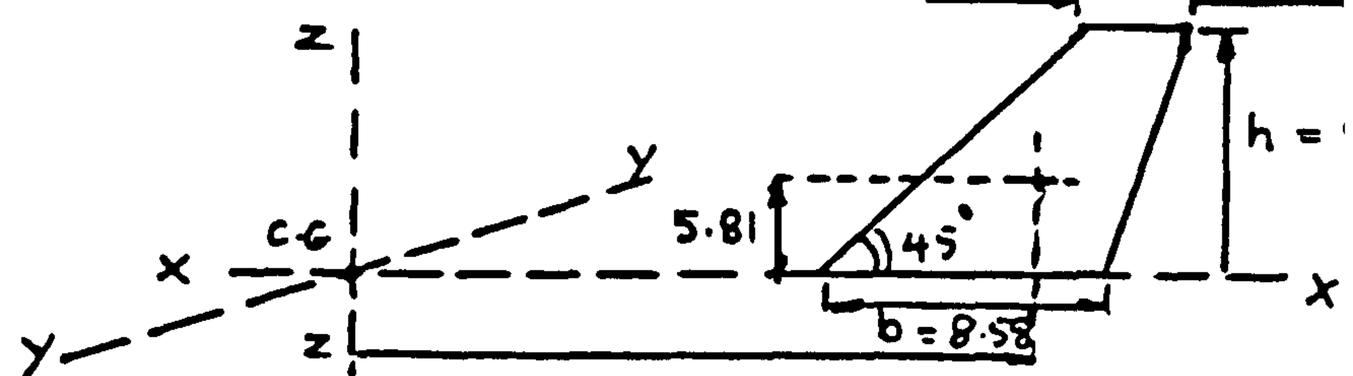

In order to estimate I_{zz}, fin + rudder planform was transformed into the following shape.

$$b = \frac{(8.58 - 3.69)}{2} + 3.69$$

$$= 6.13 \text{ ft.}$$

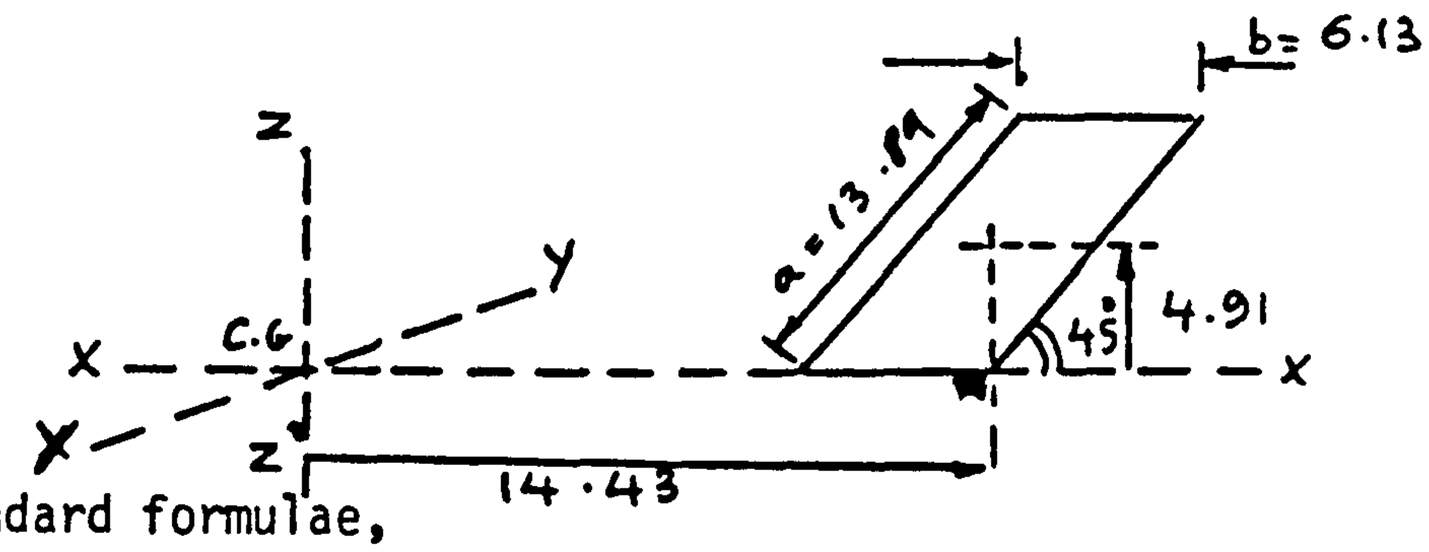

I_{zz} is then given by the standard formulae,

$$I_{zz} = 357.38\left(\frac{6.13^2 + 13.89^2\text{Cos}^2(45)}{12} + 14.4^2\right)$$

$$= 3291.1 \text{ kgm}^2$$

E.1.3 MOMENT OF INERTIA OF FUSELAGE

Assume fuselage to be a right-hollow circular cylinder of diameter 3.7 ft, which is the average width of our fuselage. Length of 45.93 ft.

Then I_{yy} is given by

$$I_{yy} = M_f\left(\frac{6a^2 + h^2}{12}\right)$$

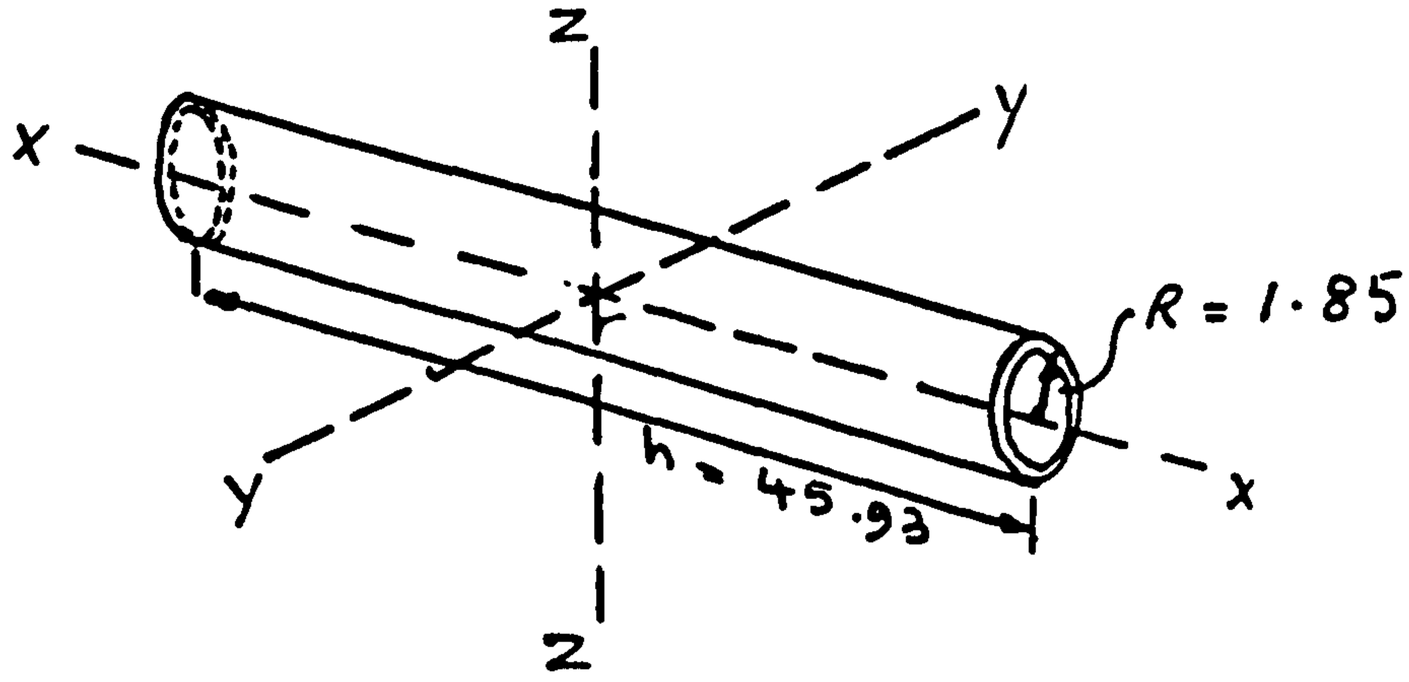

$$\simeq 5397.98\left(\frac{6 \times 1.87^2 + 45.93^2}{12}\right)$$

$$\simeq 40386.4 \text{ kgm}^2$$

and I_{xx} by,

$$I_{xx} \simeq M_f.R^2$$

$$\simeq 5397.98 \times 1.87^2 = 18876.20 \text{ lb ft}^2$$

Also

$$I_{zz} = I_{yy} \simeq 40386.4 \text{ kgm}^2$$

COMPONENT	$\bar{X}$ (m)	$\bar{Y}$ (m)	$\bar{Z}$ (m)	I_{xx} (kgm²)	I_{yy} (kgm²)	I_{zz} (kgm²)	MASS OF THE COMPONENT (kg)
MW	1.23^-	1.83	0	6622.5	3688.8	10311.3	988.0
MC	2.3	0	0.2	74.6	561.2	635.9	98.4
MFR	4.39^-	0	1.77^-	623.0	3291.1	3291.1	162.1
MF1 } ADD	2.44	0	0	} 759.4	} 40386.4	} 40386.4	1049.4
MF2 } ADD	4.56	0	0				1399.2
0.25MUC	2.06	0	0.62	33.3	403.4	370.1	89.9
0.75MUC	0.94^-	$1.75^\pm$	0.62	898.1	329.7	1028.0	260.8
ME	2.62^-	0	0	374.2	2908.0	2908.0	1450.2
MINTS	1.21	0	0.2	2.5	93.8	91.3	62.1
MIND	1.21	0	0.2	4.7	177.1	172.3	117.1
(MFC+MFSS)	1.23^-	0	0.5^-	18.3	127.1	108.8	73.2
MDD	2.44^-	0	0.5^-	2.2	54.3	52.1	8.8
(MAHP+MEC)	1.23^-	0	0.5^-	91.5	635.8	544.3	366.2
MFIN+MEIN	5.21	0	0.29^-	0.8	254.0	253.2	9.3
MELEC	3.82	0	0.1	1.6	2299.5	2297.9	157.8
MMIN	5.21	0	0.3^-	0.1	36.8	36.7	1.4
(MPIL+MEJS)	4.56	0	0.3^-	21.1	4949.8	4928.7	236.7
MACON	3.06	0	0.4^-	10.8	657.9	647.0	69.0
MEMER	4.36	0	0.3^-	1.7	359.8	358.1	18.8
MGUN	2.81	0.55	0	71.6	1883.7	1955.3	238.0
MAVIO	5.21	0	0.3^-	11.9	3634.6	3622.7	133.4
MSW	2.11	$4.65^\pm$	0	4623.6	954.8	5578.4	214.0
MAMRAAM	0.46	$0.6^\pm$	0.6	216.3	172.5	172.5	300.0
MCGC	1.23^-	0	0.5	3.3	20.5	19.7	13.3
TFF*3.637	0.26	0	0.55^-	55.7	68.4	12.7	185.1
69%TWF*3.637	0.47^-	$2.6^\pm$	0	5440.1	177.3	5617.4	804.8
31%TWF*3.637	1.89^-	$0.25^\pm$	0	22.6	1291.2	1313.8	361.6
MRADAR	6.36	0	0.2	3.4	3437.7	3432.3	84.8

$I_{xx} \cong 20025$ kgm²
$I_{yy} \cong 72854$ kgm²
$I_{zz} \cong 90146$ kgm²

TABLE E2

Details of component masses and their moments of inertia

E.2 Dynamic scaling

The aircraft was scaled down 14 times so the linear scaling ratio λ is

$$\lambda = \frac{1}{14}$$

From ref.8

Mass ratio is given by

$$\frac{m_{model}}{m_{A/C}} = \frac{\rho_{model}}{\rho_{A/C}} = \frac{\rho_{A/C}}{\rho_{A/C}} \cdot \lambda^3 = \lambda^3$$

$$\therefore \quad m_{model} = m_{A/C} * \lambda^3 = 3.23 \text{ kg.}$$

Ratio of the moment of inertia is given by

$$I_{model} = I_{A/C} \times \frac{\rho_{model}}{\rho_{A/C}} * \lambda^5$$

From Table H-2

$I_{xx_{model}}$	$\simeq$ 0.037	$kg.m^2$
$I_{yy_{model}}$	$\simeq$ 0.135	$kg.m^2$
$I_{zz_{model}}$	$\simeq$ 0.168	$kg.m^2$

Assuming a maximum tunnel speed of 30 m/s flow Reynolds number is:

$$R_e = \frac{U_{\bar{c}_{model}}}{\gamma} = \frac{30 \times 0.166}{1.461 \times 10^{-5}} \quad 3.4 \times 10^5$$

Trip wire has to be used in order to simulate a realistic air flow over the model.

TABLE E.3 DYNAMIC SIMILARITY PARAMETERS

SCALE FACTOR λ = 14			
PARAMETERS	A/C	MODEL	MEASURED
Mass (kg)	8050.5	3.0	3.0
Density I.S.A., sea level (kg m^{-3})	1.225	1.225	-
Speed (ms^{-1})	102.0	28.0	
Acceleration due to gravity (kg ms^{-2})	9.81	9.81	-
Principal moments of inertia (kg m^2)*			
I_{xx} ,	14841.74	0.028	0.026
I_{yy} ,	68586.7	0.127	0.139
I_{zz}	80957.7	0.15	0.15

PARAMETERS	RELATIONSHIP BETWEEN MODEL AND A/C
Linear displacement	$X_M/X_{A/C} = \lambda$
Angular displacement	$\theta_M/\theta_{A/C} = 1$
Linear velocity	$V_M/V_{A/C} = \frac{\lambda}{\tau}$
Angular velocity	$\dot{\theta}_M/\dot{\theta}_{A/C} = \frac{1}{\tau}$
Linear acceleration	$a_M/a_{A/C} = \frac{\lambda}{\tau^2}$
Angular acceleration	$\ddot{\theta}_M/\ddot{\theta}_{A/C} = \frac{1}{\tau^2}$
Load factor	$n_M/n_{A/C} = \frac{1}{\lambda}(\frac{V_M}{V_{A/C}})^2$
Time .	$\tau = \frac{T_M}{T_{A/C}}$

* Here the model mass and principal moments of inertia were based on the full size aircraft excluding the missile payload.

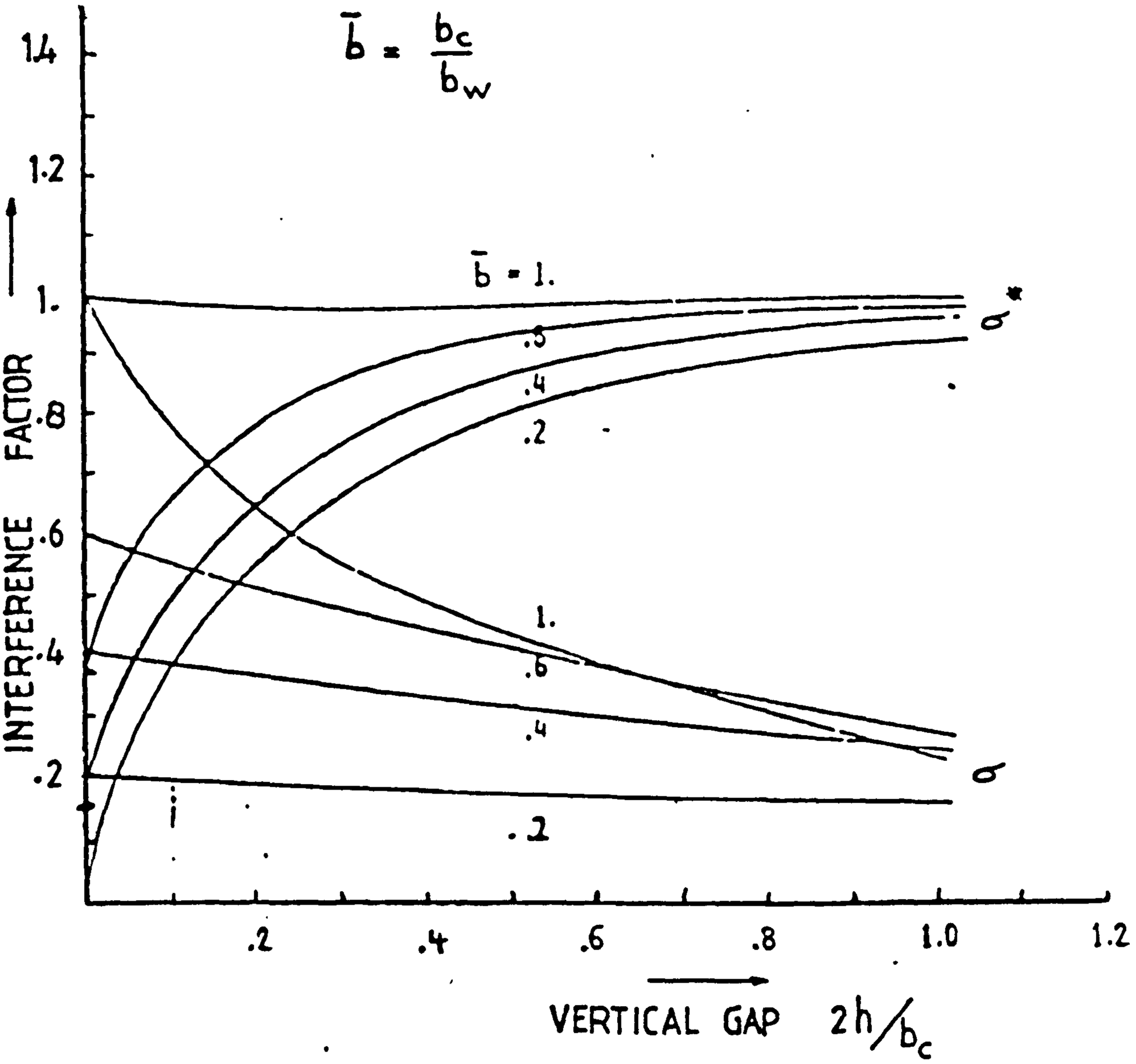

FIGURE E1.: VARIATION OF PRANDTL'S INTERFERENCE FACTOR σ AND NON ELLIPTIC INTERFERENCE FACTOR σ^* WITH NON-DIMENSIONAL VERTICAL GAP. (Ref. 3)

E.3 Evaluation of the Trimmed Flight Conditions

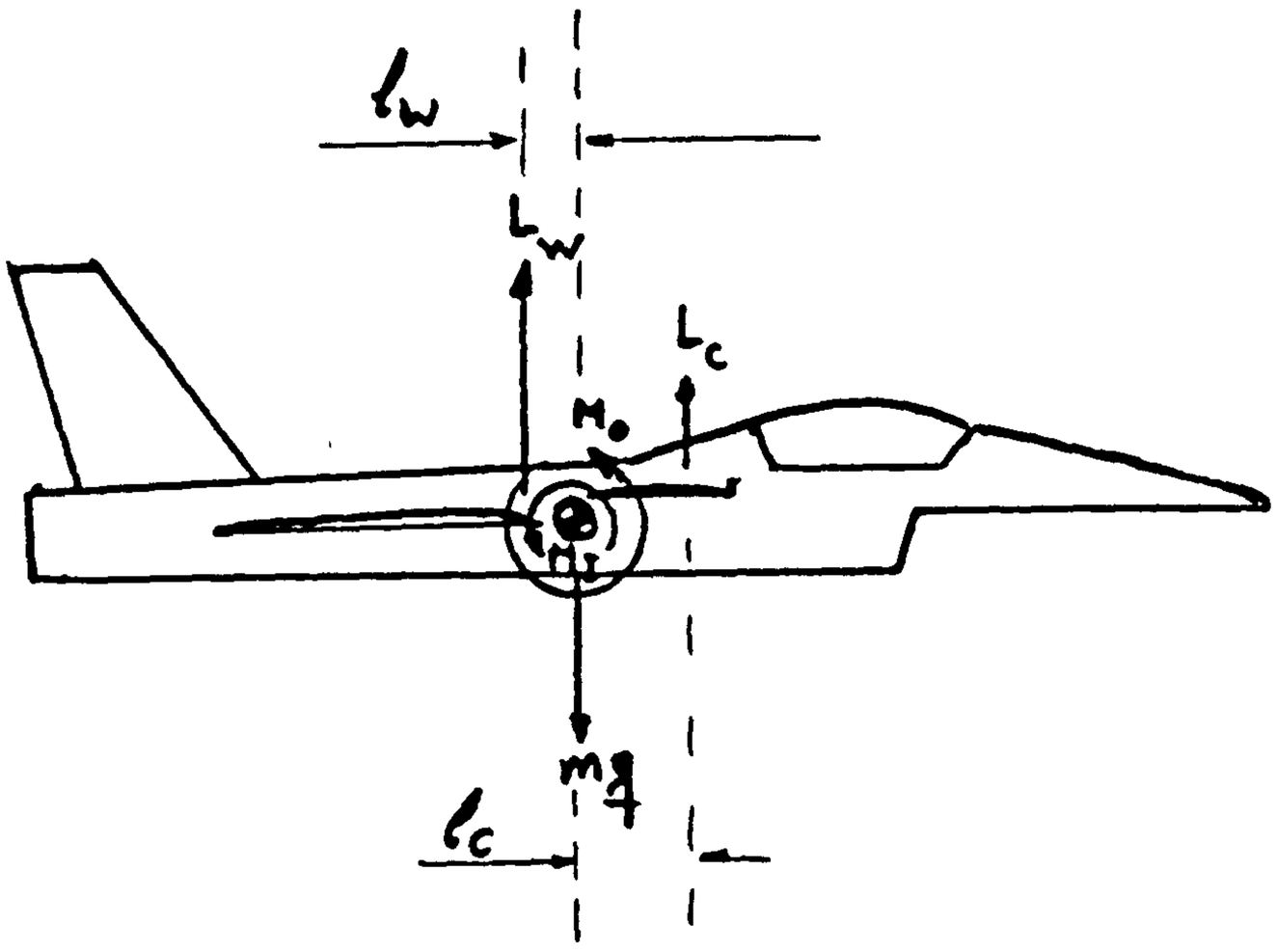

Pitching moment equation for the trim flight is

$$-L_w \ell_w + M_o + L_c \ell_c + M_1 = 0$$

where

ℓ_w = distance between wing-body aerodynamic centre and c.g.

ℓ = distance between canard-body aerodynamic centre and c.g.

Dividing by $\frac{1}{2}\rho V^2 S_w \bar{c}$ we get

$$-C_{L_{W.B.}} \cdot \frac{\ell_w}{\bar{c}} + \epsilon_{m_o} + \frac{S_c \ell_c}{S_w \bar{c}} \cdot C_{L_c} + \left(\frac{dC_M}{d\alpha}\right)_{intake} \cdot \alpha = 0$$

Let $\frac{\ell_w}{\bar{c}} = \ell_w$, $\frac{\ell_c}{\bar{c}} = \ell_c$

Now α is measured from the chord line to direction of free stream, whereas the true wing incidence is $\alpha + \alpha_o$ where for our wing section
$\simeq 1.8^o = 0.03141$ rad $= \alpha_o$

$$-a_{w.b.}\cdot\ell_w\cdot(\alpha+\alpha_o)+C_{m_o}+\frac{S_c}{S_w}\ell_c a_{c.b.}(\alpha+\eta)+\left(\frac{dc_m}{d\alpha}\right)_I\cdot\alpha=0$$

or

$$-a_{w.b.}\cdot\ell_w\cdot\alpha+a_{w.b.}\cdot\ell_w\cdot\alpha_o+C_{m_o}+\frac{S_c}{S_w}\cdot\ell_c\cdot a_{c.b}\cdot(\alpha+\eta)+\left(\frac{dc_m}{d\alpha}\right)_I\cdot\alpha=0$$

or

$$(\alpha+\eta)=\frac{(a_{w.b.}\cdot\ell_w-\left(\frac{dc_m}{d\alpha}\right)_I)\alpha-C_{m_o}+a_{w.b.}\cdot\ell_w\cdot\alpha_o}{\frac{S_c}{S_w}\cdot\ell_c\cdot a_{c.b.}}$$

or

$$(\alpha+\eta)=\left(\frac{a_{w.b.}\cdot\ell_w\cdot S_w}{a_{c.b.}\ell_c\cdot S_c}-\frac{S_w}{S_c\cdot\ell_c\cdot a_{c.b.}}-\left(\frac{dc_m}{d\alpha}\right)_I\right)\alpha-\frac{S_w}{S_c\cdot\ell_c\cdot a_{c.b.}}\cdot C_{m_o}+\frac{a_{w.b.}\ell_w\cdot S_w}{a_{c.b.}\ell_c S_c}\cdot\alpha_o \qquad \text{- - - - - EQ.E}$$

From equilibrium considerations

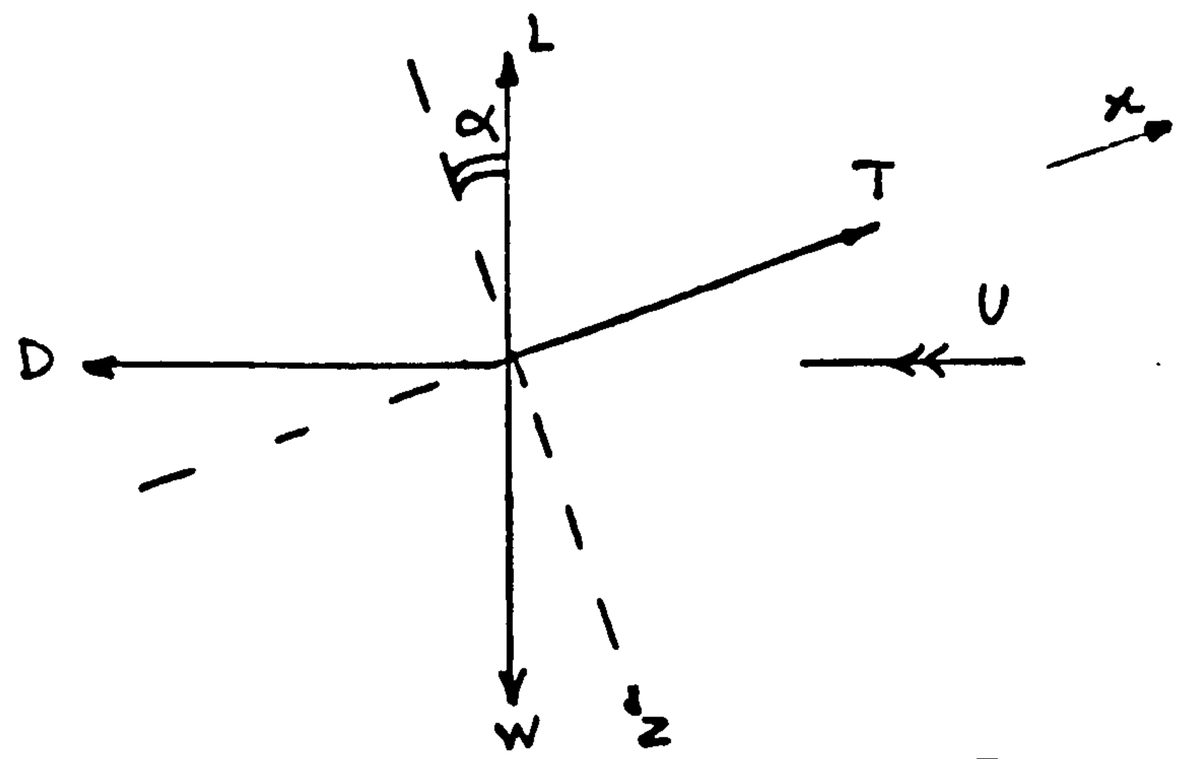

$$W = L + T\sin\alpha$$

$$D = T\cos\alpha$$

Dividing by $\frac{1}{2}\rho V^2 S_W$

$$C_W = a_{c.b.}\left(\frac{S_c}{S_w}\right)(\alpha+\eta)+a_{w.b.}(\alpha+\alpha_o)+C_T\sin\alpha \qquad \text{- - - - EQ.E2}$$

$$C_D = C_T\cos\alpha \qquad \text{- - - - EQ.E3}$$

Substituting for $(\alpha+\eta)$ from E1 in E2, ,

$$C_W = a_{c.b.}\left(\frac{S_c}{S_w}\right)\cdot\left[\left(\frac{a_{w.b.}\ell_w S_w}{a_{c.b.}\ell_c S_c}-\frac{S_w}{S_c\ell_c a_{c.b.}}\cdot\left(\frac{dc_m}{d\alpha}\right)_I\right)\alpha-\frac{S_w}{S_c\ell_c a_{c.b.}}\cdot C_{m_o}+\frac{a_{w.b.}\ell_w\cdot S_w}{a_{c.b.}\ell_c S_c}\cdot\alpha_o\right]+a_{w.b.}(\alpha+\alpha_o)+C_T.\sin\alpha \qquad \text{- - - - EQ.E4}$$

From reference 3 for a canard configuration

$$C_{D_{induced}}=\frac{S_w C_{L_{w.b.}}^2}{\pi b_w^2}+\frac{2S_c\cdot C_{L_{c.b.}}\cdot C_{L_{w.b.}}}{\pi b_c b_w}\sigma+\frac{S_c^2 C_{L_{c.b.}}^2}{S_w\pi\cdot b_c^2}\cdot\sigma^*$$

Now

$$C_{D_{total}} = C_{D_{o_{total}}} + C_{D_{induced}}$$

$$= C_{D_{o_{total}}} + \left[\frac{a_{w.b.}^2 (\alpha + \alpha_o)^2}{\pi AR_w} + \frac{2a_{w.b.} a_{c.b.}}{\pi AR_c} \left(\frac{b_c}{b_w}\right)(\alpha + \alpha_o)(\alpha + \eta).\sigma \right.$$

$$\left. + \frac{a_{c.b.}^2}{\pi AR_c} .\left(\frac{S_c}{S_w}\right)(\alpha + \eta)^2 \sigma^* \right] \qquad \text{- - - - -EQ.E5}$$

Also

$$C_T = \frac{C_D}{\cos\alpha} \qquad \text{- - - - - EQ.E6}$$

Equations 1 - 8 can be manipulated and combined to yield an equation in terms of angle of incidence 'α' of the form:

$$A_5 = A_1 + \tan(\alpha) \{C_{D_o} + A_2\alpha^2 + A_3\alpha + A_4\}$$

or

$$1 = \frac{A_5}{A_1} - \frac{\tan(\alpha)}{A_1} \{C_{D_o} + A_2\alpha^2 + A_3\alpha + A_4\} \qquad \text{- - - - - EQ.E7}$$

where the parameter $C_W = \frac{\text{weight}}{\frac{1}{2}\rho V^2 S_W}$ and ℓ_c and ℓ_w have different values at different Mach numbers. Also, coefficients A_1, A_2, A_3, A_4 and A_5 are listed in Table E4 .

Equation E7 has been incorporated in the first order optimisation code both to optimise the wing-canard interference and to estimate the longitudinal stability derivatives. Table E5 represents the flight conditions under consideration. Estimated longitudinal stability derivatives based on these flight conditions are represented in tables E6 and E7 in both concise and aeronormalised forms.

E.4 Force Velocity Derivatives.

From equilibrium conditions,

$$X = T + L \sin\alpha - D \cos\alpha$$

$$Z = -L \cos\alpha - D \sin\alpha$$

which for $\alpha < 10^{o}$ would be approximated by,

$$X = T + L\alpha - D$$

$$Z = -L - D\alpha$$

then

$$\frac{\partial X}{\partial u} = X_u = -\rho V_e S_w \left(C_D + V_e \frac{\partial C_D}{\partial V_e}\right)$$

$$\frac{\partial Z}{\partial u} = Z_u = -\rho V_e S_w \left(2C_L + V_e \frac{\partial C_L}{\partial V_e}\right)$$

$$\frac{\partial X}{\partial w} = X_w = \tfrac{1}{2}\rho V_e S_w \left[C_L - \frac{dC_D}{\partial\alpha}\right]$$

$$\frac{\partial Z}{\partial w} = Z_w = -\tfrac{1}{2}\rho V_e S_w \left[\frac{dC_L}{d\alpha} + C_D\right]$$

In concise and aeronormalised forms these derivatives become

CONCISE	AERONORMALISED
$x_u = \frac{X_u}{m}$	$\breve{X}_u = -2C_D - V \frac{\partial C_D}{\partial V}$
$x_w = \frac{X_w}{m}$	$\breve{X}_w = \left[C_L - \frac{dC_D}{d\alpha}\right]$
$z_u = \frac{Z_u}{m}$	$\breve{Z}_u = -2C_L - V_e \frac{\partial C_L}{\partial V_e}$
$z_w = \frac{Z_w}{m}$	$\breve{Z}_w = -\left[\frac{dC_L}{d\alpha} + C_D\right]$

where m = mass of the aircraft.

E.5 Moment Velocity Derivatives

M_u estimation (theoretical)

$$M \approx -\tfrac{1}{2}\rho V_e^2 S_w C_{L_{W.B.}} \cdot \ell_w + M_o + \tfrac{1}{2}\rho V_e^2 S_c C_{L_{C.B.}} \ell_c + \tfrac{1}{2}\rho V_e^2 S_w \left(\frac{dC_M}{d\alpha}\right)_{INTAKE} \bar{\bar{c}}$$

$$\therefore \quad \frac{dM}{du} \approx -\rho V_e S_w C_{L_{W.B.}} \ell_w + \rho V_e S_w \bar{\bar{c}} C_{M_o} + \rho V_e S_c C_{L_{C.B.}} \ell_c + \rho V_e S_w \left(\frac{dM}{d\alpha}\right)_{INTAKE} \alpha \bar{\bar{c}}$$

or $$M_u \approx \rho V_e\left(-S_w C_{L_{W.B.}} \ell_w + S_w \bar{\bar{c}} C_{M_o} + S_c C_{L_{C.B.}} \ell_c + S_w \left(\frac{dC_M}{d\alpha}\right)_{INTAKE} \bar{\bar{c}}\right)$$

concise form is:

$$M_u = \frac{M_v}{I_{yy}}$$

non-dimensional form is:

$$\breve{M}_u = 2\, M_v / \rho V S_w \bar{\bar{c}}$$

M_w estimation (theoretical)

Differentiating the pitching moment equation above w.r.t. w;

$$\frac{dM}{dw} = \tfrac{1}{2}\rho V^2 S_w \bar{\bar{c}} \frac{dC_M}{d_w}$$

$$\approx -\tfrac{1}{2}\rho V^2 S_w \ell_w \cdot a_{W.B.} \cdot \frac{d\alpha}{d_w} + \tfrac{1}{2}\rho V^2 S_c \ell_c \cdot a_{C.B.} \cdot \frac{d\alpha}{d_w} + \tfrac{1}{2}\rho V^2 S_w \left(\frac{dC_M}{d\alpha}\right)_{INTAKE} \frac{d\alpha}{d_w} \cdot \bar{\bar{c}}$$

since for small angles $\alpha \approx \frac{w}{V}$

$$\therefore \quad \boxed{M_w \approx \tfrac{1}{2}\rho V\left(-S_w \cdot \ell_w \cdot a_{W.B.} + S_c \ell_c a_{C.B.} + S_w \bar{\bar{c}} \cdot \left(\frac{dC_M}{d\alpha}\right)_{INTAKE}\right)}$$

concise form is;

$$m_w = \frac{M_w}{I_{yy}}$$

non-dimensional form is;

$$\breve{M}_w = 2M_w / \rho V S_w \bar{\bar{c}}$$

E.6 Force Rotary Derivatives

These derivatives are X_q, Z_q, M_q. Therefore it is necessary to find the contribution of lift and drag forces with respect to rate of rotation about y-y axis, namely q. As an approximation to this, contributions of individual components were estimated and added together as follows.

From equilibrium conditions;

$$X = T + L\,\sin\alpha - D\,\cos\alpha \qquad \simeq T + L\alpha - D$$

$$Z = -L\,\cos\alpha - D\,\sin\alpha \qquad \simeq -L - D.\alpha$$

where for small α; $\sin\alpha \simeq \alpha$, $\cos\alpha \simeq 1$ and $\alpha = \alpha_{equilibrium} + \alpha'_{perturbation}$.

$$\therefore \quad \frac{\partial X}{\partial q} = \frac{\partial T}{\partial q} + \frac{\partial L}{\partial q}.\alpha + L\,\frac{\partial \alpha}{\partial q} - \frac{\partial D}{\partial q}$$

$$\frac{\partial Z}{\partial q} = -\frac{\partial L}{\partial q} - \frac{\partial D}{\partial q}.\alpha - \frac{\partial \alpha}{\partial q}.D$$

neglecting thrust term, and since α and q are independent,

$$\frac{\partial X}{\partial q} \simeq -\frac{\partial D}{\partial q} + \frac{\partial L}{\partial q}.\alpha$$

$$\frac{\partial Z}{\partial q} \simeq -\frac{\partial L}{\partial q} - \frac{\partial D}{\partial q}.\alpha$$

E.6.1 CANARD CONTRIBUTION

Consider the figure below.

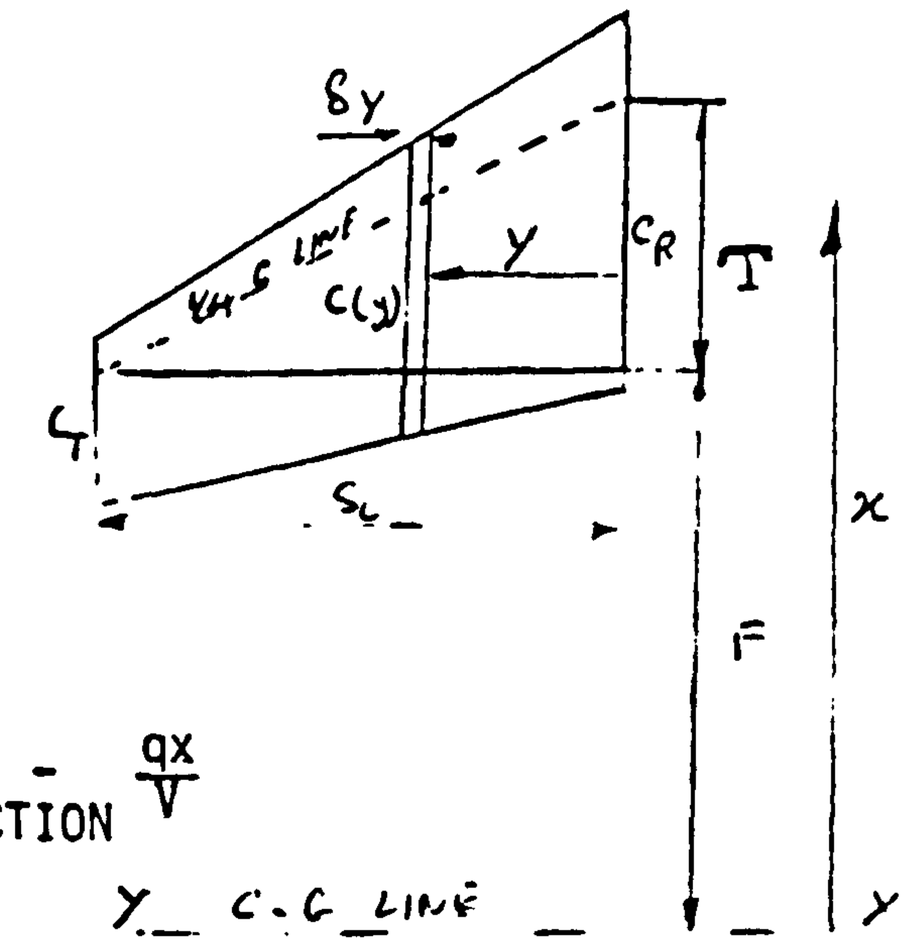

$$x = F + I\left(\frac{s - y}{s}\right)$$

Also for small α

$$\alpha = \alpha' \simeq -\frac{w}{V} = -\frac{qx}{V}$$

Applying the strip theory;

Lift on the strip is $= \frac{1}{2}\rho V^2 c(y)\delta y\left(\frac{dC_L}{d\alpha}\right)_{\text{SECTION}} c - \frac{qx}{V}$

Then the total lift due to q becomes, for half the canard,

$$= \tfrac{1}{2}\rho V q_{C.B.} q \int_0^{bc/2} c(y)x\,dy$$

$$\therefore \quad C_{L_{\substack{c \\ \text{increment} \\ \text{due to q}}}} \simeq \frac{L}{\frac{1}{2}\rho V^2 S_w} = \frac{\rho V a_{C.B.} q}{\frac{1}{2}\rho V^2 S_w} \int_0^{bc/2} c(y)x\,dy$$

$$= \frac{2a_{C.B.} q}{VS_w} \underbrace{\int_0^{bc/2} c(y)x\,dy}_{B}$$

$$B = C_R \int_0^{bc/2} \left(1 + \frac{y}{S_c}(\lambda - 1)\right)\left(F + T - \frac{Ty}{S_c}\right)dy$$

$$= C_R \int_0^{bc/2} \left(F + T - \frac{Ty}{S_c} + \frac{F}{S_c}(\lambda - 1)y + T(\lambda - 1)y/S_c - Ty^2(\lambda - 1)/S_c^2\right)dy$$

Integration gives;

$$C_{L_{\substack{c \\ \text{increment} \\ \text{due to q}}}} \simeq \frac{2a_{C.B.} q}{VS_w}\left\{\frac{3F + 2T + \lambda(3F + T)}{6}\right\} C_R S_c$$

$$\therefore \quad \boxed{\frac{dC_{L_c}}{dq} \simeq \frac{2a_{C.B.} C_R S_c}{VS_w}\left\{\frac{3F + 2T + \lambda(3F + T)}{6}\right\}}$$

where S_w = wing area
$S_c = bc/2$ = half span
λ = taper ratio.

E.6.2 WING CONTRIBUTION

Consider the figure below;

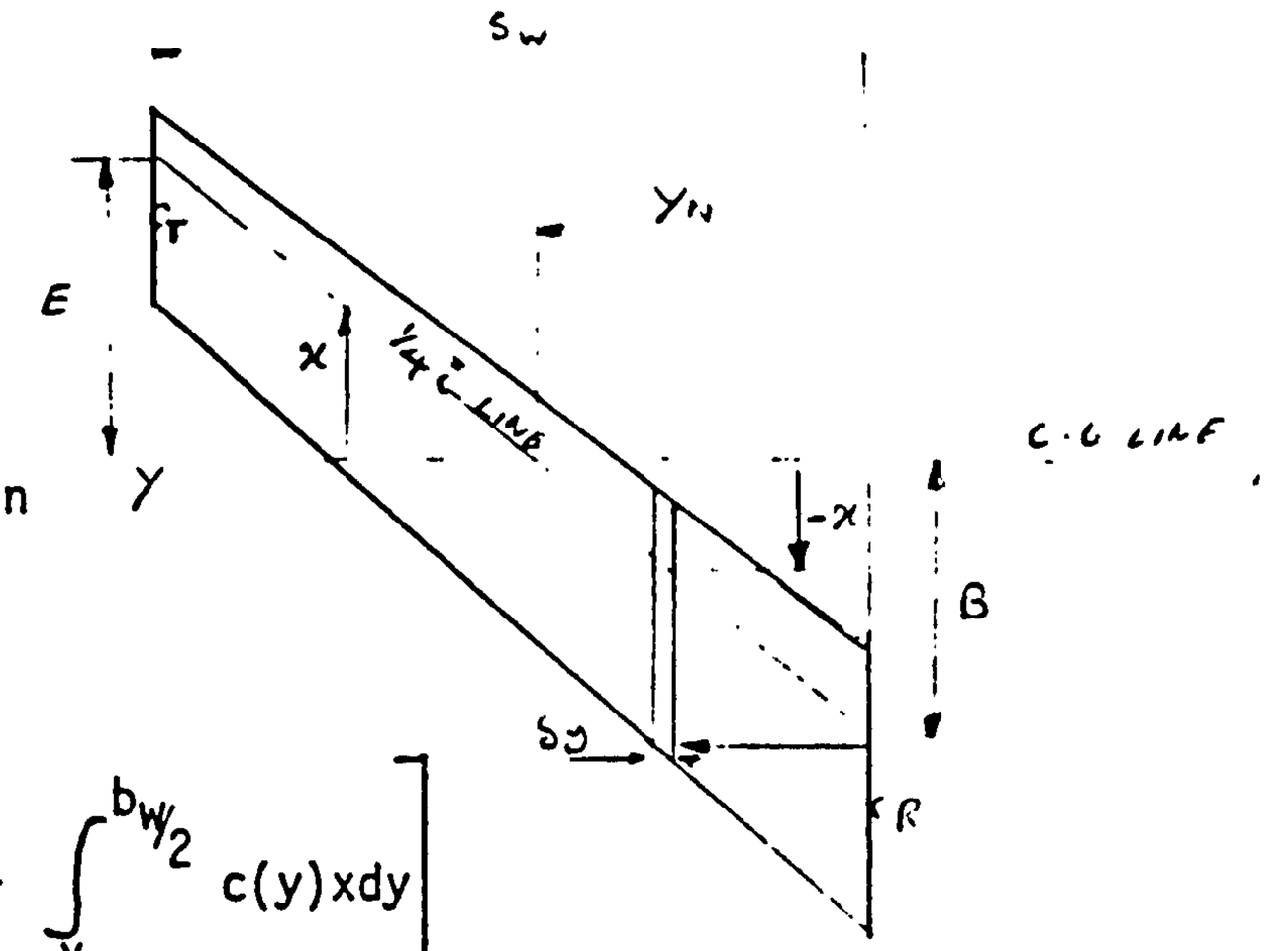

Applying the strip theory,

$$\text{Lift on strip} = \tfrac{1}{2}\rho V^2 c(y)\delta y\left(\frac{dC_L}{d\alpha}\right)_w \cdot \frac{qx}{V}$$

section

$\therefore$ total lift is given by;

$$L_{\substack{\text{increment}\\ \text{due to q}}} = \rho V a_{W.B.} q\underbrace{\left[\int_0^{Y_N} c(y)x\,dy - \int_{Y_N}^{b_{W_2}} c(y)x\,dy\right]}_{A}$$

since $x = B\left(1 - \frac{y}{Y_N}\right)$, $0 < y < Y_N$

and $x = E\left(\frac{y - y_N}{S - Y_N}\right)$, $y_N < y < S_W$

also;

$$c(y) = C_R\left(1 - \frac{y}{S_w}(\lambda - 1)\right.$$

Now;

$$A = C_R\left\{-B\int_0^{Y_N}\left(1 + \frac{y}{s}(\lambda - 1)\right)\left(1 - \frac{y}{y_N}\right)dy - E\int_{y_N}^{S_W}\left(1 + \frac{y}{s}(\lambda - 1)\right)\left(\frac{y - y_N}{s - y_N}\right)dy\right\}$$

where upon integration

$$A = \left\{C_R - B\left(\frac{y_N}{2} + \frac{(\lambda - 1)y_N^2}{6s}\right) - \frac{E}{s - Y_N}\left(-\frac{(\lambda + 1)}{2}.y_N s + \frac{y_N^2}{2} + \frac{(\lambda - 1)y_N^3}{6s} + \frac{(1 + 2\lambda)}{6}s^2\right)\right\}$$

or $$C_{L_W}{}_{\text{increment due to q}} = \frac{2a_{W.B.}qC_R}{VS_w}\left\{-B\left(\frac{y_N}{2} + \frac{(\lambda - 1)y_N^2}{6s}\right) - \frac{E}{s - y_N}\cdot\left(\frac{(1 + 2\lambda)}{6}s^2 + \frac{y_N^2}{2} + \frac{(\lambda - 1)y_N^3}{6s} - \frac{(\lambda + 1)}{2}y_N.s\right)\right\}$$

$$\therefore \quad \boxed{\frac{dC_{L_{W.B.}}}{dq} = \frac{2a_{W.B.}C_R}{VS_w}\left\{-B\left(\frac{y_N}{2} + \frac{(\lambda - 1)}{6s}y_N^2 + \frac{E}{s - Y_N}\left(\frac{(1 + 2\lambda)}{6}s^2 + \frac{y_N^2}{2} + \frac{(\lambda - 1)}{6s}y_N^3 - \frac{(\lambda + 1)}{2}y_N s\right)\right\}\right.}$$

where S_w = wing area

s_w = half span

λ = taper ratio.

Now, the induced drag is given by

$$C_{D_{induced}} = \frac{C_{L^2_{W.B.}}}{\pi AR_w} + \frac{2}{\pi AR_c}\cdot\frac{b_c}{b_w} \bullet C_{L_{W.B.}}C_{L_{C.B.}}\sigma + \frac{C_{L^2_{C.B.}}}{\pi AR_c}\cdot\sigma_*$$

integrating w.r.t. q gives

$$\left(\frac{dC_D}{dq}\right)_{total} = \frac{dC_{D_0}}{dq} + \left(\frac{dC_D}{dq}\right)_{induced}$$

$$= 2C_{L_{W.B.}} - \frac{1}{\pi AR_w}\cdot\frac{dC_{L_{W.B.}}}{dq} + \frac{2}{\pi AR_c} - \frac{b_c}{b_w}\sigma\left\{\frac{dC_{L_{W.B.}}}{dq}\cdot C_{L_{C.B.}} + C_{L_{W.B.}}\frac{dC_{L_{C.B.}}}{dq} + 2C_{L_{C.B.}}\frac{1}{\pi AR_c}\cdot\sigma_* - \frac{dC_{L_{C.B.}}}{dq}\right\}$$

The above expressions for $\frac{dC_D}{dq}$, $\frac{dC_{L_{W.B.}}}{dq}$ and $\frac{dC_{L_{C.B.}}}{dq}$ can then be used to estimate both force rotary derivatives $\frac{\partial x}{\partial q}$, $\frac{\partial z}{\partial q}$ and moment rotary derivative $\frac{\partial M}{\partial q}$ given by

$$\boxed{M_q = \tfrac{1}{2}\rho V^2 S_w \bar{c}\left(-\frac{\ell_w}{\bar{c}} - \frac{dC_{L_{W.B.}}}{dq} + \frac{S_c}{S_w}\cdot\frac{\ell_c}{\bar{c}}\cdot\frac{dC_{L_{C.B.}}}{dq} + \left(\frac{dC_M}{d\alpha}\right)_{intake}\cdot\frac{d\alpha}{dq}\right)}$$

where in concise form

$$m_q = \frac{M_q}{I_{yy}}$$

and in non-dimensional form

$$\breve{M}_q = \frac{2\,M_q}{\rho V S_w \bar{c}^2}$$

E .7 CANARD CONTROL DERIVATIVES X_η, Z_η and M_η

From equilibrium conditions;

$$X = T + L\,\sin\alpha - D\,\cos\alpha$$

$$Z + -L\,\cos\alpha - D\,\sin\alpha$$

Differentiation w.r.t. η gives

$$\frac{dX}{d\eta} = \frac{dT}{d\eta} + \frac{dL}{d\eta}.\alpha + L\cancel{\frac{d\alpha}{d\eta}}^{0} - \frac{dD}{d\eta} \qquad \text{since } \alpha \text{ is small and } \alpha = \alpha' = 0$$

$$\frac{dZ}{d\eta} = -\frac{dL}{d\eta} - \frac{dD}{d\eta}.\alpha - D.\cancel{\frac{d\alpha}{d\eta}}^{0}$$

Assuming that the only drag increase is due to the induced drag, then;

$$\frac{dX}{d\eta} = -\frac{dD}{d\eta}, \quad \frac{dZ}{d\eta} = -\frac{dL}{d\eta}$$

$$X_\eta \simeq \frac{dD}{d\eta} = -\tfrac{1}{2}\rho V^2 S_w \left(\frac{dC_D}{d\eta}\right)_{\text{induced}}$$

$$= -\left\{2C_{L_{W.B.}}\frac{1}{\pi AR_w}.\frac{dC_{L_{W.B.}}}{d\eta} + \frac{2S_c C_{L_{C.B.}}\sigma}{\pi b_c b_w}.\frac{dC_{L_{W.B.}}}{d\eta} + \right.$$

$$\left. \frac{2S_c.C_{L_{W.B.}}}{\pi b_c.b_w}.\frac{dC_{L_{C.B.}}}{d\eta}.\sigma + 2C_{L_{C.B.}}\frac{S_c^2}{S_w}.\frac{\sigma_\star}{b_c^2\pi}.\frac{dC_{L_{C.B.}}}{d\eta}\right\}.\tfrac{1}{2}\rho V^2 S_w$$

in concise form

$$x_\eta = \frac{X_\eta}{\text{A/C mass}}$$

This derivative is usually neglected for stability.

From equilibrium conditions,

$$\frac{dZ}{d\eta} \simeq -\frac{dL}{d\eta}$$

$$\frac{dZ}{d\eta} = -\tfrac{1}{2}\rho V^2 S_W\left(\frac{dC_{L_{W.B.}}}{d\eta} + \frac{S_C}{S_W}\cdot\frac{dC_{L_{C.B.}}}{d\eta}\right)\text{ , to first order in }\alpha.$$

However, α and η are assumed independent and therefore,

$$\frac{dZ}{d\eta} = -\tfrac{1}{2}\rho V^2 S_C \cdot \frac{dC_{L_{C.B.}}}{d\eta}$$

In concise form,

$$Z_\eta = \frac{Z_\eta}{m}$$

and in aeronormalised form,

$$\breve{Z}_\eta = \frac{2Z_\eta}{\rho V^2 S_W}$$

also differentiating the pitching moment equation w.r.t. η gives,

$$\frac{dM}{d\eta} \cong -\tfrac{1}{2}\rho V^2 S_W \ell_W \cdot \frac{dC_{L_{W.B.}}}{d\alpha}\ \frac{d\alpha}{d\eta} + \tfrac{1}{2}\rho V^2 S_C \ell_C \cdot \frac{dC_{L_{C.B.}}}{d\eta}$$

i.e. $$\frac{dM}{d\eta} \cong \tfrac{1}{2}\rho V^2 S_C \ell_C \cdot \frac{dC_{L_{C.B.}}}{d\eta}$$

In concise form

$$m_\eta = \frac{M_\eta}{I_{yy}}$$

and in aeronormalised form,

$$\breve{M}_\eta = \frac{2M_\eta}{\rho V^2 S_W \bar{c}}$$

$$A_1 = \left(\left(\frac{a_{w.B} \cdot l_w}{l_c} - \frac{1}{l_c} \cdot \left(\frac{dC_M}{d\alpha} \right)_{INTAKE} \right) + a_{w.B} \right)$$

$$A_2 = \left[\frac{a_{w.B}^2}{\pi R_w} + \frac{2\, a_{w.B} \cdot a_{c.B}}{\pi R_c} \cdot \frac{b_c}{b_w} \cdot \left(\frac{a_{w.B} \cdot l_w \cdot S_w}{a_{c.B} \cdot l_c \cdot S_c} - \frac{S_w}{S_c \cdot l_c \cdot a_{c.B}} \cdot \left(\frac{dC_m}{d\alpha} \right)_{INTAKE} \right) \cdot \sigma + \frac{a_{c.B}^2}{\pi R_c} \cdot \frac{S_c}{S_w} \cdot \left(\frac{a_{w.B} \cdot l_w \cdot S_w}{a_{c.B} \cdot l_c \cdot S_c} - \frac{S_w}{S_c \cdot l_c \cdot a_{c.B}} \cdot \left(\frac{dC_M}{d\alpha} \right)_{INTAKE} \right)^2 \cdot \sigma^* \right]$$

$$A_3 = \left[\left(-\frac{2\, a_{w.B} \cdot a_{c.B}}{\pi R_c} \cdot \frac{b_c}{b_w} \cdot \frac{S_w}{S_c \cdot l_c \cdot a_{c.B}} \cdot C_{m_0} \cdot \sigma \right) + \left(\frac{2\, a_{w.B} \cdot a_{c.B}}{\pi R_c} \cdot \frac{b_c}{b_w} - \frac{a_{w.B} \cdot l_w \cdot S_w}{a_{c.B} \cdot l_c \cdot S_c} + \frac{2\, a_{w.B} \cdot a_{c.B}}{\pi R_c} \cdot \frac{b_c}{b_w} \cdot \left(\frac{a_{w.B} \cdot l_w \cdot S_w}{a_{c.B} \cdot l_c \cdot S_c} - \frac{S_w}{S_c \cdot l_c \cdot a_{c.B}} \cdot \left(\frac{dC_M}{d\alpha} \right)_{INTAKE} \right) \right) \cdot \alpha_0 \cdot \sigma + \frac{2\, a_{c.B}^2}{\pi R_c} \cdot \frac{S_c}{S_w} \cdot \left(\frac{a_{w.B} \cdot l_w \cdot S_w}{a_{c.B} \cdot l_c \cdot S_c} - \frac{S_w}{S_c \cdot l_c \cdot a_{c.B}} \cdot \left(\frac{dC_M}{d\alpha} \right)_{INTAKE} \right) \cdot \left(\frac{a_{w.B} \cdot l_w \cdot S_w}{a_{c.B} \cdot l_c \cdot S_c} \cdot \alpha_0 - \frac{S_w}{S_c \cdot l_c \cdot a_{c.B}} \cdot C_{m_0} \right) \cdot \sigma^* \right]$$

$$A_4 = -\left(\frac{2 a_{w.B}}{\pi R_c} \cdot \frac{b_c}{b_w} \cdot \frac{S_w}{S_c \cdot l_c} \cdot C_{m_0} \cdot \sigma \right) \alpha_0 + \frac{a_{w.B}^2}{\pi R_w} + \frac{2\, a_{w.B}}{\pi R_c} \cdot \frac{b_c}{b_w} \cdot \frac{a_{w.B} \cdot l_w \cdot S_w}{l_c \cdot S_c} \cdot \alpha_0^2 \cdot \sigma + \frac{a_{c.B}^2}{\pi R_c} \cdot \frac{S_c}{S_w} \cdot \left(\frac{a_{w.B} \cdot l_w \cdot S_w}{a_{c.B} \cdot l_c \cdot S_c} \cdot \alpha_0 - \frac{S_w}{S_c \cdot l_c \cdot a_{c.B}} \cdot C_{m_0} \right)^2 \cdot \sigma^*$$

$$A_5 = \frac{C_{m_0}}{l_c} + C_w - \left(\frac{a_{w.B} \cdot l_w}{l_c} + a_{w.B} \right) \cdot \alpha_0$$

TABLE – E4

TABLE - E5. MODEL FLIGHT CONDITIONS

Level Flight → n = 1

m = 3.23 kg.

ρ = 1.225

CG AT 0.425 m	M	L_w (m)	L_c (m)	AWB (rad^{-1})	ACB (rad^{-1})	V (m/s)	TOTAL C_{D_o}	$(\frac{dc_m}{d\alpha})_{intake}$	C_w
	0.04	↑ 0.051	↑ 0.169	4.606	5.017	13.62	0.0257	↑ 0.004	2.734
	0.06			4.606	5.017	20.42	0.0257		1.216
	0.08			4.606	5.017	27.224	0.0257		0.684
	0.1	↓	↓	4.606	5.017	34.03	0.0257	↓	0.438

MACH NO.	α^o	η^o_{trim}	C_L	C_D	C_M	X_u	Z_u	M_u
0.06	9.42	4.12	1.19	0.16	0.0	-0.6	-2.4	0.0
0.08	4.46	3.60	0.68	0.08	0.0	-0.26	-1.36	0.0
0.1	2.13	3.35	0.44	0.05	0.0	-0.17	-0.87	0.0

X_w	Z_w	M_w	X_q	Z_q	M_q	X_η	Z_η	M_η
0.15	-4.9	-0.13	1.1	0.33	-0.42	-0.32	-1.25	1.26
0.14	-4.84	-0.13	0.64	0.33	-0.42	-0.19	-1.25	1.26
0.13	-4.82	-0.13	0.42	0.33	-0.42	-0.12	-1.25	1.26

TABLE -E6 ESTIMATED LONGITUDINAL STABILITY DERIVATIVES IN AERONORMALISED FORM

MACH NO.	α^o	η^o_{trim}	C_L	C_D	C_M	X_u	Z_u	m_u
0.06	9.42	4.12	1.19	0.16	0.0	-0.23	-0.95	0.0
0.08	4.46	3.60	0.68	0.08	0.0	-0.14	-0.72	0.0
0.1	2.13	3.35	0.44	0.05	0.0	-0.11	-0.57	0.0

x_w	z_w	m_w	x_q	z_q	m_q	x_η	z_η	m_η
0.06	-1.94	-0.21	0.08	0.1	-0.69	-2.61	-10.11	40.9
0.07	-2.55	-0.28	0.06	0.13	-0.85	-2.67	-17.97	72.7
0.09	-3.17	-0.35	0.05	0.16	-1.06	-2.73	-28.01	113.6

TABLE-E7. ESTIMATED LONGITUDINAL STABILITY DERIVATIVES IN CONCISE FORM

TABLE-E8: List of Longitudinal Stability Derivatives in Dimensional, Aeronormalised and Concise Forms

STABILITY DERIVATIVES IN DIMENSIONAL FORM	DIVISORS TO OBTAIN CONCISE FORM		DIVISORS TO OBTAIN AERONORMALISED FORM	
X_u	mass	x_u	$\frac{1}{2}\rho V S_w$	$\breve{X}_u$
X_w	"	x_w	"	$\breve{X}_w$
X_q	"	x_q	$\frac{1}{2}\rho S_w \bar{c}$	$\breve{X}_q$
Z_u	"	z_u	$\frac{1}{2}\rho V S_w$	$\breve{Z}_u$
Z_w	"	z_w	"	$\breve{Z}_w$
Z_q	"	z_q	$\frac{1}{2}\rho V S_w \bar{c}$	$\breve{Z}_q$
M_u	I_{yy}	m_u	$\frac{1}{2}\rho V S_w \bar{c}$	$\breve{M}_u$
M_w	"	m_w	"	$\breve{M}_w$
M_q	"	m_q	$\frac{1}{2}\rho V S_w \bar{c}^2$	$\breve{M}_q$
X_η	mass	x_η	$\frac{1}{2}\rho V^2 S_w$	$\breve{X}_\eta$
Z_η	"	z_η	"	$\breve{Z}_\eta$
M_η	I_{yy}	m_η	$\frac{1}{2}\rho V^2 S_w \bar{c}$	$\breve{M}_\eta$

E.8 Estimation of Lateral Derivatives

E.8.1 Moment Velocity Derivatives L_v, N_v

Here the moment derivatives L_v and N_v are estimated. These will have a different value compared to ones obtainable from C_{ℓ_β} and C_{n_β} of Appendix E since the C.G. positions of the dynamic model and that of the full-size model do not coincide.

The contributions are due to fuselage and fin. Normally the contribution of fuselage to N_v is destabilising and this effect must be overcome by the fin. In the event of a sideslip the whole aircraft is subject to the sideslip velocity whereas with the c.g. fixed the only effect is due to weathercock stability. Assuming the fin to be the only contributory part to N_v, it can be shown that

$$N_{v_{fin}} \simeq \tfrac{1}{2}\rho V S_{fin} \frac{dC_L}{d\beta_{fin}} . \ell_F . K$$

where K is the interference factor due to sidewash. However, dihedral, anhedral, wing sweep, wing-fuselage arrangement and fin all contribute to L_v. Here, dihedral, anhedral do not exist for the model and since the wing is mounted in the middle of the fuselage as regards the vertical position, this effect is also zero. Therefore, assuming the fin to be the main contributory element, it can be shown that,

$$L_{v_{fin}} \simeq -\tfrac{1}{2}\rho V \frac{dC_L}{d\beta} . S_F \, h_F . K$$

With reference to Appendix E, the contribution of wing forward sweep due to sideslip, to L_v is destructive and estimated to be

$$L_{v_{\substack{sweep \\ forward}}} \simeq \tfrac{1}{2}\rho V S_w d . C_{L_w} . \mathrm{Tan}\Lambda . K$$

Here, ℓ_F = distance from fin centre of pressure to c.g.

h_F = distance from fin centre of pressure to C_L

d = wing moment arm in θ_y direction.

It must however be noted that the wing contribution cannot be treated in isolation from the fuselage since for a sideslip to starboard say, the port wing would be blanketted by the fuselage wake. Therefore the above treatment of L_v represents a crude approximation to the important derivative L_v.

E.8.2 MOMENT ROTARY DERIVATIVE L_p

Using strip theory it can be shown that the total rolling moment due to rolling velocity is,

$$L_{total} = -\tfrac{1}{2}\rho V p \int_{-s}^{+s} \left(\frac{dC_L}{d\alpha}\right)_{local} c(y)y^2 dy$$

Assuming $\left(\frac{dC_L}{d\alpha}\right)$ to be constant, then

$$L = -\tfrac{1}{2}\rho V p \left(\frac{dC_L}{d\alpha}\right) \cdot \int_{-s}^{+s} c(y)y^2 dy$$

and $$\int_{-s}^{+s} c(y)y^2 dy = S_w k_n^2$$

where k_n is the radius of gyration of wing area about ℄.

$$\therefore \qquad \frac{dL}{dp} = -\tfrac{1}{2}\rho V \left(\frac{dC_L}{d\alpha}\right) S_w k_n^2$$

From the f.s.w. model layout and aerodynamic characteristics.

ℓ_F = 0.34 m

k ≈ 0.8

$C_{L_{W.B.}}$ ≈ 0.78 at V = 27 m/s

$C_{L_{W.B.}}$ ≈ 0.63 at V = 30 m/s

h_F ≈ 0.14 m

S_F = 0.028 m^2

d ≈ 0.13 m

I_{xx} ≈ 0.0256 kg m^2

I_{zz} ≈ 0.151 kg m^2

$I_{xx_{wing}}$ ≈ 0.0123 kg m^2

$\frac{dC_L}{d\beta}$ ≈ 2.68 rad^{-1}

model f.s.w. mass ≈ 0136 kg

k_n ≈ 0.18 m

By substitution of **these** data in expressions for L_v, L_p and N_v Table H14 below has been formed.

	LATERAL STABILITY DERIVATIVES IN					
	CONCISE FORM			AERONORMALISED FORM		
SPEED (m/s)	ℓ_v	n_v	ℓ_p	$\breve{Y}_v$	$\breve{N}_v$	$\breve{Y}_p$
30	1.21	2.48	-8.8	0.06	0.61	-1.14
27	-0.08	2.23	-7.9	0.0	0.55	-1.02

TABLE E9: ESTIMATED LATERAL DERIVATIVES (THEORETICAL)

In order to evaluate the other lateral derivatives detailed aerodynamic data is essential and in its absence no attempt was made to estimate them.

TABLE-E10: List of Lateral Stability Derivatives in Dimensional, Aeronormalised and Concise Forms.

STABILITY DERIVATIVES IN DIMENSIONAL FORM	DIVISORS TO OBTAIN CONCISE FORM		DIVISORS TO OBTAIN AERONORMALISED FORM	
L_v	I_{xx}	ℓ_v	$\frac{1}{2}\rho U S_w s$	$\breve{L}_v$
L_p	"	ℓ_p	$\frac{1}{2}\rho U S_w s^2$	$\breve{L}_p$
L_r	"	ℓ_r	"	$\breve{L}_r$
N_v	I_{zz}	n_v	$\frac{1}{2}\rho U S_w s$	$\breve{N}_v$
N_p	"	n_p	$\frac{1}{2}\rho U S_w s^2$	$\breve{N}_p$
N_r	"	n_r	"	$\breve{N}_r$
L_ξ	I_{xx}	ℓ_ξ	$\frac{1}{2}\rho U^2 S s$	$\breve{L}_\xi$
L_ζ	"	ℓ_ζ	"	$\breve{L}_\zeta$
N_ξ	I_{zz}	n_ξ	"	$\breve{N}_\xi$
N_ζ	"	n_ζ	"	$\breve{N}_\zeta$

			ESTIMATED LONGITUDINAL STABILITY DERIVATIVES											
			CONCISE FORM						AERONORMALISED FORM					
		METHOD	z_w	m_w	z_q	m_q	z_η	m_η	$\check{Z}_w$	$\check{M}_w$	$\check{Z}_q$	$\check{M}_q$	$\check{Z}_\eta$	$\check{M}_\eta$
C.G. AT 0.444 m FROM DATUM	U = 28 m/s M = 0.08	E.K.F ESTIMATES	-4.5	7.0	-31.0	-1.4	-92.0	108.0	.8.0	3.3	-328.2	-4.0	-6.1	1.9
		STATIC TEST DATA	-2.21	3.1	-	-1.96	-99.0	96.0	-3.93	1.48	-	-5.56	-6.52	1.69
		OPTIMISATION PROGRAM	-2.54	-0.28	0.13	-0.85	-17.98	72.7	-4.84	-0.13	0.33	-0.42	-1.25	1.26

TABLE E11: ESTIMATED LONGITUDINAL DERIVATIVES

	LATERAL STABILITY DERIVATIVES	E.K.F. ESTIMATES	THEORY	E.K.F. ESTIMATES	THEORY
CONCISE FORM	ℓ_v	2.0	-1.21	0.7	-0.1
	ℓ_p	-12.0	-8.8	-8.0	-7.9
	ℓ_r	-2.0	-	-3.2	-
	n_v	2.0	2.48	2.2	2.23
	n_p	26.0	-	-2.0	-
	n_r	-9.0	-	-8.0	-
	ℓ_ζ	118.0	-	100.0	-
	n_ζ	222.0	-	380.0	-
AERONORMALISED FORM	$\breve{L}_v$	0.08	-0.06	0.03	0.00
	$\breve{L}_p$	-1.15	-1.14	-1.03	-1.02
	$\breve{L}_r$	-0.26	-	-0.41	-
	$\breve{N}_v$	0.49	0.61	0.54	0.55
	$\breve{N}_p$	19.83	-	-1.53	-
	$\breve{N}_r$	-6.86	-	-6.1	-
	$\breve{L}_\zeta$	0.16	-	0.15	-
	$\breve{N}_\zeta$	1.83	-	3.49	-
		U ≈ 30 m/s		U ≈ 27 m/s	
		C.G. AT 0.444 m FROM DATUM		C.G. AT 0.44 m FROM DATUM	
		ζ POSITIVE TO STARBOARD			

TABLE E12: ESTIMATED LATERAL DERIVATIVES

PROGRAM STRUCTURE DIAGRAM

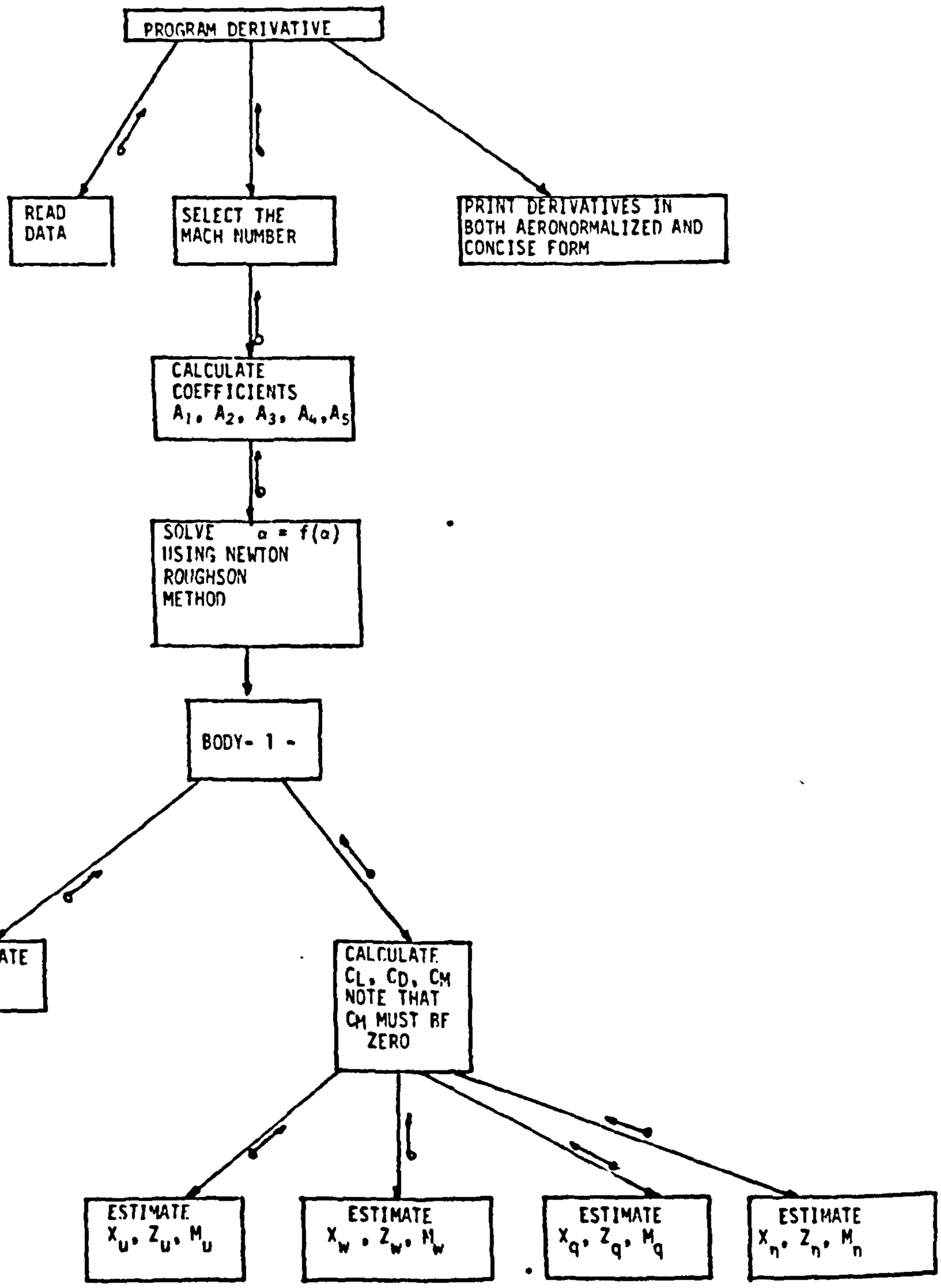

FIGURE E.1: STRUCTURE DIAGRAM OF THE SUB-ROUTINE DERIVATIVE

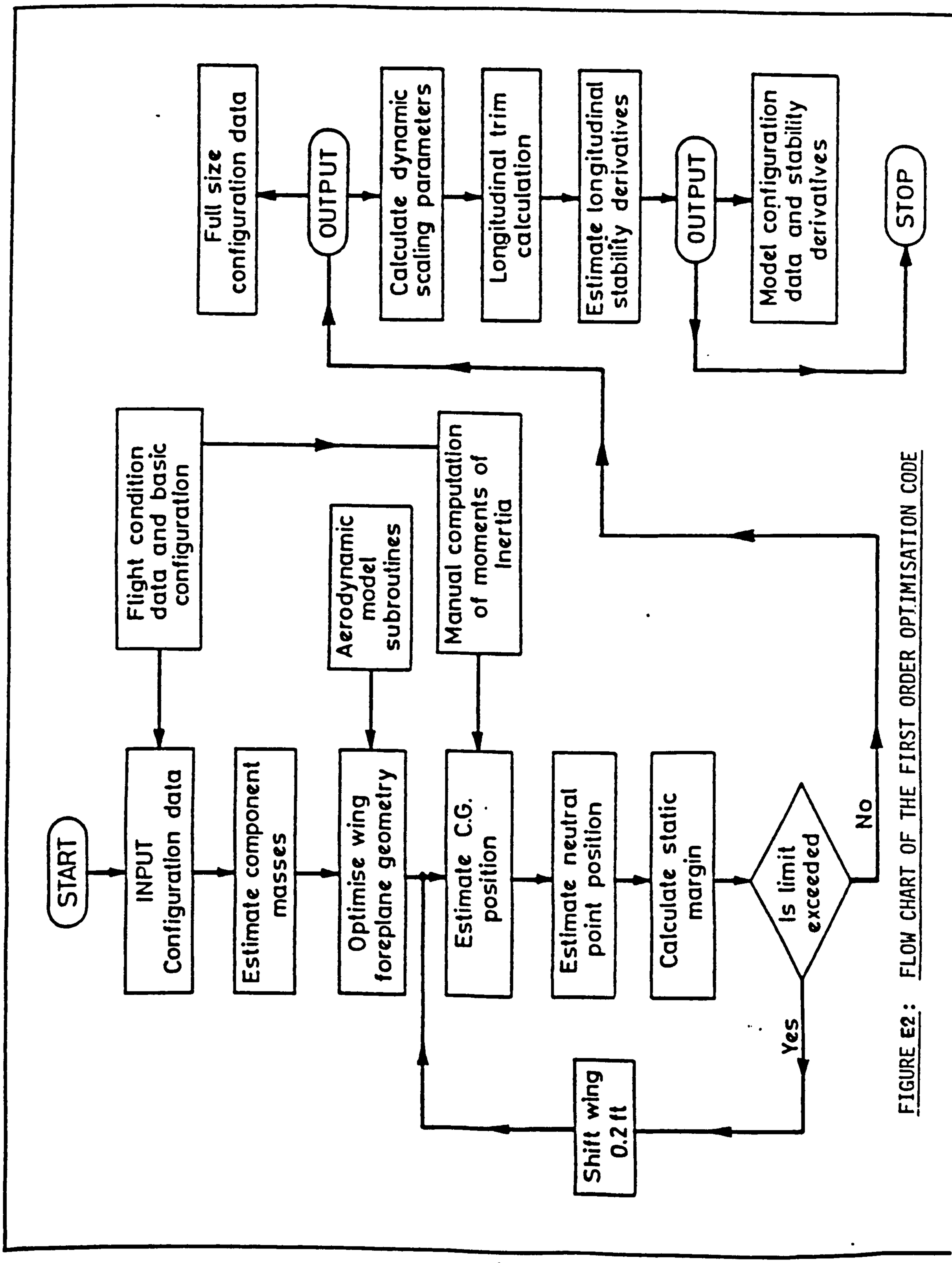

FIGURE E2 : FLOW CHART OF THE FIRST ORDER OPTIMISATION CODE

APPENDIX - F

TRIP WIRE CALCULATIONS

In order to calculate the approximate position and thickness of the trip wire the velocity distribution round the aerofoil is needed. The theory of wing sections permits the two-dimensional calculation of the pressure distribution and hence the velocity distribution with considerable accuracy. Although this method is not unduly laborious, the computations required are too long to permit the quick and easy calculations which are necessary in this case.

Here, it was assumed that the velocity distribution about the wing section is composed of the three separate and independent components listed below:

1) The distribution corresponding to the velocity distribution over the basic thickness form at zero angle of attack, $\frac{u}{U}$.

2) The distribution corresponding to the additional load distribution of the mean line at its ideal angle of attack, $\frac{\Delta u}{U}$.

3) The distribution corresponding to the additional load distribution associated with angle of attack, $\frac{\Delta u_a}{U}$.

Consider the case where the aerofoil is at an angle of incidence of 0^o (different from effective angle of incidence), in this case $\frac{\Delta u_a}{U} = 0$.

This procedure or rather superposition of velocity distributions is illustrated in Fig.F1.

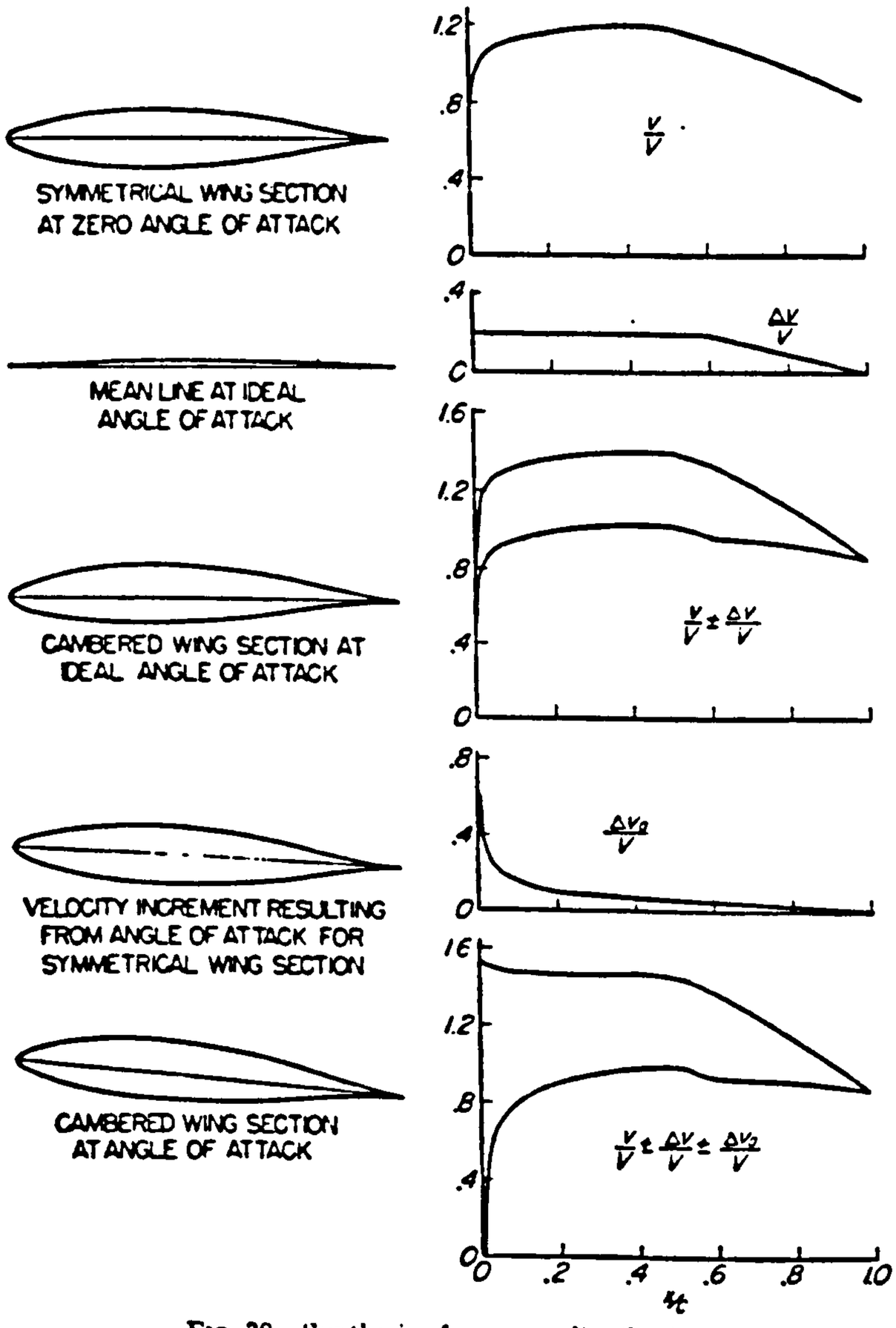

FIG. 38. Synthesis of pressure distribution.

FIG. 1 (Ref.36)

From Appendix B, the aerofoil sections chosen were from NACA, Series 6, with the following allocations.

Wing:	Outer Section	NACA 65-206
	Inner Section	NACA 66-206
Canard + Fin		NACA 65-006

Now, in order to camber NACA 6-series wing sections, mean lines are usually used which produce a uniform chordwise loading from the leading edge to the point $\frac{x}{c} = a$, where x is the chordwise distance from the leading edge and c is the chord, and, from this point onwards a linearly decreasing load to the trailing edge.

From Ref. 9, data for NACA mean lines with values of -a- equal to 0, 0.1, 0.2, ------ , 1.0 are known for NACA 6 series sections. The data are presented for a design lift coefficient of unity. All tabulated values vary directly with the design lift coefficient. Corresponding data for similar mean lines with other design lift coefficients may accordingly be obtained simply by multiplying the tabulated values by the desired design lift coefficient. In the case of 65-206 and 66-206 sections where the value of -a- is not specified, it is understood that the uniform load mean line (a = 1.0) has been used.

NACA 65-206
(Stations and ordinates given in per cent of airfoil chord)

Upper surface		Lower surface	
Station	Ordinate	Station	Ordinate
0	0	0	0
0.460	0.524	0.540	− 0.424
0.706	0.642	0.794	− 0.502
1.200	0.822	1.300	− 0.608
2.444	1.140	2.556	− 0.768
4.939	1.625	5.061	− 0.993
7.437	2.012	7.563	− 1.164
9.936	2.340	10.064	− 1.306
14.939	2.869	15.061	− 1.523
19.945	3.277	20.055	− 1.685
24.953	3.592	25.047	− 1.802
29.962	3.824	30.038	− 1.880
34.971	3.982	35.029	− 1.922
39.981	4.069	40.019	− 1.927
44.990	4.078	45.010	− 1.888
50.000	4.003	50.000	− 1.797
55.009	3.836	54.991	− 1.646
60.016	3.589	59.984	− 1.447
65.022	3.276	64.978	− 1.216
70.026	2.907	69.974	− 0.963
75.028	2.489	74.972	− 0.699
80.027	2.029	79.973	− 0.437
85.024	1.538	84.976	− 0.192
90.018	1.027	89.982	0.007
95.009	0.511	94.991	0.121
100.000	0	100.000	0

L.E. radius: 0.240
Slope of radius through L.E.: 0.084

FIG.F4.

NACA 66-206
(Stations and ordinates given in per cent of airfoil chord)

Upper surface		Lower surface	
Station	Ordinate	Station	Ordinate
0	0	0	0
0.461	0.509	0.539	− 0.409
0.707	0.622	0.793	− 0.482
1.202	0.798	1.298	− 0.584
2.447	1.102	2.553	− 0.730
4.941	1.572	5.059	− 0.940
7.439	1.947	7.561	− 1.099
9.939	2.268	10.061	− 1.234
14.942	2.791	15.058	− 1.445
19.947	3.196	20.053	− 1.604
24.954	3.513	25.046	− 1.723
29.962	3.754	30.038	− 1.810
34.971	3.929	35.029	− 1.869
39.981	4.042	40.019	− 1.900
44.990	4.095	45.010	− 1.905
50.000	4.088	50.000	− 1.882
55.009	4.020	54.991	− 1.830
60.018	3.886	59.982	− 1.744
65.026	3.641	64.974	− 1.581
70.031	3.288	69.969	− 1.344
75.034	2.848	74.966	− 1.058
80.034	2.339	79.966	− 0.747
85.031	1.780	84.969	− 0.434
90.023	1.182	89.977	− 0.148
95.012	0.578	94.988	0.054
100.000	0	100.000	0

L.E. radius: 0.223
Slope of radius through L.E.: 0.084

FIG.F5.

(Ref.36)

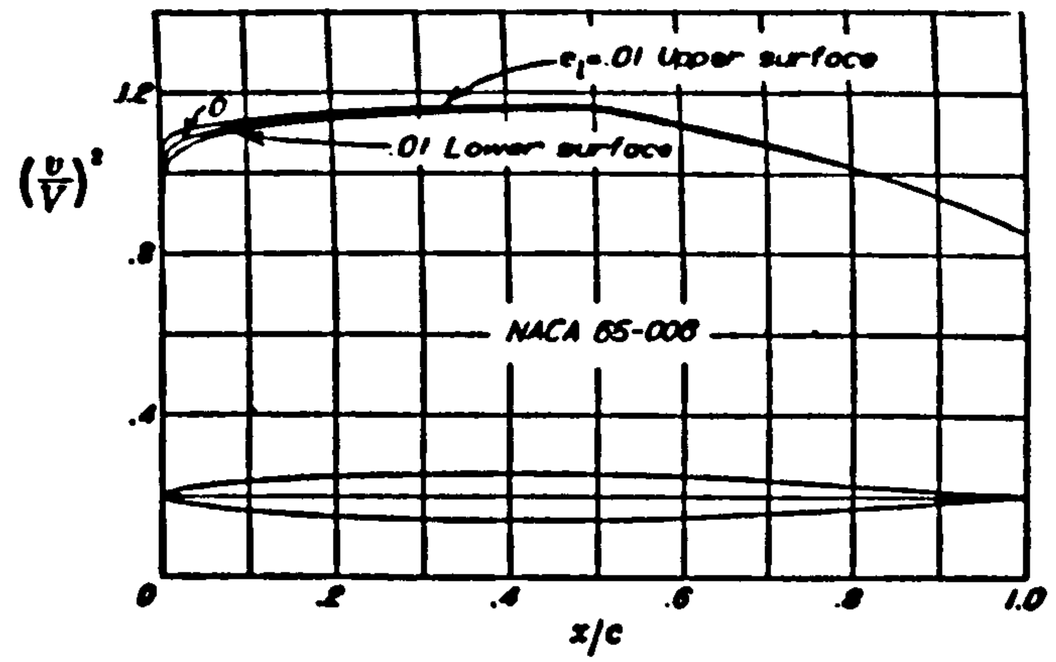

x (per cent c)	y (per cent c)	$(v/V)^2$	v/V	$\Delta v_s/V$
0	0	0	0	4.815
0.5	0.476	1.044	1.022	2.110
0.75	0.574	1.055	1.027	1.780
1.25	0.717	1.063	1.031	1.390
2.5	0.956	1.081	1.040	0.965
5.0	1.310	1.100	1.049	0.695
7.5	1.589	1.112	1.055	0.560
10	1.824	1.120	1.058	0.474
15	2.197	1.134	1.065	0.381
20	2.482	1.143	1.069	0.322
25	2.697	1.149	1.072	0.281
30	2.852	1.155	1.075	0.247
35	2.952	1.159	1.077	0.220
40	2.998	1.163	1.078	0.198
45	2.983	1.166	1.080	0.178
50	2.900	1.165	1.079	0.160
55	2.741	1.145	1.070	0.144
60	2.518	1.124	1.060	0.128
65	2.246	1.100	1.049	0.114
70	1.935	1.073	1.036	0.100
75	1.594	1.044	1.022	0.086
80	1.233	1.013	1.006	0.074
85	0.865	0.981	0.990	0.060
90	0.510	0.944	0.972	0.046
95	0.195	0.902	0.950	0.031
100	0	0.858	0.926	0
L.E. radius: 0.240 per cent c				

NACA 65-006 Basic Thickness Form

FIG_K3

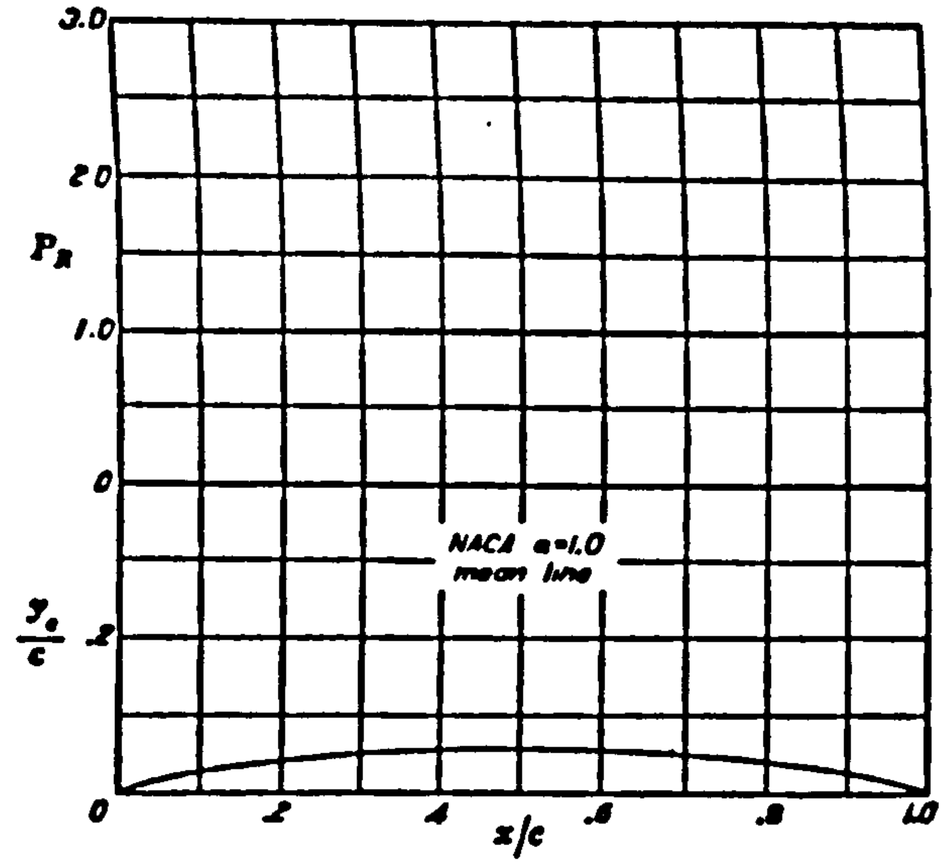

$c_{l_i} = 1.0$ $\alpha_i = 0°$ $c_{m_c/4} = -0.250$				
x (per cent c)	y_c (per cent c)	dy_c/dx	P_R	$\Delta v/V = P_R/4$
0	0			
0.5	0.250	0.42120		
0.75	0.350	0.38875		
1.25	0.535	0.34770		
2.5	0.930	0.29155		
5.0	1.580	0.23430		
7.5	2.120	0.19995		
10	2.585	0.17485		
15	3.365	0.13805		
20	3.980	0.11030		
25	4.475	0.08745		
30	4.860	0.06745		
35	5.150	0.04925		
40	5.355	0.03225	1.000	0.250
45	5.475	0.01595		
50	5.515	0		
55	5.475	− 0.01595		
60	5.355	− 0.03225		
65	5.150	− 0.04925		
70	4.860	− 0.06745		
75	4.475	− 0.08745		
80	3.980	− 0.11030		
85	3.365	− 0.13805		
90	2.585	− 0.17485		
95	1.580	− 0.23430		
100	0			

Data for NACA Mean Line $a = 1.0$

FIG_K2

(Ref.36)

From Ref.9, the design lift coefficient of NACA 65-206 is $C_{L_{design}} = 0.2$. Since the value of -a- is not specified, -a- must be equal to unity. Fig.F.2, gives the load distribution over NACA mean line a = 1.0 with a design coefficient of $C_{L_{design}} = 1.0$. However, in the case of NACA 65-206, $C_{L_{design}} = 0.2$, so multiplication of every ordinate of NACA mean line a = 1.0, by a factor of $\frac{1}{5}$ and its addition with the corresponding ordinate of "NACA 65-006, basic thickness", would yield the corresponding ordinate of the upper surface of NACA 65-206. Moreover, the value of $\frac{\Delta u}{U}$ of this mean line, multiplied by the same factor and added to the value of $\frac{u}{U}$ of NACA 65-006 would supply us with the approximate velocity distribution about NACA 65-206 section. Also, the velocity distribution about NACA 65-006 section is readily given in Fig. F3 .

It is assumed that the velocity increment on the upper surface is equal to the velocity decrement on the lower surface. This assumption is in accord with the basic concept of the distribution of the circulation used in the theory of thin wing sections.

Tables F.1 and F.2 give the approximate velocity distribution round the NACA 65-206 and NACA 65-006 respectively.

Now, for the relatively simple case of two-dimensional constant-property boundary layer the transition position can be satisfactorily calculated by using several empirical correlations. One such useful correlation suggested by Ref. 10 is that there is a connection between $R_\theta (\equiv U_1\theta/\nu)$ and $Re_x (\equiv U_1 x/\nu)$ at transition where x is the distance along the aerofoil surface.

At the transition point according to Ref. 10

$$R_{\theta_{transition}} = 1.174\left(1 + \frac{22400}{Re_{x_{transition}}}\right)Re_{x_{transition}}^{0.46} \quad \text{- - -} \quad \text{EQ. F1}$$

According to the expression above, the development of R_θ as a function of Re_x is needed. These values of R_θ and Re_x are the transitional values.

At this stage Thwaite's method was used to calculate the momentum thickness θ through

$$\theta^2 = \frac{0.45\nu}{U_1^6} \int_0^x U_1^5 \, dx \qquad \text{- - - - -} \quad \text{EQ.F2}$$

From tables F1 and F2 the values of U_1 for both NACA 65-206 and NACA 65-006 were readily available. A computer program was written to calculate θ, R_θ and R_x for both NACA 65-206 and 65-006. These were tabulated in tables K3 and K4 respectively.

One way of estimating the transition point is to use a graphical procedure in which R_θ is plotted as a function of R_{e_x} in order to find the intersection of this curve and the curve represented by EQ. F1 above. FiguresF 6 andF 7 give transition points as:

NACA 65-206 at $\approx 30\% \bar{\bar{c}}_{wing}$

NACA 65-006 at $\approx 20\% \bar{c}_{canard}$

F.S.W. $\bar{\bar{c}}_{wing}$ = 2.35m				
FULL SCALE MODEL M = 0.3 , α = 0.0°				
x%c	y%c upper surface	y%c lower surface	U_x(m/s) upper	U_x(m/s) lower
0	0	0		
0.5	0.524	-0.424	109.45	99.24
0.75	0.642	-0.502	109.96	99.75
1.25	0.822	-0.608	110.37	100.16
2.5	1.140	-0.768	111.30	101.08
5.0	1.625	-0.993	112.21	102.0
7.5	2.012	-1.164	112.82	102.61
10.0	2.340	-1.306	113.13	102.92
15.0	2.869	-1.523	113.84	103.63
20.0	3.277	-1.685	114.25	104.04
25	3.592	-1.802	114.56	104.35
30	3.824	-1.880	114.86	104.65
35	3.982	-1.922	115.07	104.86
40	4.069	-1.927	115.12	104.96
45	4.078	-1.888	115.37	105.16
50	4.003	-1.797	115.27	105.06
55	3.836	-1.646	114.35	104.14
60	3.589	-1.447	113.33	103.12
65	3.276	-1.216	112.21	102.00
70	2.907	-0.963	110.88	100.67
75	2.489	-0.699	109.45	99.24
80	2.029	-0.437	107.82	97.61
85	1.538	-0.192	106.18	95.97
90	1.027	-0.007	104.35	94.14
95	0.511	-0.121	102.1	91.89
100	0.0	0.0	99.65	89.44

TABLE F.1.

TWO-DIMENSIONAL VELOCITY DISTRIBUTION ON THE UPPER AND LOWER WING SURFACES

CANARD η = 0.0°		
FULL SCALE MODEL M = 0.3		
$x\%\bar{\bar{c}}$	$y\%\bar{\bar{c}}$	U_x m/s
0	0	0
0.5	0.476	104.35
0.75	0.574	104.86
1.25	0.717	105.265
2.5	0.956	106.18
5.0	1.31	107.10
7.5	1.589	107.71
10	1.824	108.02
15	2.197	108.74
20	2.482	109.14
25	2.697	109.45
30	2.852	109.76
35	2.952	109.96
40	2.998	110.06
45	2.983	110.27
50	2.9	110.16
55	2.741	109.25
60	2.518	108.23
65	2.246	107.10
70	1.935	105.77
75	1.594	104.35
80	1.233	102.71
85	0.865	101.08
90	0.510	99.24
95	0.195	96.99
100	0	94.54

TABLE F 2.

TWO-DIMENSIONAL VELOCITY DISTRIBUTION
OVER UPPER AND LOWER CANARD AND/OR
FIN + RUDDER SURFACES

F.S.W.			
M = 0.3 , α = 0.0 , $\bar{\bar{c}}$ = 2.35 m			
θ	Re_θ	Re_x	$x\%\bar{\bar{c}}$
2.66×10^{-5}	185.61	82113.3	0.5
3.22×10^{-5}	225.11	123170.0	0.75
4.14×10^{-5}	289.38	205283.2	1.25
5.8×10^{-5}	405.425	410566.4	2.5
8.15×10^{-5}	569.77	821132.8	5.0
9.93×10^{-5}	693.86	1231699.18	7.5
1.14×10^{-4}	800.21	1642265.6	10.0
1.39×10^{-4}	973.72	2463398.3	15.0
1.6×10^{-4}	1121.66	3284531.1	20.0
1.79×10^{-4}	1251.86	4105663.93	25.0
1.96×10^{-4}	1367.92	4926726.7	30.0
2.11×10^{-4}	1476.03	5747929.5	35.0
2.26×10^{-4}	1581.37	6569062.3	40.0
2.39×10^{-4}	1671.94	7390195.1	45.0
2.53×10^{-4}	1771.23	8211327.85	50.0
2.72×10^{-4}	1903.08	9032460.6	55.0
2.92×10^{-4}	2038.3	9853593.4	60.0
3.12×10^{-4}	2178.52	10674726.2	65.0
3.34×10^{-4}	2332.0	11495859.0	70.0
3.57×10^{-4}	2494.67	12316991.79	75.0

TABLE F.3.

VARIATION OF Re_x, Re_θ AND MOMENTUM THICKNESS θ
WITH DISTANCE ALONG THE WING SURFACE

CANARD			
M = 0.3 , η = 0.0°			
θ	R_θ	Re_x	x%c
2.05×10^{-5}	143.58	46822.0	0.5
2.49×10^{-5}	174.00	70233.06	0.75
3.2×10^{-5}	223.66	117055.1	1.25
4.48×10^{-5}	313.28	234110.2	2.5
6.3×10^{-5}	439.6	468220.4	5.0
7.66×10^{-5}	535.72	702330.6	7.5
8.84×10^{-5}	617.79	936440.8	10.0
1.07×10^{-4}	751.4	1404661.2	15
1.24×10^{-4}	865.7	1872881.6	20
1.38×10^{-4}	966.07	2341102.0	25
1.51×10^{-4}	1055.27	2809322.4	30
1.63×10^{-4}	1138.73	3277542.8	35
1.744×10^{-4}	1218.82	3745763.2	40
1.84×10^{-4}	1285.8	4213983.6	45
1.96×10^{-4}	1367.1	4682204.0	50
2.1×10^{-4}	1470.1	5150424.4	55
2.25×10^{-4}	1576.4	5618644.8	60
2.41×10^{-4}	1687.5	6086865.2	65
2.6×10^{-4}	1809.0	6555085.5	70

TABLE F.4.

VARIATION OF Re_x, Re_θ AND MOMENTUM THICKNESS θ
WITH DISTANCE ALONG THE CANARD AND/OR FIN + RUDDER SURFACE

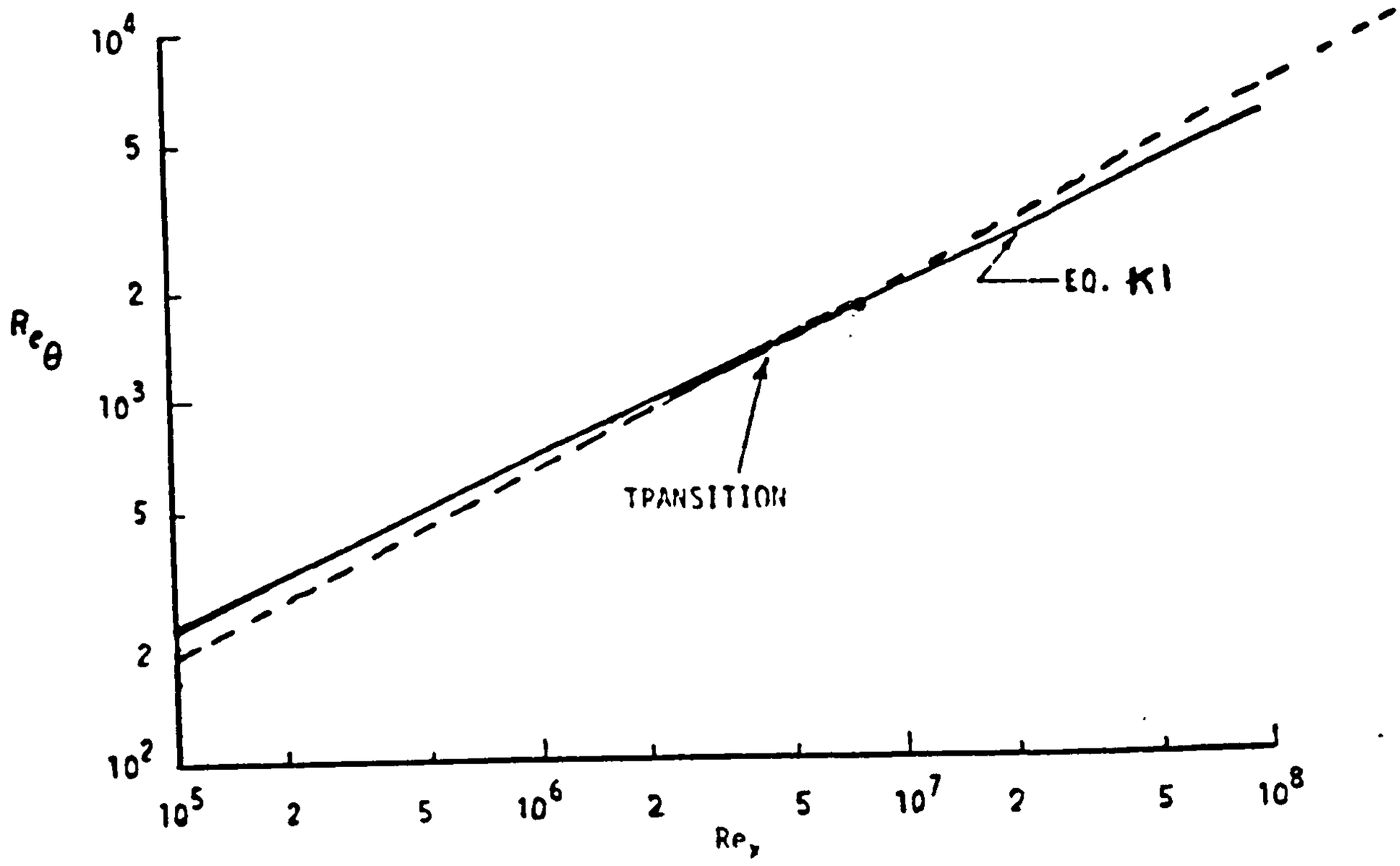

Fig.F.6 Prediction of transition for Eq. F.1 graphically.

For the 'FARJAN' FSW model the only difference is the scaling factor, but the trip-wire should still be placed at the 30% chord in case of the F.S.W. and 20% chord in case of the Canard. Fin was not treated since the flow around it was assumed to be turbulent for both full scale and model versions. This and other assumptions and approximations will be justified after the flow visualization has been completed.

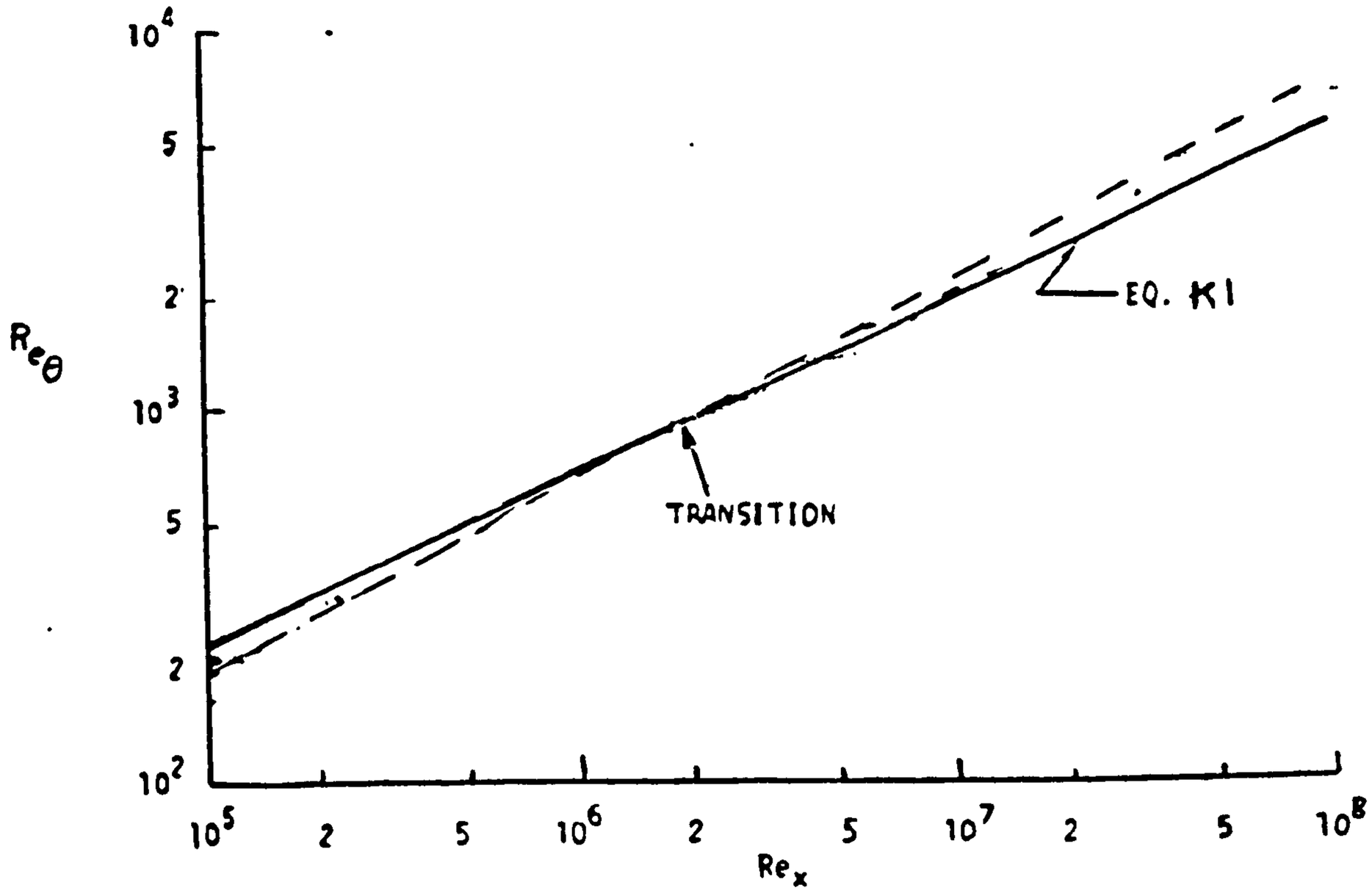

Fig.F7 Prediction of transition for Eq F1 graphically

From Ref.11, if the diameter of the trip-wire is taken to be -d-, dimensional analysis shows that in a constant-pressure laminar boundary layer the transition behaviour depends on $\frac{U_1\delta}{\gamma}$ and d/δ only. An empirical criterion for transition to occur a negligibly small distance behind the wire is

$$u_b(y = d)\,\frac{d}{\gamma} \simeq 800$$

where u_b is the boundary layer velocity at distance y from the surface. In practice, $\frac{U_1\delta}{\gamma}$ at the desired transition position may be not far short of 800 ($\frac{U_1 x}{\gamma} = 2.6 \times 10^4$ in zero pressure gradient, more in favourable gradients), so d is close to δ, $u_b(y = d)$ is close to U_1, and the above criterion is not too far from

$$U_1\frac{d}{\gamma} = 800 \qquad \text{- - - - - - - - -} \qquad \text{EQ.F3}$$

Based on a tunnel speed of 20 m/s, i.e. $U_1 = 20$ m/s, equation K3 gives

$$U_1 \frac{d}{\gamma} = 800$$

$$\therefore \quad d = \frac{1.461 \times 10^{-5} \times 800}{20}$$

$$\Rightarrow \quad d \simeq 0.6 \text{ mm}$$

As mentioned earlier on, flow visualisation would justify the usage of this trip wire.

APPENDIX - G

G.1 MEASUREMENT OF MOMENTS OF INERTIA

For this purpose the model was suspended on the vertical shaft of the rig seen in the diagram below. A relatively soft spring was chosen for the purpose of oscillation. This spring had the following characteristic:

$$\text{If tension} = \frac{\lambda}{\ell} \text{ extension}$$

$$T = \frac{\lambda}{\ell}.x$$

$$\frac{dT}{dx} = \frac{\lambda}{\ell} = 16.922 \text{ N/m}$$

I_{yy} measurement.

Assuming that the set of body-axes and the principal axis coincide, then essentially the system can be represented as:

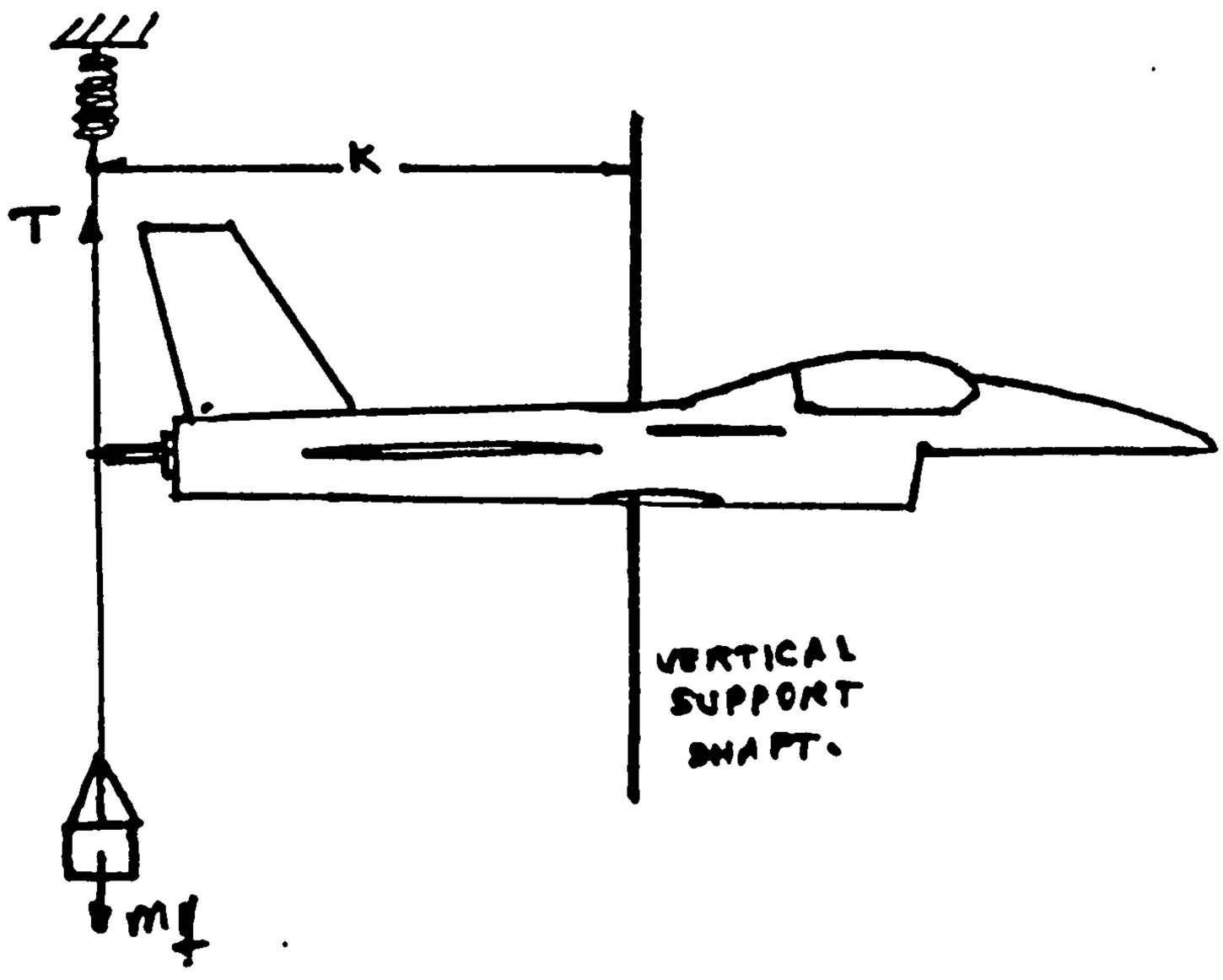

With the assumption that friction at the gimbal is negligible and that the damping due to wing + fuselage moving through the air is small, Newton's Second Law of Motion gives the relationship between frequency of oscillation and moment of inertia.

I_{yy}, I_{xx} measurements.

With reference to figures , it can be seen that the general mathematical model below can be applied to both I_{yy} and I_{xx} measurements.

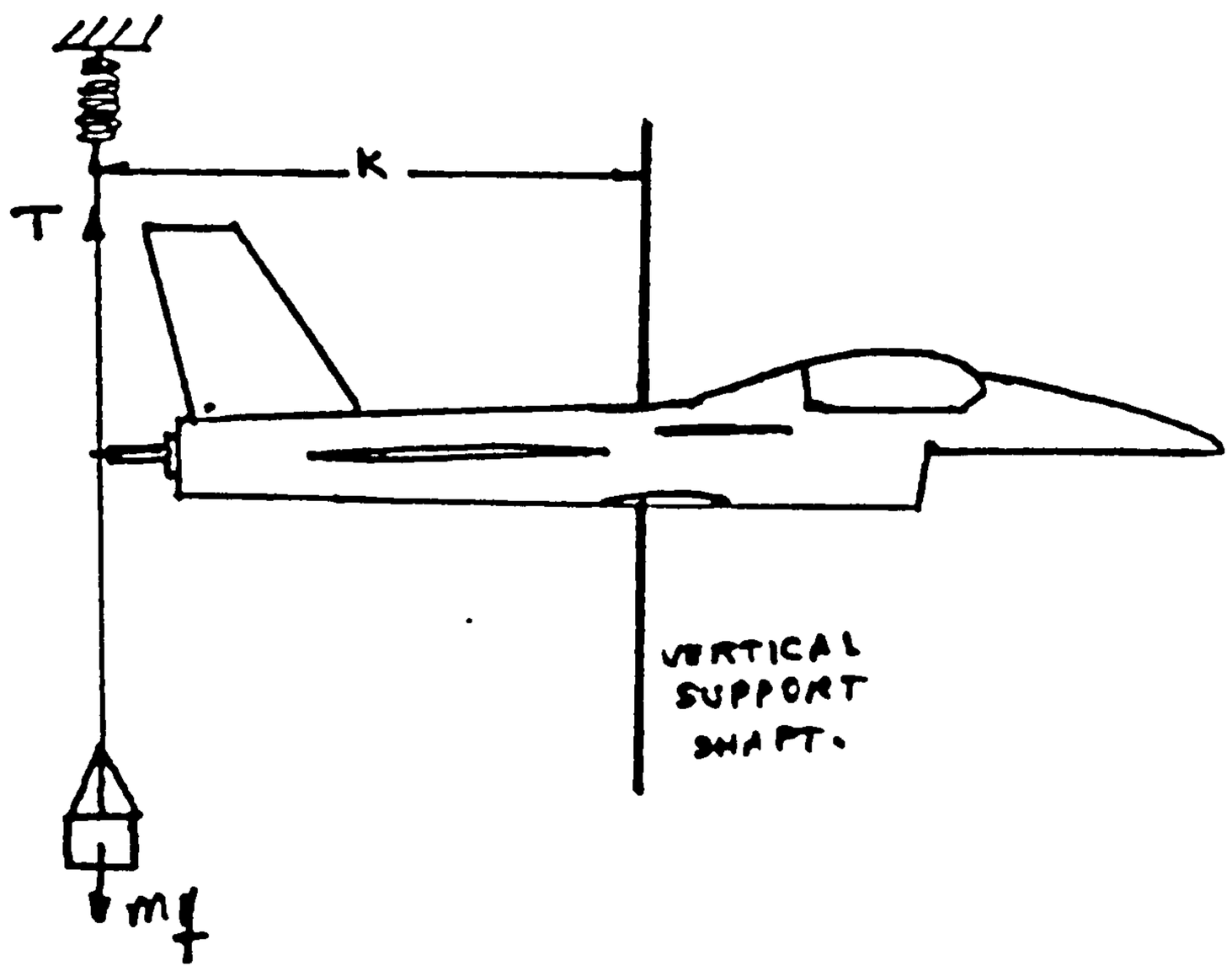

For small displacement from equilibrium position

$$mgk - Tk = I_{yy}\ddot{\theta}$$

where $T = Ax$, A = modulus of the spring

and for small θ

$$\dot{x} = k\theta$$

$$mgk - Ak^2\theta = I_{yy}\ddot{\theta}$$

Multiply both sides by $2\frac{d\theta}{dt}$ and integrate

$$2(mgk - Ak^2\theta)\frac{d\theta}{dt} = I_{yy}\cdot\frac{d}{dt}\left(\frac{d\theta}{dt}\right)^2$$

$$\Rightarrow \left(\frac{d\theta}{dt}\right)^2 = \frac{2}{I_{yy}}\int(mgk - Ak^2\theta)d\theta$$

$$\Rightarrow \left(\frac{d\theta}{dt}\right)^2 = \frac{2mgk\theta - Ak^2\theta^2 + B}{I_{yy}}$$

where B is constant.

$$\therefore \quad \frac{d\theta}{dt} = \sqrt{-\frac{Ak^2}{I_{yy}}\left(\theta^2 - \frac{2mgk}{Ak^2}.\theta - \frac{I_{yy}}{Ak^2}.B\right)}$$

$$\frac{d\theta}{dt} = \sqrt{-\frac{Ak^2}{I_{yy}}\left[\left(\theta - \frac{mgk}{Ak^2}\right)^2 - \left(\frac{mgk}{Ak^2}\right)^2 - \frac{I_{yy}}{Ak^2}.B\right]}$$

$$\frac{d\theta}{dt} = \sqrt{\frac{Ak^2}{I_{yy}}\left\{\left[\left(\frac{mgk}{Ak^2}\right)^2 + \frac{I_{yy}}{Ak^2}.B\right] - \left(\theta - \frac{mgk}{Ak^2}\right)^2\right\}}$$

or

$$\frac{d\theta}{dt} = \sqrt{\frac{Ak^2}{I_{yy}}} \cdot \sqrt{\left\{\left[\left(\frac{mgk}{Ak^2}\right)^2 + \frac{I_{yy}}{Ak^2}.B\right] - \left(\theta - \frac{mgk}{Ak^2}\right)^2\right\}}$$

Integration yields,

$$\pm \mathrm{Sin}^{-1} \frac{\left(\theta - \frac{mgk}{Ak^2}\right)}{\sqrt{\left(\frac{mgk}{Ak^2}\right)^2 + \frac{I_{yy}}{Ak^2}.B}} = \sqrt{\frac{Ak^2}{I_{yy}}}.t$$

$$\frac{\theta - \frac{mgk}{Ak^2}}{\sqrt{\left(\frac{mgk}{Ak^2}\right)^2 + \frac{I_{yy}}{Ak^2}.B}} = \mathrm{Sin}\left(\sqrt{\frac{Ak^2}{I_{yy}}}.t + C\right)$$

or

$$\theta = \sqrt{\left(\frac{mg}{Ak}\right)^2 + \frac{I_{yy}}{Ak^2}.B}.\left\{\mathrm{Sin}\left(\sqrt{\frac{Ak^2}{I_{yy}}}.t + c\right)\right\} + \frac{mg}{Ak}$$

where n = undamped angular frequency = $\sqrt{\frac{Ak^2}{I_{yy}}}$

$$\therefore \quad \text{period } T = \frac{2\pi}{n} = \frac{2\pi}{\sqrt{\frac{Ak^2}{I_{yy}}}}$$

or

$$I_{yy} = \frac{Ak^2_{yy} T^2_{yy}}{4\pi^2}$$

Similarly

$$I_{xx} = \frac{Ak^2_{xx} T^2_{xx}}{4\pi^2}$$

----- EQ.G.1

Here the weight was chosen to be 150 gr. which includes the weight and mounting assembly onto the model. The trace of the oscillations about x-x and y-y axis showed that the damping was small so the damped frequency was assumed to be the same as the natural undamped frequency of the system. Therefore, from Eq.G1,

$$I \approx \frac{Ak^2.T^2}{4\pi^2}$$

about
x-x and y-y
axis

where k is the distance between axis of rotation and point of connection to the spring.

From Fig.G4,G5, with plotter set on 500 mm/min paper feed, the periods were found to be

T_{x-x} = 0.708 S

T_{y-y} = 1.236 S

where

k_{x-x} = 0.345 m

k_{y-y} = 0.46 m

Since the gun and missiles have not been represented on the model, then their masses and moments of inertia were subtracted from those given in Table E1 of Appendix E.

This modification brought about the following changes:

Mass of aircraft = 18073.37 lb = 8050.5 kg

$$I_{xx_{A/C}} = 358650.42 \text{ lb ft}^2 = 14841.74 \text{ kg m}^2$$

$$I_{yy_{A/C}} = 1657395.36 \text{ lb ft}^2 = 68586.7 \text{ kg m}^2$$

$$I_{zz_{A/C}} = 1956341.07 \text{ lb ft}^2 = 80957.7 \text{ kg m}^2$$

When scaled down dynamically:

Mass of model $\approx$ 3.0 kg

$I_{xx_{model}}$ = 0.028 kg m^2

$I_{yy_{model}}$ = 0.127 kg m^2

$I_{zz_{model}}$ = 0.150 kg m^2

The above set of values should not be considered very accurate since the moments of inertia of the aircraft itself were found approximately. Therefore, these values would serve as a guide line. The experiments based on the mathematical model outlined earlier yielded the following results:

$$I_{xx} \approx \frac{Ak_{xx}^2 T_{xx}^2}{4\pi^2} = 0.026 \text{ kg m}^2$$

$$I_{yy} \approx \frac{Ak_{yy}^2 T_{yy}^2}{4\pi^2} = 0.139 \text{ kg m}^2$$

I_{zz} measurement

With reference to Fig.G3, it can be said that for small oscillations:

$$\Rightarrow \pm \sin^{-1} \frac{\frac{\theta}{B.I_{zz}}}{2Ak^2} = \sqrt{\frac{2Ak^2}{I_{zz}}}.t + C$$

$$\theta = \pm \frac{B.I_{zz}}{2Ak^2} . \sin\left(\sqrt{\frac{2Ak^2}{I_{zz}}}.t + C\right)$$

n = angular frequency = $\sqrt{\frac{2Ak^2}{I_{zz}}}$

$$T = \frac{2\pi}{n}$$

$$T = \frac{2\pi}{\sqrt{\frac{2Ak^2}{I_{zz}}}}$$

$$= T^2 = \frac{4\pi^2 . I_{zz}}{2Ak^2}$$

$$= I_{zz} = \frac{Ak^2}{2\pi^2} . T^2$$

Here k = 0.5 m

With reference to Fig. G.6, with plotter set to 500 mm/min paper feed, the period of the oscillations about the zz-axis was found to be

$$T_{zz} = 0.84 \text{ s}$$

$$\therefore I_{zz} \simeq \frac{16.922 \times 0.5^2}{2 \times \pi^2} . 0.84^2$$

$$I_{zz} \simeq 0.151 \quad \text{kg m}^2$$

The same argument for I_{xx} and I_{yy} applies to I_{zz} as well.

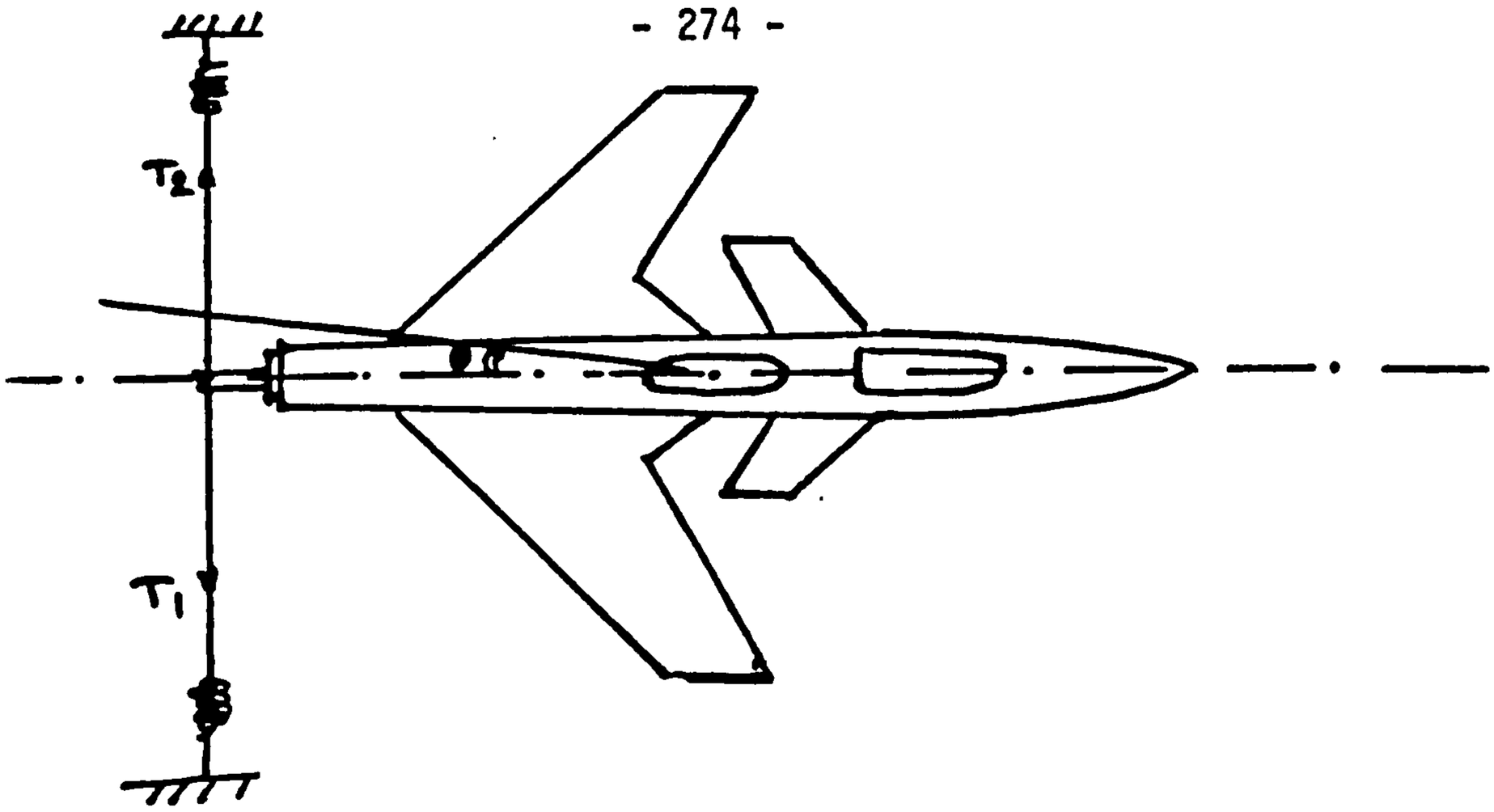

$$T_1k - T_2k = I\ddot{\theta}$$

$$A(\ell - k\theta).k - A(\ell + k\theta).k = I\ddot{\theta}$$

$$A\ell k - Ak^2\theta - A\ell k - Ak^2\theta = I\ddot{\theta}$$

$$-2Ak^2\theta = I_{zz}\ddot{\theta}$$

$$2\frac{d\theta}{dt} \cdot \frac{d^2\theta}{dt} = -4\frac{Ak^2}{I_{zz}}.\theta.\frac{d\theta}{dt}$$

$$\left(\frac{d\theta}{dt}\right)^2 = \int -\frac{4Ak^2}{I_{zz}}\,\theta d\theta$$

$$= -\frac{4Ak^2\theta^2}{I_{zz}.2} + B$$

$$\frac{d\theta}{dt} = \sqrt{-\frac{4Ak^2}{I_{zz}} \cdot \frac{\theta^2}{2} + B}$$

$$\frac{d\theta}{dt} = \sqrt{\frac{2Ak^2}{I_{zz}}} \cdot \sqrt{\frac{B.I_{zz}}{2Ak^2} - \theta^2}$$

$$\frac{d\theta}{\sqrt{\frac{B.I_{zz}}{2Ak^2} - \theta^2}} = \sqrt{\frac{2Ak^2}{I_{zz}}} \cdot dt$$

where $T_1 = A(\ell - x)$

$T_2 = A(\ell + x)$

x is the extension and

ℓ is the length of the spring

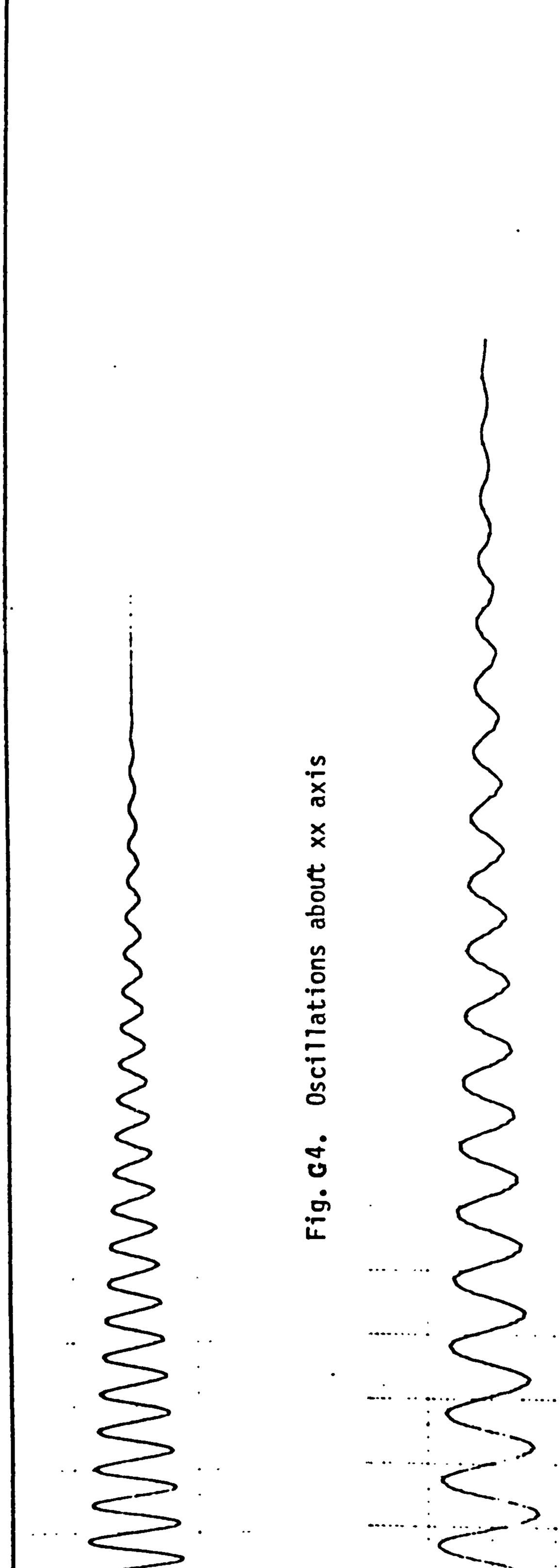

Fig. G4. Oscillations about xx axis

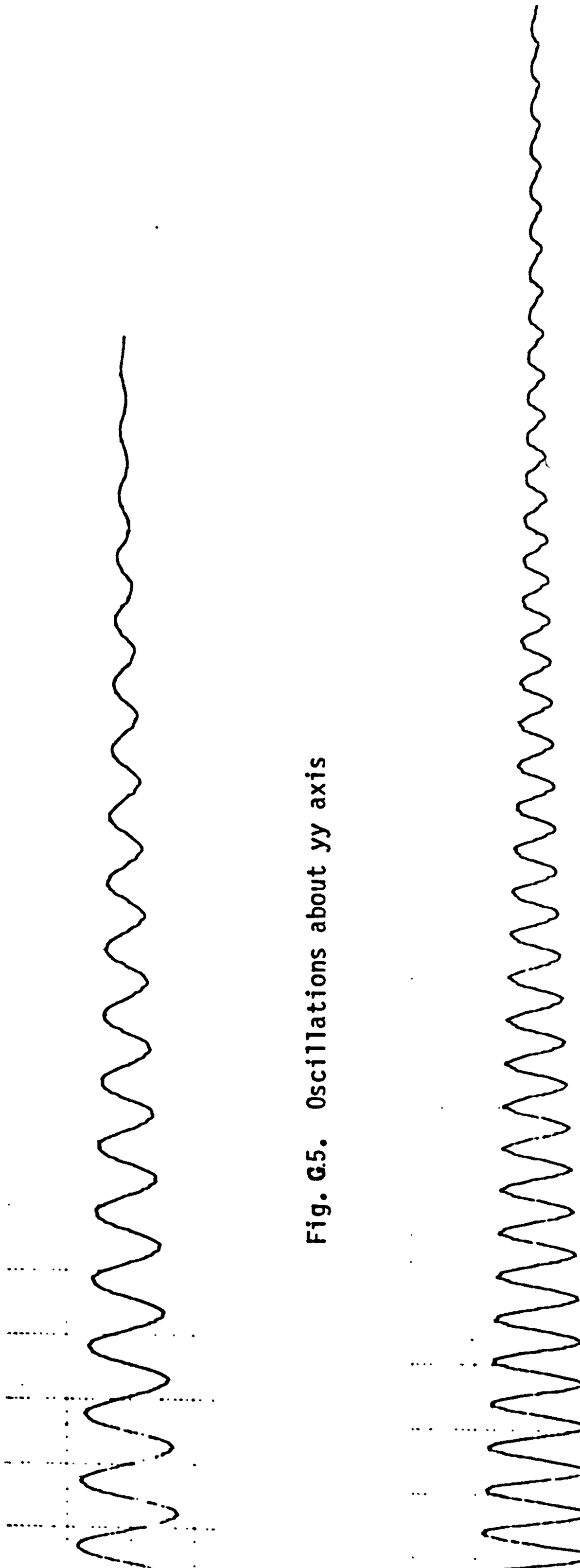

Fig. G5. Oscillations about yy axis

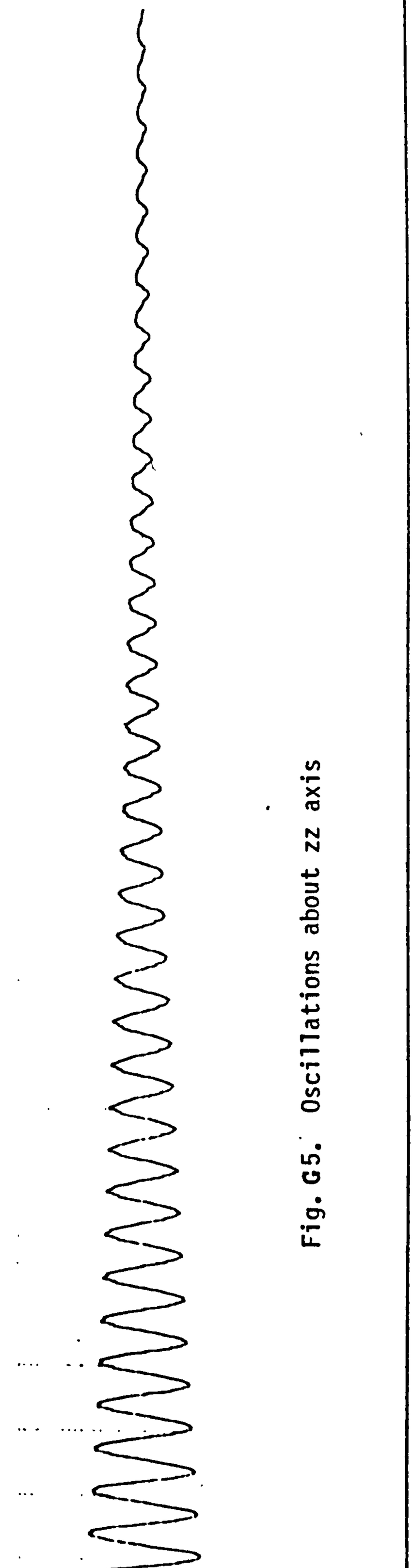

Fig. G5. Oscillations about zz axis

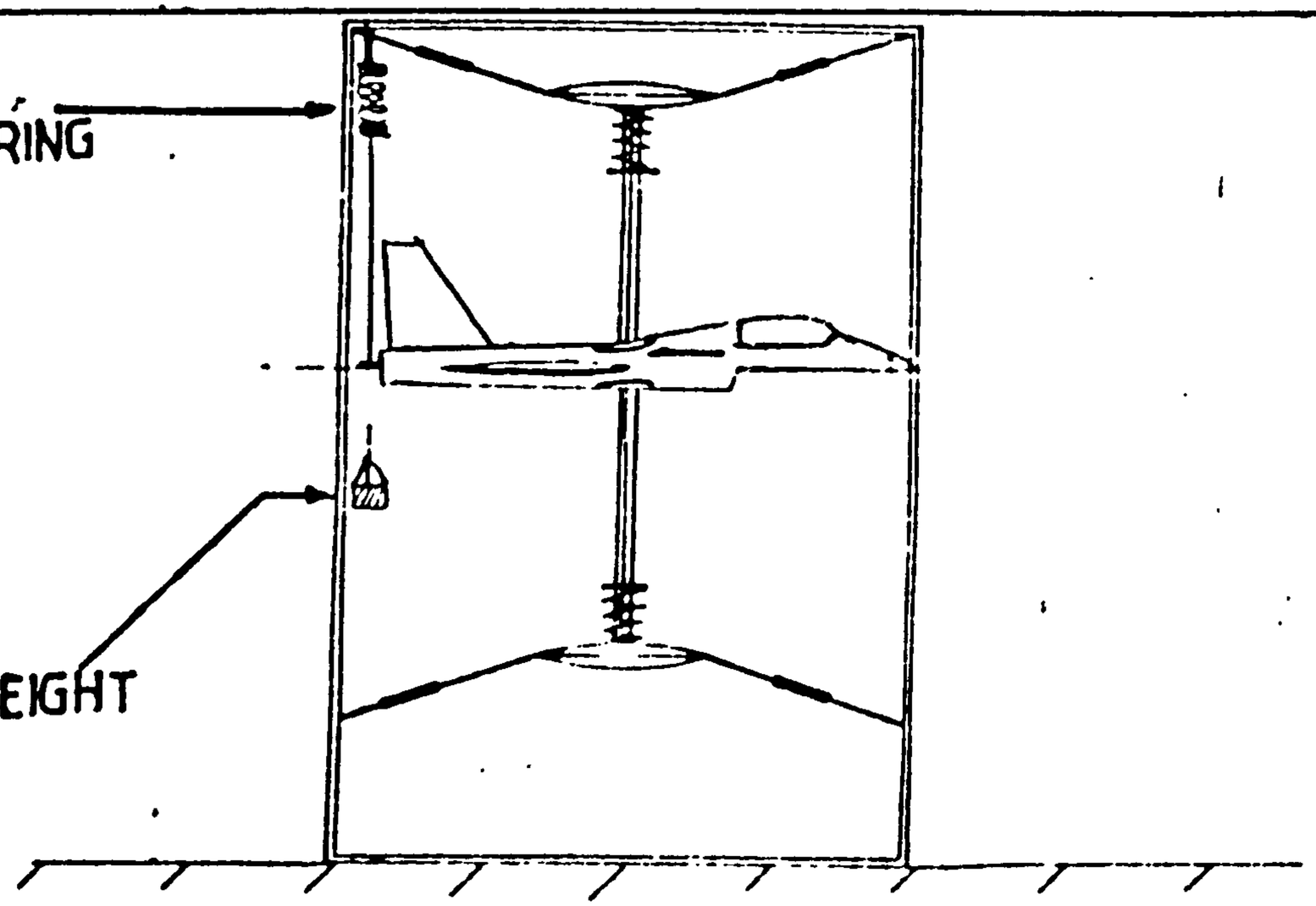

Fig. G 1.

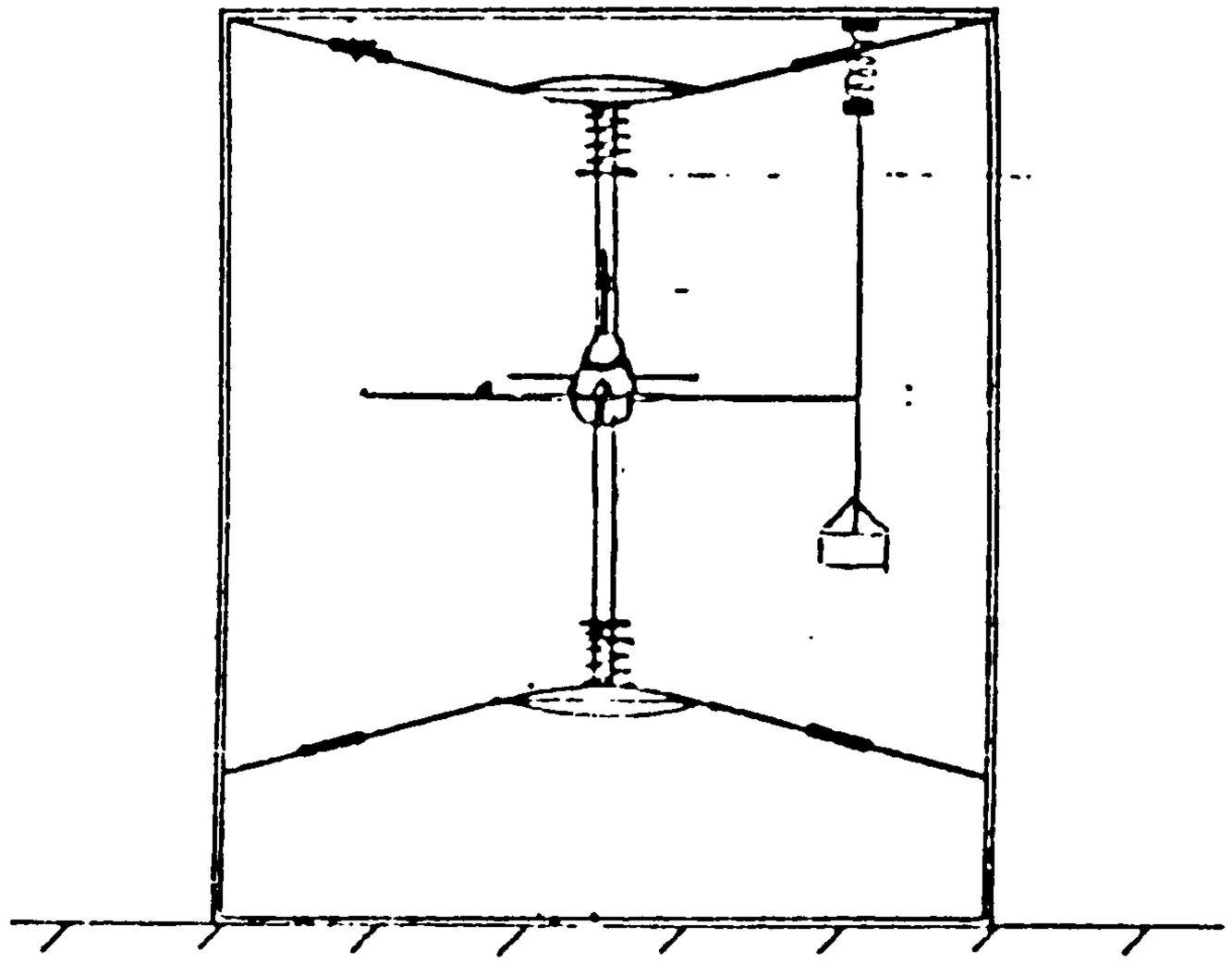

Fig. G.2.

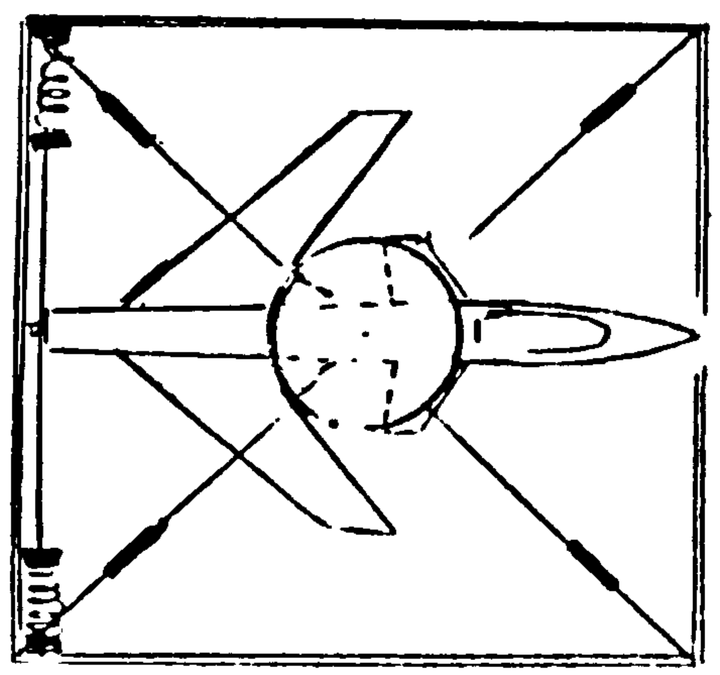

Fig. G.3.

THESE FIGURES REPRESENT THE SUSPENSION SYSTEM AND THE MASS-SPRING ARRANGEMENTS FOR THE DETERMINATION AND ADJUSTMENT OF THE PRINCIPAL MOMENTS OF INERTIA, I_{xx}, I_{yy} and I_{zz}

G.2 EXPERIMENTAL DETERMINATION OF THE NEUTRAL POINT POSITION

The pitching moment equation is given by - neglecting the downwash and unwash.

$$C_{M_{c.g.}} \simeq C_{M_O} - \frac{X_w}{\bar{c}} C_{L_{w.B}} + \bar{V}_c C_{L_c} + (C_{M_{c.g.}})_{intake}$$

where the drag component is neglected.

Differentiate w.r.t. C_L;

$$\frac{dC_{M_{c.g.}}}{dC_L} \simeq - \frac{X_w}{\bar{c}} + \bar{V}_c \cdot \frac{dC_{L_c}}{dC_L} + \left(\frac{dC_{M_{c.g.}}}{dC_L}\right)_{ontake}$$

$$= -\left(\frac{X_{c.g.} - X_{AC}}{\bar{c}}\right) + \bar{V} \cdot \frac{dC_{L_{c.B}}}{dC_{L_{w.B}}} + \frac{2\dot{m}}{\rho V_\infty S_w \bar{c}} \cdot \frac{\partial B}{\partial C_{L_{w.B}}} \cdot (X_{np} - X_{in})$$

where $\bar{V}_c$ = canard volume coefficient.

Neglecting the intake term;

$$\frac{dC_{M_{c.g.}}}{dC_L} = - \left(\frac{X_{c.g.} - X_{AC}}{\bar{c}}\right) + \bar{V} \cdot \frac{a_{c.B}}{a_{w.B}} + \bar{V} \cdot a_{c.B} \cdot \frac{d\eta}{dC_{L_{w.B}}}$$

which should equate zero when c.g. is placed on the neutral point.

$$\therefore \frac{d\eta}{dC_{L_{w.B}}} = \frac{- \frac{X_{c.g.} - X_{AC}}{\bar{c}} + \bar{V} \cdot \frac{a_{c.B}}{a_{w.B}}}{\bar{V} \cdot a_{c.B}}$$

For stick-fixed case $\frac{d\eta}{dC_L} = 0$ since canard is not moving.

Then;

$$\frac{X_{np}}{\bar{c}} = \frac{X_{AC}}{\bar{c}} + \bar{V} \cdot \frac{a_{c.B}}{a_{w.B}}$$

$$\therefore \quad \frac{d\eta}{dC_L} = \frac{X_{c.g.} - X_{np}}{\bar{V} \cdot a_{c.B}} = \frac{k_s}{\bar{V} \cdot a_{c.B}}$$

where k_s is static margin stick-fixed.

The dynamic model was then made to fly in trim at different speeds. For every speed, n_{trim} was measured and C_L calculated since,

$$C_L = \frac{mg}{\frac{1}{2}\rho U^2 S_w}$$

This process was repeated for three known C.G. positions and results given in Tables G1, G2 and G3. Variations of C_L with n_{trim} for the C.G. settings are depicted in Figure G1. Slopes of C_L - n_{trim} curves from Figure G1 were then calculated and plotted against the C.G. positions (Fig. G2). The intersection of this line and the axis representing the C.G. location was found to be approximately 0.445 m from datum. This represents a static margin stick-fixed of approximately -1% $\bar{c}$. Table G4 gives the static margin corresponding to the three C.G. settings used in this experiment.

C.G. AT 0.444m FROM DATUM		
APPROXIMATE TUNNEL SPEED U (m/s)	n_{TRIM} (deg)	C_L
24.85	8	0.93
27.04	6	0.78
28.22	5	0.72
30.17	4	0.63

TABLE G1

VARIATION OF C_L WITH n_{trim} FOR THE RESPECTIVE C.G. POSITIONS

C.G. AT 0.439m FROM DATUM		
APPROXIMATE TUNNEL SPEED U (m/s)	n_{TRIM} (deg)	C_L
22.81	8	1.1
23.16	6	1.07
23.34	5	1.05
23.51	4	1.03

TABLE G2

C.G. AT 0.435m FROM DATUM		
APPROXIMATE TUNNEL SPEED U (m/s)	η_{TRIM} (deg)	C_L
22.08	8	1.17
22.08	6	1.17
22.08	4	1.17

TABLE G3

VARIATION OF C_L WITH η_{trim} .

C.G. POSITION (m)	0.444	0.439	0.435
STATIC MARGIN STICK FIXED $\%\bar{c}$	≃ -1.0	≃ -4.0	≃ -6.0

TABLE G4

ESTIMATED STATIC MARGIN STICK-FIXED FOR THE THREE C.G. SETTINGS

η_{TRIM} VERSUS C_L GRAPHS FOR PRE-SET C.G. POSITIONS.

SYMBOL	SLOPE (deg)	C.G. POSITION RELATIVE TO DATUM.
Δ -	12.96	0.444
x -	57.14	0.439
o -	∞	0.435

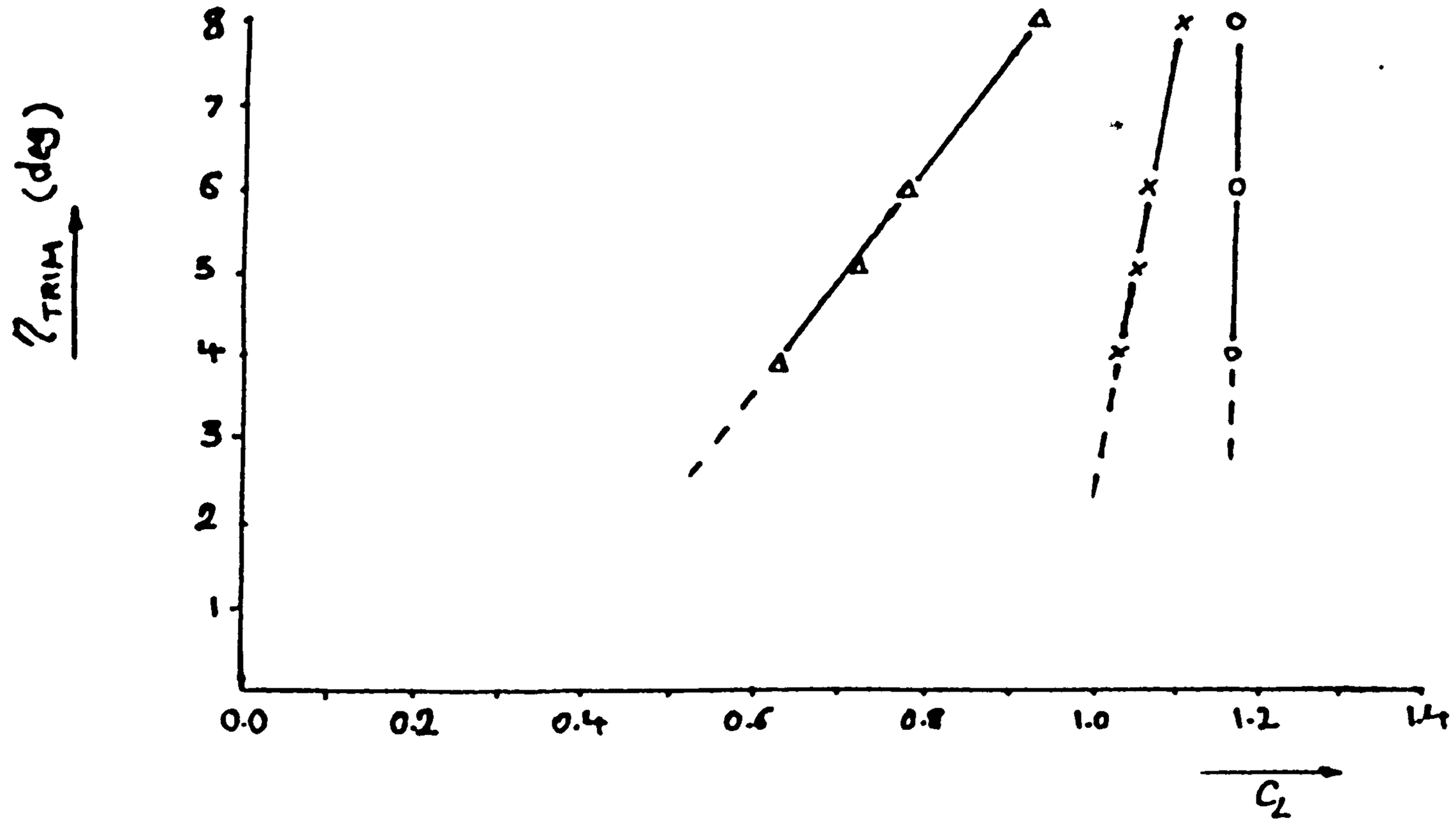

FIGURE G1

A GRAPH OF $\frac{d\ell_{TRIM}}{dC_L}$ VERSUS C.G. POSITION.

NP : POSITION OF NEUTRAL POINT RELATIVE TO DATUM. $\simeq 44.54 \times 10^{-2}$ m

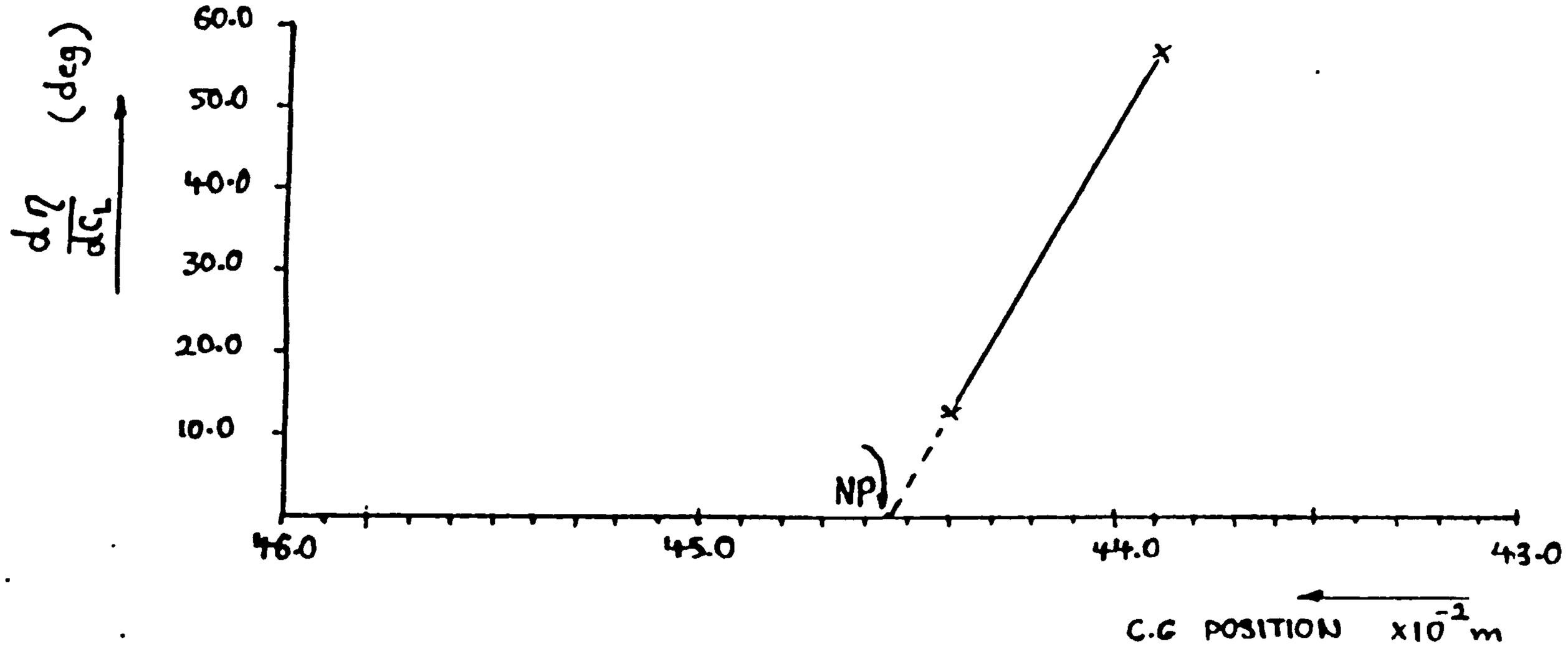

FIGURE G 2

APPENDIX - H

STATIC WIND TUNNEL RESULTS

H.1 Longitudinal Measurements

These tests were carried out at approximate tunnel speeds of 19, 25 and 28 m/s, which are corrected for tunnel interference. Results include pitching moment, lift and drag variations with incidence for various canard angle settings (see Table H1).

Aerodynamic data extracted from Table H1 are presented in TableH .2, together with the corresponding theoretical values where available from Appendix B. From available pitching moment and lift data, the position of the N.P. was estimated to be at 0.025 m ahead of the C.G. position at 0.435 m from datum. This would result in an approximate negative static margin stick-fixed of -14% $\bar{c}$.

H.2 Lateral Measurements

These tests were mainly concerned with the yaw variations, although rolling moment due to aileron deflection at zero yaw was also examined. These measurements are coded according to Table H3. As before, results have been corrected for tunnel interference. Unlike the longitudinal case above, there was not scope for a substantial comparison between theory and experiment. However, aerodynamic data obtained through Table H3 is presented in Table H4 and where treated theoretically, results are given.

PAGE

NUMBERING

AS ORIGINAL

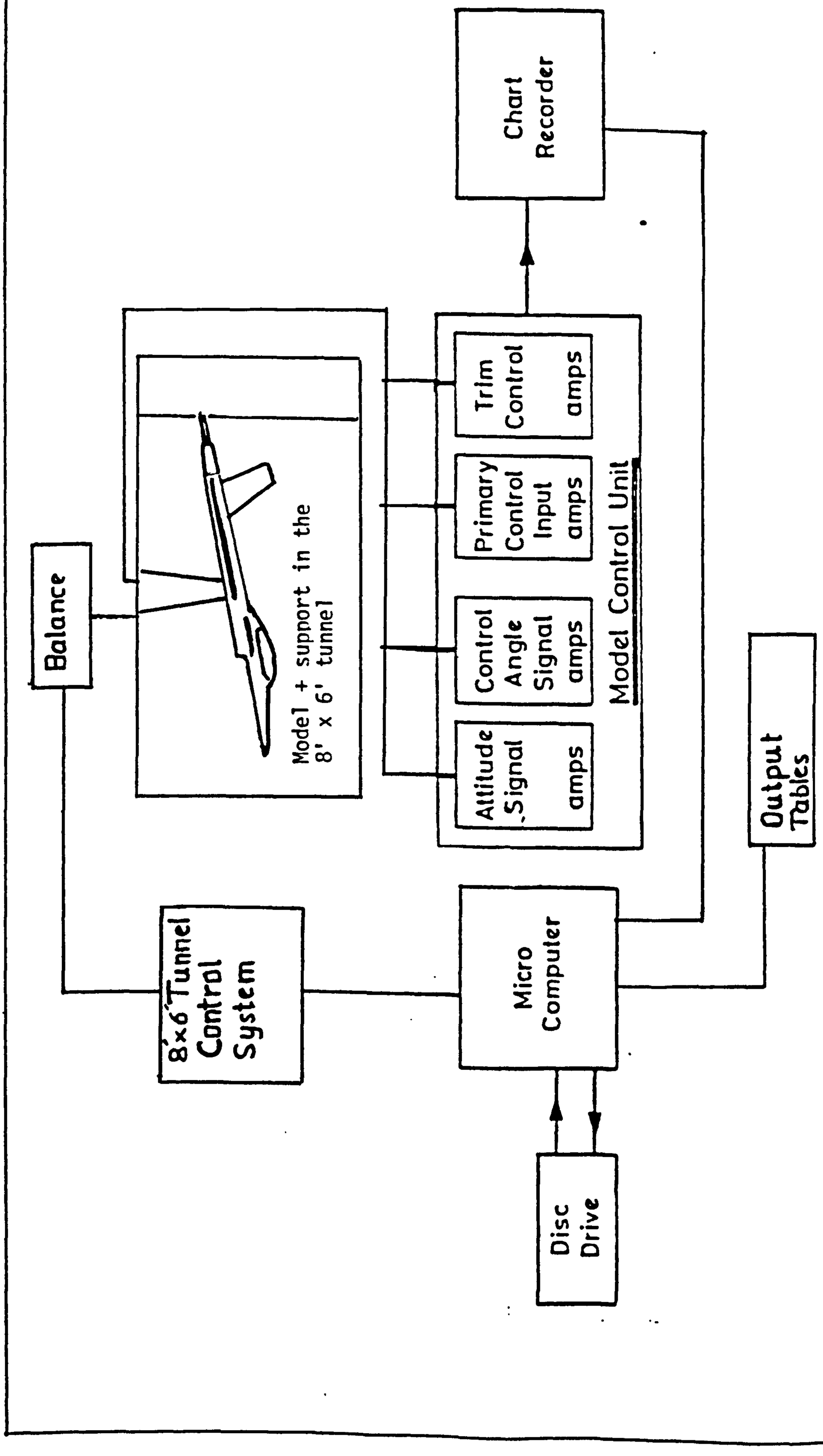

FIGURE.H DATA ACQUISITION AND INSTRUMENTATION FACILITY FOR THE STATIC TUNNEL MEASUREMENTS

C.G. AT 0.435 m FROM DATUM	TUNNEL SPEED ≈ (m/s)	VARIATION OF C_L WITH α^o (CANARD ON)	VARIATION OF C_M WITH α^o (CANARD OFF)	DRAG POLARS		VARIATION OF C_L WITH α^o (CANARD OFF)
				CANARD ON	CANARD OFF	
	19	FIG. M3	FIG. M4	FIG.M	-	-
	25	FIG. M2	-	FIG.M7	-	-
	28	FIG. M1	FIG. M5	FIG.M6	FIG.M15	FIG. M12

TABLE H.1

SYMMETRICAL FORCE-MOMENT MEASUREMENTS CORRESPONDING TO COVERED FLIGHT-ATTITUDE CONDITIONS

C.G. AT 0.435 m FROM DATUM	TUNNEL SPEED ≈ (m/s)	VARIATION OF C_n WITH ζ^o AT $\alpha = 0^o, 20^o$ WITH $\psi = 0^o$	VARIATION OF C_n WITH ζ^o AT $\alpha = 0^o, 20^o$ WITH $\psi = 10^o, 15^o$ IN EACH CASE	VARIATION OF C_ℓ WITH ξ^o AT $\alpha = 0^o$ $\psi = 0^o$
	19.0	FIG. M9	FIG. M10	-
	25.0	-	-	FIG. M11

TABLE H.3

ASYMMETRICAL FORCE-MOMENT MEASUREMENTS CORRESPONDING TO COVERED FLIGHT-ATTITUDE CONDITIONS

TUNNEL SPEED (m/s)	WING - CANARD - BODY						CANARD LIFT SLOPE A PROPORTION OF TOTAL LIFT SLOPE						
	WIND TUNNEL		THEORY (WITH THE INTERFERENCE FACTOR)		THEORY (WITHOUT THE INTERFERENCE FACTOR)		WIND TUNNEL	THEORY WITH INTER-FERENCE	THEORY WITHOUT INTER-FERENCE	WIND TUNNEL	THEORY	WIND TUNNEL	THEORY
	$(\frac{dC_L}{d\alpha})$ (rad^{-1}) total		$(\frac{dC_L}{d\alpha})$ (rad^{-1}) total		$(\frac{dC_L}{d\alpha})$ (rad^{-1}) total		$(\frac{dC_L}{d\alpha})_{\eta=0^o}$ (rad^{-1}) ≈	$(\frac{dC_L}{d\alpha})_{\eta=0^o}$ (rad^{-1})	$(\frac{dC_L}{d\alpha})_{\eta=0^o}$ (rad^{-1})	C_{D_o} for $\eta = 0^o$ ≈	C_{D_o} for $\eta=0^o$	C_{m_o}	$(\frac{dC_L}{d\eta})_{\alpha=0^o}$ (rad^{-1}) ≈
	CANARD ON $= 0^o$	CANARD OFF ≈	CANARD ON $= 0^o$	CANARD OFF	CANARD ON $= 0^o$	CANARD OFF							
19.0	3.76	3.38	4.63	3.68	3.66	3.07	0.46	0.95	0.59	0.041	0.036	-0.095	0.74
25.0												-0.098	
28.0												-0.12	

TABLE H 2

AERODYNAMIC PARAMETERS CORRESPONDING TO FLIGHT-ATTITUDES OF TABLE-H1

* All lift slopes in Table-H2 are based on the wing area

TUNNEL SPEED	$(\frac{dC_n}{d\zeta})_{\psi=0^o}(rad^{-1})$		$(\frac{dC_n}{d\zeta})_{\psi=10^o}(rad^{-1})$		$(\frac{dC_n}{d\zeta})_{\psi=15^o}(rad^{-1})$		$(\frac{dC_\ell}{d\xi})_{\psi=0^o}(rad^{-1})$	$(\frac{dC_n}{d\beta})_{\alpha=0}(rad^{-1})$	
(m/s)	$\alpha = 0^o$	$\alpha = 20^o$	$\alpha = 0^o$	$\alpha = 20^o$	$\alpha = 0^o$	$\alpha = 20^o$	$\alpha = 0^o$	WIND TUNNEL	THEORY
19.0	0.401	0.401	0.415	0.0	0.329	0.0	-	0.47	0.32
25.0	-	-	-	-	-	-	0.448	-	

TABLE H4

AERODYNAMIC PARAMETERS CORRESPONDING TO FLIGHT-ATTITUDE CONDITIONS OF TABLE-H3
BASED ON THE WING AREA

* It must be noted that the values of $\frac{dC_n}{d\zeta}$ and $\frac{dC_\ell}{d\xi}$ are average values due to non-linearity.

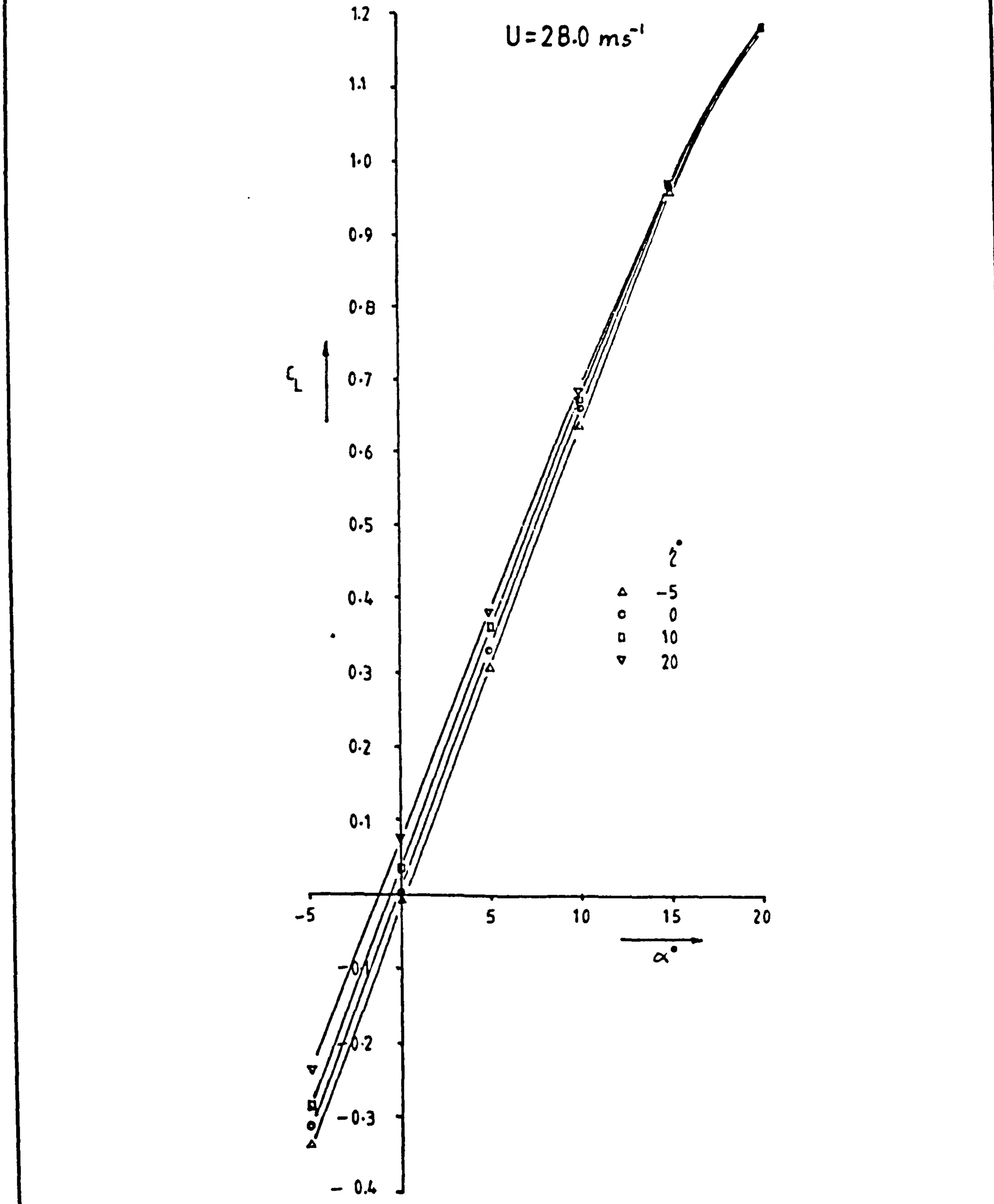

FIGURE H1

C_l - α VARIATION - CANARD ON

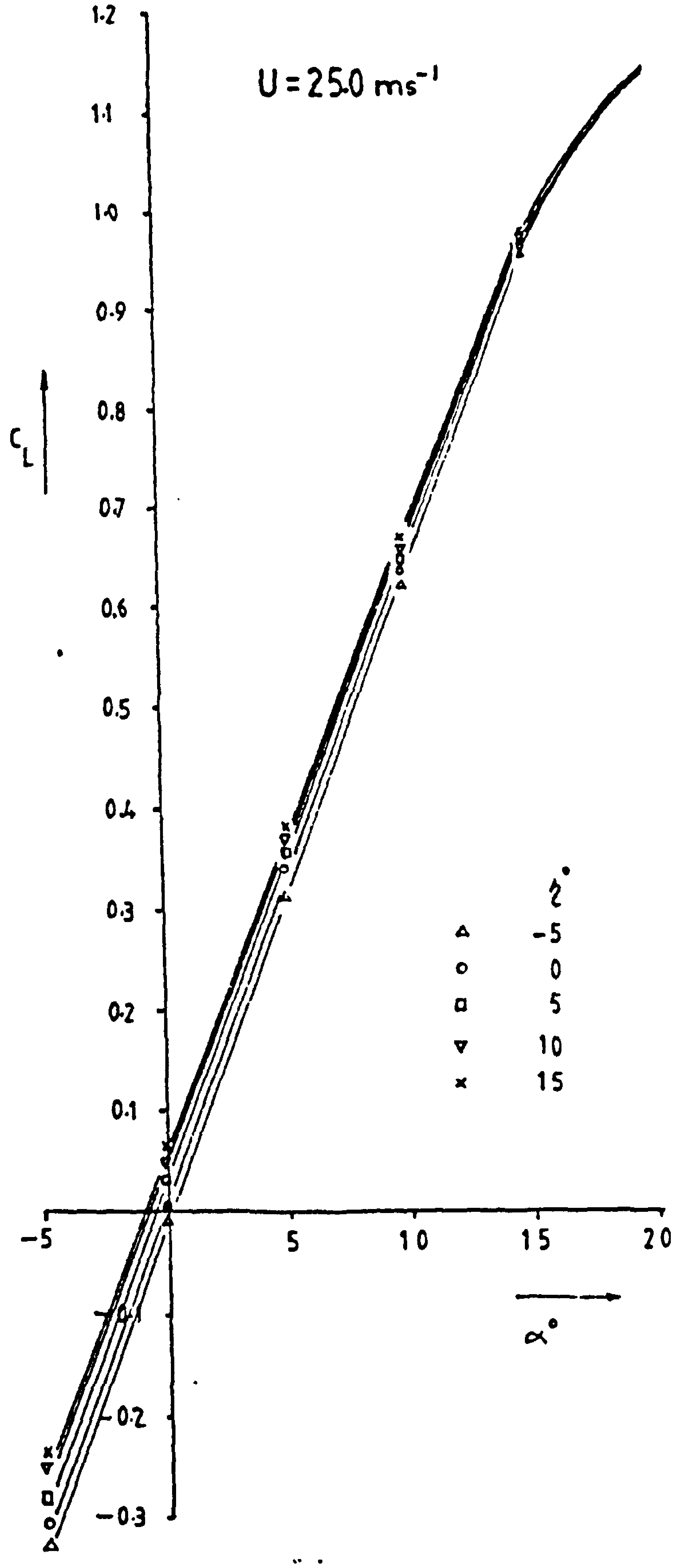

FIGURE H.2

C_L - α VARIATION - CANARD ON

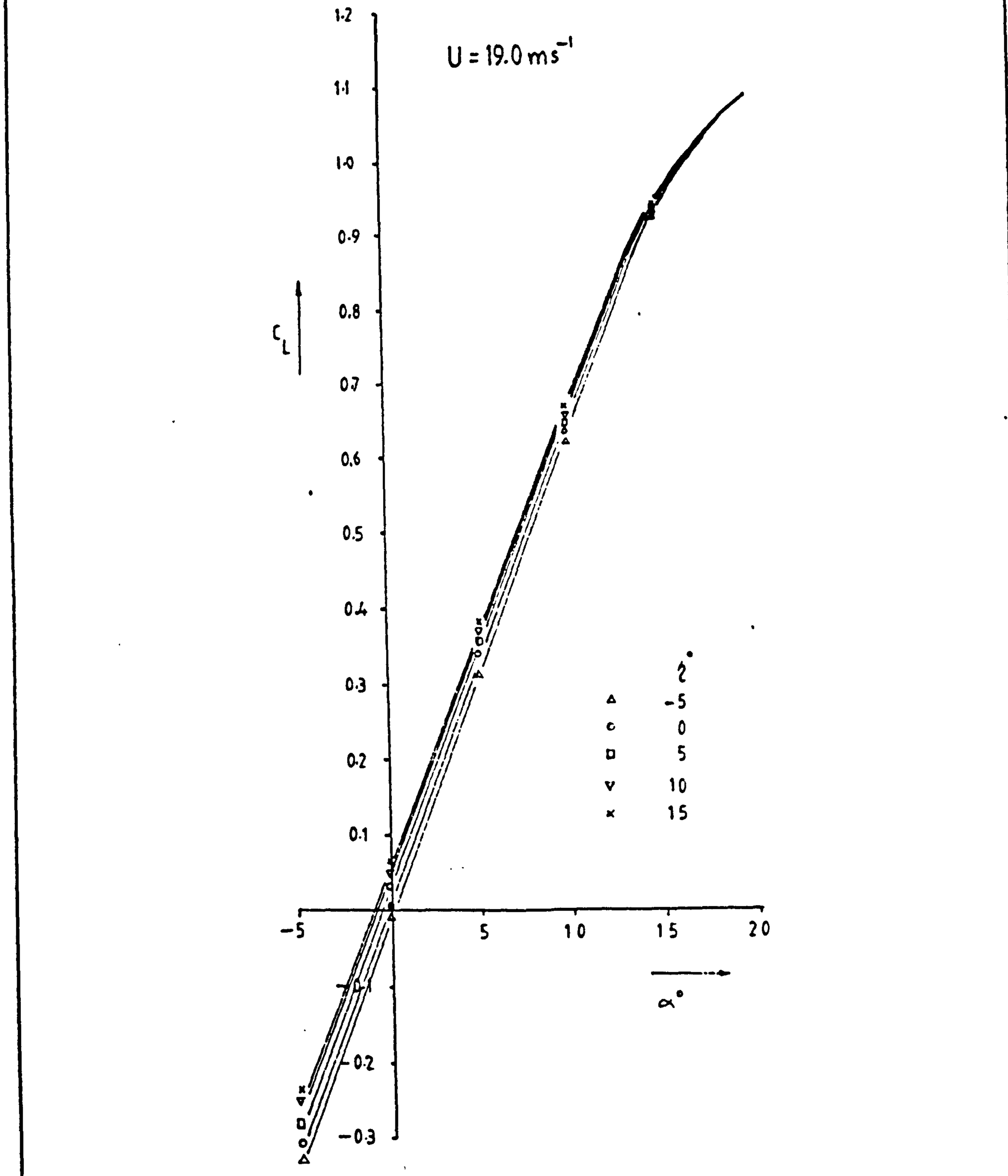

FIGURE H3

C_L - α VARIATION - CANARD ON

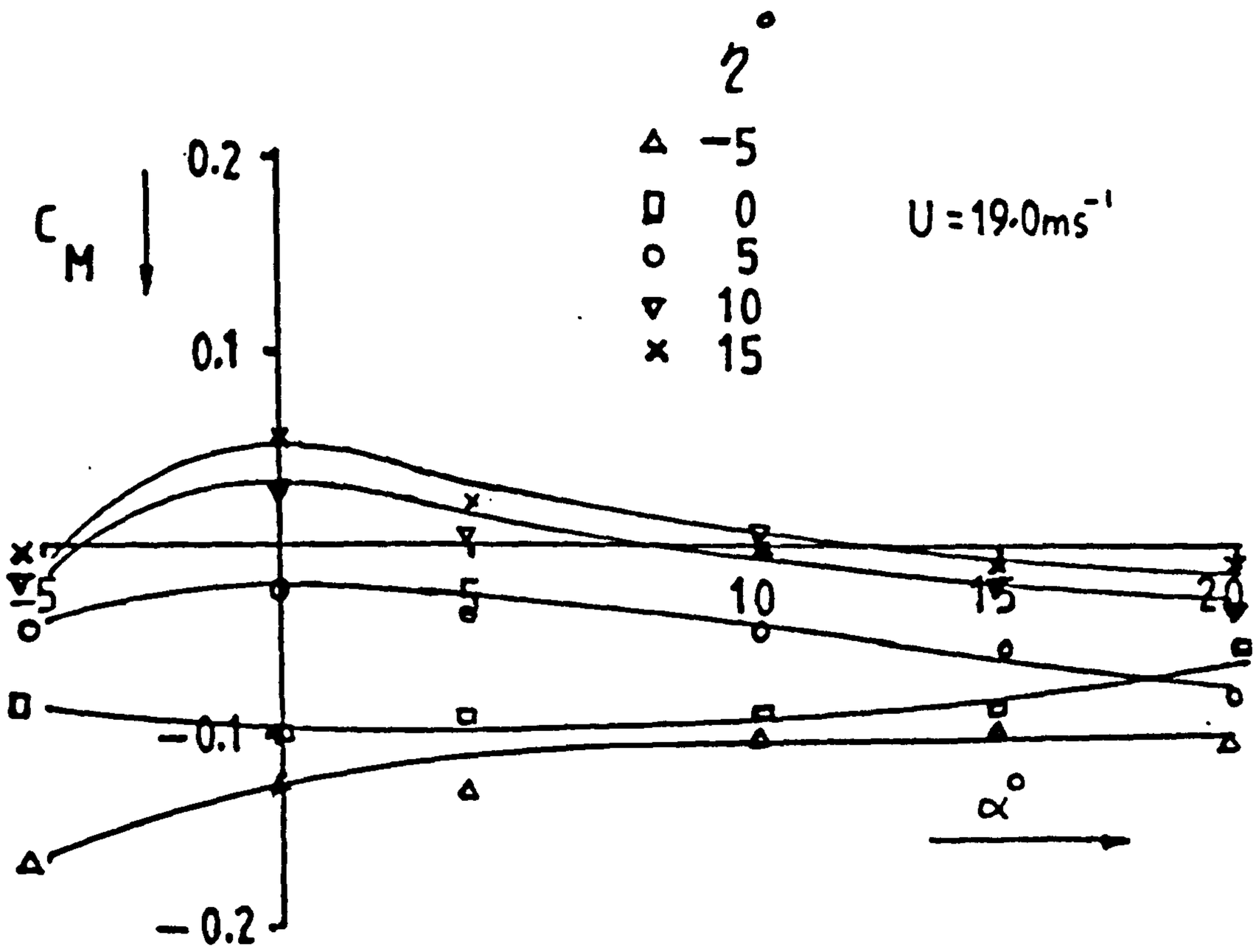

FIGURE H 4

C_m - α VARIATIONS FOR DIFFERENT CANARD SETTINGS η°

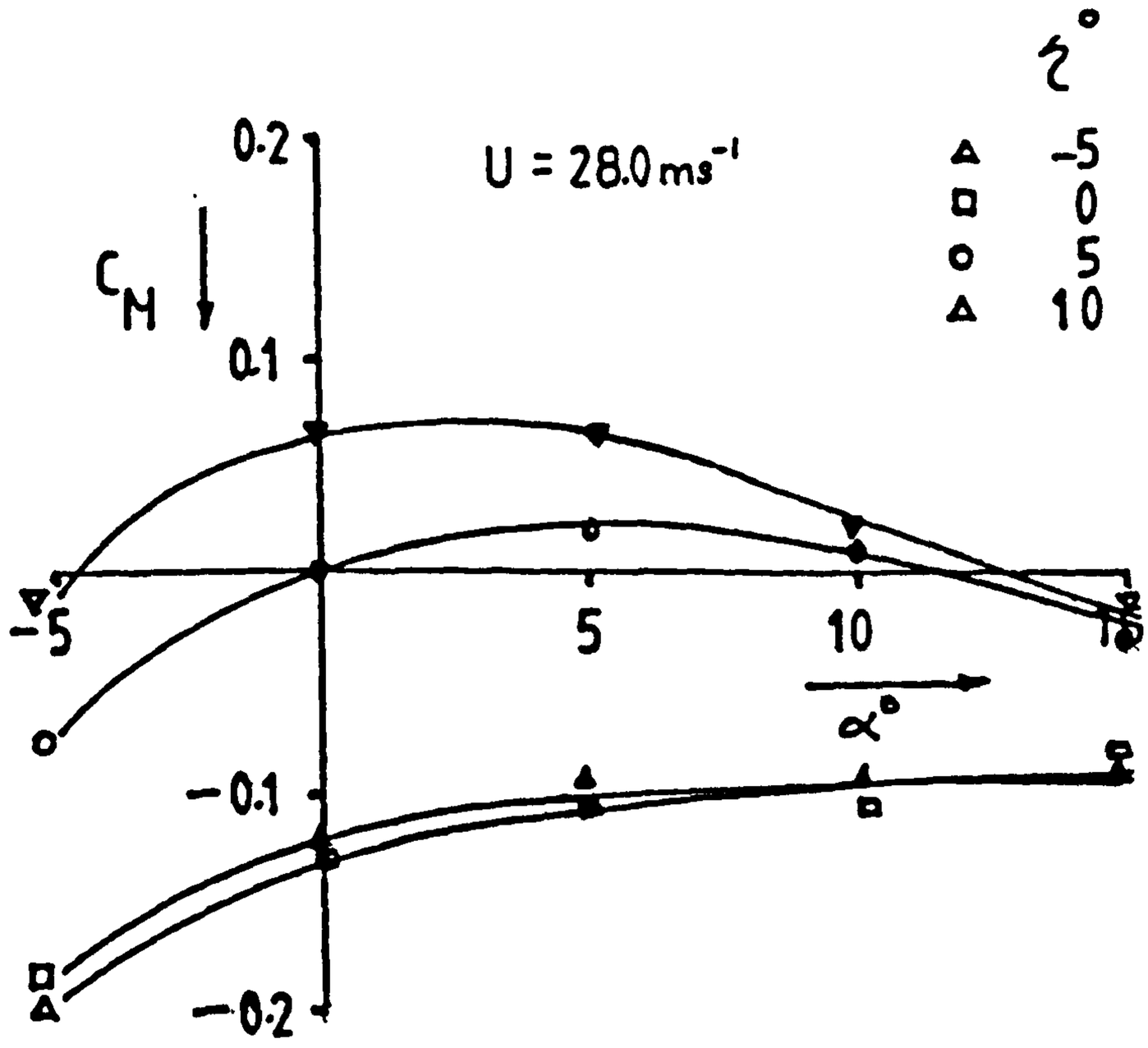

FIGURE H.5

C_m - α VARIATIONS FOR DIFFERENT CANARD SETTINGS η°

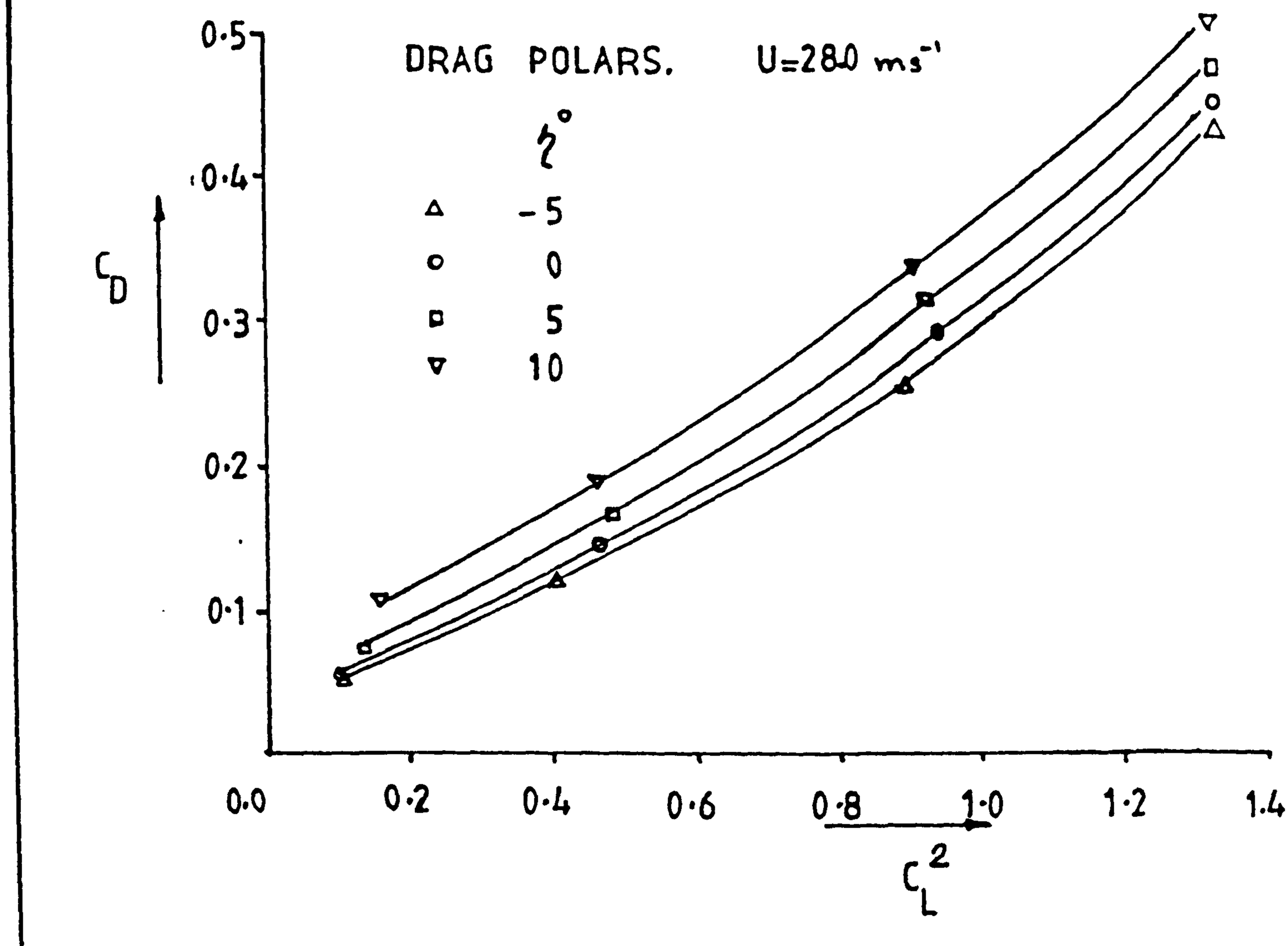

FIGURE H.6

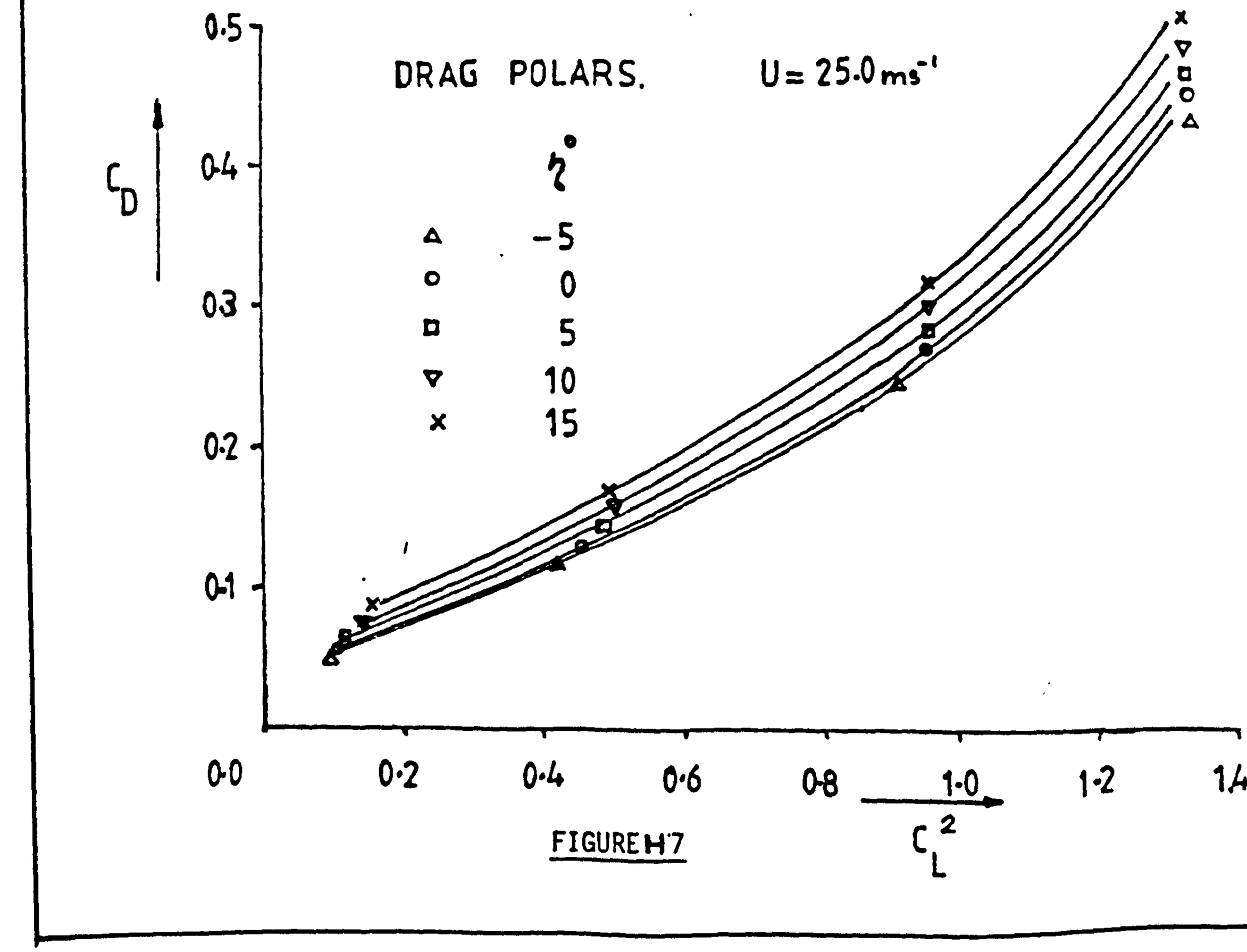

FIGURE H.7

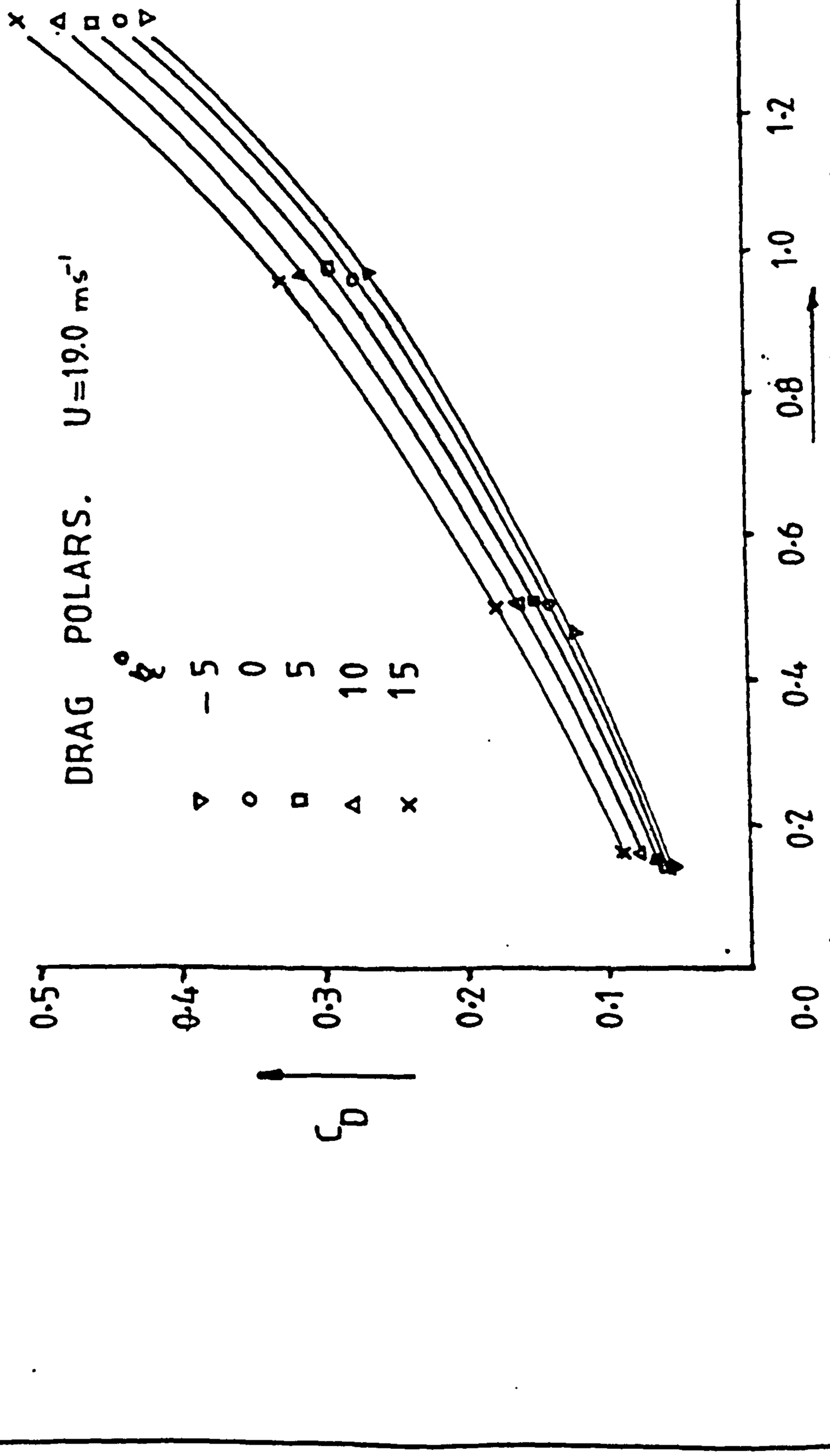
DRAG POLARS. U=19.0 ms⁻¹
ε°
−5
0
5
10
15
0.5
0.4
0.3
0.2
0.1
0.0
0.2
0.4
0.6
0.8
1.0
1.2
1.4
C_D
C_L^2

FIGURE H.8

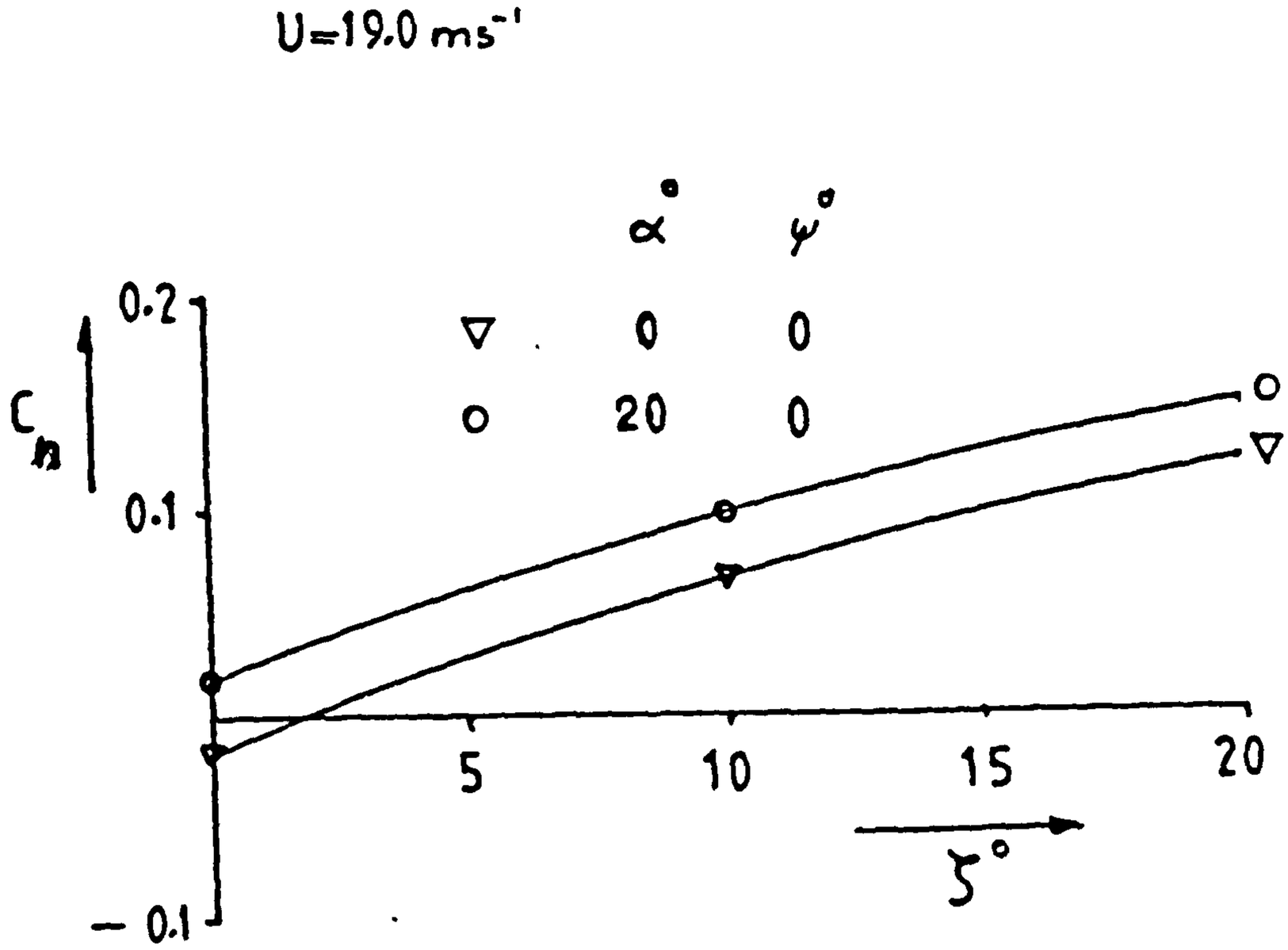

FIGURE H 9

C_n - ζ^o VARIATIONS FOR DIFFERENT INCIDENCES α^o

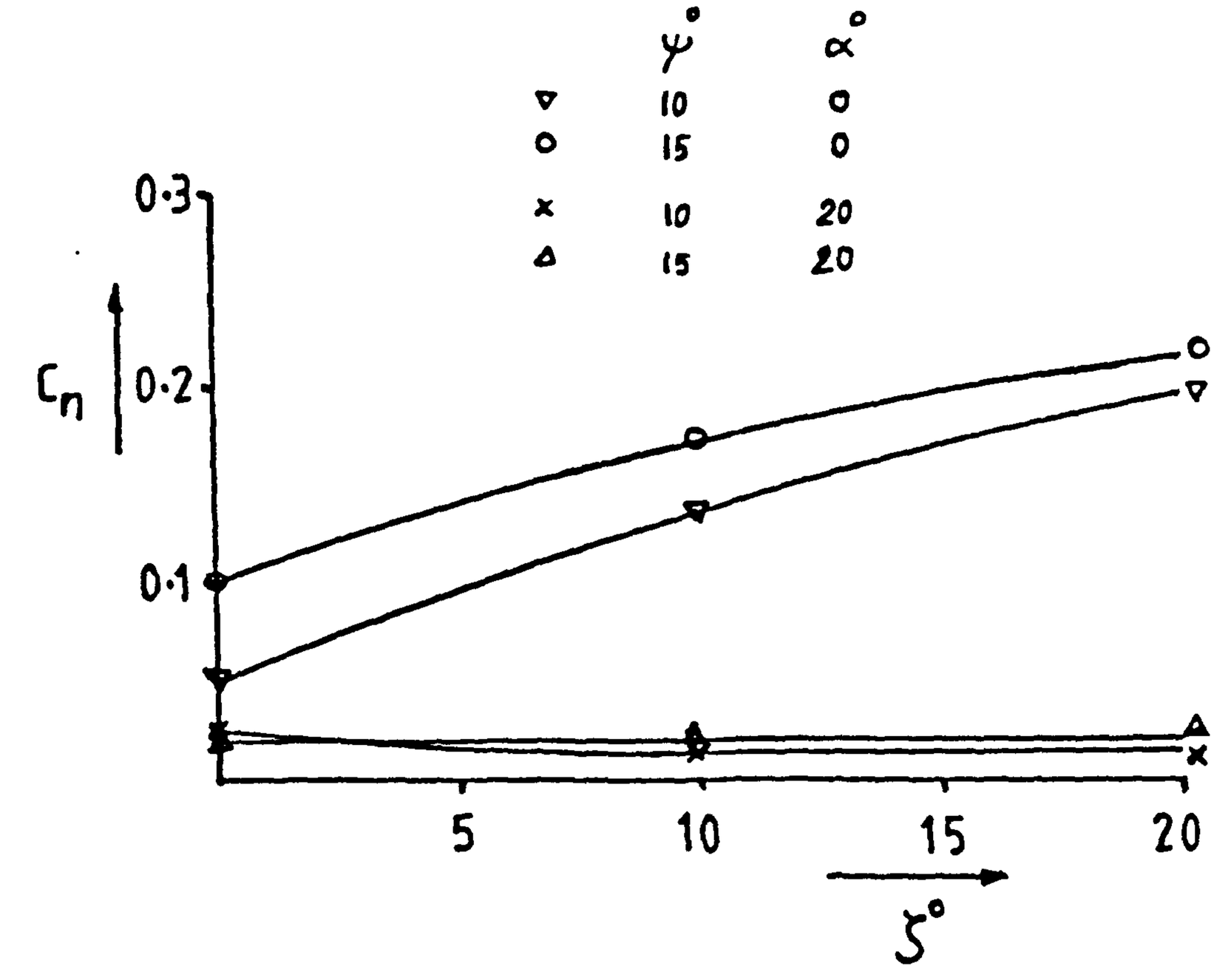

FIGURE H10

C_n - ζ^o VARIATIONS FOR DIFFERENT INCIDENCES α^o

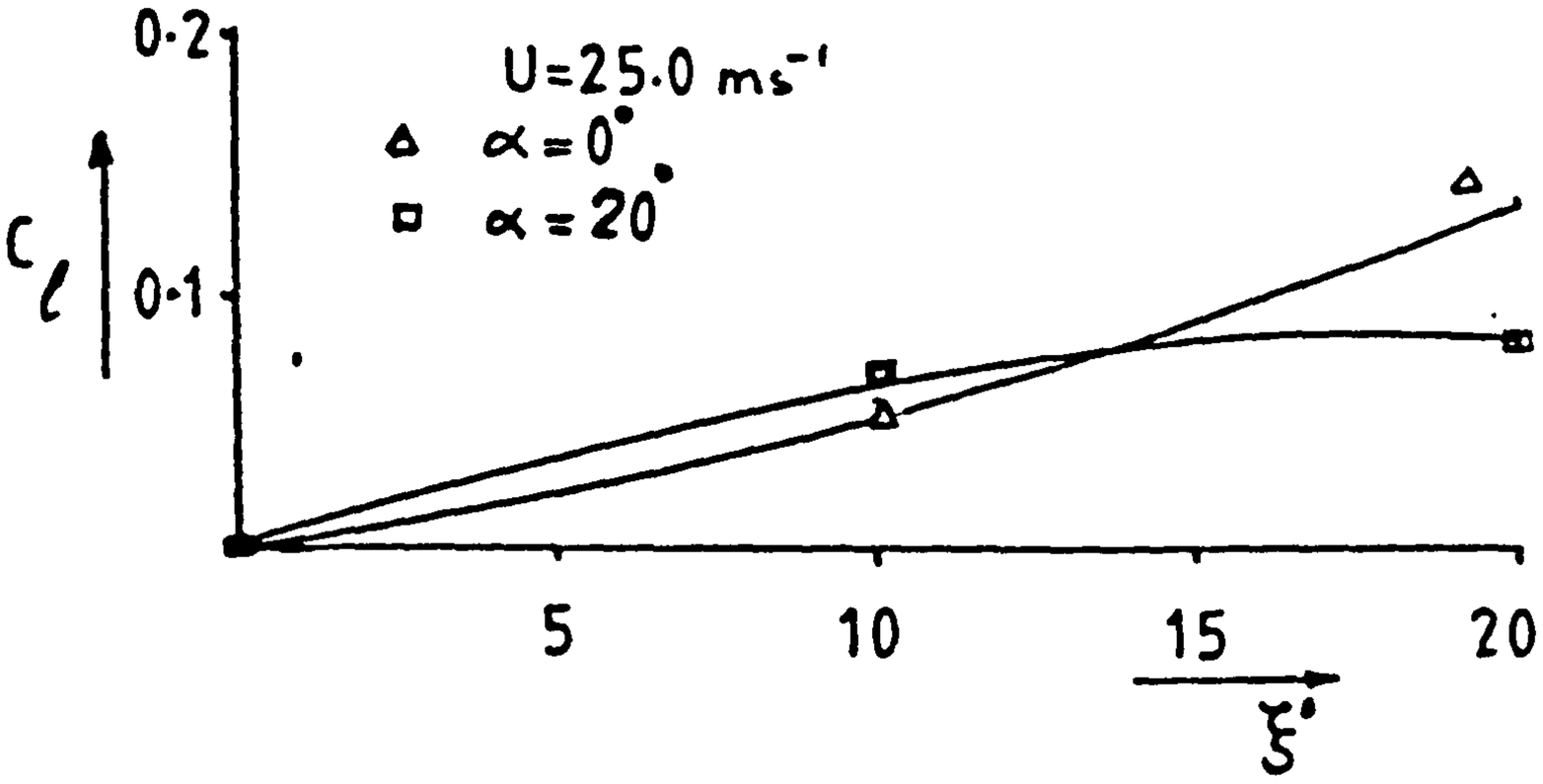

FIGURE H11

C_l - ξ^o VARIATION

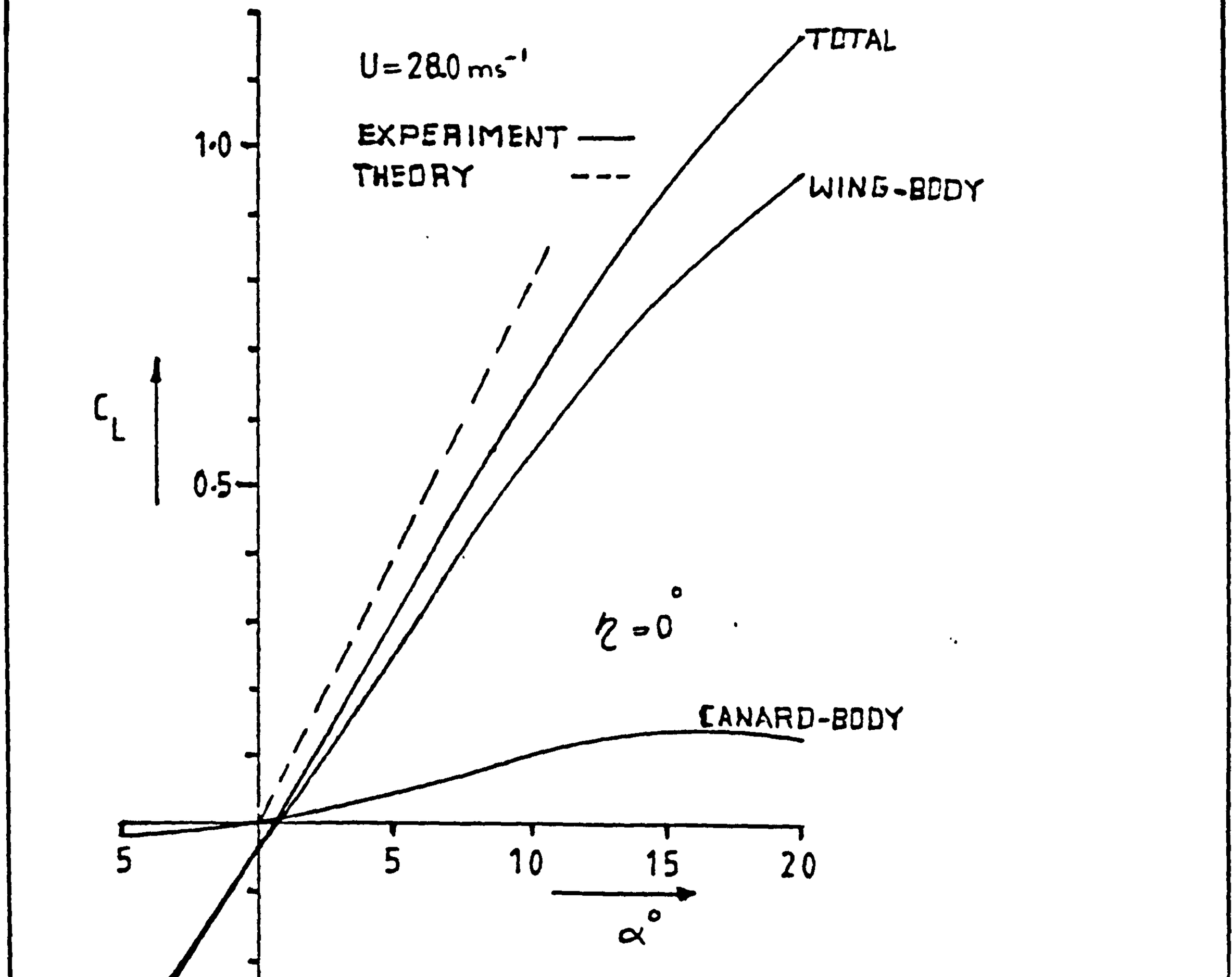

FIGURE H'12

COMPARISON BETWEEN THEORY AND EXPERIMENT

REGARDING LIFT CURVES

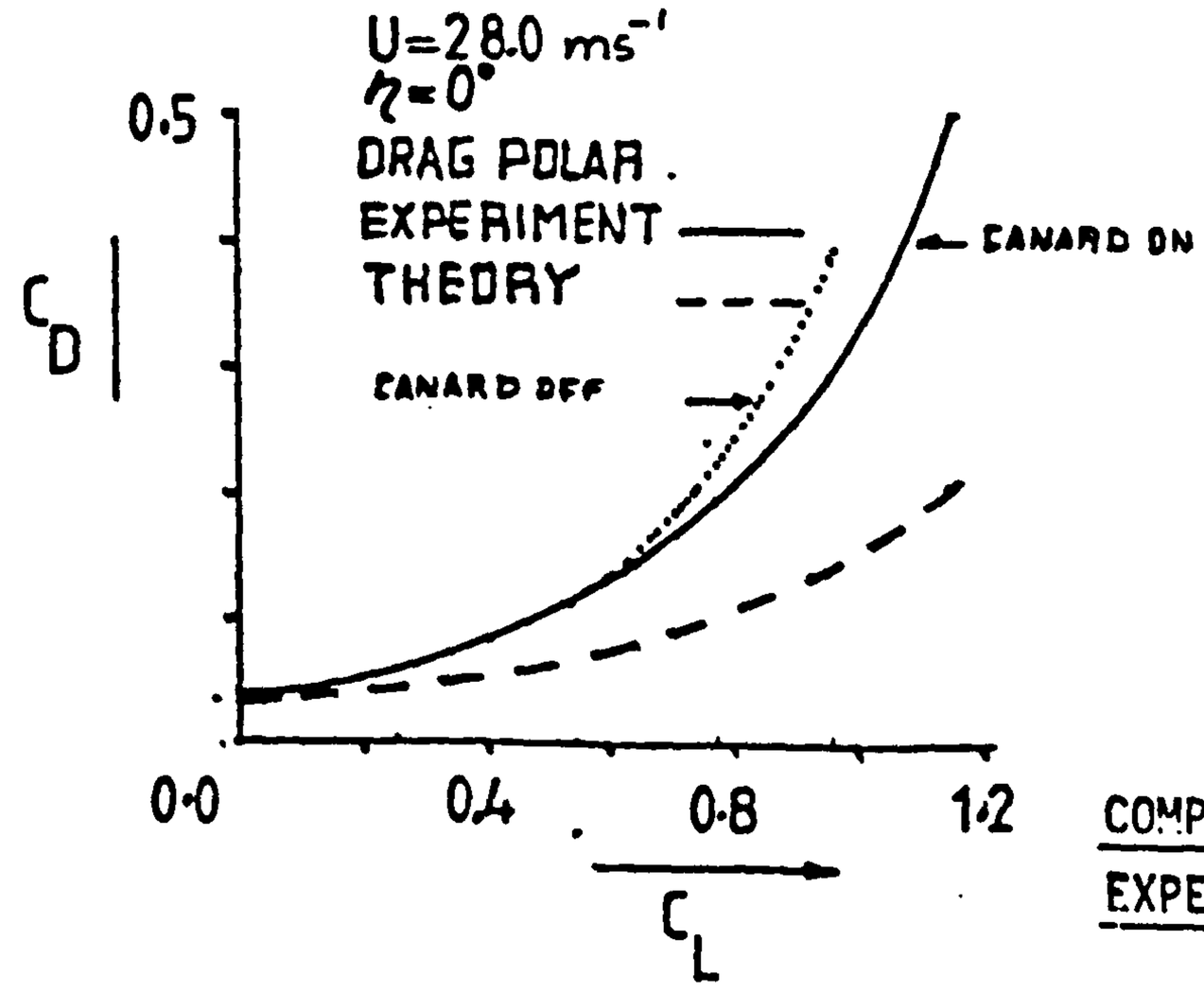

FIGURE H'14

COMPARISON BETWEEN THEORY AND EXPERIMENT REGARDING DRAG POLARS

APPENDIX - I

I.1 Control System Design Calaulations

By substituting the estimated longitudinal stability derivatives from Table J3a of Appendix J -

For U = 30.0m/s

$z_w = -6.0$
$m_w = 8.0$
$m_q = -2.7$
$z_q = -32.0$
$z_\eta = -155.0$
$m_\eta = 143..0$

The characteristic equation given by denominator of Equation (11.1) of section 11, becomes:

$$\Delta = s^2(s^2 + 7.4s + 22.4) = 0$$

$$s^2 = 0$$

or $s^2 + 7.4s + 22.4 = 0$

which represents two poles at zero and two poles at

$$s = -3.7 \pm i2.9$$

This leads to a damping ratio ζ of $\zeta \simeq 0.78$, and and un-damped frequency ω_n of $\omega_n \simeq 4.7$ rad/sec.

I.2 Pitch-Loop Analysis

Pitch control is achieved via the θ-feedback loop of Fig. 11.2, the open-loop transfer function is given by

$$\frac{\bar{\theta}}{(\theta_r - \theta)} = k_\theta k_\eta G(s)_\theta$$

$$= k_\theta k_\eta \frac{sm_\eta + z_\eta m_w - z_w m_\eta}{s(s^2 + s(-z_w - m_q) + (m_q z_w - m_w(U_e + z_q)))}$$

where on substitution of estimated stability derivatives:

$$\frac{\overline{\theta}}{(\overline{\theta_r - \theta_o})} = \frac{143k_\eta k_\theta(s - 1.6)}{s(s^2 + 7.4s + 22.4)}$$

Further, the closed-loop transfer function is given by

$$\frac{\overline{\theta}}{\overline{\theta}_r} = \frac{k_\eta k_\theta G(s)_\theta}{1 + k_\theta k_\eta G(s)_\theta}$$

$$= \frac{143k_\theta k_\eta(s - 1.6)}{s^3 + 7.4s^2 + (22.4 + 143k_\theta k_\eta)s - 227k_\theta k_\eta}$$

where for the servo-actuators

$$k_\eta = 0.7 \text{ rad/volt}$$

$$\therefore \quad \frac{\overline{\theta}}{\overline{\theta}_r} = \frac{100.1k_\theta(s - 1.6)}{s^3 + 7.4s^2 + (22.4 + 100.1k_\theta)s - 158.9k_\theta}$$

By assuming the control law:

$$\eta = k_\theta(\theta_r - \theta_o)$$

the value of k_θ to give a satisfactory response was found to be $k_\theta = -0.1$. The step response of this sub-system is given by Fig. I2 below.

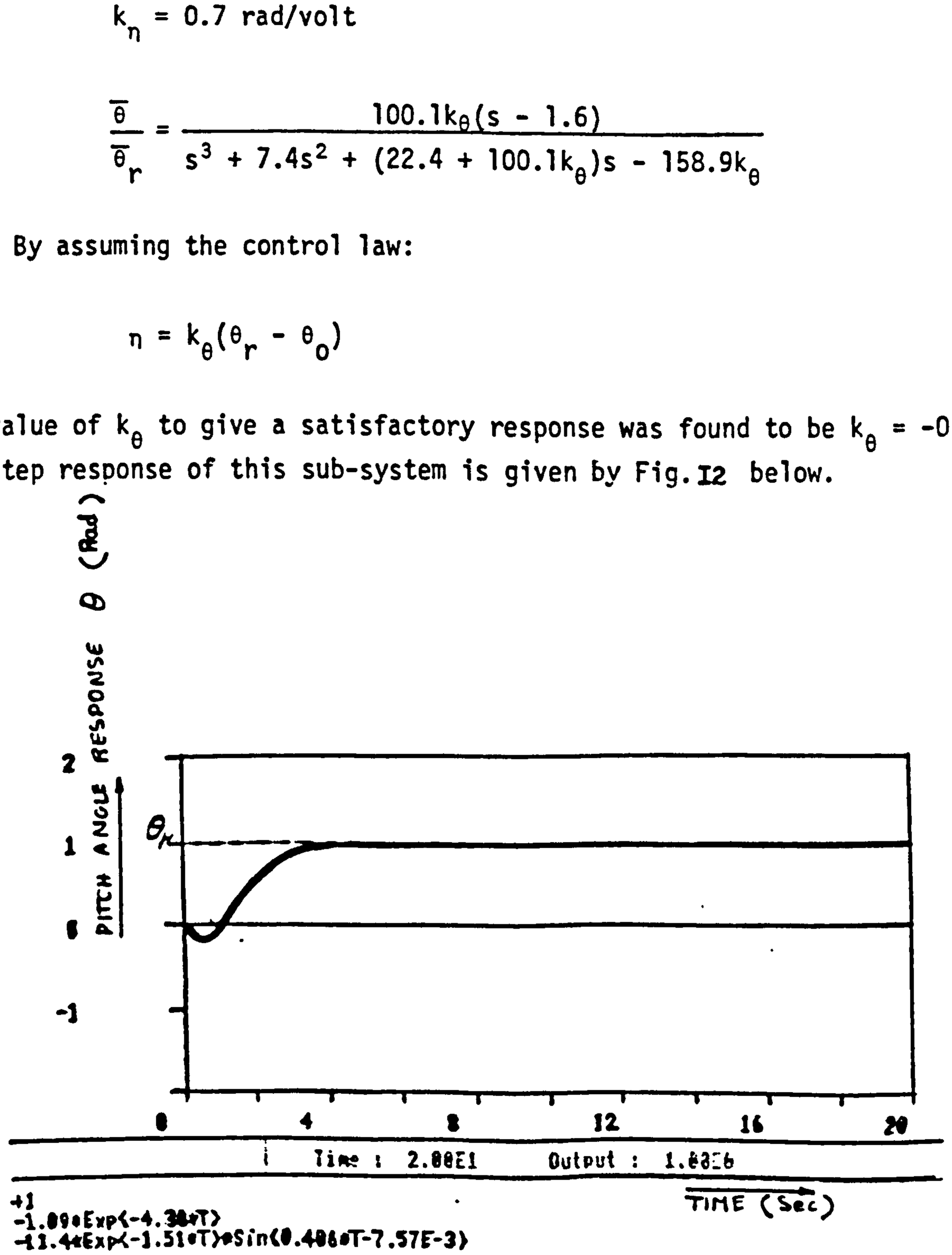

FIG. I2 CLOSED-LOOP TIME RESPONSE TO A STEP DEFLECTION OF 1 rad.

Now, by substitution of stability derivative estimates and the above control law in equation (11.3) of Section 11,

$$\frac{\bar{h}_o}{\bar{\theta}_r} = \frac{-10.85s^2 - 3.49.6s + 47.7}{s(s^3 + 8.7s^2 + 20.2s + 15.89)}$$

I.3 Height Loop Analysis with Unity Feedback

From Equation (11.4) of Section 11, the closed-loop transfer function of the height loop is given by:

$$\frac{\bar{h}_o}{\bar{h}_r} = \frac{k_h G(s)_h}{1 + k_h G(s)_h}$$

After substitution of the stability derivatives estimates and some manipulations:

$$\frac{\bar{h}_o}{\bar{h}_r} = \frac{-10.85k_h(s^2 + 32.2s - 43.94)}{s^4 + 8.7s^3 + s^2(20.2 - 10.85k_h) + s(15.89 - 349.6k_h) + 476.7k_h}$$

The value of k_h to give a satisfactory response was found to be,

$$k_h \simeq 0.01$$

Therefore, the control laws are given by

$$\underline{n = -0.1(\theta_r - \theta_o)}$$

$$\underline{\theta_r = 0.01(h_r - h_o)}$$

Figures I4 and I5 represent the computer simulations of Equation (11.5) for various values of a correction factor defined as:

$$C_F = \frac{k_\theta}{k_{\theta_o}}$$

where $k_{\theta_o} = -0.1$

I.4 Height Loop Analysis with Velocity Feedback

By substituting the estimated values of derivatives in Equation (10.6) of Section 10,

$$\frac{\bar{h}_o}{\bar{h}_r} = \frac{-10.85k_vk_hs^3+(-349.6k_vk_h-10.85k_h)s^2+(476.7k_vk_h-349.6k_h)s+476.7k_h}{s^4+(8.7-10.85k_vk_h)s^3+(20.2-349.6k_vk_h-10.85k_h)s^2+(15.89+476.7k_vk_h-349.6k_h)s+476.7k_h}$$

The optimal values of k_v and k_h are somewhere around $k_v = 2$ and $k_h = 0.015$ respectively. For these values, the poles and zeros of the system become,

$$\left.\begin{matrix}-0.6 \pm 1.54\\ -0.25\\ -7.0\end{matrix}\right\} \text{poles} \qquad \text{and} \qquad \left.\begin{matrix}1.32\\ -0.6\\ -3.3\end{matrix}\right\} \text{zeros}$$

Fig. I3 shows the response of this system to a step input. Evidently, the response time has become shorter and to about half the value of the system with no velocity feed-back. Fig. I9 represents the bode plot for this system. Despite the advantage of the velocity feed-back, the noise in the physical system, namely, the test rig, would result in oscillations in the canard servo-actuator, especially with small values of k_v.

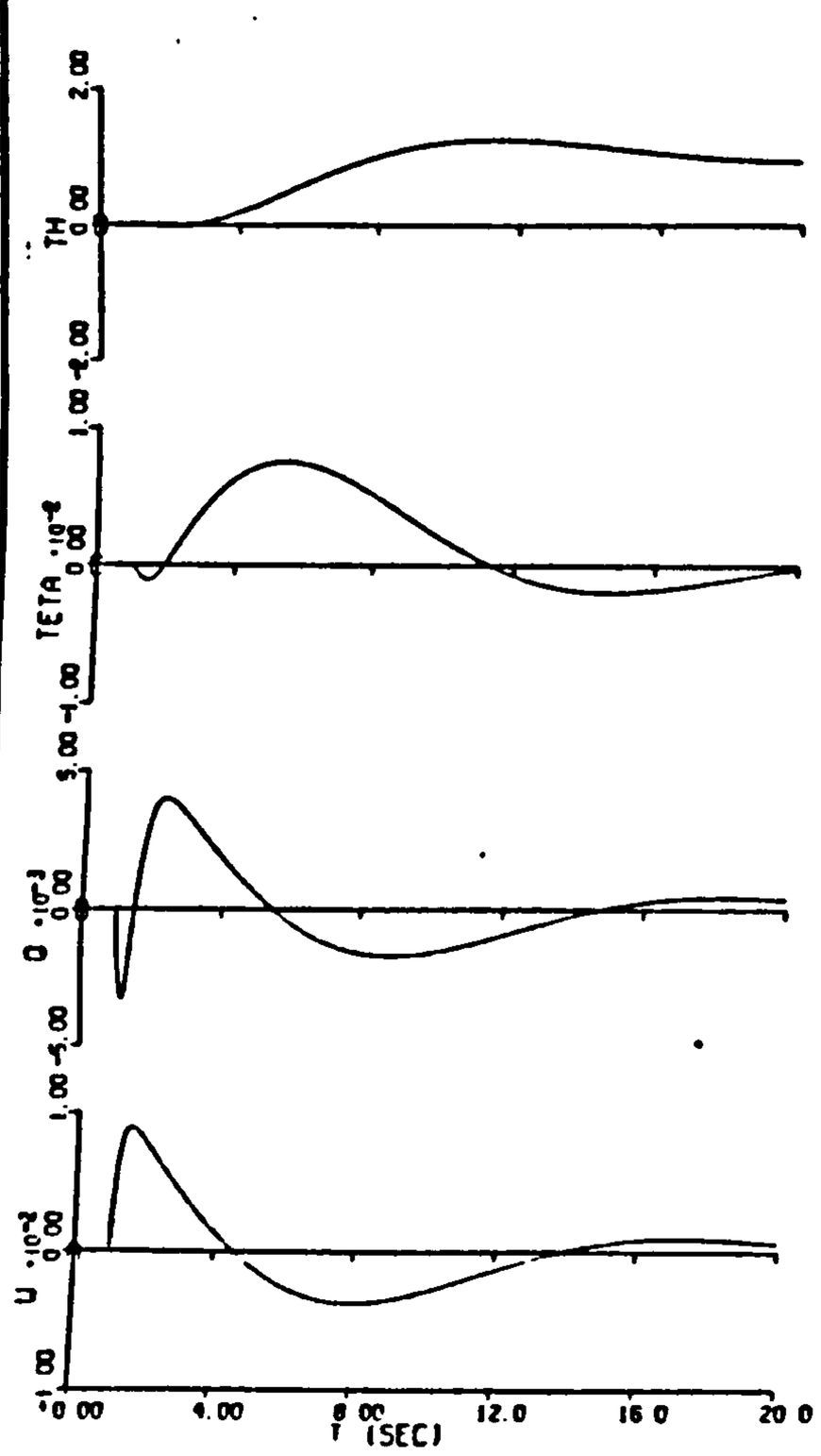

$C_F = 1$

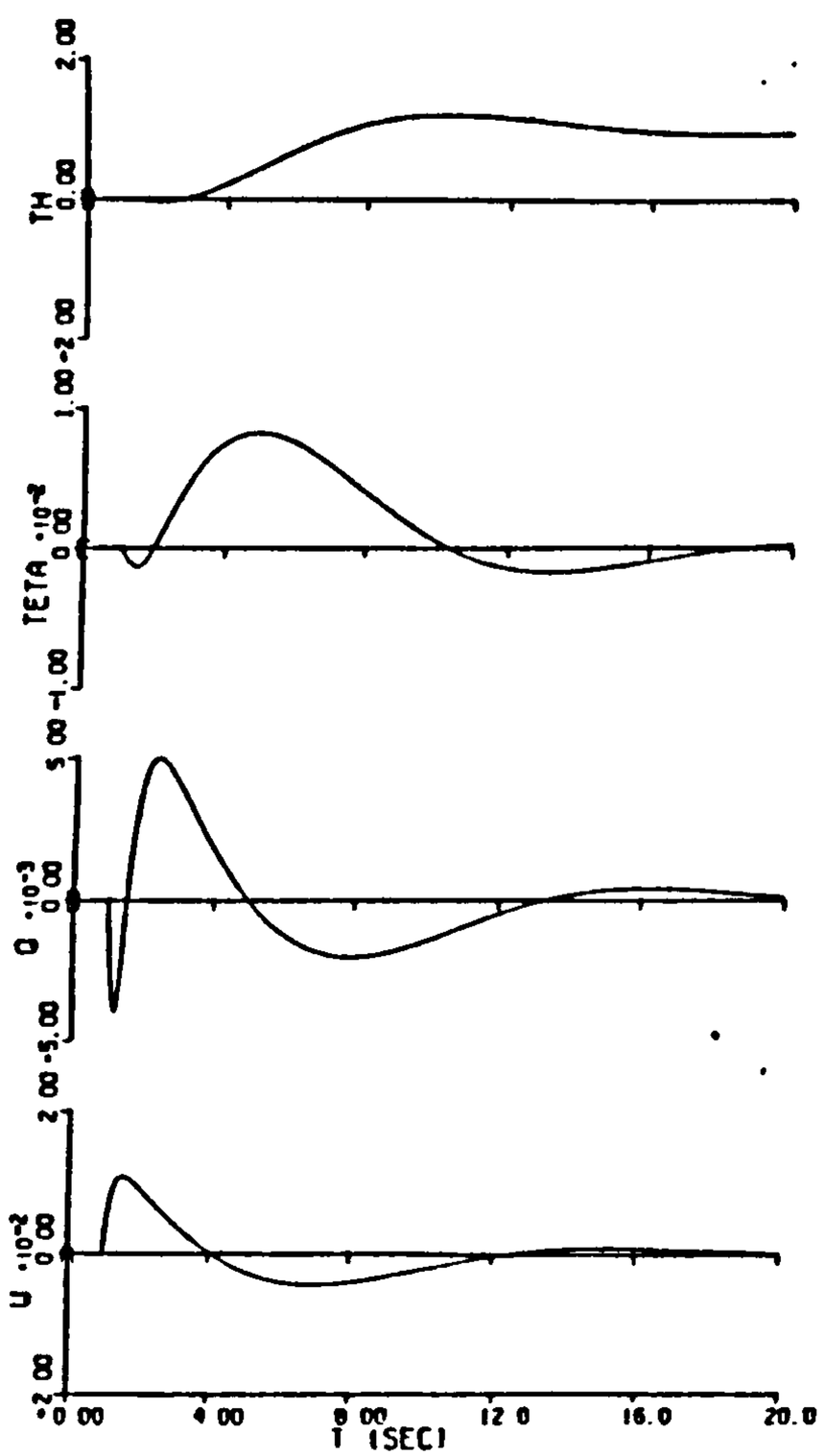

$C_F = 1.2$

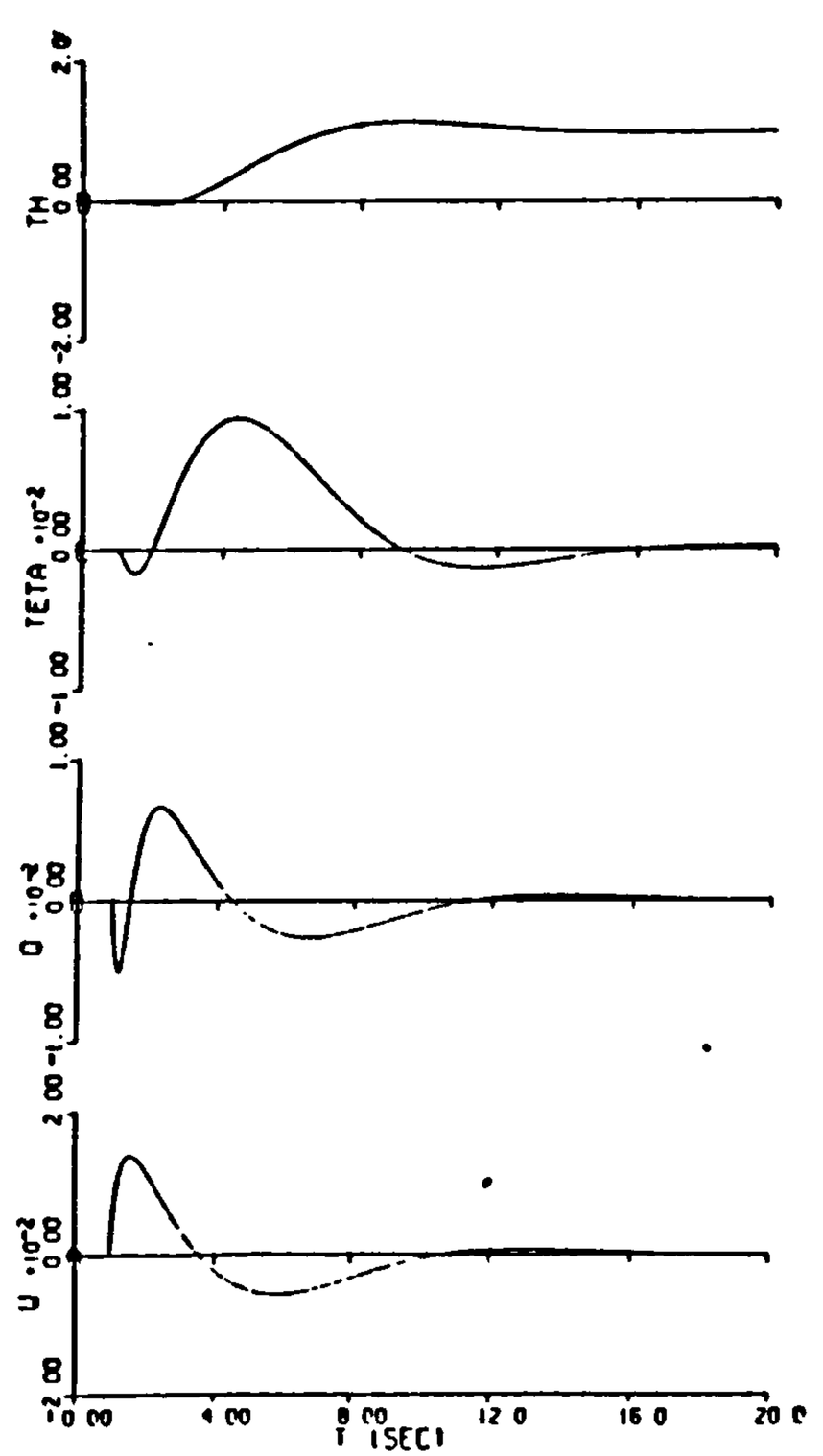

$C_F = 1.5$

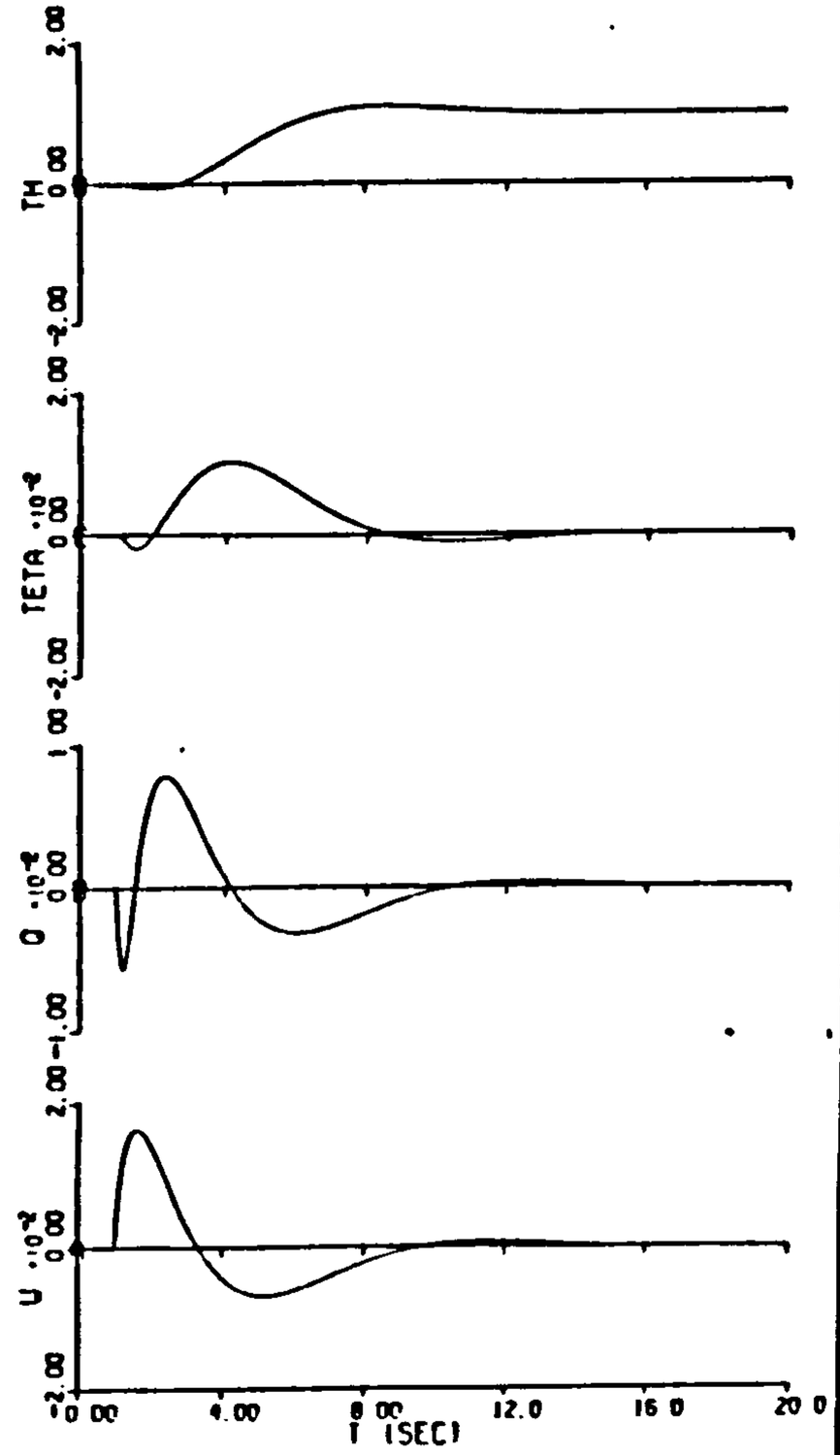

$C_F = 1.7$

FIGURE I4

SIMULATION OF EQUATIONS

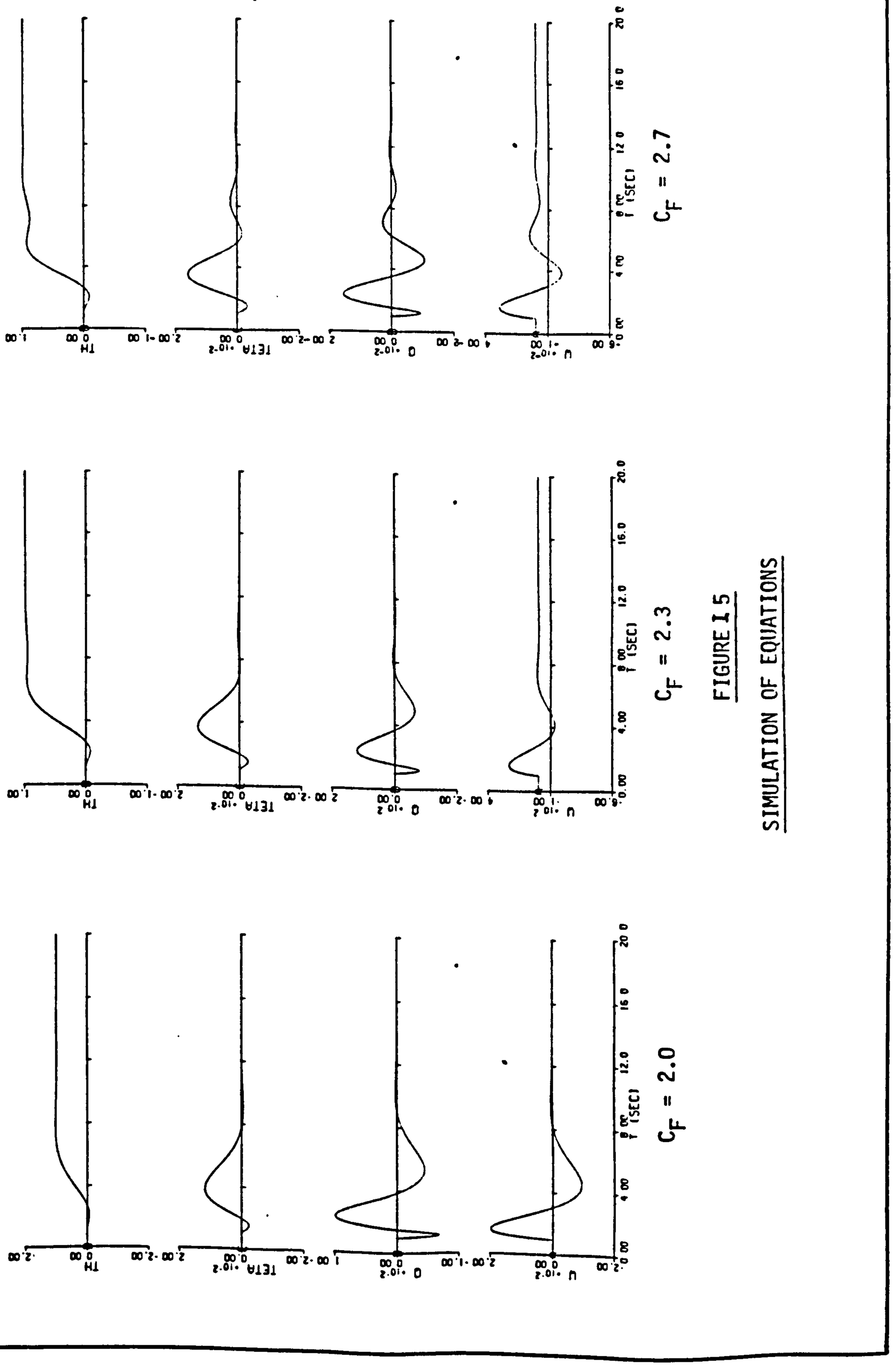

$C_F = 2.7$

$C_F = 2.3$

$C_F = 2.0$

FIGURE I 5

SIMULATION OF EQUATIONS

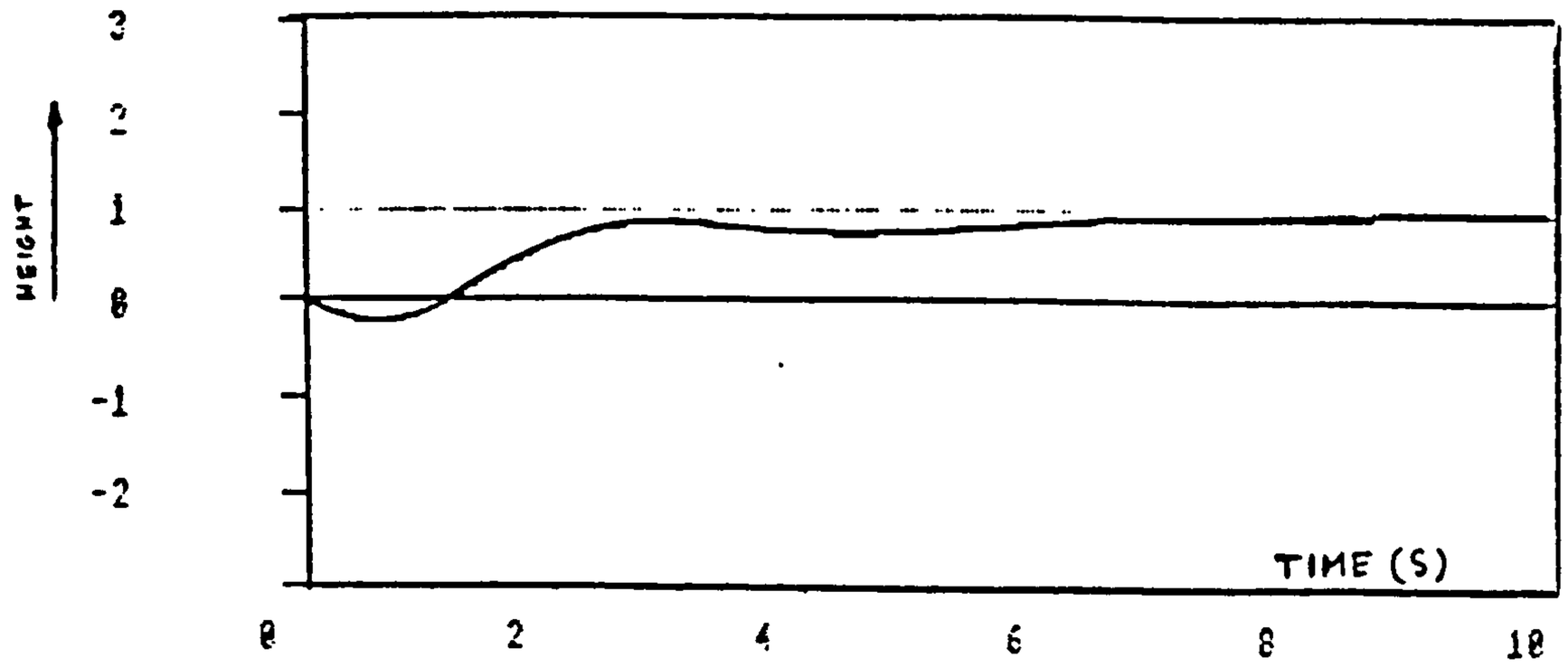

FIGURE I8

SYSTEM RESPONSE WITH VELOCITY FEEDBACK TO A HEIGHT STEP INPUT

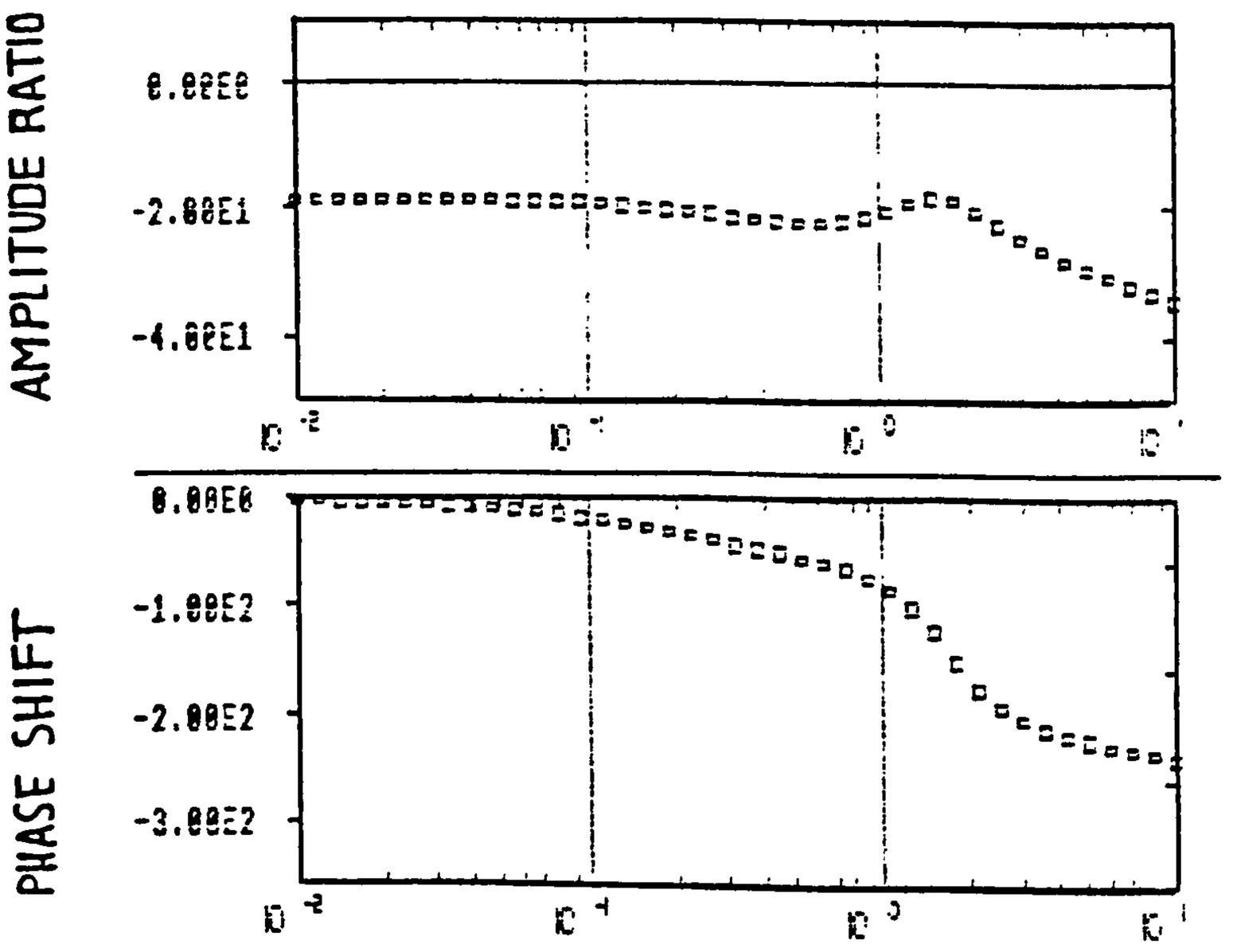

FIGURE I9

BODE PLOT OF SYSTEM WITH VELOCITY FEEDBACK

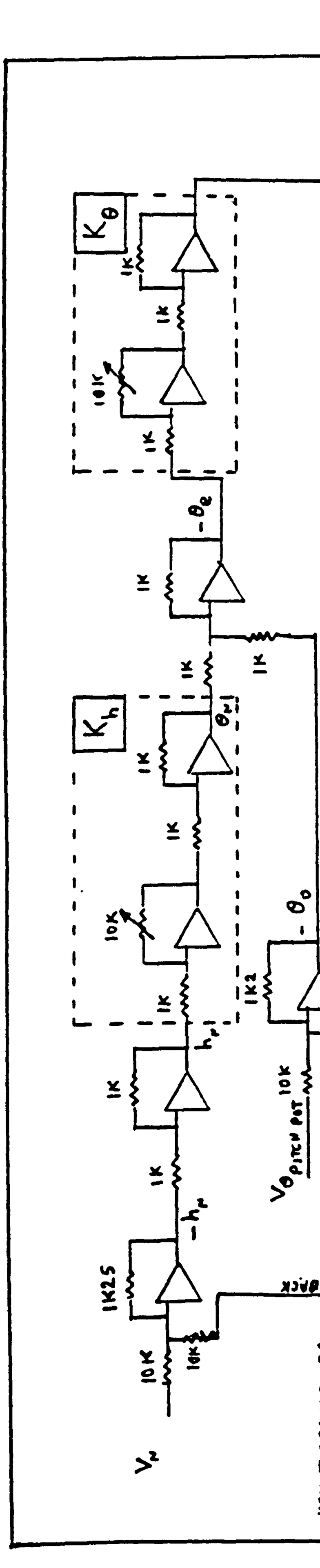

FIGURE I10

HEIGHT LOCK CONTROL SYSTEM ANALOGUE CIRCUIT

WITHOUT VELOCITY FEEDBACK

FIGURE I10

HEIGHT LOCK CONTROL SYSTEM BLOCK DIAGRAM

WITHOUT VELOCITY FEEDBACK

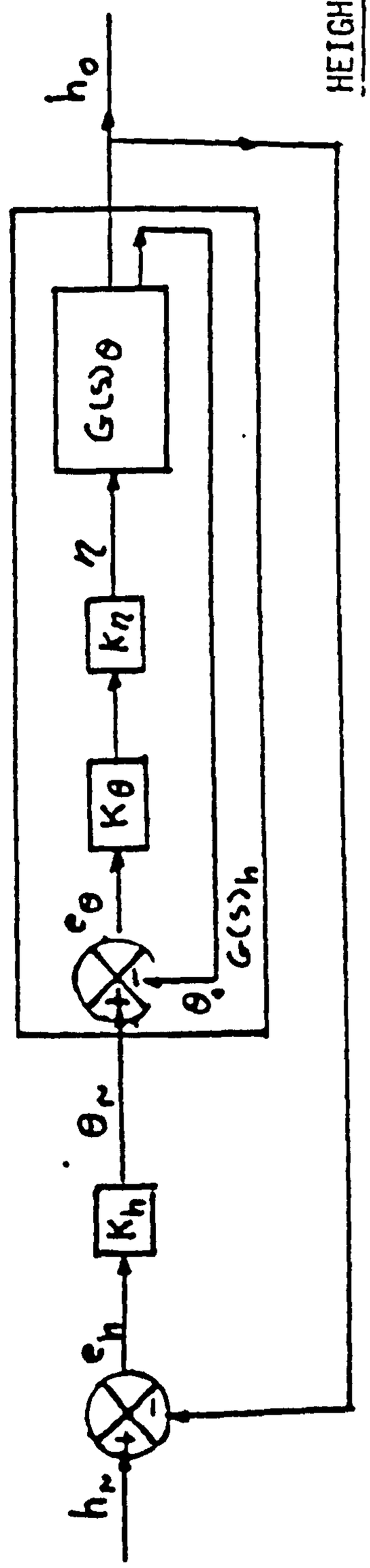

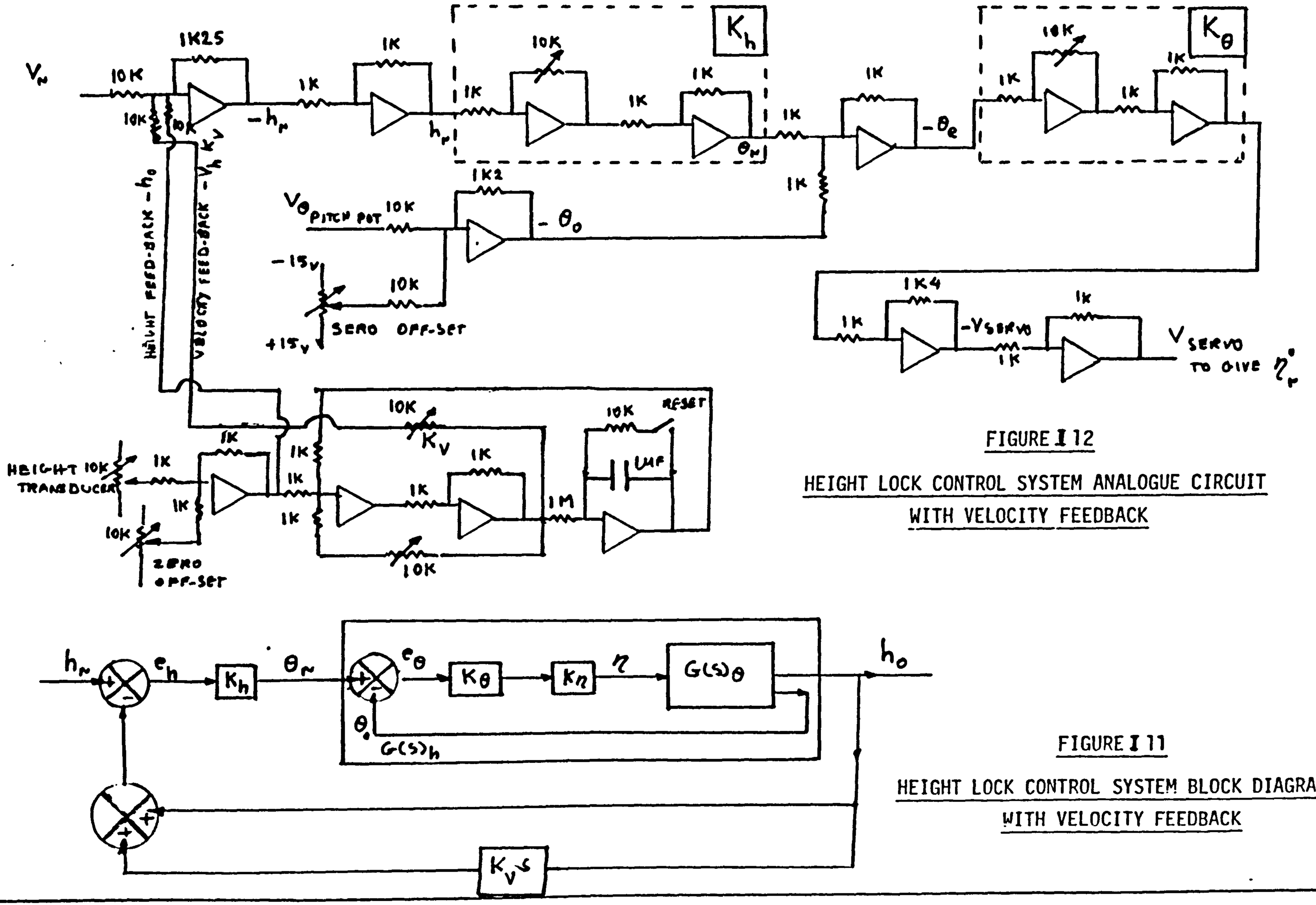

FIGURE I 12

HEIGHT LOCK CONTROL SYSTEM ANALOGUE CIRCUIT
WITH VELOCITY FEEDBACK

FIGURE I 11

HEIGHT LOCK CONTROL SYSTEM BLOCK DIAGRAM
WITH VELOCITY FEEDBACK

APPENDIX -J: Initial Estimation of the Covariance Matrices G, R and Q

Initially, the elements of G, Q and R matrices for both longitudinal and lateral computer based, parameter identification experiments were set to zero except for G where the diagonal elements which were approximated by

$$G_{ii} = \varepsilon(X_i X_i^T) \quad ,$$

since other elements were assumed un-correlated. Also a first order approximation to process and measurement intensities is given from section 5.4 by

$$r_i = q_i = \frac{(\text{r.m.s.})_i^2 \text{error}}{\pi} . 2nh$$

where $n = 100$ and $h = 0.01$ s. Since 100 samples per second are taken.

	STATES	ASSUMED INITIAL VALUES	MAXIMUM VALUE ATTAINED	r.m.s. ERROR % OF MAXIMUM VALUE	G_{ii}	q_i	r_i
LONGITUDINAL	w	0	4.0 (m/s)		1.6×10^{-3}		10^{-3}
	q	0	1.0 (rad/s)		10^{-4}		6×10^{-5}
	θ	0	0.4 (rad)		1.6×10^{-5}		10^{-5}
LATERAL	v	0	0.1 (m/s)	1%	10^{-6}		6×10^{-7}
	P	0	0.5 (rad/s)		2.5×10^{-5}		1.6×10^{-5}
	R	0	0.04(rad/s)		2×10^{-7}		1.3×10^{-7}
	ϕ	0	0.2 (rad/s)		4×10^{-6}		2.5×10^{-6}
LONGITUDINAL	z_w	-2.0	-2.0		0.04	2.5×10^{-2}	
	m_w	-0.2	-0.2		0.0004	2.5×10^{-4}	
	z_q	-	-		-		
	m_q	-0.8	-0.8		0.0064	4.1×10^{-3}	
	z_η	-10.0	-10.0	10%	1.0	0.64	
	m_η	40.0	40.0		16.0	10.2	
LATERAL	ℓ_v	-20.0	-20.0		4.0	2.5	
	ℓ_p	-5.0	-5.0		0.25	0.16	
	ℓ_r	1.5	1.5		0.0225	1.4×10^{-2}	
	n_v	15.0	15.0		2.225	1.4	
	n_p	1.5	1.5		0.0225	1.4×10^{-2}	
	n_r	-5.0	-5.0		0.25	0.16	
	ℓ_ξ	50.0	50.0		25.0	15.9	
	n_ζ	-6.0	-6.0		0.36	0.23	

These values of covariance matrices were used for the computer based experiments of sections 5 and 6. In matrix form G, Q and R can be presented as:

J.1 LONGITUDINAL CASE

$$G = \begin{bmatrix} 1.6 \times 10^{-3} & & & 0 & & & \\ & 10^{-4} & & & & & \\ & & 1.6 \times 10^{-5} & & & & \\ & & & 4 \times 10^{-2} & & & \\ 0 & & & & 4 \times 10^{-4} & & 0 \\ & & & & & 6.4 \times 10^{-3} & \\ & & & & & & 1.0 \\ & & & 0 & & & 16.0 \end{bmatrix}$$

$$R = \begin{bmatrix} 10^{-3} & 0 & 0 \\ 0 & 6 \times 10^{-5} & 0 \\ 0 & 0 & 10^{-5} \end{bmatrix}$$

$$Q = \begin{bmatrix} 2.5 \times 10^{-2} & 0 & 0 & 0 & 0 \\ 0 & 2.5 \times 10^{-4} & 0 & 0 & 0 \\ 0 & 0 & 4.1 \times 10^{-3} & 0 & 0 \\ 0 & 0 & 0 & 0.64 & 0 \\ 0 & 0 & 0 & 0 & 10.2 \end{bmatrix}$$

J.2 LATERAL CASE

$$G = \begin{bmatrix}
10^{-6} & & & & & & 0 & & & & & \\
 & 2.5 \times 10^{-5} & & & & & & & & & & \\
 & & 2 \times 10^{-7} & & & & & & & & & \\
 & & & 4 \times 10^{-6} & & & & & & & & \\
 & & & & 4.0 & & & & & & & \\
 & & & & & 0.25 & & & & & & \\
0 & & & & & & 0.0225 & & & & & 0 \\
 & & & & & & & 2.225 & & & & \\
 & & & & & & & & 0.0225 & & & \\
 & & & & & & & & & 0.25 & & \\
 & & & & & & & & & & 25.0 & \\
 & & & & & 0 & & & & & & 0.36
\end{bmatrix}$$

$$R = \begin{bmatrix}
6 \times 10^{-7} & 0 & 0 & 0 \\
0 & 1.6 \times 10^{-5} & 0 & 0 \\
0 & 0 & 1.3 \times 10^{-7} & 0 \\
0 & 0 & 0 & 2.5 \times 10^{-6}
\end{bmatrix}$$

$$Q = \begin{bmatrix}
2.5 & & & & & & & \\
 & 0.16 & & & & & & \\
 & & 1.4 \times 10^{-2} & & & & & \\
 & & & 1.4 & & & & \\
 & & & & 1.4 \times 10^{-2} & & & \\
 & & & & & 0.16 & & \\
 & & & & & & 15.9 & \\
 & & & & & & & 0.23
\end{bmatrix}$$

J.3 Results of Computer Based Experiments Regarding the Parameter Identification Code

This appendix contains the results obtained from the computer based experiments regarding the E.K.F., parameter identification algorithm. Simulated short period longitudinal and lateral responses with known stability derivatives due to various inputs to canard and aileron have been examined. These results have been coded in accordance with tables 5.6 and 6.2 of sections 5 and 6 respectively. It must be pointed out that the simulations were based on the same mathematical model as the E.K.F. algorithm. Tables J1 and J2 below represent the actual and estimated longitudinal and lateral stability derivatives respectively. The estimated values are based on the average of 10 runs.

		CONCISE LONGITUDINAL STABILITY DERIVATIVES				
CASE NO:	A/C SPEED (m/s)	z_w	m_w	m_q	z_η	m_η
Case - I	300	-2.0 / $\hat{-2.0}$	-0.02 / $\hat{-0.02}$	-1.2 / $\hat{-1.0}$	-19.2 / $\hat{-20.0}$	9.2 / $\hat{11.0}$
Case - II	20	-2.0 / $\hat{-2.0}$	-0.2 / $\hat{-0.2}$	-0.8 / $\hat{-0.7}$	-10.0 / $\hat{-15.0}$	40.0 / $\hat{45.0}$
Case - III-i	20	-2.0 / $\hat{-3.0}$	-0.2 / $\hat{-0.5}$	-0.8 / $\hat{-1.1}$	-10.0 / $\hat{-16.0}$	40.0 / $\hat{32.0}$
Case - III-ii	20	-2.0 / $\hat{-2.0}$	-0.2 / $\hat{-0.2}$	-0.8 / $\hat{-0.6}$	-10.0 / $\hat{-9.0}$	40.0 / $\hat{48.0}$

Note: Superscript '^' represents the estimated value of the stability derivative.

TABLE J1: ACTUAL AND ESTIMATED LONGITUDINAL STABILITY DERIVATIVES

A/C SPEED	CONCISE LATERAL STABILITY DERIVATIVES							
	ℓ_v	ℓ_p	ℓ_r	n_v	n_p	n_r	ℓ_ξ	n_ξ
ACTUAL	-20.0	-5.0	1.5	15.0	1.5	-5.0	50.0	-6.0
ESTIMATED	-20.0	-5.0	1.0	15.0	1.5	-5.0	50.0	-4.5

TABLE J2: ACTUAL AND ESTIMATED LATERAL STABILITY DERIVATIVES

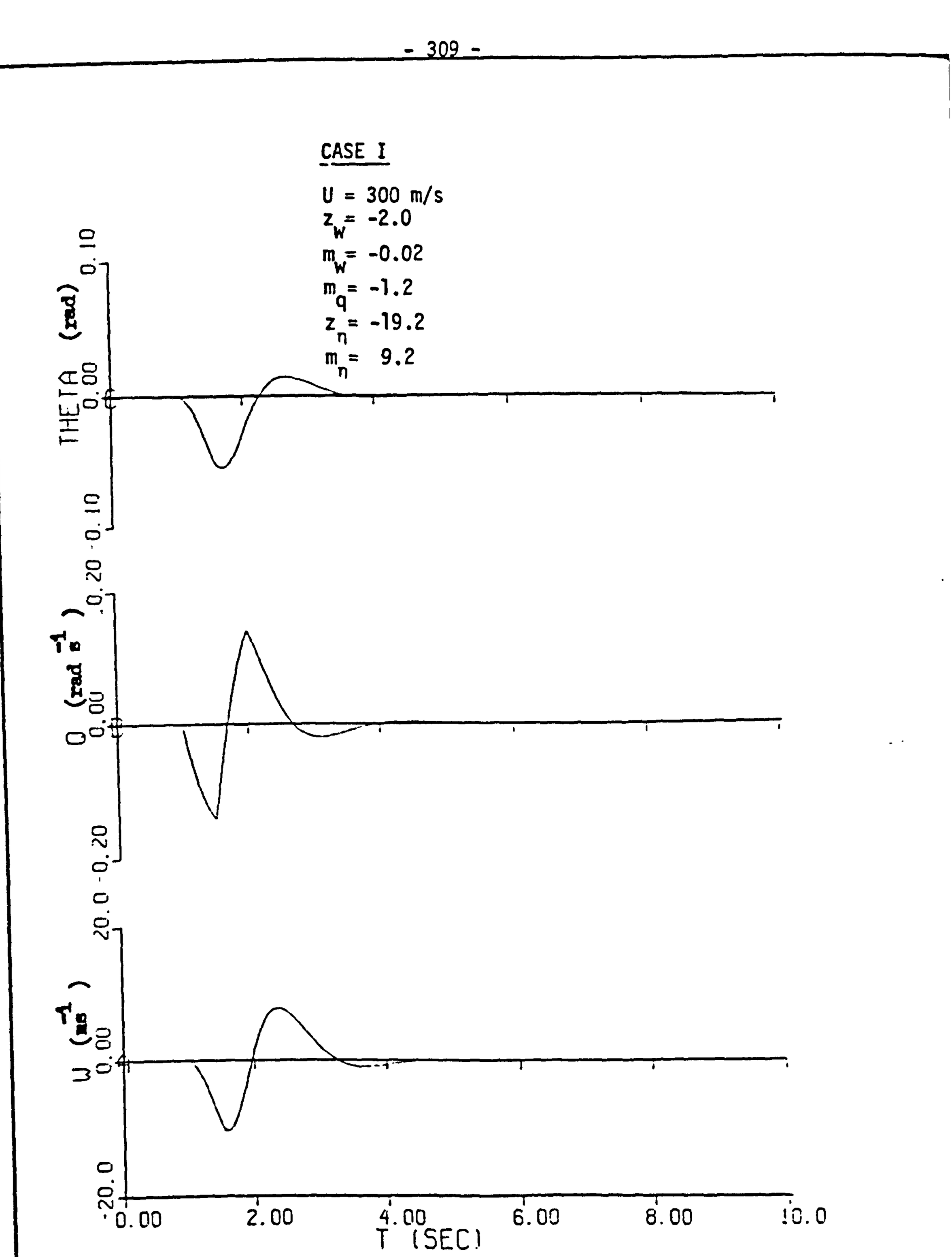

FIGURE JO

SIMULATED LONGITUDINAL RESPONSE OF THE A/C TO A DIPOLE CANARD INPUT

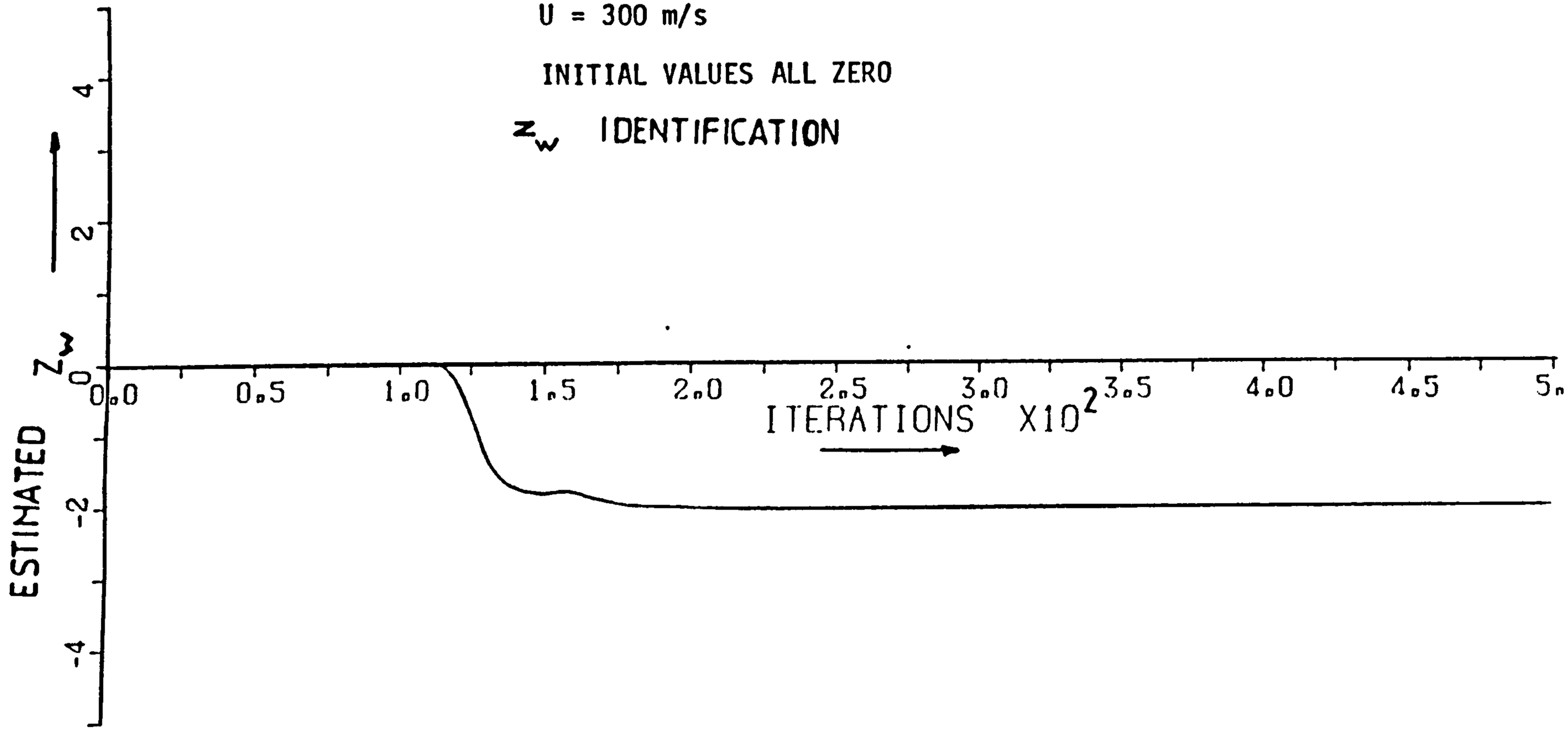

FIGURE J1

CONVERGENCE OF z_w WITH NUMBER OF ITERATIONS (CASE I)

CASE II

U_o = 20.0 m/s
z_w = -2.0
m_w = -0.2
m_q = -0.8
z_n = -10.0
m_n = 40.0

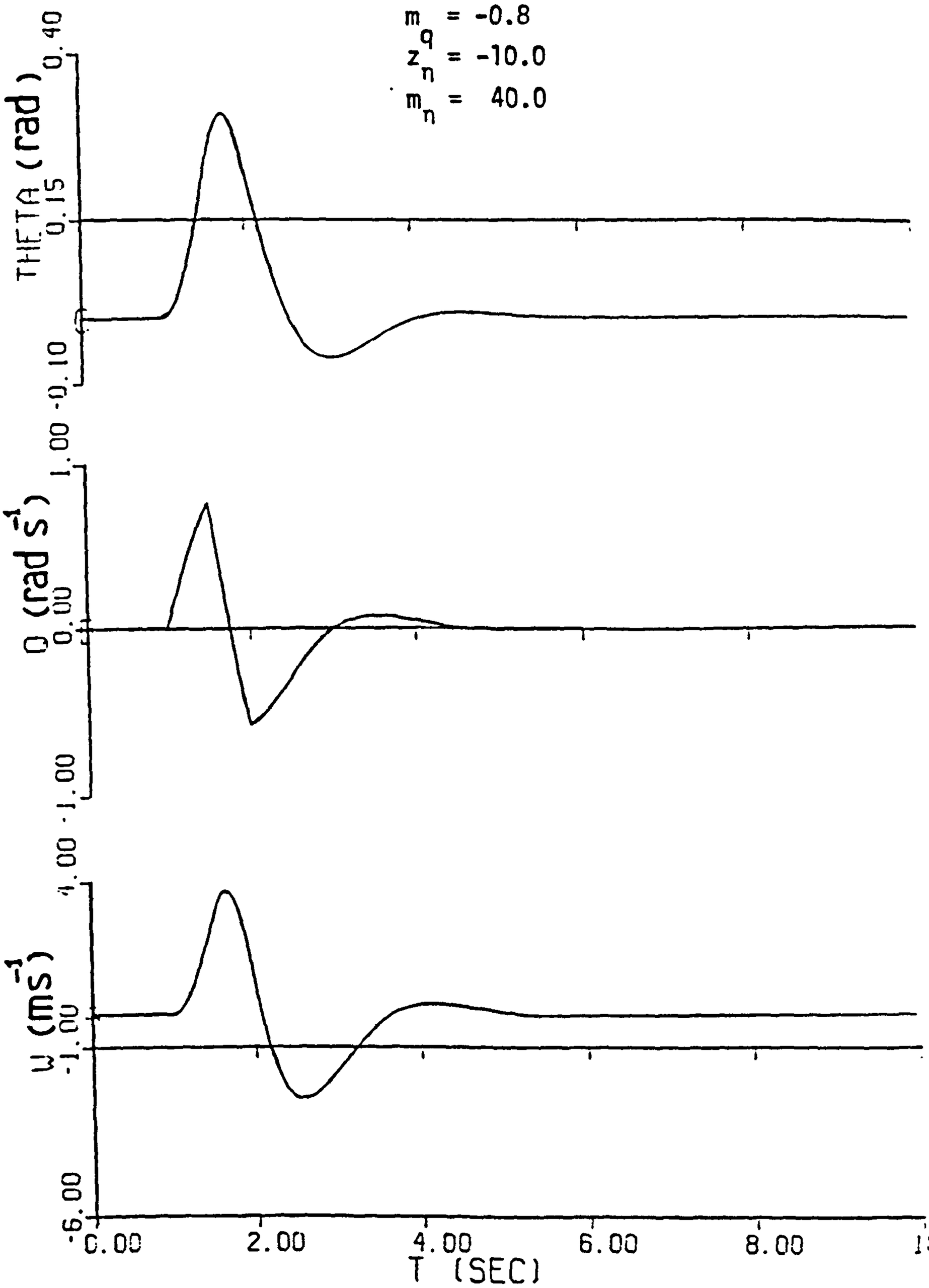

FIGURE J01

SIMULATED LONGITUDINAL RESPONSE OF THE A/C TO A DIPOLE CANARD INPUT

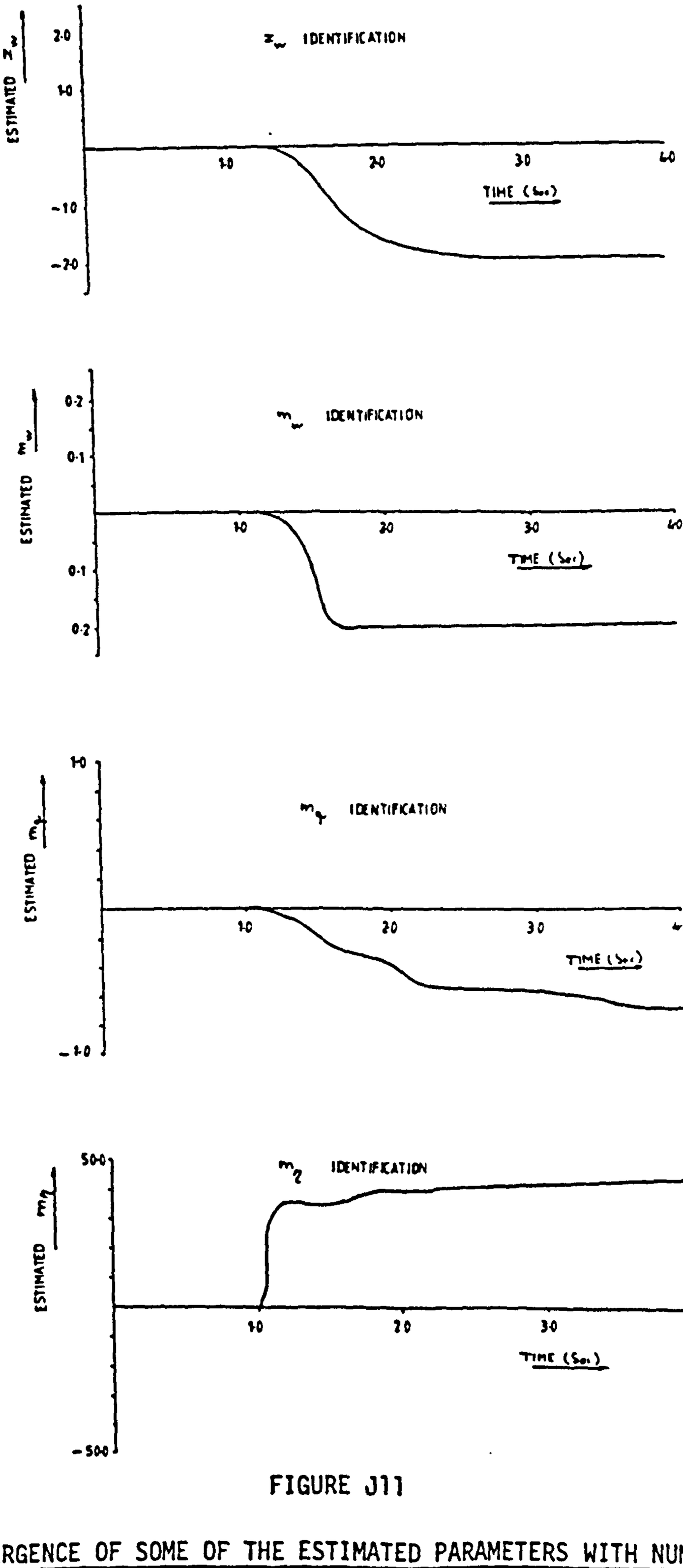

FIGURE J11

CONVERGENCE OF SOME OF THE ESTIMATED PARAMETERS WITH NUMBER OF ITERATIONS (CASE II)

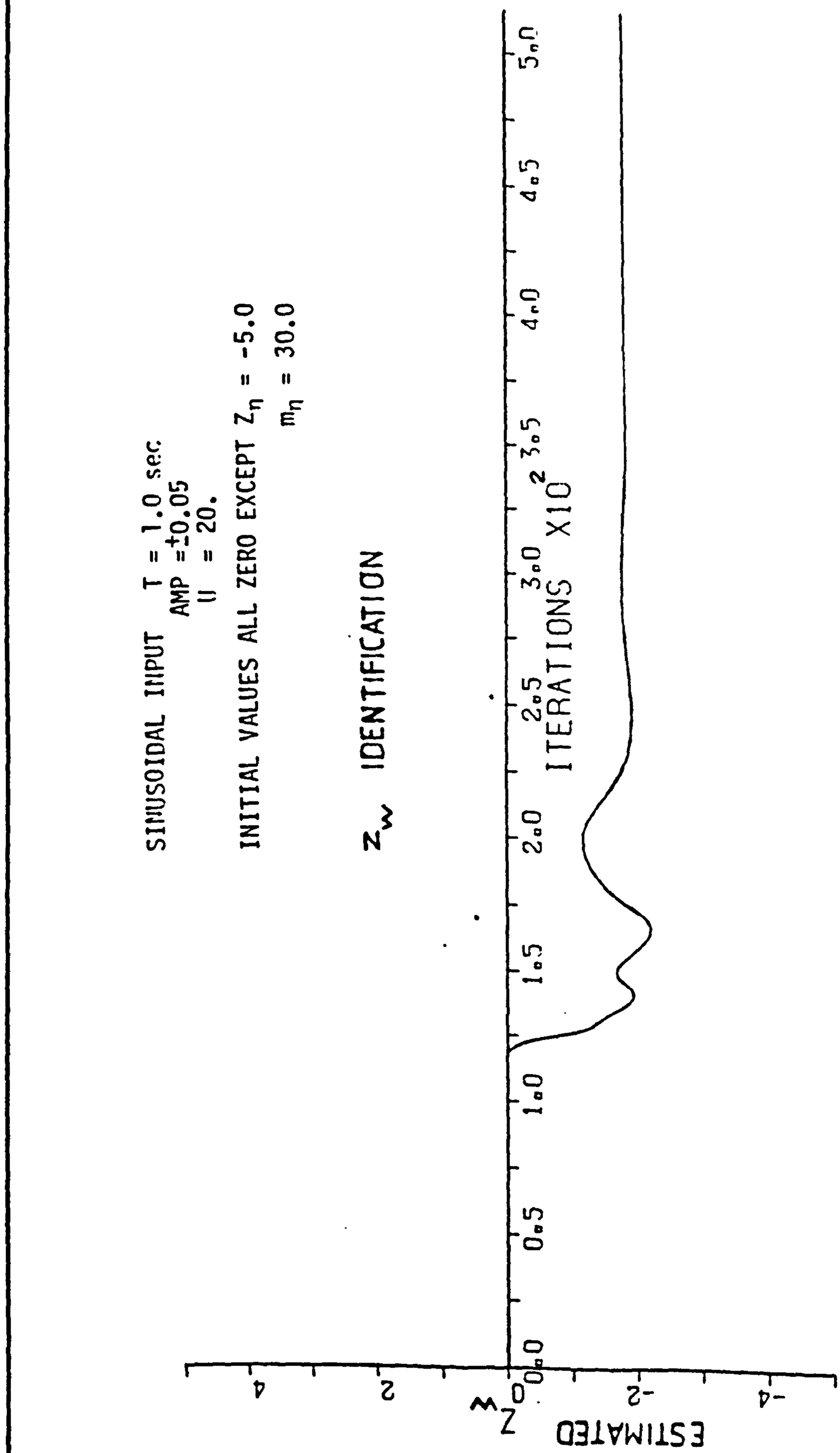

FIGURE J3

CONVERGENCE OF ESTIMATED Z_w WITH NUMBER OF ITERATIONS (CASE III-ii)

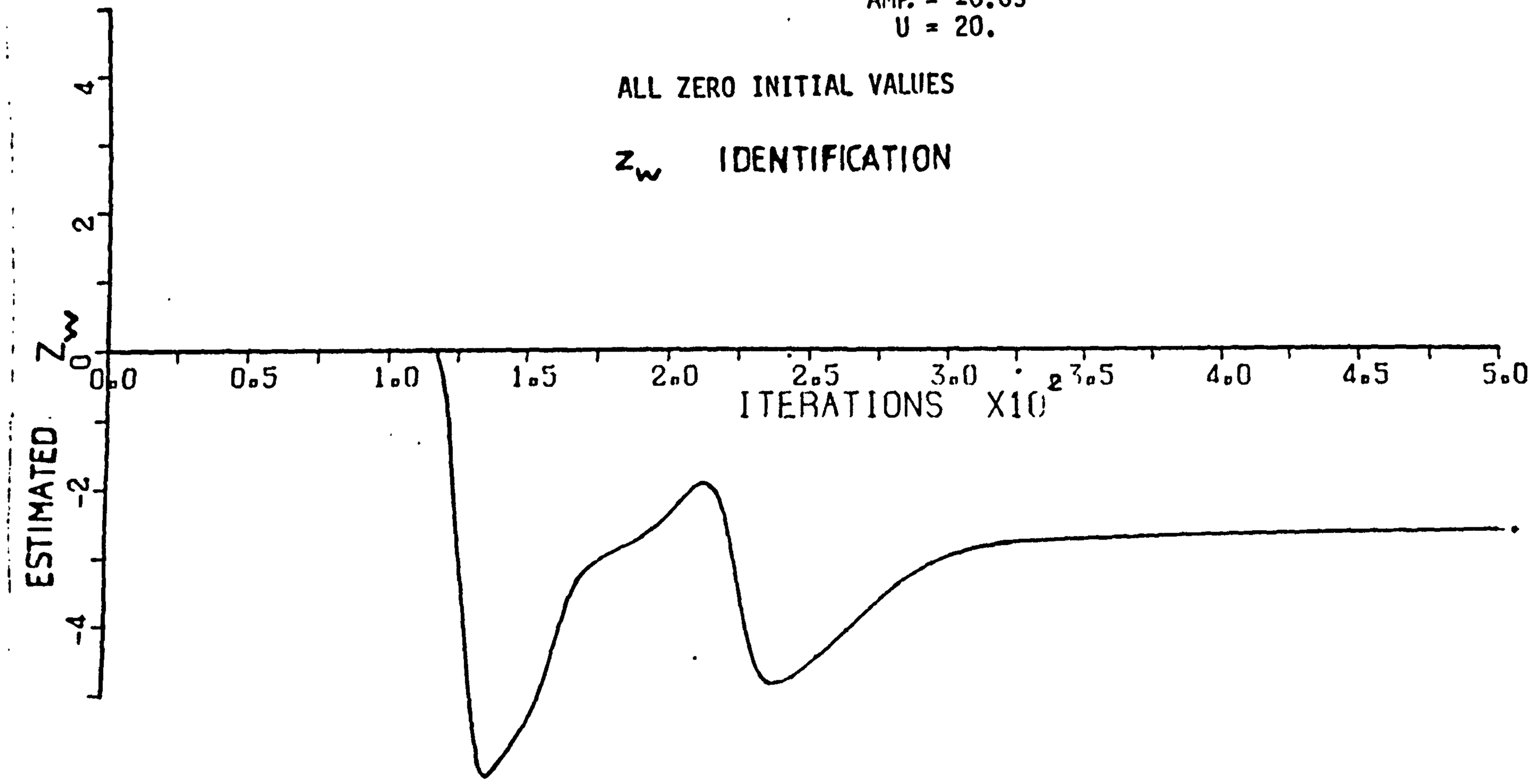

FIGURE J4

CONVERGENCE OF ESTIMATED z_w WITH NUMBER OF ITERATIONS (CASE III-1)

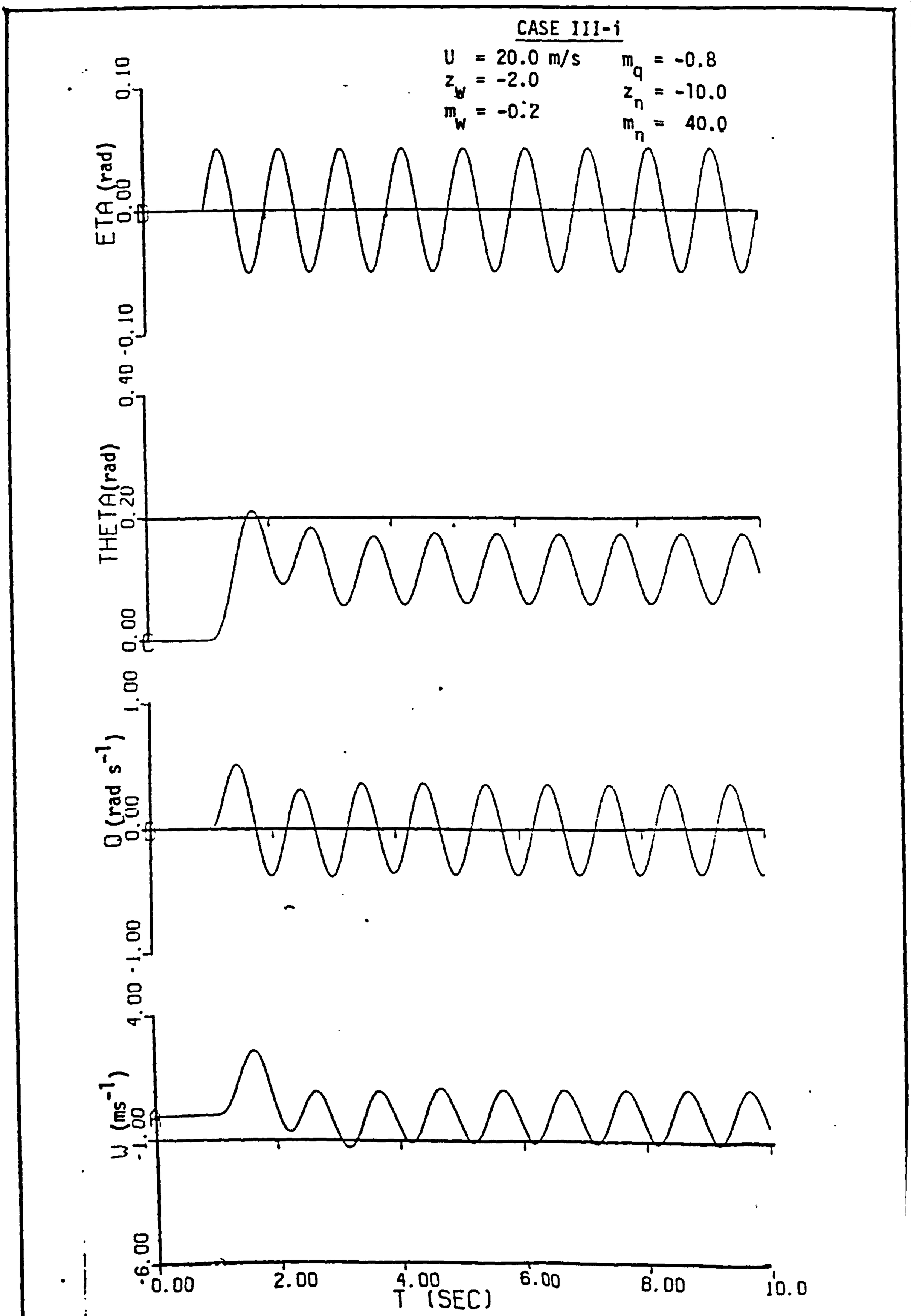

FIGURE J5: SIMULATED LONGITUDINAL RESPONSE OF A/C TO A SINUSOIDAL CANARD INPUT

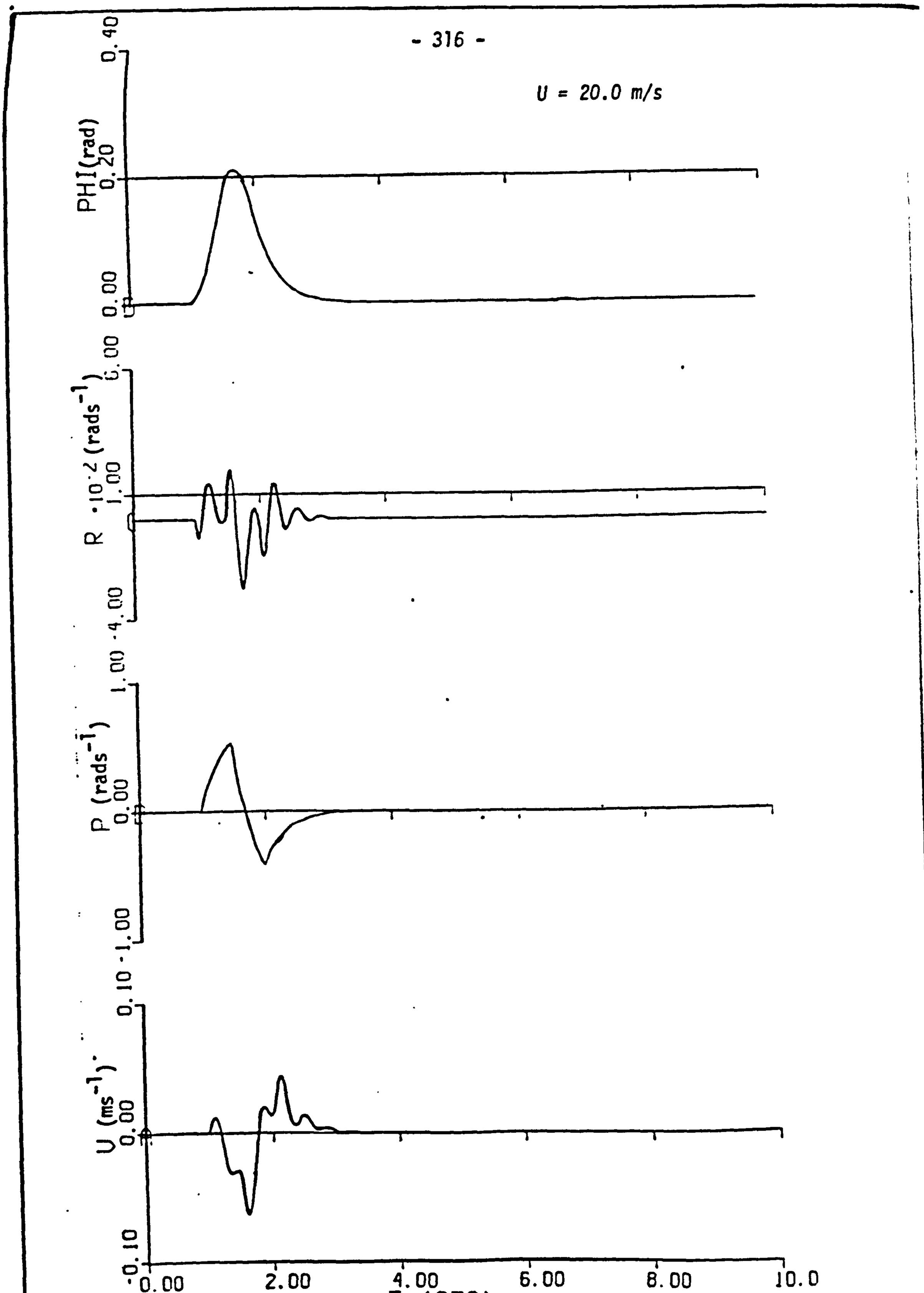

FIGURE J6

SIMULATOR LATERAL RESPONSE OF A/C TO A DIPOLE AILERON INPUT

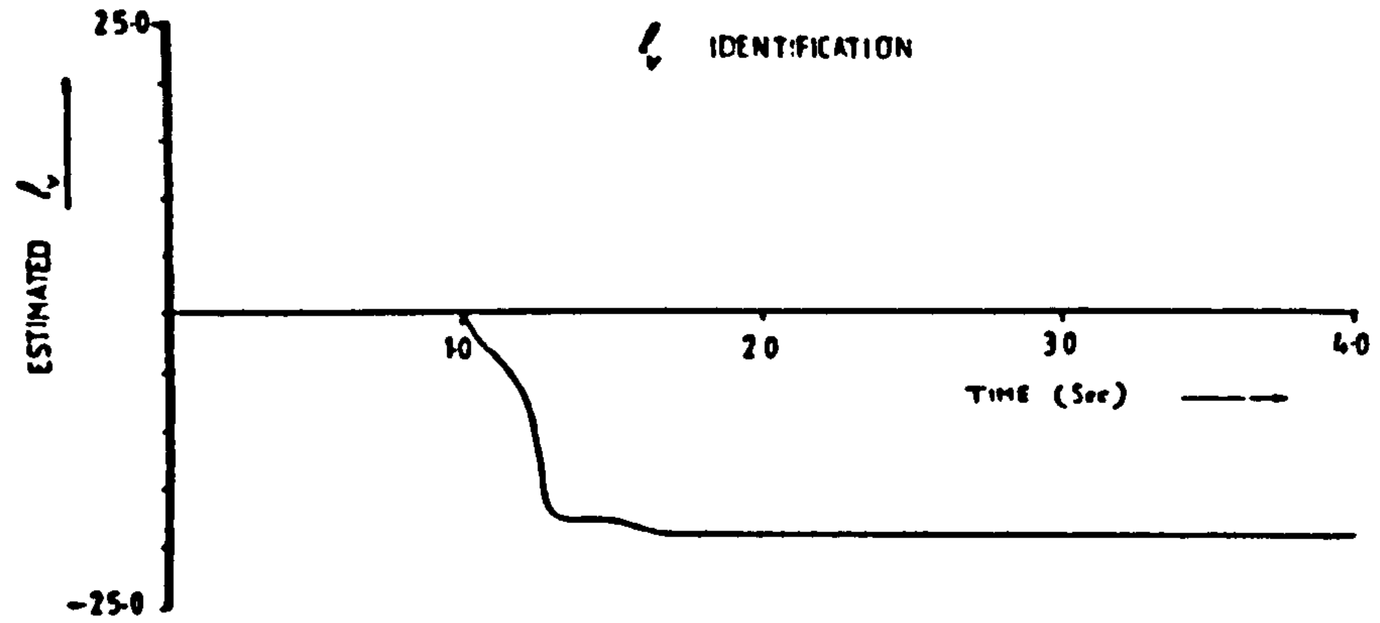

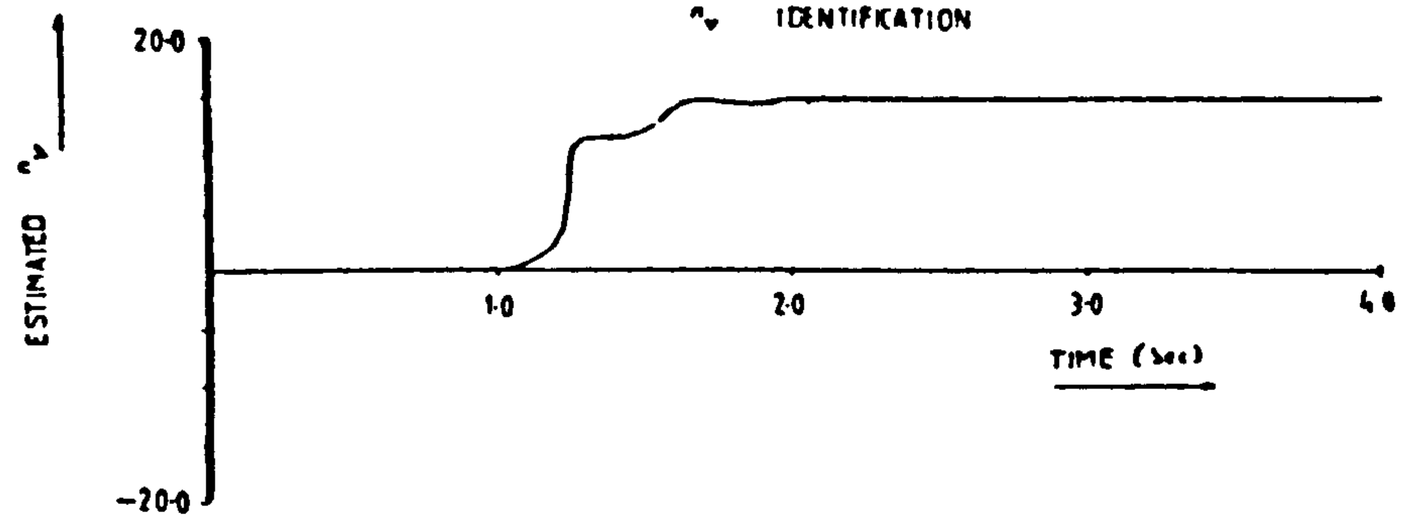

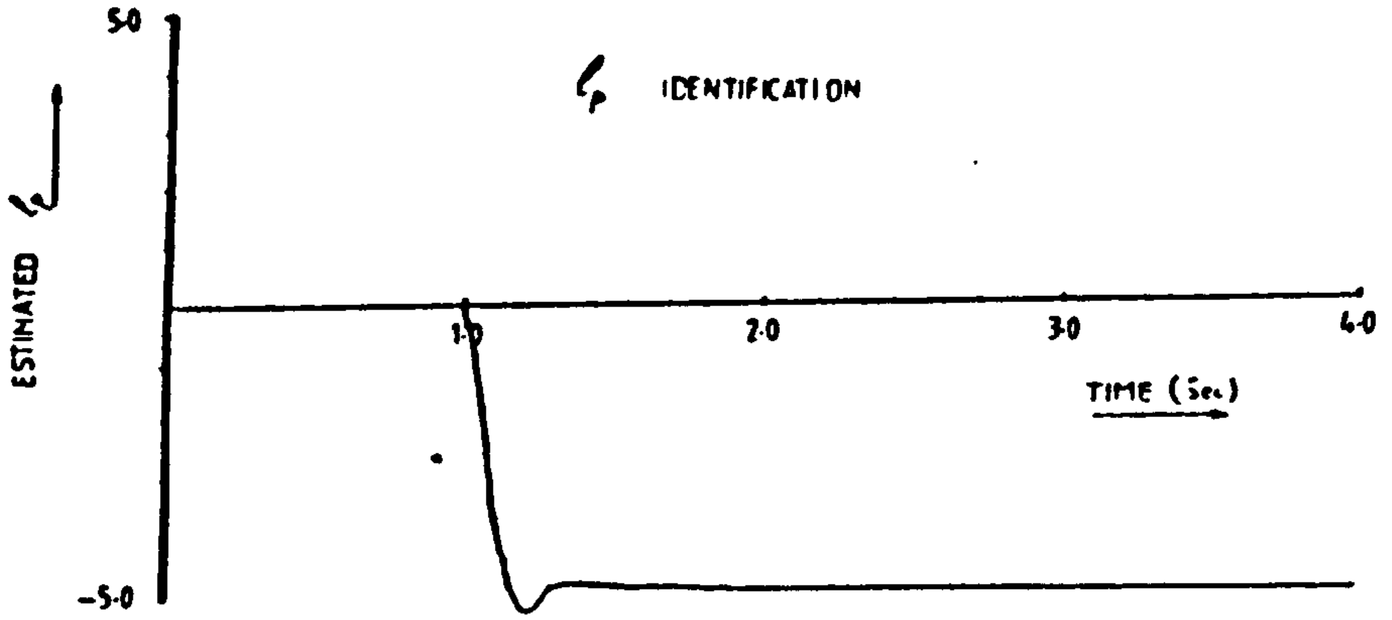

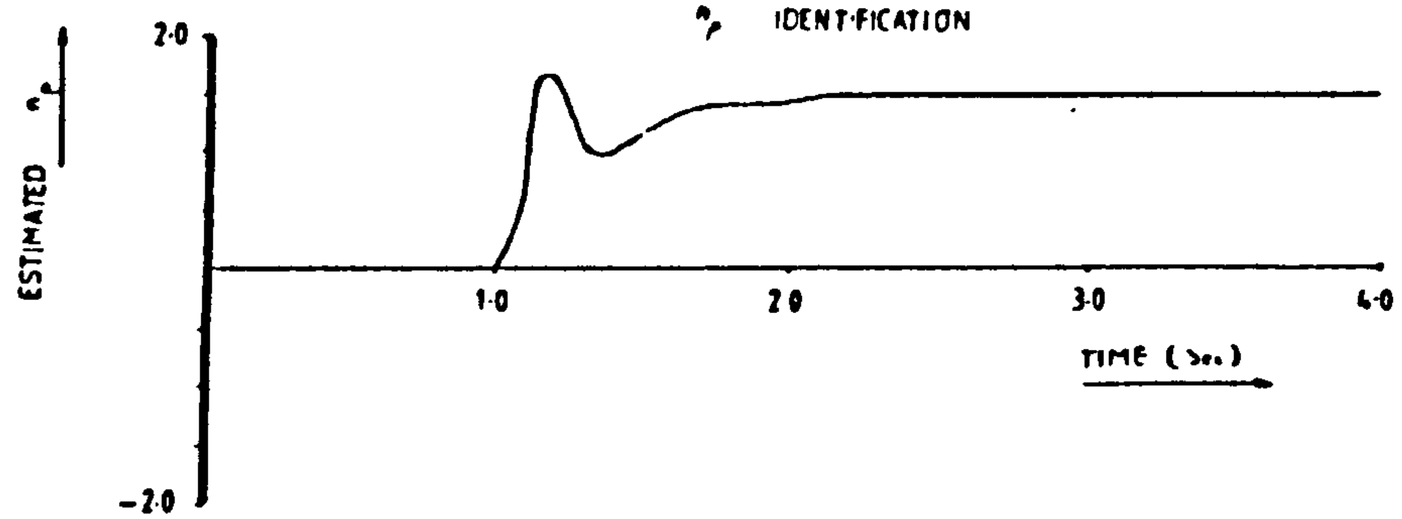

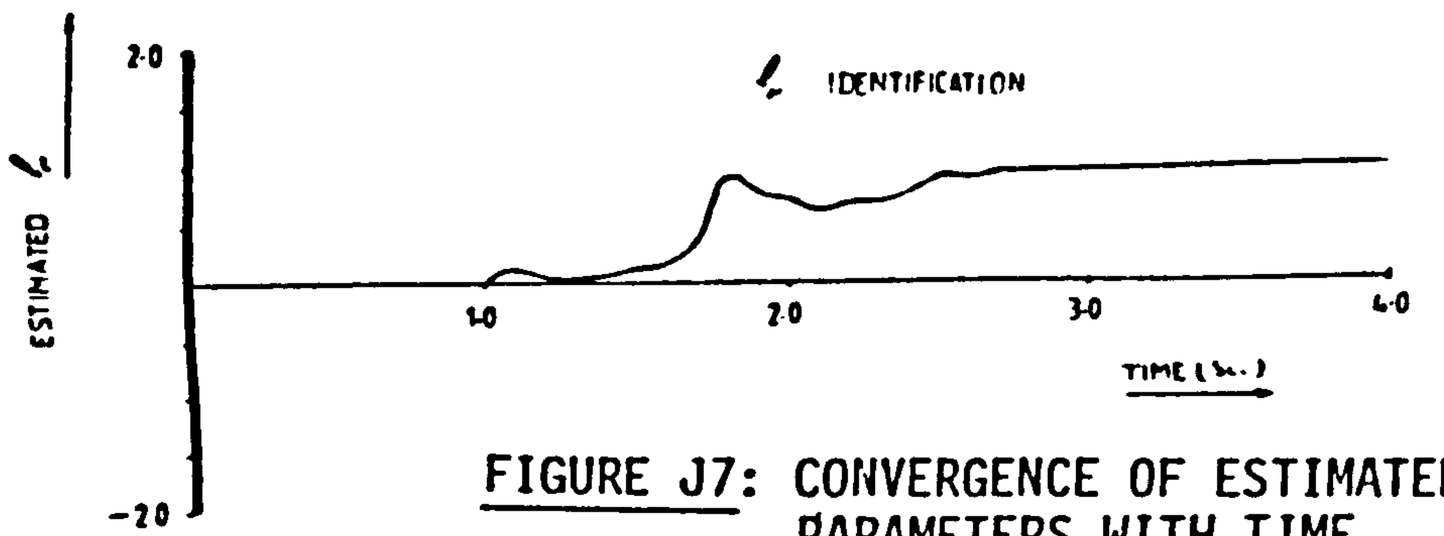

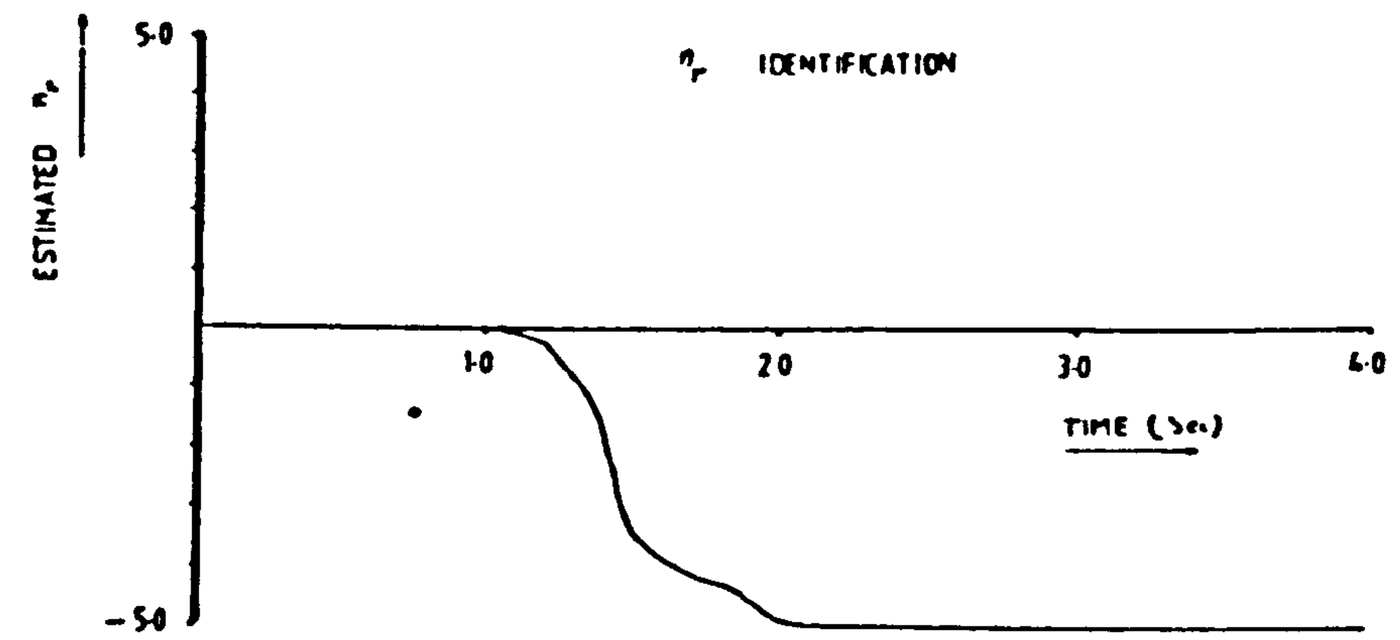

FIGURE J7: CONVERGENCE OF ESTIMATED PARAMETERS WITH TIME

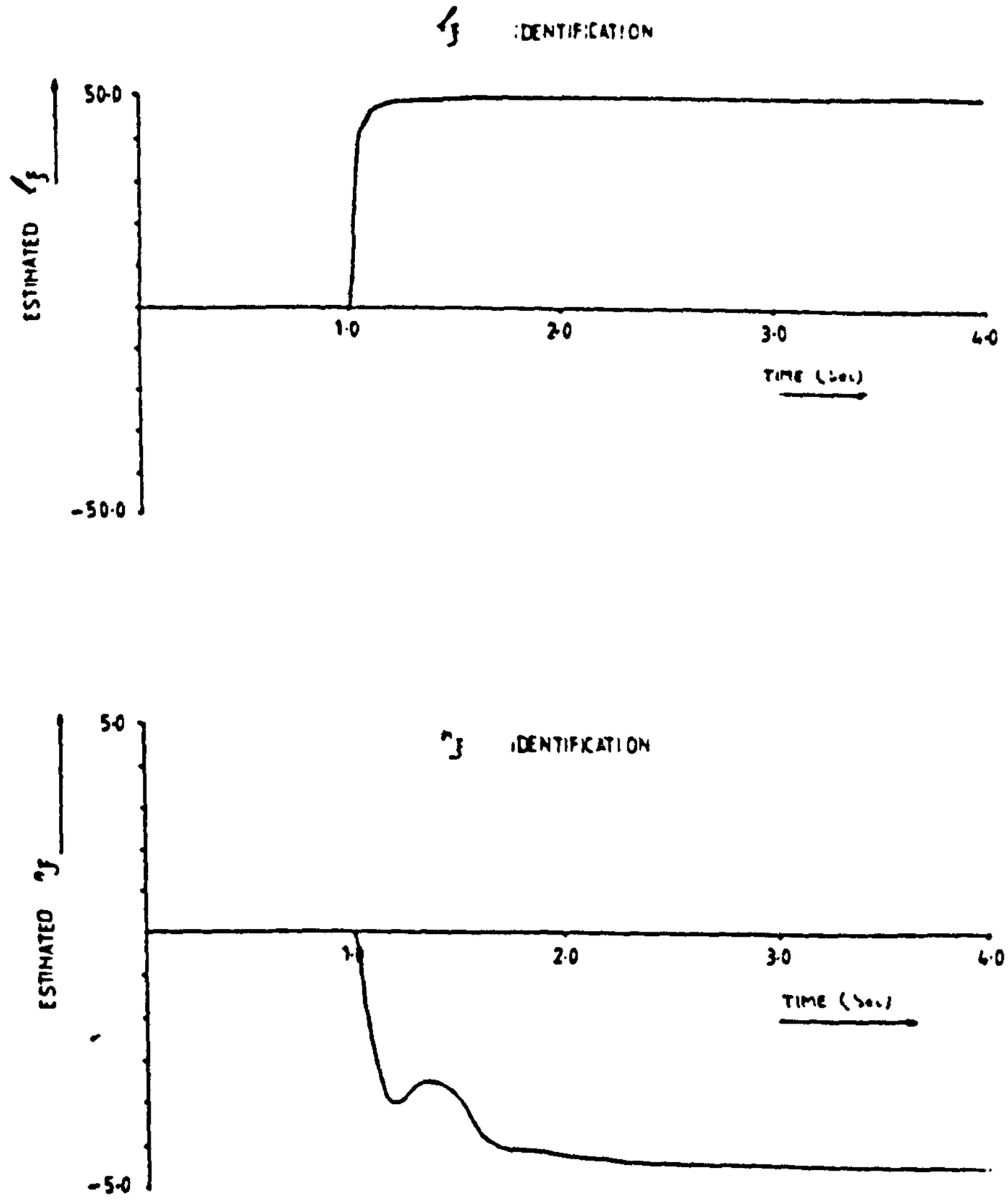

FIGURE J8: CONVERGENCE OF ESTIMATED PARAMETERS WITH TIME

PROGRAM STRUCTURE DIAGRAM

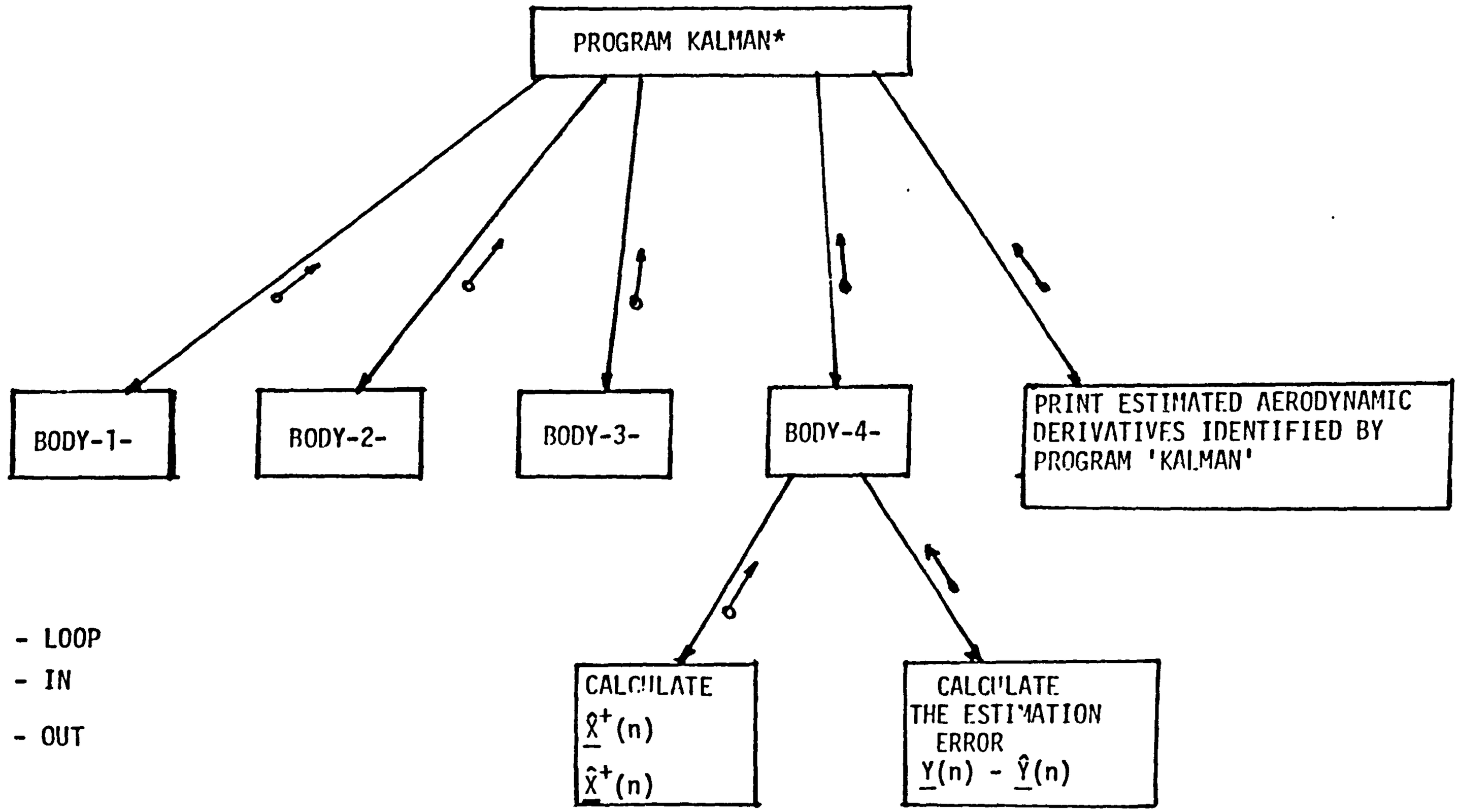

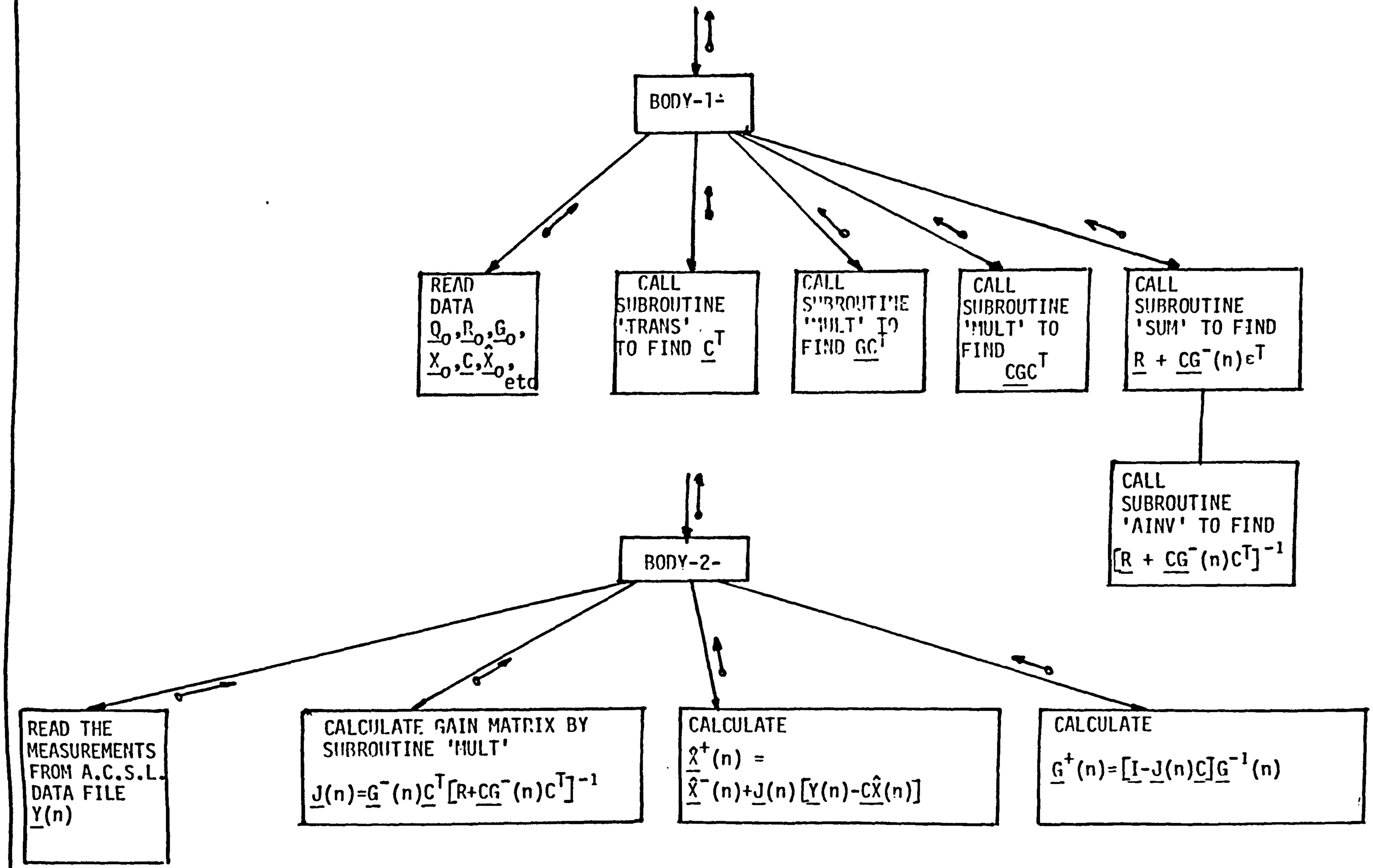
BODY-1-
READ DATA $\underline{Q}_o, \underline{R}_o, \underline{G}_o, \underline{X}_o, \underline{C}, \hat{\underline{X}}_o$, etc
CALL SUBROUTINE 'TRANS' TO FIND $\underline{C}^T$
CALL SUBROUTINE 'MULT' TO FIND $\underline{GC}^T$
CALL SUBROUTINE 'MULT' TO FIND $\underline{CGC}^T$
CALL SUBROUTINE 'SUM' TO FIND $\underline{R} + \underline{CG}^-(n)\epsilon^T$
CALL SUBROUTINE 'AINV' TO FIND $[\underline{R} + \underline{CG}^-(n)C^T]^{-1}$
BODY-2-
READ THE MEASUREMENTS FROM A.C.S.L. DATA FILE $\underline{Y}(n)$
CALCULATE GAIN MATRIX BY SUBROUTINE 'MULT'
$\underline{J}(n)=\underline{G}^-(n)\underline{C}^T[R+\underline{CG}^-(n)C^T]^{-1}$
CALCULATE
$\underline{\hat{X}}^+(n) = \underline{\hat{X}}^-(n)+\underline{J}(n)[\underline{Y}(n)-\underline{C}\hat{\underline{X}}(n)]$
CALCULATE
$\underline{G}^+(n)=[\underline{I}-\underline{J}(n)\underline{C}]\underline{G}^{-1}(n)$

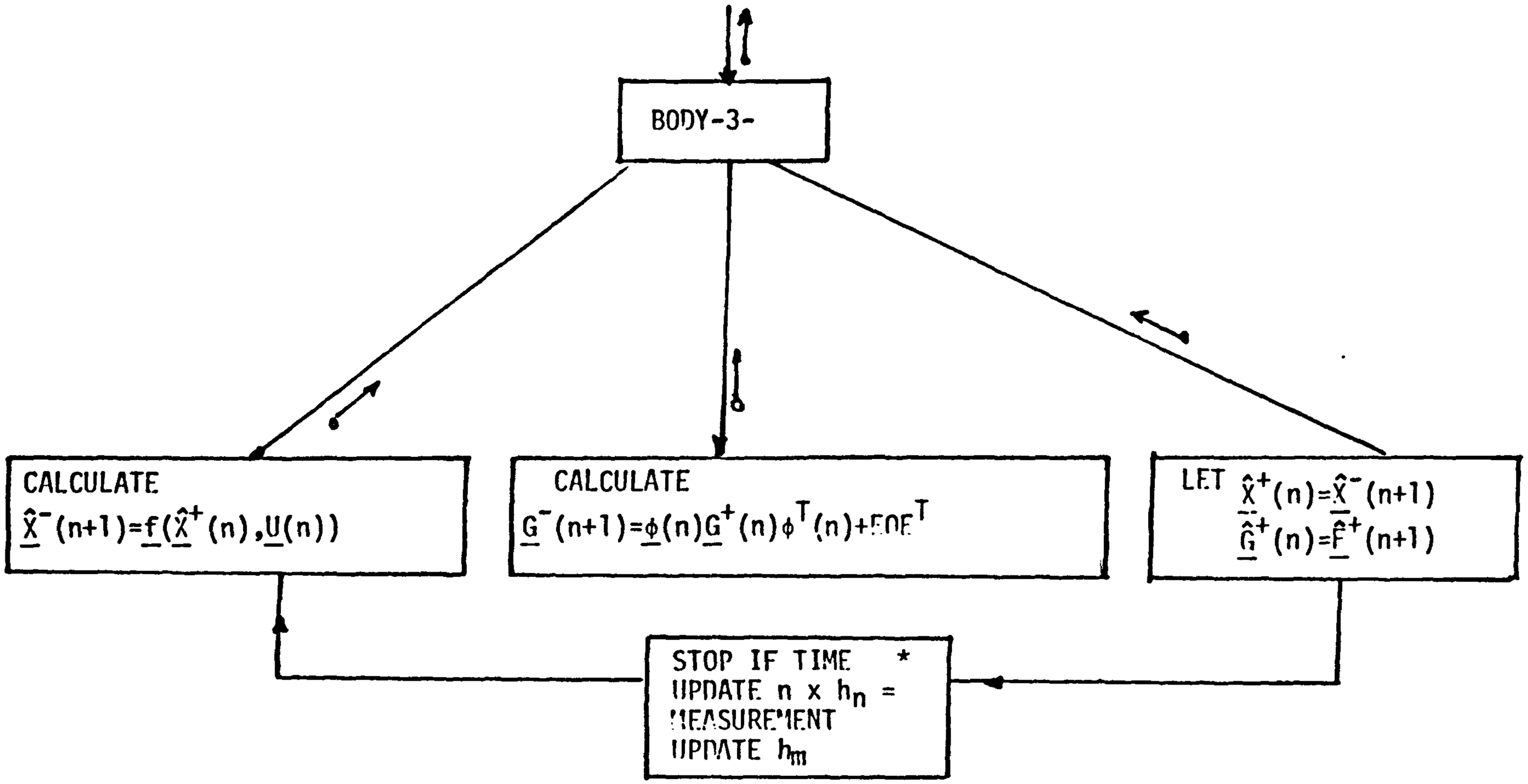
BODY-3-
CALCULATE
$\hat{\underline{X}}^-(n+1)=\underline{f}(\hat{\underline{X}}^+(n),\underline{U}(n))$
CALCULATE
$\underline{G}^-(n+1)=\underline{\phi}(n)\underline{G}^+(n)\phi^T(n)+EQE^T$
LET $\hat{\underline{X}}^+(n)=\hat{\underline{X}}^-(n+1)$
$\hat{\underline{G}}^+(n)=\hat{\underline{F}}^+(n+1)$
STOP IF TIME *
UPDATE n x h_n =
MEASUREMENT
UPDATE h_m

* - LOOP

J.4 Calculations and Results Regarding Experiments 1 - 4 of Table 8.3

Covariance matrices G, R and Q were initially estimated to be:

$$G = \begin{bmatrix} 1.6 \times 10^{-3} & 0 & 0 & 0 & 0 & 0 & 0 & 0 \\ 0 & 10^{-4} & 0 & 0 & 0 & 0 & 0 & 0 \\ 0 & 0 & 1.6 \times 10^{-5} & 0 & 0 & 0 & 0 & 0 \\ 0 & 0 & 0 & 4 \times 10^{-2} & 0 & 0 & 0 & 0 \\ 0 & 0 & 0 & 0 & 4 \times 10^{-4} & 0 & 0 & 0 \\ 0 & 0 & 0 & 0 & 0 & 6.4 \times 10^{-3} & 0 & 0 \\ 0 & 0 & 0 & 0 & 0 & 0 & 1.0 & 0 \\ 0 & 0 & 0 & 0 & 0 & 0 & 0 & 16.0 \end{bmatrix}$$

$$R = \begin{bmatrix} 10^{-3} & 0 & 0 \\ 0 & 6 \times 10^{-5} & 0 \\ 0 & 0 & 10^{-5} \end{bmatrix}$$

$$Q = \begin{bmatrix} 2.5 \times 10^{-2} & 0 & 0 & 0 & 0 \\ 0 & 2.5 \times 10^{-4} & 0 & 0 & 0 \\ 0 & 0 & 4.1 \times 10^{-3} & 0 & 0 \\ 0 & 0 & 0 & 0.64 & 0 \\ 0 & 0 & 0 & 0 & 10.2 \end{bmatrix}$$

With all initial values set to zero. The covariance matrices were based on an assumed 10% r.m.s. in the estimation of the aerodynamic derivatives and 1% r.m.s. error in measurement. Based on the average of ten runs with different R deviating from its estimated value by ±20%, Table J3 gives the mean estimated stability derivatives of the F.S.W. model with C.G. at 0.444 m from datum.

ESTIMATED DERIVATIVES IN CONCISE FORM							C.G. AT 0.444 m FROM DATUM
TUNNEL SPEED (m/s)	z_w	m_w	m_q	z_η	z_q	m_η	
U = 27	-4.5	7.0	-1.4	-92.0	-31.0	108.0	
U = 30	-6.0	8.0	-2.7	-155.0	-33.0	143.0	

ESTIMATED DERIVATIVES IN AERO-NORMALISED FORM							C.G. AT 0.444 m FROM DATUM
TUNNEL SPEED (m/s)	$\check{Z}_w$	$\check{M}_w$	$\check{M}_q$	$\check{Z}_\eta$	$\check{Z}_q$	$\check{M}_\eta$	
U = 27	-8.0	3.3	-4.0	-6.1	-328.2	1.9	
U = 30	-9.6	3.4	-6.9	-9.2	-314.4	2.3	

TABLES-J3.a

MEAN ESTIMATED STABILITY DERIVATIVES WITH C.G. AT 0.444 m FROM DATUM

ESTIMATED DERIVATIVES IN CONCISE FORM							C.G. AT 0.44 m FROM DATUM
TUNNEL SPEED (m/s)	z_w	m_w	m_q	z_η	z_q	m_η	
U = 26	-5.0	8.0	-1.0	X	-32.0	140.0	
U = 28	-7.0	10.0	-2.2	-190.0	-32.0	160.0	

ESTIMATED DERIVATIVES IN AERO NORMALISED FORM							C.G. AT 0.44 m FROM DATUM
TUNNEL SPEED (m/s)	$\check{Z}_w$	$\check{M}_w$	$\check{M}_q$	$\check{Z}_\eta$	$\check{Z}_q$	$\check{M}_\eta$	
U = 26	-9.2	3.9	-2.8	X	-338.7	X	
U = 28	-12.0	4.8	-6.2	-13.5	-338.7	3.0	

TABLES-J3.b

MEAN ESTIMATED STABILITY DERIVATIVES WITH C.G. AT 0.440 m FROM DATUM

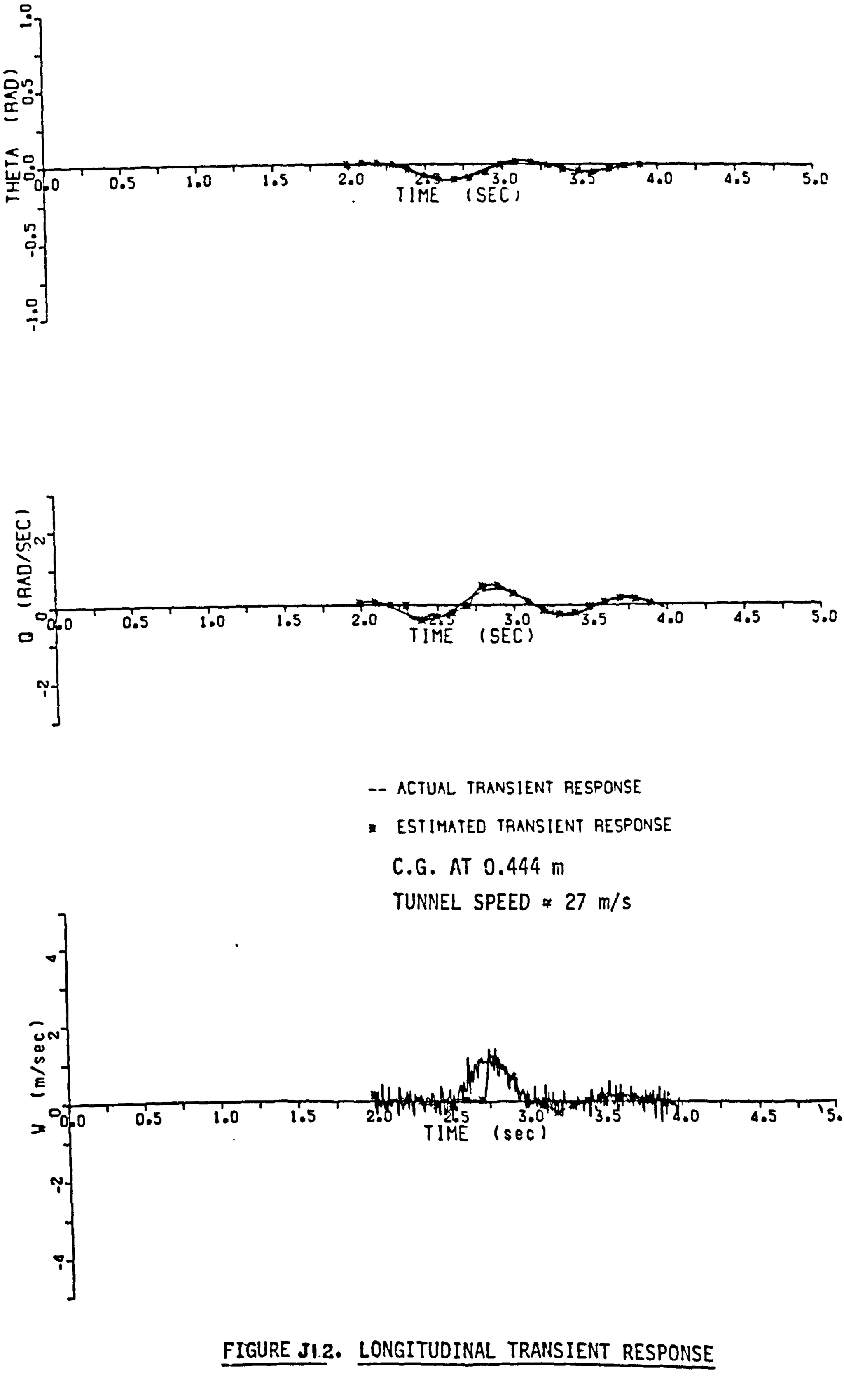

FIGURE J1.2. LONGITUDINAL TRANSIENT RESPONSE

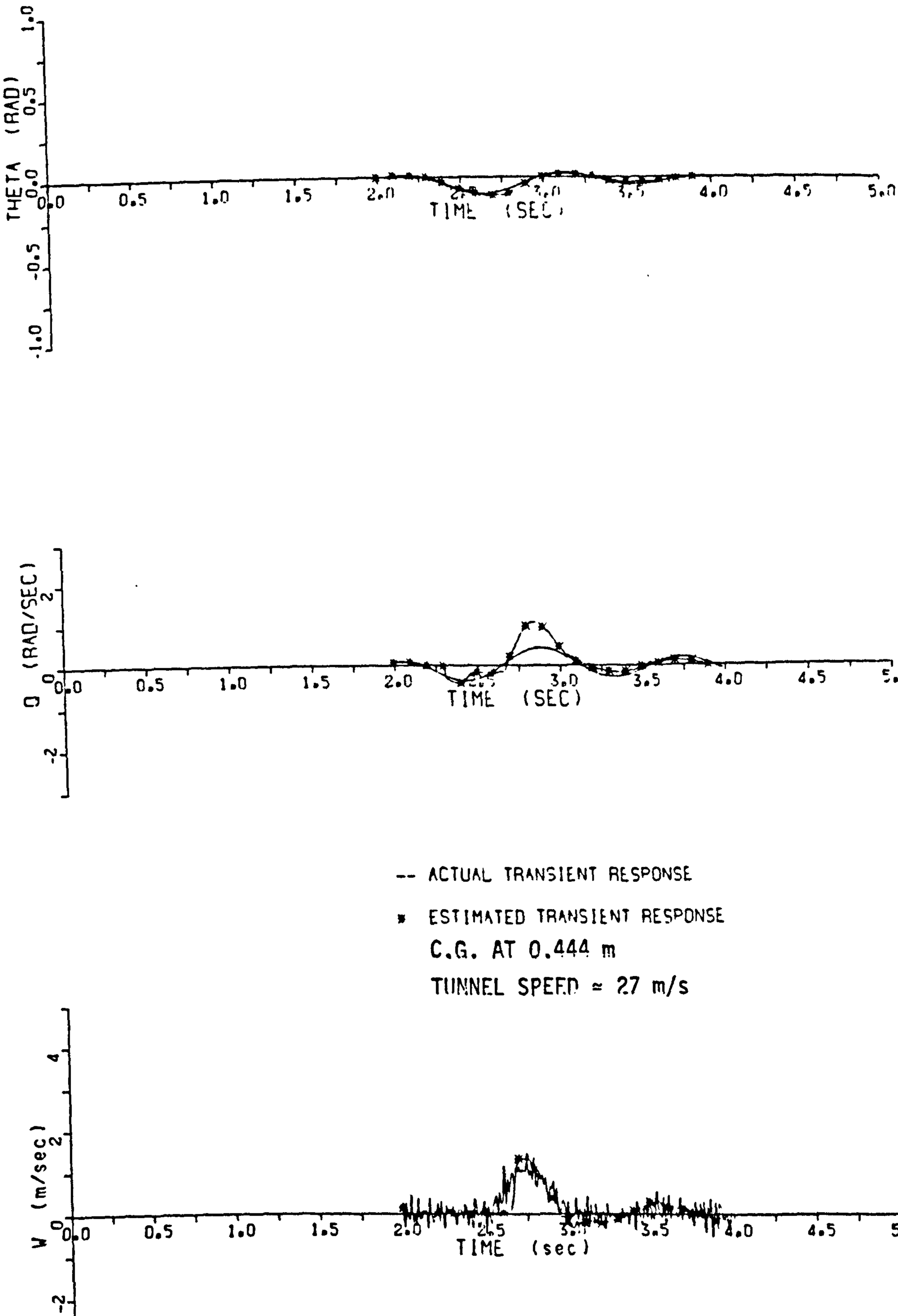

FIGURE J13. LONGITUDINAL TRANSIENT RESPONSE

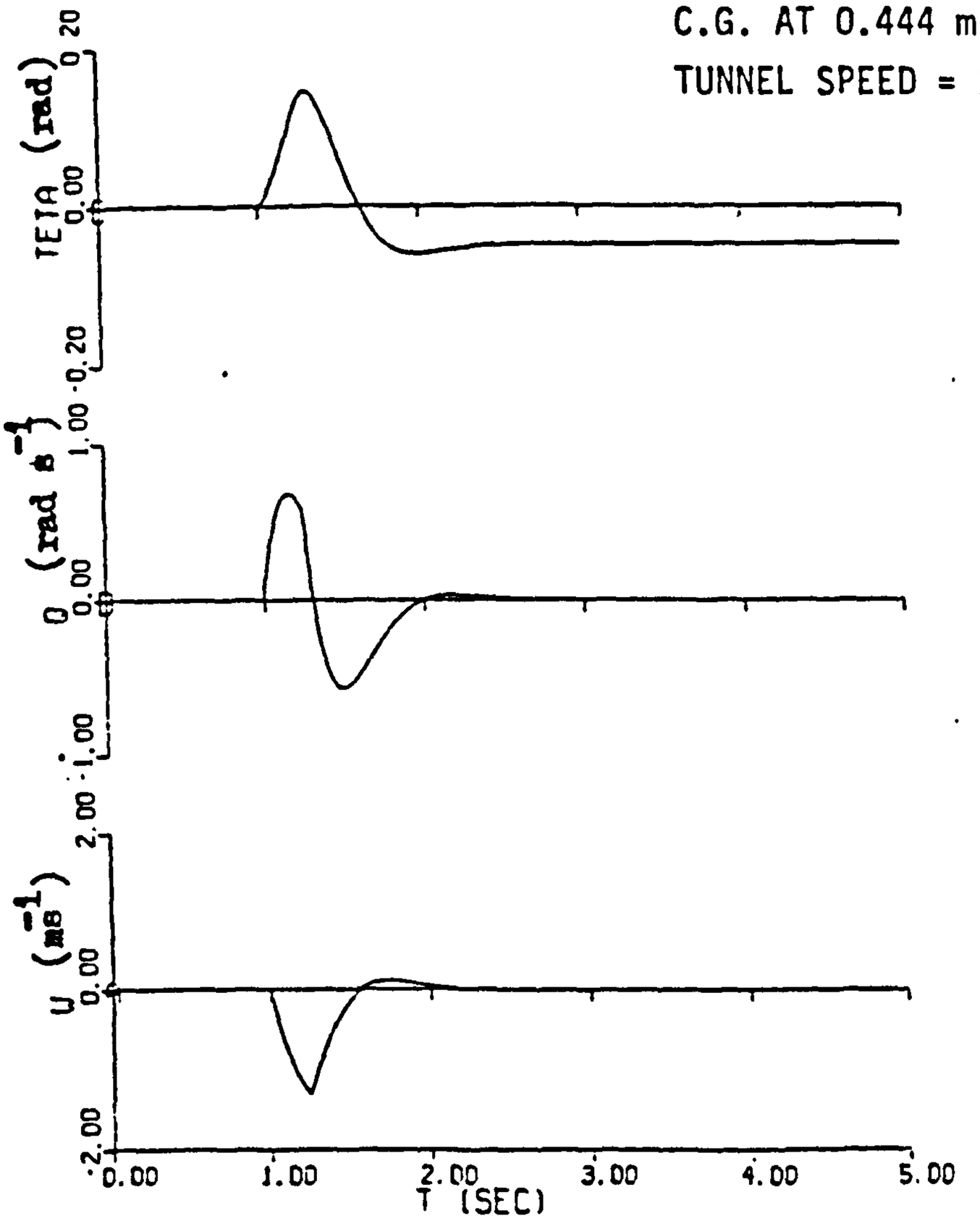

FIGURE J14. SIMULATION OF LONGITUDINAL TRANSIENT RESPONSE USING ESTIMATED DERIVATIVES

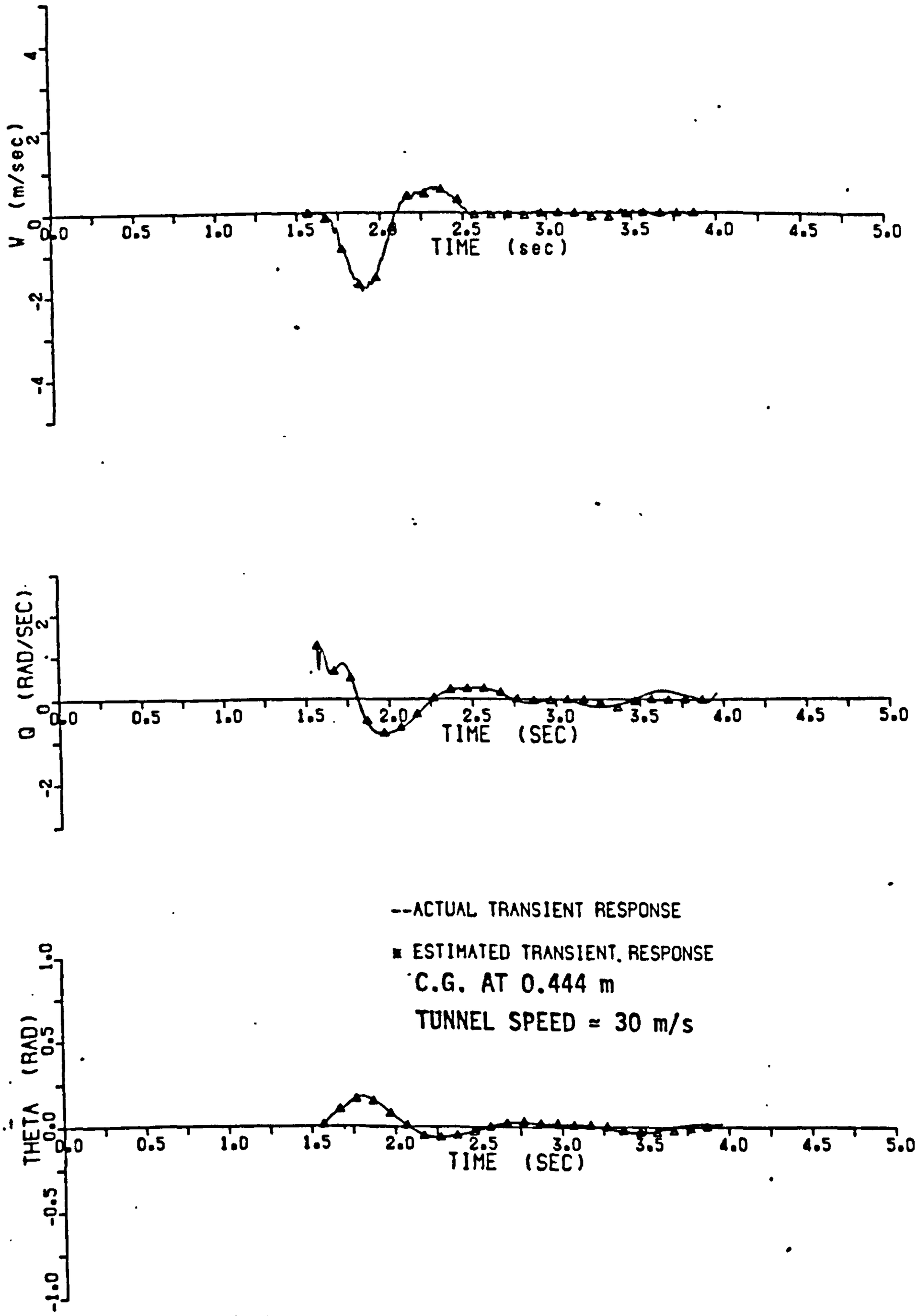

FIGURE 315. LONGITUDINAL TRANSIENT RESPONSE

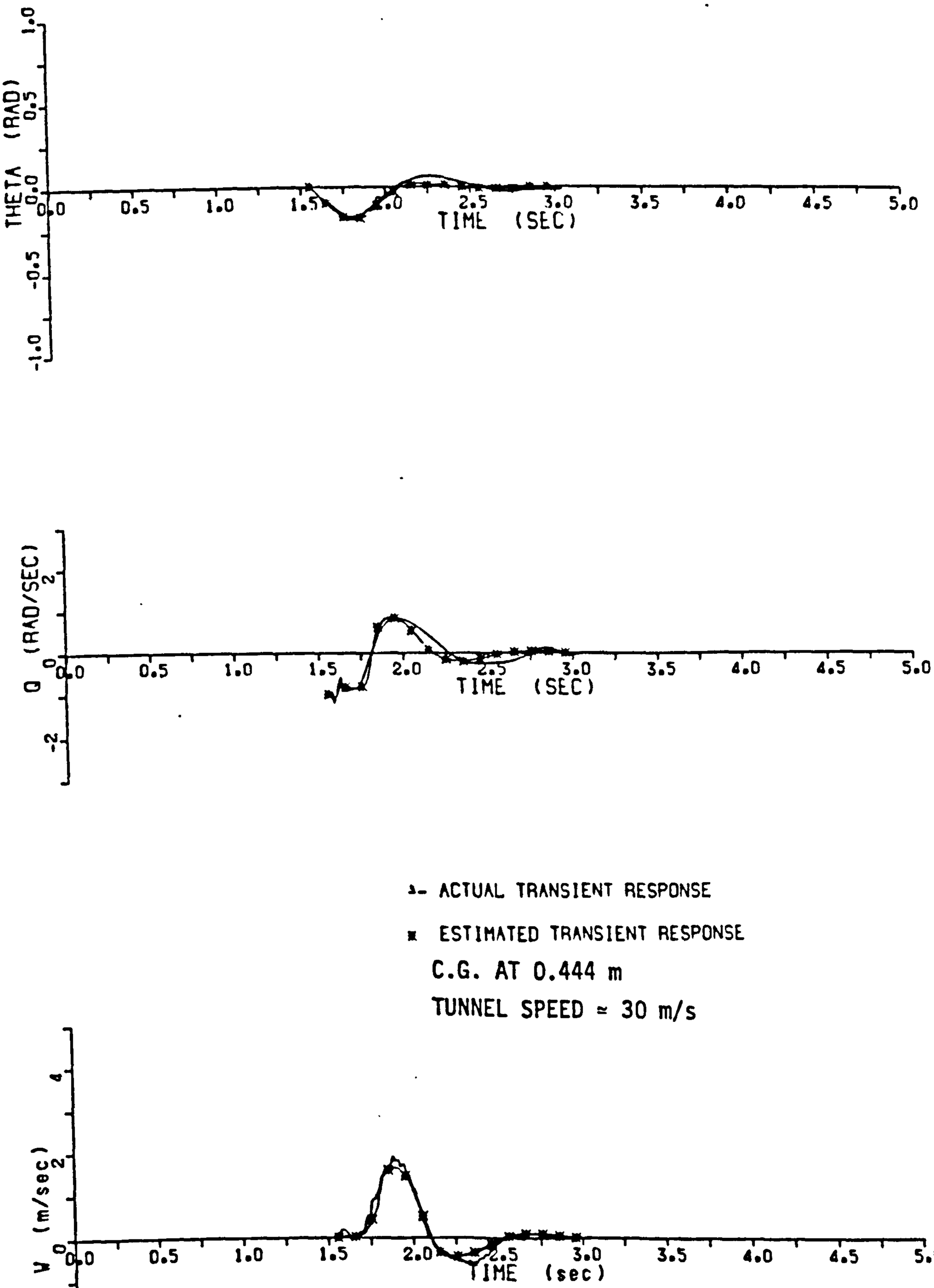

a- ACTUAL TRANSIENT RESPONSE

x ESTIMATED TRANSIENT RESPONSE

C.G. AT 0.444 m

TUNNEL SPEED ≈ 30 m/s

FIGURE J16 .LONGITUDINAL TRANSIENT RESPONSE

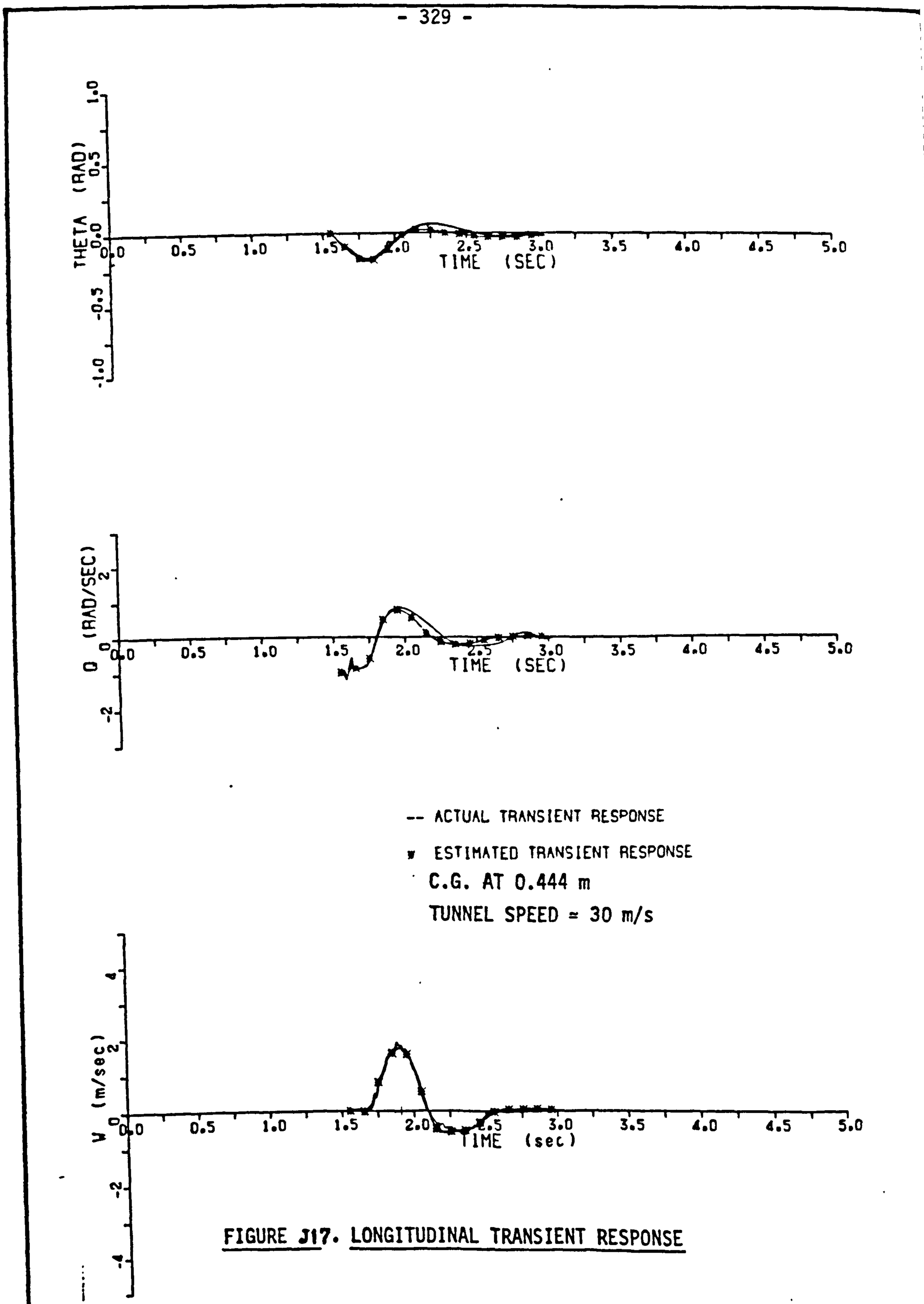

FIGURE J17. LONGITUDINAL TRANSIENT RESPONSE

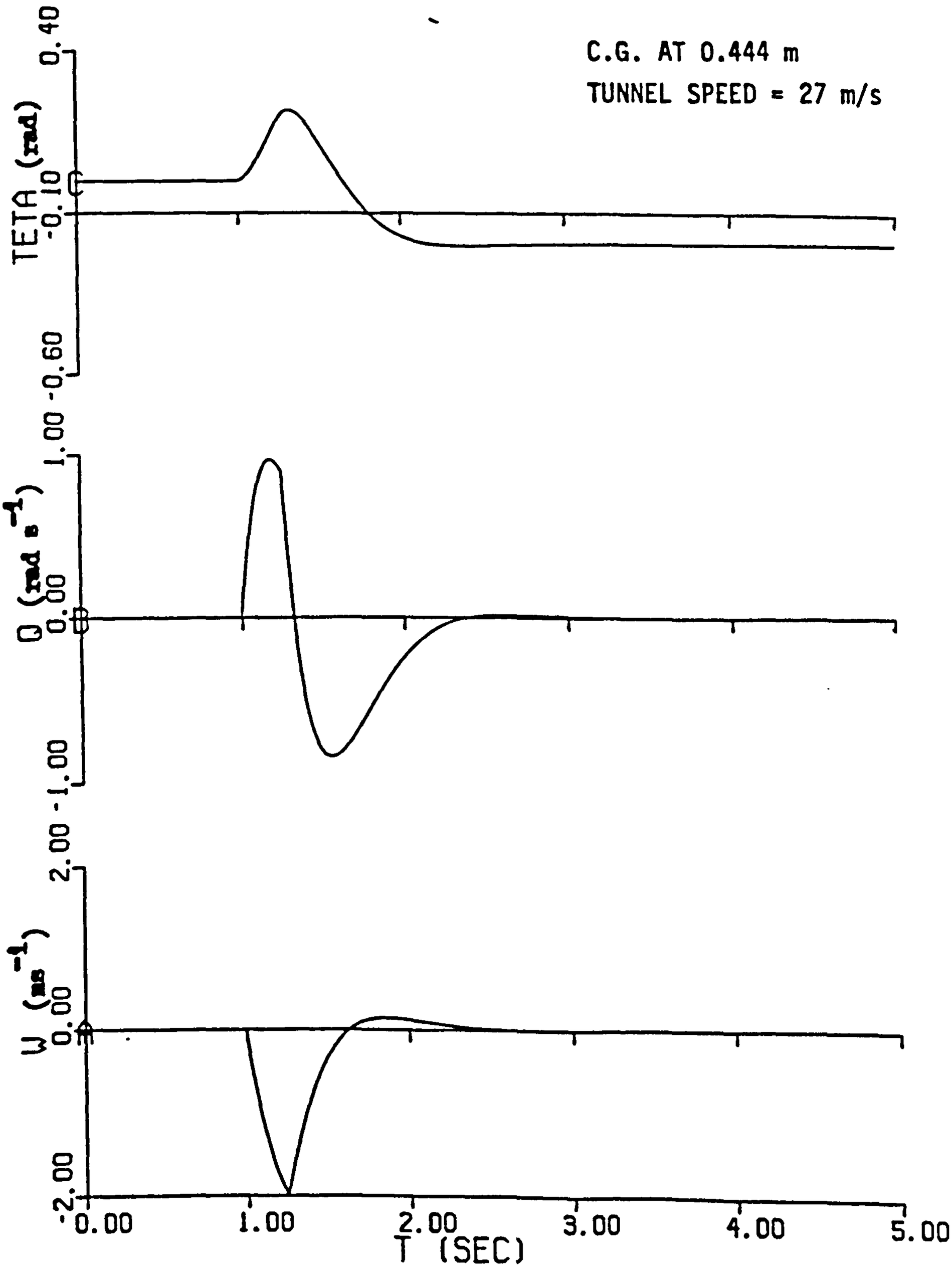

FIGURE J18. SIMULATION OF LONGITUDINAL TRANSIENT RESPONSE USING ESTIMATED DERIVATIVES

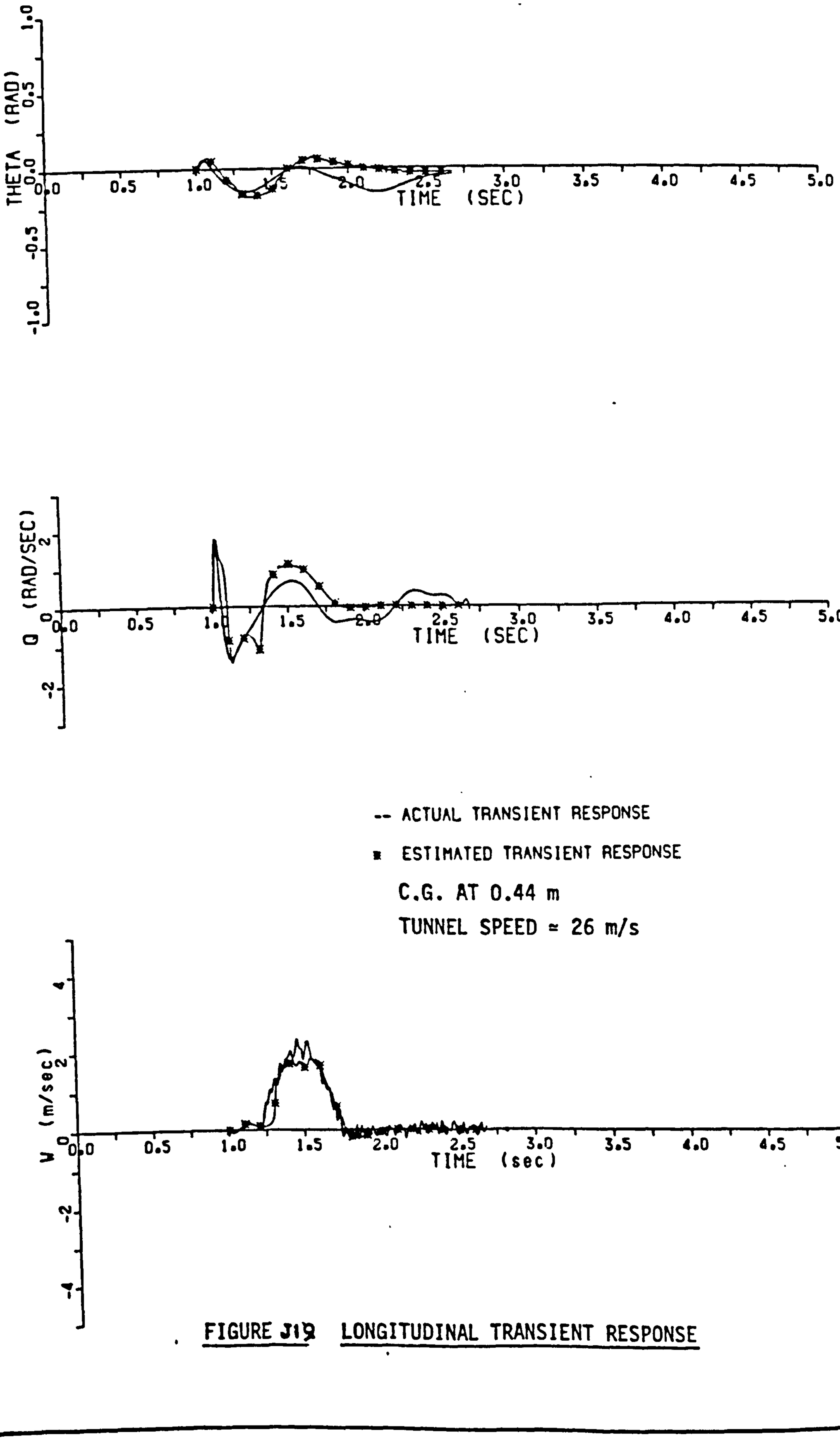

FIGURE J19 LONGITUDINAL TRANSIENT RESPONSE

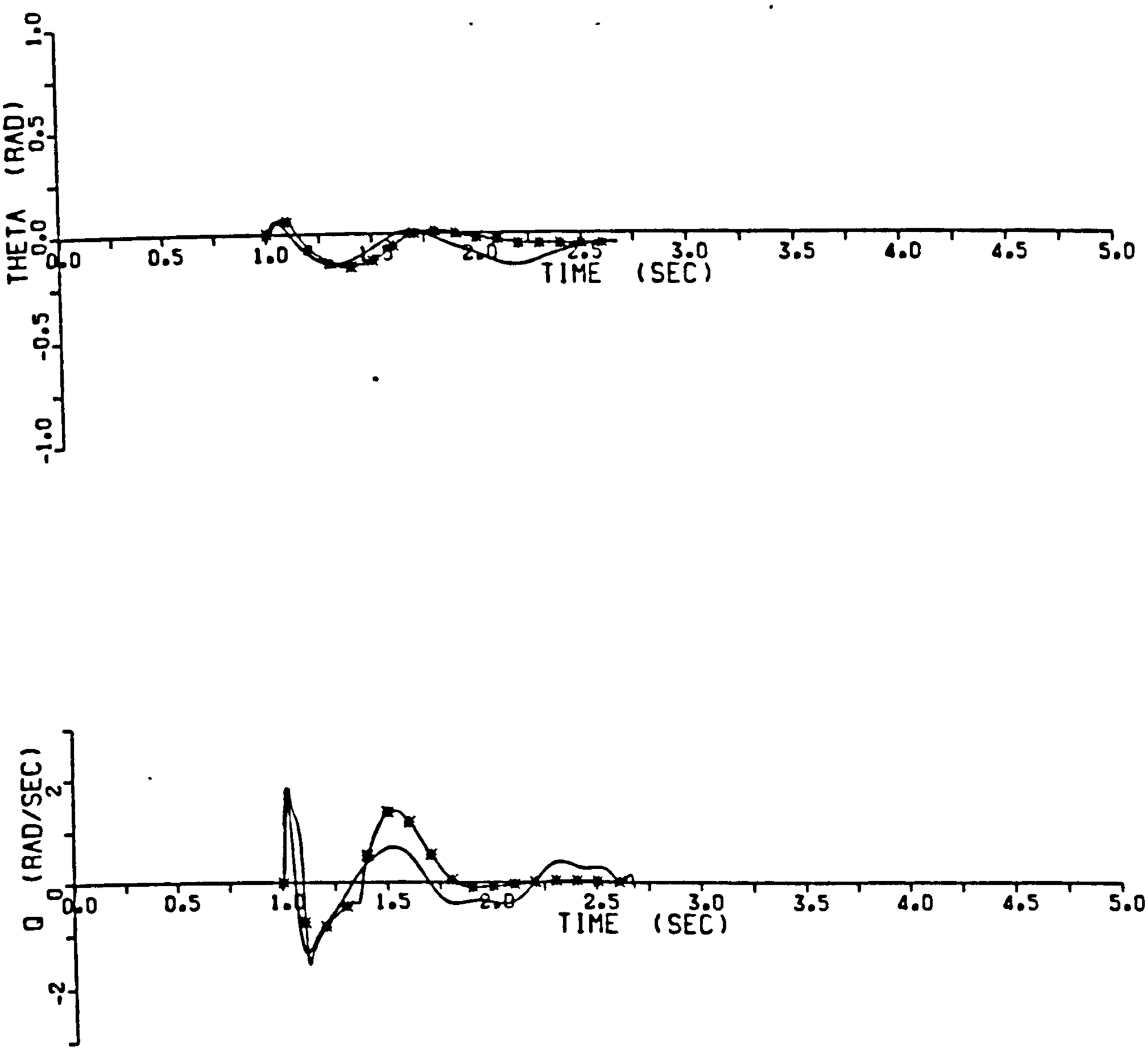

FIGURE 320. LONGITUDINAL TRANSIENT RESPONSE

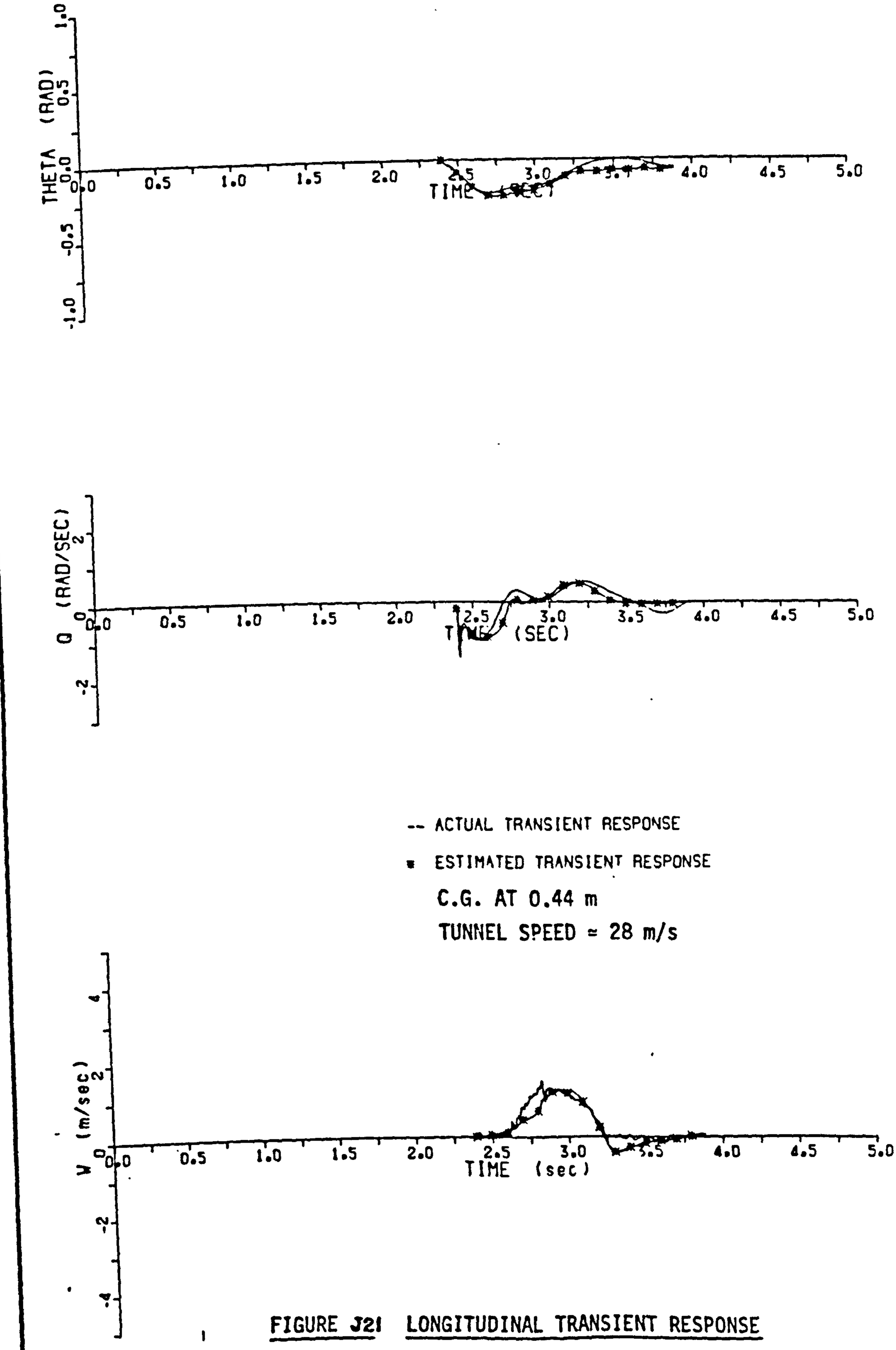

FIGURE J21 LONGITUDINAL TRANSIENT RESPONSE

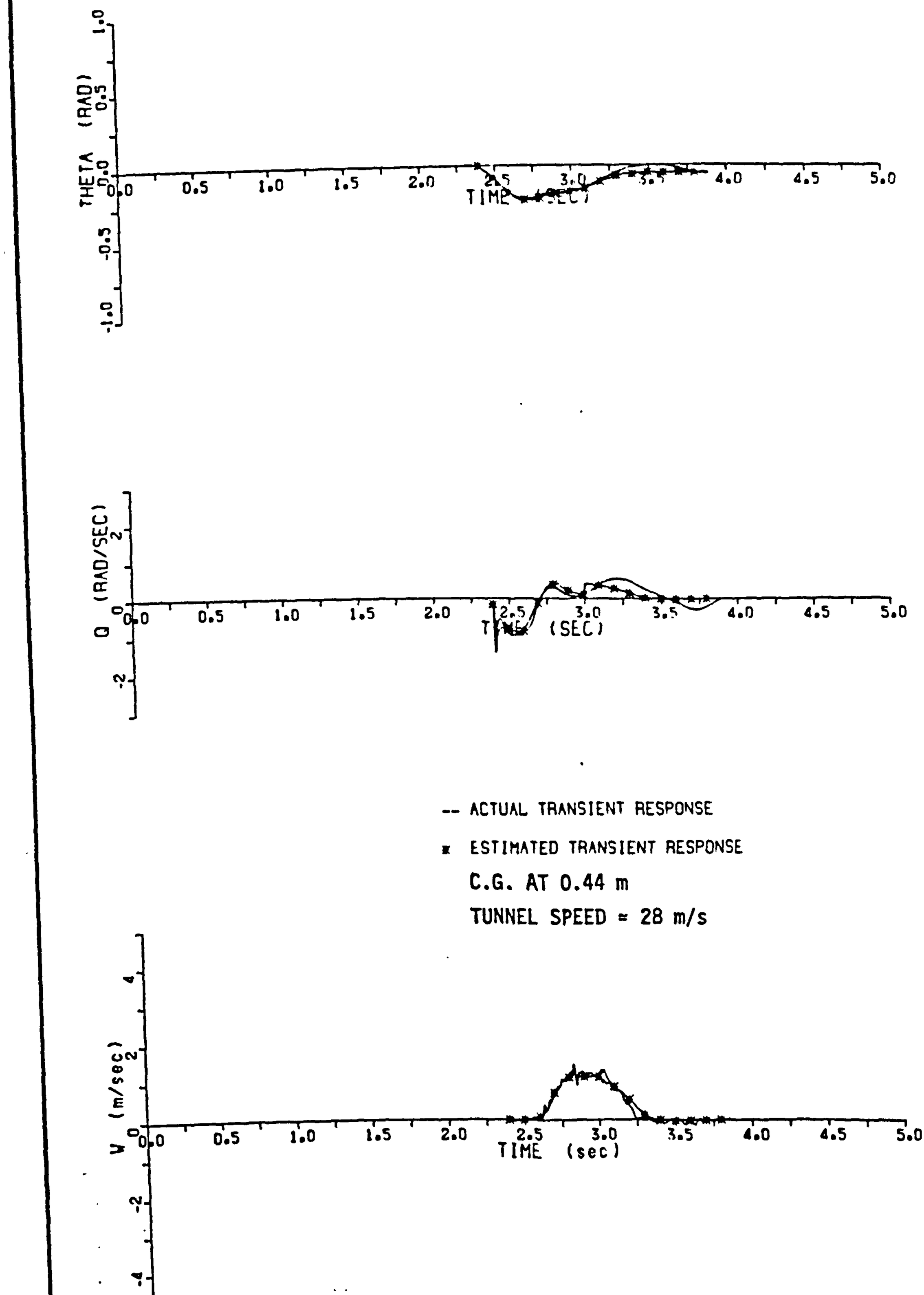

FIGURE J22. LONGITUDINAL TRANSIENT RESPONSE

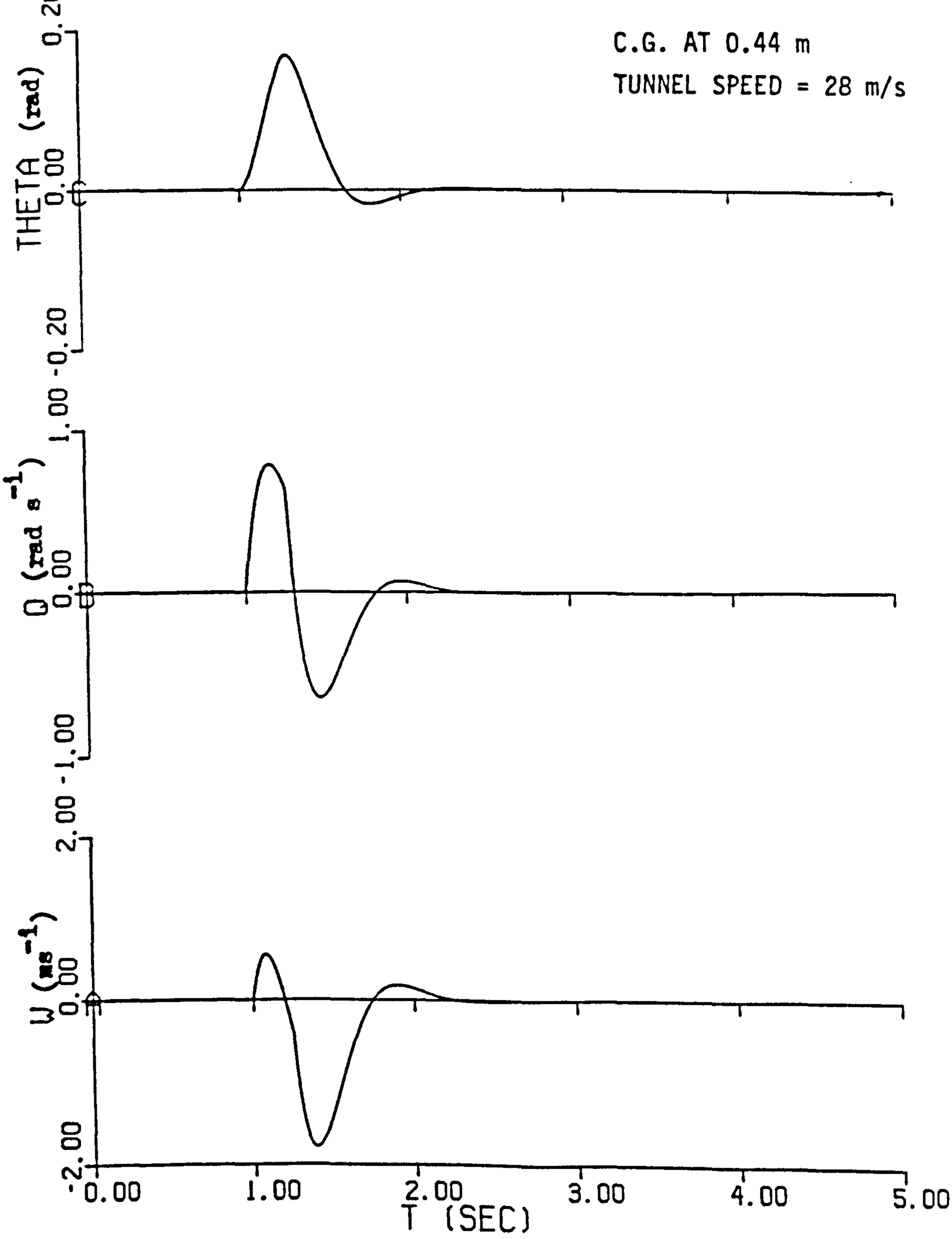

FIGURE J23. SIMULATION OF LONGITUDINAL TRANSIENT RESPONSE USING ESTIMATED DERIVATIVES

J.4 Results of the Lateral Dynamic Tests

This section contains the results of lateral experiments as given by Table 9.2 of Section 9.

Covariance Matrices G, R, Q

Based on the method of section J1., the initial value of the state covariance matrix 'G' was estimated to be:

$$G(0) = \begin{bmatrix} 0.2 & & & & & & & & & & & & & & \\ & 0.2 & & & & & & & & & & & & & \\ & & 0.158 & & & & & & & & & & & & \\ & & & 0.02 & & & & & & & & & & & \\ & & & & 0.25 & & & & & & & & & & \\ & & & & & 0.289 & & & & & & & & & \\ & & & & & & 0.09 & & & & & & & & \\ & & & & & & & 0.25 & & & & & & & \\ & & & & & & & & 0.026 & & & & & & \\ & & & & & & & & & 0.088 & & & & & \\ & & & & & & & & & & 0.0 & & & & \\ & & & & & & & & & & & 64.0 & & & \\ & & & & & & & & & & & & 0.0 & & \\ & & & & & & & & & & & & & 64.0 & \end{bmatrix}$$

Also, measurement noise covariance matrix 'R' and process noise covariance matrices 'Q' were estimated to be:

$$R = \begin{bmatrix} 10^{-6} & 0 & 0 & 0 \\ 0 & 10^{-6} & 0 & 0 \\ 0 & 0 & 10^{-6} & 0 \\ 0 & 0 & 0 & 10^{-6} \end{bmatrix}$$

$$Q = \begin{bmatrix} 0.02 & & & & & & & & & & & \\ & 0.017 & & & & & & & & & & \\ & & 0.003 & & & & & & & & & \\ & & & 0.01 & & & & & & & & \\ & & & & 0.03 & & & & & & & \\ & & & & & 0.03 & & & & & & \\ & & & & & & 0.0 & & & & & \\ & & & & & & & 3.0 & & & & \\ & & & & & & & & 0.0 & & & \\ & & & & & & & & & 3.0 & & \\ & & & & & & & & & & 0.0 & \\ & & & & & & & & & & & 3.0 \end{bmatrix}$$

ESTIMATED DERIVATIVES IN CONCISE FORM									C.G. AT 0.444 m FROM DATUM
TUNNEL SPEED (m/s)	ℓ_v	ℓ_p	ℓ_r	n_v	n_p	n_r	ℓ_ζ	n_ζ	
27	2.0	-12.0	-2.0	2.0	26.0	-9.0	118.0	222.0	
29	0.5	- 2.0	-1.2	0.8	30.0	-7.2	124.0	240.0	
31	1.5	- 4.5	-1.0	1.5	32.0	-8.0	132.0	210.0	
33	1.0	- 7.8	-0.9	1.2	33.0	-9.0	147.0	190.0	

TABLE- J4 .

ESTIMATED DERIVATIVES IN AERONORMALISED FORM									C.G. AT 0.444 m FROM DATUM
TUNNEL SPEED (m/s)	$\breve{L}_v$	$\breve{L}_p$	$\breve{L}_r$	$\breve{N}_v$	$\breve{N}_p$	$\breve{N}_r$	$\breve{L}_\zeta$	$\breve{N}_\zeta$	
27	0.09	-1.72	-0.29	0.55	22.03	-7.63	0.2	2.26	
29	0.02	-0.27	-0.16	0.2	23.67	-5.68	0.18	2.12	
31	0.08	-0.56	-0.12	0.36	23.62	-5.9	0.17	1.62	
33	0.04	-0.92	-0.11	0.27	22.88	-6.24	0.17	1.3	

TABLE -J5.

ESTIMATED DERIVATIVES IN CONCISE FORM									C.G.AT 0.44m FROM DATUM
TUNNEL SPEED (m/s)	ℓ_v	ℓ_p	ℓ_r	n_v	n_p	n_r	ℓ_ζ	n_ζ	
27	0.7	-8.0	-3.2	2.2	-2.0	-8.0	100.0	380.0	

TABLE - J6.

ESTIMATED DERIVATIVES IN AERONORMALISED FORM									C.G.AT 0.44m FROM DATUM
TUNNEL SPEED (m/s)	$\breve{L}_v$	$\breve{L}_p$	$\breve{L}_r$	$\breve{N}_v$	$\breve{N}_p$	$\breve{N}_r$	$\breve{L}_\zeta$	$\breve{N}_\zeta$	
27	0.03	-1.15	-0.46	0.6	-1.69	-6.78	0.17	3.17	

TABLE .-J7.

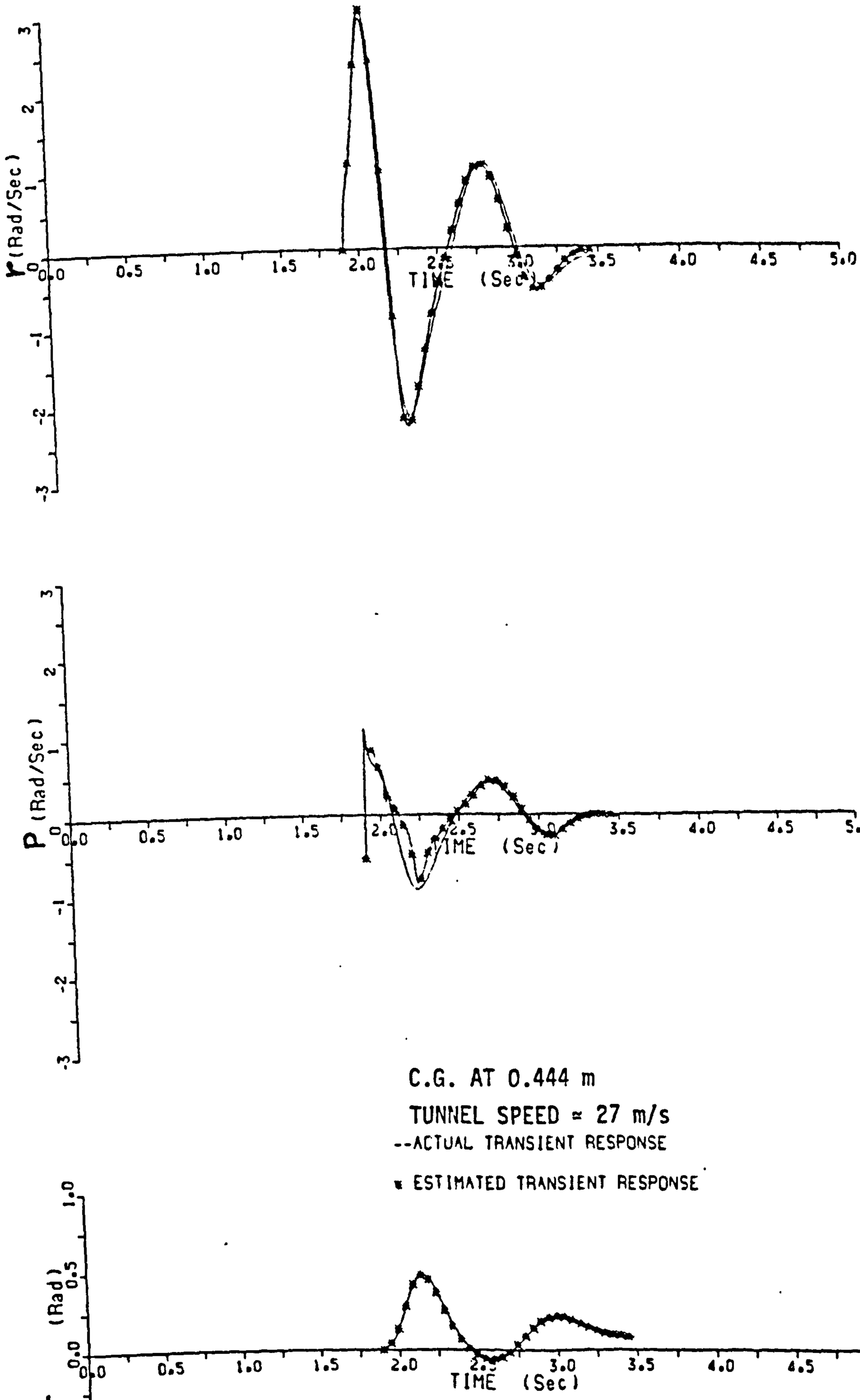

FIGURE J24. LATERAL TRANSIENT RESPONSE DUE TO RUDDER PULSE INPUT

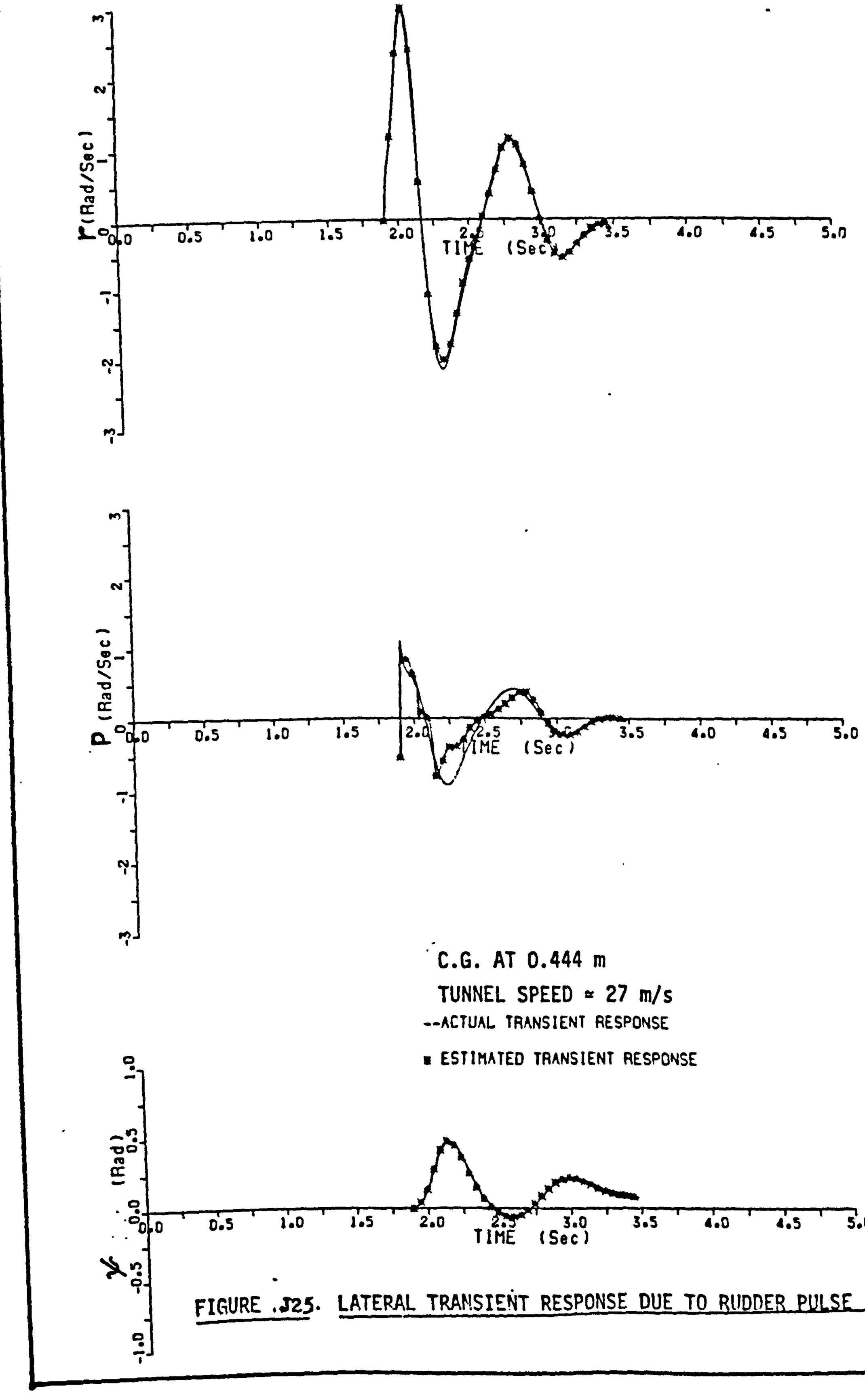

FIGURE .325. LATERAL TRANSIENT RESPONSE DUE TO RUDDER PULSE INPUT

Text cut off in original

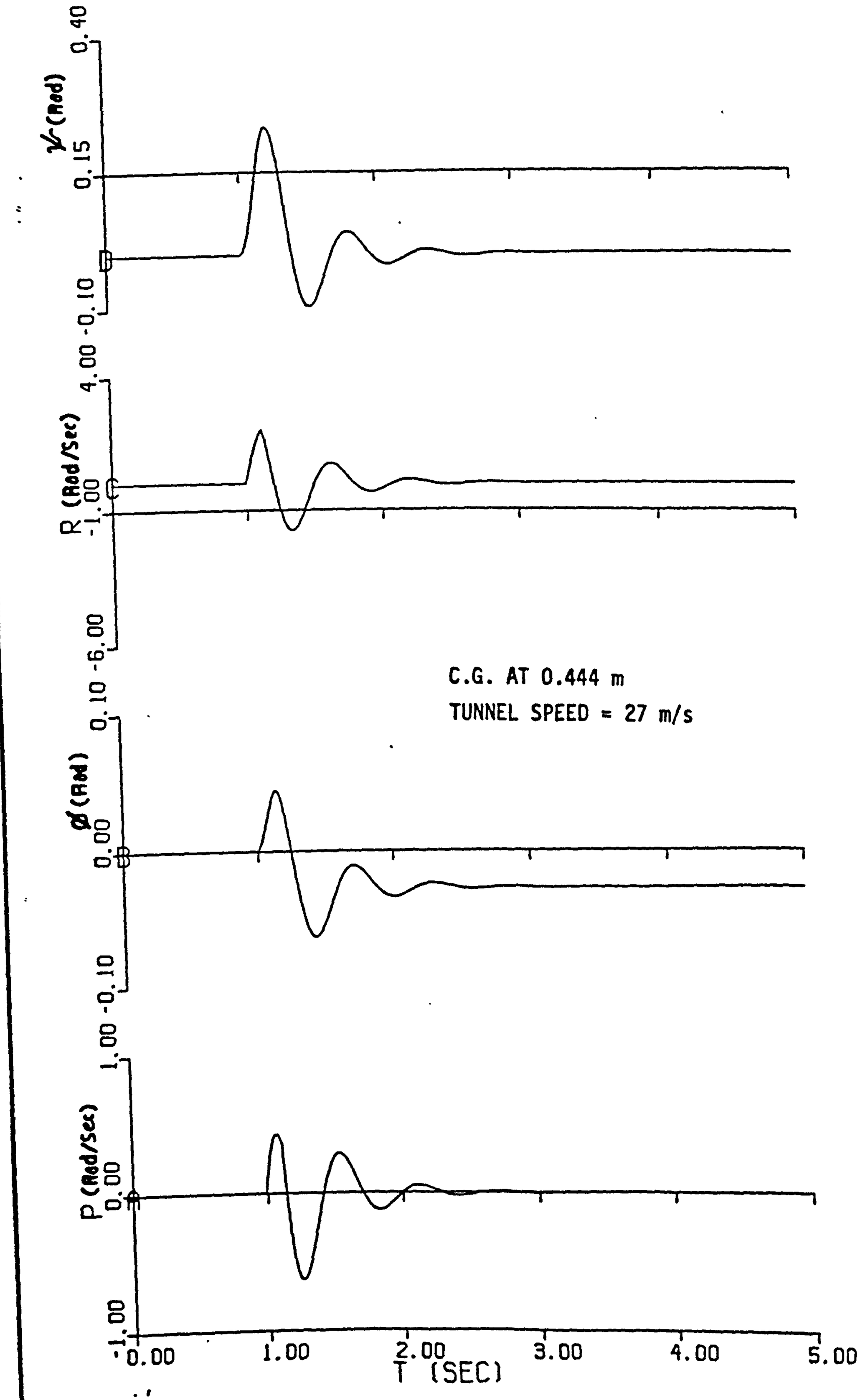

ℓ_v = 1.7
ℓ_p =-12.
ℓ_r = -1.
n_v = 2.0
n_p = 26.
n_r = -9.
ℓ_ζ = -11
n_ζ = -22

C.G. AT 0.444 m
TUNNEL SPEED = 27 m/s

FIGURE J26 SIMULATED LATERAL TRANSIENT RESPONSE USING ESTIMATED DERIVATIVES

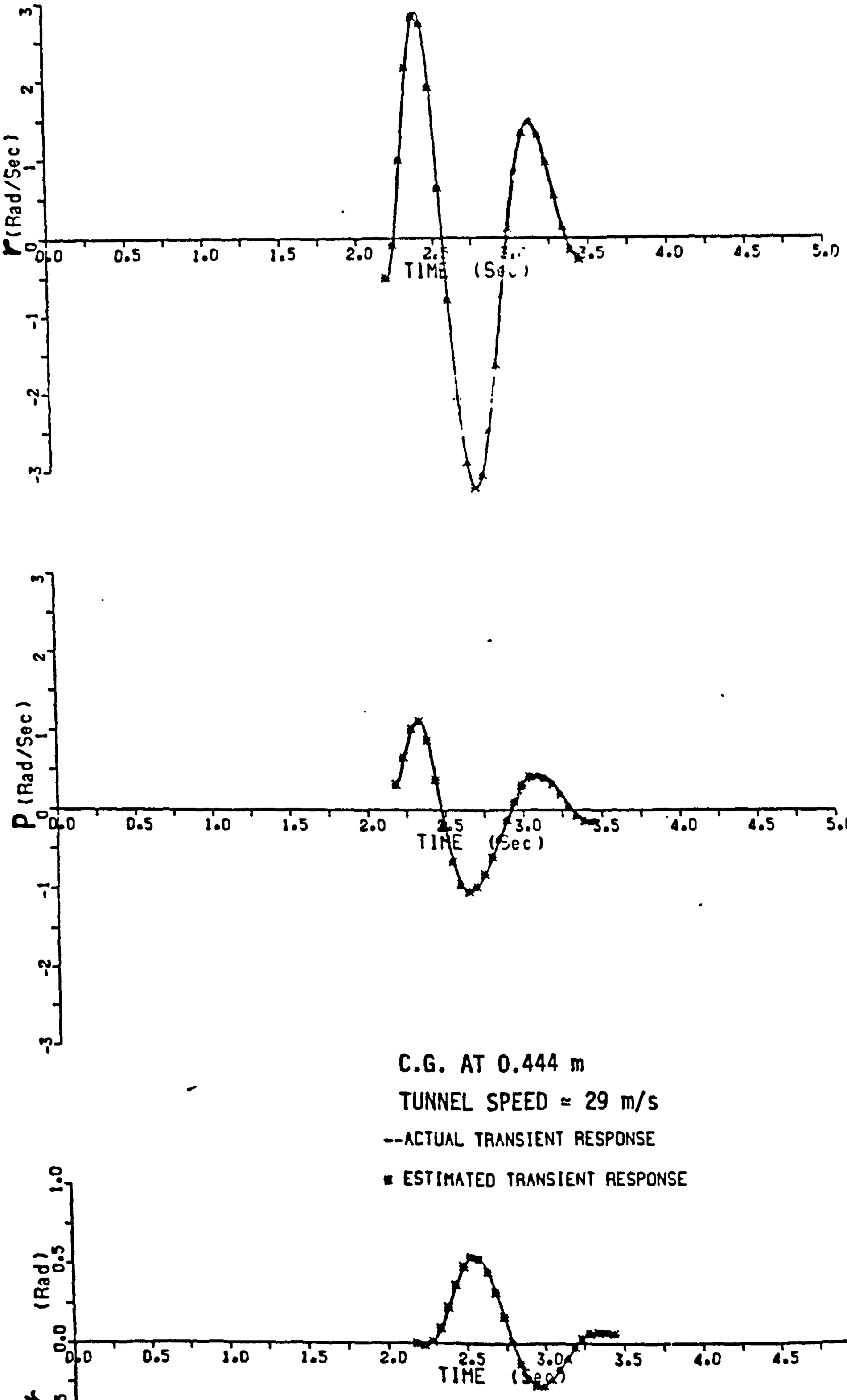

FIGURE 27. LATERAL TRANSIENT RESPONSE DUE TO RUDDER PULSE INPUT

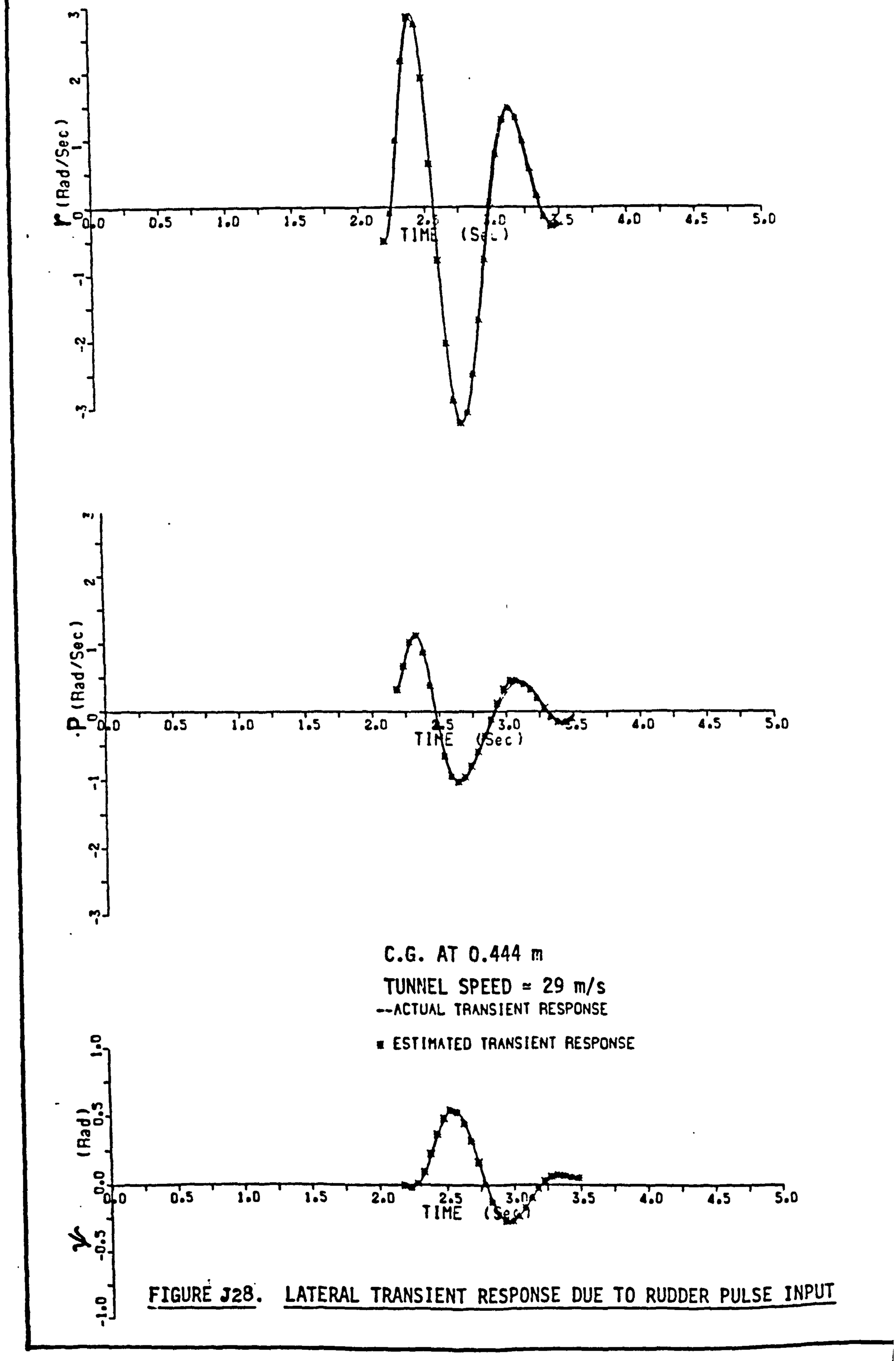

FIGURE J28. LATERAL TRANSIENT RESPONSE DUE TO RUDDER PULSE INPUT

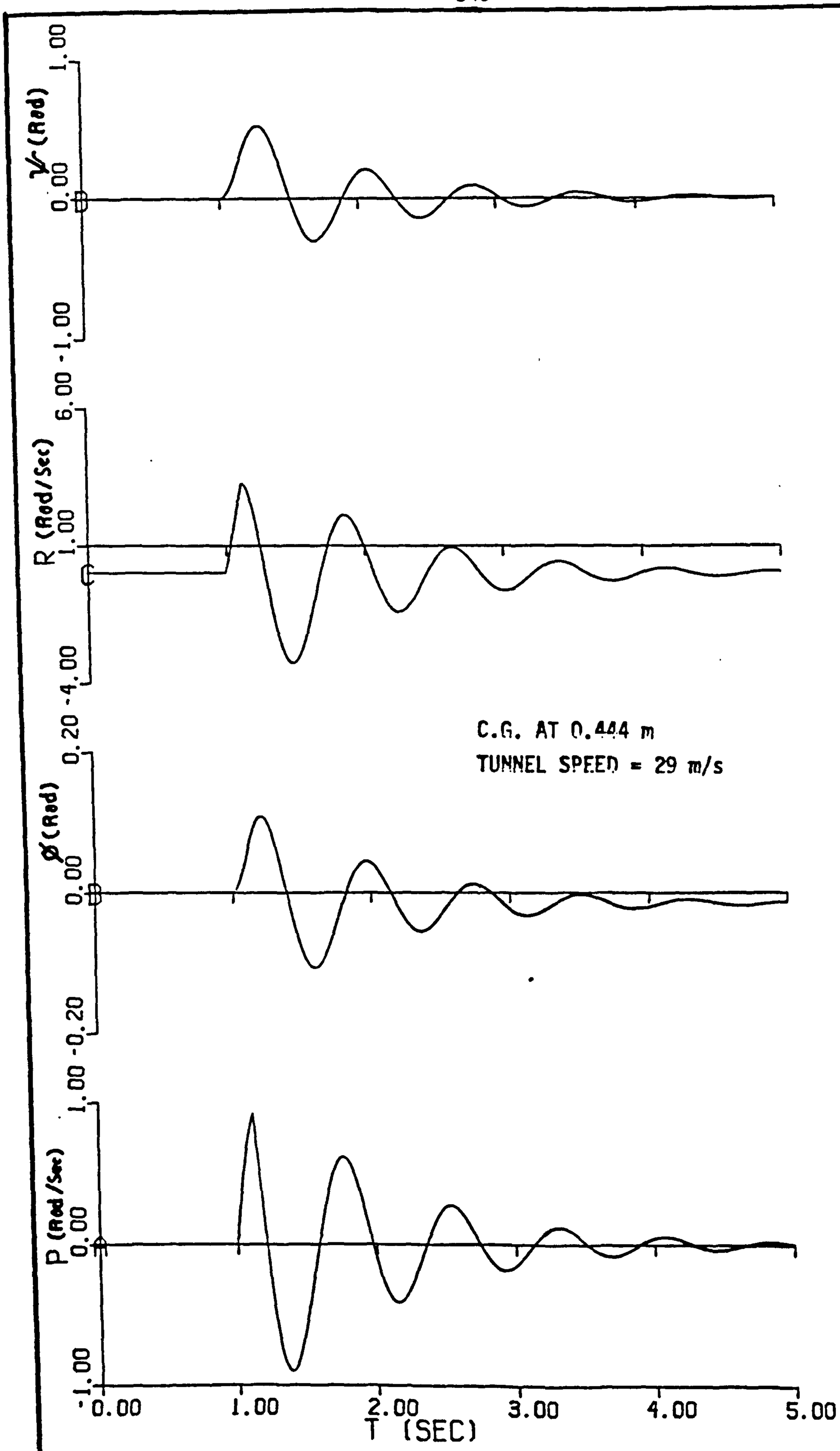

FIGURE J29. SIMULATED LATERAL TRANSIENT RESPONSE USING ESTIMATED DERIVATIVES WITH MODIFIED DATA SO THAT $\phi_{FINAL} = 0^o$

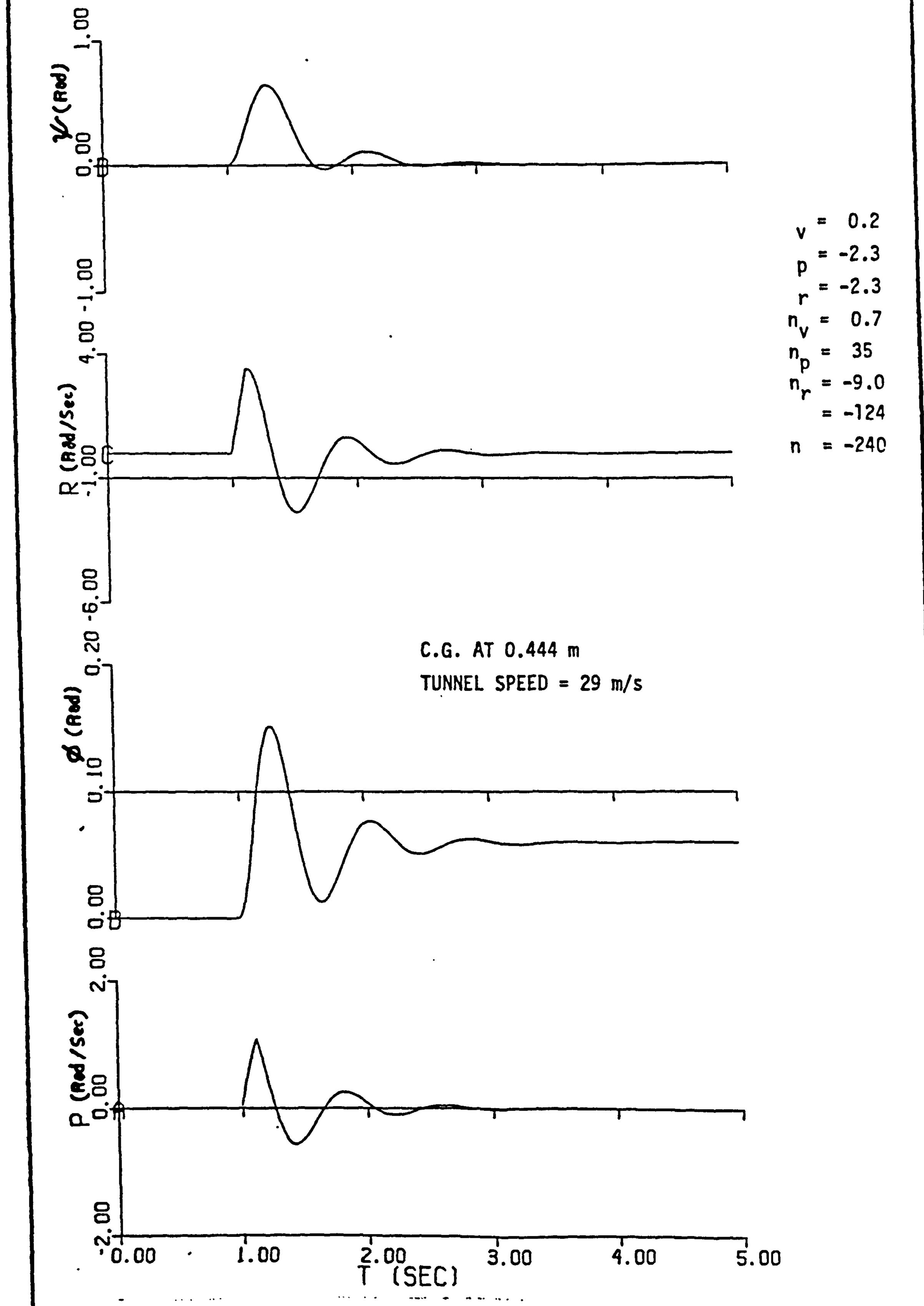

FIGURE J30 SIMULATED LATERAL TRANSIENT RESPONSE USING ESTIMATED DERIVATIVES WITH DATA NOT MODIFIED

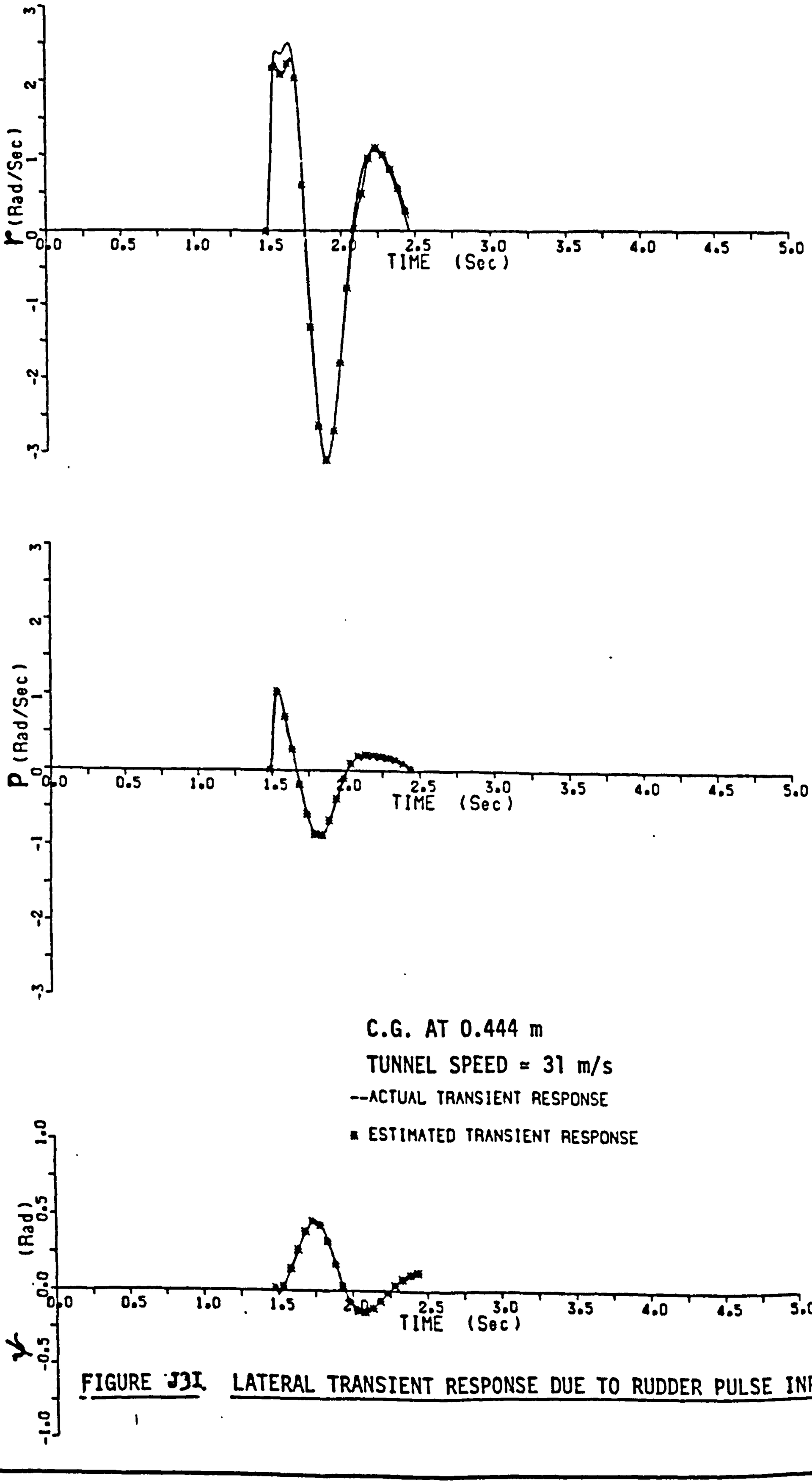

FIGURE J3I LATERAL TRANSIENT RESPONSE DUE TO RUDDER PULSE INPUT

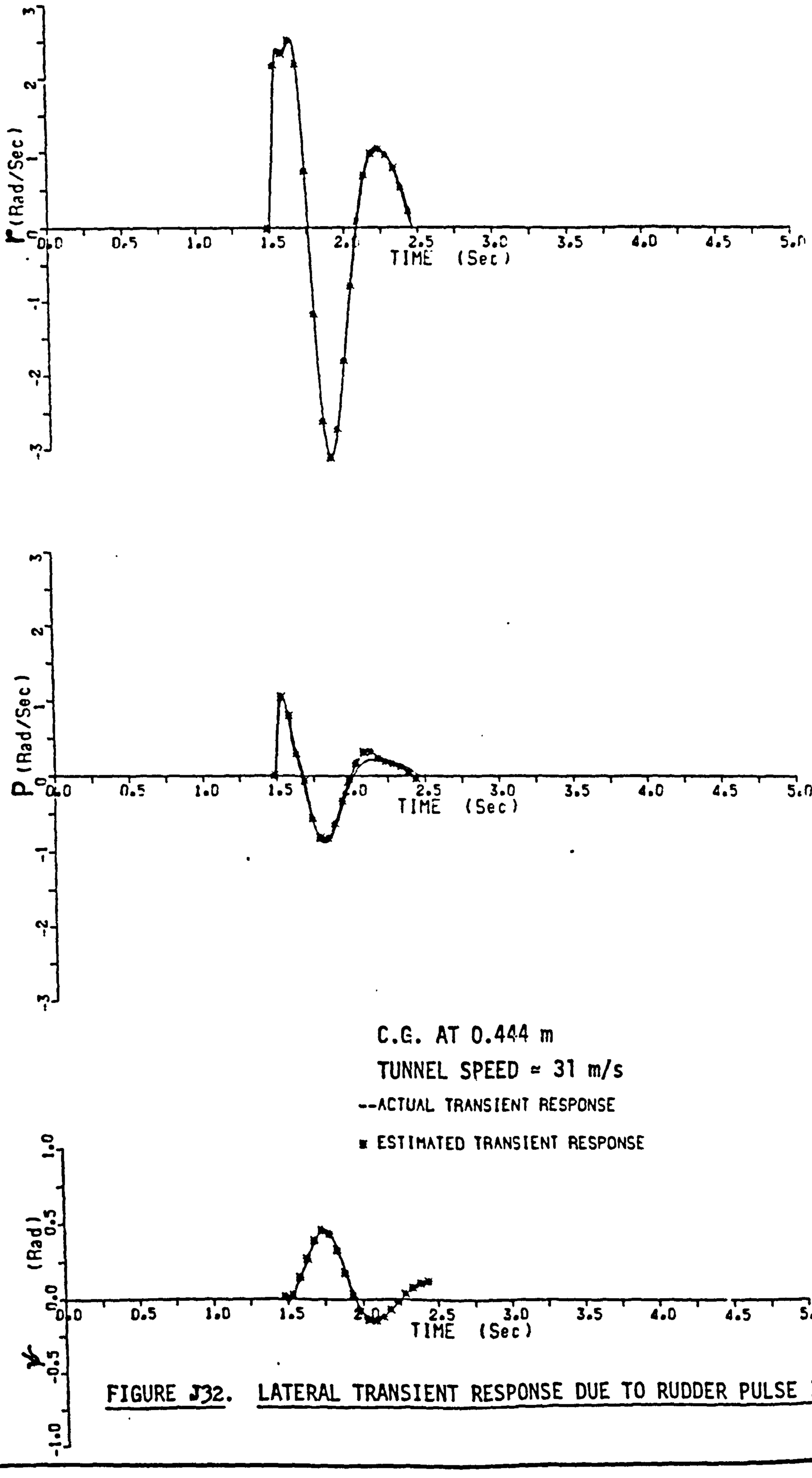

FIGURE J32. LATERAL TRANSIENT RESPONSE DUE TO RUDDER PULSE INPUT

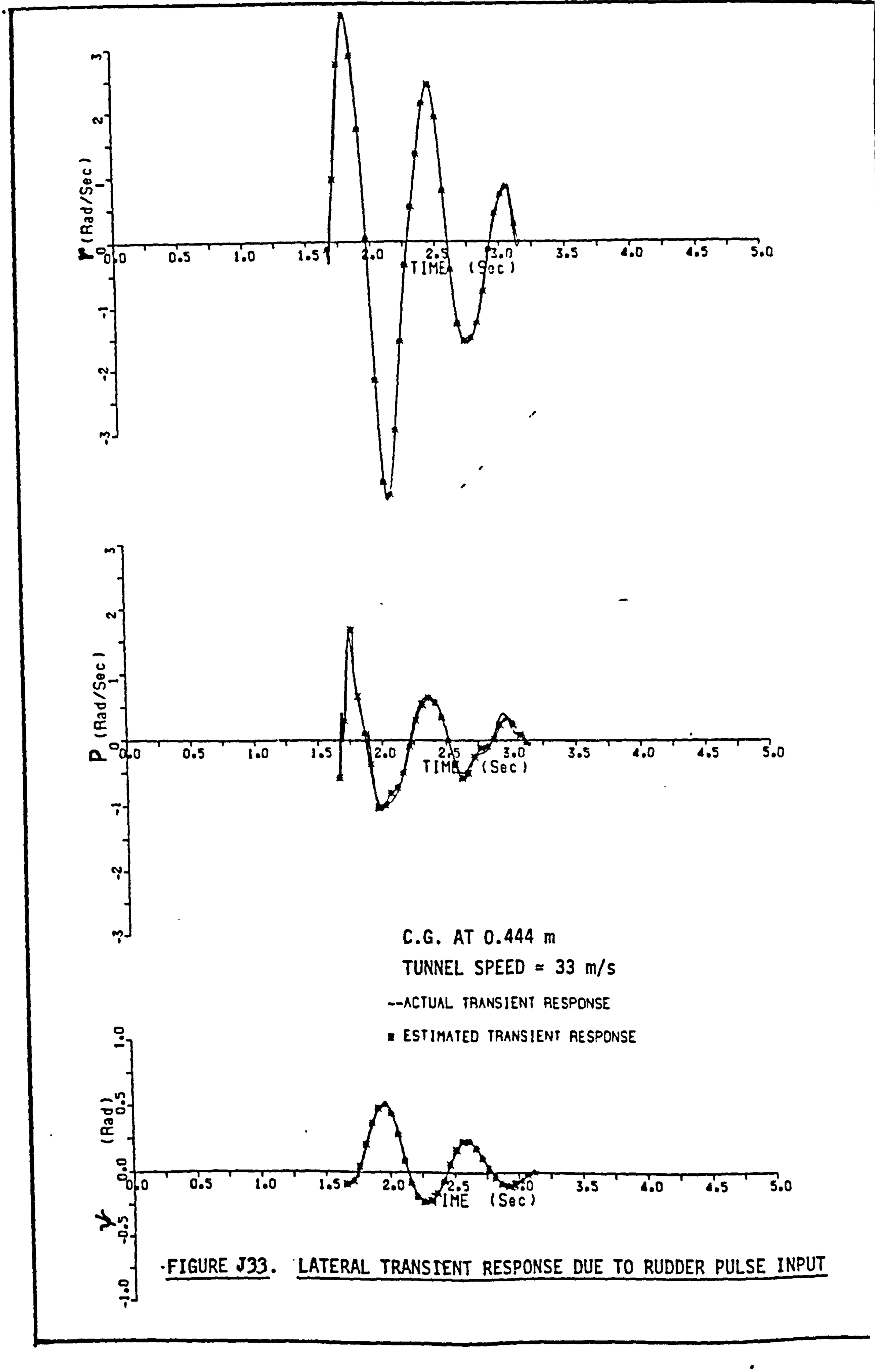

FIGURE J33. LATERAL TRANSIENT RESPONSE DUE TO RUDDER PULSE INPUT

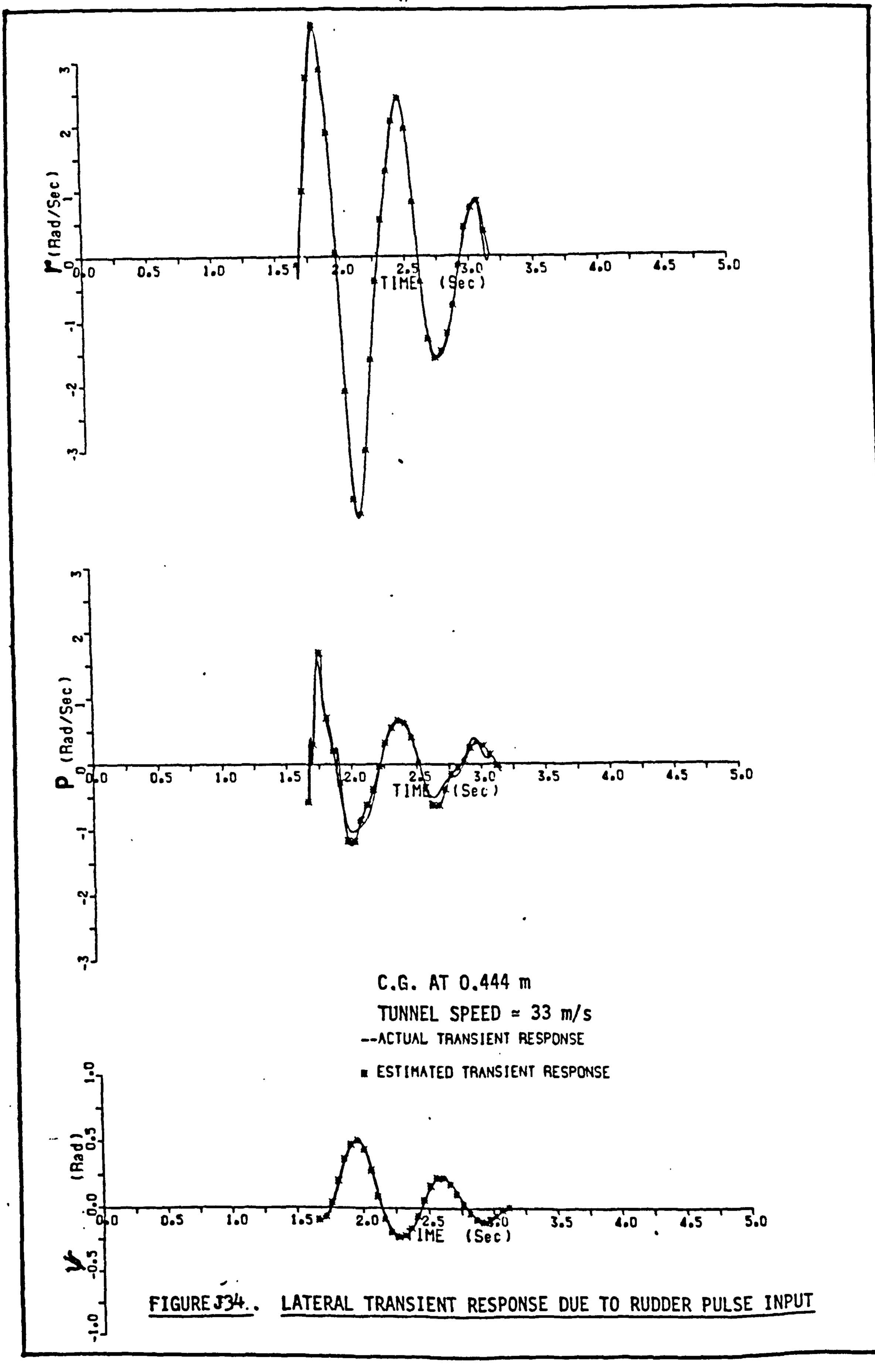

FIGURE 34. LATERAL TRANSIENT RESPONSE DUE TO RUDDER PULSE INPUT

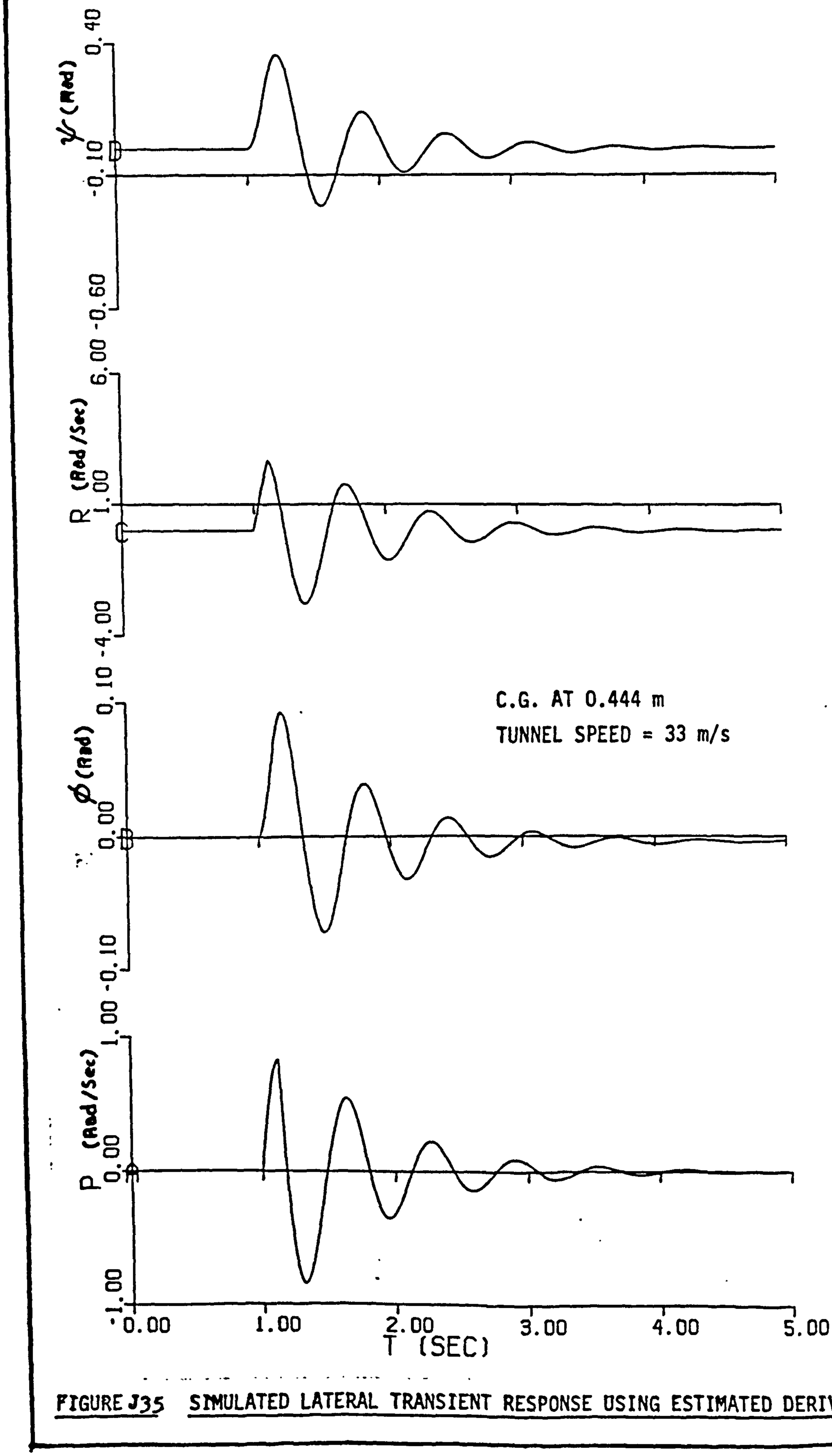

FIGURE J35 SIMULATED LATERAL TRANSIENT RESPONSE USING ESTIMATED DERIVATIVES

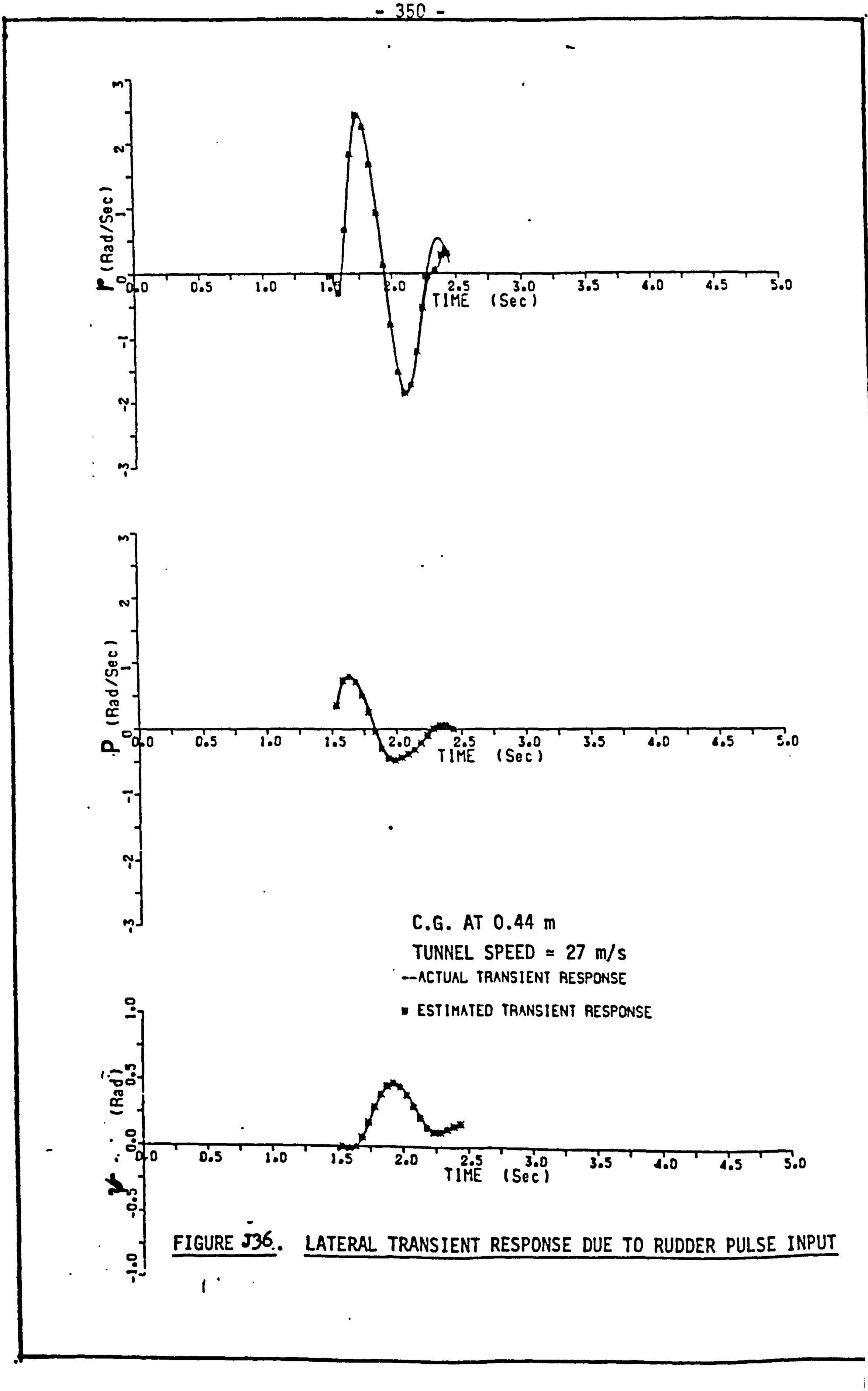

FIGURE 36. LATERAL TRANSIENT RESPONSE DUE TO RUDDER PULSE INPUT

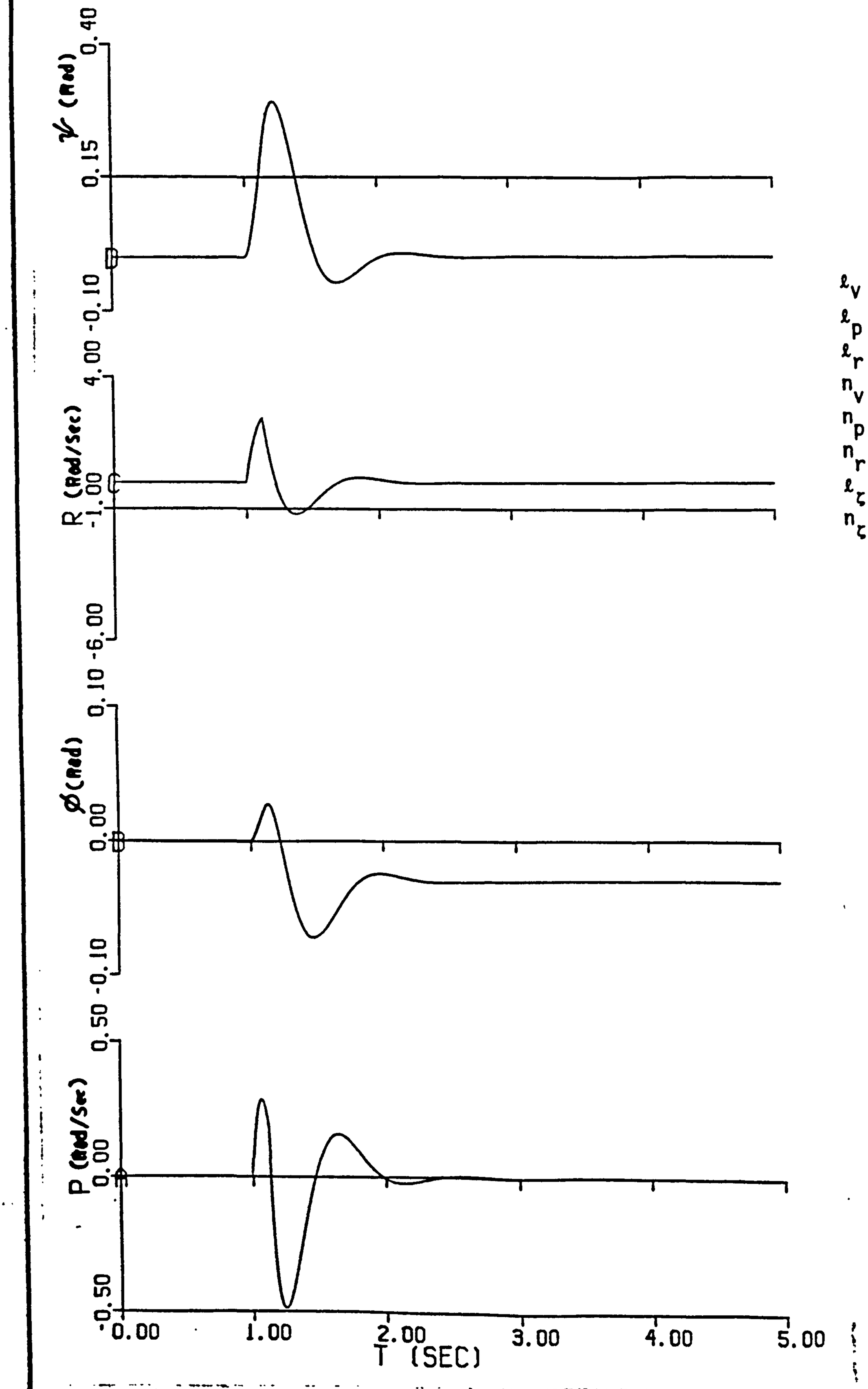

ℓ_v = 0.7
ℓ_p = -8.0
ℓ_r = -3.2
n_v = 2.2
n_p = -2.0
n_r = -8.0
ℓ_ζ = -100
n_ζ = -380

FIGURE 137. SIMULATED LATERAL TRANSIENT RESPONSE USING ESTIMATED DERIVATIVES

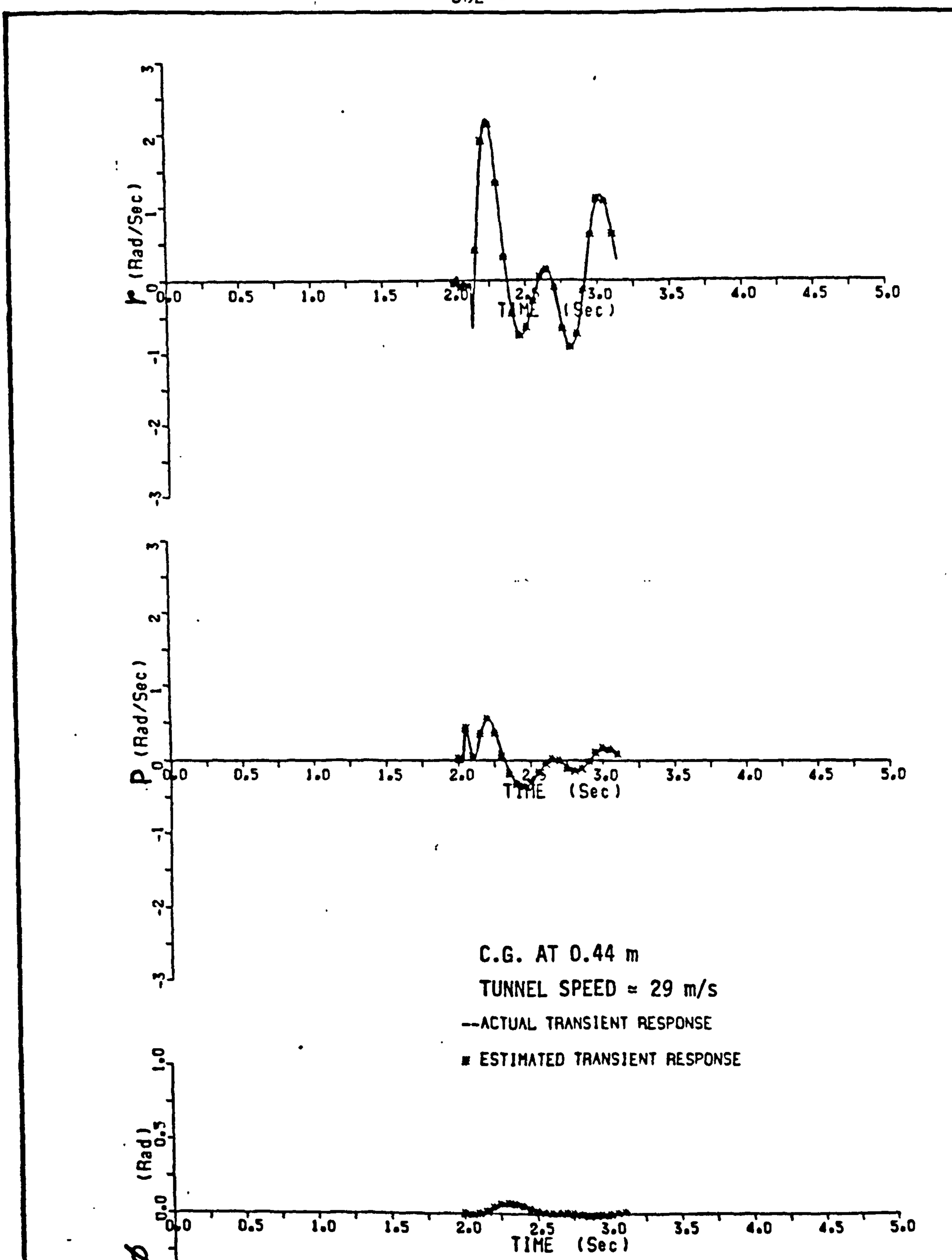

FIGURE 38 LATERAL TRANSIENT RESPONSE DUE TO RUDDER DEFLECTION